# Stony Brook University

# Synthesis and Characterization of Late Transition Metal Complexes as Models for the Active Site of Hydrogenases

A Dissertation Presented

by

**Daniel Amarante**

to

The Graduate School

in Partial Fulfillment of the

Requirements

for the Degree of

**Doctor of Philsophy**

in

**Chemistry**

Stony Brook University

**August 2011**

**Stony Brook University**

The Graduate School

**Daniel Amarante**

We, the dissertation committee for the above candidate for the

Doctor of Philosophy degree, hereby recommend

acceptance of this dissertation.

**Dr. Stephen A. Koch – Dissertation Advisor**
**Professor, Department of Chemistry**

**Dr. Joseph W. Lauher – Chairperson of Defense**
**Professor, Department of Chemistry**

**Dr. Andreas Mayr – Third Member**
**Professor, Department of Chemistry**

**Dr. Elise G. Megehee – Outside Member**
**Associate Professor, Department of Chemistry, St. John's University**

This dissertation is accepted by the Graduate School

Lawrence Martin
Dean of the Graduate School

Abstract of the Dissertation

**Synthesis and Characterization of Late Transition Metal Complexes as Models for the Active Site of Hydrogenases**

by

**Daniel Amarante**

**Doctor of Philosophy**

in

**Chemistry**

Stony Brook University

**2011**

Researchers have turned to biological systems that utilized hydrogen in order to develop new catalysts that do not require platinum. In nature, hydrogen is oxidized or reduced with certain efficiency by using metalloenzymes called hydrogenases. Currently there are three types of hydrogenases: [NiFe], [FeFe], and [Fe]–hydrogenase. These hydrogenases have shown unusual structures, such as having carbonyl and cyanide ligands bound to the active site.

The synthesis of the potentially tridentate ligands, *bis*–(2–thiophenyl)phenylphosphine ($H_2$PS2) and *bis*–(2–thiobenzyl)benzylamine ($H_2$NS2), has been optimized. These ligands contain the rich sulfur environment that is found in the metalloenzyme and have shown prior success in making stable metal complexes in various oxidation states. Metal complexes of ruthenium and osmium containing these ligands were successfully synthesized and characterized.

The discovery of $[Fe(CN)_x(CO)_y]$ units in hydrogenase enzymes has prompted the study of iron–cyanide–carbonyl compounds. Recently, compounds of the general structure $[Fe^{II,III}(CN)_4L_2]^{2-,1-}$, where L = DMSO, CO, pyridine, were synthesized for the first time. This prompted studies of related compounds of the congener elements of iron, specifically using ruthenium and osmium. These studies have produced the first compounds of ruthenium with the general structure, $[Ru^{II}(CN)_4L_2]^{2-}$ where L = CO and pyridine.

Iron carbonyl complexes with the $H_2PS2$ ligand have been previously used to mimic the iron centers in hydrogenase enzymes. To expand on these studies, ruthenium was used to replace iron in the general structure $[M^{II}(CO)_3(PS2)]$. Studies show that the monomer loses carbonyls producing a trimer, $[Ru^{II}{}_3(CO)_5(PS2')_3]$. Various compounds were also synthesized using $Li_2NS2$ in place of $Li_2PS2$.

The synthesis of analogs for the binuclear [NiFe] and [FeFe] hydrogenase active sites has been sought for some time. Only a few such compounds had been previously characterized. Using $[Fe^{II}(CN)_2(CO)_3I]^-$ as a starting compound, the synthesis of a binuclear compound, $[Fe^{II}(CN)_2(CO)_2Ni^{II}(S4)]$ (S4 is 3,7–dithianoane–1,9–dithiolate). The X–ray structure of this compound reproduces certain aspect of the active site of [NiFe] hydrogenase enzymes.

Characterization of synthesized compounds was done using single crystal X–ray crystallography, infrared spectroscopy, NMR and electrochemistry.

## Table of Contents

## List of Figures

## List of Tables

## List of Abbreviations

| | |
|---|---|
| dppe | 1,2–*bis*–(diphenylphosphino)ethane |
| *n*–PrOH | 1–propanol |
| tmbt | 2,3,5,6–tetramethylbenzenethiolate |
| Stip | 2,4,6–triisopropylbenzenethiolate |
| CN–dmph | 2,6–dimethylphenylisocyanide |
| *i*–PrOH | 2–propanol or isopropanol |
| $H_2O2S2$ | 3,7–dithianoane–1,9–diol |
| $H_2S4$ | 3,7–dithianoane–1,9–dithiol |
| $CH_3CN$ | acetonitrile |
| A | amp |
| Å | angstrom |
| *aq* | aqueous |
| $[PPN]^+$ | *bis*–(triphenylphosphine)iminium cation |
| NBr2' | *bis*–[2–bromobenzyl]4–methylbenzylamine |
| NBr2 | *bis*–[2–bromobenzyl]benzylamine |
| $Li_2NS2'$ | litho–(*bis*–[2–thiobenzyl]4–methylbenzylamine) |
| $Li_2NS2$ | litho–(*bis*–[2–thiobenzyl]benzylamine) |
| $H_2POS2$ | *bis*–[2–thiophenyl]oxophenylphosphine |
| $H_2PS2$ | *bis*–[2–thiophenyl]phenylphosphine |
| $H_2PS2'$ | *bis*–[5–methyl–2–thiophenyl]phenylphosphine |
| $CaH_2$ | calcium hydride |
| CO | carbonyl |
| cm | centimeter |
| $CN^-$ | cyanide |
| CV | cyclic voltammetry |
| $^o$ | degree |
| $CDCl_3$ | deuterated chloroform |
| DMSO–$d_6$ | deuterated dimethylsulfoxide |

| | |
|---|---|
| $P_2O_5$ | diphosphorous pentoxide |
| d | doublet |
| ddd | doublet of doublet of doublets |
| dd | doublet of doublets |
| $S_8$ | elemental sulfur |
| EtOH | ethanol |
| *fac* | facial |
| g | gram |
| IR | infrared |
| kV | kilovolt |
| L | ligand |
| $Li_3$NSe3 | litho–(*tris*–[2–selenobenzyl]amine) |
| $Li_3$NS3 | litho–(*tris*–[2–thiobenzyl]amine) |
| MHz | megahertz |
| *mer* | meridial |
| MeOH | methanol |
| mA | milliamp |
| mL | milliliter |
| mM | millimolar |
| mmol | millimole |
| M | molar |
| mol | mole |
| m | multiplet |
| DMF | *N*,*N*–dimethylmethanamide |
| nm | nanometer |
| *n*–BuLi | *n*–butyllithium |
| ndt | norbornanedithiolate |
| NMR | nuclear magnetic resonance |
| *o*–xyl | *o*–xylene–*α*,*α*'–dithiolate |
| ppm | parts per million |
| $K_2CO_3$ | potassium carbonate |

| | |
|---|---|
| py | pyridine |
| R.T. | room temperature |
| sh | shoulder |
| s | singlet |
| $Na_2SO_4$ | sodium sulfate |
| $H_2SO_4$ | sulfuric acid |
| $[Bu_4N]^+$ | tetrabutylammonium cation |
| $TBABF_4$ | tetrabutylammonium tetrafluoroborate |
| $[Et4N]^+$ | tetraethylammonium cation |
| THF | tetrahydrofuran |
| TMEDA | *N, N, N′,N′*–tetramethylethylenediamine |
| TMS | tetramethylsilane |
| $[PPh_4]^+$ | tetraphenylphosphonium cation |
| $[n–Pr_4N]^+$ | tetrapropylammonium cation |
| $[Me_3NBz]^+$ | trimethylbenzylammonium cation |
| t | triplet |
| td | triplet of doublets |
| NBr3 | *tris*–[2–bromobenzyl]amine |
| $H_3PS3$ | *tris*–[2–thiophenyl]phosphine |
| $H_3PS3'$ | *tris*–[5–methyl–2–thiophenyl]phosphine |
| UV–Vis | Ultraviolet–visible |
| V | volt |

**Acknowledgments**

I would like to thank my advisor Dr. Stephen A. Koch for his guidance and support throughout my years at Stony Brook University. Thank you for sharing your knowledge and expertise with me. I would like to give a special and warm thanks to the late Dr. Michelle Millar, not only for acting as a second research advisor but, for making chemistry fun and exciting as well as making the research group feel like a family. Your love and determination toward chemistry will live on forever through all the people you have touched, again thank you Dr. Millar.

I would like to thank my Ph.D. committee members, Dr. Joseph W. Lauher, Dr. Andreas Mayr and Dr. Elise G. Megehee. Thank you Dr. Lauher for helping and guiding me when using the X–ray diffractometers (Bruker and Oxford) and for being the chairperson of my committee. Thank you Dr. Mayr for helping and guiding me all these years and for being the third member of my committee. Thank you Dr. Megehee for introducing me to the world of research, for all the years at St. John's University and helping me throughout my Ph.D.

I would like to thank all the people from the Koch and Millar groups: Dr. Lu Gan, Su'aad Zaman, Soumya Bhattacharya, David Spritzer, Anthony Pesiri, Jason Ng and Eric Rus. I would also like to thank the people from other research groups: Dr. Ruchi Gupta, Trisha Barua, Dr. Joseph Kaloko, Dr. Stephen Chaterpaul, Dr. Nick Getter, Shawn Fisher, Natalie St. Fleur and Perry Woo. Thank you for your advice, your help and especially your friendship.

I would like to thank the chemistry main office staff. Especially Katherine Hughes, who always went beyond the call of duty to ensure that I have everything completed for my graduation. I would like to thank Liz Perez for our discussions about life. I would like to thank Charmine Yapchin for helping me order the liquid nitrogen for the X–ray diffractometer.

I am thankful for the love and support that I have from my family. My parents, Maritza and Genaro, have always been there for me with endless love, encouragement and advice. I would like to thank my sisters, Krystle, Priscilla and Ivette, for their love, understanding and support. I would like to thank my nieces, Annamarie, Angelina, Isabella and Karla for their love. I want to give a very special thanks to my grandparents, Italia (Wala) and Cipriano (Papito) Guzman, who have always been there for me and shown me so much love and how to love

others. Thank you Papito for starting me on the road toward science and thank you Wala for helping me become the person I am today. Your love and memory will always be a part of me. Finally, I would like to thank my wonderful wife, Sarswati Ramoutar, for her unconditional love, support, understanding and patience.

Once again, I would like to say thank you to my wife, family and friends for always being there for me when I needed you. Your love and support have been more than I could ever ask for, God has truly blessed me.

# CHAPTER 1. Hydrogenase: An Introduction

## 1.1 Metalloproteins and Metalloenzymes: An Overview

Metalloproteins, by definition, are proteins that contain transition metals which are involved in a wide range of biological processes. For this reason, many chemists and other scientists are determined to understand the mechanisms and the roles of these enzymes.

One function that is uniquely performed by metalloproteins is respiration, dioxygen transport. There are three known classes of this metalloproteins: hemoglobin–myoglobin, hemocyanins, and hemerythrins. These metalloproteins are illustrated in **Figure I–1**. In these metalloproteins, dioxygen molecules binds to either iron (hemoglobin or hemerythrin) or copper (hemocyanin) center without undergoing an irreversible electron transfer reaction, which results to dioxygen bond cleavage. In the case of hemoglobin and myoglobin, the dioxygen binding site in an iron porphyrin complex that undergoes a structural change upon dioxygen binding. This triggers subtle movement of the protein chains which results in the uptake of dioxygen.

In hemocyanin, which is found in mollusks and arthropods, dioxygen binds between two copper atoms. In this case, the dioxygen binding reaction results in an oxidative addition to the reduced, deoxy, form of the dimetallic center that generates a peroxide derivative of the oxidized, oxy, form. The chemical strategies that are performed in all three reactions are quite similar. Nature uses different transition metals in different organisms to carry out similar functions.

Another function that involves metalloproteins is electron transfer reactions. These proteins, which are involved in a net electron transfer, undergo redox transformations without catalyzing an overall chemical change in the substrate. Such carriers usually pass their electrons to or from enzymes that require redox chemistry in order to perform a specific task. Two examples of these electron transfer metalloproteins are iron–sulfur clusters and cytochromes, which are illustrated in **Figure I–2**.

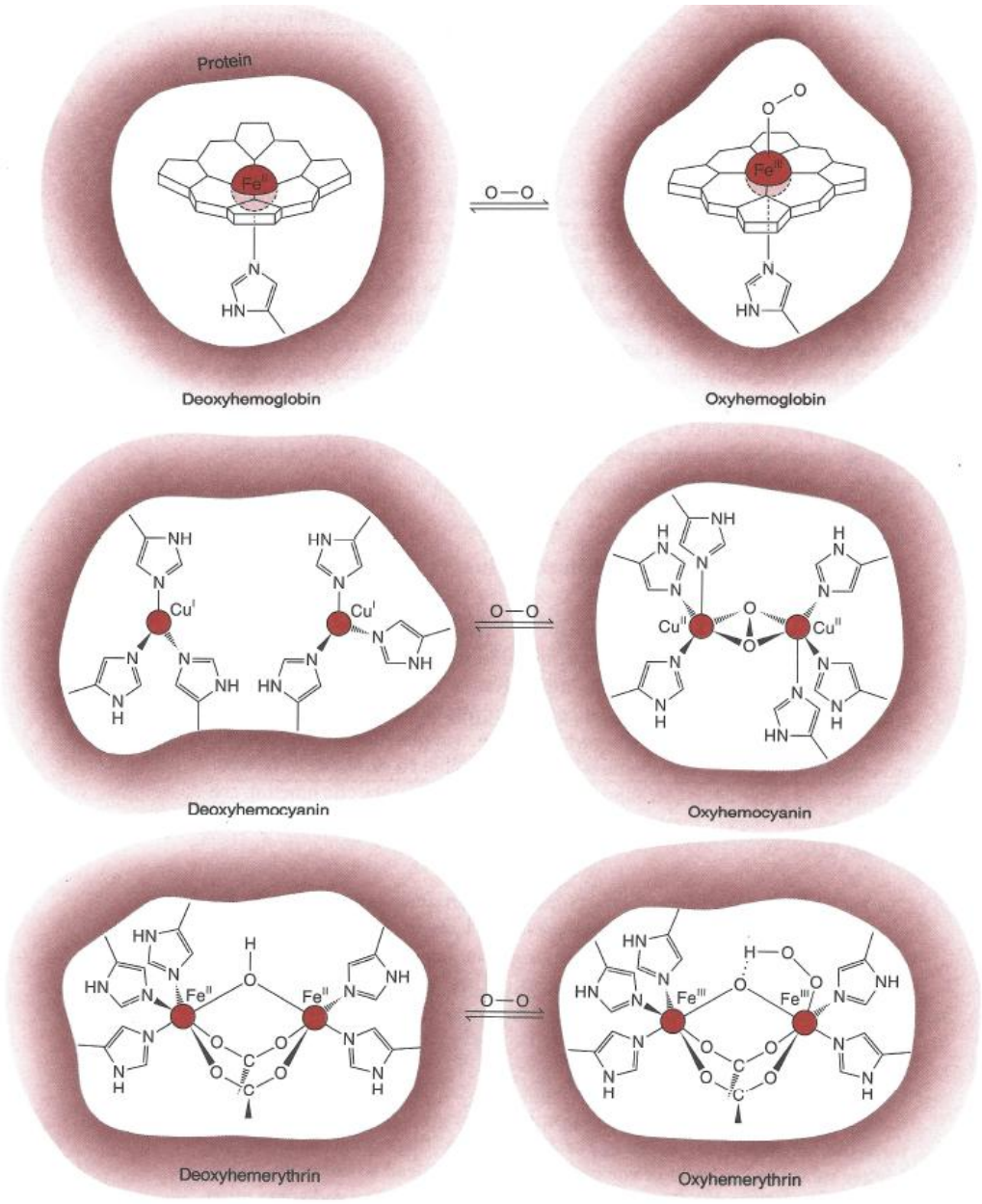


**Figure I–1. Examples of different types of metalloenzymes.**[1]

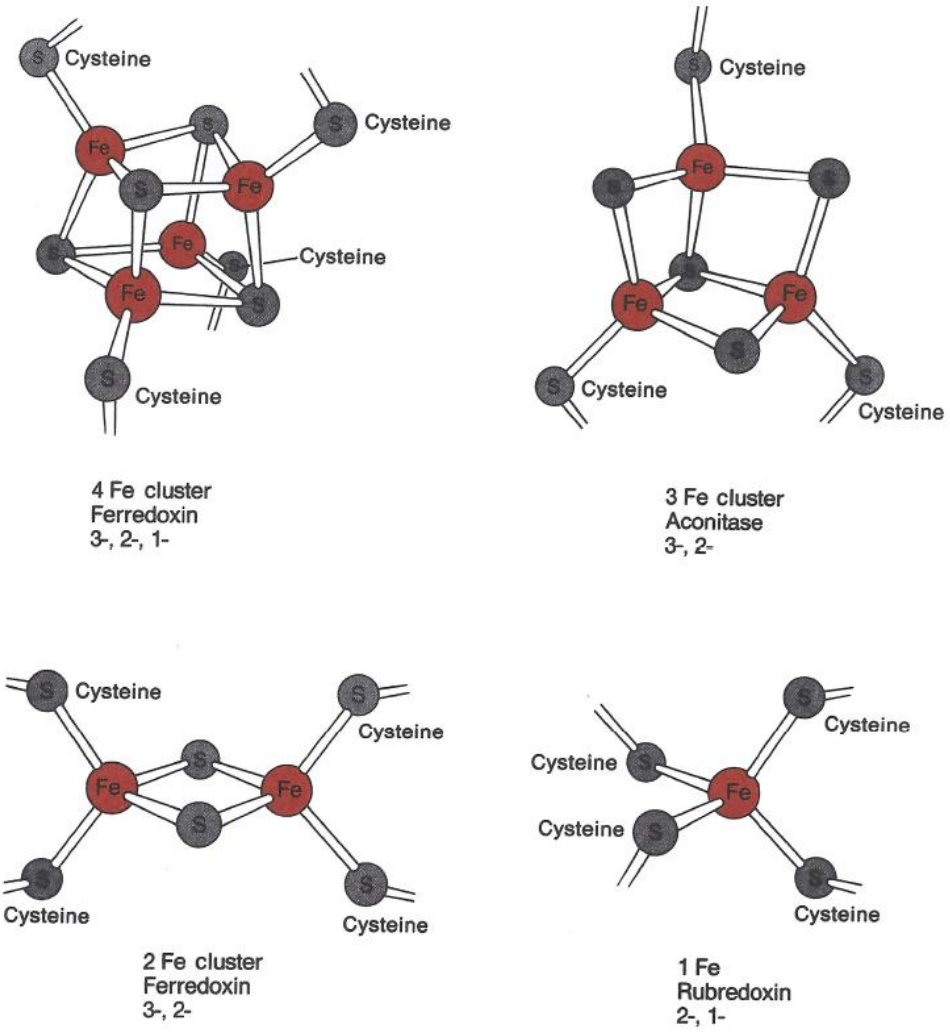


**Figure I–2. Examples of different classes of Fe–S clusters.**[1]

Metalloenzymes are a subclass of metalloproteins, which perform specific catalytic functions. **Table I–1** summarizes some of the reactions catalyzed by metalloenzymes. Metalloenzymes are grouped depending on the functions they perform. Some of these functions can be performed by more than one metalloenzyme. This type of diversity cannot be explained and is shrouded by nature itself.

| Table I–1. Selected Metalloenzyme Functions.[1] | | |
|---|---|---|
| **Function** | **Enzyme** | **Reaction** |
| Hydrolytic enzymes | Carboxypeptidase | Removes terminal amino acids from proteins |
| | Carbonic anhydrase | $H_2O + CO_2 \rightarrow H^+ + HCO_3^-$ |
| Protective Metalloenzymes | Superoxide dismutase | $2O_2^- + 2H^+ \rightarrow H_2O_2 + O_2$ |
| Dehydrogenases | Liver alcohol dehydrogenase | $CH_3CH_2OH + NAD^+ \rightarrow CH_3CHO + NADH + H^+$ |
| Nitrogen fixation | Nitrogenase | $N_2 + 8e^- + 8H^+ \rightarrow 2NH_3 + H_2$ |
| Photosynthesis | Photosystem II | $2H_2O \rightarrow O_2 + 4H^+ + 4e^-$ |

There are several metalloenzymes that catalyze reactions which involve either oxidation or reduction of the substrate. Unlike the metalloproteins that function as electron transport, these metalloenzymes generally function as two–electron redox components. One example of these processes is the oxidation of hydrocarbons to alcohols, which is catalyzed by the iron–porphyrin center in cytochrome P–450.

Dehydrogenation is another class of a two–electron redox process. Within the substrate there is a loss of dihydrogen when the removal of two electrons and two protons has been achieved. Some enzymes can generate or consume dihydrogen. This class of metalloenzymes is called hydrogenase, which contains iron–sulfur clusters, and, depending on the class of hydrogenase, nickel.

## 1.2 Hydrogenases and Hydrogen fuel

Currently, the energy infrastructure is dominated by fossil fuel production and combustion. This is causing massive emission of greenhouse gases, which are harming the planet. Hydrogen is often suggested as alternative fuel, sometimes called as the "fuel of the future." This statement has been mentioned for at least a generation, usually with greater seriousness during high petroleum prices. Since hydrogen is derived from fuels, such as methane, it cannot be viewed as a fuel. It is more correct to call hydrogen an energy currency.[2]

Several fundamental problems need to be solved in order to make hydrogen a reliable source of energy. The realization of these possibilities depends upon significant progress in hydrogen generation, storage, transportation and utilization. It is critical to develop new ways of generating hydrogen that do not use hydrocarbons.

The technology to utilized hydrogen is highly advanced, however it is the scaling up that remains an issue. Hydrogen fuel cells have been designed and used, but because of the high cost and limited availability of platinum group metals, this technology has not widespread to the retail market.[3]

Recent studies by the Department of Energy and Stanford University (**Figure I–3**) shows the different type of fuels used today and compares the specific energies and carbon dioxide emissions.[4] From this study, this shows that hydrogen has the most specific energy out of all the other types of fuels, which is extremely valuable from the point of power usage. However, hydrogen has the lowest energy density, which is insufficient from the point–of–view of using this fuel in a car for example. The most important aspect of this study is the amount of carbon dioxide emissions that are released by these fuels. Hydrogen, of course, has no carbon dioxide emissions, which is a positive result due to current global energy and pollution problems. Research has been on going in order to use this type of fuel in our technological world.

Specific Energy, Energy Density & CO2

| Fuel | Specific Energy kj/g | Density KWH/gal | Chemical Formula | lbs CO2/gal |
|---|---|---|---|---|
| Propane | 50.4 | 26.8 | C3H8 | 13 |
| Ethanol | 29.7 | 24.7 | C2H5OH | 13 |
| Gasoline | 46.5 | 36.6 | C7H16 | 20 |
| Diesel | 45.8 | 40.6 | C12H26 | 22 |
| Biodiesel | 39.6 | 35.0 | C18H32O2 | 19 |
| Methane | 55.8 | 27.0 | CH4 | 3 |
| Oil | 47.9 | 40.5 | C14H30 | 20 |
| Wood | 14.9 | 11.3 | approx weight | 9 |
| Coal | 30.2 | 22.9 | approx weight | 19 |
| Hydrogen | 141.9 | 10.1 | H2 | 0 |

Source: DOE, Stanford University, College of the Desert, & Green Econometrics research

**Figure I–3. Comparison of fuels and their specific energies.**

Scientists have turned to biological systems that utilized hydrogen in order to develop new catalysts that do not require platinum group metals. In nature, hydrogen is consumed or produced with certain efficiency by hydrogenase enzymes. These enzymes are characterized as metalloenzymes which contain iron and/or nickel core. The general reaction of dihydrogen consumption and production is indicated in **Scheme I–1**.

$$H_2 \rightleftharpoons 2H^+ + 2e^-$$

**Scheme I–1. Redox reaction of $H_2$.**

In 1931, this enzymatic activity was first reported with the discovery of *Escherichia coli* evolves hydrogen under certain conditions.[3] Hydrogenase has been found in various different microorganisms, from prokaryotic microbes to eukaryotic protozoa and fungi.[5] Depending on the conditions, these hydrogenase enzymes can catalyze the uptake and production of hydrogen.

These enzymes are separated into three main groups (**Figure I–4**)[6] which is [NiFe]–hydrogenases, [FeFe]–hydrogenase and [Fe]–hydrogenase.

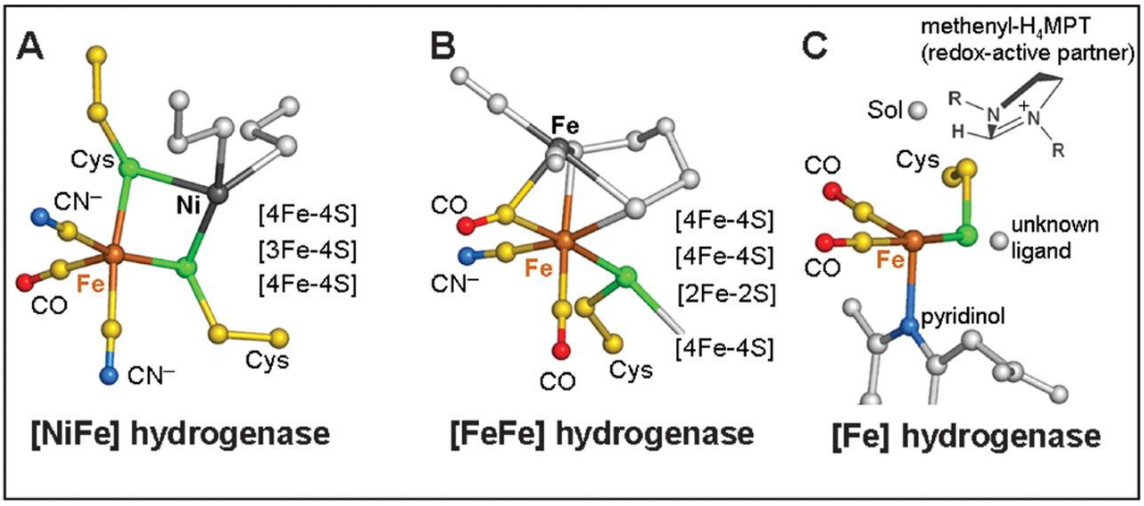


**Figure I–4. The different classes of Hydrogenases. (A) [NiFe]–hydrogenase from *Desulfovibrio gigas*; (B) [FeFe]–hydrogenase from *Clostridium pasteurianium* and *Desulfovibrio desulfuricans*. (C) [Fe]–hydrogenase from *Methanocaldococcus jannaschii*.**

## 1.3 [NiFe]–Hydrogenases

### 1.3.1 Structure and Mechanisms of [NiFe]–Hydrogenases

It has long been thought that the nickel center in the [NiFe]–hydrogenase was the active site for the activation of hydrogen. These lead scientists to discover that dihydrogen adducts of various transition metals can propose the intermediacy of a nickel dihydrogen complex in hydrogen activation by the enzyme.[7] With a large emphasis on the nickel site, scientists synthesized various nickel complexes for the electrocatalytic reduction of protons to dihydrogen.[8]

In 1995, the crystal structure of *Desulfovibrio gigas* (**Figure I–5**)[8], a [NiFe] hydrogenase, was discovered. The crystallographic studies showed the active site of the enzyme to contain one nickel and one iron atom.[8–9] The coordination sphere of the iron atom includes three diatomic ligands, which could not be properly be identified by crystallography. Infrared studies combined with isotopic labeling has been used to concluded that there are two cyanide and one carbon monoxide ligands bound to the iron atom. Two bridging thiolate groups, from the cysteine residues, complete the iron coordination sphere. It has been proposed that the bridging species could be a $\mu$–oxo, sulfide, hydroxo, peroxide or sulfoxide group.[10–12]

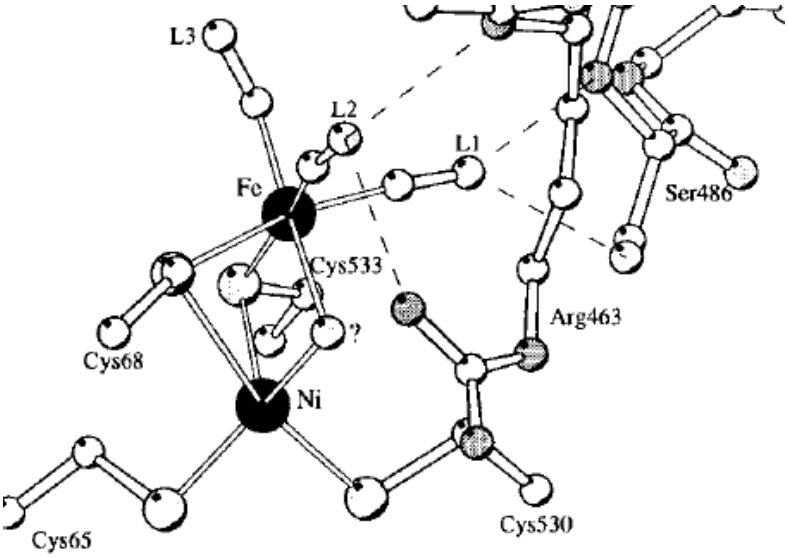


**Figure I–5. X–ray structure of [NiFe]–hydrogenase from *Desulfovibrio gigas*.**

It was determined that the iron center remains at oxidation state 2+ in a low spin (S = 0) diamagnetic system in the inactive (Ni–A) and active (Ni–B) forms of the enzyme.[8] Besides Ni–A and Ni–B forms, researchers have used crystallographic studies, which reported the Ni–C, Ni–CO, and Ni–R structures and proposed the potential proton and gas channel pathways.[13–15]

There are three structural units that are composed within the [NiFe]–hydrogenase active site.[16] The first unit is the {Ni(μ–S–Cys)$_2$Fe} arrangement, which is formed by the bridging cysteine ligands. This orientation has sometimes been referred as the "butterfly" arrangement. The second unit is the distorted square–planar arrangement, which is composed of the four cysteine ligands that are bound to the nickel center. The last unit is the {Fe(CN)$_2$(CO)} motif. The bond distance between the dinuclear center of the active site ranges from 2.9 Å to approximately 2.5 Å for the inactive forms Ni–A, Ni–B and the reduced active form Ni–SI respectively.[10,13–15]

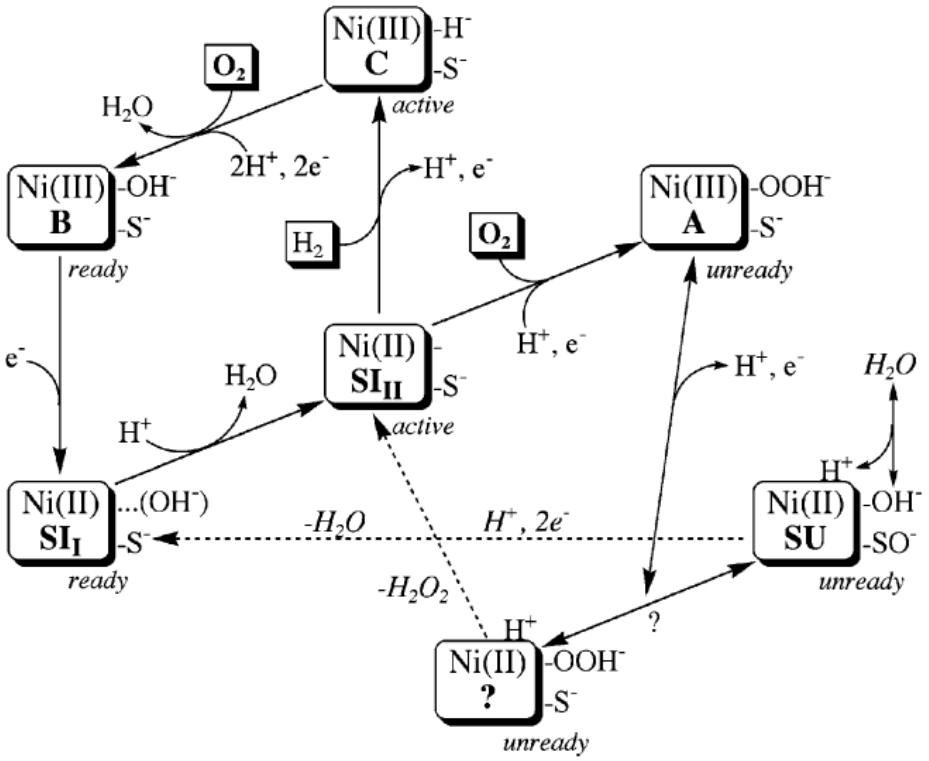


**Figure I–6. Possible aerobic oxidation reactions in that lead to the ready Ni–B state and the unready Ni–A state, as well as all different redox states of active site [NiFe]–hydrogenase.[11]**

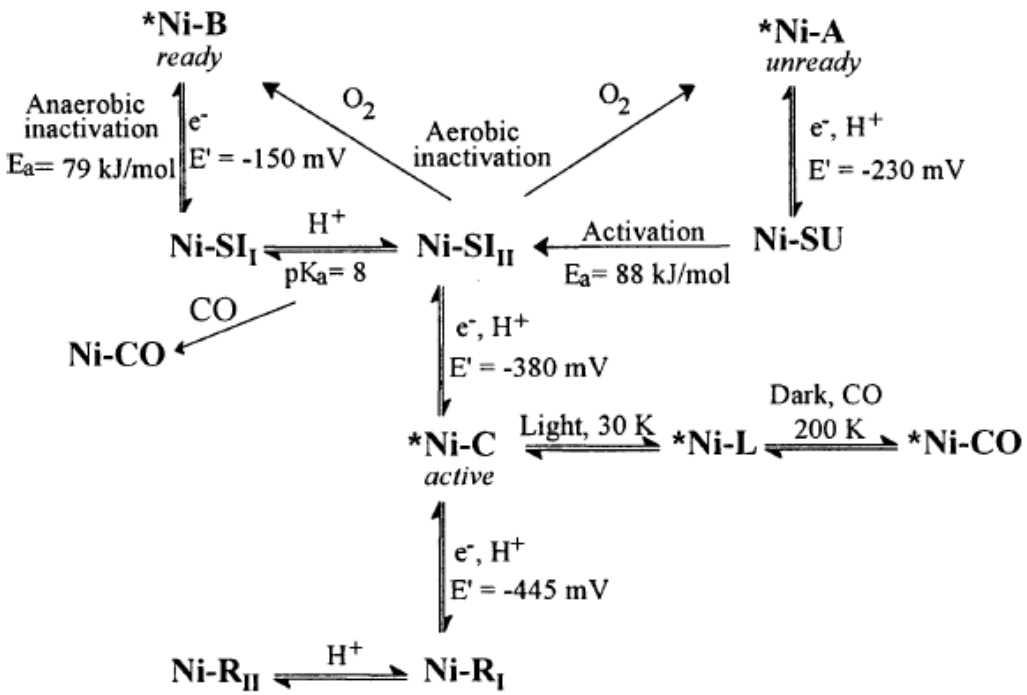


**Figure I–7. Scheme of different redox states of the active site [NiFe]–hydrogenase (* = EPR–active states) and redox potential at pH 8.0.[17]**

Dioxygen studies by Van der Zwaan *et al.* shows that oxygen was bound near the [NiFe] site in both the Ni–A and the Ni–B states.[18] It was proven, by the same group, that there was no direct interaction between nickel and oxygen. In related studies there was some unexpected conclusions which suggests that the bridging ligand, in the Ni–A state, could possibility be either dioxygen or water.[19–21] Investigation of the different redox states of [NiFe]–hydrogenase present a series of complex schemes of the inactive and active forms of the [NiFe] core, which are illustrated in **Figure I–6** and **Figure I–7**.

There are possible reaction fragments, i.e. $HOO^-$, $SO^-$, $OH^-$, $H^+$, $O_2$ and $S^-$, have been labeled in these multi–step states. However, not all of these states have been fully characterized. Electron paramagnetic resonance, EPR, have been used to probe the redox states of the dinuclear active site. It was determined that the square planar $Ni^{II}$, which is EPR silent (S = 0), is being oxidized or reduced to $Ni^{III}$ or $Ni^{I}$, which are both EPR active (S = ½). Upon further investigation it was determined that the nickel, $Ni^{II}$, was the inactive form of the enzyme and was oxidized to $Ni^{III}$ for the active form of the enzyme (**Figure I–6**).

Based on spectroscopic data, there have been some detailed mechanisms for the hydrogen activation involving hydrides, $H^-$, for both the nickel and iron centers. To date, it has been generally accepted by researchers that the redox states of the active site, which correspond to the catalytic activity, have been determined to be Ni–R, Ni–C and Ni–SI.[17] This three–step mechanism, which involves these redox states, has been supported by kinetic data using spectroscopic redox titrations.[22–24] These studies showed a shift in the vibrational frequencies, using FTIR of the Ni–$SI_I$ and Ni–$SI_{II}$, which suggests that there are different levels of protonation of the terminal cysteines bound to the nickel atom. This would, also, be consistent with the broad pH range to which the [NiFe]–hydrogenase are in the active form.[25] However, it has been accepted that the Ni–C form is the key intermediate of the catalytic cycle. This key intermediate was proven by experimental and theoretical results showing that the Ni–C form has the presence of a bridging hydride.[26–31] It was previously mentioned that EPR studies show that the nickel center was responsible for the catalytic activity; this was later supported by the crystal structures, which indicated that the gas channel of the enzyme end at the nickel center in 2002, this work was done by Ogata *et al.*[13] and later supported by developing research in 2005 by Volbeda *et al*.[32]

Experimental techniques were not the only route researchers have chosen. Some researchers have used computational methods to solve how this catalytic activity works, however there has been some controversy between the experimental results and the computational. Computational studies of these intermediates and transition states of this catalytic activity have pointed to the iron center as the primary binding site for dihydrogen. In 2002, Leger *et al*. calculated that the energy barrier, for the heterolytic cleavage, was similar to the electrochemical data.[33] In 2004, Siegbahn showed through DFT (density functional theory) studies that the bridging cysteines might act as a base during the catalytic cycle.[29] In 2006, Pardo *et al*. used the computational studies that other researchers have reported and formulated a proposed mechanism of the catalytic activity for the dihydrogen oxidation and production by the [NiFe]–hydrogenase (**Figure I–8**). However, this proposed mechanism favors the iron center as the primary binding site for dihydrogen.[27]

The catalytic cycle has been separated into two components: (1) the outer cycle, which represents the dihydrogen oxidation and (2) the inner cycle, which represents the dihydrogen production or reduction. The Ni–$SI_{II}$ form, the first step of this process of the outer cycle, starts

with the binding of the dihydrogen to the iron center. There has been some debate, from the DFT calculations, whether the kinetic barrier for the heterolytic cleavage would have been lowered if the nickel center were in the 3+ oxidation state or not. Those researchers who believe that the nickel is not in the 3+ oxidation state have concluded that both transition metals, Ni and Fe, are in the 2+ oxidation states.[17] Some researchers have concluded that the amino acid residues, which surround the active site, do not interfere with the binding of the dihydrogen binding to the iron center.[29] As a result, the Ni–C state is formed after the transfer of one proton during the heterolytic cleavage. The Ni–C state then forms a transient intermediate, which has been concluded to be similar to Ni–L state, and quickly oxidizes back to the Ni–$SI_{II}$ state.

The starting point of the inner cycle is the Ni–$SI_{II}$ form, which, in a one–electron/one–proton step, forms a stable intermediate called Ni–C. A possible transient intermediate, $Ni^{I}$–$Fe^{II}$, might occur within the first step; however, this process haS not been detected by spectroscopy. This transient intermediate has been concluded to be similar to the Ni–L species, which has been detected by photodissociation at low temperatures.[34–35] The existence of this transient intermediate was discovered when the $H_2/D_2$ exchange activity of the [NiFe]–hydrogenase was observed. The Ni–C intermediate, in a second one–electron/one–proton step, forms the Ni–R state. This transition was proven using infrared spectroscopy where the CO/CN stretching frequencies have shifted when reducing Ni–C to Ni–R, which suggested that the Ni–R state contains the bridging hydride.[26–31] To date, there have been no further experimental developments of the hydrogen species bound to the Ni–R state; however, DFT calculation has proposed the structure of the Ni–R state (**Figure I–8**). The final step of the inner cycle is the formation of the dihydrogen ligand on the iron center and the release of the dihydrogen gas that passes through a gas transport channel and the formation of the Ni–$SI_{II}$ state.

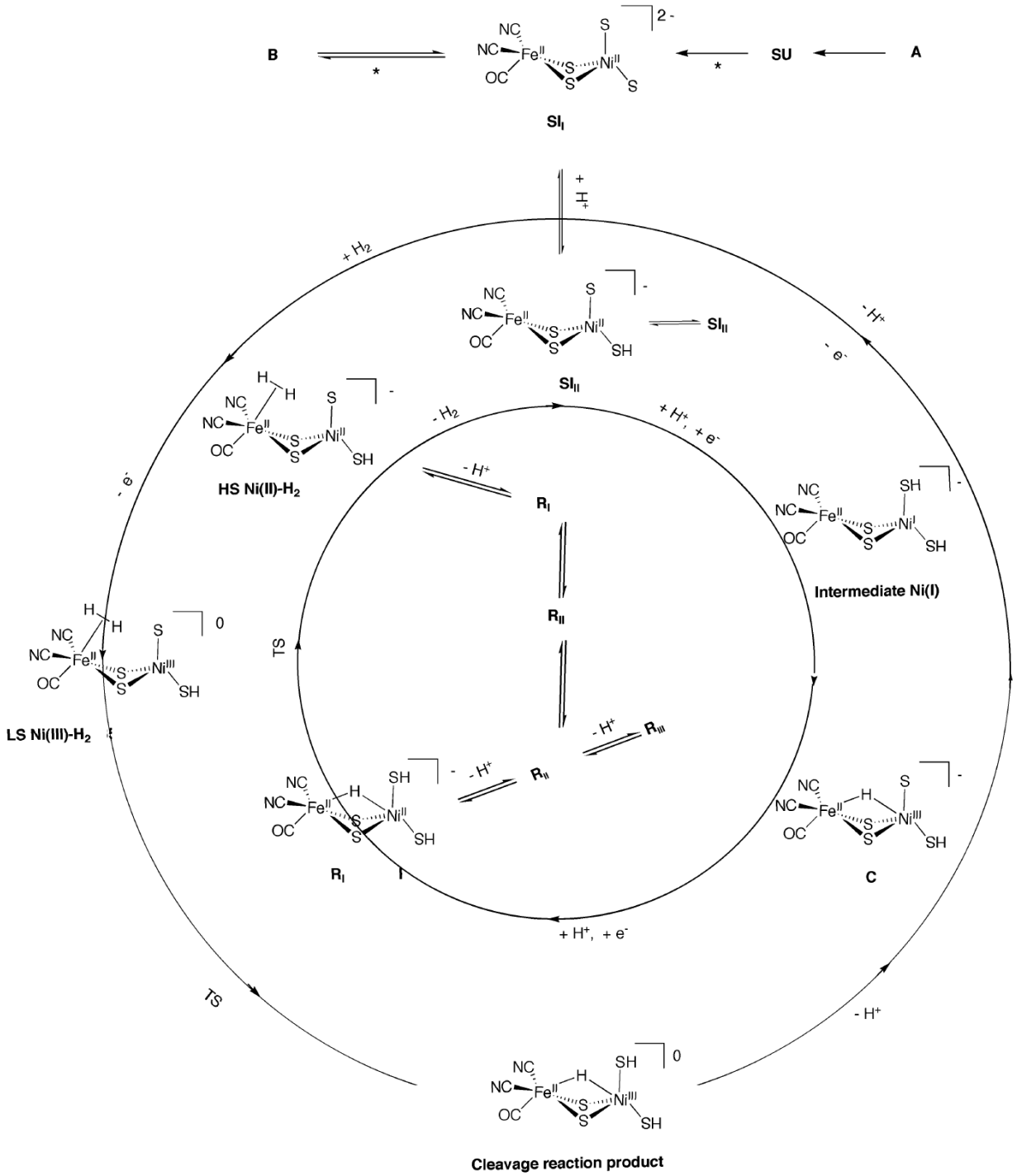


**Figure I–8. Catalytic cycle, using computational studies, for [NiFe]–hydrogenase (where * = show process).**

### 1.3.2 Models of [NiFe]–Hydrogenases

In the past, modeling studies of [NiFe]–hydrogenase has been divided into four categories: (1) the synthesis and characterization of the nickel complexes containing sulfur ligands, (2) the synthesis and characterization of iron complexes that contain cyanide and carbonyl ligands, (3) the development of hetero–dinuclear complexes, which primarily focuses on the x–ray structure, (4) the catalytic activity of the modeled structures using dihydrogen.

There has been extensive research on nickel complexes, containing sulfur ligands, that predates the discovery of the structure on the active site of [NiFe]–hydrogenase. These complexes contained a wide variety of ligands from mixed S/N/O molecules to thioether.[36] Initially, this research was performed to investigate tetrahedral $Ni^{II}$ complexes that can be reversibly oxidized to $Ni^{III}$ using monodentate ligands. To date there are only eight $Ni^{II}$ complexes that can do this reversible oxidization (**Figure I–9**),[36] which is similar to what is found in the active site. Square planar $Ni^{II}$ complexes were synthesized and characterized, by X–ray crystallography, using bidentate and porphyrin–type ligands, i.e. 1,2–ethanedithiol (edt), norboranedithiol (ndt), chlorin, oxo–phlroin etc. (**Figure I–10**). It is worth noting that some of these $Ni^{II}$ complexes show similar electrochemical to that found in the nickel center of the enzyme.[36]

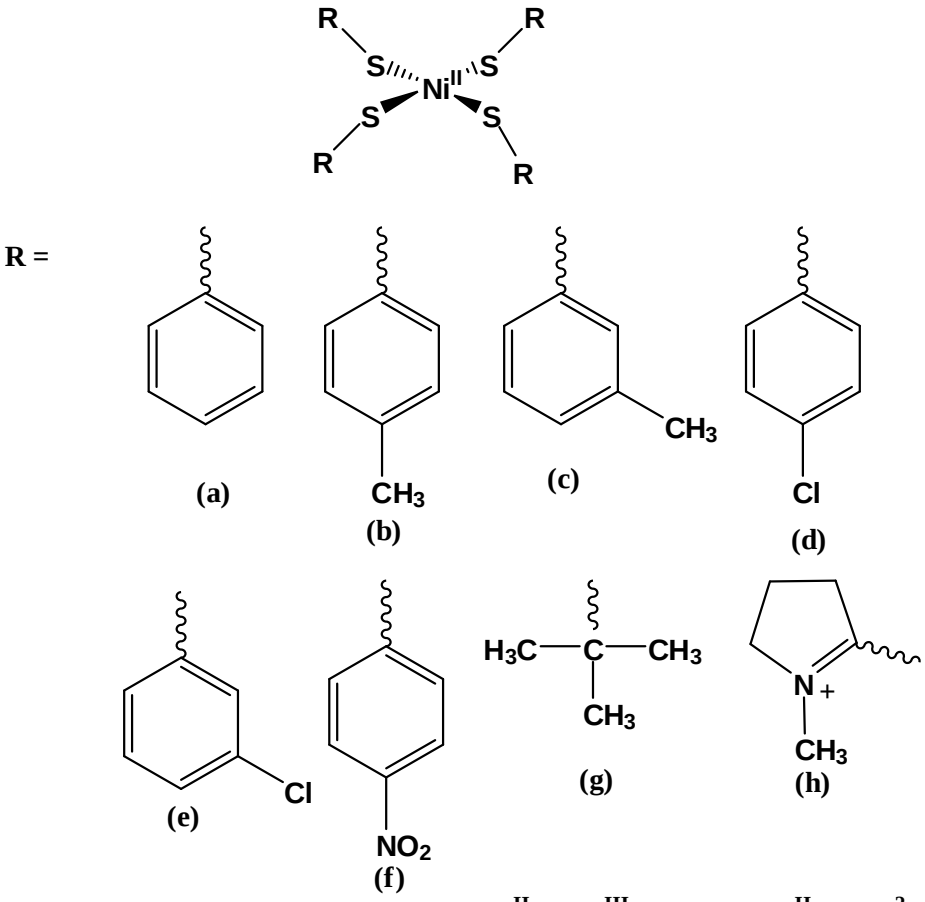


**Figure I–9. Nickel complexes reversible redox $Ni^{II}$ to $Ni^{III}$ (a) – (g) $[Ni^{II}(SR)_4]^{2-}$ complexes; (h) $[Ni^{II}(SR)_4]^{2+}$complex.**

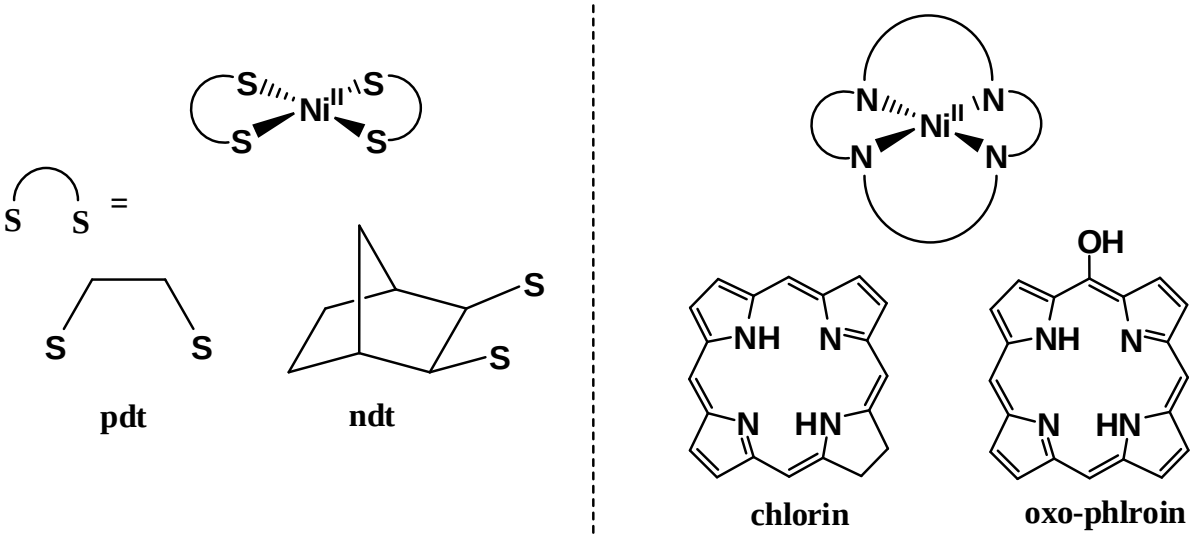


**Figure I–10. Nickel complexes containing bidentate and tetradentate ligands. (left) Sulfur bidentate ligands; (right) Porphyrin–type ligands.**

The synthesis of iron–cyanide and iron–carbonyl complexes has been investigated for nearly three hundred years and one hundred years, respectively. This predates the discovery of the [NiFe]–hydrogenase by over 250 years. The oldest iron–cyanide/carbonyl complex, $[Fe^{II}(CN)_5(CO)]^{3-}$, was discovered and reported in 1887 by Mullar *et. al*.[37] Approximately thirty years later, researchers found that $[Fe^{II}(CN)_5(CO)]^{3-}$ could be synthesized by a ligand displacement reaction using $[Fe^{II}(CN)_5(NH_3)]^{3-}$ under CO atmosphere.[38–39] In 1959, Cotton *et al*. discovered, under extreme temperature and high CO pressure, the same iron complex can be synthesized.[40] However, due to the extreme measures needed to synthesize complexes like $[Fe^{II}(CN)_5(CO)]^{3-}$ this hindered scientists from pursuing further investigation in the field. In 2001, Jiang *et al*. synthesized two geometric isomers of $[Fe^{II}(CN)_4(CO)_2]^{2-}$ (**Figure I–11**) under mild reaction conditions.[41] This research opened a new era of $[Fe(CN)_x(CO)_y]$ complexes to be synthesized and characterized in order to study the second component of the [NiFe]–hydrogenase.[42]

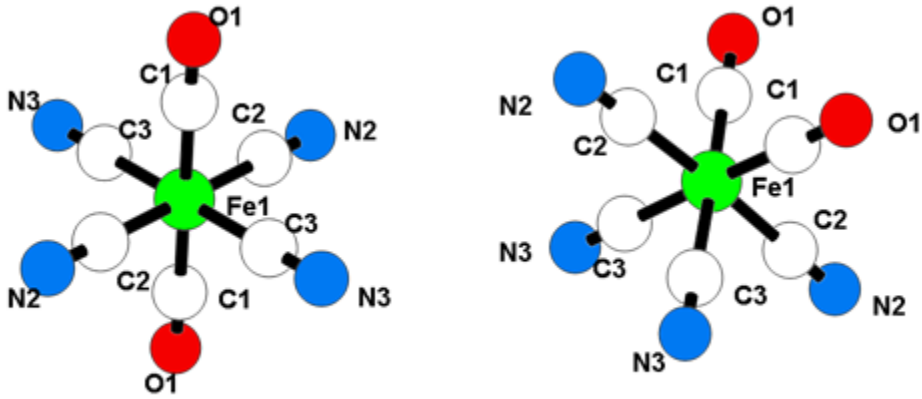


**Figure I–11. X–ray structure of *trans* and *cis* $[Fe^{II}(CN)_4(CO)_2]^{2-}$.**

In 1996, Lai *et al*. reported the first structurally characterized thiolate–bridged Ni–Fe carbonyl complex[43] (**Figure I–12a**); however the Fe was bridged by one of the thiolate. It was shown that the Ni–Fe bond distance was 3.76 Å, which was longer than the reported bond distance in the enzyme (2.6 to 2.9 Å). Osterloh *et. al*., in 1997, reported the first Ni–Fe dimer where the complex was bridged by two thiolates (**Figure I–12b**).[44] It was reported that the Ni–Fe bond distance was 2.8 Å, which shows the advantage of a di–bridged system with a difference of approximately 1 Å. This was the first Ni–Fe dimer where both transition metals have similar geometries, i.e. square planar. The first structurally reported Ni–Fe dimer, containing (1) two

bridging thiolate and (2) Fe–CO ligation, was reported by Davies *et. al*. in 1999 (**Figure I–12c**).[45–46] This structure contained a tetradentate N/S ligand; however, the Ni–Fe bond distance was measured to be 3.5 Å. This elongated bond distance was due to the ethane bridge between the thiolate and the amine, which adds more flexibility to the tetradentate ligand. This structure showed the $Fe^{II}$ center to have a distorted octahedral geometry while the $Ni^{II}$ had a square pyramidal arrangement. Researchers moved from nitrogen–based ligands to phosphine–based due to phosphorous being a soft donor as compared to nitrogen. Sellmann *et al*., in 2002, reported a Ni–Fe dimer that has a tridentate thiolate ligand; however, in this case the phosphine ligands were bound to the iron center as opposed to the nickel (**Figure I–12d**).[47] The nickel showed four thiolates bound to it as was found in the enzyme with cysteine ligation. The structure confirmed that one carbonyl ligand was bound to the iron; however, the Ni–Fe bond distance was 3.3 Å. In 2005, the first Ni–Fe dimer which contained a phosphine–type ligand, 1,2–*bis*–(diphenylphosphino)ethane (dppe), where the Ni–Fe bond distance was the shortest at 2.5 Å (**Figure I–12e**).[48] The structure showed a square pyramidal geometry at the $Fe^{0}$ center while the $Ni^{II}$ center showed a distorted tetrahedron. During this time, Tatsumi synthesized and structurally characterized the first Ni–Fe dimer that closely mimics the structure of the enzyme (**Figure I–12f**).[49] The structure confirmed two carbonyl and cyanide ligands bound to iron and a bridging bidentate thiolate where the nickel is coordinated to four thiolates. The $Fe^{II}$ showed an octahedral geometry, where the cyanides are in the *trans* arrangement while the carbonyls are *cis*, and the $Ni^{II}$ showed a square planar geometry. The Ni–Fe bond distance was measured to be 3.05 Å which is close to the bond distance reported for the oxidized form of the [NiFe]–hydrogenase.[41–42,50–57] Recently, in 2009, Jiang *et al*. synthesize the first Ni–Fe dimer that closely mimics the native active site and the structure was found to be neutral, where Tatsumi's compound was charged (**Figure I–12g**).[41b] The Ni–Fe bond distance was measured at 2.81 Å, one of the shortest bond distances known. This bond distance, like Tatsumi's, are similar to the bond distances found in the native active site of *D. gigas* and *D. fructosovorans*.

The complexes, in **Figure I–12(a–f)** and similar structures, have not shown to be effective catalysts as the native active site. Currently, **Figure I–12g**, catalytic studies have not been reported; however, **Figure I–12h** showed positive results.[58] The Fe–Fe and Ni–$Fe_{avg}$ bond distances were measured to be 2.66 Å and 2.50 Å, respectively. The Fe–Ni–Fe trimer was found to catalyze the reduction of trifluoroacetic acid to dihydrogen with an activity of six.

Unfortunately, the compound only remains stable for approximately one hour before decomposition occurs.

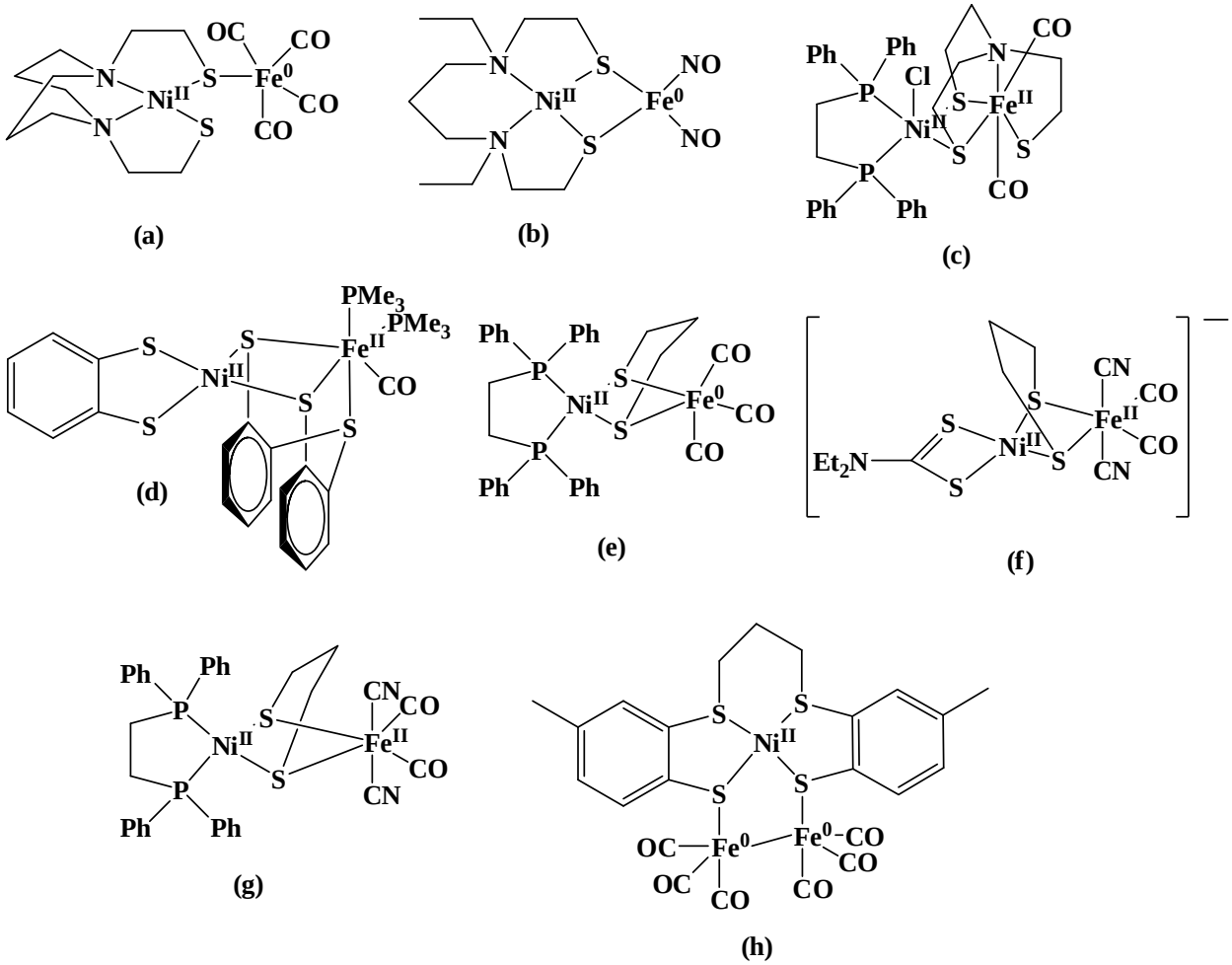


**Figure I–12. Ni–Fe dimers models of [NiFe]–hydrogenase.**

## 1.4[FeFe]–hydrogenases

### 1.4.1 Structure and Mechanisms of [FeFe]–Hydrogenases

The [FeFe]–hydrogenase, unlike the [NiFe]–hydrogenase, contains two iron atoms and it is structurally different with some similarities. This type of hydrogenase is responsible for the production, or reduction, of dihydrogen.[59–60] The activity of the [FeFe]–hydrogenase is approximately ten times greater than the [NiFe]–hydrogenase and binds more strongly to hydrogen.[61]

In early 1999, the crystal structures, the active sites, of two [FeFe]–hydrogenase, *Clostridium pasteurianum* (CpI) and *Desulfovibrio desulfricans* (DdH), were discovered conjointly by two independent groups.[62–63] The X–ray structure, shown in **Figure I–13**, contains two distinct iron atoms where one iron center is coordinated to an iron–sulfur cluster [$Fe_4S_4$]; called the H–cluster.[16] The active site is buried deeply within the protein. According to crystallographic data, three iron–sulfur clusters are contained within the enzyme. The clusters are given names relative to their position from the active site, which are called proximal, medial, and distal (**Figure I–14**).[64] The H–cluster is composed on an [$Fe_4S_4$]–cubane core linked by one cysteinyl residue to a [$Fe_2S_2$]–subsite. The cubane is linked to the protein, from the backbone, by three cysteines. The dinuclear metal center is bridged by a dithiolate ligand with two carbonyls one bridging carbonyl, one solvent ($H_2O$) and two cyanide ligands, which completes the coordination sphere. Carbonyl and cyanide ligands are highly unusual for biological systems; however, since both the [NiFe] and [FeFe]–hydrogenases contain those ligands it allows scientists to consider that these ligands are essential for this catalytic activity. Another novel feature is the presence of low spin iron(II) centers, which are unusual in a non–heme environment.

One of the major debates is the nature of the dithiolate ligand, marked X in **Figure I–13**. Currently, it remains undecided experimentally as to whether X is $CH_2$, NH or O. The use high–resolution X–ray crystallography combined with DFT optimizations of the dithiolate ligand, which has a 3.5 to 3.9 Å protein environment, favors oxygen as the mysterious component.[16] Other researchers have used crystallographic data and shown that the bridging ligand is either 2–azapropane–1,3–dithiol or propane–1,3–dithiol.[62–63]

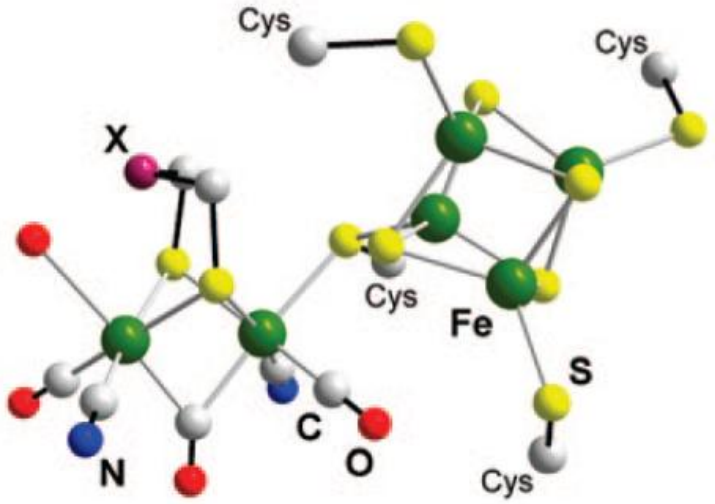


**Figure I–13. X–ray structure of [FeFe]–hydrogenase active site.**

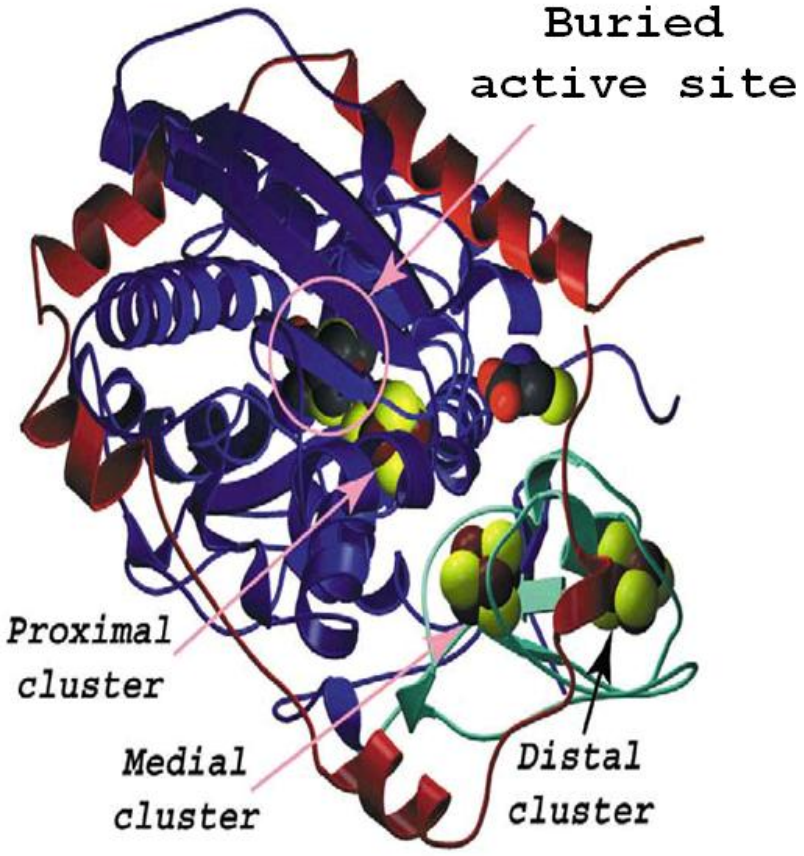


**Figure I–14.** ***Desulfovibrio desulfuricans*****.**

The different redox states of the active site were first studied by EPR spectroscopy, which gave a signal (S= ½) in the active form called $H_{ox}$ (**Figure I–15**).[65] The aerobic inactive site, $H_{inact}$, is diamagnetic, from which it could form a paramagnetic state, called $H_{trans}$, by a one–electron reduction process (**Figure I–16**).[65] Redox titrations showed that these signals disappeared upon reduction, potential at –0.400 V vs NHE at pH 8.0, to produce a diamagnetic species called $H_{red}$ (**Figure I–16** and **Figure I–17**). According to DFT calculations, the $H_{inact}$ or $H_{ox}^{air}$ forms are low spin due to the presence of the $Fe^{II}$–$Fe^{II}$ system. In the $H_{ox}$ form, the cluster is paramagnetic and it showed that one of the CO ligands acts a bridge between the dinuclear centers.

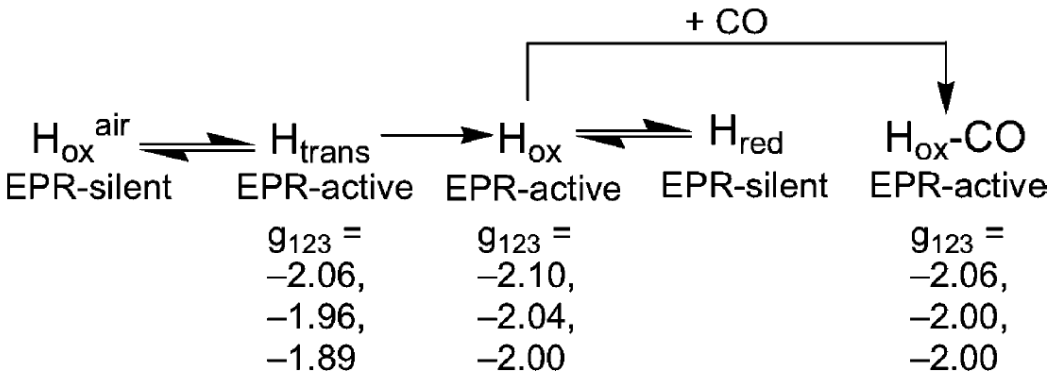


**Figure I–15. EPR studies on [FeFe]–hydrogenase.**

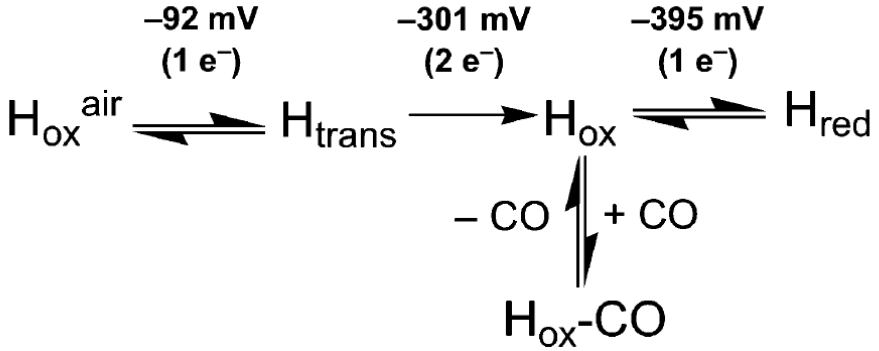


**Figure I–16. Electrochemical studies on [FeFe]–hydrogenase (pH 8.0).**

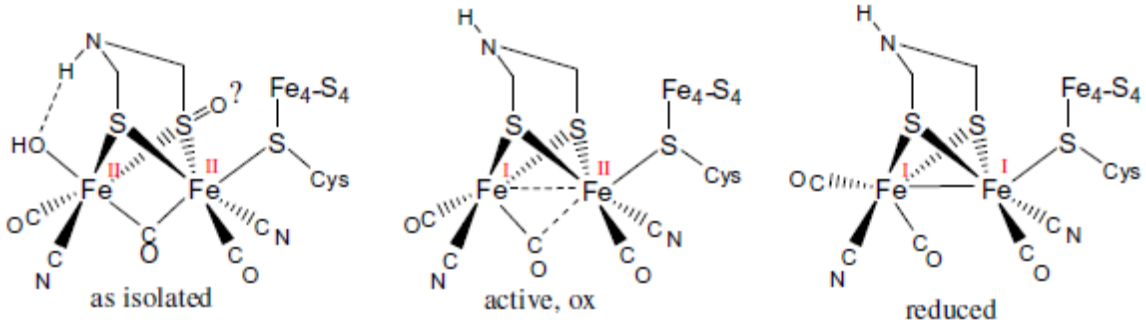


**Figure 1–17. Proposed forms of [FeFe]–hydrogenase active site.**

Experimentally it was shown that the [$Fe_4S_4$] cluster remains diamagnetic while an unpaired spin was centered on one of the irons in the dinuclear subsite. Using isotopic $^{13}CO$ labeling[66], magnetic studies[67] and DFT calculations[68] it was shown that the $H_{ox}$ and $H_{ox}$–CO forms were $Fe^{II}$–$Fe^{I}$ systems with the unpaired spin located on the distal iron relative to the cubane. Mössbauer studies, along with DFT calculations, revealed that the iron atoms, in the dinuclear center, were indistinguishable in the $H_{red}$ form, and concludes that the $Fe^{I}$–$Fe^{I}$ system was favored.[69–70] Infrared spectroscopy and electrochemistry were able to detect the transition between $H_{inact}$ to $H_{red}$ at various redox potentials; however, due to high instability, information beyond this point is non–existent.

As with the [NiFe]–hydrogenase, the [FeFe]–hydrogenase has a narrow range of redox potentials (**Figure I–16**), due to the presence of ligands bound to the transition metals. The ligand was not chosen by nature accidentally and the properties of these ligands, i.e thiolates are good π donors, carbonyls are good π acceptors and cyanides are good σ donors, are what makes these enzymes perform their catalytic activity. Scientists have been investigating different combinations of these ligands in order to discover the hidden power of these enzymes.

DeGioia and co–workers suggested the proposed catalytic cycle, shown in **Figure I–18**.[71–72] The cycle begins with the inactive, $Fe^{II}$–$Fe^{II}$ ($H_{ox}^{air}$), oxidized form that was isolated from *Desulfovibrio desulfricans.* The protonation of the hydroxide ligand, with a one–electron reduction, leads to a loss of water yielding the catalytically active $Fe^{I}$–$Fe^{II}$ form ($H_{ox}$).

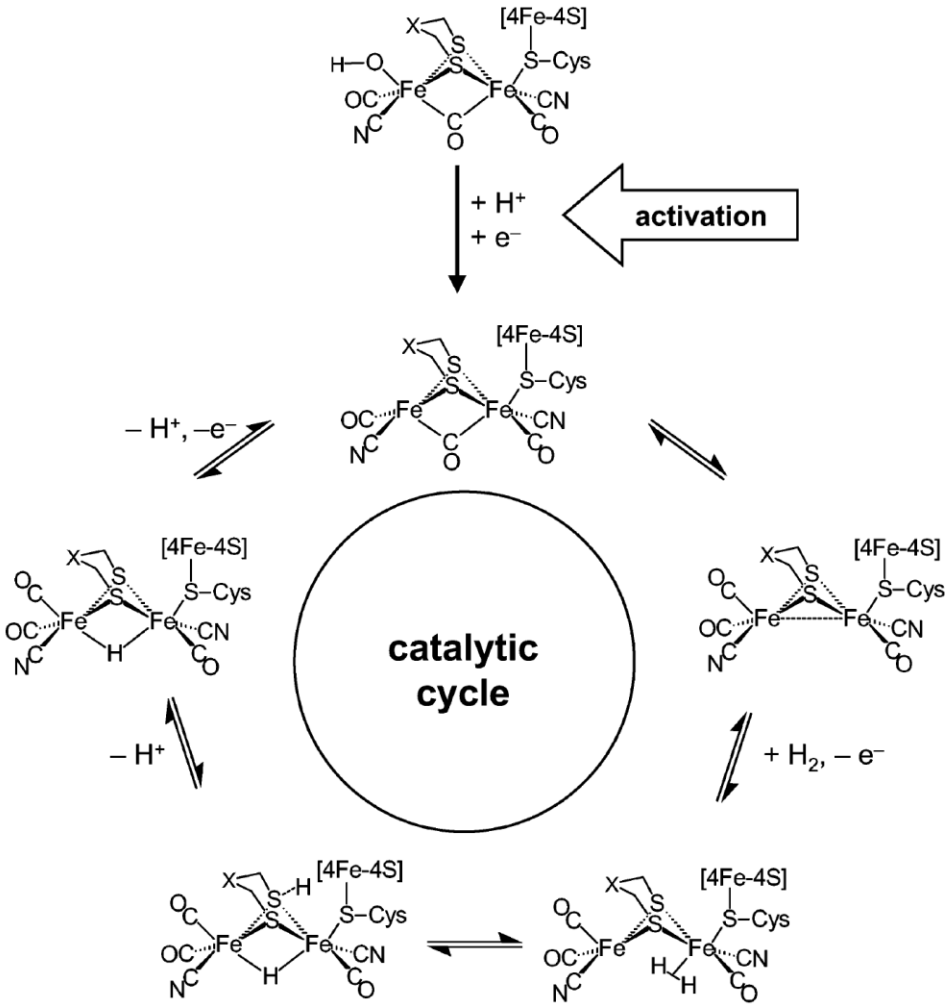


**Figure I–18. Proposed catalytic cycle for [FeFe]–hydrogenase with unknown bridging thiolate.**

The bridging CO $Fe^{I}$–$Fe^{II}$ form rearranges itself to produce an "all terminal" CO form. Dihydrogen gas binds to the proximal iron center resulting in a one–electron oxidation to form $Fe^{II}(H_2)$–$Fe^{II}$ form. A proton is transferred from the bound dihydrogen to the dithiolate resulting in a bridging hydride between the two iron centers. The active site undergoes another one–electron oxidation to reproduce the $Fe^{I}$–$Fe^{II}$ form and thereby completing the cycle. Some researchers believe that the proton transfers to the nitrogen atom on the bridging 2–azapropane–1,3–dithiol (**Figure 1–19**).[16] Regardless of which mechanism is correct both have one component in common, that the binding of the dihydrogen in the $H_{ox}$ ($Fe^{I}$–$Fe^{II}$) form is the key to the catalytic cycle. This theory was proven experimentally in 2006 by Albracht and co–workers.[73]

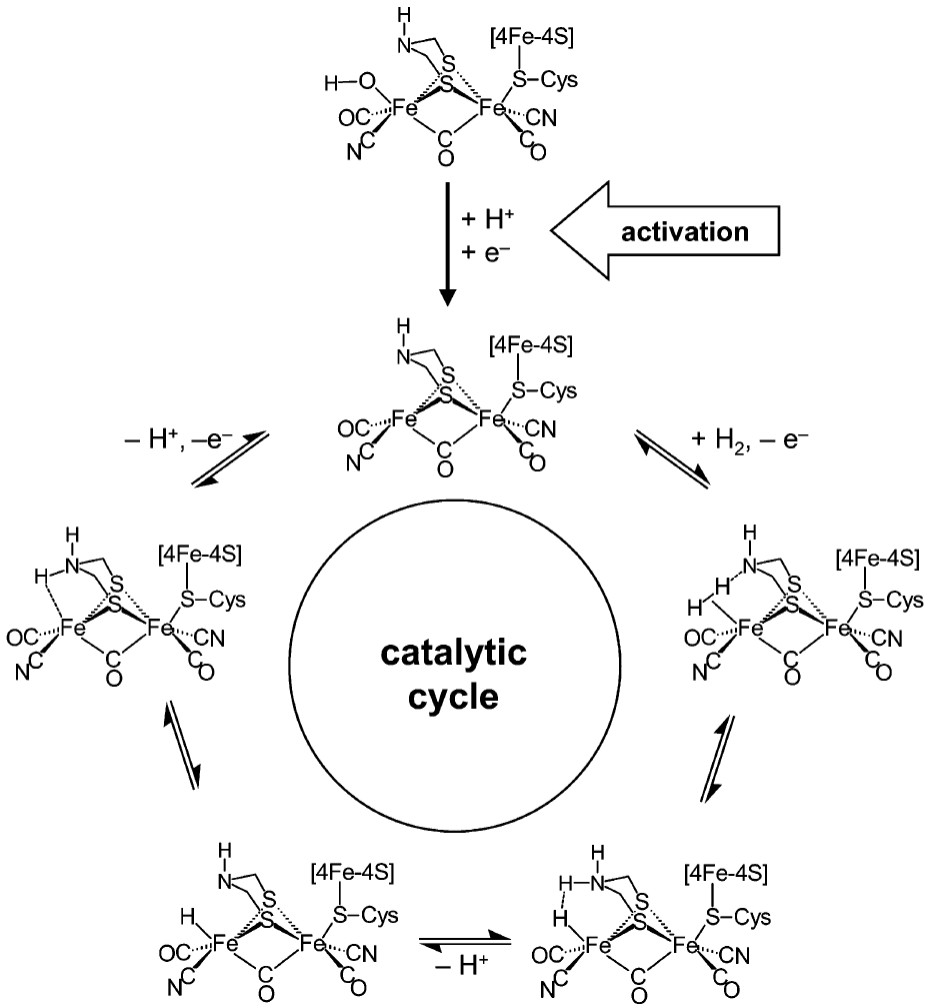


**Figure I–19. Proposed catalytic cycle for [FeFe]–hydrogenase with 2–azapropane–1,3–dithiolate.**

### 1.4.2 Models of [FeFe]–hydrogenase

The two key components when trying to model the [FeFe]–hydrogenase are (1) focusing on the bridging thiolate and (2) the carbonyl and cyanide ligation. Synthesis and characterization of diiron carbonyl compounds has been known for almost ninety years; however, synthetic methods and techniques have greatly developed within the last thirty years.

In 1999, Lyon *et al*. were the first to report a diiron compound with a Fe–Fe bond distance, 2.510 Å, that is similar to that reported for the enzyme active site[74] and they were the first to report the preparation of the dianionic dicyanide complex (**Figure I–20**).

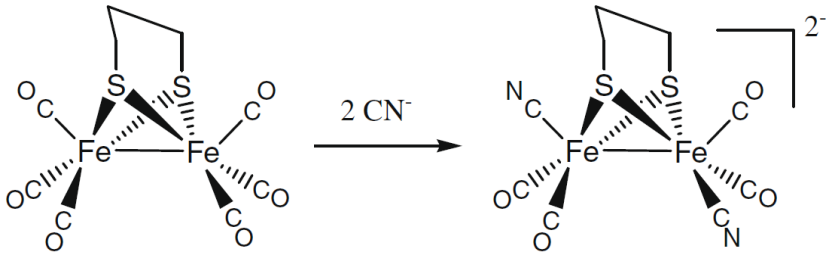


**Figure I–20. Structural models of [FeFe]–hydrogenase: (left) $[Fe^{I}_{2}(pdt)(CO)_{6}]$, (right) $[Fe^{I}_{2}(pdt)(CN)_{2}(CO)_{4}]^{2-}$.**

Rauchfuss and Pickett, along with their coworkers, independently utilized ligand substitution using $[Fe^{I}_{2}(pdt)(CO)_{6}]$ as the starting material.[76–77] Darensbourg and coworkers were the first to report the synthesis of $[Fe^{I}_{2}(pdt)(CN)_{2}(CO)_{4}]^{2-}$; however, Rauchfuss and coworkers were the first to identify its X–ray structure.[77] The $[Fe^{I}_{2}(pdt)(CN)_{2}(CO)_{4}]^{2-}$ complex resembles the active site and generates dihydrogen when reacted with acid. The product of this reaction was described as an insoluble polymeric series with an unknown structure. Darensbourg and coworkers reported the same protonation affording a transient bridging hydride, which was characterized spectroscopically; however, the complex could not be isolated.[75–76]

Rauchfuss and coworkers synthesized and characterized a monoanionic $Fe^{I}$–$Fe^{I}$ complex with one $CN^{-}$ and one phosphine. This diiron complex reacted with acid to form a stable dinuclear species containing a bridging hydride (**Figure I–21**).[77] The catalysis of the proton reduction was shown using electrochemical studies in the presence of solutions at various acid concentrations.

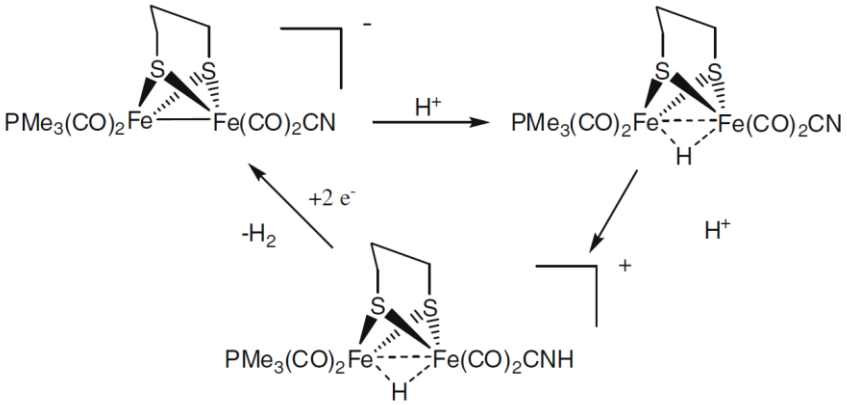


**Figure I–21. A *mono*–phosphine diiron complex to model [FeFe]–hydrogenase.**

In 2003, Heineky and coworkers reported using isonitrile ligands (C≡N–R) rather than cyanide to synthesize neutral species, which tested positive for the production of dihydrogen (**Figure I–22**). Darensbourg showed, using the isonitrile species with the bridging hydride, that it undergoes an isotope exchange with $D_2$ upon photolysis.[78] This was quite an achievement because very few models actually react with hydrogen.

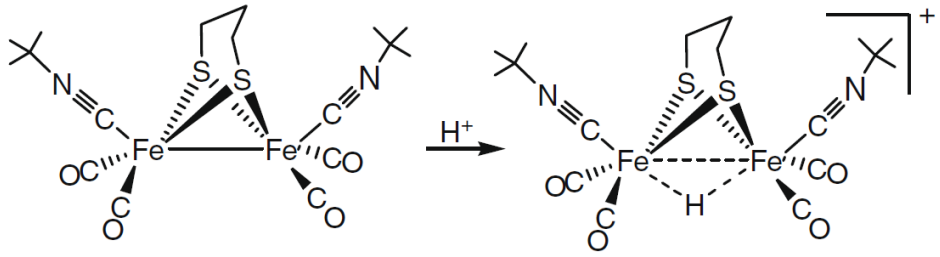


**Figure I–22. Modeling [FeFe]–hydrogenase using isonitriles.**

Darensbourg *et al.*have reported the synthesis and characterization of a *bis*–phosphine $Fe^{I}$–$Fe^{I}$ complex that upon protonation gave a stable bridging hydride species (**Figure I–23**).[79] This complex showed isotopic exchange with $D_2$ upon photolysis. There have been conflicting reports on the reduction of $[Fe^{I}_2(pdt)(CO)_6]$, shown in **Figure I–20**. Based on electrochemical studies it was shown that the diiron complex underwent a reversible two–electron reduction in DMF in the presence of a CO atmosphere. In 2003, Darensbourg and coworkers, using cyclic voltammetry and bulk electrolysis, showed a consistent one–electron reduction in CO–saturated $CH_3CN$. A further one–electron reduction to the dianionic complex occurs; however, only at extremely high reducing potentials.[80]

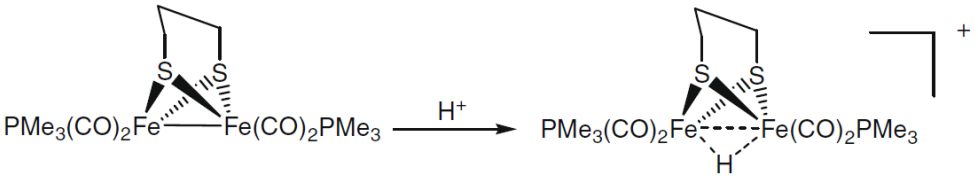


**Figure I–23. A *bis*–phosphine diiron complex to model [FeFe]–hydrogenase.**

In 2004, Pickett and coworkers demonstrated that dihydrogen evolved from protic media using $[Fe^{I}_{2}(pdt)(CO)_6]$ under reducing conditions.[81] They also reported a detailed study on a one–electron reduction product, which proposed a disproportionation/ligand redistribution reduction that affords a dimeric species containing four iron atoms (**Figure I–24**). The structure shown was proposed based on spectroscopic data, since the complex could not be isolated.

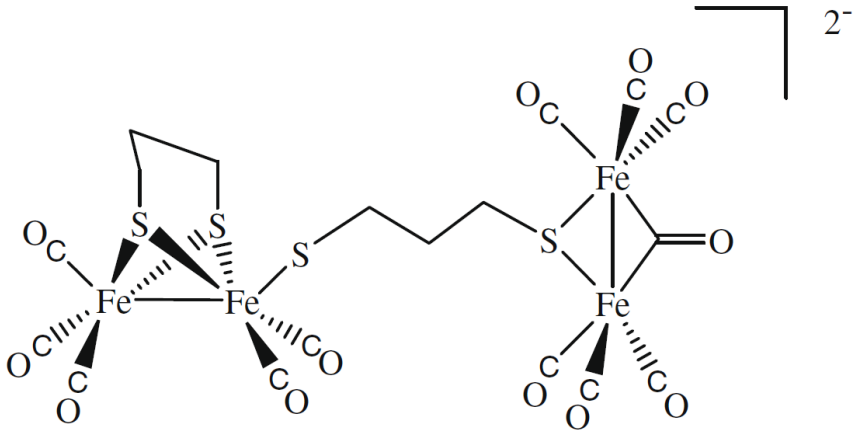


**Figure I–24. Dimeric species containing four Fe atoms to model [FeFe]–hydrogenase.**

A $Fe_2S_3$ system, using a tridentate thioether ligand, has shown promise since it mimics the active site.[82] This new ligand system, interestingly, showed a transient bridging CO species upon reaction with cyanide. This observation was important since the existence of a bridging CO was only been demonstrated using infrared spectroscopy on the different redox states of the enzyme (**Figure I–24**).

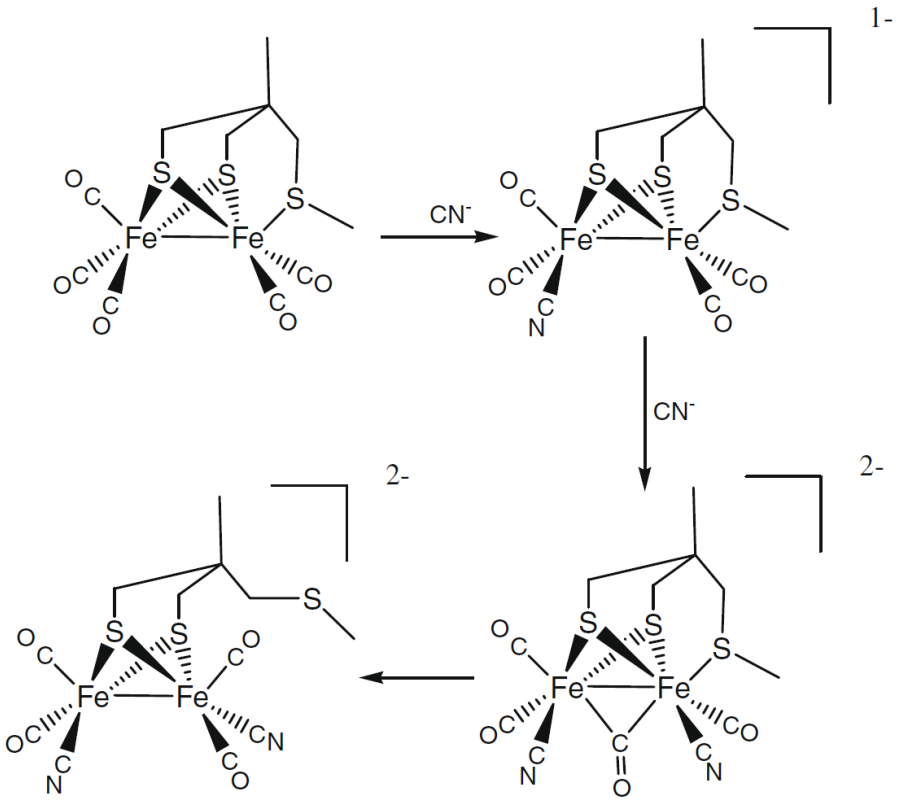

**Figure I–24. Modeling [FeFe]–hydrogenase using tridentate thiother.**

It was previously stated that there has been debate on whether the bridgehead of the dithiolate in the enzyme is $CH_2$, NH or O. Crystallographic studies have pointed toward NH[83] while DFT calculations pointed toward O.[84] In 2001, Rauchfuss and coworkers developed model complexes using 2–azapropane–1,3–dithiol which surprisingly can be synthesize by a condensation reaction using formaldehyde with a primary amine and a dimeric iron sulfide (**Figure I–25**).[85]

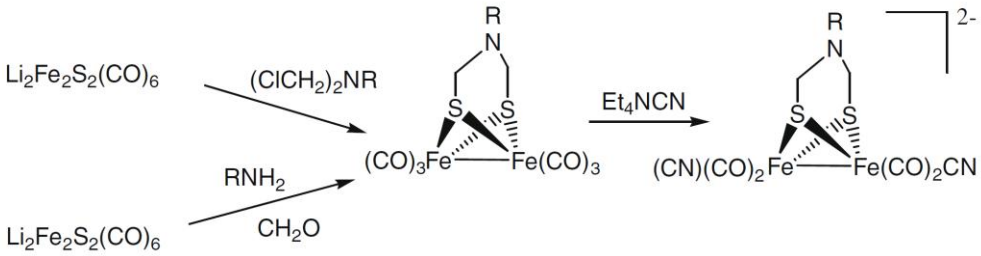

**Figure I–25. Synthesis of diiron complex using 2–azapropane–1,3–dithiolate.**

In 2005, Picket and coworkers synthesized the first complete structural model of the [FeFe] active site (**Figure I–26**).[82] Mössbauer studies revealed that the complex showed similar results to those reported for the reduced form of the [FeFe]–hydrogenase found in *Clostridia pasteurianum*. This complex, shown in **Figure I–26**, has shown to be so extremely efficient at proton reduction that it promoted other researchers to design similar models and study their catalytic activity.[86]

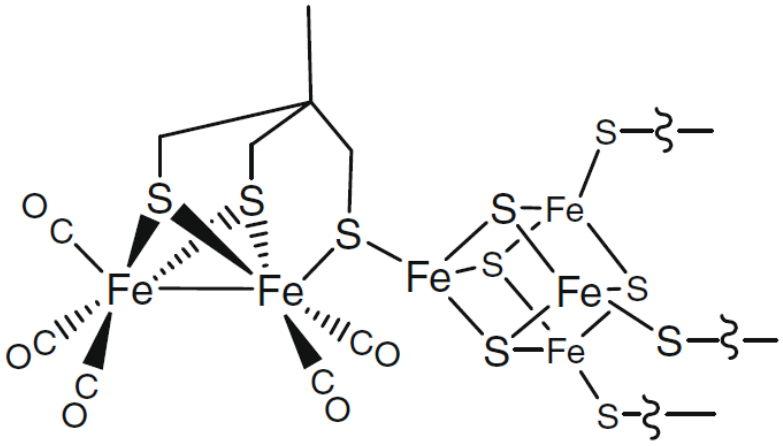


**Figure I–26. First complete structural model of [FeFe]–hydrogenase.**

## 1.5 [Fe]–hydrogenases

### 1.5.1 Structure and Mechanisms of [Fe]–Hydrogenases

In the past, this type of hydrogenase was referred to as $H_2$–forming methylene–tetrahydromethanopterin dehydrogenase (Hmd) or as an "iron–sulfur cluster" free hydrogenase. Hmd was first discovered in 1990 by Thauer and coworkers.[87] It was found to be phylogenetically unrelated to the [NiFe] and [FeFe]–hydrogenases; Hmd is a homodimer, composed of two identical subunits that contains two iron atoms per homodimer. Purity of this enzyme proved to be difficult due to thermal and photo instability.[88] The most stable form of the Hmd enzyme is from *Methanothermobacter marburgensis*; however, sequence homologies suggested that all Hmd enzymes are similar. Thauer and coworkers discovered that Hmd plays a key role in $CO_2$ reduction to methane.[88] Hmd is not the same as [NiFe] and [FeFe]–hydrogenases as it does not catalyze the reduction of dihydrogen, but rather facilitates the stereoselective transfer of a hydride from $H_2$ (**Figure I–27**).[61]

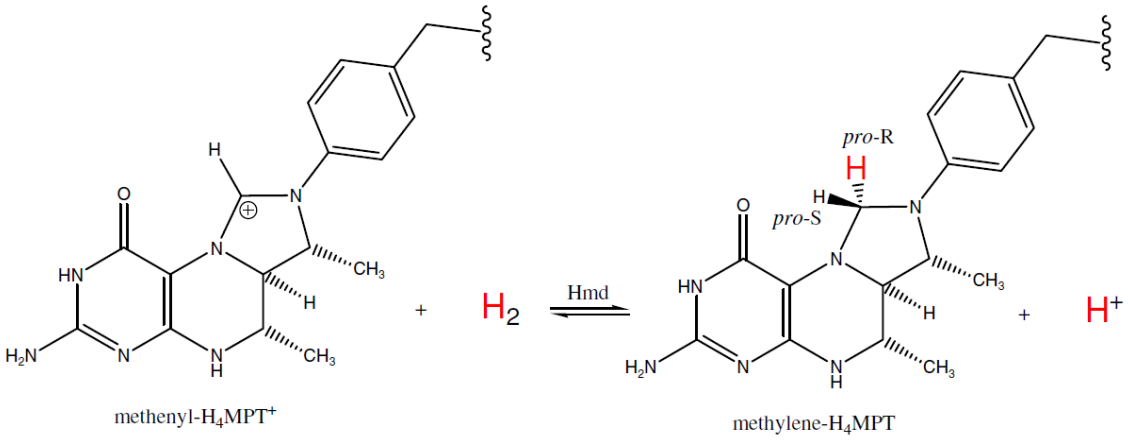


**Figure I–27. Stereoselective transfer of a hydride by Hmd.**

The Hmd was thought to be "metal–free" until 2004 where Thauer and coworkers discovered the enzyme contains one iron atom.[89–90] Spectroscopic studies suggested that the active site contained two *cis*–CO, one thiolate and two N/O ligands. Studies showed that treating the Hmd with CO lead to a tricarbonyl complex, which suggested that the CO replaced a weakly bound solvent molecule. Mössbauer studies suggested that the active site was diamagnetic under a wide range of conditions, which suggested the iron was $Fe^{II}$.[91]

In 2008, Thauer and coworkers solved the crystal structure of the Hmd active site, which confirmed the presence of iron atom bound to two *cis*–CO ligands. Studies suggested that the previously unknown ligand may in fact be an acyl moiety derived from the pendant acid group on the pyridine ring (**Figure I–28**).[92–93]

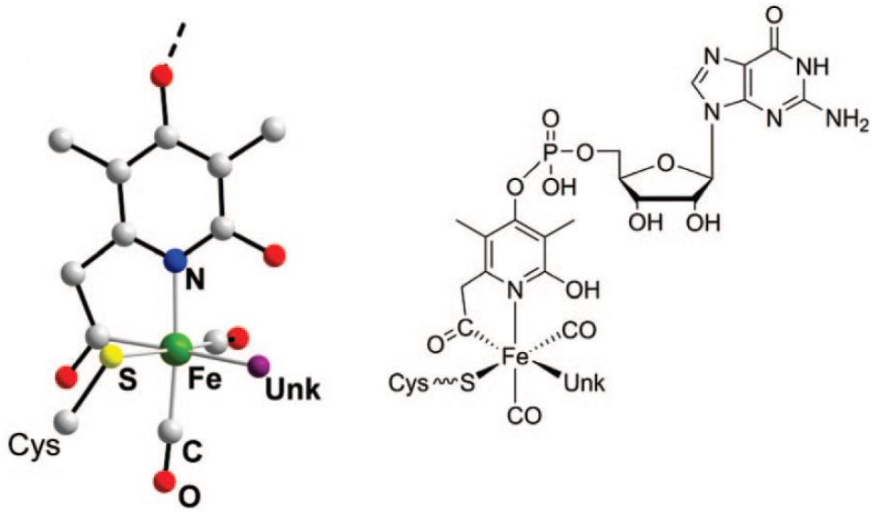


**Figure I–28. X–ray and skeletal structure of the Hmd active site.**

### 1.5.2 Models of [Fe]–hydrogenase

Since the crystal structure was reported in 2008, several functional models have been reported. Pickett and coworkers, prior to the publication of the Hmd crystal structure, synthesized and characterization an iron complex that exhibited IR spectra similar to that of the enzyme active site (**Figure I–29**).[94]

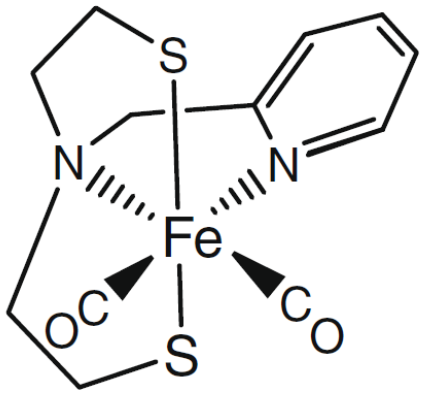


**Figure I–29. Structure of $Fe^{II}$–complex to model Hmd active site.**

## 1.6 Conclusions/Goals

Hydrogenase active sites have been investigated for the past thirty years. Chemical, computational and spectroscopic (i.e. IR, EPR, X–ray crystallography and DFT) studies have illustrated that these active sites contain transition, nickel and/or iron. Researchers have synthesized and characterized several models of the specific active sites. However, only a few of these models have similar catalytic activity found in the enzymes.

The primary goal of this research is synthesize and characterized models of the [NiFe] and [FeFe]–hydrogenases. There are various pathways to achieve this goal. First, synthesis and structural characterization of dimeric complexes using individual components, i.e. $[Fe(CN)_x(CO)_y]$ and $Ni(SR)_4$. Second, synthesis and characterization of the individual components as previously stated. Cyanide and carbon monoxide are poisonous by nature; however, these ligands are found in the enzyme active sites, which researchers are investigating, the same can be said for the $Ni(SR)_4$ component. Another approach was synthesizing

polydentate–thiolate ligands and using them with various transition metals to model the active sites of hydrogenase and other transition metal–sulfur containing enzymes, e,g. nitrogenase.

Research has expanded to ruthenium and osmium in place of iron for two reasons: (1) same group as iron, i.e. similar chemical properties and (2) less susceptible to oxidation. The goals are to synthesized and characterized ruthenium and osmium analogs of the existing iron complexes and compare their chemical and physical properties.

## 1.7 Experimental Techniques

All chapters in this dissertation follow these general procedures and use these instruments unless otherwise stated.

### 1.7.1 General Methods

Syntheses of ligands and metal complexes were carried out under dinitrogen atmosphere using conventional Schlenk techniques unless otherwise specified. Transfer of air sensitive materials was carried out under a dinitrogen atmosphere by either cannulation (solutions) or in the Dry–Box (solids). All chemicals used are either commercially available or were synthesized according to the literature procedure. All solvents were distilled prior to use. Cyclohexane, hexane, diethyl ether, toluene, benzene and tetrahydrofuran (THF) were distilled using Na/benzophenone. Methanol, 2–propanol and ethanol were distilled using $Mg/I_2$. Acetonitrile and tetramethylethylenediamine (TMEDA) were distilled using calcium hydride ($CaH_2$). Dichloromethane and chloroform were distilled using diphosphorus pentoxide ($P_2O_5$). Solvents were stored in a dinitrogen gas filled flask. Dinitrogen gas was purged through these solvents before use. Tetrabutylammonium tetrafluoroborate ($TBABF_4$) was recrystallized using ethyl acetate and pentane. All other solvents were used as purchased unless otherwise specified.

## 1.8 Instrumentation

### 1.8.1 Electrochemistry

Cyclic voltammetry (CV) studies were recorded on a BAS–100W electrochemical analyzer with a platinum working electrode, a platinum wire auxiliary electrode, and a Ag/AgCl

reference electrode. Samples (ca. 1.0 mM) were measured in the specified solvent with tetra–*n*–butylammonium tetrafluoroborate (0.1 M), $TBABF_4$, as the supporting electrolyte. The samples were measured in a 2 mL micro–electrochemical cell.

### 1.8.2 Electronic Spectroscopy (UV–Vis)

UV–Vis spectra were measured using an HP 8453 UV–Visible Spectrophotometer. A tungsten lamp was used for the visible region and a deuterium lamp was used for the ultraviolet region. All samples were scanned using two quartz cells of different path lengths, 0.1 mm and 1.0 mm. Samples (ca. 1.0 mM) were measured in the specified solvent under dinitrogen atmosphere.

### 1.8.3 $^{1}$H–NMR, $^{13}$C–NMR and $^{31}$P–NMR Spectroscopy

$^{1}$H–NMR, $^{13}$C–NMR and $^{31}$P–NMR spectra were recorded using a Varian–300 spectrometer operating at 300 MHz and a Varian–400 spectrometer operating at 400 MHz. All chemicals shifts were referenced using tetramethylsilane (TMS), at 0.00 parts per million (ppm), for $^{1}$H–NMR. All chemicals shifts were referenced to the reported deuterated solvents for $^{13}$C–NMR. All chemical shifts were referenced using an external standard of 85% $H_3PO_4$ (0.0 ppm) for $^{31}$P–NMR.

### 1.8.4 Infrared Spectroscopy

The infrared spectra were recorded using a Thermo Fisher Scientific Nicolet iS10. The spectra were analyzed using Omnic IR software, version 8.0.342. Solid samples were prepared using a potassium bromide (KBr) pellet. Solution samples were injected into a solution $CaF_2$ IR cell with a typical path length of 1 mm.

### 1.8.5 X–ray Structure Determinations

Cell parameters and data collection summaries for the complexes are given throughout the chapters. X–ray data of these complexes were collected on an Oxford single crystal X–ray diffractometer operating at 50 kV and 40 mA using Mo Kα ($\lambda$ = 0.71073 Å) radiation. The X–ray diffractometer was operated using CrysAlisPro, version 171.33.66. All samples were collected at 100 K. The structure refinement was done with SHELXL–97 (Sheldrick). All of the crystal structures were solved by direct methods using WinGX, version 1.80.05. Anisotropic refinement for all non–hydrogen atoms was done by a full–matrix least squares method. X–ray structure figures were created using ChemRay, x–ray imaging software developed by Dr. Joseph W. Lauher at Stony Brook University.

## 1.9 References


1. Lippard, S. J.; Berg, J. M. *Principles of Bioinorganic Chemistry*; University Science Books; 1994.
2. Lubitz, W.; Tumas, W. *Chem. Rev.* **2007**, *107*, 3900.
3. Gordon, R.B.; Bertram, M.; Graedel, T.E. *Proc. Natl. Acad. Sci. USA* **2006**, *103*, 1209.
4. http://greenecon.net/solar–and–hydrogen–energy–economics/energy_economics.html
5. Akhmanova, A.; Voncken, F.; van Alen, T.; van Hoek, A.; Boxma, B.; Vogels, G.; Veehuis, M.; Hackstein, J. H. P. *Nature* **1998**, *396*, 527.
6. Shima, S.; Pilak, O.; Vogt, S; Schick, M.; Stagni, M. S.; Meyer–Klaucke, W.; Warkentin, E.; Thauer, R. K.; Ermler, U. *Science* **2008**, *321*, 572.
7. Crabtree, R. H.. *Inorg. Chim. Acta* **1986**, *125*, L7.
8. Volbeda, A.; Charon, M. H.; Piras, C.; Hatchikian, E. C.; Frey, M.; Fontecilla–Camps J. C. *Nature* **1995**, *373*, 580.
9. Volbeda, A.; Garcin, E.; Pirasl, C.; De Lacey, A .L.; Fernandez, V. M.; Hatchikian, E. C.; Frey, M.; Fontecilla–Camps, J. C.. *J. Am. Chem. Soc.* **1996**, *118*, 12989.
10. Ogata, H.; Hirota, S.; Nakahara, A.; Komori, H.; Shibata, N.; Kato, T.; Kano, K.; Higuchi, Y. *Structure* **2005**, *13*, 1635.
11. Volbeda, A.; Martin, L; Cavazza, C.; Matho, M.; Faber, B. W.; Roseboom, W.; Albracht, S. P. J.; Garcin, E.; Rousset, M.; Fontecilla–Camps J. C. *J. Biol. Inorg. Chem.* **2005**, *10*, 239.
12. Lamle, S. E.; Albracht, S. P. J.; Armstrong, F. A. *J. Am. Chem. Soc.* **2004**, *126*, 14899.
13. Ogata, H.; Mizoguchi, Y.; Mizuno, N.; Miki, K.; Adachi, S.; Yasuoka, N.; Yagi, T.; Yamacuchi, O; Hirota, S.; Higuchi, Y. *J. Am. Chem. Soc.* **2002**, *124*, 11628.
14. Higuchi, Y.; Ogata, H.; Miki, K.; Yasuoka, N.; Yagi, T. *Structure* **1999**, *7*, 549.
15. Leroux, F.; Dementin, S.; Burlatt, B.; Cournac, L.; Volbeda, A,; Champ, S.; Martin, L.; Guigliarelli, B.; Bertrand, P.; Fontecilla–Camps J. C.; Rousset, M.; Leger, C. *Proc. Natl. Acad. Sci. U. S. A.* **2008**, *105*, 11188.
16. Tard, C.; Pickett, C. J. *Chem. Rev.* **2009**, *109*, 2245.
17. De Lacey, A. L.; Fernandez, V. M.; Rousset, M.; Cammack, R. *Chem. Rev.* **2007**, *107*, 4304.

18. Van der Waan, J. W.; Coremans, J.; Bouwens, E. C. M.; Albracht, S. P. J.; *Biochim. Biophys. Acta* **1990**, *1041*, 101.
19. Trofanchuk, O.; Stein, M.; Gessner, C.; Lendzin, F.; Higuchi, Y.; Lubitz, W. *J. Biol. Inorg. Chem.* **2000**, *5*, 36.
20. Gessner, C.; Trofanchuck, O.; Kawagoe, K.; Higuchi, Y.; Yasuoka, N.; Lubitz, W. *Chem. Phys. Lett.* **1996**, *256*, 518.
21. Carepo, M.; Tierney, D. L.; Brondino, C. D.; Yang, T. C.; Pamplona, A; Telser, J.; Moura, I.; Moura, J. J. G.; Hoffman, B. M. *J. Am. Chem. Soc.* **2002**, *124*, 281.
22. Osz, J.; Bagyinka, C. *Biophys. J.* **2005**, *89*, 1984.
23. De Lacey, A. L.; Moiroux, J.; Bourdillon, C. *Eur. J. Biochem.* **2000**, *267*, 6560.
24. Leger, C.; Jones, A. K.; Roseboom, W.; Albracht, S. P. J.; Armstrong, F. A.*Biochemistry* **2002**, *41*, 15736.
25. Niu, S. Q.; Thomson, L. M.; Hall, M. B. *J. Am. Chem. Soc.* **1999**, *121*, 4000.
26. Foerster, S.; Stein, M.; Brecht, M.; Ogata, H.; Higuchi, Y.; Lubitz, W. *J. Am. Chem. Soc.* **2003**, *125*, 83.
27. Pardo, A.; De Lacey, A. L.; Fernandez, V. M.; Fan, H. J.; Fan, Y. B.; Hall, M. B. *J. Biol. Inorg. Chem.* **2006**, *11*, 286.
28. Brecht, M.; van Gastel, M.; Buhrke, T.; Friedrich, B.; Lubtiz, W. *J. Am. Chem. Soc.* **2003**, *125*, 13075.
29. Siegbahn, P. E. M. *Advances in Inorganic Chemistry – Including Bioinorganic Studies, Vol 56*; Elsevier Academic Press Inc: San Diego, 2004; p 101.
30. Foerster, S.; van Gastel, M.; Brecht, M; Lubtiz, W. *J. Biol. Inorg. Chem.* **2005**, *10*, 51.
31. De Gioia, L.; Fantucci, P.; Guigliarelli; B.; Bertrand, P. *Int. J. Quantum Chem.* **1999**, *73*, 187.
32. Volbeda, A.; Fontecilla–Camps J. C. *Coord. Chem. Rev.* **2005**, *249*, 1609.
33. Leger, C.; Jones, A. K.; Albracht, S. P. J.; Armstrong, F. A. *J. Phys. Chem. B* **2002**, *106*, 13058.
34. Foerster, S.; Stein, M.; Brecht, M.; Ogata, H.; Higuchi, Y.; Lubitz, W. *J. Am. Chem. Soc.* **2003**, *125*, 83.
35. Fichtner, C.; van Gastel, M.; Lubitz, W. *Phys. Chem. Chem. Phys.* **2003**, *5*, 5507.
36. Halcrow, M. A.; Christou, G. *Chem. Rev.* **1994**, *94*, 2421.

37. Mullar, J. A.; Hebd, C. R. *Seances, Acad. Sci.*; **1887**, *104*, 992.

38. Manchot, W.; Merry, E., Woringer, P. *Chem. Ber.*, **1912**, *45*, 2879.

39. Kenney, D. J.; Flynn, T. P.; Gallini, J. B. *J. Inorg. Nucl. Chem.*, **1961**, *20*, 75.

40. Cotton, F. A.; Monchamp, R. R.; Henry, R. J. M.; Young, R. C.; *J. Inorg. Nucl. Chem.*, **1959**, *10*, 28.

41. (a) Jiang, J.; Koch, S. A. *Angew. Chem., Int. Ed.* **2001**, *40*, 2629–2631. (b) Jiang, J.; Maruani, M.; Sclaimanzadeh, J.; Lo, W.; Koch, S. A.; Millar, M. *Inorg. Chem.* **2009**, *48*, 6359.

42. Chiarella, G. M.; Melgarejo, D. Y.; Koch, S. A. *J. Am. Chem. Soc.*, **2006**, *128*, 1416–1417.

43. Lai, C. H.; Reibenspies, J. H.; Darenbourg, M. Y.; *Angew. Chem. Int. Ed.* **1996**, *35*, 2390.

44. Osterloh, F.; Saak, W.; Haase, D.; Pohl, S. *Chem. Commun.* **1997**, 979.

45. Davies, S. C.; Evans, D. J.; Hughes, D. L.; Longhurst, S.; Sanders, J. R.*Chem. Commun.* **1999**, 1935.

46. Smith, M. C.; Barcely, J. E.; Cramer, S. P.; Davies, S. C.; Gu, W. W.; Hughes, D. L.; Longhurst, S.; Evans, D. J. *J. Chem. Soc. Dalton Trans.* **2002**, 3410.

47. Zhu, W. F.; Marr, A. C.; Wang, Q.; Neese, F.; Spencer, D. J. E.; Blake, A .J.; Cooke, P. A.; Wilson, C.; Schroder, M. *Proc. Natl. Acad. Sci. U. S. A.* **2005**, *102*, 18280.

48. Sellmann, D.; Geipel, F.; Lauderbach, F.; Heinemann, F. W.; *Angew Chem. Int. Ed.* **2002**, *41*, 632.

49. Li, Z. L.; Ohki, Y.; Tatsumi, K. *J. Am. Chem. Soc.* **2005**, *127*, 8950.

50. Chen, C. H.; Chang, Y. S.; Yang, C. Y.; Chen, T. N.; Lee, C.; Liaw, W .F. *Dalton Trans.* **2004**, 137.

51. Contakes, S. M.; Hsu, S.C. N.; Rauchfuss, T. B.; Wilson, S. R.; *Inorg. Chem.* **2002**, *41*, 4610.

52. Jiang, J. F.; Koch, S. A. *Inorg. Chem.* **2002**, *41*, 158.

53. Jiang, J. F.; Acunzo, A.; Koch, S. A. *J. Am. Chem. Soc.* **2001**, *123*, 12109.

54. Liaw, W. F.; Lee, J. H.; Gau, H. B.; Chen, C. H.; Jung, S. J.; Hung, C. H.; Chen, W. Y.; Hu, C. H.; Lee, G. H. *J. Am. Chem. Soc.* **2002**, *124*, 1680.

55. Liaw, W. F.; Lee, J. H.; Chen, C. H.; Lee, C. H.; Lee, G. H.; Peng, S. M. *J. Am. Chem. Soc.* **2000**, *122*, 488.

56. Kayal, A.; Rauchfuss, T. B. *Inorg. Chem.* **2003**, *42*, 5046.
57. Sellmann, D.; Geipel, F.; Heinemann, F. W. *Chem. Eur. J.* **2002**, *8*, 958.
58. Perra, A.; Davies, E .S.; Hyde, J. R.; Wang, Q.; McMaster, J.; Schroder, M. *Chem. Commun.* **2006**, 1103.
59. Adams, M. W. W. *Biochim. Biophys. Acta* **1990**, *1020*, 115.
60. Vignais, P. M.; Billoud, B.; Meyer, J. *Fems Microbiol. Rev.* **2001**, *25*, 455.
61. Heinekey, D. M. *J. Organomet. Chem.* **2009**, *694*, 2671.
62. Peters, J. W.; Lanzilotta, W. N.; Lemon, B. J.; Seefeldt, L. C. *Science*, **1998**, *282*, 1853.
63. Nicolet, Y.; Piras, C.; Legrand, P.; Hatchikian, C. E.; Fontecilla–Camps J. C. *Struct. Fold. Des.* **1999**, *7*, 13.
64. Nicolet, Y.; Cavazza, C.; Fontecilla–Camps, J.C. *Journal of Inorganic Biochemistry* **2002**, *91*, 1.
65. Siegbahn, P. E. M.; Tye, J. W.; Hall, M. B. *Chem. Rev.* **2007**, *107*, 4414.
66. De Lacey, A. L.; Standler, C.; Cavazza, C.; Hatchikian, E. C.; Fernandez, V. M. *J. Am. Chem. Soc.* **2000**, *122*, 11232.
67. Popescu, C. V.; Munck, E. *J. Am. Chem. Soc.* **1999**, *121*, 7877.
68. Cao, Z. X.; Hall, M. B. J. *J. Am. Chem. Soc.* **2001**, *123*, 3734.
69. Bruschi, M.; Fantucci, P.; De Dioia, L. *Inorg. Chem.* **2003**, *42*, 4773.
70. Zhou, T. J.; Mo, Y. R.; Liu, A. M.; Zhou, Z. H.; Tsai, K. R. *Inorg. Chem.* **2004**, *43*, 923.
71. Zhou, T.; Mo, Y.; Zhou, Z.; Tsai, K. *Inorg. Chem.* **2005**, *44*, 4941.
72. Bruschi, M.; Fantucci, P.; De Gioia, L. *Inorg. Chem.* **2002**, *41*, 1421.
73. Albracht, S. P. J.; Roseboom, W.; Hatchikian, E. C. *J. Biol. Inorg.Chem.* **2006**, *11*, 88.
74. Lyon, E. J.; Georgakai, I. P.; Reibenspies, J. H.; Darensbourg, M. Y. *Angew. Chem. Int. Ed.* **1999**, *38*, 3178.
75. Schmidt, M.; Contakes, S. M.; Rauchfuss T. B. *J. Am. Chem. Soc.* **1999**, *121*, 9736.
76. Le Cloirec A.; Best, S. P.; Borg, S.; Davies, S. C.; Evans, D. J.; Hughes, D. L.; Pickett, C. J. *Chem. Commun*. **1999**, 2285.
77. Gloaguen, F.; Lawrence, J. D.; Rauchfuss, T. B. *J. Am. Chem. Soc.* **2001**, *123*, 9476.
78. Nehring, J. L.; Heinekey, D. M. *Inorg. Chem.* **2003**, *42*, 4288.
79. Zhao, X.; Georgakaki, I. P.; Miller, M. L.; Mejia–Rodriguez, R.; Chiang, C. Y.; Darensbourg, M. Y. *Inorg. Chem.* **2002**, *41*, 3917.

80. Chong, D.; Georgakaki, I. P.; Mejia–Rodriguez, R.; Sanabria–Chinchilla, J.; Soriaga, M. P.; Darensbourg, M. Y. *J. Chem. Soc., Dalton Trans.* **2003**,*89*, 4158.
81. Aguirre De Carcer, I.; DiPasquale, A.; Rheingold, A. L.; Heinekey, D. M. *Inorg.Chem.* **2006**, *45*, 8000.
82. Tard, C.; Liu, X.; Ibrahim, S. K.; Bruschi, M.; De Gioia, L.; Davies, S.; Yang, X.; Wang, L. S.; Sawers, G.; Pickett, C. J. *Nature* **2005** *434*, 610.
83. Nicolet, Y.; De Lacey, A. L.; Vernde, X.; Fernandez, V. M.; Hatchikian, E.C.; Fontecilla–Camps, J. C. *J. Am. Chem. Soc.* **2001**, *123*, 1596.
84. Pandey, A. S.; Harris, T. V.; Giles, L. J.; Peters, J. W.; Szilagyi, R. K. *J. Am. Chem. Soc.* **2008**, *130*, 4533.
85. Li, H.; Rauchfuss, T. B. *J. Am. Chem. Soc.* **2002**, *124*, 726.
86. Popescu, C. V.; Münck, E. J. *J. Am. Chem. Soc.* **1999**, *121*, 7877.
87. Zirngibl, C.; Hedderich, R.; Thauer, R. K. *FEBS Lett.* **1990**, *216*, 112.
88. Thauer, R. K.; Klein, A. R.; Hartmann, G. C. *Chem. Rev.* **1996**, *96*, 3031.
89. Lyon, E. J.; Shima, S.; Buurman, G.; Chowdhuri, S.; Batschauer, A.; Steinbach, K.; Thauer, R. K. *Eur. J. Biochem.* **2004**, *271*, 195.
90. Lyon, E. J.; Sordel–Kippert, M. S.; Kauss, M.; Kahnt, J.; Thauer, R. K.; Steinbach, K.; Xie, X. L.; Verdier, L.; Griesenger, C. *Angew. Chem., Int. Ed. Engl.* **2004**, *43*, 2547.
91. Shima, S.; Lyon, E. J.; Thauer, R. K.; Mienert, B.; Bill, E. *J. Am. Chem. Soc.* **2005**, *127*, 10430.
92. Shima, S.; Pilak, O.; Vogt, S.; Schick, M.; Stagni, M. S.; Meyer–Klaucke, W.; Warkentin, E.; Thauer, R. K.; Ermler, U. *Science* **2008**, *321*, 572.
93. Hiromoto, T.; Ataka, K.; Pilak, O.; Vogt, S.; Stagni, M. S.; Meyer–Klaucke, W.; Warkentin, E.; Thauer, R. K.; Shima, S.; Ermler, U. *FEBS Lett.* **2009**, *583*, 585.
94. Wang, X.; Li, Z.; Zeng, X.; Luo, Q.; Evans, D. J.; Pickett, C. J.; Liu, X. *Chem. Commun.* **2008**, 3555.

# CHAPTER 2. Synthesis of Phosphine–Thiolate, Amine–Thiolate, and Amine–Selenate Ligands

## 2.1 Introduction

Systematic studies of coordination compounds using phenylene–bridged phosphinothiols suffered due to the lack of a general preparative route of the ligands. In 1989, an efficient method was developed for the *ortho*–lithiation of lithium thiophenolate.[1–3] Block *et al.* reported a series of substituted phosphanylarylthiols that were prepared using the reaction of lithium 2–lithiobenzenethiolate with organochlorophosphines.[4] Since this discovery, research groups have been developing new substituted phosphanylarylthiols by using substituted benzenethiol as starting materials (e.g. 4–methylbenzenethiol). A number of coordination compounds have been explored over the recent years.

However, until recently, most studies have focused on the bidentate ligand (HPS1, illustrated in **Figure II–1**).[5] Tridentate ($H_2$PS2) and tetradentate ($H_3$PS3) ligands, illustrated in **Figure II–1**, have shown to have a wide interest among scientists in the recent years.

There are several reasons for choosing a ligand such as [PS2] or [PS3] etc. First, sulfur is an excellent donor atom for a wide range of metals and, due to the low ionization energy of sulfur including the lone pairs of electrons, offers the possibility of rich sulfur–based chemistry for these complexes.[6] The main function of these ligands is to model the hydrogenase active site since the enzyme contains a rich source of sulfur which is bound to the metal active site, discussed in Chapter 1. This modeling have been extended to the second row and third row transition metals, discussed in Chapter 3, due to previous studies of promising catalytic properties. The steric hindrance provided by the aryl ring can prevent polymerization.

The sulfur atoms play an important role in the functionality of the ligand; however, the phosphorous plays an equal role in this system. Phosphorous, also, is an electron rich ligand donor atom for a wide range of metals. Despite the fact that phosphorous is not native to the enzyme systems, the additional electron donor capacity of the atom provides an extra stabilization of the metal center toward redox activity.

The chelate effect of these ligands offers greater stability than monodentate thiolate ligands. The advantages that these polydentate ligands have are stereochemistry, stoichiometry and control over the coordination number.[7]

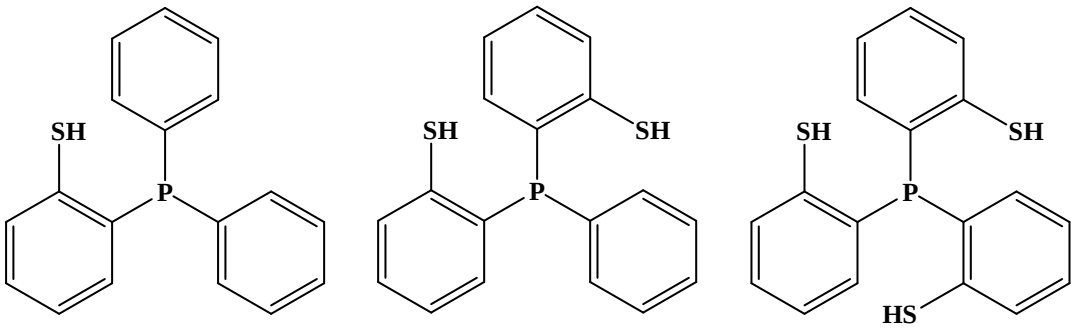


**HPS1** **$H_2$PS2** **$H_3$PS3**

**Figure II–1. The family of [PS] ligands.**

The purpose of designing the NS2 or NS3 ligands, shown in **Figure II–2**, is to obtain ligands that can mimic the H cluster of the [FeFe] hydrogenase. The framework of the [NS(e)] ligand is similar to the [PS] ligand but with two major differences. The first major difference is the replacement of the phosphorous atom with a nitrogen atom. This change is important due to the fact that nitrogen is native to the [FeFe] hydrogenase enzyme. The second difference is the addition of the methylene groups, —$CH_2$—, which adds to the flexibility of the [NS(e)] ligands versus the [PS] ligands.

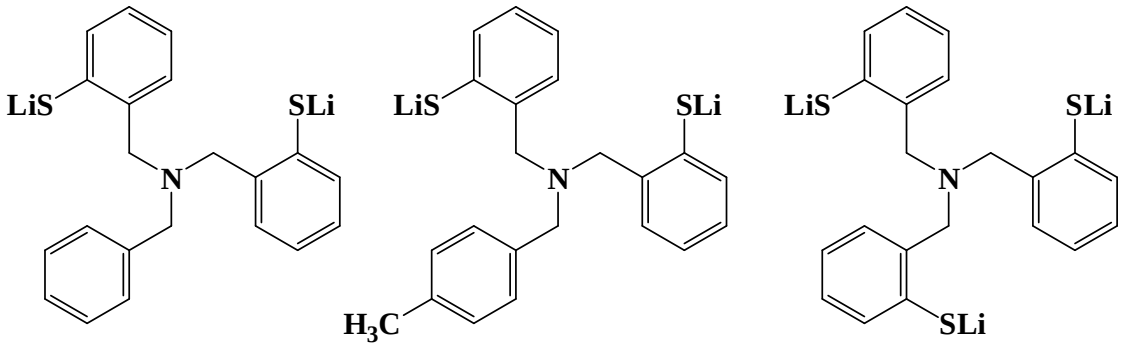


**$Li_2$NS2** **$Li_2$NS2'** **$Li_3$NS3**

**Figure II–2. The family of [NS] ligands.**

In the past, whether in the reported literature procedure or by previous students in the Koch or Millar groups, the synthesis of the [PS] and [NS(e)] ligands has not been described

thoroughly. In this chapter, the total synthesis will be discussed; the critical steps of each procedure have been investigated and have been carefully tested. Optimization of these multistep reactions has, also, been performed by using various solvents for recrystallization.

## 2.2 Experimental

All [PS] ligands were prepared by a modified literature procedure.[4]

**Synthesis of $H_2$PS2 (*bis*–[2–thiophenyl]phenylphosphine)**

In a 500 mL Schlenk flask, a solution of TMEDA (45.0 mL, 0.299 moles) and 2.5 M *n*–butyllithium (120 mL, 0.299 moles) in 200 mL of freshly distilled cyclohexane were prepared at 0 $^{o}$C (ice bath). A solution of thiophenol (15 g, 0.136 moles) in 100 mL cyclohexane was added dropwise to the TMEDA/*n*–butyllithium solution. The mixture was allowed to slowly warm to room temperature; a precipitate (white creamy slurry) was observed. After stirring overnight, the white solid was filtered, under nitrogen, *via* closed frit. The solid was washed with approximately 100 mL of distilled cyclohexane and dried under vacuum. The white solid was brought into the Dry–Box, weighed and transferred to a separate 500 mL Schlenk flask. Yield: ~31 g, 96% yield. The white solid was dissolved in freshly distilled THF (250 mL) and cooled to –78 $^{o}$C using a dry ice/acetone bath. A solution of dichlorophenylphosphine (8.8 mL, 0.065 moles) in 50 mL of freshly distilled THF was added dropwise to the THF slurry. The mixture was allowed to slowly warm to room temperature and stirred overnight. The clear orange solution was cooled to 0 $^{o}$C (ice bath) and brought to pH ~ 5 using 10% $H_2SO_4$ (aq). After acidification, the flask was opened to air. The mixture was separated using a separatory funnel. The aqueous layer was washed with diethyl ether (2 × 100 mL). The THF layer and diethyl ether layers were combined and washed with 200 mL saturated aqueous solution of NaCl. The solution was separated and the organic layer was dried using $Na_2SO_4$ and left to stir for ~2 hours, filtered and the solvent was removed by rotary evaporator to give thick green oil. The oil was further dried under vacuum to give a green residue which was recrystallized in methanol (~50 mL). The solution was left to stir for several hours, filtered, and dried. A pure white solid was obtained (16.1 g, 76% yield). $^{1}$H–NMR, $^{31}$P–NMR and $^{13}$C–NMR are shown in **Figure II–9**, **Figure II–10** and **Figure II–11** respectively. Crystal structure is shown in **Figure II–40**.

**$^{1}$H–NMR (400 MHz, $CDCl_3$) [ppm]:** 7.41–7.35 (m, *J* = 7.38, 5H, aromatic), 7.32–7.26 (td, *J* = 7.29, 2H, aromatic), 7.25–7.20 (td, *J* = 7.23, 2H, aromatic), 7.11–7.05 (td, *J* = 7.08, 2H, aromatic), 6.82–6.77 (ddd, *J* = 6.79, 2H, aromatic), 4.08 (s, 2H, –S*H*).

**$^{13}$C–NMR (100 MHz, $CDCl_3$) [ppm]:** 138.4, 138.1, 134.6, 134.5, 134.5, 134.3, 134.1, 133.9, 133.8, 130.8, 130.8, 129.8, 129.6, 129.1, 129.1, 126.3 (aromatic).

**$^{31}$P–NMR (162 MHz, $CDCl_3$) [ppm]:** –17.85 (s).

**Unit cell:** Monoclinic, $P2_1/n$, a = 7.6555(2) Å, b = 8.0505(2) Å, c = 26.6533(6) Å, $\alpha = \gamma = 90^o$, $\beta = 97.476(2)^o$, V = 1628.70(7) $Å^3$.

A colorless crystal measuring 0.45 × 0.35 × 0.25 $mm^3$ was mounted using a nylon loop and centered on the X–ray beam at 100 K. Crystals were grown from a concentrated diethyl ether solution at –20$^o$C. The accurate unit cell was obtained using reflection with $2\theta = 3.31 – 29.70^o$: a = 7.6555(2) Å, b = 8.0505(2) Å, c = 26.6533(6) Å, $\alpha = \gamma = 90^o$, $\beta = 97.476(2)^o$, V = 1628.70(7) $Å^3$. The structure was solved under a primitive monoclinic crystal system (space group $P2_1/n$) using 4238 reflections. The asymmetric unit consists of one molecule of the $H_2$PS2. The data reduction was done using CryAlisPro and the structure refinement was done with SHELXL–97 (Sheldrick). All the non–hydrogen atoms were located by Direct Methods and were refined anisotopically by a full–matrix least–squares method. The thiol protons were located using Fourier difference maps. The positions of the remaining hydrogen atoms were calculated. The crystallographic parameters and atomic coordinates for this compound are located in **Table A–1**.

**Synthesis of $H_2$PS2' (*bis*–[5–methyl–2–thiophenyl]phenylphosphine)**

In a 500 mL Schlenk flask, a solution of TMEDA (40.0 mL, 0.266 moles) and 2.5 M *n*–butyllithium (106 mL, 0.266 moles) in 200 mL of freshly distilled cyclohexane were prepared at 0 $^o$C (ice bath). A solution of *p*–methylthiophenol (15 g, 0.121 moles) in 100 mL cyclohexane was added dropwise to the TMEDA/*n*–butyllithium solution. The mixture was allowed to slowly warm to room temperature; a precipitate (white creamy slurry) was observed. After stirring overnight, the white solid was filtered, under nitrogen, *via* closed frit. The solid was washed with approximately 100 mL of distilled cyclohexane and dried under vacuum. The white solid was brought into the Dry–Box, weighed and transferred to a separate 500 mL Schlenk flask. Yield: ~28 g, 97% yield. The white solid was dissolved in freshly distilled THF (250 mL) and cooled to –78 $^o$C using a dry ice/acetone bath. A solution of dichlorophenylphosphine (8.0 mL, 0.059 moles) in 50 mL of freshly distilled THF was added dropwise to the THF slurry. The mixture

was allowed to slowly warm to room temperature and stirred overnight. The clear orange solution was cooled to 0 $^{o}$C (ice bath) and brought to pH ~ 5 using 10% $H_2SO_4$ (aq). After acidification, the flask was opened to air. The mixture was separated using a separatory funnel. The aqueous layer was washed with diethyl ether (2 × 100 mL). The THF layer and diethyl ether layers were combined and washed with 200 mL saturated aqueous solution of NaCl. The solution was separated and the organic layer was dried using $Na_2SO_4$ and left to stir for ~2 hours, filtered and the solvent was removed by rotary evaporator to give thick green oil. The oil was further dried by vacuum to give a green residue which was recrystallized in methanol (~50 mL). The solution was left to stir for several hours, filtered, and dried. A pure white solid was obtained (12.4 g, 60% yield). Crystals were grown from a concentrated solution of diethyl ether at –20 $^{o}$C. $^{1}$H–NMR, $^{31}$P–NMR and $^{13}$C–NMR are shown in **Figure II–12**, **Figure II–13** and **Figure II–14** respectively. Crystal structure is shown in **Figure II–41**.

**$^{1}$H–NMR (400 MHz, $CDCl_3$) [ppm]:** 7.40–7.34 (m, *J* = 7.38, 3H, aromatic), 7.31–7.26 (m, *J* = 7.28, 4H, aromatic), 7.07– 7.03 (dd, *J* = 7.05, 2H, aromatic), 3.94 (s, 2H, –S*H*), 2.16 (s, 6H, –C$H_3$).

**$^{13}$C–NMR (100 MHz, $CDCl_3$) [ppm]:** 136.18, 135.00, 134.94, 134.58, 134.49, 134.32, 134.30, 134.24, 134.02, 131.19, 131.15, 130.72, 129.45, 129.08, 129.00 (aromatic); 21.31, 21.29 (–*C*$H_3$).

**$^{31}$P–NMR (162 MHz, $CDCl_3$) [ppm]:** –17.16 (s).

**Unit cell:** Monoclinic, $P2_1/n$, a = 9.4007(2) Å, b = 9.5810(2) Å, c = 20.0653(5) Å, α = γ = 90$^{o}$, β = 98.492(2)$^{o}$, V = 1787.43(7) Å$^3$.

A colorless crystal measuring 0.85 × 0.40 × 0.35 mm$^3$ was mounted using a nylon loop and centered on the X–ray beam at 100K. Crystals were grown from a concentrated diethyl ether solution at –20$^{o}$C. The accurate unit cell was obtained using reflection with 2θ = 3.49 – 31.40$^{o}$: a = 9.4007(2) Å, b = 9.5810(2) Å, c = 20.0653(5) Å, α = γ = 90$^{o}$, β = 98.492(2)$^{o}$, V = 1787.43(7) Å$^3$. The structure was solved under a primitive monoclinic crystal system (space group $P2_1/n$) using 5301 reflections. The asymmetric unit consists of one molecule of the $H_2PS2'$. The data reduction was done using CryAlisPro and the structure refinement was done with SHELXL–97 (Sheldrick). All the non–hydrogen atoms were located by Direct Methods and were refined anisotopically by a full–matrix least–squares method. The thiol and methyl protons were located using Fourier difference maps. The positions of the remaining hydrogen atoms were calculated.

The crystallographic parameters and atomic coordinates for this compound are located in **Table A–2**.

**Synthesis of $H_2$POS2 (*bis*–[2–thiophenyl]oxophenylphosphine)**

In a 500 mL Schlenk flask, a solution of TMEDA (30.0 mL, 0.199 moles) and 2.5 M *n*–butyllithium (80 mL, 0.199 moles) in 200 mL of freshly distilled cyclohexane were prepared at 0 $^{o}$C (ice bath). A solution of thiophenol (10 g, 0.136 moles) in 100 mL cyclohexane was added dropwise to the TMEDA/*n*–butyllithium solution. The mixture was allowed to slowly warm to room temperature; a precipitate (white creamy slurry) was observed. After stirring overnight, the white solid was filtered, under nitrogen, *via* closed frit. The solid was washed with approximately 100 mL of distilled cyclohexane and dried under vacuum. The white solid was brought into the Dry–Box, weighed and transferred to a separate 500 mL Schlenk flask. Yield: ~21 g, 97% yield. The white solid was dissolved in freshly distilled THF (250 mL) and cooled to –78 $^{o}$C using a dry ice/acetone bath. A solution of phenylphosphonic dichloride (6.5 mL, 0.044 moles) in 50 mL of freshly distilled THF was added dropwise to the THF slurry. The mixture was allowed to slowly warm to room temperature and stirred overnight. The clear orange solution was cooled to 0 $^{o}$C (ice bath) and brought to pH ~ 5 using 10% $H_2SO_4$ (aq). After acidification, the flask was opened to air. The mixture was separated using a separatory funnel. The aqueous layer was washed with diethyl ether (2 × 100 mL). The THF layer and diethyl ether layers were combined and washed with 200 mL saturated aqueous solution of NaCl. The solution was separated and the organic layer was dried using $Na_2SO_4$ and left to stir for ~2 hours, filtered and the solvent was removed by rotary evaporator to give thick green oil. The oil was further dried by vacuum to give a green residue which was recrystallized in 2–propanol (~50 mL). The solution was left to stir for several hours, filtered, and dried. A pure white solid was obtained (8.9 g, 59% yield). $^{1}$H–NMR, $^{31}$P–NMR and $^{13}$C–NMR are shown in **Figure II–15**, **Figure II–16** and **Figure II–17** respectively.

**$^{1}$H–NMR (400 MHz, $CDCl_3$) [ppm]:** 7.68–7.58 (m, *J* = 7.63, 3H, aromatic), 7.55–7.48 (td, *J* = 7.52, 2H, aromatic), 7.46–7.36 (m, *J* = 7.42, 4H, aromatic), 7.12–7.05 (td, *J* = 7.09, 2H, aromatic), 7.00–6.91 (dd, *J* = 6.95, 2H, aromatic), 6.21 (s, 2H, –S*H*).

**$^{13}$C–NMR (100 MHz, $CDCl_3$) [ppm]:** 140.37, 140.31, 134.22, 134.09, 132.68, 132.59, 132.49, 132.47, 131.94, 131.85, 129.00, 128.87, 128.16, 127.09, 124.78, 124.66 (aromatic).

**$^{31}$P–NMR (162 MHz, $CDCl_3$) [ppm]:** 40.75 (s).

**Synthesis of $H_3PS3$ (*tris*–[2–thiophenyl]phosphine)**

In a 500 mL Schlenk flask, a solution of TMEDA (45.0 mL, 0.299 moles) and 2.5 M *n*–butyllithium (120 mL, 0.299 moles) in 200 mL of freshly distilled cyclohexane were prepared at 0 $^{o}$C (ice bath). A solution of thiophenol (15 g, 0.136 moles) in 100 mL cyclohexane was added dropwise to the TMEDA/*n*–butyllithium solution. The mixture was allowed to slowly warm to room temperature; a precipitate (white creamy slurry) was observed. After stirring overnight, the white solid was filtered, under nitrogen, *via* closed frit. The solid was washed with approximately 100 mL of distilled cyclohexane and dried under vacuum. The white solid was brought into the Dry–Box, weighed and transferred to a separate 500 mL Schlenk flask. Yield: ~31 g, 96% yield. The white solid was dissolved in freshly distilled THF (250 mL) and cooled to –78 $^{o}$C using a dry ice/acetone bath. A solution of phosphorus trichloride (3.4 mL, 0.065 moles) in 50 mL of freshly distilled THF was added dropwise to the THF slurry. The mixture was allowed to slowly warm to room temperature and stirred overnight. The clear orange solution was cooled to 0 $^{o}$C (ice bath) and brought to a pH ~ 5 using 10% $H_2SO_4$ (aq). After acidification, the flask was opened to air. The mixture was separated using a separatory funnel. The aqueous layer was washed with diethyl ether (2 × 100 mL). The THF layer and diethyl ether layers were combined and washed with 200 mL saturated aqueous solution of NaCl. The solution was separated and the organic layer was dried using $Na_2SO_4$ and left to stir for ~2 hours, filtered and the solvent was removed by rotary evaporator to give thick green oil. The oil was further dried by vacuum to give a green residue which was recrystallized in methanol (~50 mL). The solution was left to stir for several hours, filtered, and dried. A pure white solid was obtained (9.1 g, 65% yield). $^{1}$H–NMR, $^{31}$P–NMR and $^{13}$C–NMR are shown in **Figure II–18**, **Figure II–19** and **Figure II–20** respectively.

**$^{1}$H–NMR (400 MHz, $CDCl_3$) [ppm]:** 7.42–7.37 (dd, *J* = 7.40, 3H, aromatic), 7.29–7.24 (td, *J* = 7.26, 3H, aromatic), 7.13–7.07 (td, *J* = 7.10, 3H, aromatic), 6.82–6.78 (ddd, *J* = 6.80, 3H, aromatic), 4.10–4.09 (d, 4.09, 3H, –S*H*).

**$^{13}$C–NMR (100 MHz, $CDCl_3$) [ppm]:** 138.80, 138.48, 134.26, 132.96, 132.92, 131.03, 130.99, 130.12, 126.53 (aromatic).

**$^{31}$P–NMR (162 MHz, $CDCl_3$) [ppm]:** –24.39 (s).

**Synthesis of $H_3PS3'$ (*tris*–[5–methyl–2–thiophenyl]phosphine)**

In a 500 mL Schlenk flask, a solution of TMEDA (40.0 mL, 0.266 moles) and 2.5 M *n*–butyllithium (106 mL, 0.266 moles) in 200 mL of freshly distilled cyclohexane were prepared at 0 $^{o}$C (ice bath). A solution of *p*–methylthiophenol (15 g, 0.136 moles) in 100 mL cyclohexane was added dropwise to the TMEDA/*n*–butyllithium solution. The mixture was allowed to slowly warm to room temperature; a precipitate (white creamy slurry) was observed. After stirring overnight, the white solid was filtered, under nitrogen, *via* closed frit. The solid was washed with approximately 100 mL of distilled cyclohexane and dried under vacuum. The white solid was brought into the Dry–Box, weighed and transferred to a separate 500 mL Schlenk flask. Yield: ~28 g, 97% yield. The white solid was dissolved in freshly distilled THF (250 mL) and cooled to –78 $^{o}$C using a dry ice/acetone bath. A solution of phosphorous trichloride (3.1 mL, 0.035 moles) in 50 mL of freshly distilled THF was added dropwise to the THF slurry. The mixture was allowed to slowly warm to room temperature and stirred overnight. The clear orange solution was cooled to 0 $^{o}$C (ice bath) and brought to a pH ~ 5 using 10% $H_2SO_4$ (aq). After acidification, the flask was opened to air. The mixture was separated using a separatory funnel. The aqueous layer was washed with diethyl ether (2 × 100 mL). The THF layer and diethyl ether layers were combined and washed with 200 mL saturated aqueous solution of NaCl. The solution was separated and the organic layer was dried using $Na_2SO_4$ and left to stir for ~2 hours, filtered and the solvent was removed by rotary evaporator to give a thick green oil. The oil was further dried by vacuum to give a green residue which was recrystallized in methanol (~50 mL). The solution was left to stir for several hours, filtered, and dried. A pure white solid was obtained (8.1 g, 57% yield). $^{1}$H–NMR, $^{31}$P–NMR and $^{13}$C–NMR are shown in **Figure II–21**, **Figure II–22** and **Figure II–23** respectively.

**$^{1}$H–NMR (400 MHz, $CDCl_3$) [ppm]:** 7.34–7.28 (dd, *J* = 7.30, 3H, aromatic), 7.10–7.05 (dd, *J* = 7.08, 3H, aromatic), 6.60–6.57 (dd, *J* = 6.59, 3H, aromatic), 3.97–3.96 (d, 3.97, 3H, –S*H*), 2.18 (s, 9H, –C$H_3$).

**$^{13}$C–NMR (100 MHz, $CDCl_3$) [ppm]:** 136.29, 134.66, 134.36, 133.48, 133.44, 131.26, 131.22, 130.95 (aromatic); 21.35, 21.33 (–*C*$H_3$).

**$^{31}$P–NMR (162 MHz, $CDCl_3$) [ppm]:** –23.38 (s).

**Synthesis of NBr2 (*bis*–[2–bromobenzyl]benzylamine)**

Into a 500 mL Schlenk flask with $K_2CO_3$ (49.7 g, 360 mmoles) and 2–bromobenzylbromide (30 g, 120 mmoles), 200 mL of freshly distilled $CH_3CN$ was added by cannula under $N_2$. Benzylamine (6.55 mL, 59.9 mmoles, density: 0.981 g/mL) was added by syringe. The mixture was stirred under reflux for 8 hours. The reaction was cooled down to room temperature and the $CH_3CN$ was removed by a rotary evaporator and the solid was further dried by vacuum. The solid was extracted three times with water and diethyl ether (150:100 mL). The ether fractions were collected in a 500 mL Erlenmeyer flask and dried by adding solid $Na_2SO_4$ and stirring for ~1 hour. The solution was filtered and was placed in a preweighed 500 mL flask. The solvent was removed under vacuum to produce a yellow residue which was recrystallized by addition of methanol (~50 mL). The solution was left to stir for several hours, filtered, and dried. A pure white solid was obtained (25.5 g, 95.5%). $^{1}$H–NMR and $^{13}$C–NMR are shown in **Figure II–24** and **Figure II–25** respectively.

**$^{1}$H–NMR (400 MHz, $CDCl_3$) [ppm]:** 7.70–7.66 (dd, *J* = 7.68, 2H, aromatic), 7.52–7.48 (dd, *J* = 7.50, 2H, aromatic), 7.42–7.38 (d, *J* = 7.40, 2H, aromatic), 7.36–7.27 (m, *J* = 7.30, 5H, aromatic), 7.10–7.04 (td, *J* = 7.07, 2H, aromatic), 3.74–3.72 (s, 4H, –C*H*$_2$($C_6H_4$)Br), 3.69–3.70 (s, 2H, –C*H*$_2$($C_6H_5$)).

**$^{13}$C–NMR (100 MHz, $CDCl_3$) [ppm]:** 139.15, 138.70, 132.83, 130.50, 128.93, 128.49, 128.46, 127.55, 127.25, 124.51 (aromatic); 58.82 (–*C*H$_2$($C_6H_5$)) 57.80 (–C*H*$_2$($C_6H_4$)Br).

**Synthesis of $Li_2$NS2 (litho–(*bis*[2–thiobenzyl]benzylamine))**

In a 500 mL Schlenk flask, NBr2 (25.5 g, 57.2 mmoles) was dissolved in 250 mL of freshly distilled diethyl ether and the solution was cooled to –78$^{o}$C (dry ice/acetone); the solution becomes yellow when dissolved. In a Schlenk graduated cylinder, 2.5 M *n*–butyllithium (46 mL, 115 mmoles) was measured and added dropwise to the NBr2 solution. Red vapor was seen above the yellow solution. The reaction was allowed to stir at –78$^{o}$C for approximately 30 minutes. The dry ice/acetone bath was removed and the solution was brought to room temperature to speed up the reaction, which resulted in the solution turning clear orange. The solution was brought back to –78 $^{o}$C and sulfur powder (3.67 g, 115 mmoles) was slowly added via addition funnel. The solution was allowed to stir at –78 $^{o}$C to room temperature overnight. The off–white precipitate that formed was filtered, via closed frit, and washed with distilled diethyl ether and dried under vacuum. This compound is sensitive to air forming disulfide, which is yellow in color. This

compound was brought into the Dry–Box, weighed, and stored (15.8 g, 76%). $^{1}$H–NMR and $^{13}$C–NMR are shown in **Figure II–30** and **Figure II–31** respectively.

**$^{1}$H–NMR (400 MHz, DMSO–$d_6$) [ppm]:** 7.49–7.45 (d, *J* = 7.47, 2H, aromatic), 7.40–7.35 (d, *J* = 7.38, 2H, aromatic), 7.31–7.24 (t, *J* = 7.28, 2H, aromatic), 7.20–7.13 (t, *J* = 7.17, 1H, aromatic), 7.07–7.03 (dd, *J* = 7.05, 2H, aromatic), 6.56–6.49 (td, *J* = 6.53, 2H, aromatic), 6.47–6.41 (td, *J* = 6.45, 2H, aromatic), 3.61–3.58 (s, 2H, –C*H*$_2$($C_6H_5$)), 3.58–3.56 (s, 4H, –C*H*$_2$($C_6H_4$)Br).

**$^{13}$C–NMR (100 MHz, DMSO–$d_6$) [ppm]:** 158.04, 141.64, 139.97, 133.92, 127.99, 127.48, 126.03, 124.25, 123.22, 116.06 (aromatic); 58.85 (–*C*H$_2$($C_6H_5$)); 58.72 (–*C*H$_2$($C_6H_4$)Br).

**Synthesis of NBr2' (*bis*–[2–bromobenzyl]4–methylbenzylamine)**

Into a 500 mL Schlenk flask with $K_2CO_3$ (49.7 g, 360 mmoles) and 2–bromobenzylbromide (30 g, 120 mmoles), 200 mL of freshly distilled $CH_3CN$ was added by cannula under $N_2$. 4–methylbenzylamine (7.64 mL, 60.0 mmoles, density: 0.952 g/mL) was added by syringe. The mixture was stirred under reflux for 8 hours. The reaction was cooled down to room temperature and the $CH_3CN$ was removed by a rotary evaporator and was further dried by vacuum. The solid was extracted three times with water and diethyl ether (150:100 mL). The ether fractions were collected in a 500 mL Erlenmeyer flask and dried by adding solid $Na_2SO_4$, and stirring for ~1 hour. The solution was filtered and was placed in a preweighed 500 mL flask. The solvent was removed under vacuum to produce a yellow residue which was recrystallized by addition of methanol (~50 mL). The solution was left to stir for several hours, filtered, and dried. A pure white solid was collected (21.3 g, 77.4%). Crystals were grown from layering the yellow residue with methanol and allowed to stand for two weeks. $^{1}$H–NMR and $^{13}$C–NMR are shown in **Figure II–26** and **Figure II–27** respectively. The crystal structure is shown in **Figure II–43**.

**$^{1}$H–NMR (400 MHz, $CDCl_3$) [ppm]:** 7.70–7.65 (dd, *J* = 7.68, 2H, aromatic), 7.52–7.47 (dd, *J* = 7.49, 2H, aromatic), 7.32–7.26 (td, *J* = 7.29, 4H, aromatic), 7.14–7.10 (d, *J* = 7.12, 2H, aromatic), 7.09–7.03 (td, *J* = 7.07, 2H, aromatic), 3.72 (s, 4H, –C*H*$_2$($C_6H_4$)Br), 3.64 (s, 2H, –C*H*$_2$($C_6H_4$)$CH_3$), 2.32 (s, 3H, –C*H*$_3$).

**$^{13}$C–NMR (100 MHz, $CDCl_3$) [ppm]:** 138.79, 136.80, 135.98, 132.79, 130.45, 129.18, 128.90, 128.39, 127.53, 124.48 (aromatic); 58.48 (–*C*H$_2$($C_6H_4$)Br); 57.69 (–*C*H$_2$($C_6H_4$)$CH_3$); 21.32, 21.30 (–*C*H$_3$).

**Unit cell:** Monoclinic, $P2_1/c$, a = 7.5884(4) Å, b = 29.730(2) Å, c = 8.8523(4) Å, α = γ = 90°, β = 94.891(5)°, V = 1989.8(2) Å$^3$.

A colorless crystal measuring 0.90 × 0.70 × 0.40 mm$^3$ was mounted using a nylon loop and centered on the X–ray beam at 100K. Crystals were grown from layering methanol to the reaction flask, which was left undisturbed for one week. The accurate unit cell was obtained using reflection with 2θ = 3.39 – 32.78°: a = 7.5884(4) Å, b = 29.730(2) Å, c = 8.8523(4) Å, α = γ = 90°, β = 94.891(5)°, V = 1989.8(2) Å$^3$. The structure was solved under a primitive monoclinic crystal system (space group $P2_1/c$) using 6147 reflections. The asymmetric unit consists of one molecule of the NBr2'. The data reduction was done using CryAlisPro and the structure refinement was done with SHELXL–97 (Sheldrick). All the non–hydrogen atoms were located by Direct Methods and were refined anisotopically by a full–matrix least–squares method. The positions of the hydrogen atoms were calculated. The crystallographic parameters and atomic coordinates for this compound are located in **Table A–3**.

**Synthesis of $Li_2$NS2' (litho–(*bis*–[2–thiobenzyl]4–methylbenzylamine))**

In a 500 mL Schlenk flask, NBr2' (21.3 g, 46.4 mmoles) was dissolved in 250 mL of freshly distilled diethyl ether and the solution was cooled to –78 °C (dry ice/acetone); the solution becomes yellow when dissolved. In a Schlenk graduated cylinder, 2.5 M *n*–butyllithium (37 mL, 92.8 mmoles) was measured and added dropwise to the NBr2' solution. Red vapor was seen above the yellow solution. The reaction was allowed to stir at –78 °C for approximately 30 minutes. The dry ice/acetone bath was removed and the solution was brought to room temperature to speed up the reaction, which resulted in the solution turning clear orange. The solution was brought back to –78 °C and sulfur powder (2.97 g, 92.8 mmoles) was slowly added via addition funnel. The solution was allowed to stir at –78°C to room temperature overnight. The off–white precipitate that formed was filtered, via closed frit, and washed with distilled diethyl ether and dried by vacuum. This compound is sensitive to air forming disulfide, which is yellow in color. The product was brought into the Dry–Box, weighed, and stored (12.1 g, 69.0%). $^1$H–NMR and $^{13}$C–NMR are shown in **Figure II–32** and **Figure II–33** respectively.

**$^1$H–NMR (400 MHz, DMSO–$d_6$) [ppm]:** 7.68–7.60 (d, *J* = 7.64, 2H, aromatic), 7.44–7.40 (m, *J* = 7.42, 2H, aromatic), 7.37–7.32 (d, *J* = 7.34, 2H, aromatic), 7.07–7.03 (d, *J* = 7.05, 2H, aromatic), 6.82–6.77 (m, *J* = 6.80, 4H, aromatic), 4.00 (s, 4H, –C$H_2$($C_6H_4$)Br), 3.79 (s, 2H, –C$H_2$($C_6H_4$)$CH_3$), 2.26 (s, 3H, –C$H_3$).

**$^{13}$C–NMR (100 MHz, DMSO–$d_6$) [ppm]:** 158.03, 140.05, 138.51, 134.93, 133.88, 128.57, 127.52, 124.24, 123.20, 116.04 (aromatic); 64.88 (–*C*$H_2$($C_6H_4$)$CH_3$); 58.70, 58.59(–*C*$H_2$($C_6H_4$)SLi); 20.65 (–*C*$H_3$).

**Synthesis of NBr3 (*tris*–[2–bromobenzyl]amine)**

In a 500 mL beaker, 2–bromobenzylbromide (30 g, 120 mmoles) was dissolved in 200 mL of absolute ethanol. Ammonium hydroxide (6.31 g, 180 mmoles) was added to the ethanol solution. The mixture was allowed to stir for 24 hours which produced a white powder. The white solid was filtered, washed with absolute ethanol, and air dried (17.8 g, 94.2%). $^1$H–NMR and $^{13}$C–NMR are shown in **Figure II–28** and **Figure II–29** respectively. The crystal structure is shown in **Figure II–44**.

**$^1$H–NMR (400 MHz, $CDCl_3$) [ppm]:** 7.67–7.61 (dd, *J* = 7.64, 3H, aromatic), 7.53–7.48 (dd, *J* = 7.50, 3H, aromatic), 7.30–7.23 (td, *J* = 7.27, 3H, aromatic), 7.11–7.04 (td, *J* = 7.08, 3H, aromatic), 3.80 (s, 6H, –C*H*$_2$($C_6H_4$)Br).

**$^{13}$C–NMR (100 MHz, $CDCl_3$) [ppm]:** 138.37, 132.88, 130.40, 128.54, 127.56, 124.51 (aromatic); 58.28 (–*C*$H_2$($C_6H_4$)Br).

**Unit cell:** Triclinic, *P*–1, a = 7.6219(2) Å, b = 9.0494(3) Å, c = 14.5748(4) Å, α = 79.071(3)$^o$, β = 81.768(2)$^o$, γ = 85.510(3)$^o$, V = 975.52(5) Å$^3$.

A colorless crystal measuring 0.65 × 0.50 × 0.30 mm$^3$ was mounted using a nylon loop and centered on the X–ray beam at 100K. Crystals were grown by slow cooling of a hot concentrated acetonitrile solution. The accurate unit cell was obtained using reflection with 2θ = 3.34 – 32.81$^o$: a = 7.6219(2) Å, b = 9.0494(3) Å, c = 14.5748(4) Å, α = 79.071(3)$^o$, β = 81.768(2)$^o$, γ = 85.510(3)$^o$, V = 975.52(5) Å$^3$. The structure was solved under a primitive monoclinic crystal system (space group *P*–1) using 6394 reflections. The asymmetric unit consists of one molecule of the NBr2'. The data reduction was done using CryAlisPro and the structure refinement was done with SHELXL–97 (Sheldrick). All the non–hydrogen atoms were located by Direct Methods and were refined anisotopically by a full–matrix least–squares method. The positions of the hydrogen atoms were calculated. The crystallographic parameters and atomic coordinates for this compound are located in **Table A–4**.

**Synthesis of $Li_3NS3$ (litho–(*tris*–[2–thiobenzyl]amine))**

In a 500 mL Schlenk flask, NBr3 (15.0 g, 28.6 mmoles) was dissolved in 250 mL of freshly distilled diethyl ether and the solution was cooled to –78 $^o$C (dry ice/acetone); the

solution becomes yellow when dissolved. In a Schlenk graduated cylinder, 2.5 M *n*–butyllithium (37 mL, 91.4 mmoles) was measured and added dropwise to the NBr3 solution. From the yellow solution red vapor was seen. The reaction was allowed to stir at –78 $^{o}$C for approximately 30 minutes. The dry ice/acetone bath was removed and the solution was brought to room temperature to speed up the reaction, which resulted in the solution turning clear orange. The solution was brought back to –78 $^{o}$C and sulfur powder (2.93 g, 91.4 mmoles) was slowly added via addition funnel. The solution was allowed to stir at –78 $^{o}$C to room temperature overnight. The off–white precipitate that formed was filtered, via closed frit, and washed with distilled diethyl ether and dried by vacuum. This compound is sensitive to air forming disulfide/polysulfide, which is yellow in color. This compound was brought into the Dry–Box, weighed, and stored (9.8 g, 85.2%). $^{1}$H–NMR and $^{13}$C–NMR are shown in **Figure II–34** and **Figure II–35** respectively.

**$^{1}$H–NMR (400 MHz, $D_2O$) [ppm]:** 7.30–7.20 (ddd, *J* = 7.26, 6H, aromatic), 6.95–6.87 (td, *J* = 6.91, 3H, aromatic), 6.83–6.76 (td, *J* = 6.80, 3H, aromatic), 4.20 (s, 6H, –C*H*$_2$($C_6H_4$)SLi).

**$^{13}$C–NMR (100 MHz, DMSO–$d_6$) [ppm]:** 157.66, 141.28, 133.68, 124.34, 122.94, 116.00 (aromatic); 59.95 (–*C*H$_2$($C_6H_4$)SLi).

**Synthesis of $Li_3NSe3$ (litho–(*tris*–[2–selenobenzyl]amine))**

In a 500 mL Schlenk flask, NBr3 (15.0 g, 28.6 mmoles) was dissolved in 250 mL of freshly distilled diethyl ether and the solution was cooled to –78 $^{o}$C (dry ice/acetone); the solution becomes yellow when dissolved. In a Schlenk graduated cylinder, 2.5 M *n*–butyllithium (37 mL, 91.4 mmoles) was measured and added dropwise to the NBr3 solution. From the yellow solution red vapor was seen. The reaction was allowed to stir at –78 $^{o}$C for approximately 30 minutes. The dry ice/acetone bath was removed and the solution was brought to room temperature to speed up the reaction, which resulted in the solution turning clear orange. The solution was brought back to –78 $^{o}$C and selenium powder (7.21 g, 91.4 mmoles) was slowly added via addition funnel. The solution was allowed to stir at –78 $^{o}$C to room temperature overnight. The off–white precipitate that formed was filtered, *via* closed frit, and washed with distilled diethyl ether and dried by vacuum. This compound is sensitive to air forming diselenide/polyselenide, which is yellow in color. This compound was brought into the Dry–Box, weighed, and stored (10.9 g, 69.0%). $^{1}$H–NMR and $^{13}$C–NMR are shown in **Figure II–36** and **Figure II–37** respectively.

**$^{1}$H–NMR (400 MHz, $D_2O$) [ppm]:** 7.35–7.17 (dd, *J* = 7.25, 6H, aromatic), 6.95–6.86 (t, *J* = 6.92, 3H, aromatic), 6.85–6.75 (t, *J* = 6.81, 3H, aromatic), 4.25 (s, 6H, –C*H*$_2$($C_6H_4$)SeLi).

**$^{13}$C–NMR (100 MHz, DMSO–$d_6$) [ppm]:** 156.98, 141.75, 134.12, 125.10, 123.15, 115.85 (aromatic); 64.91 (–*C*$H_2$($C_6H_4$)SeLi).

**Synthesis of $H_2S4$ (3,7–dithianoane–1,9–dithiol)**

This product was synthesized using a literature procedure.[8] The synthesis is broken into two parts.

*Part 1: Synthesis of 3,7–dithianoane–1,9–diol ($H_2O2S2$)*

A 500 mL, three–necked, round–bottomed flask is fitted with a reflux condenser which was attached to a $N_2$ inlet, contained a magnetic stir bar and sealed off with septa. The flask was flushed with $N_2$ and absolute ethanol (200 proof) was added. Septum was removed and 5.75 grams (250 mmol) of sodium metal was added to the ethanol solution cautiously. After the sodium dissolves, the solution was heated to about 50 $^{o}$C and 13.5 g (125 mmol) of 1,3–propanedithiol was added dropwise *via* cannula. To the ethanol solution, 20.1 g (250 mmol) of 2–chloroethanol was added dropwise and the mixture was refluxed for four hours. The mixture was allowed to cool to room temperature and filtered. The solvent was removed on a rotary evaporator to produce a clear viscous liquid. The product was purified by distillation at low pressure. Yield: 18.2 g, 73.6%. $^{1}$H–NMR is shown in **Figure II–38**.

**$^{1}$H–NMR (400 MHz, $CDCl_3$) [ppm]:** 3.66–3.57 (q, *J* = 3.62, 4H), 3.40–3.34 (t, *J* = 3.37, 2H), 2.63–2.51 (dt, *J* = 2.57, 8H), 1.82–1.71 (q, *J* = 1.77, 2H).

*Part 2: Synthesis of 3,7–dithianoane–1,9–dithiol*

In a 1000 mL, round–bottomed flask equipped with a reflux condenser and a magnetic stir bar was placed 18.0 g (90.7 mmol) of 3,7–dithianoane–1,9–diol, 13.8 g (181 mmol) of thiourea, and 94 mL of concentrated HCl. The mixture was stirred and refluxed for twelve hours. The resulting solution was cooled to 0 $^{o}$C using an ice bath. Potassium hydroxide 34.1 g (608 mmol) was dissolved in 400 mL of distilled water and added to the mixture cautiously. The resulting mixture was refluxed for three hours. The solution was cooled to room temperature and was acidified with dilute HCl. The solution was extracted with 300 mL of diethyl ether and dried over anhydrous magnesium sulfate. The solution was filtered and the solvent was removed using a rotary evaporator producing a clear off–yellow liquid. The product was purified by distillation at low pressure. Yield: 11.7 g, 55.9%. $^{1}$H–NMR is shown in **Figure II–39**.

**$^1$H–NMR (400 MHz, $CDCl_3$) [ppm]:** 2.70–2.65 (m, *J* = 2.67, 8H), 2.61–2.54 (t, *J* = 2.58, 4H), 1.85–1.74 (p, *J* = 1.79, 2H), 1.72–1.66 (m, *J* = 1.70, 2H)

## 2.3 Results and Discussion

### 2.3.1 Synthesis of [PS] Ligands

**Step 1: Ortholithiation of Substituted Benzenethiol Derivatives**

The following explanation can be used for any of the substituted benzenethiol derivatives. Cyclohexane, TMEDA and THF were freshly distilled prior to any synthetic workup. Working under a dinitrogen atmosphere and in the absence of light; the substituted benzenethiol was dissolved in freshly distilled cyclohexane and cooled to 0 $^oC$ (ice water bath). In the case of 4–methylbenzenethiol, the thiol becomes insoluble when cooled to 0 $^oC$; hence the solution was cooled to approximately 15 $^oC$ for the thiol compound to remain in solution. Approximately 2.2 molar equivalents of TMEDA and of 2.5 M *n*–BuLi were added and cooled to 0 $^oC$. The substituted benzenethiol solution was added dropwise to the TMEDA/*n*–BuLi solution. The mixture was stirred overnight and a yellow–white precipitate was observed. The dilithiated substituted benzenethiolate salt, which is pyrophoric, was filtered under a dinitrogen atmosphere. Exposure of the dilithiated substituted benzenethiolate salt to air will result in an exothermic reaction which results in the solid changing from off–white to black. The resulting off–white solid was washed with distilled cyclohexane and dried under vacuum. The product was taken into the Dry–Box where the product was weighed and transferred to a separate flask. The product should not be kept in the Dry–Box for longer than two days. The product is unstable even under Dry–Box environment.

**Step 2: Synthesis of $H_x$[P(=O)Sy] Ligands (where x = y = 2; x = y = 3)**

The following explanation can be used for any of the dilithiated substituted benzenethiolate salt derivatives. All manipulations were done under a dinitrogen atmosphere. The off–white dilithiated substituted benzenethiolate salt was dissolved in freshly distilled THF. The solution was cooled to –78 $^oC$ using a dry ice/acetone bath. Dichlorophenylphosphine ($H_2$PS2 or $H_2$PS2'), trichlorophosphine ($H_3$PS3 or $H_3$PS3') or phenylphosphonic dichloride ($H_2$POS2) was syringed into freshly distilled THF solution, which is cooled to –78 $^oC$. The phosphine solution was added to the dilithiated substituted benzenethiolate salt solution dropwise

and the mixture was stirred overnight. The solution was brought to room temperature as the reaction proceeded overnight. The transparent solution, the color can range from orange to a dark red depending on the concentration of the solution, was cooled to 0 $^{o}$C using an ice water bath. A 10% aqueous solution of sulfuric acid ($H_2SO_4$) in degassed water was added to the reaction mixture until pH 5. The volume of acid solution depended on the dilithiated substituted benzenethiolate salt used. Addition of the acid solution was a critical step, allowing the pH to become lower than 5 resulted in either no product or low yields due to the protonation of the phosphorous atom.

Once the solution was at pH 5, all manipulations at this point could safely be carried out under air. The reaction mixture was opened to the air and extracted. The organic (THF) layer was collected and stored. The aqueous layer was washed twice with anhydrous diethyl ether. All organic layers were combined. A brine solution, a saturated aqueous solution of sodium chloride, was added to the organic layers that were collected. The brine solution was used to remove any micelles that could or had formed in the mixture. The mixture was stirred after which it was extracted and the organic layer was collected once again. The organic solution was dried using anhydrous sodium sulfate. The sodium sulfate was filtered off and the filtrate was place on the rotary evaporator until a green oil was observed. The oil was treated with methanol and stirred overnight. The resulting white solid was filtered, washed with cold methanol and dried by vacuum. Due to the hydrogen bonding of the $H_2$POS2, 2–propanol was used instead of methanol for recrystallization. Yields varied depending on which reaction that was performed; however, the yields ranged from 50% to 80%. The products were tested for purity using $^{1}$H–NMR and $^{31}$P–NMR. Various solvents were used in order to maximize the yields of these [PS] ligands, which is described in **Table II–1**. 2–propanol gave the highest yield in all cases.

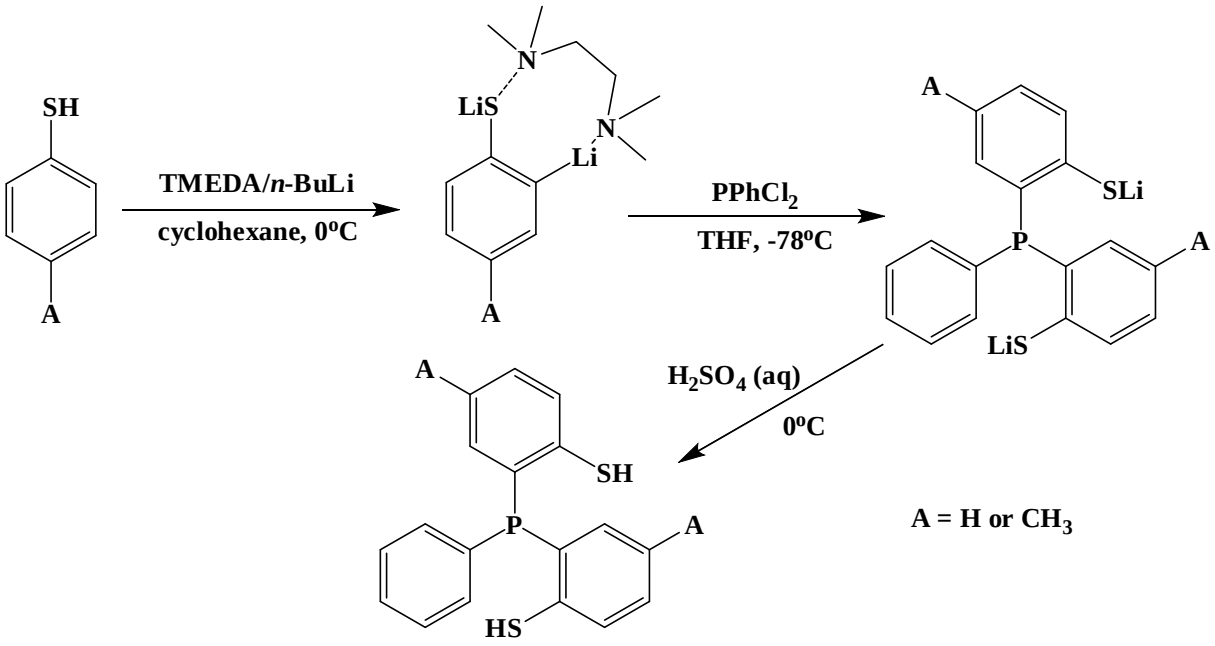


**Figure II–3. Overall synthesis of $H_2$PS2 and $H_2$PS2'.**

| Table II–1. Optimization of Yields for [PS] Ligands Using Different Solvents for Recrystallization. | | |
|---|---|---|
| **Ligand** | **Solvent** | **% Yield** |
| $H_2$PS2 | Methanol | 76 |
| | Ethanol | 79 |
| | 2–Propanol | 80 |
| $H_2$PS2' | Methanol | 60 |
| | Ethanol | 72 |
| | 2–Propanol | 76 |
| $H_3$PS3 | Methanol | 65 |
| | Ethanol | 68 |
| | 2–Propanol | 72 |
| $H_3$PS3' | Methanol | 57 |
| | Ethanol | 63 |
| | 2–Propanol | 71 |
| $H_2$POS2 | Methanol | N/A |
| | Ethanol | N/A |
| | 2–Propanol | 59 |

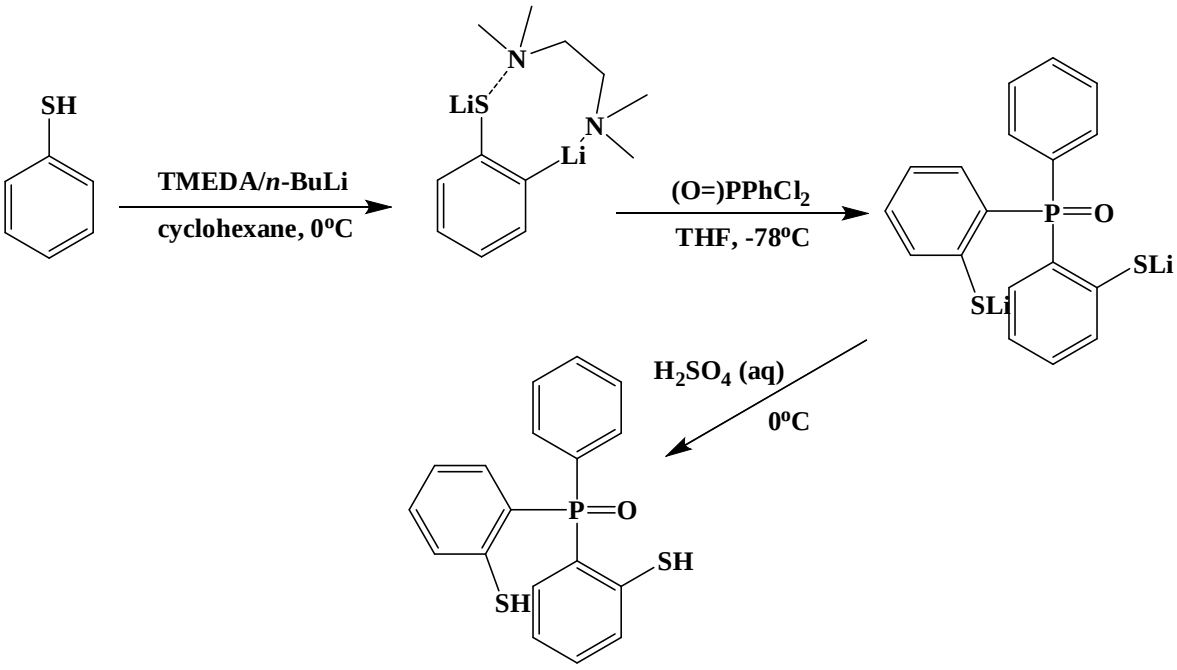


**Figure II–4. Overall synthesis of $H_2POS2$.**

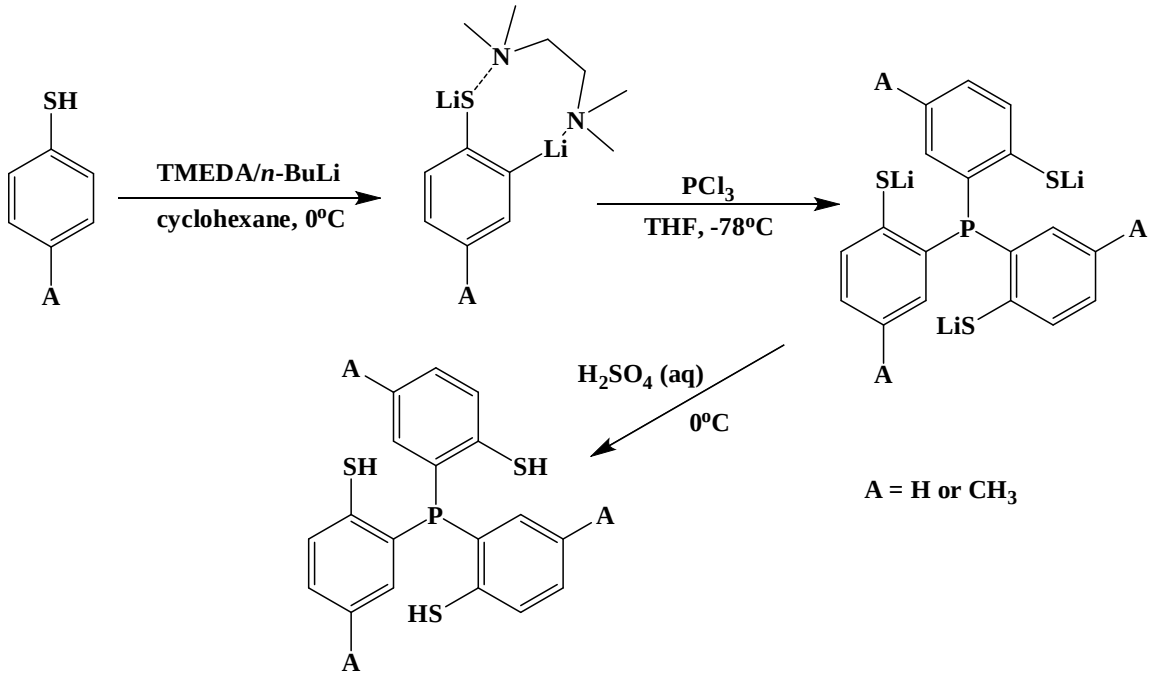


**Figure II–5. Overall synthesis of $H_3PS3$ and $H_3PS3'$.**

### 2.3.2 Synthesis of [NS] and [NSe] ligands

**Part 1: Synthesis of NBr2 and NBr2' compounds**

The following explanation can be used for of the any substituted primary amines. All manipulations were carried out under dinitrogen atmosphere. A six molar excess of potassium carbonate ($K_2CO_3$) and two molar excess of 2–bromobenzylbromide were dissolved in freshly distilled $CH_3CN$. Benzylamine (NBr2) or 4–methylbenzylamine (NBr2') was added dropwise to the potassium carbonate/2–bromobenzylbromide mixture followed by reflux. As the reaction proceeded a white powder was observed which was identified to be potassium bromide, KBr. The solution was cooled to room temperature and the $CH_3CN$ was removed using a rotary evaporator. The solid was extracted using a water/diethyl ether mixture (1.5:1). After each extraction, the diethyl ether layers were combined. The organic layer (diethyl ether layer) was dried using anhydrous sodium sulfate. The sodium sulfate was filtered off and the filtrate was placed on the rotary evaporator and the solvent removed, which produced a light yellow oil. Methanol was added and the resulting mixture was stirred overnight. A white powder was observed, which was filtered off and washed with methanol. Yields varied depending on the starting primary amine; however, yields ranged from 75% to 90%. The products were tested for purity by $^1$H–NMR.

**Part 2: Synthesis of $Li_2$NS2 and $Li_2$NS2' ligands**

The following explanation can be used for any substituted [NBr] compounds. All manipulations were carried out under dinitrogen atmosphere. NBr2 or NBr2' was partially dissolved in freshly distilled diethyl ether. The flask was cooled to –78 $^o$C using a dry ice/acetone bath. Approximately 2.2 molar excess of 2.5M *n*–BuLi was measured and transferred, dropwise, *via* cannula to the [NBr]/ether solution. As the *n*–BuLi was transferred, the yellow solution became red and a red vapor was observed, which was identified as elemental bromine. The reaction was stirred at –78 $^o$C for several minutes. The dry ice/acetone bath was removed and the solution was allowed to return to room temperature to speed up the reaction. As the reaction proceeded the NBr2 or NBr2' completely dissolved in the diethyl ether. Once at room temperature the solution was left to stir. The flask was then placed back at –78 $^o$C and 2.2 molar excess of elemental sulfur, $S_8$, was slowly added. The sulfur did not immediately dissolve in the diethyl ether. Upon completion of the addition of sulfur, the mixture was allowed to stir overnight leaving the reaction to slowly return to room temperature. Leaving the solution to stir

for longer periods of time resulted in decomposition and/or polymerization of the desired product. The next day, an off–white precipitate was observed and was filtered. The off–white solid was washed twice with distilled diethyl ether. The solid was dried *in vacuo* and transferred to the Dry Box where it was weighed and stored. This procedure was also performed by substituting selenium for sulfur.

**Part 3: Synthesis of NBr3**

Manipulations of this procedure can be done in the air. 2–bromobenzylbromide was dissolved in absolute ethanol. Approximately 1.5 molar excess of ammonium hydroxide was added slowly, using a glass pipette, to the ethanol solution. The solution was stirred for twenty–four hours, which resulted in a white precipitate. Leaving the solution to stir for longer periods of time can result in higher yields. Yields after twenty–four hours ranged from 75% to 85%. Yields after thirty–six to forty–eight hours ranged from 85% to 96%. The white solid was collected by filtration and washed with absolute ethanol. The solid was air dried, weighed and can be stored under air.

**Part 4: Synthesis of $Li_3NS3$ and $Li_3NSe3$**

All manipulations were carried out under dinitrogen atmosphere. NBr3 was partially dissolved in freshly distilled diethyl ether. The flask was cooled to –78 $^{o}$C using a dry ice/acetone bath. Approximately 3.3 molar excess of 2.5 M *n*–BuLi was measured and transferred, dropwise, *via* cannula to the NBr3/ether solution. As the *n*–BuLi was being transferred the yellow solution became red and a red vapor was observed, which was identified to be elemental bromine. The reaction was stirred at –78 $^{o}$C for several minutes. The dry ice/acetone bath was removed and the solution was allowed to return to room temperature to speed up the reaction. As the reaction proceeded, the NBr3 completely dissolved in the diethyl ether. Once at room temperature the solution was left to stir. The flask was then placed back at –78 $^{o}$C and 3.3 molar excess of elemental sulfur, $S_8$, was slowly added. The sulfur did not immediately dissolve in diethyl ether. Upon completion of the addition of sulfur the mixture was allowed to stir overnight leaving the reaction to slowly return to room temperature. Unlike the NBr3 procedure, leaving the solution to stir for longer periods of time resulted in decomposition and/or polymerization of the desired product. The next day an off–white precipitate was observed and filtered. The off–white solid was washed twice with distilled diethyl ether, dried *in*

*vacuo* and transferred to the Dry Box where it was weighed and stored. This procedure was also performed by substituting selenium for sulfur.

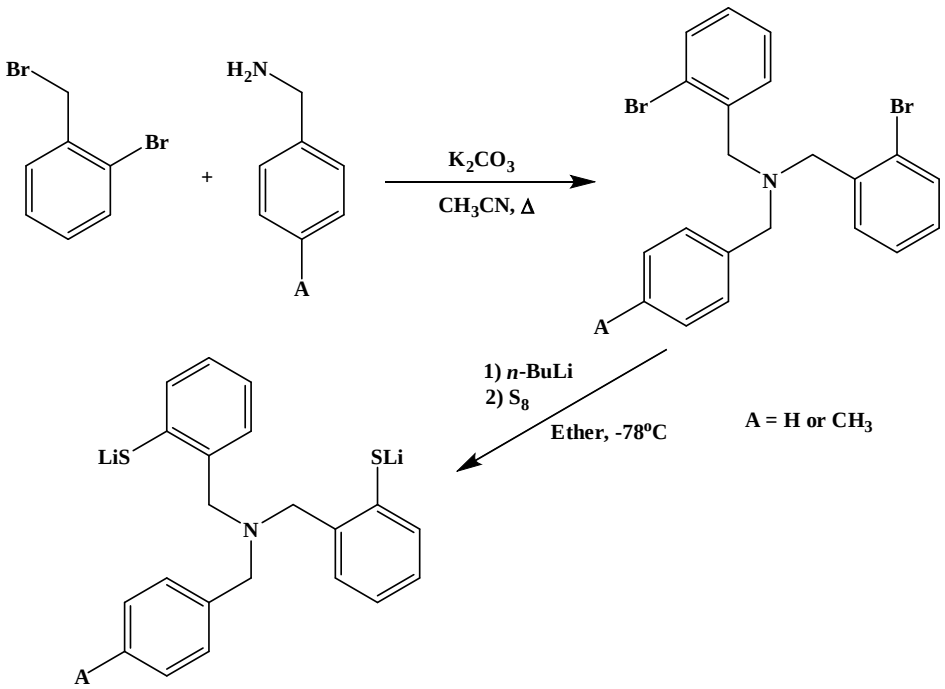


**Figure II–6. Overall synthesis of $Li_2NS2$ and $Li_2NS2'$.**

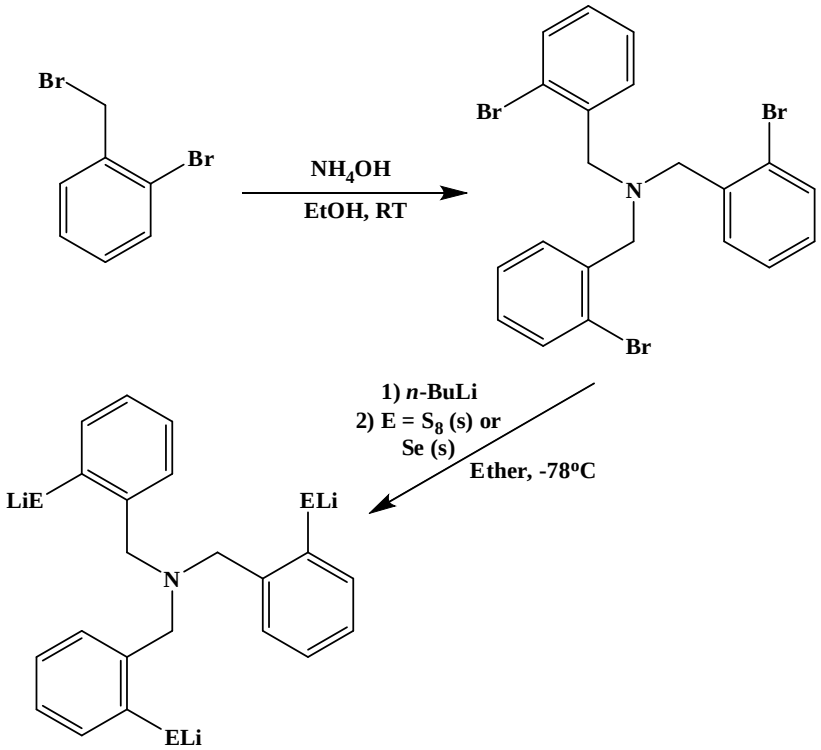


**Figure II–7. Overall Synthesis of $Li_3NS3$ and $Li_3NSe3$.**

### 2.3.3 Synthesis of $H_2S4$ (3,7–dithianoane–1,9–dithiol)

**Part 1: Synthesis of 3,7–dithianoane–1,9–diol**

The system was flushed with dinitrogen and a two molar excess of sodium metal was slowly added to the ethanol solution. Once the sodium metal had dissolved the solution was heated to approximately 50 $^{o}$C and approximately one molar excess of 1,3–propandithiol was added dropwise *via* cannula followed by the addition of a two molar excess of 2–chloroethanol. As the reaction proceeded a white powder was observed, which was identified as sodium chloride (NaCl). The mixture was cooled to room temperature and filtered. The filtrate was collected and the solvent was removed using a rotary evaporator. This resulted in a clear viscous liquid which was purified by distillation at low pressure to give the desired product. The approximate percent yield for this reaction is 75%.

**Part 2: Synthesis of 3,7–dithianoane–1,9–dithiol**

Thiourea and 3,7–dithianoane–1,9–diol were dissolved in concentrated hydrochloric acid (HCl). The mixture was stirred and refluxed. After refluxing, the solution was cooled to 0 $^{o}$C and an aqueous solution of potassium hydroxide was added cautiously to the reaction mixture. The resulting mixture was reflux for additional time. The reaction was cooled to room temperature and acidified with dilute hydrochloric acid until a pH 4 was achieved. Diethyl ether was added to the mixture and stirred for several minutes. The organic layer was extracted, collected and dried using anhydrous magnesium sulfate. The solution was filtered and the solvent was removed using a rotary evaporator which produced a clear off–yellow liquid. The product was purified by distillation at low pressure to afford clear oil. The approximate percent yield of this reaction was 55%.

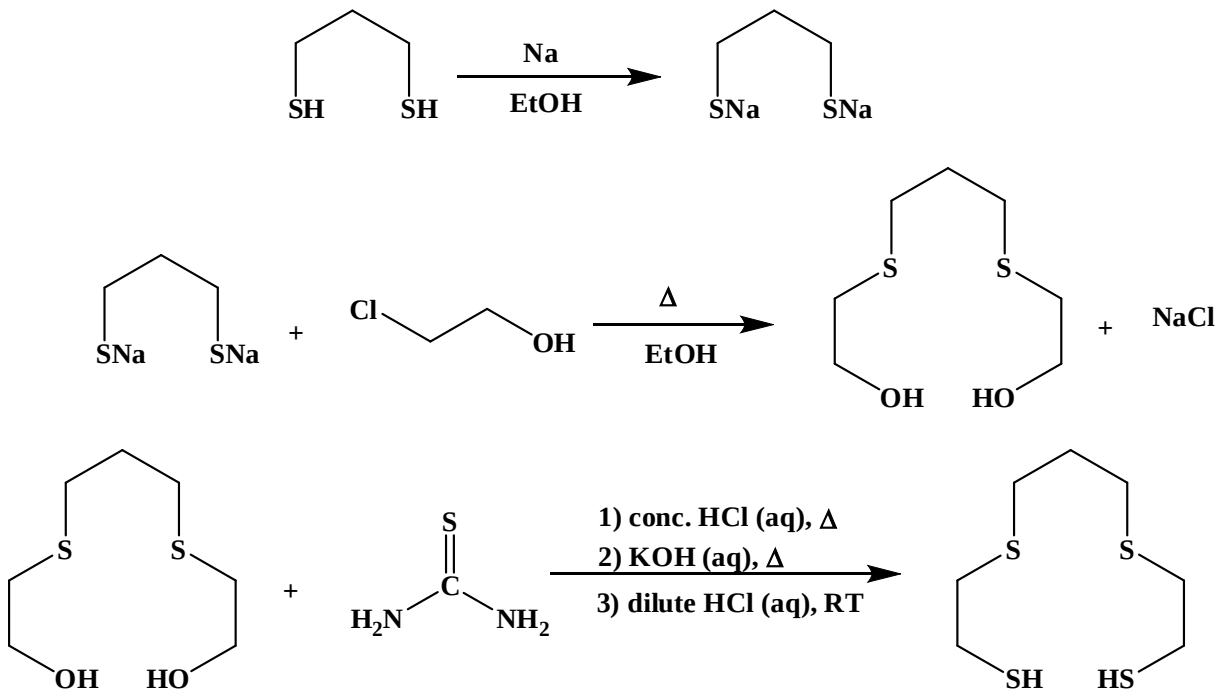


**Figure II–8. Overall Synthesis of $H_2S4$.**

### 2.3.4 NMR Spectra of Compounds and Ligands

In the next three sections are the NMR spectra of the compounds and ligands that were described in the experimental section (Section 2.2). In the $^1$H–NMR spectra for PS3 (**Figure II–12**) and PS3' (**Figure II–15**) the –SH peak shows a doublet, which shows the –SH is split by the phosphorous atom. In the $^1$H–NMR spectrum for POS2 (**Figure II–9**) the –SH peak is shifted downfield relative to the –SH peaks for the PS2, PS3 etc. due to the presence of the electronegative oxygen atom.

### 2.3.4.1 NMR Spectra of [PS] Ligands

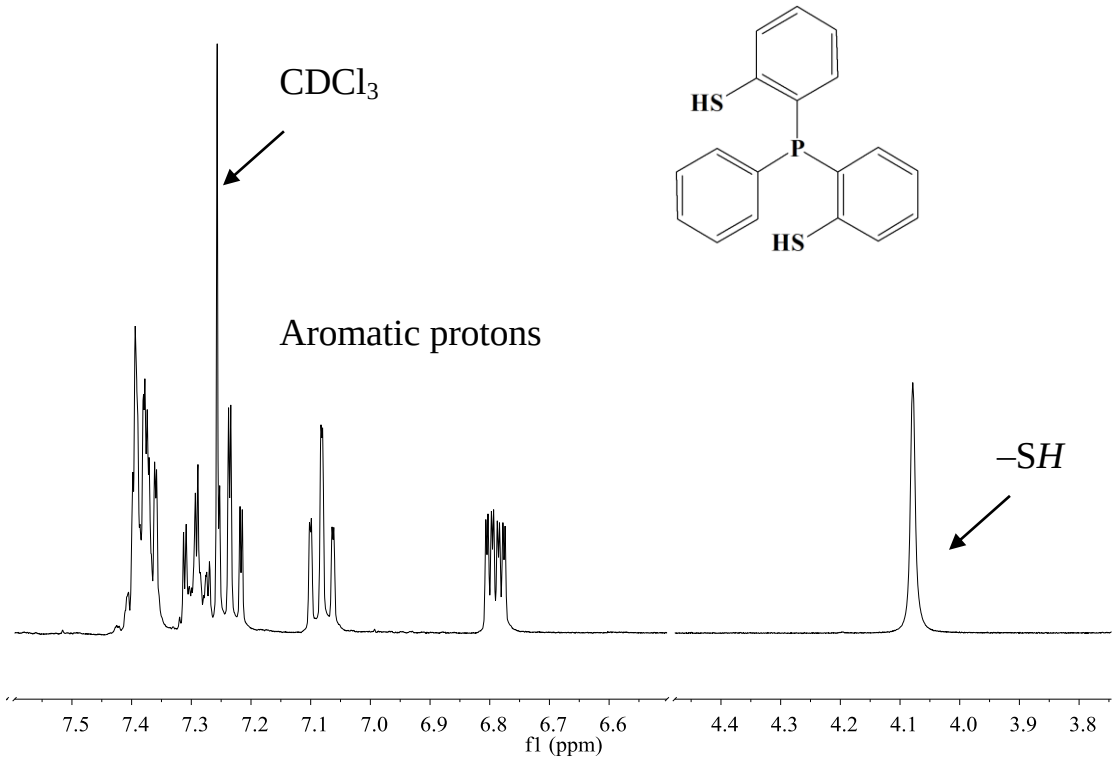


**Figure II–9. $^{1}$H–NMR spectrum of the $H_2$PS2 ligand in $CDCl_3$.**

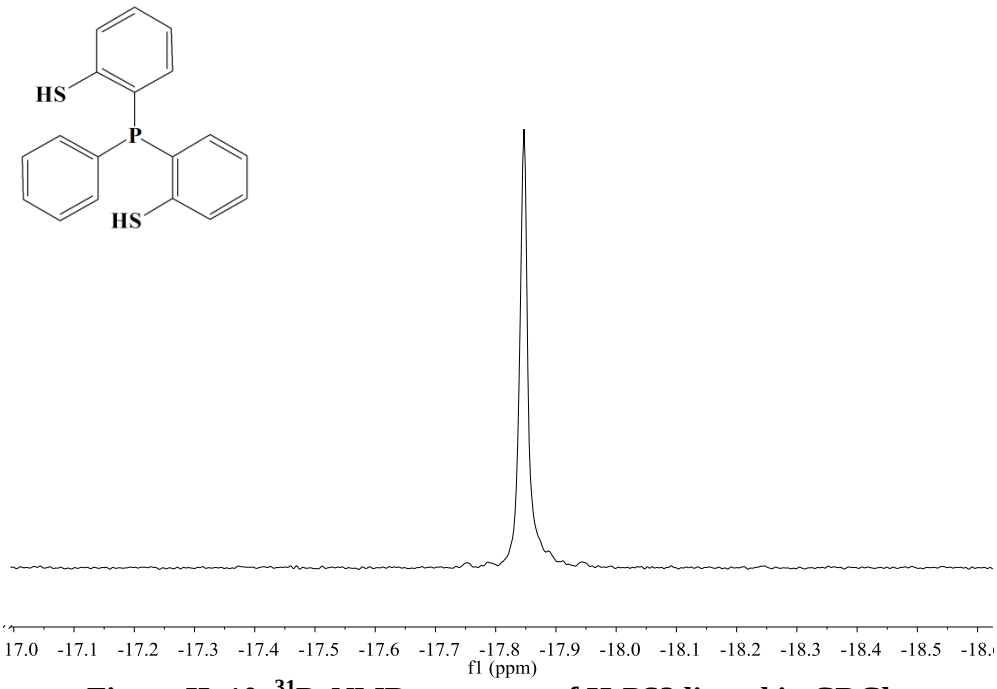


**Figure II–10. $^{31}$P–NMR spectrum of $H_2$PS2 ligand in $CDCl_3$.**

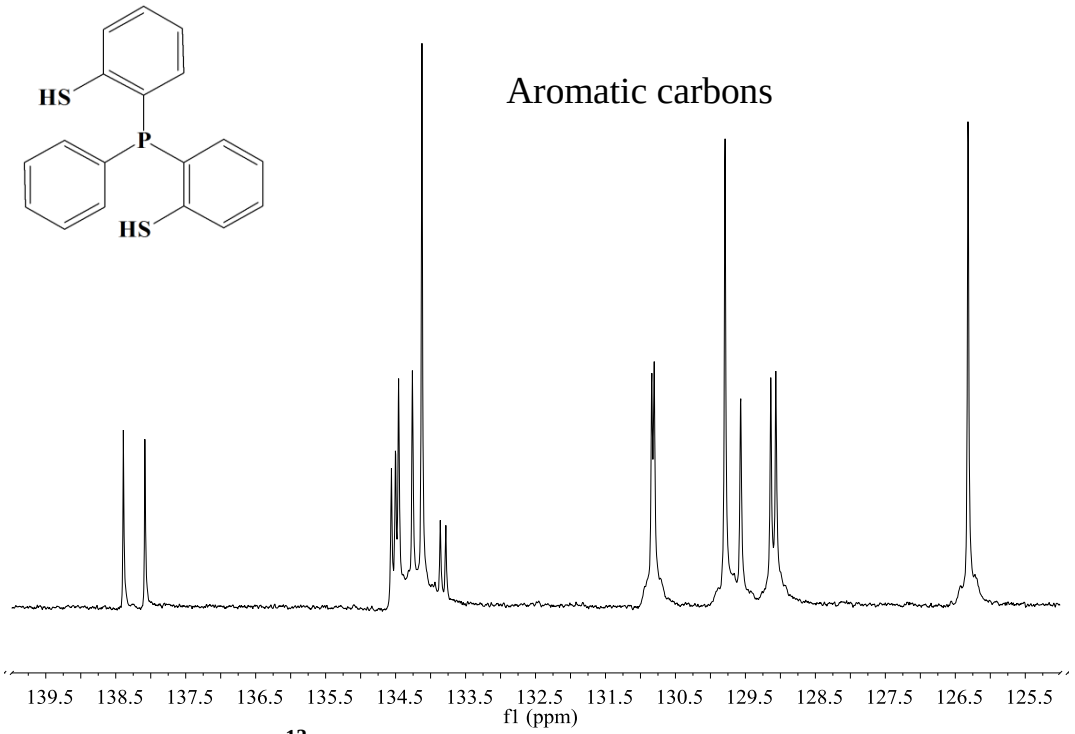


**Figure II–11. $^{13}$C–NMR spectrum of the $H_2$PS2 ligand in $CDCl_3$.**

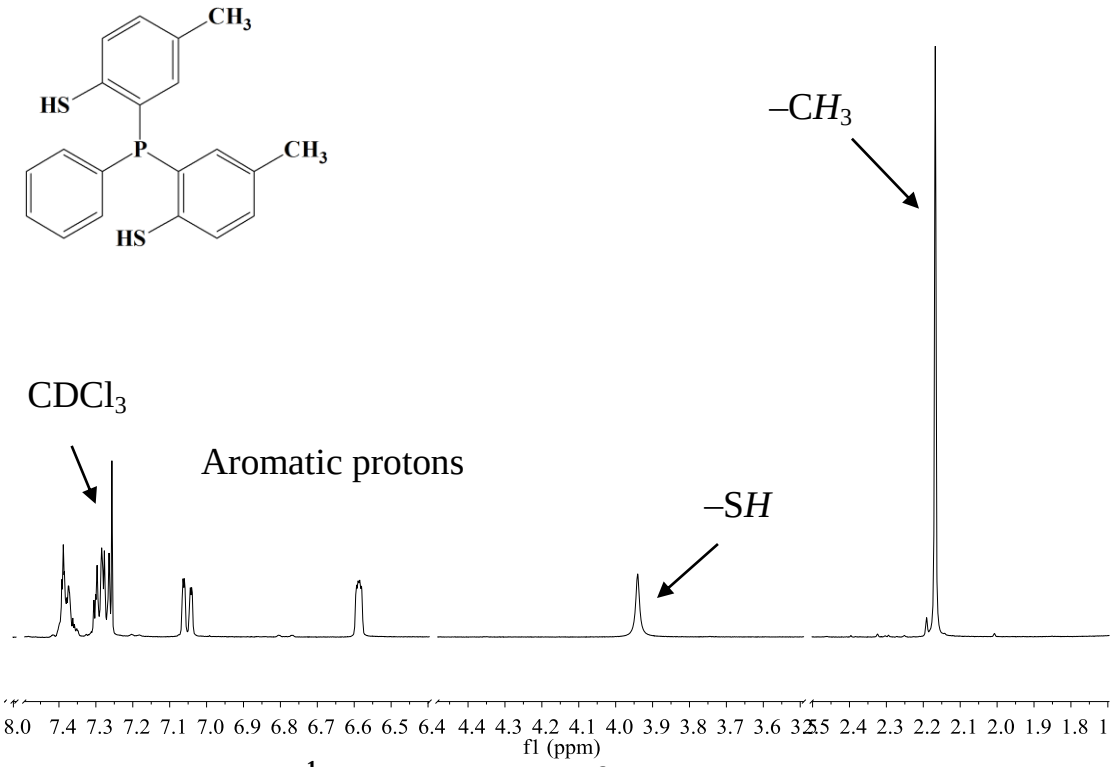


**Figure II–12. $^{1}$H–NMR spectrum of the $H_2$PS2' ligand in $CDCl_3$.**

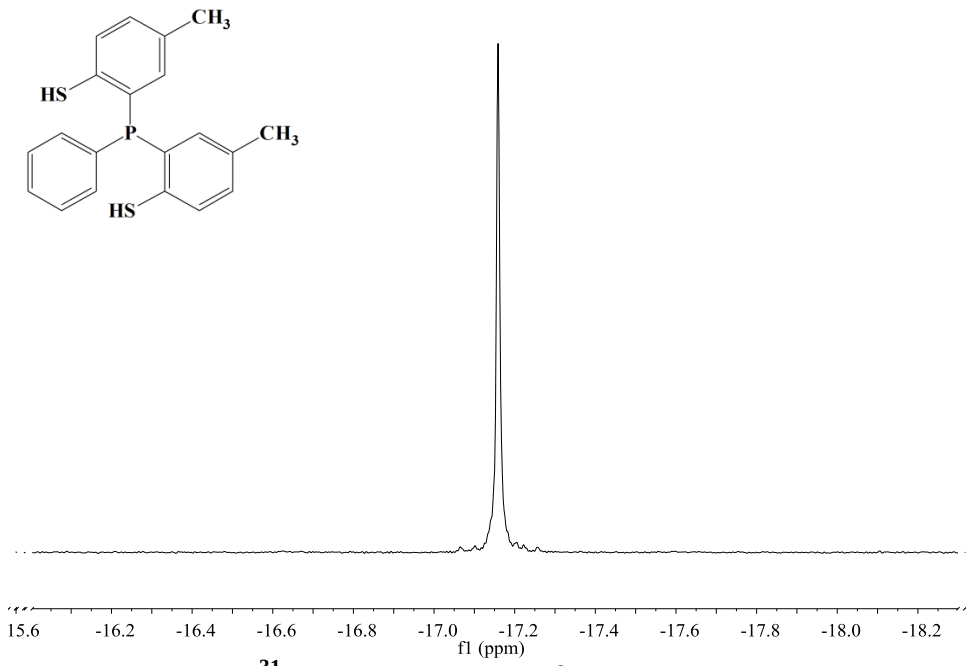


**Figure II–13. $^{31}$P–NMR spectrum of $H_2$PS2' ligand in $CDCl_3$.**

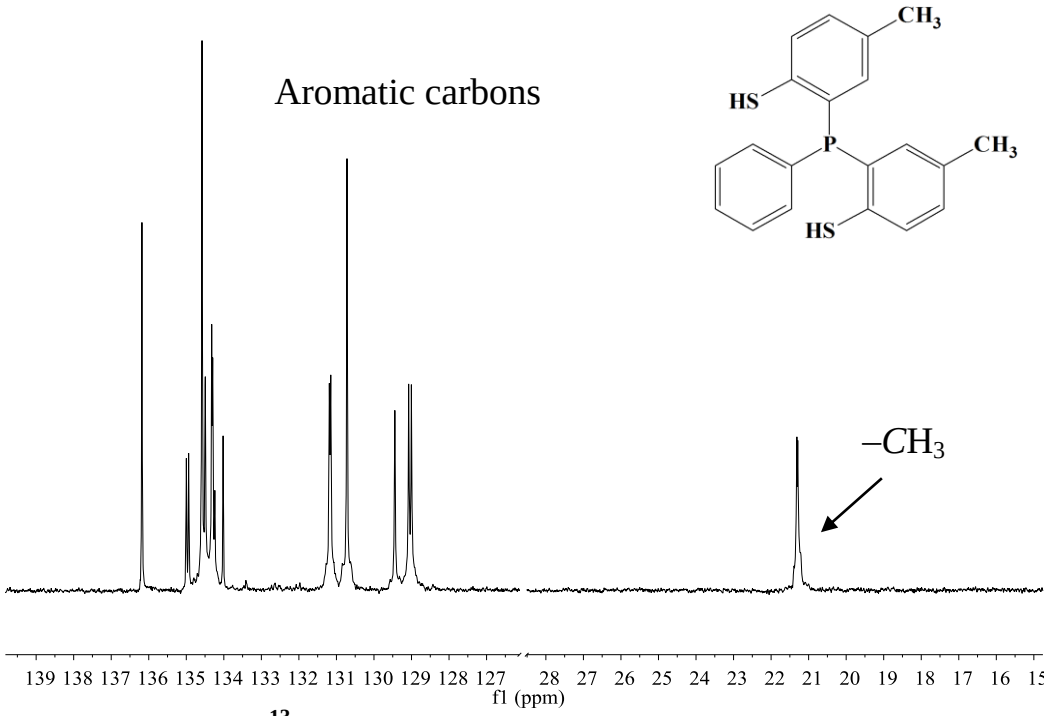


**Figure II–14. $^{13}$C–NMR spectrum of the $H_2$PS2' ligand in $CDCl_3$.**

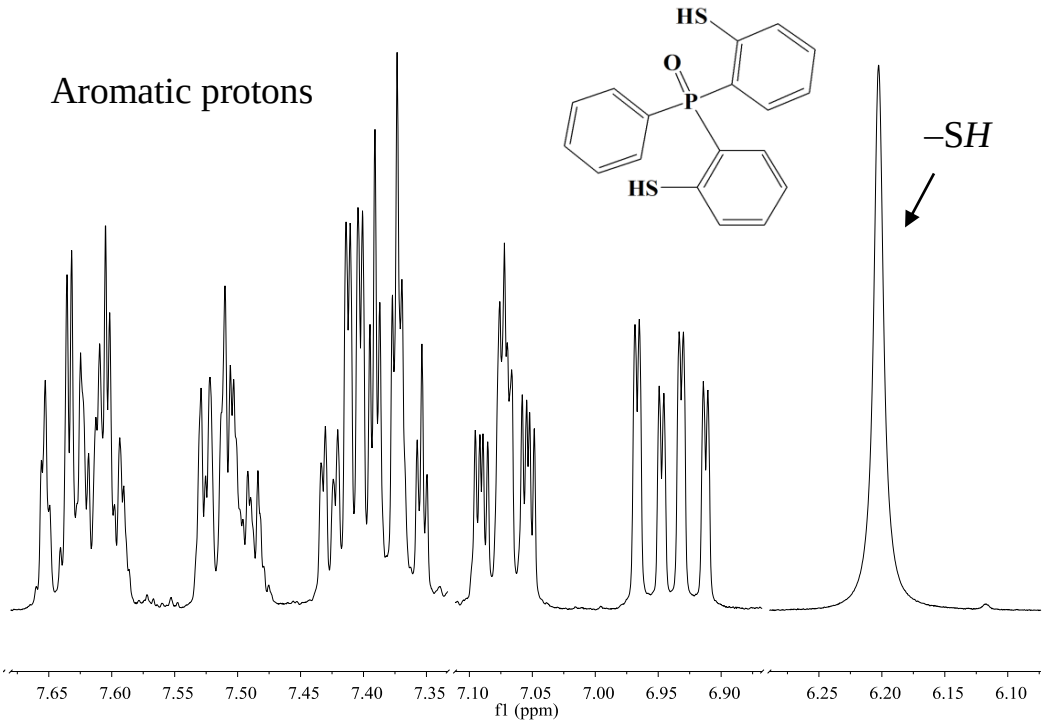


**Figure II–15. $^{1}$H–NMR spectrum of the $H_2$POS2 ligand in $CDCl_3$.**

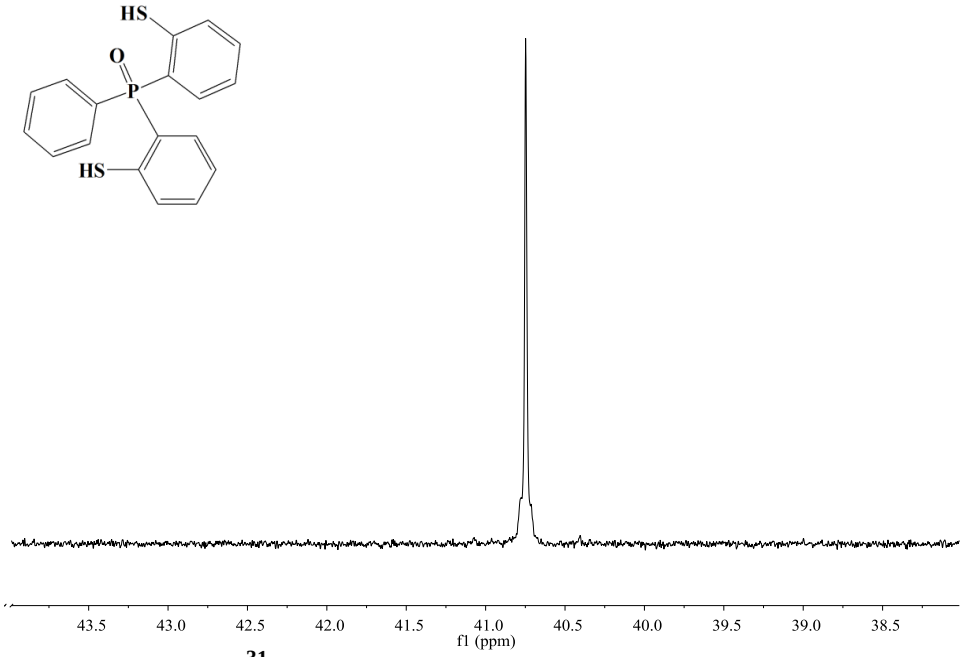


**Figure II–16. $^{31}$P–NMR spectrum of $H_2$POS2 ligand in $CDCl_3$.**

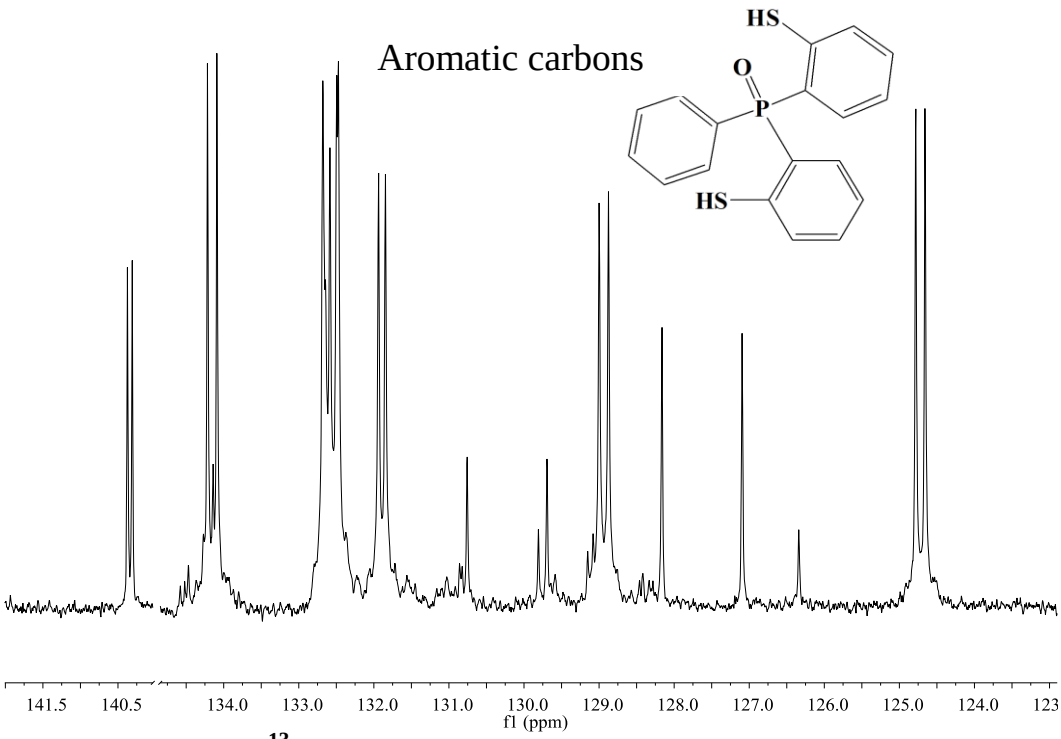


**Figure II–17. $^{13}$C–NMR spectrum of the $H_2POS2$ ligand in $CDCl_3$.**

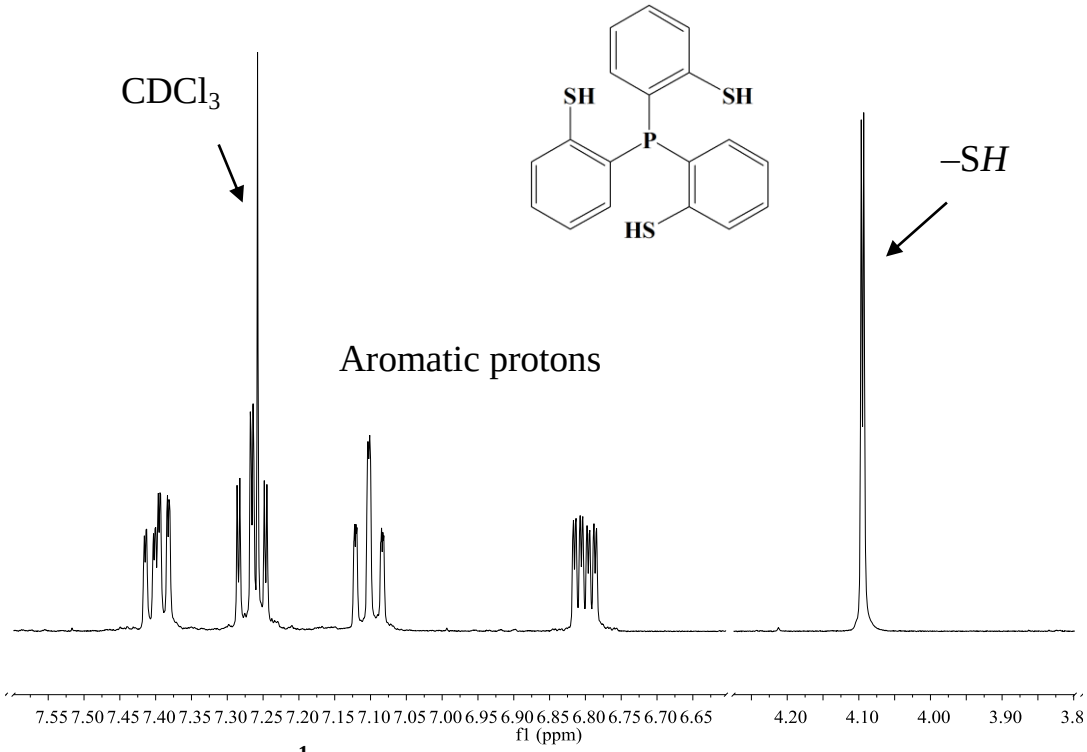


**Figure II–18. $^{1}$H–NMR spectrum of the $H_3PS3$ ligand in $CDCl_3$.**

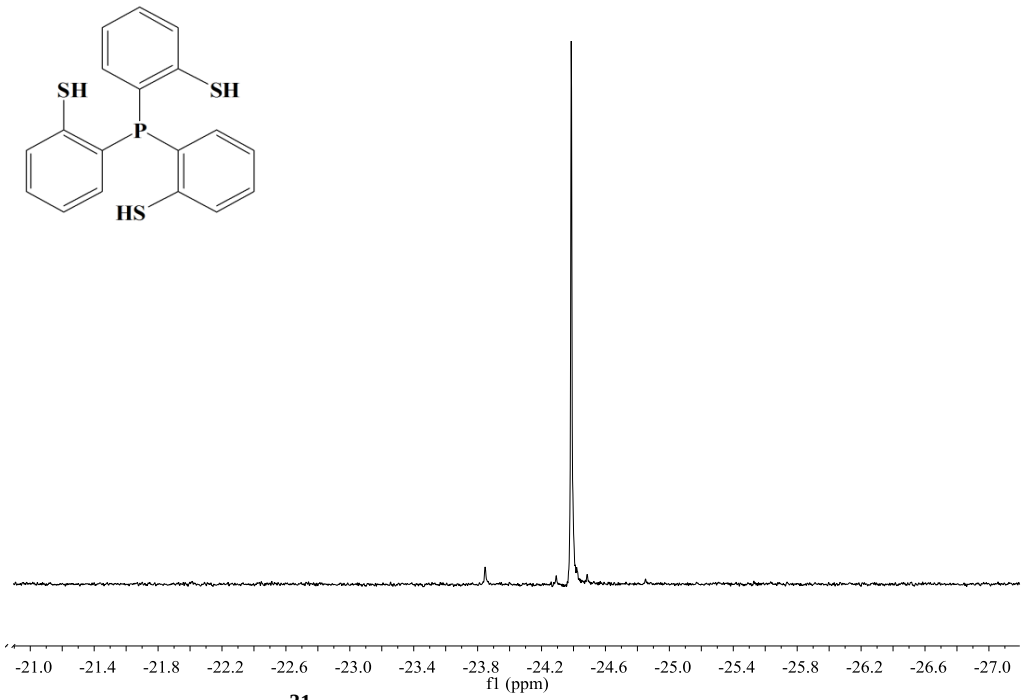


**Figure II–19. $^{31}$P–NMR spectrum of $H_3PS3$ ligand in $CDCl_3$.**

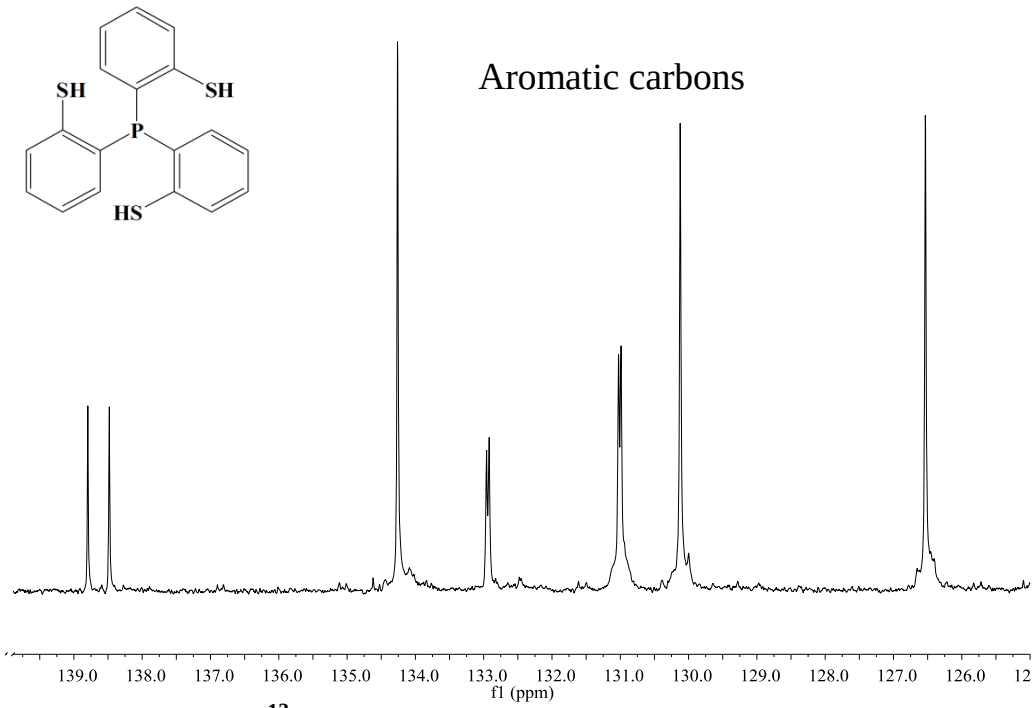


**Figure II–20. $^{13}$C–NMR spectrum of the $H_3PS3$ ligand in $CDCl_3$.**

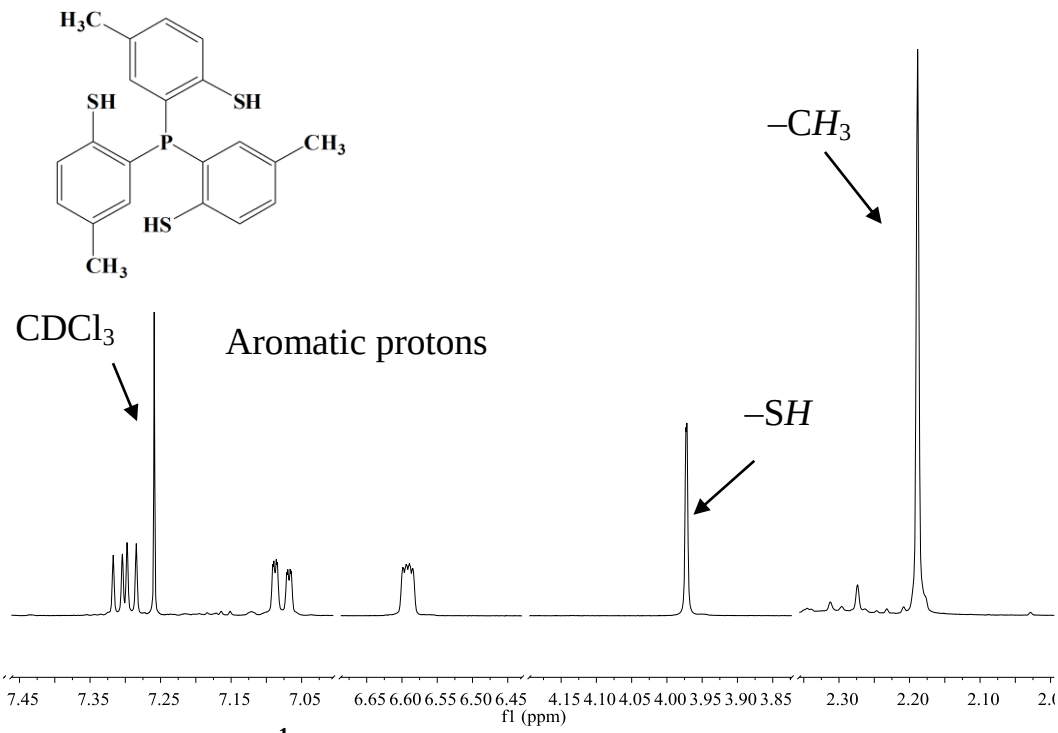


**Figure II–21. $^{1}$H–NMR spectrum of the $H_3PS3'$ ligand in $CDCl_3$.**

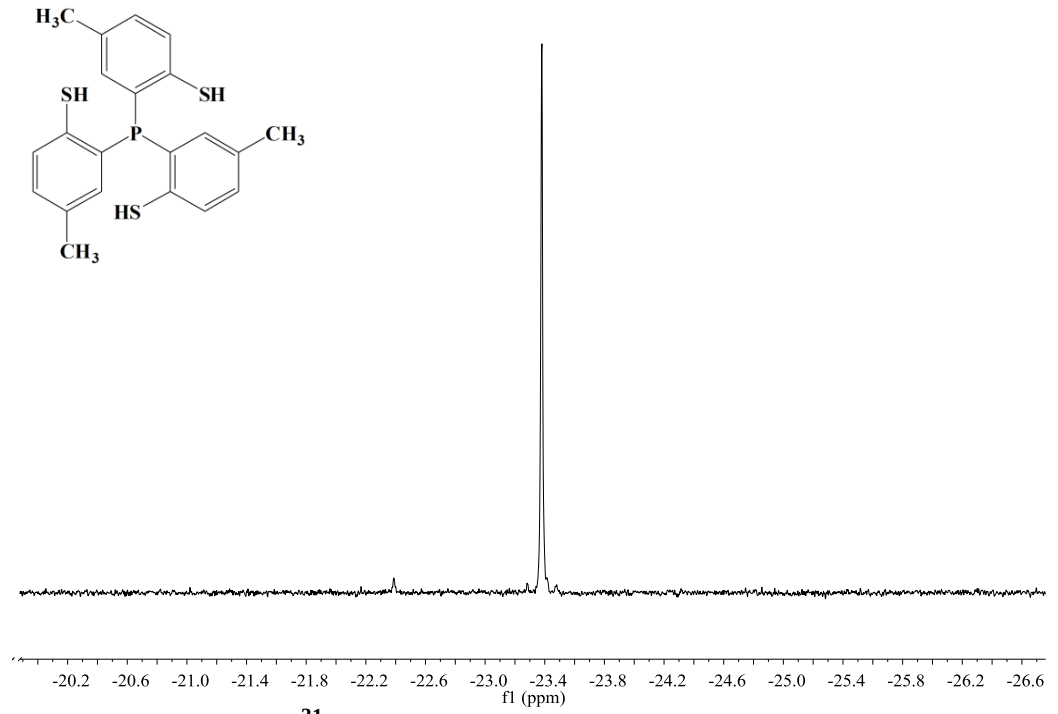


**Figure II–22. $^{31}$P–NMR spectrum of $H_3PS3'$ ligand in $CDCl_3$.**

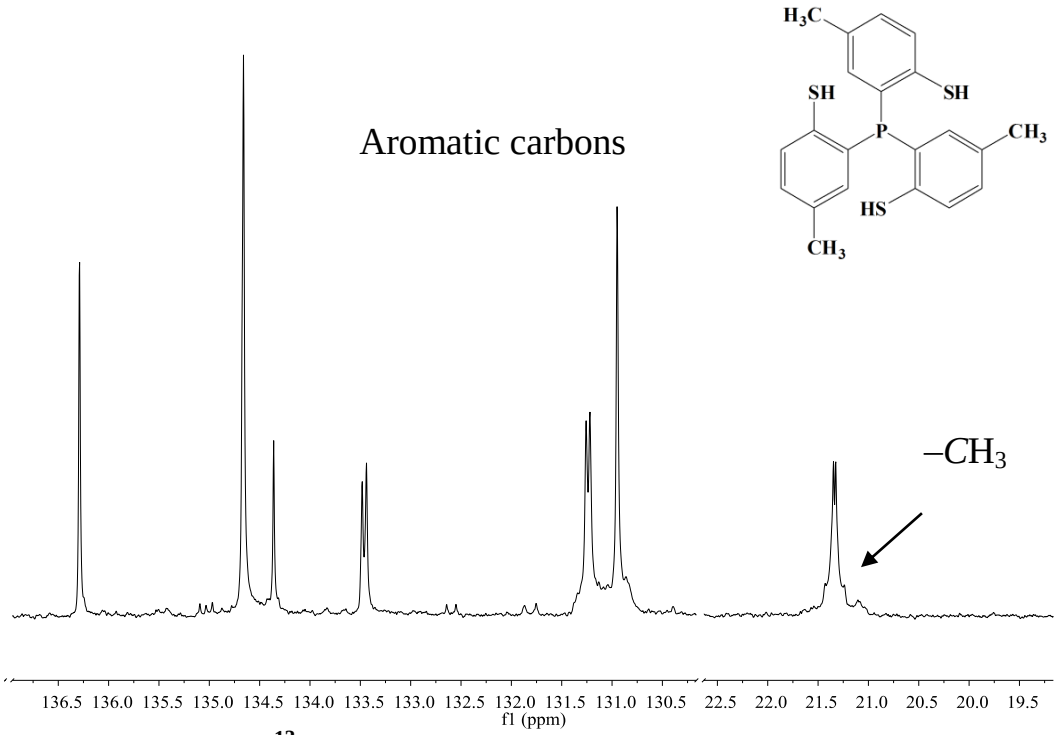


**Figure II–23. $^{13}$C–NMR spectrum of the $H_3$PS3' ligand in $CDCl_3$.**

### 2.3.4.2 NMR Spectra of [NBr] Compounds

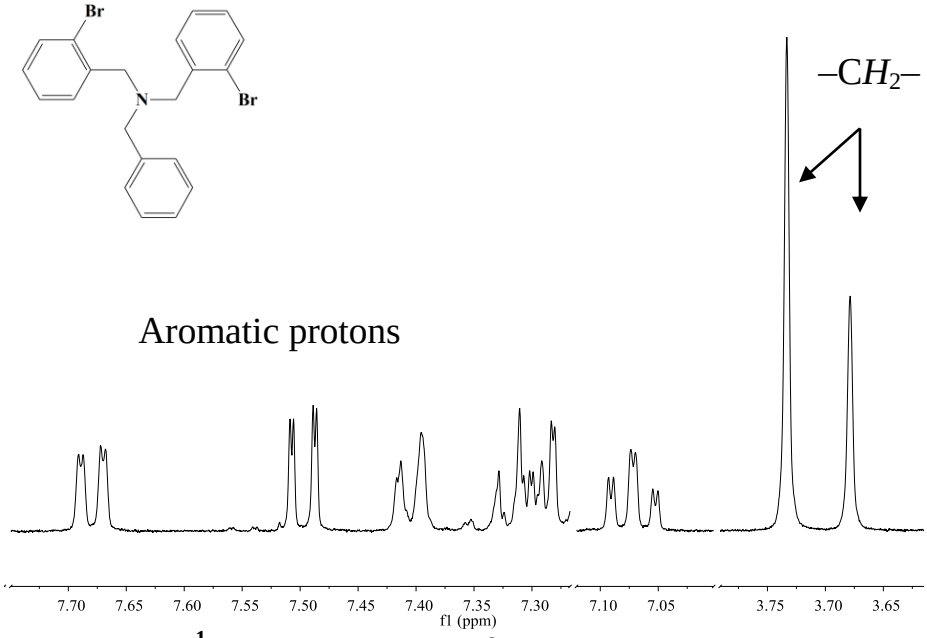


**Figure II–24. $^{1}$H–NMR spectrum of the NBr2 compound in $CDCl_3$.**

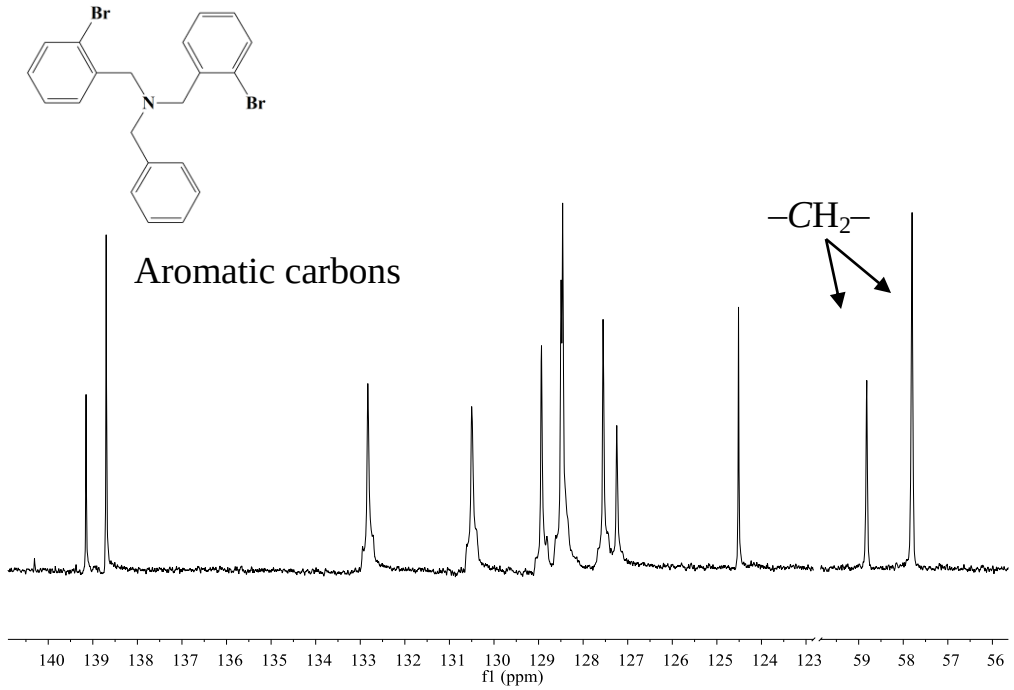


**Figure II–25. $^{13}$C–NMR spectrum of the NBr2 compound in $CDCl_3$.**

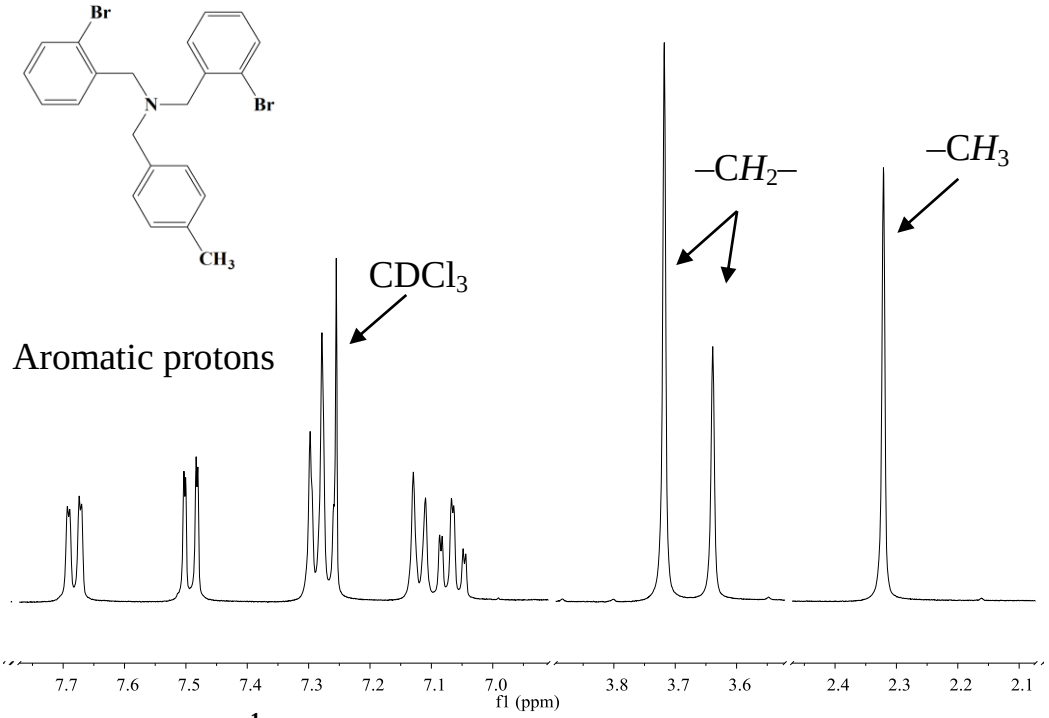


**Figure II–26. $^{1}$H–NMR spectrum of the NBr2' compound in $CDCl_3$.**

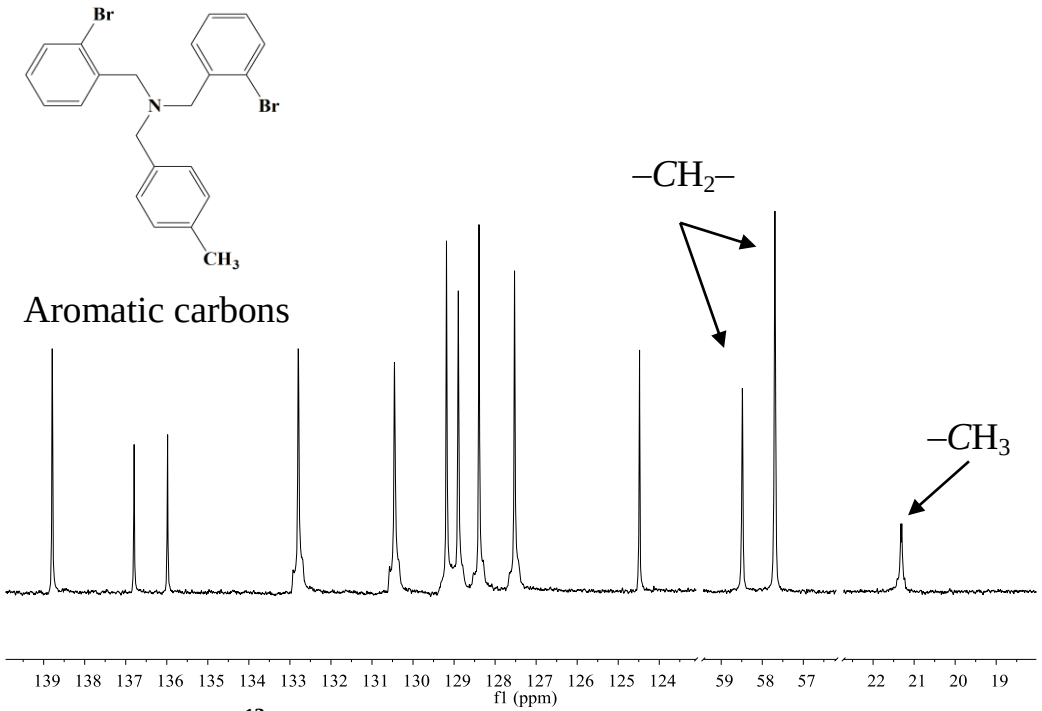


**Figure II–27. $^{13}$C–NMR spectrum of the NBr2' compound in $CDCl_3$.**

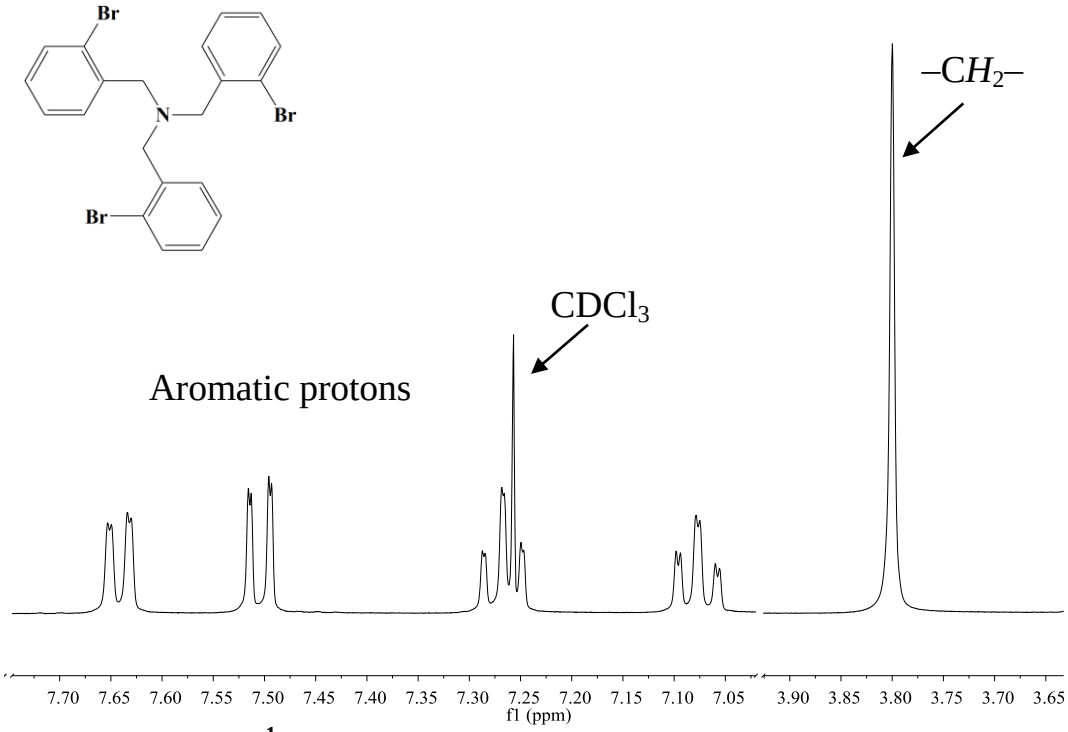


**Figure II–28. $^{1}$H–NMR spectrum of the NBr3 compound in $CDCl_3$.**

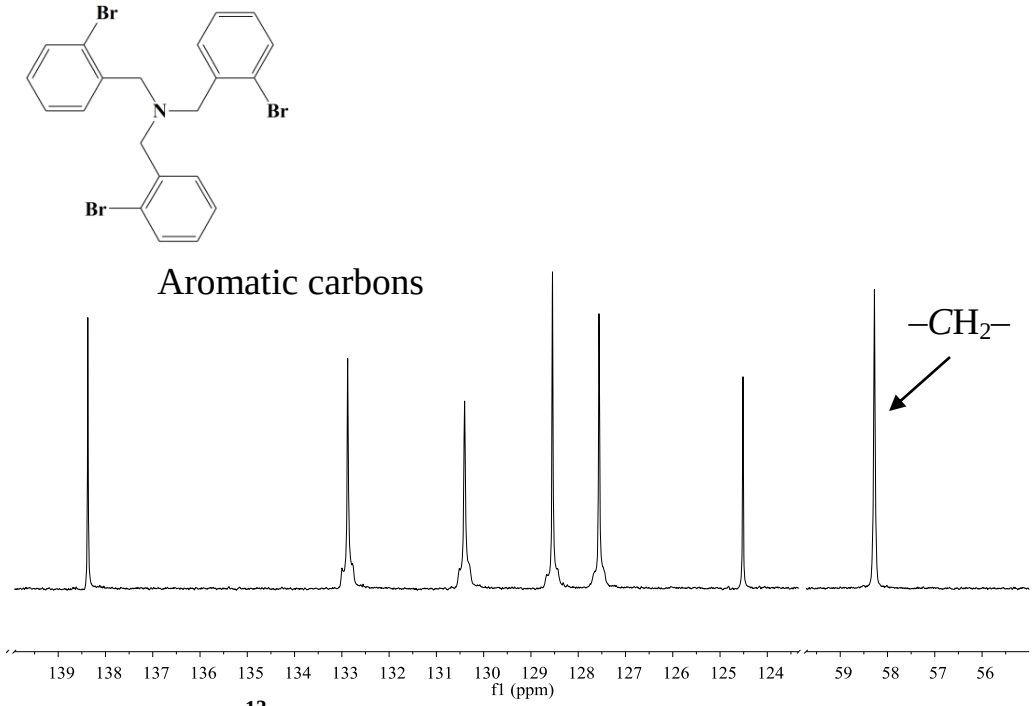


**Figure II–29. $^{13}$C–NMR spectrum of the NBr3 compound in $CDCl_3$.**

### 2.3.4.3 NMR Spectra of [NS] and [NSe] Ligands

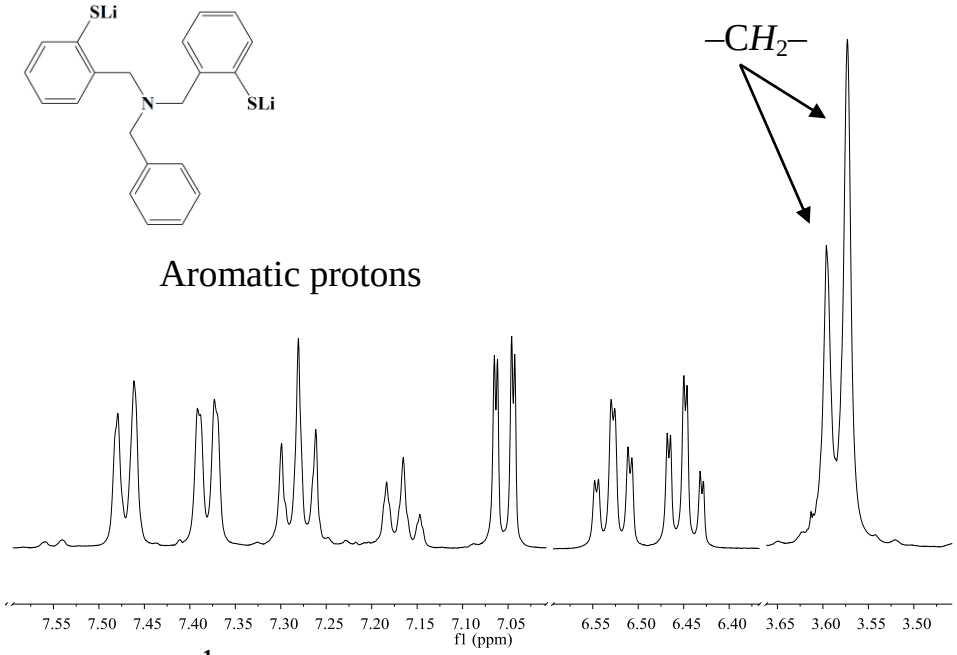


**Figure II–30. $^{1}$H–NMR spectrum of the $Li_2$NS2 ligand in DMSO–$d_6$.**

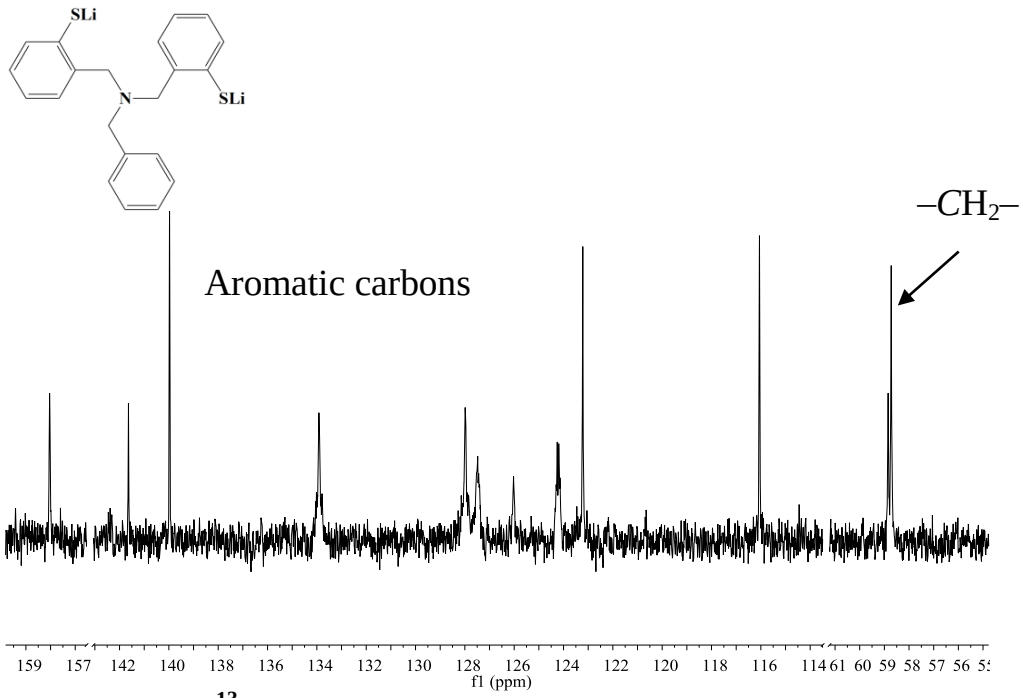


**Figure II–31. $^{13}$C–NMR spectrum of the $Li_2$NS2 ligand in DMSO–$d_6$.**

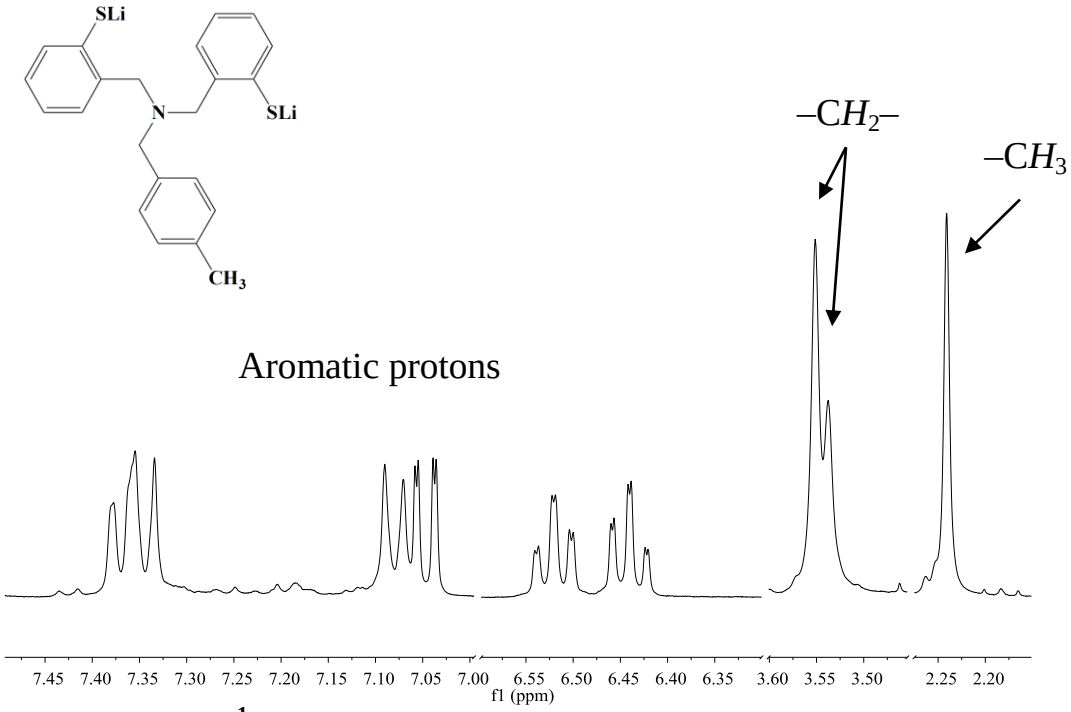


**Figure II–32. $^{1}$H–NMR spectrum of the $Li_2$NS2' ligand in DMSO–$d_6$.**

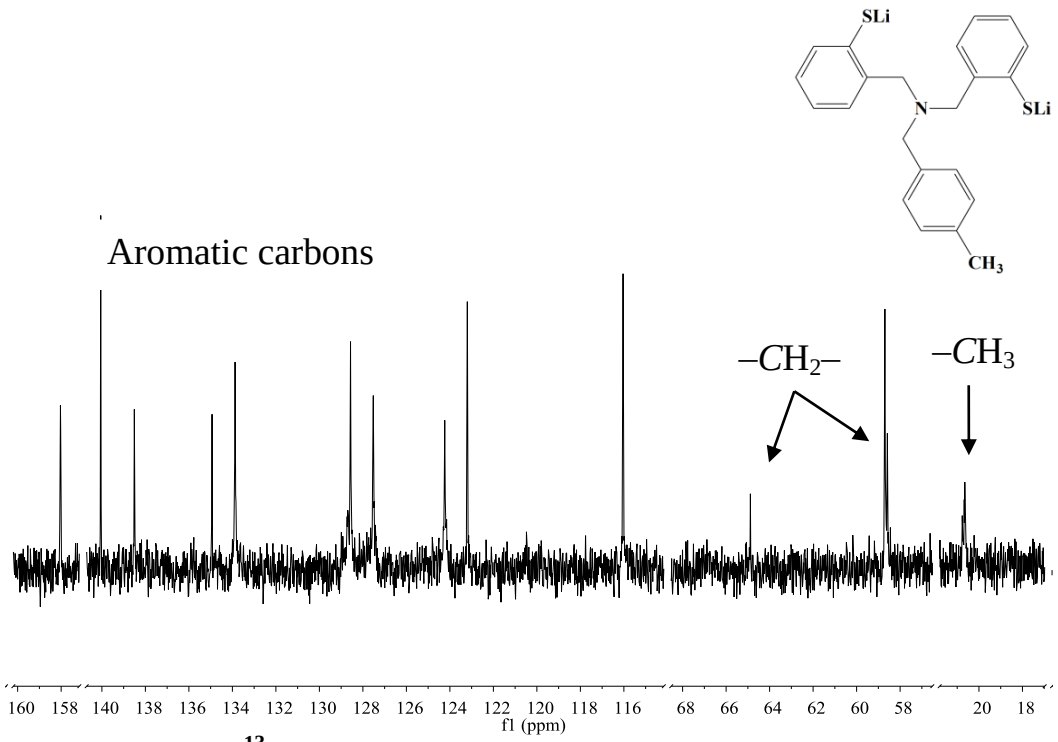


**Figure II–33. $^{13}$C–NMR spectrum of the $Li_2$NS2' ligand in DMSO–$d_6$.**

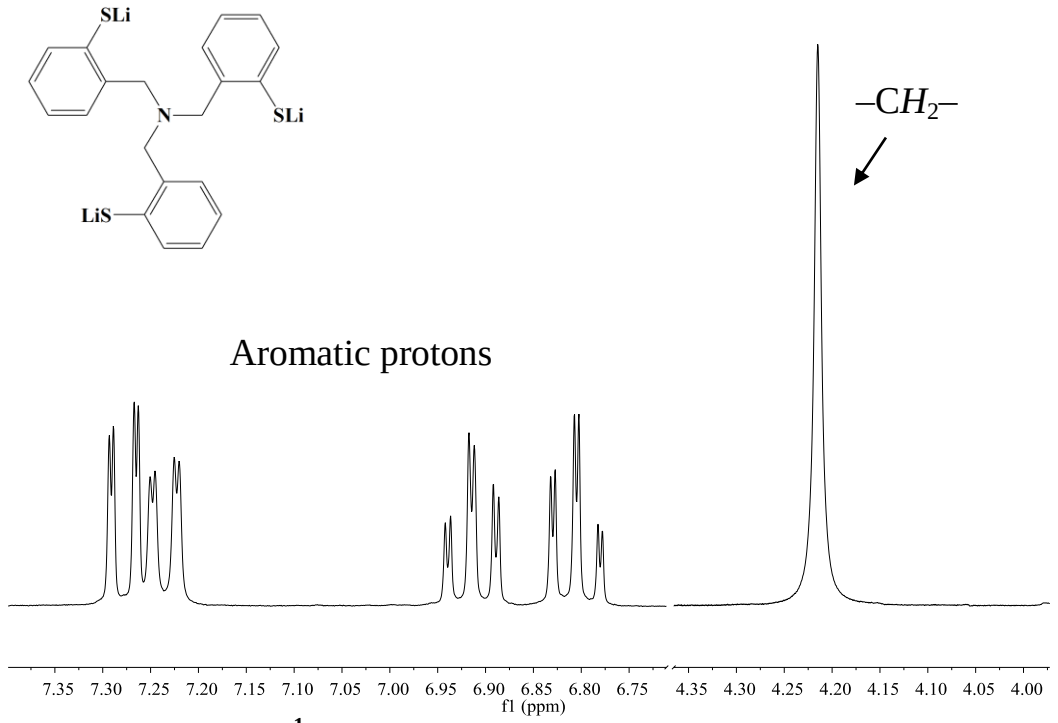


**Figure II–34. $^{1}$H–NMR spectrum of the $Li_3$NS3 ligand in $D_2O$.**

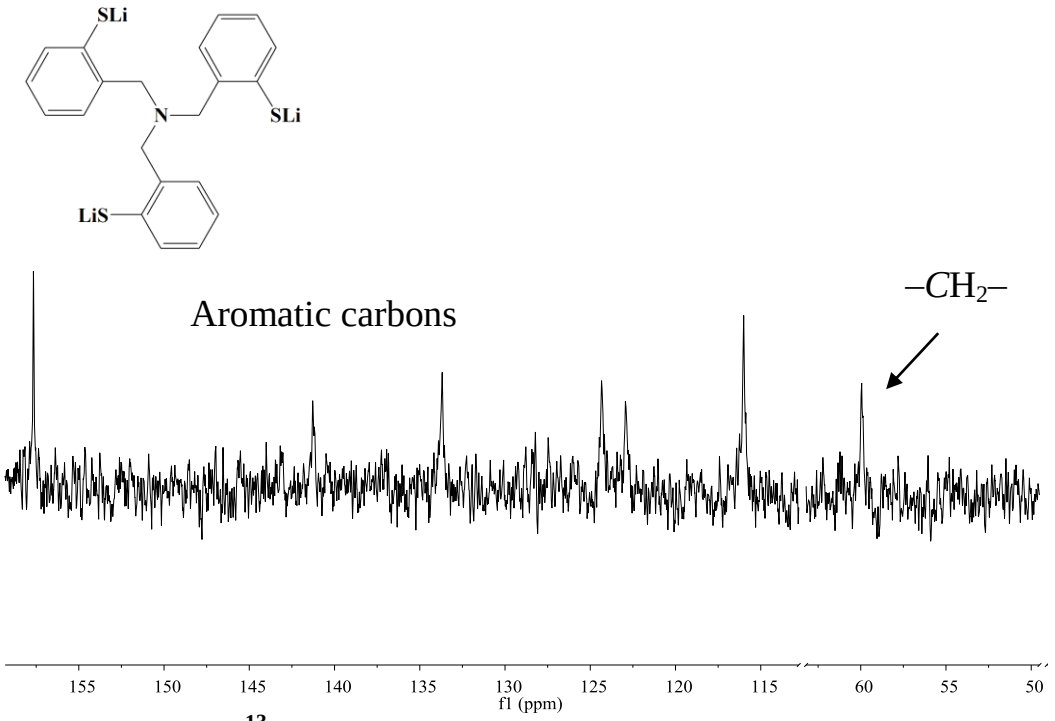


**Figure II–35. $^{13}$C–NMR spectrum of the $Li_3NS3$ ligand in DMSO–$d_6$.**

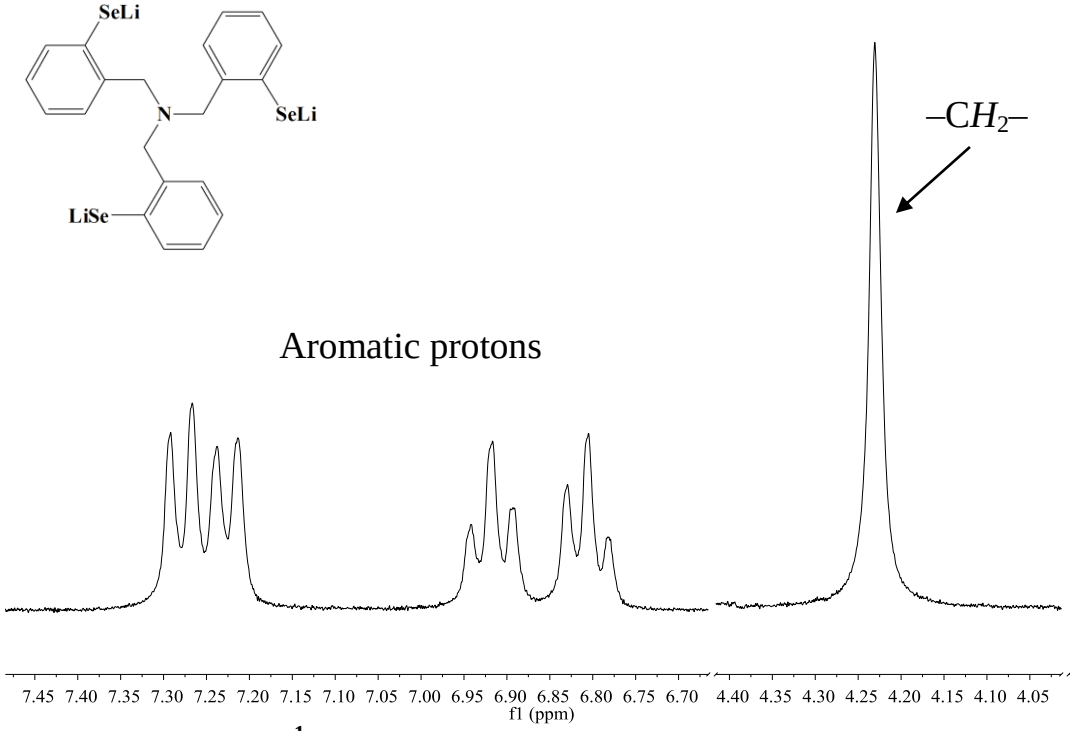


**Figure II–36. $^{1}$H–NMR spectrum of the $Li_3NSe3$ ligand in $D_2O$.**

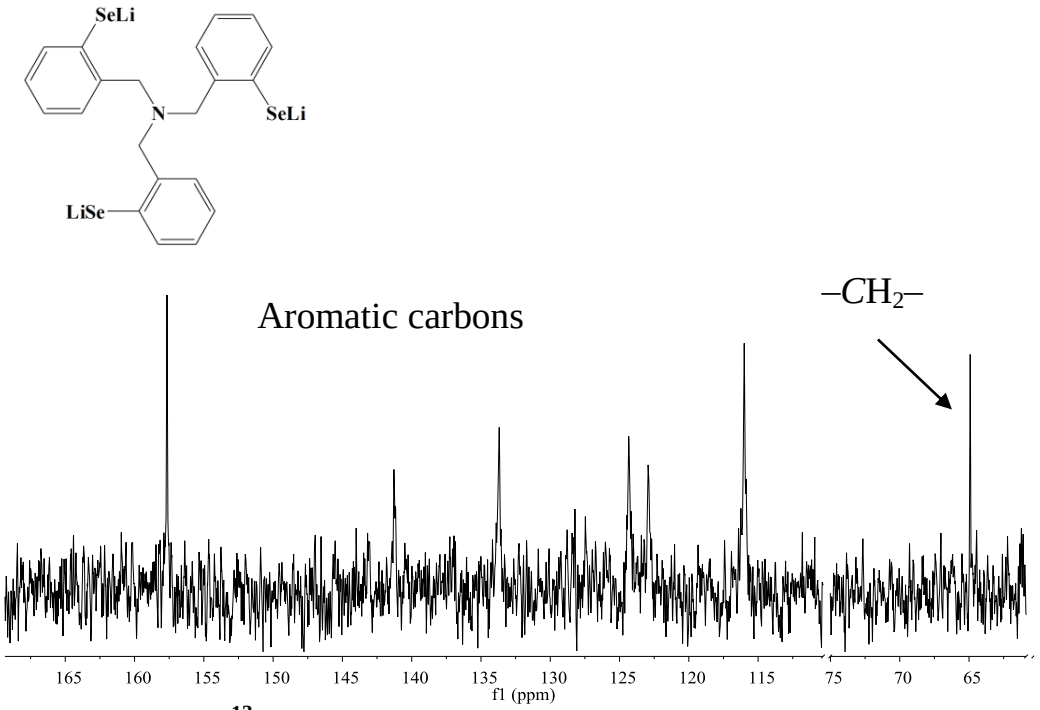


**Figure II–37. $^{13}$C–NMR spectrum of the $Li_3NSe3$ ligand in DMSO–$d_6$.**

### 2.3.4.4 NMR Spectra of $H_2O2S2$ Compound and $H_2S4$ Ligand

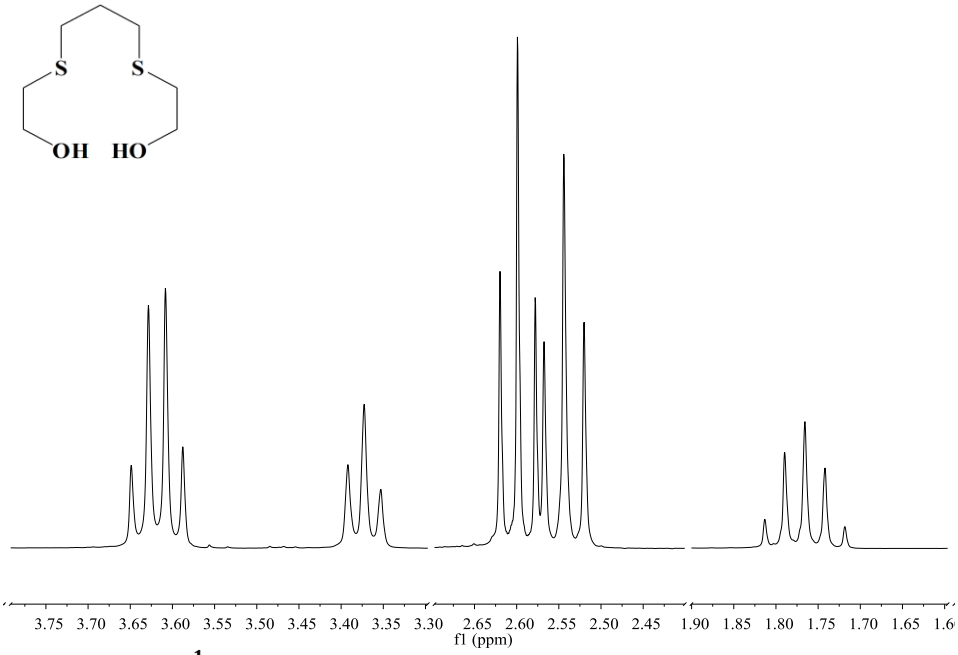


**Figure II–38. $^{1}$H–NMR spectrum of the $H_2O2S2$ compound in $CDCl_3$.**

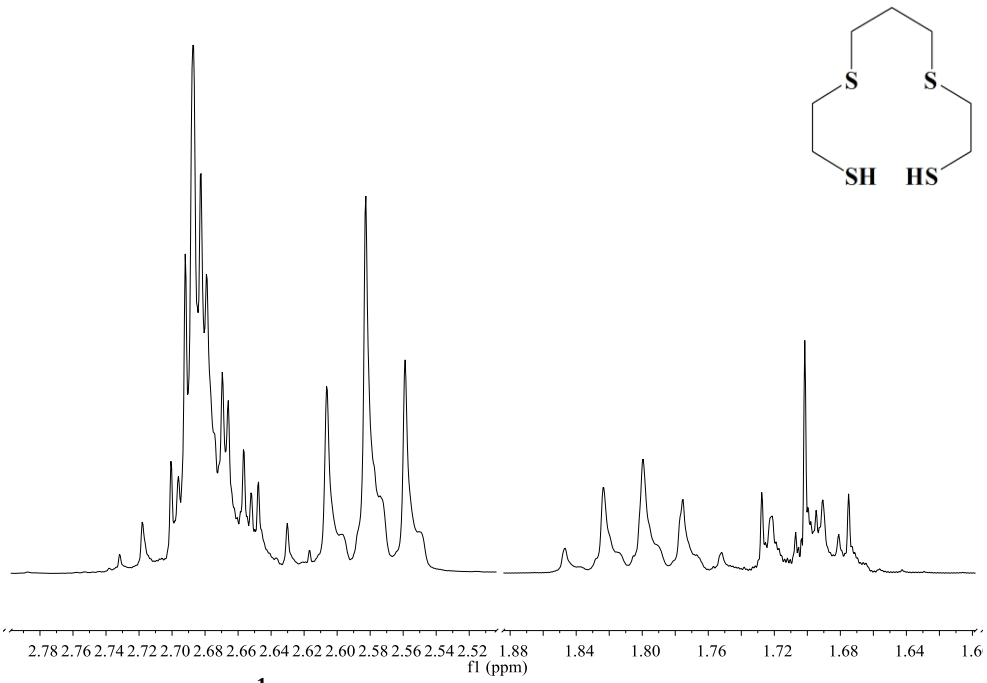


**Figure II–39. $^{1}$H–NMR spectrum of the $H_2S4$ ligand in $CDCl_3$.**

### 2.3.5 X–Ray Structures of Compounds and Ligands

Various crystals of these organic compounds were grown in order to understand their structures. Several crystal structures have been reported either in the literature or in previous group member's thesis. However, none of these compounds have been reported using the X–ray diffractometer described in the general procedures as well as having the data set collected at 100K.

The PS2 and PS2' ligand crystal structures show a slightly distorted trigonal pyramidal geometry, which is illustrated in **Figure II–34** and **Figure II–35**. $H_2PS2$ and $H_2PS2'$ crystals were grown from a concentrated solution of diethyl ether at –20 $^{o}$C. Both structures crystallize in a monoclinic space group, $P2_1/n$, with four molecules in the unit cell. For a trigonal pyramidal geometry the bond angles are typically <109.5$^{o}$ or ≈ 107$^{o}$. This distortion of the geometry is confirmed by the C—P—C bond angles of 103.00(7)$^{o}$, 102.41(7)$^{o}$ and 101.67(7)$^{o}$ for the PS2 ligand and 101.96(7)$^{o}$, 101.94(7)$^{o}$ and 105.44(7)$^{o}$ for the PS2' ligand. These values are slightly smaller than from corresponding C—P—C bond angles from similar compounds, which range from ~106$^{o}$ to 108$^{o}$.[9]

The packing diagram of $H_2PS2$, which is illustrated in **Figure II–36**, shows a weak intermolecular S—H $\cdots$ P interaction of 3.03(9) Å, forming a zigzag chain along the *b* axis. The

second –SH group points towards the π system of the adjacent aryl ring. The shortest S—H ··· C distance is 3.344(1) Å.

For each molecule, one of the –SH protons points in the direction of the phosphorous lone pair, suggesting a weak intramolecular S—H ··· P interaction of 2.585(1) Å. The second SH group points towards the π ring system of the adjacent molecule. The shortest S—H ··· C distance is 3.132(1) Å. This intramolecular interaction has been observed in the $H_3PS3$ crystal structure.[10]

The NBr2' and NBr3 compound crystal structures show a trigonal pyramidal geometry, which is illustrated in **Figure II–37** and **Figure II–38**. The NBr2' crystals were grown by layering methanol to reaction flask, which was left undisturbed. The NBr2' was crystallized in a monoclinic space group, $P2_1/c$, with four molecules in the unit cell. The NBr3 crystals were grown by slow cooling of a hot concentrated acetonitrile solution. The NBr3 was crystallized in a triclinic space group, P–1, with two molecules in the unit cell.

The trigonal pyramidal nitrogen, C—N—C, gave average bond angles of 111.2(7)$^o$ for NBr2' and 111.13(18)$^o$ for NBr3. These angles are slightly larger compared to the average C—N—C bond angle of 110.0(9)$^o$ for tribenzylamine.[11] This change in the C—N—C bond angles can be caused by the greater steric demand of the bromine atoms, which has been seen for similar structures as NBr3.[12] A summary of selective bond distances and bond angles for PS2 are listed in **Table II–2**, for PS2' **Table II–3**, for NBr2' **Table II–4**, and for NBr3 **Table II–5**.

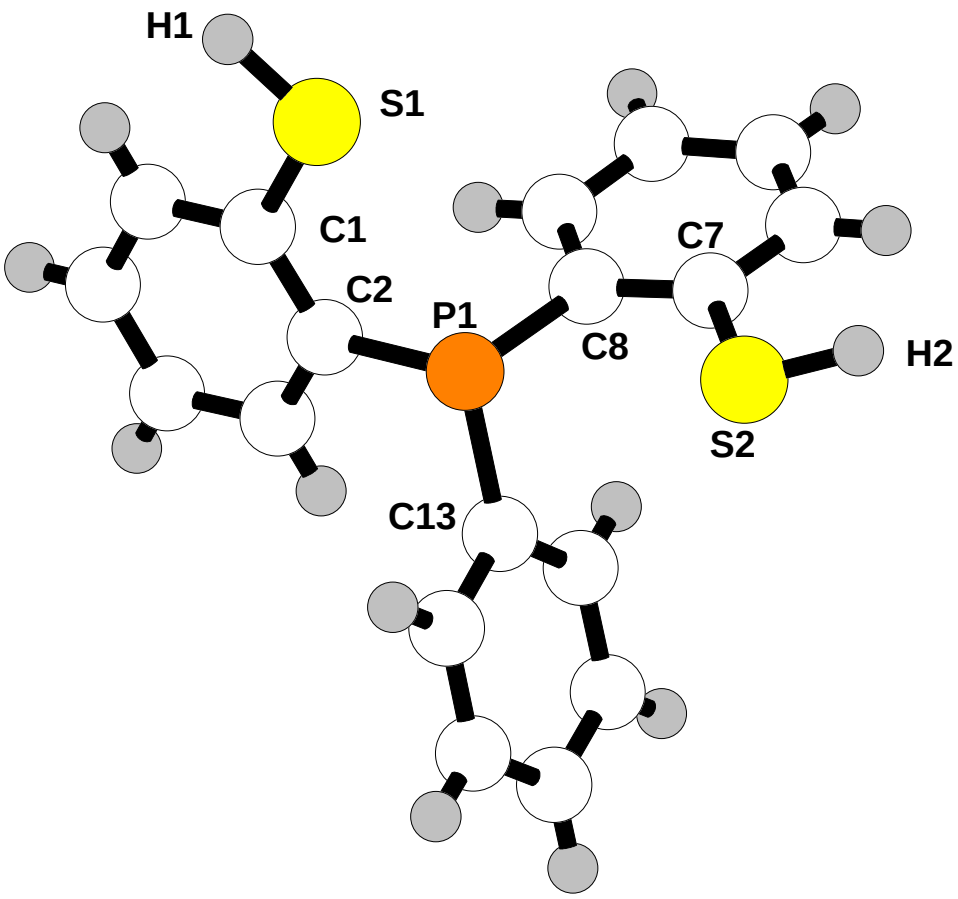


**Figure II–40. X–ray structure of $H_2$PS2 ligand.**

| Table II–2. Selective Crystallographic Data for PS2. | | | |
|---|---|---|---|
| **Bond Distances (Å)** | | **Bond Angles (°)** | |
| P(1) – C(2) | 1.8292(17) | C(2) – P(1) – C(13) | 103.00(7) |
| P(1) – C(8) | 1.8339(16) | C(2) – P(1) – C(8) | 102.41(7) |
| P(1) – C(13) | 1.8330(16) | C(8) – P(1) – C(13) | 101.67(7) |
| C(1) – S(1) | 1.7700(18) | C(2) – C(1) – S(1) | 118.75(13) |
| C(7) – S(2) | 1.7725(18) | C(8) – C(7) – S(2) | 118.65(15) |
| S(1) – H(1) | 1.29(4) | C(1) – S(1) – H(1) | 99.7(17) |
| S(2) – H(2) | 1.25(3) | C(7) – S(2) – H(2) | 95.6(15) |

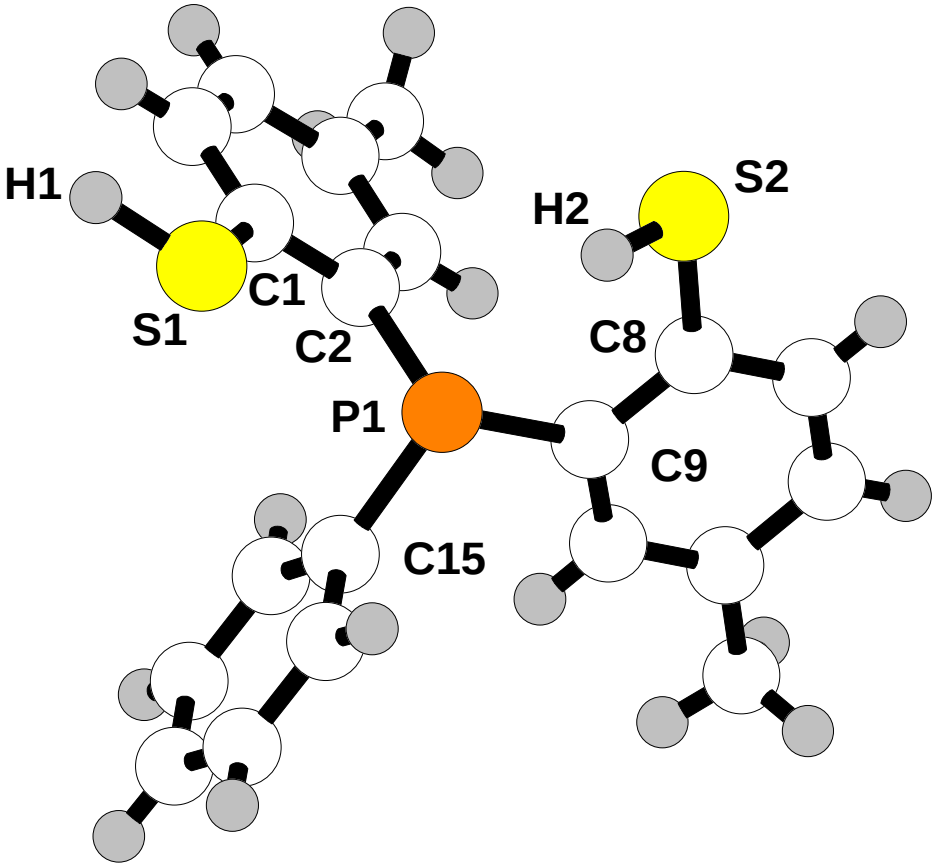


**Figure II–41. X–ray structure of $H_2$PS2' ligand.**

| Table II–3. Selective Crystallographic Data for PS2'. | | | |
|---|---|---|---|
| **Bond Distances (Å)** | | **Bond Angles (°)** | |
| P(1) – C(2) | 1.8391(16) | C(2) – P(1) – C(15) | 101.96(7) |
| P(1) – C(9) | 1.8255(17) | C(2) – P(1) – C(9) | 101.94(7) |
| P(1) – C(15) | 1.8311(16) | C(9) – P(1) – C(15) | 105.44(7) |
| C(1) – S(1) | 1.7765(18) | C(2) – C(1) – S(1) | 118.91(13) |
| C(7) – S(2) | 1.7808(17) | C(9) – C(8) – S(2) | 122.96(13) |
| S(1) – H(1) | 1.29(4) | C(1) – S(1) – H(1) | 98.4(15) |
| S(2) – H(2) | 1.17(3) | C(8) – S(2) – H(2) | 98.9(17) |

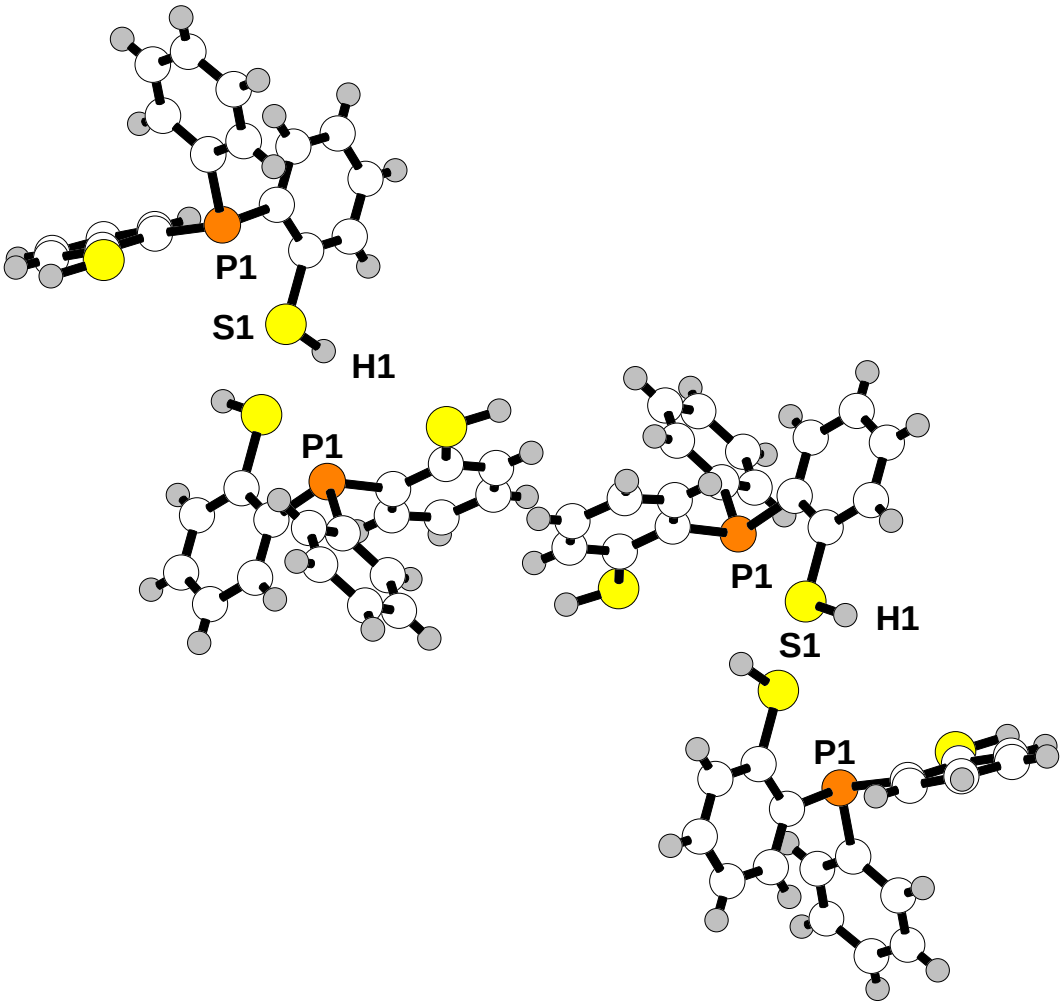


**Figure II–42: Unit cell packing diagram of $H_2$PS2 ligand.**

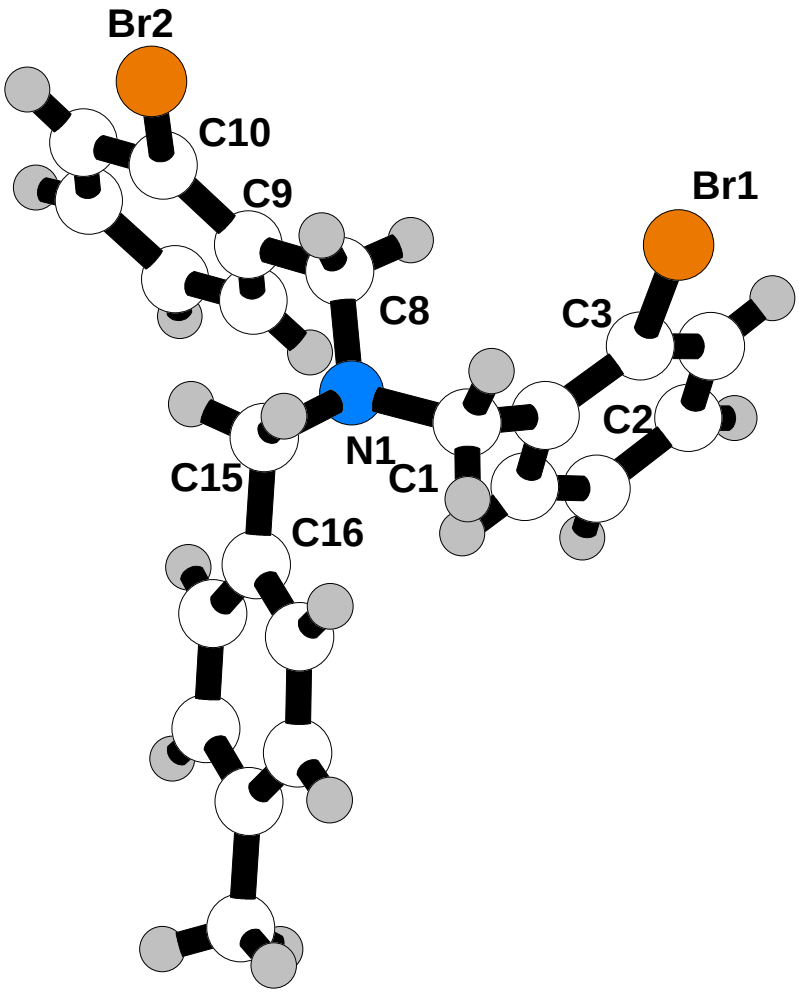


**Figure II–43. X–ray structure of NBr2' compound.**

| **Table II–4. Selective Crystallographic Data for NBr2'.** | | | |
|---|---|---|---|
| **Bond Distances (Å)** | | **Bond Angles (°)** | |
| N(1) – C(1) | 1.480(12) | N(1) – C(1) – C(2) | 108.9(8) |
| N(1) – C(8) | 1.461(12) | N(1) – C(8) – C(9) | 111.3(7) |
| N(1) – C(15) | 1.496(13) | N(1) – C(15) – C(16) | 110.5(8) |
| C(1) – C(2) | 1.494(13) | C(1) – N(1) – C(8) | 111.3(7) |
| C(8) – C(9) | 1.512(13) | C(1) – N(1) – C(15) | 111.0(7) |
| C(15) – C(16) | 1.506(13) | C(8) – N(1) – C(15) | 111.2(7) |
| C(3) – Br(1) | 1.904(9) | C(2) – C(3) – Br(1) | 120.0(10) |
| C(10) – Br(2) | 1.903(10) | C(9) – C(10) – Br(2) | 120.6(8) |

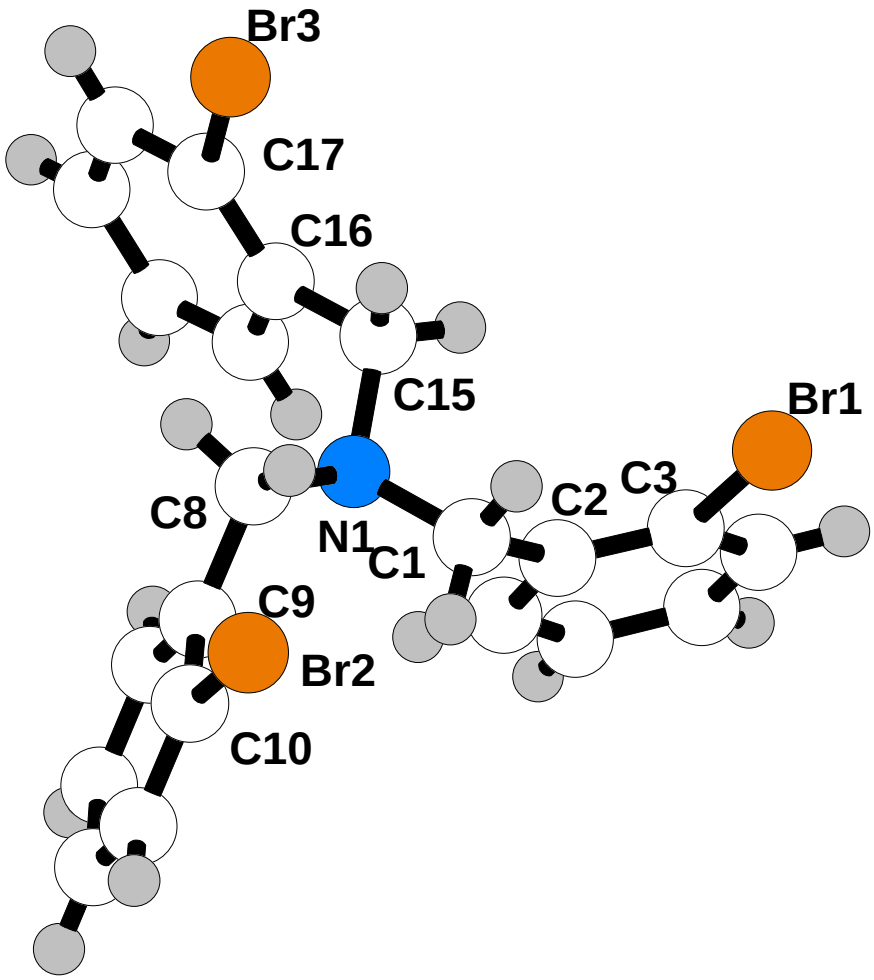


**Figure II–44. X–ray structure of NBr3 compound.**

| Table II–5. Selective Crystallographic Data for NBr3. | | | |
|---|---|---|---|
| **Bond Distances (Å)** | | **Bond Angles (°)** | |
| N(1) – C(1) | 1.468(3) | N(1) – C(1) – C(2) | 110.90(18) |
| N(1) – C(8) | 1.462(3) | N(1) – C(8) – C(9) | 110.95(18) |
| N(1) – C(15) | 1.471(3) | N(1) – C(15) – C(16) | 111.07(19) |
| C(1) – C(2) | 1.508(3) | C(8) – N(1) – C(15) | 111.24(18) |
| C(8) – C(9) | 1.507(3) | C(1) – N(1) – C(8) | 111.13(18) |
| C(15) – C(16) | 1.505(3) | C(1) – N(1) – C(15) | 111.01(19) |
| C(3) – Br(1) | 1.916(2) | C(2) – C(3) – Br(1) | 120.68(17) |
| C(10) – Br(2) | 1.909(2) | C(9) – C(10) – Br(2) | 120.60(17) |
| C(17) – Br(3) | 1.906(2) | C(16) – C(17) – Br(3) | 121.20(18) |

## 2.4 Conclusions

In conclusion, various [PS] and [NS] ligands can be synthesized using substituted benzenethiols and primary amines, respectively. It was shown that the acidification, pH ~5, for the [PS] ligands was critical step for successful completion of the ligand. Studies have shown that acidifying below pH ~5 resulted in minimum to no product formed. Yields were maximized by varying the recrystallization solvent from methanol to 2–propanol, 60% to 80%, with the exception of $H_2$POS2.

Ligands were characterized by NMR ($^{1}$H, $^{13}$C and $^{31}$P) while some by X–ray crystallography. The $H_2$PS2 X–ray structure showed one –SH proton pointed toward the adjacent $H_2$PS2's phosphorous atom, which suggests weak intermolecular interactions that forms a zigzag chain along the *b* axis within the unit cell. The $H_2$PS2' X–ray structure showed one –SH proton pointed toward the phosphorous lone pair, which suggests a weak intramolecular interaction.

## 2.5 References


1. Figuly, G. D.; Loop, C. K.; Martin, J. C. *J. Am. Chem. Soc.* **1989**, *111*, 654.
2. Block, E.; Eswarakrishnan, V.; Gernon, M.; Ofori–Okai, G.; Saha, C.; Tang, K.; Zubieta, J. *J. Am. Chem. Soc.* **1989**, *111*, 658.
3. Smith, K.; Lindsay, C. M.; Pritchard, G. J. *J. Am. Chem. Soc.* **1989**, *111*, 665.
4. Block, E.; Ofori–Okai, G.; Zubieta, J. *J. Am. Chem. Soc.* **1989**, *111*, 2327.
5. Fernandez, P.; Sousa–Pedrares, A.; Romero, J.; Garcia–Vazquez, J. A.; Sousa, A.; Perez–Lourido, P. *Inorg. Chem.* **2008**, *47*, 2121.
6. Dilworth, J. R.; Wheatley, N. *Coord. Chem. Rev.* **2000**, *199*, 89.
7. Cotton, F. A.; Eglin, J. L.; Hong, B.; James, C. A. *J. Am. Chem. Soc.* **1992**, *114*, 4915.
8. *Organic Synthesis* **1987**, *65*, 150.
9. Perez–Lourido, P.; Garcia–Vasquez, J. A.; Romero, J.; Sousa, A.; Block, E.; Maresca, K. P.; Zubieta, J. *Inorg. Chem.* **1999**, *38*, 538.
10. Hildebrand, A.; Lönnecke, P.; Silaghi–Dumitrescu, L.; Hey–Hawkins, E. *Dalton Trans.* **2008**, 4639.

11. Iwasaki, F.; Iwasaki, H. *Acta Crystallogr. B* **1972**, *28*, 3370.

12. Chen, Q.; Buss, C. B.; Young, V. G.; Fox, S. *J. Chem. Crystallogr.* **2005**, *35*, 177.

# CHAPTER 3. Synthesis and Characterization of Ruthenium(III) and Osmium(III) Complexes using Phosphine–Thiolate and Amine–Thiolate Ligands

## 3.1 Introduction

There has been considerable interest in the coordination chemistry of thiolate ligands; however, very little research has been directed toward the platinum group metals.[1–3] The chemistry of iron with thiolate ligands has received particular attention due to its known involvement in hydrogenase (**Figure III–1a**) and in iron–sulfur species in the FeMo–Co cluster of nitrogenase (**Figure III–1b**) and ferredoxins (**Figure III–1c**).

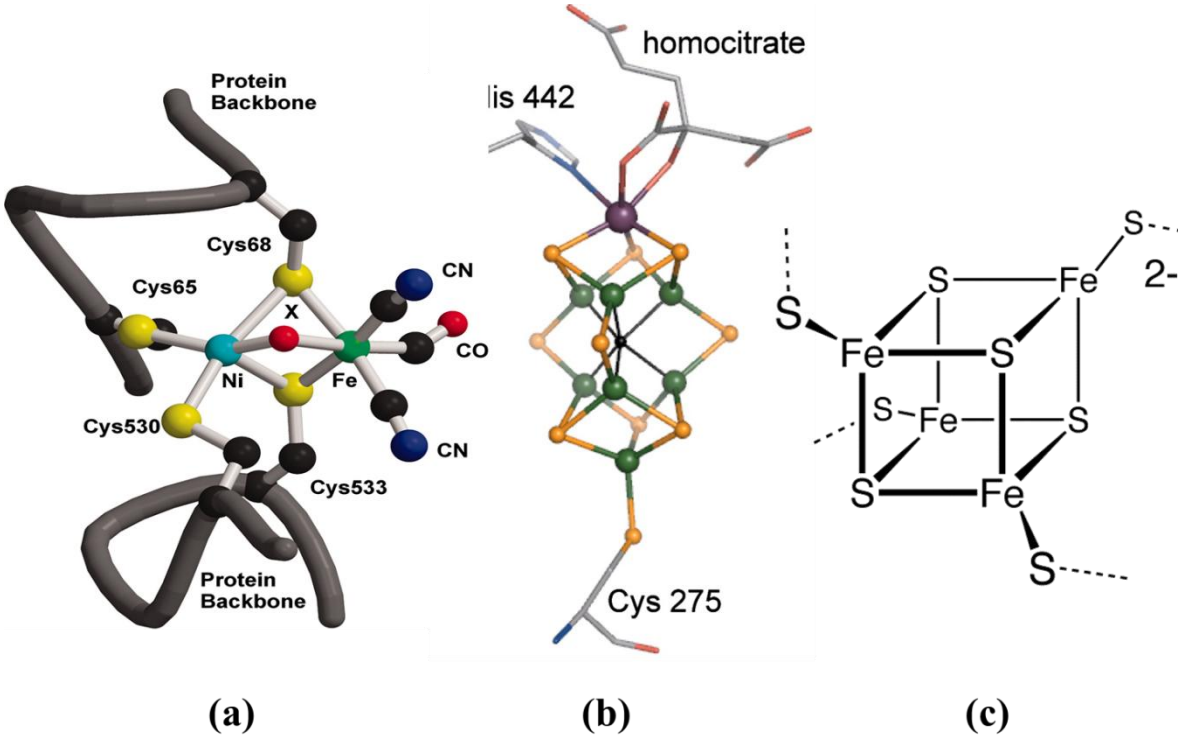


**Figure III–1. (a) [NiFe] hydrogenase[4], (b) FeMo–Co cluster[5] and (c) Fe–S cluster.[6]**

The chemistry of ruthenium with polydentate ligands with thiolate and sulfide donors have been explored[3, 7–13]; however, only a few of these complexes involved tertiary phosphine ligands. The purpose of the phosphine co–ligands is to provide a binding site as well as stabilization of the complex. There have been reports of complexes using

phosphinoalkanethiolates (e.g. $HSCH_2CH_2PPh_2$) and phosphinophenylthiolates (See Chapter 2); however reports of these types of complexes are limited.[14–18] These reports used transition metal complexes such as ruthenium, osmium, tungsten etc, which are believed to be monomeric with an octahedral geometry.

Due to the paramagnetic nature of most of these complexes as well as the absence of carbonyl (CO) and cyanide ($CN^-$) ligands, analysis using NMR and infrared spectroscopy are not used. Most researchers have claimed the formation of these complexes by using elemental analysis. A limited amount of complexes have been structurally characterized, one example being $Re^{VI}(PS2)_2$ (**Figure III–2**).[19]

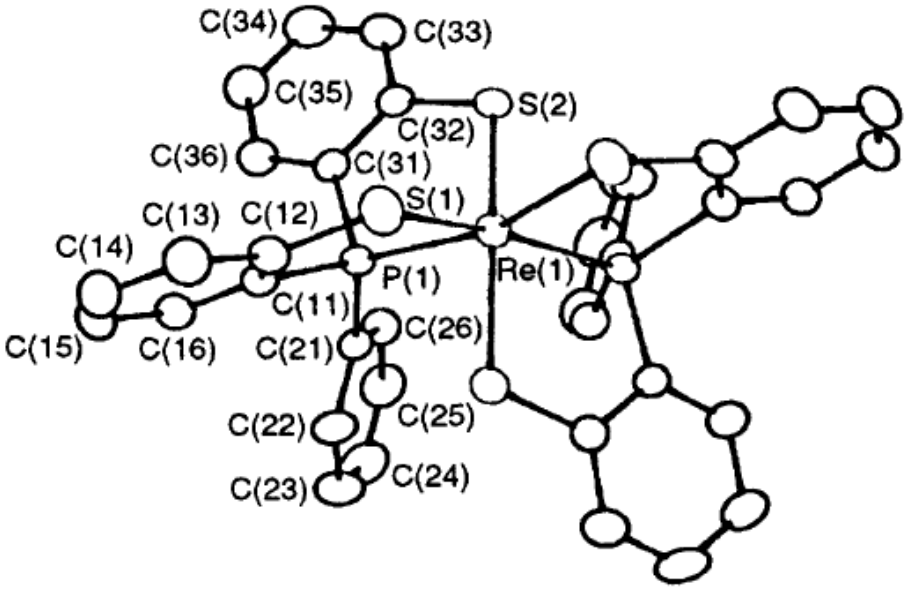


**Figure III–2. X–ray structure of $Re^{VI}(PS2)_2$.[19]**

The [PS2] ligand system has been extensively investigated by the Millar group for first row transition metals.[23–25] Among the compounds investigated were a series of octahedral complexes $[M(PS2)_2]^{0,1-}$ for Fe, Co and Ni. All the structures had the PS2 ligands coordinating in a tridentate fashion to octahedral faces. With one exception, all the structures were observed to have the geometry with the phosphorous donors in a *cis* arrangement. The one exception, $[Fe(PS2)_2]^-$, had a structure observed with the phosphorous donors having a *trans* arrangement. The complex was only obtained as a side product from the reaction of $Li_2PS2$ with $[Fe_2S_2Cl_4]^{2-}$.[23] Attempts to reproduce this synthesis were unsuccessful; attempts to directly prepare the *trans* structure only led to the *cis* isomer. The crystal structures of $[M(PS2)_2]^{0,1-}$ (M =

Fe, Co and Ni) complexes with different cations were obtained but in all these cases, only the *cis* isomer was structurally characterized. An examination of the *cis* and *trans* structures provides no structural explanation for the greater stability of the *cis* isomer. In fact, the reduced interligand steric interaction between the phenyl groups in the *trans* isomer suggests that the trans isomer might be more stable. The lack of reproducible synthetic access to a *trans* isomer, limited evaluation of their relative stabilities.

Assuming a facial coordination of the [PS2] ligand there are only one possible structure for each of the *cis* and *trans* isomers. The *cis* isomer has $C_2$ point group symmetry and is thus chiral. The *trans* isomer has $C_{2h}$ symmetry and is thus centrosymmetric. If the [PS2] ligand coordinates in a meridional, tridentate fashion, a second *trans* structure is possible. There are two diastereomers with this *trans* structure depending on the relative arrangement of the phenyl groups. The [PS2] ligand has been observed to coordinate in a tridentate, distorted planar mode in square planar $[Ni^{II}(PS2)L]$ complexes. However, it was not surprising that this structure type was not observed since this structure should be energetically unfavorable. Previous attempts to extend the studies of $[M^n(PS2)_2]^{(n-4)}$ to first row transition metal complexes with the NS2 ligand series were uniformly unsuccessful. Extension of these studies to second and third row Ru and Os complexes was initiated. The increase in size of the metal atoms and the possible reduced lability of these metal ions suggested the possibility of isolating both *cis* and *trans* isomers of these complexe.

The purpose of this research is to synthesis and characterized ruthenium and osmium complexes containing phosphine–thiolate (PS2) and amine–thiolate ligands (NS2). In the introduction of Chapter 2, the purpose of designing and reason for using these ligands was explained. It should be noted that complexes of the same type as $Re^{VI}(PS2)_2$ containing ruthenium and osmium are limited. Previous reports using $Li_2NS2$ ligand with transition metals produced dimeric complexes.[26] Complexes of the general formula, $[M^n(NS2)_2]^{(n-4)}$, have not been previously synthesized using any transition metal. One of the primary goals of this research is to expand using transition metals that are not traditionally found in biological systems. The other goal is the characterization of these transition metal compounds in the hopes that these compounds can be used as catalysts to generate hydrogen, e.g. hydrogenases, or electron transfer species, e.g. ferredoxins. These complexes could provide an alternative view on designing a model for these metalloenzymes.

## 3.2 Experimental

**Synthesis of *cis*–[$Ru^{II}(DMSO)_4Cl_2$]**

The product was prepared similar to a literature procedure.[20] In a 100 mL Schlenk flask, "$RuCl_3$•$3H_2O$" (2.0 g, 7.65 mmol) was dissolved in 20 mL of DMSO and refluxed for four hours. The solution was cooled to room temperature. Acetone (30 mL) was added to the solution and stirred for one hour, which yielded a yellow precipitate. The yellow product was filtered and washed with acetone followed by diethyl ether. Yield: 2.6 g, 70.2%

**Synthesis of [$Et_4N$][$Ru^{III}Cl_4(CH_3CN)_2$]**

The product was prepared by a literature procedure.[21] "$RuCl_3$•$3H_2O$" (1.0 g, 3.82 mmol) and $Et_4NCl$ (0.63 g, 3.82 mmol) were placed in a 250 mL Schlenk flask. A mixture of $CH_3CN$ (30 mL) and MeOH (70 mL) was transferred to the flask *via* cannula. The solution was refluxed for four hours. As the solution was being heated the color changes from a dark opaque red to a bright clear red. After refluxing, the solution was cooled to room temperature. The solution was concentrated, under vacuum, to approximately half the original volume. Diethyl ether (60 mL) was added to the solution and stirred for one hour. An orange–yellow precipitate was observed and was filtered using an open medium frit. The solid was washed with diethyl ether and dried under vacuum. Yield: 1.1 g, 63.2%.

**Synthesis of *trans*–[*n*–$Pr_4N$][$Ru^{III}(PS2)_2$]**

Synthesis of this compound can be performed by four different methods.

**Method A**

The product was prepared similar to a literature procedure.[19] In a 100 mL Schlenk flask, *cis*–[$Ru^{II}(DMSO)_4Cl_2$] (0.15 g, 0.310 mmol) was dissolved in 20 mL of MeOH. In a separate 100 mL Schlenk flask, $H_2PS2$ (0.405 g, 1.24 mmol) and lithium wire (0.018 g, 2.59 mmol) were dissolved in 20 mL of MeOH. The solution was stirred, at room temperature, until all reagents were dissolved. The ruthenium solution was added, *via* cannula, to the $Li_2PS2$ solution and the mixture was refluxed for three hours. The mixture was cooled to room temperature and a concentrated methanol solution of [*n*–$Pr_4N$]Br (0.083 g, 0.312 mmol) was layered to produce yellow–green plate crystals. Crystals were filtered using a closed frit, washed with diethyl ether and dried *in vacuo*. Yield: 0.215 g, 74.2%.

**Method B**

In a 100 mL Schlenk flask, $[Et_4N][Ru^{III}Cl_4(CH_3CN)_2]$ (0.15 g, 0.573 mmol) was dissolved in 20 mL of MeOH. In a separate 100 mL Schlenk flask, $H_2PS2$ (0.75 g, 2.30 mmol) and lithium wire (0.032 g, 4.61 mmol) were dissolved in 20 mL of MeOH. The solution was stirred, at room temperature, until all reagents were dissolved. The ruthenium solution was added, *via* cannula, to the $Li_2PS2$ solution and the mixture was refluxed for three hours. The mixture was cooled to room temperature. The dark red–orange solution was allowed to stand for three days until yellow–brown plate crystals formed. The crystals were filtered using a closed frit, washed with diethyl ether and dried *in vacuo*. Yield: 0.32 g, 63.4%.

**Method C**

In a 100 mL Schlenk flask, *cis*–$[Ru^{II}(DMSO)_4Cl_2]$ (0.15 g, 0.310 mmol) was dissolved in 30 mL of $CH_3CN$. In a separate 100 mL Schlenk flask, $H_2PS2$ (0.405 g, 1.24 mmol) and lithium wire (0.018 g, 2.59 mmol) were dissolved in 20 mL of MeOH. The solution was stirred, at room temperature, until all reagents were dissolved. The methanol was removed *in vacuo*, which resulted in a white powder ($Li_2PS2$). Approximately 30 mL of $CH_3CN$ was added to dissolve the $Li_2PS2$ solid. The ruthenium solution was added, *via* cannula, to the $Li_2PS2$ solution and the mixture was refluxed for three hours. The red mixture was cooled to room temperature and filtered through celite. A concentrated acetonitrile solution of [*n*–$Pr_4N$]Br (0.083 g, 0.312 mmol) was layered to produce yellow–brown plate crystals. Crystals were filtered using a closed frit, washed with diethyl ether and dried *in vacuo*. Yield: 0.195 g, 68.9%.

**Method D**

In a 100 mL Schlenk flask, $[Et_4N][Ru^{III}Cl_4(CH_3CN)_2]$ (0.15 g, 0.573 mmol) was dissolved in 20 mL of $CH_3CN$. In a separate 100 mL Schlenk flask, $H_2PS2$ (0.75 g, 2.30 mmol) and lithium wire (0.032 g, 4.61 mmol) were dissolved in 20 mL of MeOH. The solution was stirred, at room temperature, until all reagents were dissolved. The methanol was removed *in vacuo* and the resulting in a white powder ($Li_2PS2$). Approximately 30 mL of $CH_3CN$ was added to dissolve the $Li_2PS2$. The ruthenium solution was added, *via* cannula, to the $Li_2PS2$ solution and the mixture was refluxed for three hours. The mixture was cooled to room temperature and filtered through celite. The dark red–orange solution was allowed to stand for six days which resulted in two types of crystals being formed. The light orange plate crystals were structurally characterized as *trans*–$[Ru^{II}Cl_2(CH_3CN)_4]$. The yellow plate crystals were structurally

characterized as $[Et_4N][Ru^{III}(PS2)_2]$. Yield and separation could not be determined due to the co–crystallization of the two products.

**UV–Vis:** $\lambda_{max}$, nm ($\varepsilon_m$, $M^{-1}$ $cm^{-1}$) = 276 (49000), 315 (33300).

**Electrochemistry:** $E_{½}$ ($\Delta E_p$) = 555 mV (58 mV); 1.0 mM in DMF vs. Ag/AgCl, oxidation.

**Unit cell:** [*n*–$Pr_4N$][$Ru^{III}(PS2)_2$]: Monoclinic, $P2_1/n$, a = 9.39420(10)Å, b = 23.2295(4)Å, c = 20.5371(3)Å, α = 90°, β = 101.551(2)°, γ = 90°, V = 4390.89(11)Å$^3$.

**Unit cell:** [PPN][$Ru^{III}(PS2)_2$]: Triclinic, *P*–1, a = 11.186(5)Å, b = 12.750(5)Å, c = 12.761(5)Å, α = 71.422(5)°, β = 78.101(5)°, γ = 78.245(5)°, V = 1669.3(12)Å$^3$.

A yellow–green plate crystal measuring 0.25 × 0.15 × 0.15 mm$^3$ was mounted using a nylon loop and centered on the X–ray beam at 100 K. Crystals were grown by layering a concentrated methanol solution of [*n*–$Pr_4N$]Br onto a methanolic solution of Li[$Ru^{III}(PS2)_2$]. Crystals were grown within one day. The accurate unit cell was obtained using reflection with 2θ = 3.16 – 28.47°: a = 9.394(1) Å, b = 23.229(4) Å, c = 20.537(3) Å, α = γ = 90°, β = 101.551(2)°, V = 4390.62(4) Å$^3$. The structure was solved under a primitive monoclinic crystal system (space group $P2_1/n$) using 10184 reflections. The asymmetric unit consists of one molecule of the ruthenium complex and one cation. The data reduction was done using CryAlisPro and the structure refinement was done with SHELXL–97 (Sheldrick). All the non–hydrogen atoms were located by Direct Methods and were refined anisotopically by a full–matrix least–squares method. The positions of the remaining hydrogen atoms were calculated. The crystallographic parameters and atomic coordinates for this compound are located in **Table A–5**.

**Synthesis of *trans*–[$Et_4N$][$Ru^{III}(PS2')_2$]**

Synthesis of this compound can be made by four different methods.

**Method A**

In a 100 mL Schlenk flask, *cis*–[$Ru^{II}(DMSO)_4Cl_2$] (0.15 g, 0.310 mmol) was dissolved in 20 mL of MeOH. In a separate 100 mL Schlenk flask, $H_2PS2'$ (0.440 g, 1.24 mmol) and lithium wire (0.018 g, 2.59 mmol) were dissolved in 20 mL of MeOH. The solution was stirred, at room temperature, until all reagents were dissolved. The ruthenium solution was added, *via* cannula, to the $Li_2PS2'$ solution and the mixture was refluxed for three hours. The mixture was cooled to room temperature and a concentrated methanol solution of [$Et_4N$]Br (0.065 g, 0.310 mmol) was layered to produce red–brown microcrystals. These microcrystals were filtered using closed frit, washed with diethyl ether, and dried *in vacuo*. Yield: 0.195 g, 67.3%.

**Method B**

In a 100 mL Schlenk flask, $[Et_4N][Ru^{III}Cl_4(CH_3CN)_2]$ (0.15 g, 0.573 mmol) was dissolved in 20 mL of MeOH. In a separate 100 mL Schlenk flask, $H_2PS2'$ (0.82 g, 2.31 mmol) and lithium wire (0.032 g, 4.63 mmol) were dissolved in 20 mL of MeOH. The solution was stirred, at room temperature, until all reagents were dissolved. The ruthenium solution was added, *via* cannula, to the $Li_2PS2$ solution and the mixture was refluxed for three hours. The mixture was cooled to room temperature and filtered through celite. The dark red–orange solution was allowed to stand for three days until red–orange needle crystals formed. The crystals were filtered using a closed frit, washed with diethyl ether and dried *in vacuo*. Yield: 0.28 g, 52.1%.

**Method C**

In a 100 mL Schlenk flask, *cis*–$[Ru^{II}(DMSO)_4Cl_2]$ (0.15 g, 0.310 mmol) was dissolved in 30 mL of $CH_3CN$. In a separate 100 mL Schlenk flask, $H_2PS2'$ (0.405 g, 1.24 mmol) and lithium wire (0.018 g, 2.59 mmol) were dissolved in 20 mL of MeOH. The solution was stirred, at room temperature, until all reagents were dissolved. The methanol was removed *in vacuo* which resulted in a white powder ($Li_2PS2'$). Approximately 30 mL of $CH_3CN$ was added to dissolve the $Li_2PS2'$. The ruthenium solution was added, *via* cannula, to the $Li_2PS2'$ solution and the mixture was refluxed for three hours. The mixture was cooled to room temperature and a concentrated acetonitrile solution of $[Et_4N]Br$ (0.065 g, 0.310 mmol) was layered to produce red–brown needle crystals. Crystals were filtered using closed frit, washed with diethyl ether and dried *in vacuo*. Yield: 0.175 g, 61.8%.

**Method D**

In a 100 mL Schlenk flask, $[Et_4N][Ru^{III}Cl_4(CH_3CN)_2]$ (0.15 g, 0.573 mmol) was dissolved in 20 mL of MeOH. In a separate 100 mL Schlenk flask, $H_2PS2'$ (0.82 g, 2.31 mmol) and lithium wire (0.032 g, 4.63 mmol) were dissolved in 20 mL of MeOH. The solution was stirred, at room temperature, until all reagents were dissolved. The methanol was removed *in vacuo* and the resulting in a white powder ($Li_2PS2$). Approximately 30 mL of $CH_3CN$ was added to dissolve the $Li_2PS2$. The ruthenium solution was added, *via* cannula, to the $Li_2PS2$ solution and the mixture was refluxed for three hours. The mixture was cooled to room temperature and was filtered through celite. The dark red–orange solution was allowed to stand for four days which resulted in two types of crystals being formed. The orange plate crystals were structurally

characterized as *trans*–$RuCl_2(CH_3CN)_4$. The dark red–orange needle crystals were structurally characterized as $[Et_4N][Ru^{III}(PS2')_2]$. Yield and separation could not be determined due to the co–crystallization of the two products.

**UV–Vis:** $\lambda_{max}$, nm ($\varepsilon_m$, $M^{-1}$ $cm^{-1}$) = 277 (53200), 318 (38400).

**Electrochemistry:** $E_{½}$ ($\Delta E_p$) = 510 mV (77 mV); 1.0 mM in DMF vs. Ag/AgCl, oxidation

**Unit cell:** Triclinic, *P*–1, a = 9.2808(2)Å, b = 13.8541(4)Å, c = 19.3704(6)Å, α = 78.968(3)°, β = 88.488(2)°, γ = 80.802°, V = 2350.19(11)Å$^3$.

A red–brown needle crystal measuring 0.35 × 0.15 × 0.15 mm$^3$ was mounted using a nylon loop and centered on the X–ray beam at 100 K. Crystals were grown by layering a concentrated methanol solution of $[Et_4N]Br$ onto a methanolic solution of $Li[Ru^{III}(PS2')_2]$. Crystals were grown within two days. The accurate unit cell was obtained using reflection with 2θ = 3.12 – 29.53°: a = 9.2808(2) Å, b = 13.8541(4) Å, c = 19.3704(3) Å, α = 72.968(3)°, β = 88.488(2)°, γ = 80.802(2)°, V = 2350.19(11) Å$^3$. The structure was solved under a primitive triclinic crystal system (space group *P*–1) using 40425 reflections. The asymmetric unit consists of two molecules of the ruthenium complex, which contain an inversion center, and one cation. The data reduction was done using CryAlisPro and the structure refinement was done with SHELXL–97 (Sheldrick). All the non–hydrogen atoms were located by Direct Methods and were refined anisotopically by a full–matrix least–squares method. The positions of the remaining hydrogen atoms were calculated. The crystallographic parameters and atomic coordinates for this compound are located in **Table A–6**.

**Synthesis of *cis*–$[Et_4N][Ru^{II}(PS3')(HPS3')]$("S–S" disulfide)**

In a 100 mL Schlenk flask, *cis*–$[Ru^{II}(DMSO)_4Cl_2]$ (0.15 g, 0.310 mmol) was dissolved in 20 mL of MeOH. In a separate 100 mL Schlenk flask, $H_3PS3'$ (0.496 g, 1.24 mmol) and lithium wire (0.017 g, 2.45 mmol) were dissolved in 20 mL of MeOH. The solution was stirred, at room temperature, until all reagents were dissolved. The ruthenium solution was added, *via* cannula, to the $Li_2HPS3'$ solution and the mixture was refluxed for three hours. The mixture was cooled to room temperature and exposed to air followed by the addition of a concentrated methanol solution of $[Et_4N]Br$ (0.065 g, 0.309 mmol) which was layered to produce red–brown plate crystals. Crystals were filtered using a closed frit, washed with diethyl ether and dried *in vacuo*. Yield: 0.157 g, 49.4%.

**Unit cell:** Monoclinic, $P2_1/c$, a = 15.094(5)Å, b = 17.482(5)Å, c = 18.799(5)Å, $\alpha = \gamma = 90^o$, $\beta$ = 93.140(5)$^o$, V = 4953.11(3)Å$^3$.

A red–brown prism crystal measuring 0.30 × 0.30 × 0.20 mm$^3$ was mounted using a nylon loop and centered on the X–ray beam at 100 K. Crystals were grown by layering a concentrated methanol solution of $[Et_4N]Br$ onto a methanolic solution of $Li[Ru^{II}(PS3')(HPS3')]$–("S–S" disulfide). Crystals were grown within one day. The accurate unit cell was obtained using reflection with $2\theta$ = 3.18 – 27.12$^o$: a = 15.094(5) Å, b = 17.482(5) Å, c = 18.799(5) Å, $\alpha = \gamma = 90^o$, $\beta$ = 93.140(5)$^o$, V = 4953.11(3) Å$^3$. The structure was solved under a primitive monoclinic crystal system (space group $P2_1/c$) using 9493 reflections. The asymmetric unit consists of one molecule of the ruthenium complex and one cation. The data reduction was done using CryAlisPro and the structure refinement was done with SHELXL–97 (Sheldrick). All the non–hydrogen atoms were located by Direct Methods and were refined anisotopically by a full–matrix least–squares method. The thiol proton was located using Fourier difference maps. The positions of the remaining hydrogen atoms were calculated. The crystallographic parameters and atomic coordinates for this compound are located in **Table A–7**.

**Synthesis of *trans*–[*n*–Pr$_4$N][Ru$^{III}$(NS2)$_2$]**

In a 100 mL Schlenk flask, *cis*–$[Ru^{II}(DMSO)_4Cl_2]$ (0.15 g, 0.310 mmol) was dissolved in 20 mL of MeOH. In a separate 100 mL Schlenk flask, $Li_2NS2$ (0.450 g, 1.24 mmol) was dissolved in 20 mL of MeOH. The solution was stirred, at room temperature, until all reagents were dissolved. The ruthenium solution was added to the $Li_2NS2$ solution and the dark green mixture was refluxed for three hours. The mixture was cooled to room temperature and a concentrated methanol solution of [*n*–Pr$_4$N]Br (0.082 g, 0.312 mmol) was layered to produce emerald green microcrystals. The microcrystals were filtered *via* closed frit, washed with diethyl ether, and dried *in vacuo*. Yield: 0.275 g, 90.0%.

**UV–Vis:** $\lambda_{max}$, nm ($\varepsilon_m$, M$^{-1}$ cm$^{-1}$) = 283 (35100), 312 (30000).

**Electrochemistry:** $E_{½}$ ($\Delta E_p$) = 395 mV (55 mV); 1.0 mM in DMF vs. Ag/AgCl, oxidation.

**Unit cell:** Monoclinic, $P2_1/n$, a = 11.4340(3)Å, b = 23.6791(6)Å, c = 18.3050(4)Å, $\alpha = \gamma = 90^o$, $\beta$ = 96.415(2)$^o$, V = 4925.0(2)Å$^3$.

An emerald green plate crystal measuring 0.30 × 0.20 × 0.10 mm$^3$ was mounted using a nylon loop and centered on the X–ray beam at 100 K. Crystals were grown by layering a concentrated methanol solution of [*n*–Pr$_4$N]Br onto a methanolic solution of $Li[Ru^{III}(NS2)_2]$.

Crystals were grown within two days. The accurate unit cell was obtained using reflection with $2\theta = 3.14 – 29.57^{o}$: a = 11.4340(3) Å, b = 23.6791(6) Å, c = 18.3050(4) Å, $\alpha = \gamma = 90^{o}$, $\beta = 96.415(2)^{o}$, V = 4925.0(2) $Å^3$. The structure was solved under a primitive monoclinic crystal system (space group $P2_1/n$) using 11700 reflections. The asymmetric unit consists of one molecule of the ruthenium complex and one cation. The data reduction was done using CryAlisPro and the structure refinement was done with SHELXL–97 (Sheldrick). All the non–hydrogen atoms were located by Direct Methods and were refined anisotopically by a full–matrix least–squares method. The positions of the remaining hydrogen atoms were calculated. The crystallographic parameters and atomic coordinates for this compound are located in **Table A–8**.

**Synthesis of *trans*–[*n*–$Pr_4N$][$Ru^{III}(NS2')_2$]**

In a 100 mL Schlenk flask, *cis*–[$Ru^{II}(DMSO)_4Cl_2$] (0.15 g, 0.310 mmol) was dissolved in MeOH (20 mL). In a separate 100 mL Schlenk flask, $Li_2$NS2' (0.470 g, 1.25 mmol) was dissolved in MeOH (20 mL). The solution was stirred, at room temperature, until all reagents were dissolved. The ruthenium solution was added to the $Li_2$NS2' solution and the dark green mixture was refluxed for three hours. The mixture was cooled to room temperature and a concentrated methanol solution of [$Pr_4N$]Br (0.083 g, 0.312 mmol) was layered to produce emerald green microcrystals. The microcrystals were filtered *via* closed frit, washed with diethyl ether, and dried *in vacuo*. Yield: 0.245 g, 78.0%.

**UV–Vis:** $\lambda_{max}$, nm ($\varepsilon_m$, $M^{-1}$ $cm^{-1}$) = 281 (31000), 313 (26400).

**Electrochemistry:** $E_{½}$ ($\Delta E_p$) = 393 mV (55 mV); 1.0 mM in DMF vs. Ag/AgCl.

**Unit cell:** Monoclinic, $P2_1/n$, a = 11.417(5)Å, b = 24.770(5)Å, c = 18.287(5)Å, $\alpha = \gamma = 90^{o}$, $\beta = 95.739(5)^{o}$, V = 5145.63(4)$Å^3$.

An emerald green plate crystal measuring 0.25 × 0.20 × 0.10 $mm^3$ was mounted using a nylon loop and centered on the X–ray beam at 100 K. Crystals were grown by layering a concentrated methanol solution of [*n*–$Pr_4N$]Br to a methanolic solution of Li[$Ru^{III}(NS2')_2$]. Crystals were grown within two days. The accurate unit cell was obtained using reflection with $2\theta = 3.19 – 29.44^{o}$: a = 11.417(5) Å, b = 24.770(5) Å, c = 18.287(5) Å, $\alpha = \gamma = 90^{o}$, $\beta = 95.739(5)^{o}$, V = 5145.63(4) $Å^3$. The structure was solved under a primitive monoclinic crystal system (space group $P2_1/n$) using 10576 reflections. The asymmetric unit consists of one molecule of the ruthenium complex and one cation. The data reduction was done using

CryAlisPro and the structure refinement was done with SHELXL–97 (Sheldrick). All the non–hydrogen atoms were located by Direct Methods and were refined anisotopically by a full–matrix least–squares method. The positions of the remaining hydrogen atoms were calculated. The crystallographic parameters and atomic coordinates for this compound are located in **Table A–9**.

**Synthesis of $[Et_4N]_2[Os^{IV}Cl_6]$**

Synthesis of desired product was prepared by a literature procedure.[31] All manipulations were performed in air. Osmium tetroxide (2 g, 7.87 mmol) was added to a solution of $[Et_4N]Cl•H_2O$ (4 g, 24 mmol) in 30 mL of concentrated HCl. The solution was refluxed for nineteen hours and cooled to room temperature. Ethanol (30 mL) and diethyl ether (15 mL) was added to the acid solution. The flask was kept at –20°C for three hours. An orange solid precipitated and was filtered. The orange solid was washed with minimum amount of ethanol (4 × 10 mL) and dried for one hour at 100°C. Yield: 4.95 g, 94.8%.

**Synthesis of *trans*–$[Os^{II}Cl_2(PPh_3)_3]$**

The synthesis of desired product was prepared by using a modified literature procedure.[22] A solution of *tert*–butyl alcohol (300 mL) and distilled water (120 mL) was degassed for thirty minutes under a dinitrogen atmosphere. Tetraethylammonium hexachloroosmate(IV) (2.00 g, 3.01 mmol) and triphenylphosphine (5.54 g, 21.12 mmol) were added to the solution and was heated to reflux for three hours. The solution changed from yellow to dark green. The mixture was filtered using an open medium porous frit while the solution was hot. The resulting dark solid was washed with absolute ethanol (3 × 20 mL) and diethyl ether (4 x 30 mL) and dried under vacuum. Yield: 1.45 g, 45.9%

**Synthesis of *trans*–$[Me_3NBz][Os^{III}(PS2)_2]$**

The product was prepared by a similar literature procedure.[19] In a 100 mL Schlenk flask, *trans*–$[Os^{II}Cl_2(PPh_3)_3]$ (0.15 g, 0.143 mmol) was dissolved in MeOH (20 mL). In a separate 100 mL Schlenk flask, $H_2PS2$ (0.190 g, 0.582 mmol) and lithium wire (0.009 g, 1.29 mmol) were dissolved in MeOH (20 mL). The solution was stirred, at room temperature, until all reagents were dissolved. The osmium solution was added, *via* cannula, to the $Li_2PS2$ solution and the dark green mixture was refluxed for three hours. The mixture was cooled to room temperature and a concentrated methanol solution of $[Me_3NBz]Cl$ (0.027 g, 0.145 mmol) was layered to produce

emerald green needle crystals. Crystals were filtered *via* closed frit, washed with diethyl ether, and dried *in vacuo*. Yield: 0.067 g, 47.1%.

**UV–Vis:** $\lambda_{max}$, nm ($\varepsilon_m$, $M^{-1}$ $cm^{-1}$) = 275 (31000).

**Electrochemistry:** $E_{½}$ ($\Delta E_p$) = 127 mV (67 mV); 1.0 mM in DMF vs. Ag/AgCl, oxidation.

**Unit cell:** Triclinic, *P*–1, a = 9.309(3)Å, b = 12.829(4)Å, c = 18.442(5)Å, α = 83.487(3)°, β = 77.074(3)°, γ = 71.731(3)°, V = 2036.20(6)Å$^3$.

A green needle crystal measuring 0.35 × 0.15 × 0.10 mm$^3$ was mounted using a nylon loop and centered on the X–ray beam at 100 K. Crystals were grown by layering a concentrated methanol solution of [$Me_3$NBz]Cl onto a methanolic solution of Li[$Os^{III}(PS2)_2$]. Crystals were grown within three days. The accurate unit cell was obtained using reflection with 2θ = 3.27 – 29.69°: a = 9.309(3) Å, b = 12.829(4) Å, c = 18.442(5) Å, α = 83.487(2)°, β = 77.074(3)°, γ = 71.731(3)°, V = 2036.20(6) Å$^3$. The structure was solved under a primitive triclinic crystal system (space group *P*–1) using 10607 reflections. The asymmetric unit consists of two molecules of the osmium complex, which contain an inversion center, and one cation. The data reduction was done using CryAlisPro and the structure refinement was done with SHELXL–97 (Sheldrick). All the non–hydrogen atoms were located by Direct Methods and were refined anisotopically by a full–matrix least–squares method. The positions of the remaining hydrogen atoms were calculated. The crystallographic parameters and atomic coordinates for this compound are located in **Table A–10**.

**Synthesis of *cis*–[$Me_3$NBz][$Os^{III}(PS2')_2$]**

In a 100 mL Schlenk flask, *trans*–[$Os^{II}Cl_2(PPh_3)_3$] (0.15 g, mmol) was dissolved in MeOH (20 mL). In a separate 100 mL Schlenk flask, $H_2$PS2' (0.205 g, 0.578 mmol) and lithium wire (0.009 g, 1.30 mmol) were dissolved in MeOH (20 mL). The solution was stirred, at room temperature, until all reagents were dissolved. The osmium solution was added, *via* cannula, to the $Li_2$PS2' solution and the dark green mixture was refluxed for three hours. The mixture was cooled to room temperature and a concentrated methanol solution of [$Me_3$NBz]Cl (0.027 g, 0.145 mmol) was layered to produce green microcrystals. These microcrystals were filtered *via* closed frit, washed with diethyl ether, and dried *in vacuo*. Yield: 0.060 g, 40.1%.

**UV–Vis:** $\lambda_{max}$, nm ($\varepsilon_m$, $M^{-1}$ $cm^{-1}$) = 282 (15000).

**Electrochemistry:** $E_{½}$ ($\Delta E_p$) = 457 mV (64 mV), 292 mV (79 mV); 1.0 mM in DMF vs. Ag/AgCl, oxidation.

**Unit cell:** Triclinic, *P*–1, a = 9.0659(3)Å, b = 15.3938(5)Å, c = 16.6074(5)Å, α = 78.314(3)°, β = 88.340(2)°, γ = 86.192(2)°, V = 2264.37(2)Å$^3$.

A light green needle crystal measuring 0.35 × 0.15 × 0.05 mm$^3$ was mounted using a nylon loop and centered on the X–ray beam at 100 K. Crystals were grown by layering a concentrated methanol solution of $[Me_3NBz]Cl$ onto a methanolic solution of $Li[Os^{III}(PS2')_2]$. Crystals were grown within two days. The accurate unit cell was obtained using reflection with 2θ = 3.20 – 28.40°: a = 9.0659(3) Å, b = 15.3938(5) Å, c = 16.6074(5) Å, α = 78.314(3)°, β = 88.340(2)°, γ = 86.192(2)°, V = 2264.37(2) Å$^3$. The structure was solved under a primitive triclinic crystal system (space group *P*–1) using 9484 reflections. The asymmetric unit consists of one molecule of the osmium complex and one cation. The data reduction was done using CryAlisPro and the structure refinement was done with SHELXL–97 (Sheldrick). All the non–hydrogen atoms were located by Direct Methods and were refined anisotopically by a full–matrix least–squares method. The positions of the remaining hydrogen atoms were calculated. The crystallographic parameters and atomic coordinates for this compound are located in **Table A–11**.

## 3.3 Results and Discussion

A series of high–valent thiolate monomers of the general formula $[M^{III}(PS2^{(\prime)})_2]^-$ and $[M^{III}(NS2^{(\prime)})_2]^-$ (M = Ru and Os) have been synthesized and characterized. The notation $[PS2^{(\prime)}]$ symbolizes complexes using either [PS2] or [PS2']. Similar notation, $[NS2^{(\prime)}]$, is used for [NS2] and [NS2']. These six compounds have octahedral geometries about the metal center. All $M^{III}$ complexes were prepared from their respective $M^{II}$ compounds. Presumably, the electron lost from the metal center was used to reduce protons to hydrogen. Further studies need to be performed to confirm this hypothesis.

### 3.3.1 Synthesis of $[R_4N][Ru^{III}(PS2^{(\prime)})_2]$ (where R = *n*–Pr (PS2) and Et (PS2'))

The synthesis of *trans*–$[n\text{–}Pr_4N][Ru^{III}(PS2)_2]$ and *trans*–$[Et_4N][Ru^{III}(PS2')_2]$ were performed by four different synthetic routes. Method A was based on a modified literature procedure. The reported literature procedure used *trans*–$[Ru^{II}Cl_2(PPh_3)_3]$ as the ruthenium starting material whereas the new synthetic route used *cis*–$[Ru^{II}(DMSO)_4Cl_2]$.

Under dinitrogen atmosphere, *cis*–[$Ru^{II}(DMSO)_4Cl_2$] was dissolved in methanol upon gentle heating. Four molar equivalents of $H_2PS2$ and two molar equivalents of lithium wire were dissolved in methanol until complete dissolution. The ruthenium solution was transferred *via* cannula to the $Li_2PS2$ solution and refluxed. Excess ligand was used to prevent any dimers from forming as side or main products. As the solution was refluxing, the color changed from yellow–red to red–brown. The solution was cooled to room temperature and a concentrated methanol solution of 1.1 molar equivalents of [*n*–$Pr_4N$]Br was transferred *via* cannula and layered onto the solution in the reaction flask. The flask was left undisturbed to form yellow–green plate crystals which were suitable for x–ray crystallography in 74% yield. The desired product was, also, formed by adding the ruthenium starting material with four molar equivalents of $Li_2PS2$ and allowing the solution to stir overnight at room temperature under a dinitrogen atmosphere which produced 55% yield.

This procedure can be performed similarly using $Li_2PS2'$ and using [$Et_4N$]Br as the counter cation source which produced red–brown plate crystals. Comparative yields are 67% for refluxing and 45% for stirring. The overall reaction scheme is shown below (**Figure III–3**).

Methods B, C and D were designed to find synthetic routes to synthesize the *cis*–isomer. These routes were formulated by following synthetic routes that were known to produce the iron analogues.[23–24] It was shown that reacting [$Et_4N]_2[Fe_2^{III}S_2Cl_4$] with two equivalents of $Li_2PS2$ in acetonitrile can produce the *trans*–[$Et_4N$][$Fe^{III}(PS2)_2$] compound.[23] However, when two equivalents of $Li_2PS2$ was reacted with $Fe^{II}Cl_2 \bullet 4H_2O$ the *cis*–isomer can be synthesized.[24] The different synthetic routes proved to be unsuccessful for synthesizing the *cis*–isomer of the $[Ru^{III}(PS2)_2]^-$ or $[Ru^{III}(PS2')_2]^-$ complexes.

Despite the lack of energetic studies of these compounds, it was thought that the *trans*–$[Ru^{III}(PS2)_2]^-$ was the thermodynamically favored product while the *cis*–$[Ru^{III}(PS2)_2]^-$ was kinetically favored.

A series of experiments were performed to understand and/or prove this hypothesis. Since kinetically favored products are the first to be synthesized in a chemical reaction, various techniques can be used to isolate this product. One technique that was used was cooling the reaction to various temperatures.

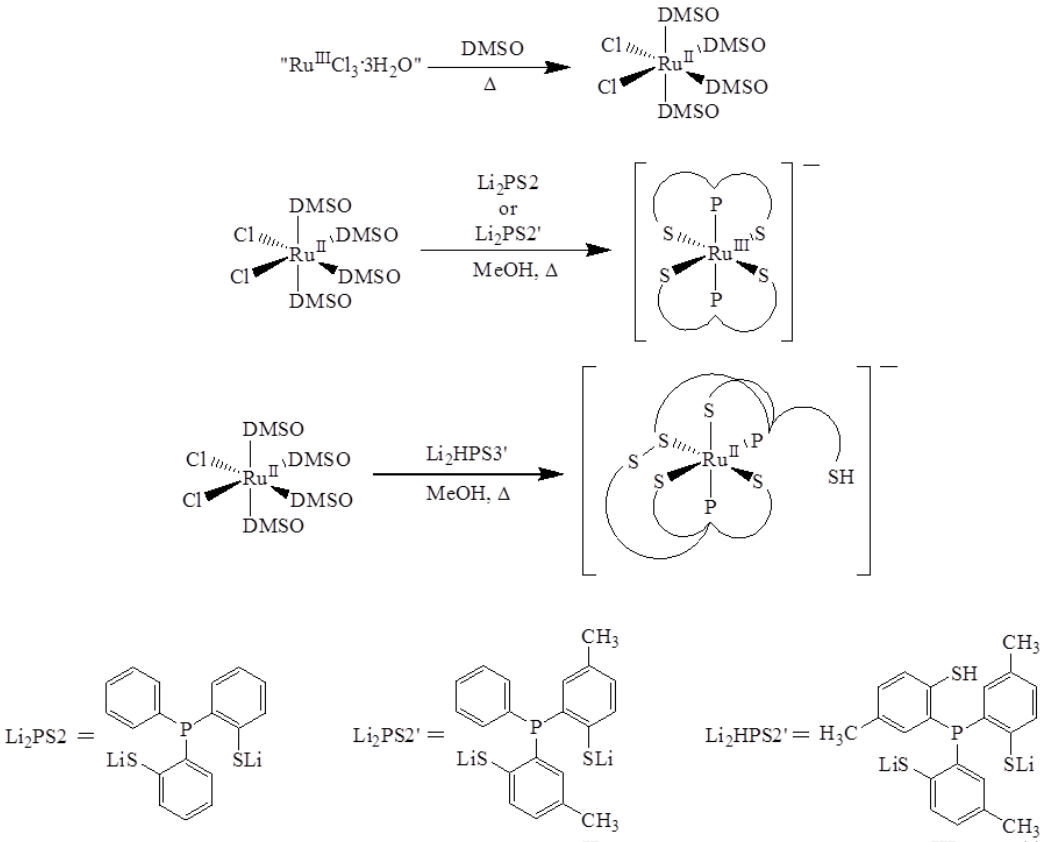


**Figure III–3. Overall synthesis of *cis*–[$Ru^{II}(DMSO)_4Cl_2$], *trans*–[$Ru^{III}(PS2^{(')})]^-$ and *cis*–[$Ru^{II}(PS3')(HPS3')]^-$ complexes.**

The temperature range over which this study was performed was 0 $^oC$ to –20 $^oC$. It was shown by carrying out the reaction as described in the experimental section, that cold conditions does not produce the desired *cis*–$[Ru^{III}(PS2)_2]^-$ or *cis*–$[Ru^{III}(PS2')_2]^-$ complexes. Yields were consistent with varying cold temperatures. Further studies need to be performed in order to understand this mechanism as well as to isolate the *cis*–isomer. Methods A to D and temperature studies are summarized in **Table III–1**.

| Table III–1. Method and Temperature Studies of Synthesizing $[Ru^{III}(PS2^{(\prime)})_2]^-$. | | | | |
|---|---|---|---|---|
| **Experiment** | **Reagent** | **Solvent** | **Temperature ($^oC$)** | **Isomer Obtained (PS2/PS2')** |
| 1 | *cis*–$[Ru^{II}(DMSO)_4Cl_2]$ | MeOH | 65 | *trans/trans* |
| 2 | *cis*–$[Ru^{II}(DMSO)_4Cl_2]$ | $CH_3CN$ | 82 | *trans/trans* |
| 3 | *cis*–$[Ru^{II}(DMSO)_4Cl_2]$ | MeOH | 0 | *trans/trans* |
| 4 | *cis*–$[Ru^{II}(DMSO)_4Cl_2]$ | $CH_3CN$ | 0 | *trans/trans* |
| 5 | *cis*–$[Ru^{II}(DMSO)_4Cl_2]$ | MeOH | –20 | *trans/trans* |
| 6 | *cis*–$[Ru^{II}(DMSO)_4Cl_2]$ | $CH_3CN$ | –20 | *trans/trans* |
| 7 | $[Et_4N][Ru^{III}Cl_4(CH_3CN)_2]$ | MeOH | 65 | *trans/trans* |
| 8 | $[Et_4N][Ru^{III}Cl_4(CH_3CN)_2]$ | $CH_3CN$ | 82 | *trans/trans* |
| 9 | $[Et_4N][Ru^{III}Cl_4(CH_3CN)_2]$ | MeOH | 0 | *trans/trans* |
| 10 | $[Et_4N][Ru^{III}Cl_4(CH_3CN)_2]$ | $CH_3CN$ | 0 | *trans/trans* |
| 11 | $[Et_4N][Ru^{III}Cl_4(CH_3CN)_2]$ | MeOH | –20 | *trans/trans* |
| 12 | $[Et_4N][Ru^{III}Cl_4(CH_3CN)_2]$ | $CH_3CN$ | –20 | *trans/trans* |

The synthesis *cis*–$[Et_4N][Ru^{II}(PS3')(HPS3')]$ was performed under reaction conditions similar to those of the $[Ru^{III}(PS2')_2]^-$ complexes, except replacing $Li_2PS2'$ with $Li_2HPS3'$. The $H_3PS3'$ was placed in a methanolic solution with two equivalence of lithium to produce the desired reactant, $Li_2HPS3'$. The main objective was to synthesize a ruthenium complex with two free thiol groups (−SH), where the general formula is $[Ru^{m+}(PS2SH)_2]^{(m-4)}$ (**Figure III–4**). This type of complex is also known as the "pendant" complex.

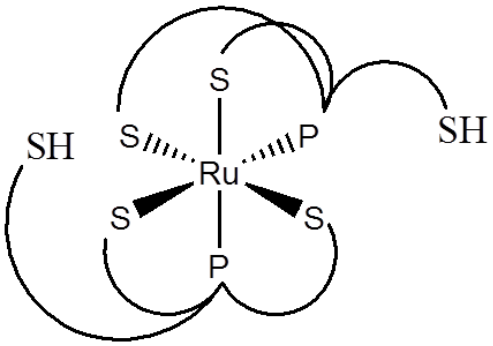


**Figure III–4. Ruthenium–PS3 "pendant" complex.**

Reacting this complex (**Figure III–4**) with various transition metal chloride compounds, $M^{II}Cl_2$ or $M^{III}Cl_3$ (where M = transition metal), could produce dimers of the general formula $[M^{m+}Ru^{n+}(PS3)_2]^{(m+n-6)}$. In the past, these complexes have been synthesized using only first row transition metals.[25] However, the isolation of the ruthenium pendant complex was not successful after multiple attempts. While the reaction was processing, air was introduced causing the oxidation of one free thiol which created a disulfide bond from the free thiol of one PS3' ligand to the bound sulfide of the adjacent [PS3']. This disulfide bond was verified by the X–ray crystal structure. This disulfide bond formation was also seen under the same reaction conditions when iron replaced ruthenium.[25] In the case of the iron complex the disulfide bond was made using the free thiolate of both [PS3] ligands (**Figure III–5**).

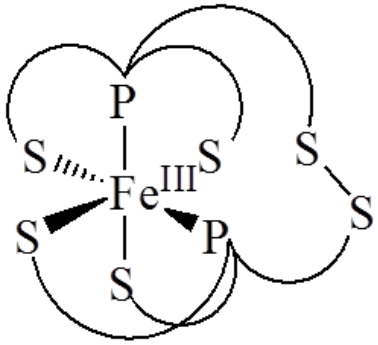


**Figure III–5. $[Fe^{III}(PS3)_2]^-$ ("S–S" disulfide).**

### 3.3.2 Synthesis of $[Me_3NBz][Os^{III}(PS2^{(\prime)})_2]$

The synthesis of $[Os^{III}(PS2)]^-$ was carried out according to a literature procedure.[19] However, characterizations of this compound were not reported in the literature with the exception of elemental analysis. Reaction conditions were similar to those of the ruthenium analog. While the reaction was heated, the solution changed from light green to dark green. The solution was cooled to room temperature and a concentrated methanol solution of 1.1 molar equivalents of $[Me_3NBz]Cl$ was transferred, *via* cannula, and layered into the reaction flask. The flask was left undisturbed for several days to form emerald green needle crystals which were suitable for X–ray crystallography in 45% yield. The desired product was, also, formed by adding the osmium starting material to four molar equivalents of $Li_2PS2$ and allowing the solution to stir overnight at room temperature under a dinitrogen atmosphere; yield 30%.

This procedure was performed in a similar manner using $Li_2PS2'$ and the same countercation which produced emerald green needle crystals. Comparative yields are 40% for refluxing and 35% for stirring. The overall reaction scheme is shown below (**Figure III–6**).

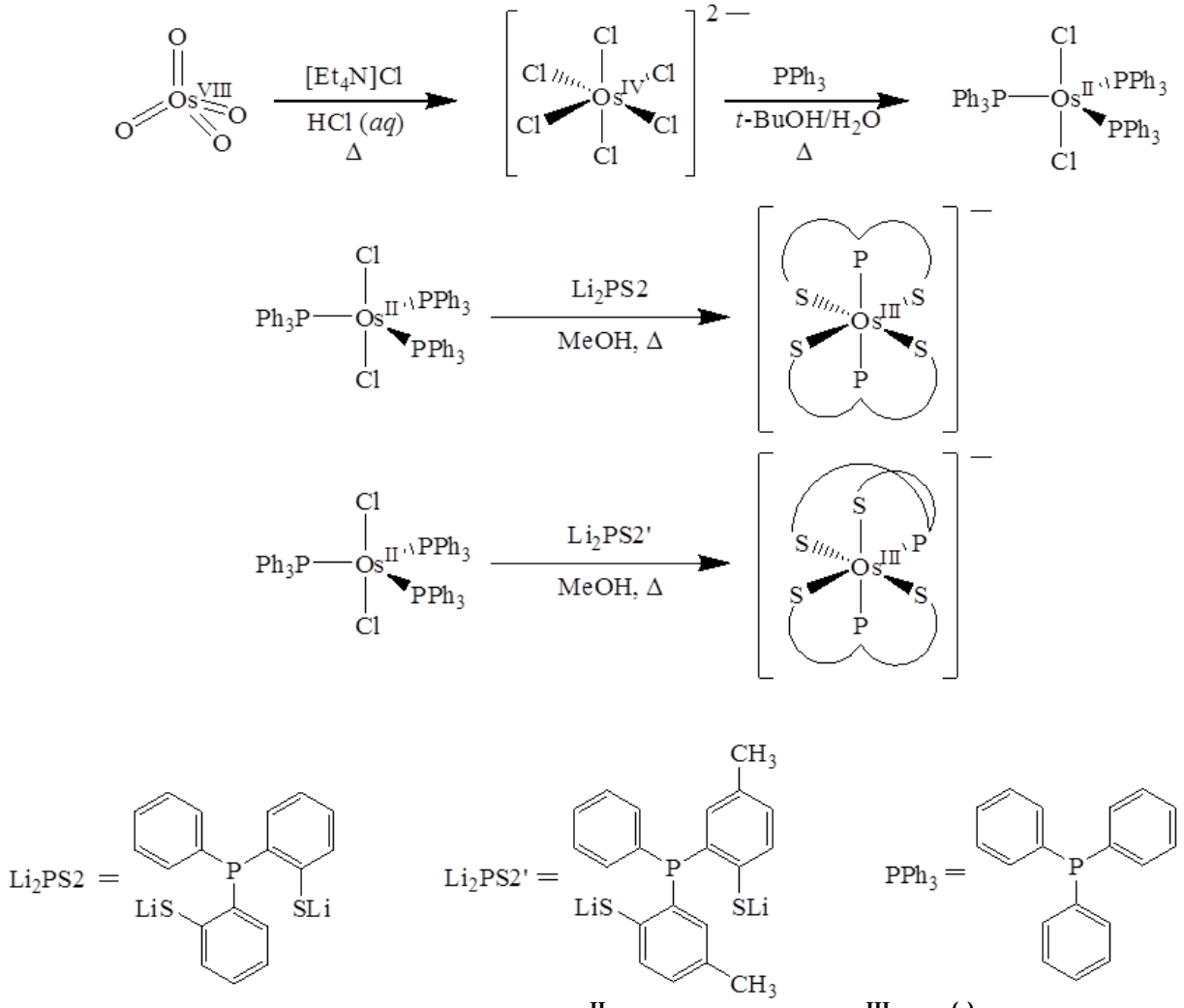


**Figure III–6. Overall synthesis of *trans*–$[Os^{II}Cl_2(PPh_3)_3]$ and $[Os^{III}(PS2^{(\prime)})_2]^-$ complexes.**

Temperature studies were done with the osmium analogues similar to those described for ruthenium. Isolation of the *cis*–$[Os^{III}(PS2)_2]^-$ and *trans*–$[Os^{III}(PS2')_2]^-$ complexes was unsuccessful. Further studies need to be performed to understand the mechanism as well as the isolation of the other isomers. The temperature studies for synthesizing $[Os^{III}(PS2^{(\prime)})_2]^-$ complexes are summarized in **Table III–2.**

| Table III–2. Method and Temperature Studies of Synthesizing $[Os^{III}(PS2^{(\prime)})_2]^-$. | | | | |
|---|---|---|---|---|
| **Experiment** | **Reagent** | **Solvent** | **Temperature ($^oC$)** | **Isomer Obtained (PS2/PS2')** |
| 1 | *trans*–$[Os^{II}Cl_2(PPh_3)_3]$ | MeOH | 65 | *trans/cis* |
| 2 | *trans*–$[Os^{II}Cl_2(PPh_3)_3]$ | $CH_3CN$ | 82 | *trans/cis* |
| 3 | *trans*–$[Os^{II}Cl_2(PPh_3)_3]$ | MeOH | 0 | *trans/cis* |
| 4 | *trans*–$[Os^{II}Cl_2(PPh_3)_3]$ | $CH_3CN$ | 0 | *trans/cis* |
| 5 | *trans*–$[Os^{II}Cl_2(PPh_3)_3]$ | MeOH | –20 | *trans/cis* |
| 6 | *trans*–$[Os^{II}Cl_2(PPh_3)_3]$ | $CH_3CN$ | –20 | *trans/cis* |

### 3.3.3 Synthesis of $[n\text{–}Pr_4N][Ru^{III}(NS2^{(\prime)})_2]$

Under dinitrogen atmosphere, $Ru^{II}(DMSO)_4Cl_2$ was dissolved in methanol upon gentle heating. Four molar equivalents of $Li_2NS2$ were dissolved in methanol until complete dissolution occurred. The ruthenium solution was transferred *via* cannula to the $Li_2NS2$ solution and refluxed. Excess ligand was used to prevent any dimers from forming as side or main products. As the solution was refluxing, the color changed from yellow–red to dark green. The solution was cooled to room temperature and a concentrated methanol solution of 1.1 molar equivalents of $[Pr_4N]Br$ was transferred *via* cannula and layered into the reaction flask. The flask was left undisturbed, overnight, to form emerald green prism crystals which were suitable for x–ray crystallography in 90% yield. The desired product was, also, formed by adding the ruthenium starting material with four molar equivalents of $Li_2NS2$ and allowing the solution to stir overnight at room temperature under a dinitrogen atmosphere which produced 80% yield.

This procedure was also performed using $Li_2NS2'$ and the same countercation which produced emerald green prism crystals of $[n\text{–}Pr_4N][Ru^{III}(NS2')_2]$. Comparative yields are 64% for refluxing and 59% for stirring. The overall reaction scheme is shown below (**Figure III–7**).

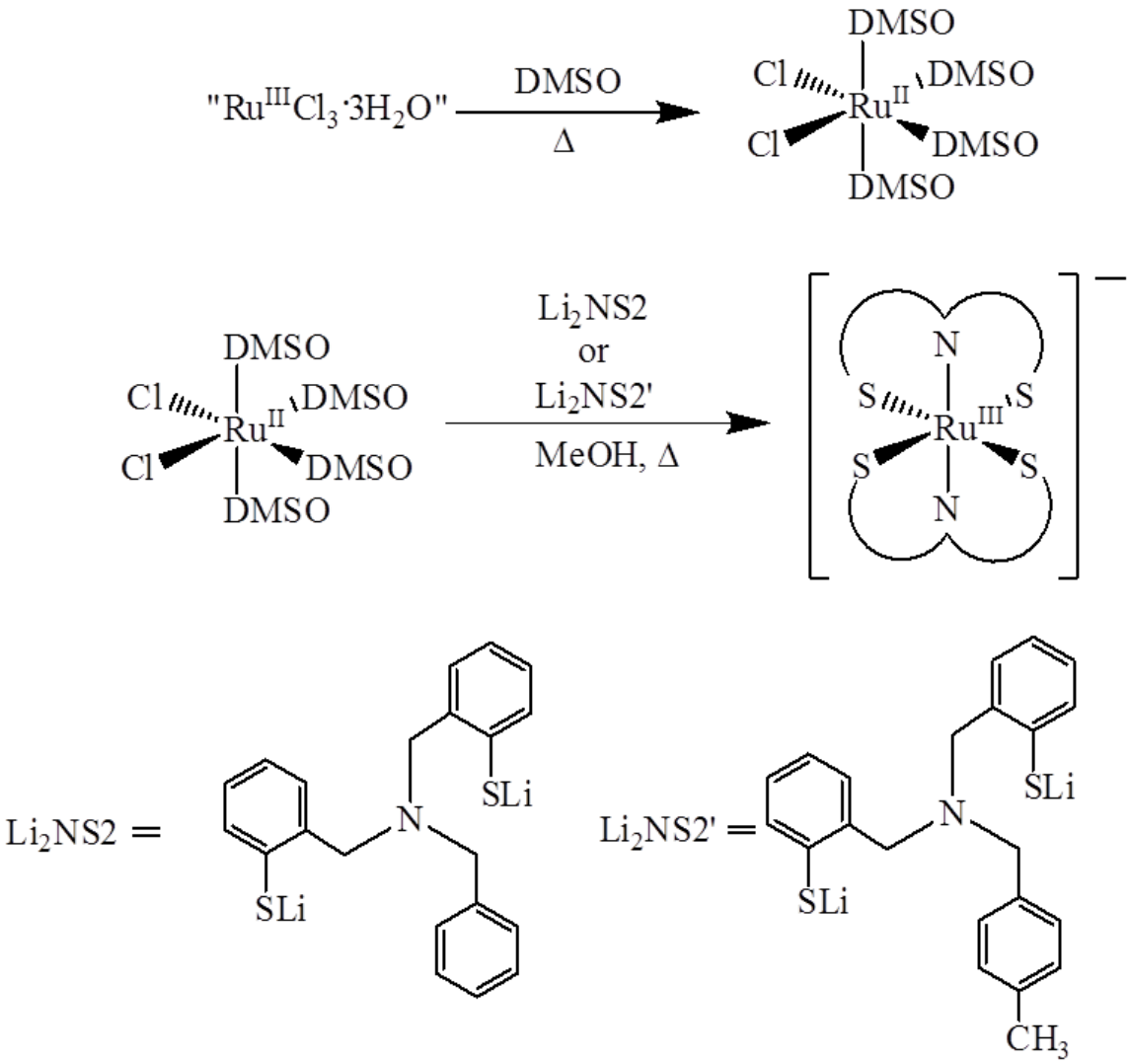


**Figure III–7. Overall reaction of *cis*–[$Ru^{II}(DMSO)_4Cl_2$] and [$Ru^{III}(NS2(')]^-$ compounds.**

### 3.3.4 X–ray Structures of Ruthenium and Osmium Complexes with Phosphine–Thiolate and Amine–Thiolate Ligands

The X–ray structure of *trans*–[$M^{III}(PS2)_2]^-$, where M = Fe[23], Ru and Os, confirmed an octahedral structure consisting of two [PS2] ligands and the corresponding cation. The X–ray structure shows the PS2 ligands to be in a *trans* orientation for all transition metal compounds. In all three X–ray structures, the [PS2] ligands are coordinated to the transition metal in a *facial* arrangement. The *trans*–[$Fe^{III}(PS2)_2]^-$ was synthesized by John Franolic[23] while the *cis*–[$Fe^{III}(PS2)_2]^-$ isomer was synthesized by Susan Beatty[24]. The X–ray structures of these complex anions are isostructural.

The X–ray structure of the *trans*–$[Fe^{III}(PS2)_2]^-$ contains a crystallographic $C_2$ axis which bisects the anion across of the equatorial S–Fe–S bond angles as well as the $[Et_4N]^+$ cation. The X–ray structure of the *trans*–$[Ru^{III}(PS2)_2]^-$ contains no crystallographic symmetry; therefore, the complex anion and cation are located in a general position. The X–ray structure of the *trans*–$[Os^{III}(PS2)_2]^-$ contains a crystallographic inversion center which is located across the osmium and one [PS2] ligand. The general structure for the iron anion can be found in John Franolic's PhD dissertation, while the general structure for the ruthenium and osmium anions are illustrated in **Figure III–8** and **Figure III–9** respectively. Selective bond distances and angles for the Fe[23], Ru and Os structures are summarized in **Table III–3**, **Table III–4** and **Table III–5** respectively. The $Fe–S_{avg}$, $Ru–S_{avg}$ and $Os–S_{avg}$ bond distances are 2.298(2) Å, 2.3686(6) Å and 2.3655(16) Å respectively. The bond Fe–P and Os–P distances are 2.199(2) Å and 2.2822(15) Å respectively, while the $Ru–P_{avg}$ bond distance was 2.2831(6) Å. The bond distance from iron to ruthenium increases due to the change in atomic radii of the transition metal center; however, the bond distances for ruthenium and osmium do not exhibit a significant change due to the lanthanide contraction.

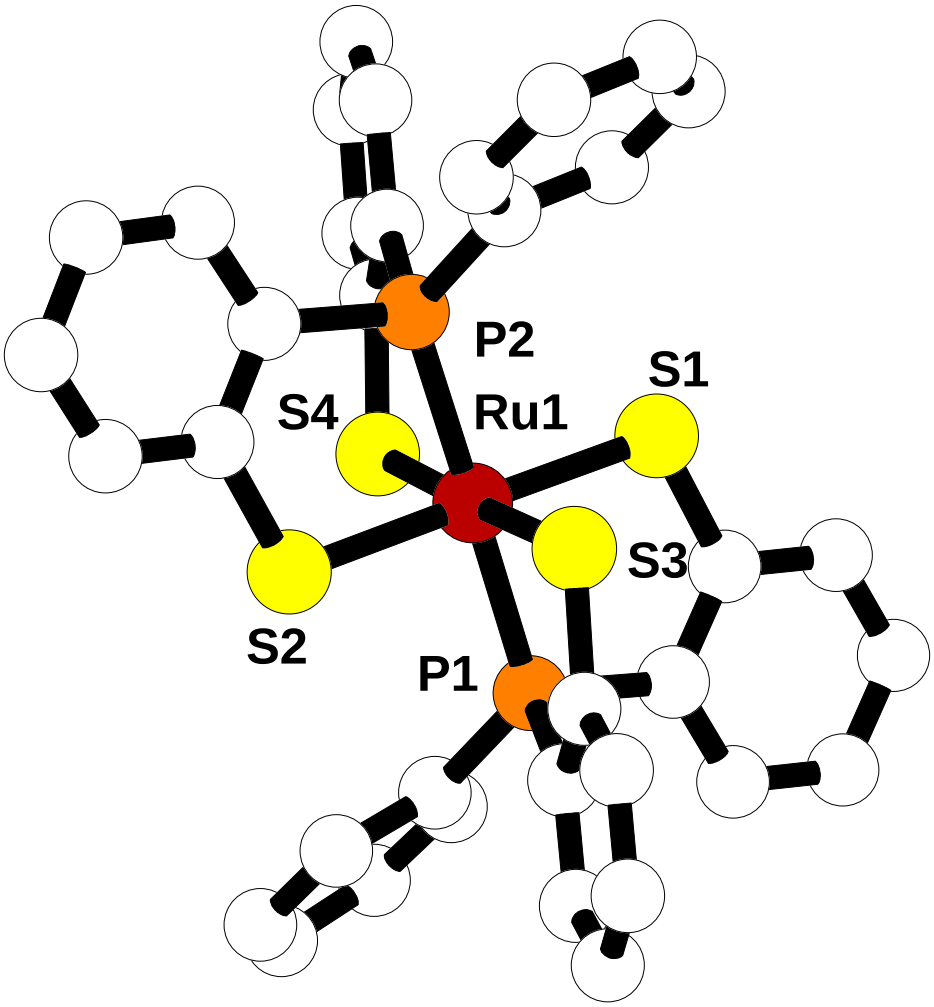


**Figure III–8. X–ray structure of *trans*–[*n*–$Pr_4N$][$Ru^{III}(PS2)_2$] (hydrogens and cation were removed for clarity).**

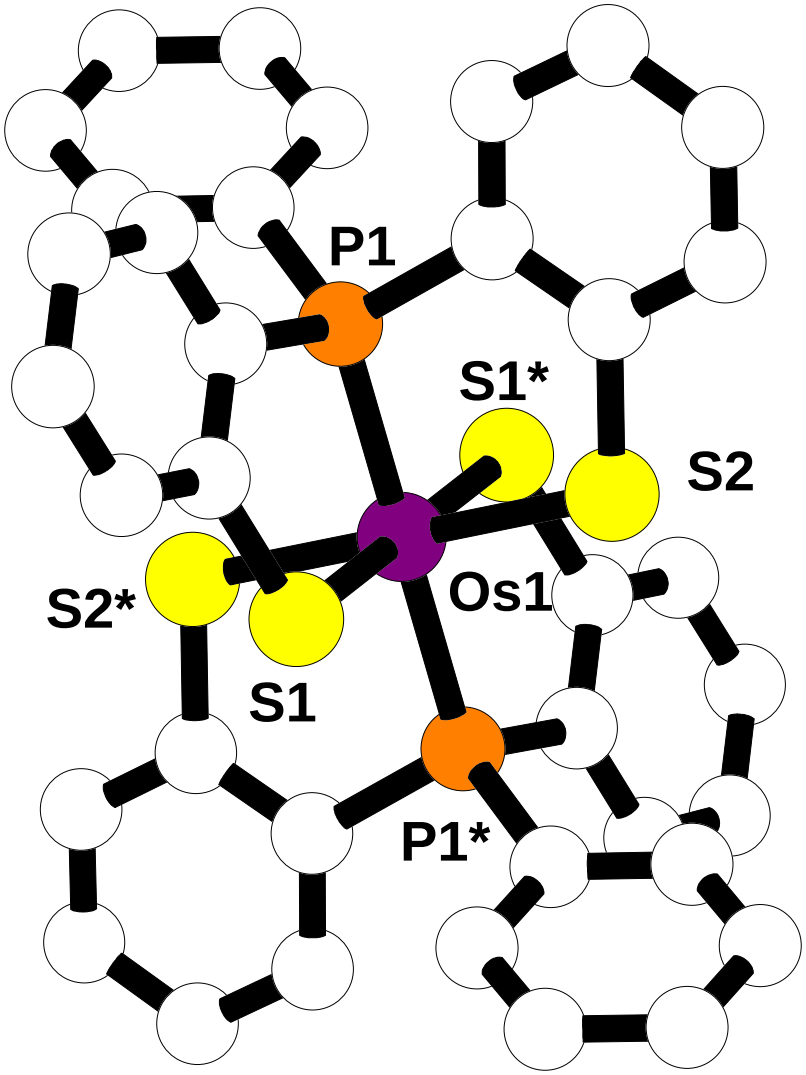


**Figure III–9. X–ray structure of *trans*–[$Me_3NBz$][$Os^{III}(PS2)_2$] (hydrogens and cation were removed for clarity).**

| Table III–3. Selective Crystallographic Data for *trans*–[Et4N][$Fe^{III}(PS2)_2$]. | | | |
|---|---|---|---|
| **Bond Distances (Å)** | | **Bond Angles (°)** | |
| Fe(1) – S(1) | 2.284(2) | S(1) – Fe(1) – S(2) | 87.47(7) |
| Fe(1) – S(2) | 2.311(2) | S(1) – Fe(1) – S(2)* | 92.53(7) |
| Fe(1) – P(1) | 2.199(1) | S(1) – Fe(1) – P(1) | 92.08(4) |
| | | S(1) – Fe(1) – P(1)* | 87.92(4) |
| | | S(2) – Fe(1) – P(1) | 96.52(3) |
| | | S(2) – Fe(1) – P(1)* | 83.48(3) |

| Table III–4. Selective Crystallographic Data for *trans*–[*n*–$Pr_4N$][$Ru^{III}(PS2)_2$]. | | | |
|---|---|---|---|
| **Bond Distances (Å)** | | **Bond Angles (°)** | |
| Ru(1) – S(1) | 2.3666(6) | S(1) – Ru(1) – S(2) | 179.33(2) |
| Ru(1) – S(2) | 2.3738(5) | S(1) – Ru(1) – S(3) | 90.71(2) |
| Ru(1) – S(3) | 2.3498(5) | S(1) – Ru(1) – S(4) | 87.312(19) |
| Ru(1) – S(4) | 2.3841(5) | S(2) – Ru(1) – S(3) | 89.37(2) |
| Ru(1) – P(1) | 2.2784(6) | S(2) – Ru(1) – S(4) | 92.61(2) |
| Ru(1) – P(2) | 2.2878(6) | S(3) – Ru(1) – S(4) | 178.01(2) |
| | | P(1) – Ru(1) – S(1) | 86.37(2) |
| | | P(1) – Ru(1) – S(2) | 92.98(2) |
| | | P(1) – Ru(1) – S(3) | 84.57(2) |
| | | P(1) – Ru(1) – S(4) | 95.576(19) |
| | | P(2) – Ru(1) – S(1) | 94.34(2) |
| | | P(2) – Ru(1) – S(2) | 86.32(2) |
| | | P(2) – Ru(1) – S(3) | 95.70(2) |
| | | P(2) – Ru(1) – S(4) | 84.183(19) |
| | | P(1) – Ru(1) – P(2) | 179.24(2) |

| Table III–5. Selective Crystallographic Data for *trans*–[$Me_3NBz$][$Os^{III}(PS2)_2$]. | | | |
|---|---|---|---|
| **Bond Distances (Å)** | | **Bond Angles (°)** | |
| Os(1) – S(1) | 2.3703(15) | S(1) – Os(1) – S(2) | 92.59(6) |
| Os(1) – S(2) | 2.3628(17) | S(1) – Os(1) – S(2)* | 87.41(6) |
| Os(1) – P(1) | 2.2822(15) | S(1) – Os(1) – P(1) | 85.60(5) |
| | | S(1) – Os(1) – P(1)* | 94.40(5) |
| | | S(2) – Os(1) – P(1) | 85.23(6) |
| | | S(2) – Os(1) – P(1)* | 94.77(6) |

The X–ray structure of $[M^{III}(PS2')_2]^-$, where M = Ru and Os, confirmed an octahedral structure consisting of two [PS2'] ligands and the corresponding cation. The x–ray structure shows the PS2 ligands to be in a *trans* orientation for the ruthenium compound; however, for the osmium compound the [PS2'] ligands are in a *cis* orientation. In both X–ray structures, the [PS2'] ligands are coordinated to the transition metal in a *facial* arrangement. The ruthenium complex ion has a crystallographic inversion center on the metal center, while the $[Et_4N]^+$ cation is located on a general position. This implies that the ratio of the ruthenium complex ion and the cation is 1:1. The general structure of the ruthenium complex anion is shown in **Figure III–10**. Selective

bond distances and angles for *trans*–$[Ru^{III}(PS2')_2]^-$ are summarized in **Table III–6**. The $Ru–S_{avg}$ bond distance is 2.3765(5) Å and the Ru–P bond distance was 2.2935(6) Å. The osmium complex anion and the $[Me_3NBz]^+$ are located on general positions. Crystals were grown directly from the reaction mixture upon slow addition of the corresponding countercation. The general structure of the osmium complex anion is shown in **Figure III–11**. The osmium X–ray structure shows a distorted octahedral geometry of the $[OsP_2S_4]$ center caused by the [PS2'] ligands being in the *cis* arrangement. Selective bond distances and angles for *cis*–$[Os^{III}(PS2')_2]^-$ are summarized in **Table III–7**. The $Os–S_{avg}$ bond distance was 2.3794(14) Å and the $Os–P_{avg}$ bond distance was 2.2879(14) Å.

The two ruthenium complexes, *trans*–$[Ru^{III}(PS2)_2]^-$ and *trans*–$[Ru^{III}(PS2')_2]^-$, are structurally similar except that the [PS2'] ligands contain a methyl group *para* to the binding thiolate. Due to the similarity of the two complexes, the bond distances should not be affected in any significant way. The $Ru–S_{avg}$ bond distance for the *trans*–$[Ru^{III}(PS2)_2]^-$ was 2.3686(6) Å while for the *trans*–$[Ru^{III}(PS2')_2]^-$ the average bond distance was 2.3765(5) Å. The $Ru–P_{avg}$ bond distance for *trans*–$[Ru^{III}(PS2)_2]^-$ was 2.2831(6) Å while the Ru–P bond distance for *trans*–$[Ru^{III}(PS2')_2]^-$ was 2.2935(6) Å. The Ru–L bond distances for the *trans*–$[Ru^{III}(PS2')_2]^-$ complex are longer than *trans*–$[Ru^{III}(PS2)_2]^-$ complex. The extra methyl groups on the [PS2'] are positioned so that they should not contribute structurally to the Ru–L bond distances. Electron donating groups, e.g. methyl groups, affect the structure by adding electron density thus decreasing the Ru–L bond distances. However, the longer bond distances for the [PS2'] complex are consistent with the observation that [PS2'] is a bulkier ligand. The bond angles for both complexes are not appreciably different. The extra methyl group has little effect on the cone angle of the ligand. There would have been a noticeable difference had the methyl groups been *ortho* to the thiolate functional group.

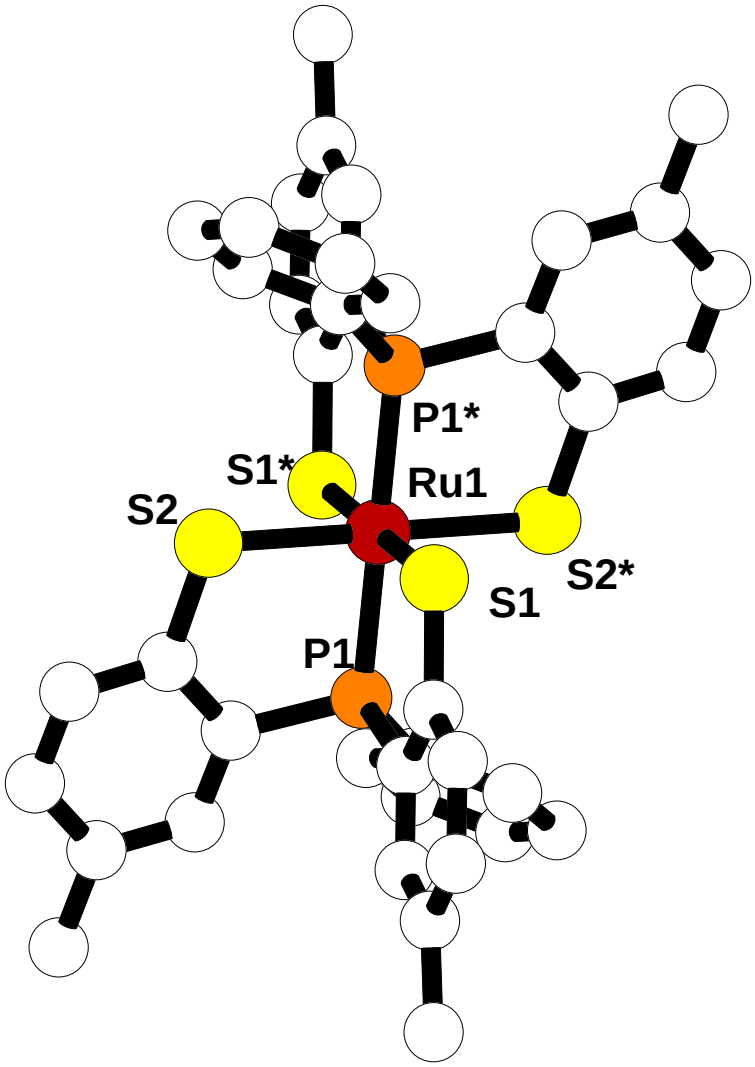


**Figure III–10. X–ray structure of *trans*–[$Et_4N$][$Ru^{III}(PS2')_2$] (hydrogens and cation were removed for clarity).**

| Table III–6 Selective Crystallographic Data for *trans*–[$Et_4N$][$Ru^{III}(PS2')_2$]. | | | |
|---|---|---|---|
| **Bond Distances (Å)** | | **Bond Angles (°)** | |
| Ru(1) – S(1) | 2.3661(6) | S(1) – Ru(1) – S(1)* | 180.00(3) |
| Ru(1) – S(2) | 2.3870(6) | S(1) – Ru(1) – S(2) | 91.79(2) |
| Ru(1) – P(1) | 2.2935(6) | S(1) – Ru(1) – S(2)* | 88.21(2) |
| | | S(2) – Ru(1) – S(2)* | 180.000(11) |
| | | P(1) – Ru(1) – S(1) | 93.82(2) |
| | | P(1) – Ru(1) – S(1)* | 86.18(2) |
| | | P(1) – Ru(1) – S(2) | 96.13(2) |
| | | P(1) – Ru(1) – S(2)* | 83.87(2) |
| | | P(1) – Ru(1) – P(1)* | 180.00(3) |

| Table III–7. Selective Crystallographic Data for *cis*–[$Me_3NBz$][$Os^{III}(PS2')_2$]. | | | |
|---|---|---|---|
| **Bond Distances (Å)** | | **Bond Angles (°)** | |
| Os(1) – S(1) | 2.4151(15) | S(1) – Os(1) – S(2) | 97.62(5) |
| Os(1) – S(2) | 2.3427(13) | S(1) – Os(1) – S(3) | 88.30(5) |
| Os(1) – S(3) | 2.3784(13) | S(1) – Os(1) – S(4) | 86.27(5) |
| Os(1) – S(4) | 2.3814(13) | S(2) – Os(1) – S(3) | 91.28(5) |
| Os(1) – P(1) | 2.2978(14) | S(2) – Os(1) – S(4) | 170.46(5) |
| Os(1) – P(2) | 2.2781(14) | S(3) – Os(1) – S(4) | 97.56(5) |
| | | P(1) – Os(1) – S(1) | 82.63(5) |
| | | P(1) – Os(1) – S(2) | 85.08(5) |
| | | P(1) – Os(1) – S(3) | 169.68(5) |
| | | P(1) – Os(1) – S(4) | 86.80(5) |
| | | P(2) – Os(1) – S(1) | 167.41(5) |
| | | P(2) – Os(1) – S(2) | 93.15(5) |
| | | P(2) – Os(1) – S(3) | 84.96(5) |
| | | P(2) – Os(1) – S(4) | 84.09(5) |
| | | P(1) – Os(1) – P(2) | 104.85(5) |

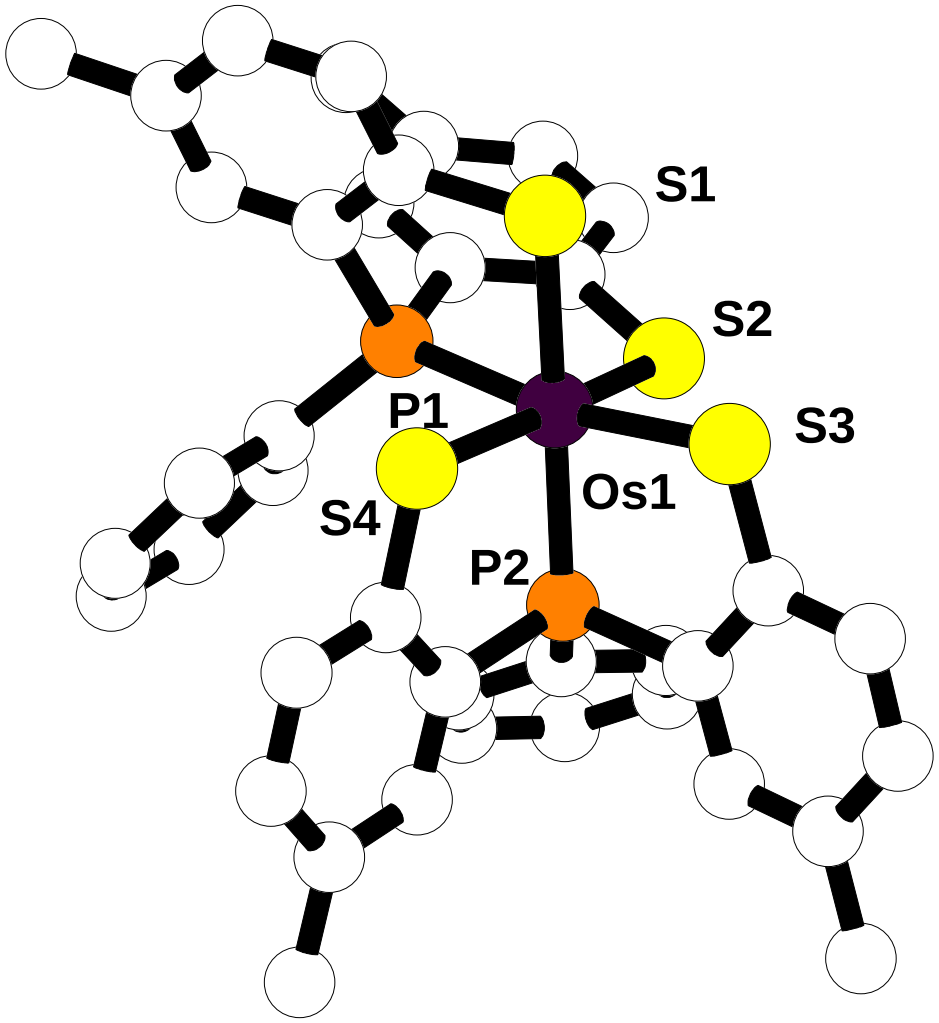


**Figure III–11. X–ray structure of *cis*–[$Me_3NBz$][$Os^{III}(PS2')_2$] (hydrogens and cation were removed for clarity).**

The X–ray structure of the $[Ru^{III}(NS2^{(\prime)})_2]^-$ confirmed an octahedral structure consisting of two [NS2] or [NS2'] ligands and $[n\text{–}Pr_4N]^+$ cation. The X–ray structure shows the [NS2] and [NS2'] ligands to be in a *trans* orientation. In both X–ray structures the [NS2] and [NS2'] ligands are coordinated in a *mer* arrangement. Crystals were grown directly from the reaction mixture upon slow addition of the $[n\text{–}Pr_4N]^+$ cation. In both structures, the ruthenium complex anion and the counteraction are located in general positions. The compounds are shown to be isomorphous and the structures were solved under a monoclinic crystal system $P2_1/n$. The general structures

for *trans*–[$Ru^{III}(NS2)_2]^-$ in **Figure III–12** and *trans*–[$Ru^{III}(NS2')_2]^-$ in **Figure III–13**. The only structural difference between *trans*–[$Ru^{III}(NS2)_2]^-$ and *trans*–[$Ru^{III}(NS2')_2]^-$ is the non–coordinated benzyl has a methyl group located in the *para* position. Selective bond distances and angles for *trans*–[$Ru^{III}(NS2)_2]^-$ are summarized in **Table III–8** and for *trans*–[$Ru^{III}(NS2')_2]^-$ in **Table III–9**. For the [$Ru^{III}(NS2)_2]^-$, the Ru–$S_{avg}$ bond distance was 2.3697(7) Å and the Ru–$N_{avg}$ bond distance was 2.225(2) Å. For the [$Ru^{III}(NS2')_2]^-$, the Ru–$S_{avg}$ bond distance was 2.3668(11) Å and the Ru–$N_{avg}$ bond distance was 2.221(3) Å. The bond distances are slightly shorter for the [$Ru^{III}(NS2')_2]^-$ complex than [$Ru^{III}(NS2)_2]^-$ complex. This observation is due to the presence of the extra methyl group on each of the [NS2'] ligand. Methyl groups act as an electron donating group which causes the binding atoms, sulfur and nitrogen, to be more electron–rich and results in stronger binding to the ruthenium. The bond angles are similar for the two complexes. This is because the [NS2] ligand and [NS2'] ligand are nearly identical. Since the [NS2'] ligand has a methyl group *para* to the free benzyl group, this has very little effect on the bond angles. If the methyl group had been *ortho*, then there would have been a noticeable change in the bond angles. The methyl group adds no steric hindrance to the complex.

**Table III–8. Selective Crystallographic Data for *trans*–[*n*–$Pr_4N$][$Ru^{III}(NS2)_2$].**

| **Bond Distances (Å)** | | **Bond Angles (°)** | |
|---|---|---|---|
| Ru(1) – S(1) | 2.3562(6) | S(1) – Ru(1) – S(2) | 175.24(3) |
| Ru(1) – S(2) | 2.3867(7) | S(1) – Ru(1) – S(3) | 96.94(2) |
| Ru(1) – S(3) | 2.3490(7) | S(1) – Ru(1) – S(4) | 88.88(2) |
| Ru(1) – S(4) | 2.3869(7) | S(2) – Ru(1) – S(3) | 87.77(2) |
| Ru(1) – N(1) | 2.234(2) | S(2) – Ru(1) – S(4) | 86.41(2) |
| Ru(1) – N(2) | 2.215(2) | S(3) – Ru(1) – S(4) | 174.15(3) |
| | | N(1) – Ru(1) – S(1) | 85.33(5) |
| | | N(1) – Ru(1) – S(2) | 94.03(2) |
| | | N(1) – Ru(1) – S(3) | 89.96(5) |
| | | N(1) – Ru(1) – S(4) | 89.92(6) |
| | | N(2) – Ru(1) – S(1) | 90.16(5) |
| | | N(2) – Ru(1) – S(2) | 90.82(5) |
| | | N(2) – Ru(1) – S(3) | 86.44(5) |
| | | N(2) – Ru(1) – S(4) | 94.17(6) |
| | | N(1) – Ru(1) – N(2) | 173.85(8) |

| **Table III–9. Selective Crystallographic Data for *trans*–[*n*–$Pr_4N$][$Ru^{III}(NS2')_2$].** | | | |
|---|---|---|---|
| **Bond Distances (Å)** | | **Bond Angles (°)** | |
| Ru(1) – S(1) | 2.3817(11) | S(1) – Ru(1) – S(2) | 176.55(3) |
| Ru(1) – S(2) | 2.3509(11) | S(1) – Ru(1) – S(3) | 87.11(4) |
| Ru(1) – S(3) | 2.3555(11) | S(1) – Ru(1) – S(4) | 87.22(4) |
| Ru(1) – S(4) | 2.3891(11) | S(2) – Ru(1) – S(3) | 96.33(4) |
| Ru(1) – N(1) | 2.227(3) | S(2) – Ru(1) – S(4) | 89.34(4) |
| Ru(1) – N(2) | 2.214(3) | S(3) – Ru(1) – S(4) | 174.25(4) |
| | | N(1) – Ru(1) – S(1) | 94.24(8) |
| | | N(1) – Ru(1) – S(2) | 85.47(8) |
| | | N(1) – Ru(1) – S(3) | 90.98(7) |
| | | N(1) – Ru(1) – S(4) | 88.50(7) |
| | | N(2) – Ru(1) – S(1) | 90.70(8) |
| | | N(2) – Ru(1) – S(2) | 89.77(8) |
| | | N(2) – Ru(1) – S(3) | 86.31(7) |
| | | N(2) – Ru(1) – S(4) | 94.69(7) |
| | | N(1) – Ru(1) – N(2) | 174.24(11) |

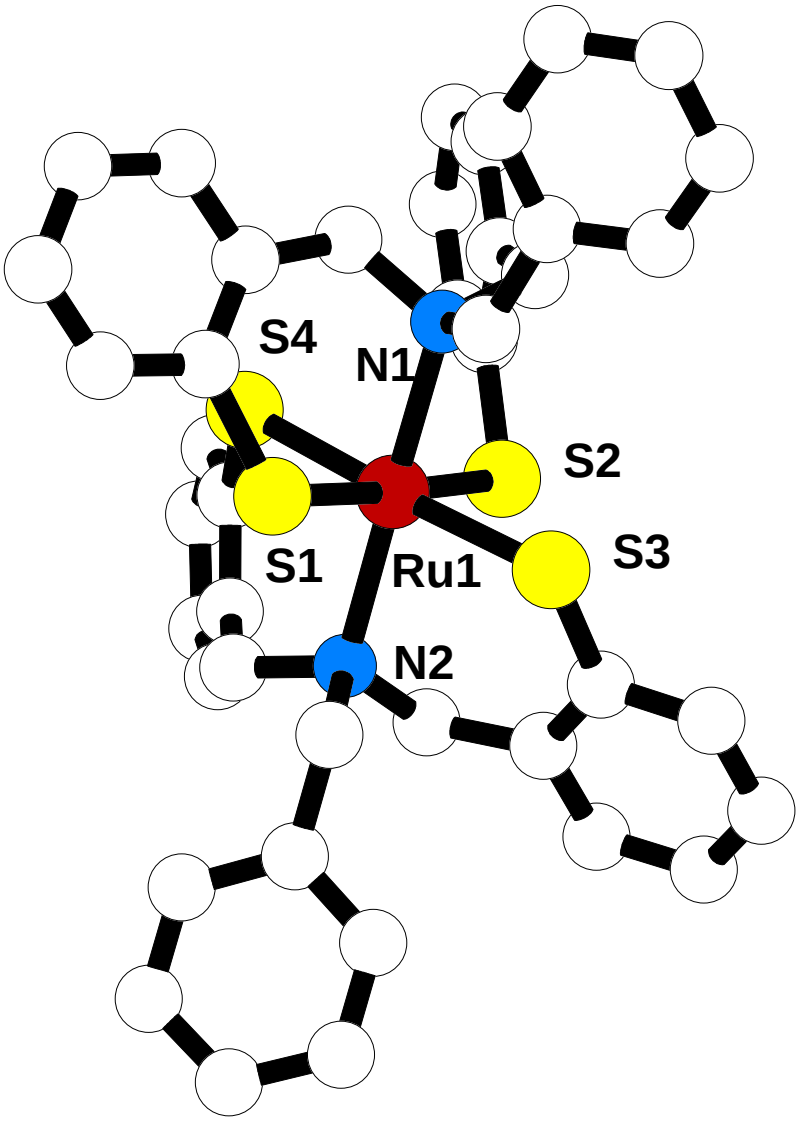


**Figure III–12. X–ray structure of *trans*–[*n*–$Pr_4N$][$Ru^{III}(NS2)_2$] (hydrogens and cation were removed for clarity).**

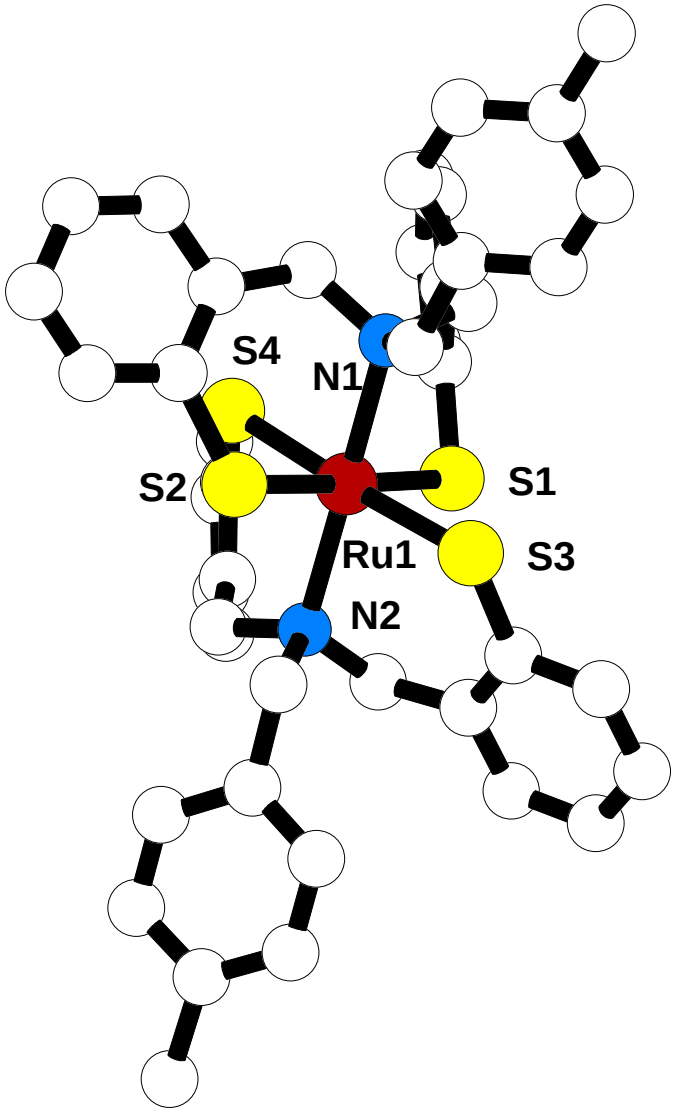


**Figure III–13. X–ray structure of *trans*–[*n*–$Pr_4N$][$Ru^{III}(NS2')_2$] (hydrogens and cation were removed for clarity).**

The X–ray structure of the *cis*–[$Ru^{II}$(PS3')(HPS3')]$^-$(“S–S” disulfide) confirmed a distorted octahedral structure consisting of two [PS3] ligands, where two thiolate are bridged and one thiol is free, and there is one $[Et_4N]^+$ cation. The [PS3'] ligands are coordinated to the transition metal in a *facial* arrangement while at the same time the phosphorous atoms are *cis* each other. The ruthenium complex anion and the $[Et_4N]^+$ cation are located on general positions. The general structure of the ruthenium complex anion is shown in **Figure III–14**. Selective bond distances and angles for *cis*–[$Ru^{II}$(PS3')(HPS3')]$^-$(“S–S” disulfide) are summarized in **Table III–**

**10**. The Ru–$S_{avg}$ bond distance is 2.3835(14) Å and the Ru–$P_{avg}$ bond distance was 2.2401(14) Å. The structure shows that the free thiol has strong hydrogen bonding to the thiolate of the adjacent [PS3] ligand. The hydrogen bond distance between S(6) – H(1) was 2.205(5) Å. The S–S bond distance was 2.1113(18) Å.

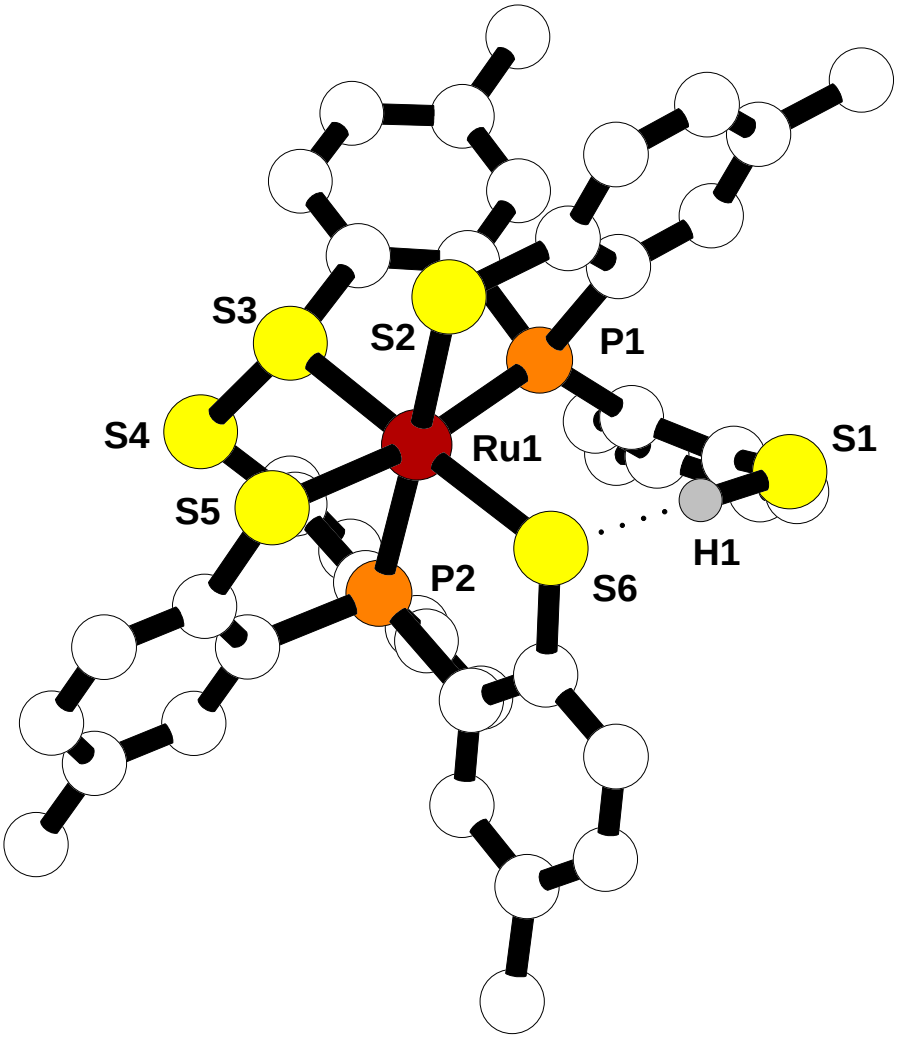


**Figure III–14. X–ray structure of *cis*–[$Et_4N$][$Ru^{II}$(PS3')(HPS3')](“S–S” disulfide) (hydrogens and cation were removed for clarity).**

| Table III–10. Selective Crystallographic Data for *cis*–[$Et_4N$][$Ru^{II}$(PS3')(HPS3')]("S–S" disulfide). | | | |
|---|---|---|---|
| **Bond Distances (Å)** | | **Bond Angles (°)** | |
| Ru(1) – S(2) | 2.4287(15) | P(1) – Ru(1) – P(2) | 104.45(5) |
| Ru(1) – S(3) | 2.2835(13) | P(1) – Ru(1) – S(2) | 83.70(5) |
| Ru(1) – S(5) | 2.4440(15) | P(1) – Ru(1) – S(3) | 87.04(5) |
| Ru(1) – S(6) | 2.3778(14) | P(1) – Ru(1) – S(5) | 170.69(5) |
| S(3) – S(4) | 2.1113(18) | P(1) – Ru(1) – S(6) | 91.98(5) |
| Ru(1) – P(1) | 2.2553(14) | S(2) – Ru(1) – S(3) | 89.55(5) |
| Ru(1) – P(2) | 2.2247(14) | S(2) – Ru(1) – S(5) | 88.88(5) |
| H(1) – S(6) | 2.205(5) | S(2) – Ru(1) – S(6) | 89.91(5) |
| | | S(3) – Ru(1) – S(5) | 87.28(5) |
| | | S(3) – Ru(1) – S(6) | 178.93(5) |
| | | S(5) – Ru(1) – S(6) | 93.63(5) |
| | | P(2) – Ru(1) – S(2) | 171.02(5) |
| | | P(2) – Ru(1) – S(3) | 94.56(5) |
| | | P(2) – Ru(1) – S(5) | 83.36(5) |
| | | Ru(1) – S(3) – S(4) | 112.80(6) |

### 3.3.5 Electrochemistry

The cyclic voltammetry of *trans*–[$M^{III}(PS2)_2]^-$ (where M = Ru and Os) in *N*,*N*–dimethylformamide shows a quasi–reversible oxidation at $E_{½}$ = 0.555 V for Ru (**Figure III–15**) and a reversible oxidation at 0.127 V for Os vs Ag/AgCl (**Figure III–16**). It is easier to oxidize the osmium compound than the ruthenium. This follows a general trend of the periodic table, as one goes down the periodic table the elements are easier to get oxidized.

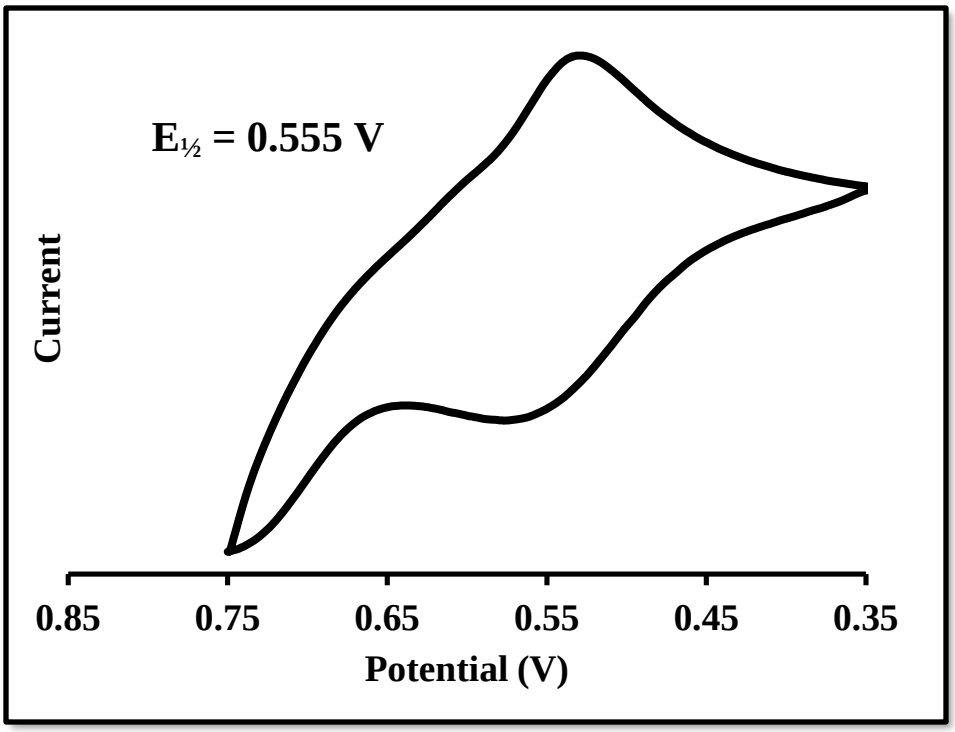


**Figure III–15. Cyclic Voltammogram of *trans*–[*n*–$Pr_4N$][$Ru^{III}(PS2)_2$] in DMF.**

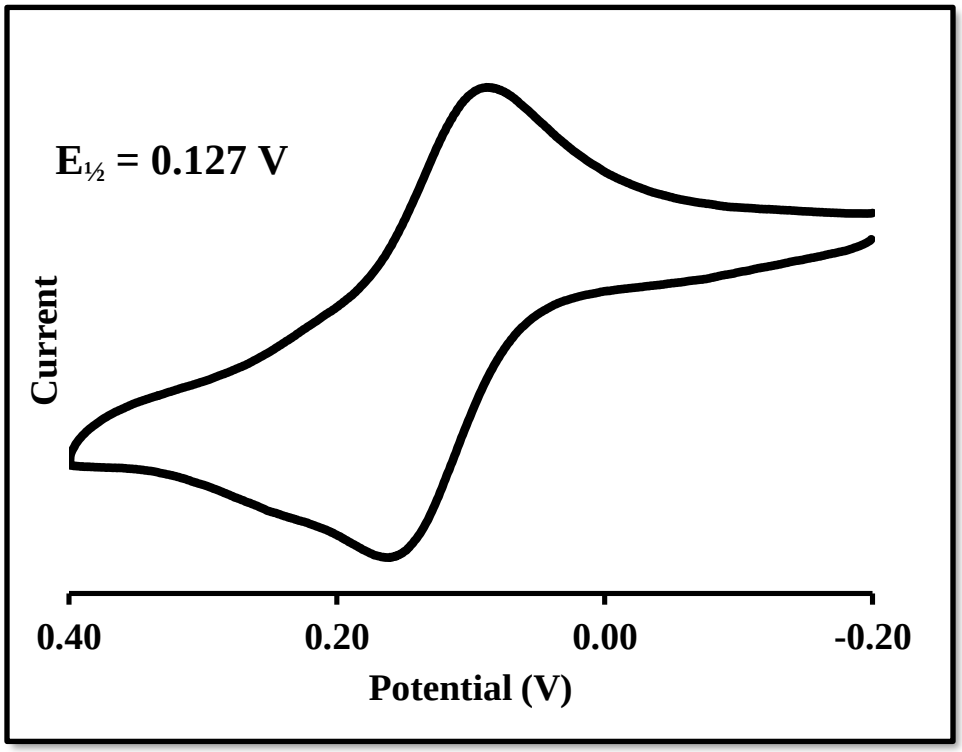


**Figure III–16. Cyclic Voltammogram of *trans*–[$Me_3NBz$][$Os^{III}(PS2)_2$] in DMF.**

The cyclic voltammetry of *trans*–$[Ru^{III}(PS2')_2]^-$ in *N*,*N*–dimethylformamide shows a quasi–reversible oxidation at $E_{½}$ = 0.510 V vs Ag/AgCl (**Figure III–17**). Electrochemically, the *trans*–$[Ru^{III}(PS2')_2]^-$ is similar to *trans*–$[Ru^{III}(PS2)_2]^-$ with the exception of the methyl groups on the [PS2'] ligand. Both complexes show a quasi–reversible one electron oxidation to a $Ru^{IV}$ species. Comparison of the $E_{½}$ for both complexes, 0.555 V for [PS2] complex and 0.510 V for the [PS2'] complex, showed that the *trans*–$[Ru^{III}(PS2')_2]^-$ was easier to oxidize than the *trans*–$[Ru^{III}(PS2)_2]^-$. This is due to the presence of the methyl groups and the fact that methyl groups are electron donors. This extra electron donation serves to stabilize the $Ru^{IV}$ complex.

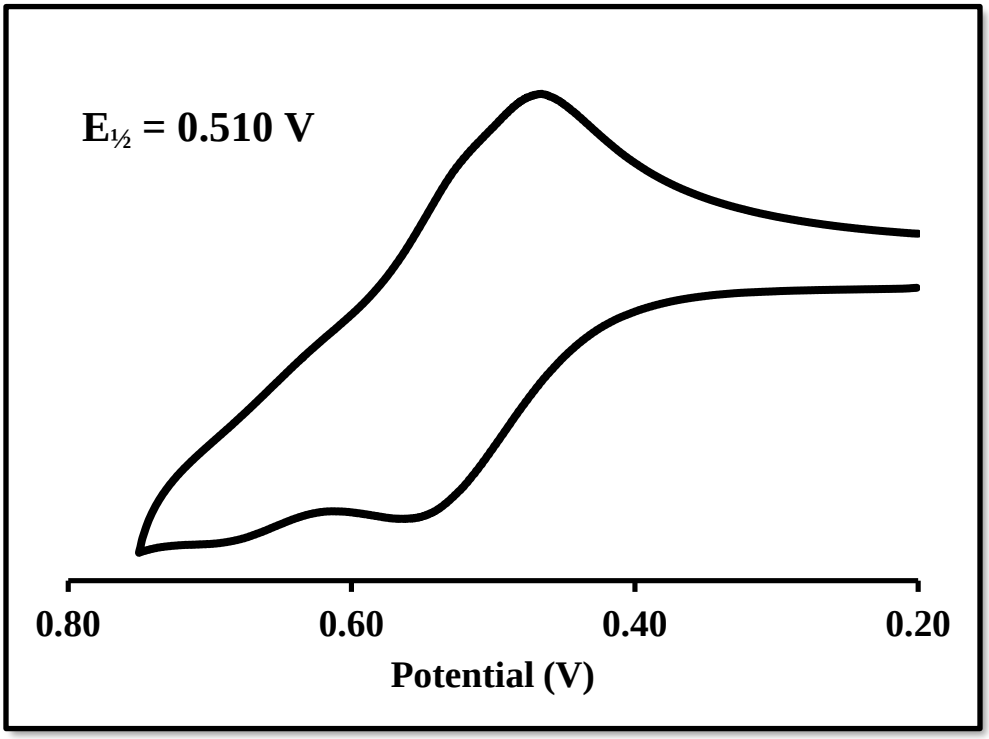


**Figure III–17. Cyclic Voltammogram of *trans*–$[Et_4N][Ru^{III}(PS2')_2]$ in DMF.**

The cyclic voltammetry of *cis*–$[Os^{III}(PS2')_2]^-$ in *N*,*N*–dimethylformamide shows two reversible oxidations at $E_{½}$ = 0.457 V and 0.292 V vs Ag/AgCl (**Figure III–18**). There are two theories on the identification of the two reversible oxidation peaks. The first theory is that the first reversible oxidation peak corresponds to the $Os^{IV}$ species and the second reversible oxidation peak corresponds to the $Os^{V}$ species. The second theory is that the first reversible oxidation peak still belongs to the $Os^{IV}$ species; however, the second reversible oxidation peak belong to the oxidation of *trans*–$[Os^{III}(PS2')_2]^-$. Isolation and characterization of the *trans*–

$[Os^{III}(PS2')_2]^-$ must be performed to prove this theory. As stated before, various attempted synthetic schemes have been performed to isolate the *trans* isomer with no success to date.

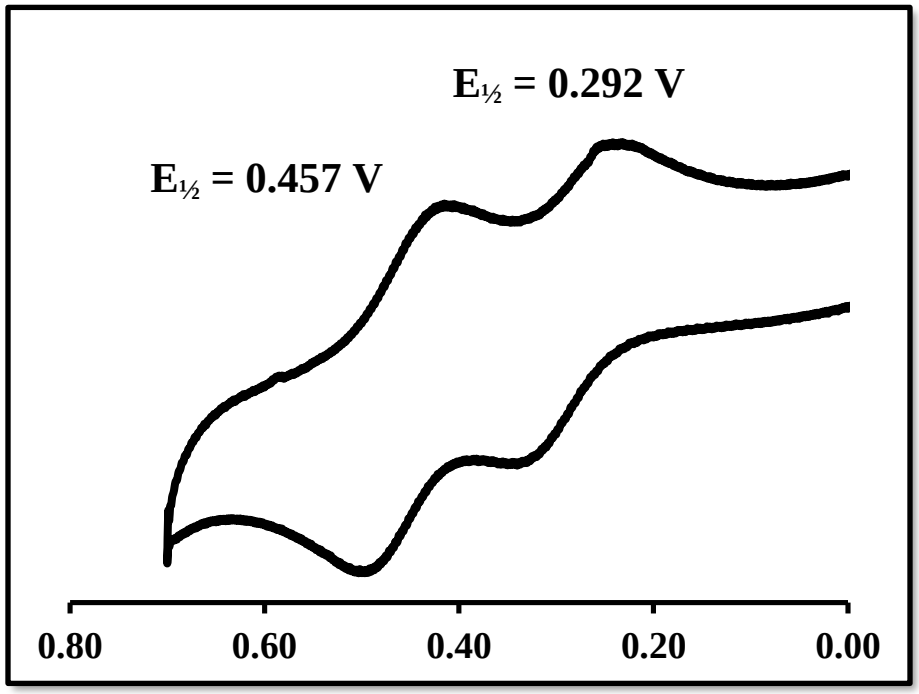


**Figure III–18. Cyclic Voltammogram of *cis*–$[Me_3NBz][Os^{III}(PS2')_2]$ in DMF.**

The cyclic voltammetry of *trans*–$[Ru^{III}(NS2)_2]^-$ and *trans*–$[Ru^{III}(NS2')_2]^-$ in *N*,*N*–dimethylformamide shows a reversible oxidation at $E_{½}$ = 0.395 V for [NS2] (**Figure III–20**) and a reversible oxidation at 0.393 V for [NS2'] vs Ag/AgCl (**Figure III–21**). Electrochemically, the *trans*–$[Ru^{III}(NS2')_2]^-$ is similar to *trans*–$[Ru^{III}(NS2)_2]^-$ with the exception of the methyl groups on the [NS2'] ligand. Both complexes show a reversible one electron oxidation to a $Ru^{IV}$ species. Upon comparison of the $E_{½}$ for both complexes shows that the *trans*–$[Ru^{III}(NS2')_2]^-$ was slightly easier to oxidized than the *trans*–$[Ru^{III}(NS2)_2]^-$. This is due to the electron donating properties of the methyl groups, as previously stated for the [PS2] and [PS2'] complexes.

Comparison of the [PS2] and [NS2] complexes shows an extreme difference in electrochemical potentials. The structures of the two ligands have two major differences. The first major difference is the phosphorous for the [PS2] ligand while the nitrogen for the [NS2] ligand and the second major difference are the methylene groups on the [NS2] ligand (**Figure III–19**).

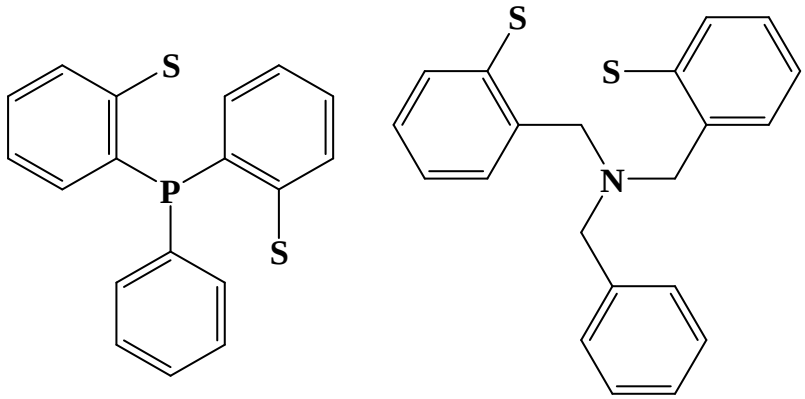


**Figure III–19. [PS2] ligand versus [NS2] ligand.**

Previous results have shown that moving down the periodic table would make it easier to oxidize.[24–25] This would suggest that the [PS2] complex would be easier to oxidize due to the presence of phosphorous; however, this is not the case. The methylene groups act as electron donating groups as do the methyl groups making it harder to oxidize the [PS2] complex. The same is true for the [PS2'] complex compared to the [NS2'] complex.

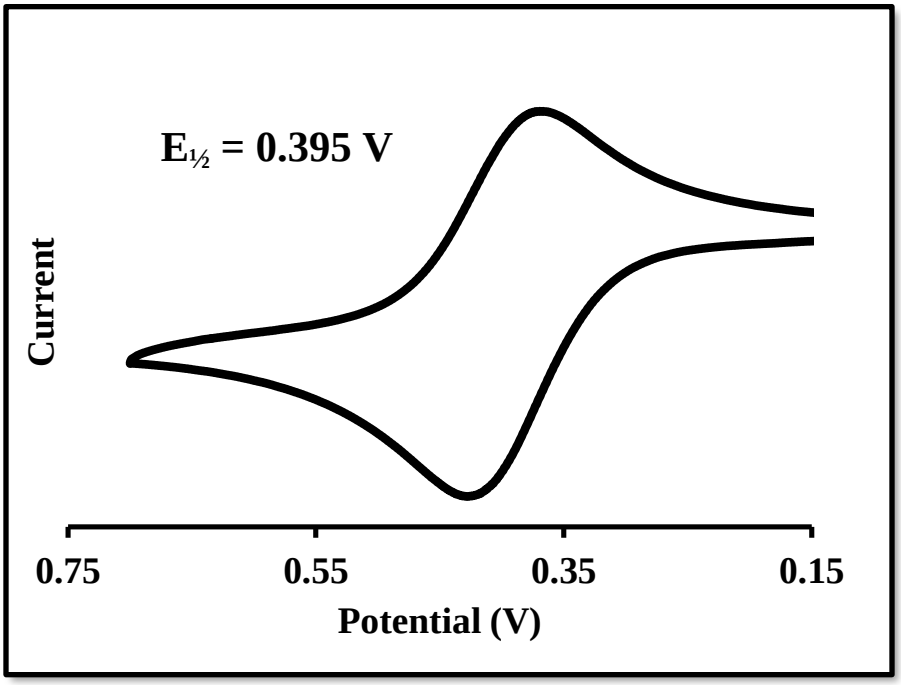


**Figure III–20. Cyclic Voltammogram of *trans*–[*n*–$Pr_4N$][$Ru^{III}(NS2)_2$] in DMF.**

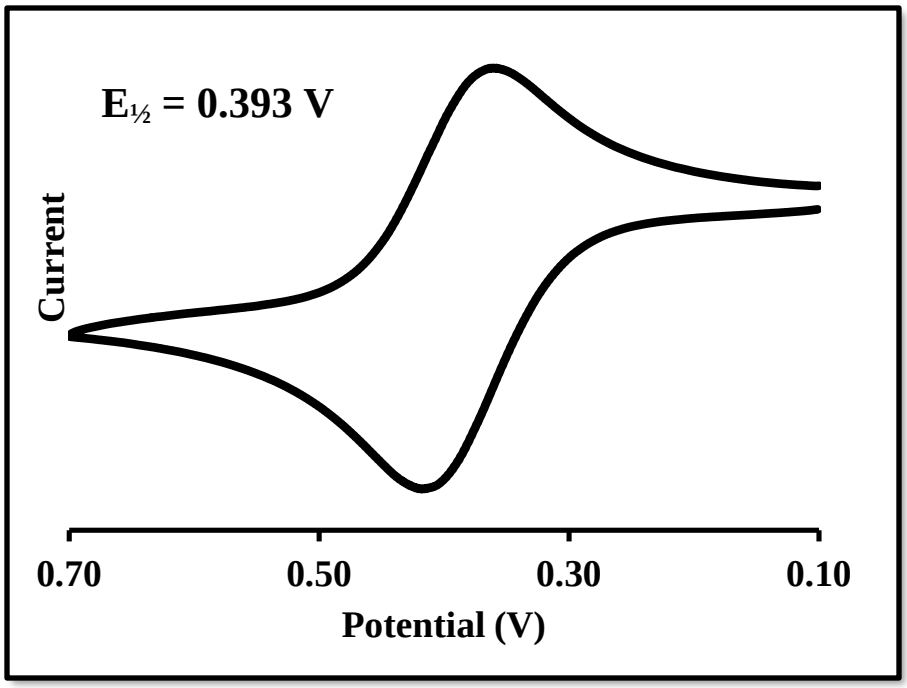


**Figure III–21. Cyclic Voltammogram of *trans*–[*n*–$Pr_4N$][$Ru^{III}(NS2')_2$] in DMF.**

## 3.4 Conclusions

In conclusion, $[M^{III}(PS2^{(\prime)})_2]^-$ (where M = Ru and Os) and $[Ru^{III}(NS2^{(\prime)})_2]^-$ were synthesized and characterized by X–ray crystallography, UV–Vis and electrochemistry. The X–ray structures confirmed that all the transition metal complexes were the *trans* isomers with the exception of *cis*–$[Os^{III}(PS2')_2]^-$.

Temperature studies and alternating the ruthenium/osmium starting materials was performed to isolate the other geometric isomer with no success. Mechanistic studies are still on going to determine the isolation of both geometric isomers. The syntheses of $[Ru^{III}(NS2^{(\prime)})_2]^-$ are the first monomeric transition metal complexes using [NS] ligands. The X–ray structures showed the [NS] ligands in the meridial arrangement while the [PS] ligands were facial. The X–ray structure comparison of the $[M^{III}(PS2^{(\prime)})_2]^-$, where M = Fe, Ru and Os, illustrated one of the basic periodic trends where the M–L bond distances increased due to the increasing change of atomic radii.

Electrochemical studies showed oxidation potentials decreased from $[Ru^{III}(PS2)_2]^-$ to $[Ru^{III}(PS2')_2]^-$ due to the electron donating effects of the methyl groups on the [PS2'] ligand. The same observation was seen with $[Ru^{III}(NS2)_2]^-$ and $[Ru^{III}(NS2')_2]^-$ due to the methylene groups on the [NS] ligands when compared to the Ru–[PS] complexes.

## 3.5 References


1. Berg, J. M.; Holm, R. H. *Metals Ions in Biology*; Spiro, T. G., Ed; Wiley: New York, 1982; vol. 4; pp. 1–66.
2. Blower, P. J.; Dilworth, J. R. *Coord. Chem. Rev.* **1987**, *76*, 121.
3. Dilworth, J. R.; Zheng, Y.; Miller, J. R. *J. Chem. Soc, Dalton Trans.* **1992**, 1757–1758.
4. Zhu, W.; Marr, A. C.; Wang, Q.; Neese, F.; Spencer, D. J. E.; Blake, A. J.; Cooke, P. A.; Wilson, C.; Schröder, M. *PNAS*, **2005**, *102*, 18280–18285.
5. Corbett, M. C.; Hu, Y.; Fay, A. W.; Ribbe, M. W.; Hedman, B.; Hodgson, K. O. *PNAS*, **2006**, *103*, 1238–1243.
6. Lippard, S. J.; Berg, J. M. *Principles of Bioinorganic Chemistry*; University Science Books; 1994.
7. Sellmann, D.; Geck, M.; Knoch, F.; Ritter, G.; Dengler, J. *J. Am. Chem. Soc.*, **1991,** *113*, 1819.
8. Sellmann, D.; Lechner, P.; Knoch, F.; Moll, M. *Angew. Chem., Int. Ed. Engl.*, **1991**, *30*, 552.
9. Sellmann, D.; Barth, I.; *Z. Anorg. Allg. Chem.*, **1989,** *577*, 234.
10. Sellmann, D.; Binker, G.; Moll, M.; Herdtweck, E. *J. Organomet. Chem.* **1987**, *327*, 403.
11. Sellmann, D.; Kaeppler, O. *Z. Naturforsch., Teil B*, **1987**, *42*, 1291.
12. Sellmann, D.; Binker, G.; Moll, M.; Campana, C. E. *Inorg. Chim. Acta* **1987**, *130*, 221.
13. Sellmann, D.; Reineke, U.; Huttner, G.; Zsolnai, L. *J. Organomet. Chem.* **1987**, *310*, 83.
14. Issleib, V. K.; Gans, W. *Z. Anorg. Allg. Chem.* **1982**, *491*, 163.
15. Stephan, D. W.; *Inorg. Chem.* **1984**, *23*, 2207.
16. Block, E.; Eswarakrishman, V.; Gernon, M.; Ofori–Okai, G.; Saha, C.; Tang, K.; Zubieta, J. *J. Am. Chem. Soc.* **1989**, *111*, 658.
17. Block, E.; Ofori–Okai, G.; Zubieta, J. *J. Am. Chem. Soc.* **1989**, *111*, 2647.

18. Vries, N.; Davison, A.; Jones, A. G. *Inorg. Chim. Acta* **1989**, *165*, 346.
19. Dilworth, J. R.; Hutson, A. J.; Lewis, J. S.; Miller, J. R.; Zheng, Y.; Chen, Q.; Zubieta, J. *J. Chem. Soc., Dalton Trans.* **1996**, 1093–1104.
20. I.P. Evans; A. Spencer; G. Wilkinson. *J. Chem. Soc. Dalton* **1973**, 204.
21. Dehand, J.; Rose, J. *Inorg. Chim. Acta* **1979**, *37*, 249.
22. Elliott, G. P.' McAuley, N. M.; Roper, W. R. *Inorg. Synth.* **1989**, *26*, 185.
23. John Franolic, PhD dissertation, Stony Brook University, Stony Brook, **1993**.
24. Susan T. Beatty, PhD dissertation, Stony Brook University, Stony Brook, **1995**.
25. Kou–Suein Ai, PhD dissertation, Stony Brook University, Stony Brook, **1996**.
26. Doris Melgarejo, PhD dissertation, Stony Brook University, Stony Brook, **2006**.

# CHAPTER 4. Synthesis and Characterization of Ruthenium(II) and Osmium(II) Carbonyl–Cyanide Complexes

## 4.1 Introduction

Until the discovery of [NiFe] and [FeFe] hydrogenases, cyanide ($CN^-$) was an unheard native biological ligand. Cyanide was publicly known as a deadly poison, since cyanide is the active ingredient in "suicide pill." Considering how fatal cyanide can be, why did nature go through the trouble of using this type of ligand in a biological system? This question and several others has prompted researchers to investigate complexes containing the [$Fe^{II}$(CN)] moiety.

Looking back, about 300 years ago, the study of [$Fe(CN)_xL_{6-x}$] has captured the interest of chemist. The chemistry of iron–cyanide complexes are one of the oldest in coordination chemistry. These complexes have been the basis of many chemical reactions as well as industrial and mining processes.[1–2]

For example Prussian blue, [$(Fe^{III})_4(Fe^{II}(CN)_6)_3 \bullet xH_2O$], was initially utilized as a pigment in painting. One painting where Prussian blue was used as a pigment was Vincent van Gogh's "Starry Night" (**Figure IV–1**).

**Figure IV–1. "Starry Night" by Vincent van Gogh painted in 1889.[3]**

Currently, Prussian blue is used to treat thallium and radioactive cesium poisoning.[4] This compound can also be used to prevent hydration, an anti–caking agent called yellow prussiate of soda, is used in some commercial and cooking salt.[5]

Prussian blue is an example of the first class of mixed valent compounds. The crystal structure (**Figure IV–2**) shows cyano ligands that are bridging $Fe^{II}$ and $Fe^{III}$ ions.[6] The deep blue color comes from inter–valent change transfer, ICT, from the $Fe^{II}$ to $Fe^{III}$ through the cyanide

ligands. However, when a voltage is applied to the solution the color changes from deep blue to white because oxidation of $Fe^{II}$ to $Fe^{III}$ eliminates the ICT interaction. When exposed to visible light the compound undergoes spin–crossover behavior. This behavior converts the system from low spin to high spin, which makes this compound one of the few materials that contains a magnetic response to light.

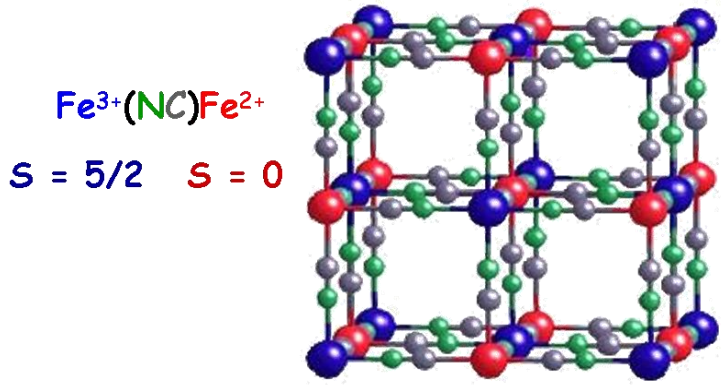


**Figure IV–2. X–ray Structure of Prussian blue.**

For over a hundred years, compounds with the basic structure of $[Fe(CN)_5L]^{n-}$ (where L = monodentate ligand) have been known. However, while many of these compounds have been chemically or spectroscopically characterized but very few have been structurally characterized. The first examples of $[Fe^{II,III}(CN)_4(L–L)]^{n-}$ (where L–L = 2,2–bipyridine and 1,10–phenanthroline) complexes with bidentate ligands were reported approximately 70 years ago.[7]

In the past, syntheses of pentacyano and tetracyano iron complexes (**Scheme IV–1**) were generated under extremely harsh conditions (e.g. high temperature, high pressure and long reaction times).[8]

$$[Fe^{II}(CN)_6]^{2-} + L \rightarrow [Fe^{II}(CN)_5(L)]^{n-}$$

$$[Fe^{II}(CN)_6]^{2-} + L–L \rightarrow [Fe^{II}(CN)_5(L–L)]^{n-}$$

**Scheme IV–1. Iron cyanide complexes reacting with mono– and bi– dentate ligands.**

The oldest iron complex containing exclusively CO and $CN^-$ ligands is $[Fe^{II}(CN)_5(CO)]^{3-}$. Despite the fact that this complex is over one hundred years old, it was only periodically studied in the 20$^{th}$ century.[9–12] In 1887, was the first reported synthesis of $[Fe^{II}(CN)_5(CO)]^{3-}$ appeared in the literature.[13] In 1912, it was found that the complex, $[Fe^{II}(CN)_5(CO)]^{3-}$, could be synthesized by a ligand displacement reaction using

$[Fe^{II}(CN)_5(NH_3)]^{3-}$ under CO atmosphere.[14–15] It was not until 1959, that Cotton *et al.* found that $[Fe^{II}(CN)_5(CO)]^{3-}$ can be synthesized using $[Fe^{II}(CN)_6]^{4-}$ under a CO atmosphere. However, the procedure requires the reaction to be carried out under extremely high temperature and pressure.[8] In 2001, Jiang *et al.* synthesized two geometric isomers of $[Fe^{II}(CN)_4(CO)_2]^{2-}$ (**Figure IV–3**) using simple reaction conditions.[16] Normally synthesis of these complexes came from the $[Fe^{II}(CN)_6]^{2-}$ starting material; however, Jiang *et al.* started with $Fe^{II}Cl_2 \cdot 4H_2O$ reacting with a calculated amount of cyanide while under CO atmosphere.

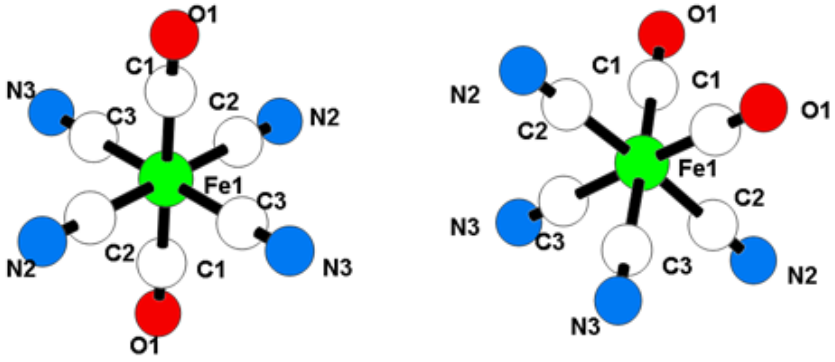


**Figure IV–3. X–ray structure of *trans* and *cis*–$[Fe^{II}(CN)_4(CO)_2]^{2-}$.**

In 2006, Chiarella *et. al.* used this concept and expended it using other monodentate ligands, e.g. DMSO and pyridine (**Scheme IV–2**).[17] These complexes were both characterized spectroscopically as well as structurally (**Figure IV–4**).

$$Fe^{II}Cl_2 \;+\; 4\ XCN \xrightarrow{\text{DMSO or pyridine}} \begin{matrix}[Fe^{II}(CN)_4(DMSO)_2]^{2-} \\ \text{or} \\ [Fe^{II}(CN)_4(py)_2]^{2-}\end{matrix}$$

**Scheme IV–2. Ferrous chloride reaction with cyanide (where X = $[Et_4N]^+$ for pyridine and $Na^+$ for DMSO)**

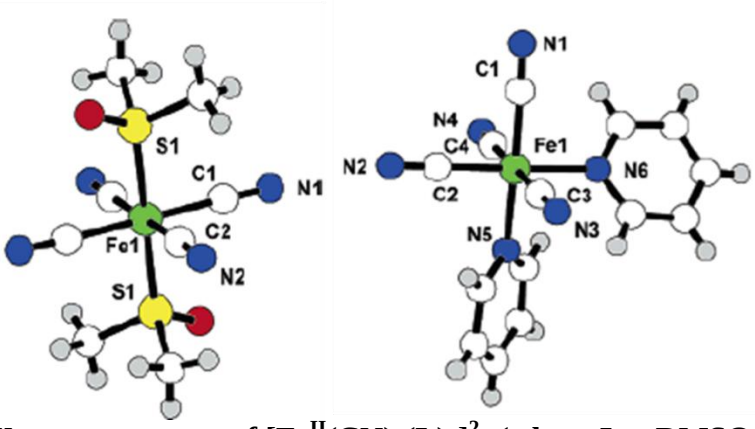


**Figure IV–4. X–ray structures of $[Fe^{II}(CN)_4(L)_2]^{2-}$ (where L = DMSO and pyridine).**

In this chapter, the goal was to extend the research done by Jiang and Chiarella by synthesizing and characterizing ruthenium and osmium analogs and comparing them to the original iron complexes. Analogs containing these two transition metals were, so far, non–existent.

## 4.2 Experimental

**Synthesis of $[PPN]_4[Ru^{II}(CN)_6]$**

The product was prepared by a literature procedure.[18] In a 250 mL Schlenk flask, [PPN]Cl (1.40 g, 2.44 mmol) was dissolved in 50 mL of hot degassed water. In a separate 50 mL Schlenk flask, $K_4[Ru^{II}(CN)_6]$ (0.500 g, 1.21 mmol) was dissolved in 10 mL of degassed water. The metal solution was added to the hot [PPN]Cl solution dropwise. A white solid was observed which was filtered off using a closed frit and washed with warm degassed water. While the solid was dried *in vacuo* the color changed from white to yellow to brown. The brown product was kept in the dry box (Yield: 1.57 g, 53.8%).

**$^1$H–NMR (400 MHz, $CD_3OD$) [ppm]:** 7.72 – 7.48 (aromatic, 30H, $PPN^+$).

**$^{13}$C–NMR (100 MHz, $CD_3OD$) [ppm]:** 165.15 (*C*≡$N^-$); 135.08, 133.67, 133.63, 133.58, 133.52, 133.49, 130.85, 130.83, 130.76, 130.69, 130.67, 129.29, 129.27, 128.21, 128.20 ($PPN^+$).

**Electrochemistry:** $E_{½}$ ($\Delta E_p$) = 139 mV (159 mV) 1.0 mM in $CH_3CN$ vs. Ag/AgCl, oxidation.

**Infrared ($CH_3OH$):** $\nu_{CN}$ = 2043 $cm^{-1}$.

**UV–Vis:** $\lambda_{max}$, nm ($\varepsilon_m$, $M^{-1}cm^{-1}$) = 266 (21600), 273 (17800), 295 (1800), 328 (1700), 356 (1300).

**Synthesis of $[PPN]_3[Ru^{III}(CN)_6]$**

In a 100 mL Schlenk flask, $[PPN]_4[Ru^{II}(CN)_6]$ (0.25 g, 0.104 mmol) was dissolved in 50 mL of $CH_2Cl_2$. The solution was stirred for 24 hours at room temperature. The reaction was monitored by IR. Crystals were grown by vapor diffusion of methylene chloride and diethyl ether (Yield: 0.087 g, 44.8%)

**Unit Cell:** Orthorhombic, *Pbcn*, a = 24.009(3) Å, b = 20.583(2) Å, c = 19.4679(19) Å, $\alpha = \beta = \gamma = 90^o$, V = 9620.6(17) $Å^3$.

A yellow needle crystal measuring 0.60 × 0.30 × 0.10 $mm^3$ was mounted using a nylon loop and centered on the X–ray beam at 298 K. Crystals were grown by vapor diffusion using methylene chloride and diethyl ether within one week. The accurate unit cell was obtained using reflection with $2\theta = 1.67 – 20.83^o$: a = 24.009(3) Å, b = 20.583(2) Å, c = 19.4679(19) Å, $\alpha = \beta = \gamma = 90^o$, V = 9620.6(17) $Å^3$. The structure was solved under a primitive orthorhombic crystal system (space group *Pbcn*) using 5047 reflections. The asymmetric unit consists of one–half molecule of the ruthenium complex anion and 1.5 molecules of the $PPN^+$ cation. The data reduction was done using CryAlisPro and the structure refinement was done with SHELXL–97 (Sheldrick). All the non–hydrogen atoms were located by Direct Methods and were refined anisotopically by a full–matrix least–squares method. The positions of the remaining hydrogen atoms were calculated. The crystallographic parameters and atomic coordinates for this compound are located in **Table A–12**.

**Infrared ($CH_2Cl_2$):** $\nu_{CN}$ = 2089 and 2078 $cm^{-1}$.

**Synthesis of $[PPN]_3[Ru^{II}(CN)_5(CO)]$**

In a 100 mL Schlenk flask, $[PPN]_4[Ru^{II}(CN)_6]$ (0.500 g, 0.207 mmol) was dissolved in methanol (50 mL). The solution was placed under a carbon monoxide atmosphere and refluxed for six hours. The reaction was monitored by IR. The solution was cooled to room temperature and was placed under dinitrogen atmosphere. The solvent was removed *in vacuo*, which resulted in a yellow solid. The yellow solid was purified by adding 20 mL of 1:1 $CH_2Cl_2/H_2O$ mixture. The organic layer was separated by using a separatory funnel. The organic layer was dried using anhydrous magnesium sulfate. The solution was filtered and the solvent was removed *in vacuo*, which resulted in a yellow solid (Yield: 0.28 g, 74.6%).

**$^{1}$H–NMR (400 MHz, $CD_3OD$) [ppm]:** 7.72 – 7.48 (aromatic, 30H, $PPN^+$).

**$^{13}$C–NMR (100 MHz, $CD_3OD$) [ppm]:** 200.55 (*C*≡O); 151.17, 150.65 (*C*≡$N^-$); 135.06, 133.70, 133.66, 133.61, 133.55, 133.52, 130.86, 130.83, 130.77, 130.70, 130.67, 129.32, 129.30, 128.25, 128.23 ($PPN^+$).

**Electrochemistry:** $E_{½}$ ($\Delta E_p$) = 995 mV (63 mV) 1.0 mM in DMF vs. Ag/AgCl, oxidation.

**Infrared ($CH_3OH$):** $\nu_{CO}$ = 1983 $cm^{-1}$; $\nu_{CN}$ = 2109(sh), 2086 $cm^{-1}$.

**UV–Vis:** $\lambda_{max}$, nm ($\varepsilon_m$, $M^{-1}cm^{-1}$) = 265 (9000), 272 (6600).

**Synthesis of *trans*–$[PPN]_2[Ru^{II}(CN)_4(CO)_2]$**

In a 100 mL Schlenk flask, $[PPN]_3[Ru^{II}(CN)_5(CO)]$ (0.200 g, 0.107 mmol) was dissolved in $CH_3CN$ (50 mL). The solution was placed under CO atmosphere and refluxed for twelve hours. The reaction was monitored by IR. The solution was cooled to room temperature and the solution was placed under dinitrogen atmosphere. The solvent was removed *in vacuo*, which resulted in a tan solid. The tan solid was purified by adding 20 mL of 1:1 $CH_2Cl_2/H_2O$ mixture. The organic layer was separated by using a separatory funnel. The organic layer was dried using anhydrous magnesium sulfate. The solution was filtered and the solvent was removed *in vacuo*, which resulted in a tan solid (Yield: 0.101 g, 70.7%).

**$^{1}$H–NMR (400 MHz, $CD_3OD$) [ppm]:** 7.74 – 7.26 (aromatic, 30H, $PPN^+$).

**$^{13}$C–NMR (100 MHz, $CD_3OD$) [ppm]:** 193.87 (*C*≡O); 134.85 (*C*≡$N^-$); 134.15, 132.27, 132.24, 132.18, 132.13, 132.10, 129.88, 129.86, 129.79, 129.72, 129.70, 127.59, 127.58, 126.52, 126.51 ($PPN^+$).

**Infrared ($CH_3CN$):** $\nu_{CO}$ = 2007 $cm^{-1}$; $\nu_{CN}$ = 2107 $cm^{-1}$.

**UV–Vis:** $\lambda_{max}$, nm ($\varepsilon_m$, $M^{-1}cm^{-1}$) = 267 (9400), 271 (7600).

**Unit Cell:** Monoclinic, $P2_1/n$, a = 12.9848(2) Å, b = 13.21920(10) Å, c = 19.8902(3) Å, $\alpha = \gamma = 90^o$, $\beta = 106.5600(10)^o$, V = 3272.51(7) $Å^3$.

A gold plate crystal measuring 0.45 × 0.25 × 0.10 $mm^3$ was mounted using a nylon loop and centered on the X–ray beam at 100 K. Crystals were grown by vapor diffusion using methylene chloride and diethyl ether in three days. The accurate unit cell was obtained using reflection with $2\theta = 3.26 – 32.97^o$: a = 12.9848(2) Å, b = 13.21920(10) Å, c = 19.8902(3) Å, $\alpha = \gamma = 90^o$ $\beta = 106.5600(10)^o$, V = 3272.51(7) $Å^3$. The structure was solved under a primitive monoclinic crystal system (space group $P2_1/n$) using 10534 reflections. The asymmetric unit consists of one–half molecule of the ruthenium complex anion and one molecule of the $PPN^+$

cation. The data reduction was done using CryAlisPro and the structure refinement was done with SHELXL–97 (Sheldrick). All the non–hydrogen atoms were located by Direct Methods and were refined anisotopically by a full–matrix least–squares method. The positions of the remaining hydrogen atoms were calculated. The crystallographic parameters and atomic coordinates for this compound are located in **Table A–13**.

**Synthesis of *cis*–[PPN]$_2$[Ru$^{II}$(CN)$_4$(CO)$_2$]**

In a 100 mL Schlenk flask, $Ru^{II}(CO)_3Cl_2THF$ (0.200 g, 0.61 mmol) was dissolved in methanol (25 mL). To the stirred solution, solid NaCN (0.12 g, 2.44 mmol) was added, after which the solution was allowed to stir overnight at room temperature. The solvent was removed *in vacuo*, which resulted in a white solid. Approximately 20 mL of degassed distilled water, *via* cannula, was added to redissolved the product, $Na[Ru^{II}(CN)_4(CO)_2]$. In a separate 100 mL Schlenk flask, [PPN]Cl (0.70 g, 1.22 mmol) was dissolved in warm degassed water and transferred to the aqueous *cis*–$Na_2[Ru^{II}(CN)_4(CO)_2]$ solution, dropwise *via* cannula. Upon the addition of the [PPN]Cl, a white precipitate was obtained. Solution was stirred for approximately thirty minutes. The white precipitate was filtered using a closed frit, washed 2 x 20 mL of diethyl ether and dried *in vacuo* (Yield: 0.655 g, 80.2%).

**Infrared ($CH_3OH$):** $\nu_{CO}$ = 2050 and 2006 $cm^{-1}$; $\nu_{CN}$ = 2123 and 2083 $cm^{-1}$.

**UV–Vis:** $\lambda_{max}$, nm ($\varepsilon_m$, $M^{-1}cm^{-1}$) = 257 (sh, 8600), 265 (9500), 267 (8500).

**Unit Cell:** Monoclinic, $P2_1/c$, a = 25.0458(8) Å, b = 13.0964(6) Å, c = 20.6277(5) Å, $\alpha = \gamma = 90^o$, $\beta = 107.143(3)^o$, V = 6465.5(4) $Å^3$.

A colorless prism crystal measuring 0.35 x 0.25 x 0.20 $mm^3$ was mounted using a nylon loop and centered on the X–ray beam at 100 K. Crystals were grown by vapor diffusion using methylene chloride and diethyl ether in one week. The accurate unit cell was obtained using reflection with $2\theta = 3.35 – 28.12^o$: a = 25.0458(8) Å, b = 13.0964(6) Å, c = 20.6277(5) Å, $\alpha = \gamma = 90^o$ $\beta = 107.143(3)^o$, V = 6465.5(4) $Å^3$. The structure was solved under a primitive monoclinic crystal system (space group $P2_1/c$) using 7515 reflections. The asymmetric unit consists of one molecule of the ruthenium complex anion and two molecules of the $PPN^+$ cation. The data reduction was done using CryAlisPro and the structure refinement was done with SHELXL–97 (Sheldrick). All the non–hydrogen atoms were located by Direct Methods and were refined anisotopically by a full–matrix least–squares method. The positions of the remaining hydrogen

atoms were calculated. The crystallographic parameters and atomic coordinates for this compound are located in **Table A–14**.

**Synthesis of *fac*–[AsPh$_4$][Ru$^{II}$(CN)$_3$(CO)$_3$]**

In a 100 mL Schlenk flask, Ru$^{II}$(CO)$_3$Cl$_2$THF (0.200 g, 0.61 mmol) was dissolved in methanol (25 mL). To the stirred solution, solid NaCN (0.089 g, 1.83 mmol) was added, after which the solution was allowed to stir overnight at room temperature. The solvent was removed *in vacuo*, which resulted in a white solid. Approximately 20 mL of degassed distilled water, *via* cannula, was added to redissolved the product, Na[Ru$^{II}$(CN)$_3$(CO)$_3$]. In a separate 100 mL Schlenk flask, [AsPh$_4$]Cl (0.51 g, 1.22 mmol) was dissolved in warm degassed water and transferred to the aqueous Na[Ru$^{II}$(CN)$_3$(CO)$_3$] solution, dropwise *via* cannula. Upon the addition of the [AsPh$_4$]Cl, a white precipitate was obtained. Solution was stirred for approximately thirty minutes. The white precipitate was filtered using a closed frit, washed 2 x 20 mL of diethyl ether and dried *in vacuo* (Yield: 0.271 g, 68.7%).

**$^1$H–NMR (400 MHz, CDCl$_3$) [ppm]:** 7.92 – 7.66 (aromatic, 20H, [AsPh$_4$]$^+$)

**$^{13}$C–NMR (100 MHz, CDCl$_3$) [ppm]:** 186.14 (*C*≡O); 123.16 (*C*≡N$^-$); 135.05, 133.33, 131.57, 120.78 ([AsPh$_4$]$^+$).

**Infrared (CH$_3$CN):** $\nu_{CO}$ = 2118 and 2077 cm$^{-1}$; $\nu_{CN}$ = 2164 and 2145 cm$^{-1}$.

**Synthesis of *trans*–[PPN]$_2$[Ru$^{II}$(CN)$_4$(CO)(py)]**

In a 100 mL Schlenk flask, [PPN]$_3$[Ru$^{II}$(CN)$_5$(CO)] (0.200 g, 0.107 mmol) was dissolved in pyridine (30 mL). The solution was refluxed for overnight under a dinitrogen atmosphere. The reaction is monitored by IR. The solution was cooled to room temperature and the solvent was removed, *in vacuo*, which resulted in a tan oil. The oil was purified by adding 20 mL of 1:1 $CH_2Cl_2/H_2O$ mixture. The organic layer was separated by using a separatory funnel. The organic layer was dried using anhydrous magnesium sulfate. The solution was filtered and the solvent was removed *in vacuo* which resulted in a dark tan solid (Yield: 0.104 g, 70.2%).

**$^1$H–NMR (400 MHz, CD$_3$OD) [ppm]:** 9.12 – 9.09 (d, 2H, *J* = 9.11, *ortho* hydrogens on bound pyridine), 7.81 – 7.75 (t, 1H, *J* = 7.78, *para* hydrogen on bound pyridine), 7.34 – 7.29 (t, 2H, *J* = 7.78, *meta* hydrogens on bound pyridine), 7.72– 7.48 (aromatic, 60H, PPN$^+$).

**$^{13}$C–NMR (100 MHz, CD$_3$OD) [ppm]:** 202.81 (*C*≡O); 156.86 (*C*≡N$^-$); 152.43, 138.33, 125.35 (bound pyridine); 135.04, 133.72, 133.69, 133.63, 133.58, 133.54, 130.86, 130.83, 130.76, 130.70, 130.67, 129.35, 129.33, 128.28, 128.26 (PPN$^+$).

**Electrochemistry:** $E_{½}$ ($\Delta E_p$) = 538 mV (71 mV) 1.0 mM in $CH_3CN$ vs. Ag/AgCl, oxidation.

**UV–Vis:** $\lambda_{max}$, nm ($\varepsilon_m$, $M^{-1}cm^{-1}$) = 261 (sh, 12100), 267 (13300), 271 (11200), 380 (br, 1800).

**Infrared (pyridine):** $\nu_{CO}$ = 1950 $cm^{-1}$; $\nu_{CN}$ = 2089 $cm^{-1}$.

**Unit Cell:** Triclinic, *P*–1, a = 13.7375(4) Å, b = 16.1926(5) Å, c = 17.1100(5) Å, α = 73.931(3) $^o$, β = 71.636(2)$^o$, γ = 71.625(3)$^o$, V = 3360.84(17) $Å^3$.

A brown prism crystal measuring 0.45 × 0.30 × 0.15 $mm^3$ was mounted using a nylon loop and centered on the X–ray beam at 100 K. Crystals were grown by vapor diffusion using acetonitrile and diethyl ether in four days. The accurate unit cell was obtained using reflection with 2θ = 3.26 – 32.97$^o$: a = 13.7375(4) Å, b = 16.1926(5) Å, c = 17.1100(5) Å, α = 73.931(2)$^o$ β = 71.636(2)$^o$, γ = 71.625(3)$^o$, V = 3360.84(17) $Å^3$. The structure was solved under a primitive triclinic crystal system (space group *P*1bar) using 16991 reflections. The asymmetric unit consists of one molecule of the ruthenium complex anion and two molecules of the $PPN^+$ cation. The data reduction was done using CryAlisPro and the structure refinement was done with SHELXL–97 (Sheldrick). All the non–hydrogen atoms were located by Direct Methods and were refined anisotopically by a full–matrix least–squares method. The positions of the remaining hydrogen atoms were calculated. The crystallographic parameters and atomic coordinates for this compound are located in **Table A–15**.

**Attempted Synthesis of *trans*–$[PPN]_2[Ru^{II}(CN)_4(CO)(CN–dmph)]$**

In a 100 mL Schlenk flask, $[PPN]_3[Ru^{II}(CN)_5(CO)]$ (0.200 g, 0.107 mmol) and 2,6–dimethylphenylisocyanide (0.070 g, 0.533 mmol) were dissolved in acetonitrile (30 mL). The solution was refluxed overnight. The reaction was monitored by IR. The solution was cooled to room temperature and the solvent was removed *in vacuo*, which resulted in a dark yellow oil. The oil was purified by adding 20 mL of 1:1 $CH_2Cl_2/H_2O$ mixture. The organic layer was separated by using a separatory funnel. The organic layer was dried using anhydrous magnesium sulfate. The solution was filtered and the solvent was removed *in vacuo*, which resulted in a dark yellow solid (Yield: 0.101 g, 65.7%).

**Infrared ($CH_3CN$):** $\nu_{CO}$ = 1986 $cm^{-1}$; $\nu_{CN}$ = 2096 $cm^{-1}$; $\nu_{CN–dmph}$ = 2121 $cm^{-1}$.

**Synthesis of $[Et_4N]_2[Os^{IV}Cl_6]$**

The product was prepared by a literature procedure.[19] All manipulations were performed in air. Osmium tetroxide (2.0 g, 7.87 mmol) was added to a solution of $[Et_4N]Cl•H_2O$ (4.0 g, 24 mmol) in 30 mL of concentrated HCl. The solution was refluxed for 19 hours and cooled to room

temperature. Ethanol (30 mL) and diethyl ether (15 mL) were added to the acid solution. The flask was kept at –20°C for three hours. An orange solid precipitated and was filtered. The orange solid was washed with minimum amount of ethanol (4 × 10 mL) and dried for one hour at 100°C. Yield: 4.95 g, 94.8%

**Synthesis of $[PPN]_4[Os^{II}(CN)_6]$**

In a 100 mL Schlenk flask, $[Et_4N]_2[Os^{IV}Cl_6]$ (0.500 g , 0.754 mmol) was dissolved with 30 mL of degassed water. To this solution, $[Et_4N]CN$ (1.20 g, 7.54 mmol) was added. The mixture was allowed to reflux for three days and then was allowed to cool to room temperature. In a separate 100 mL Schlenk flask, [PPN]Cl (1.30 g, 2.26 mmol) was dissolved in 25 mL of hot degassed water. The metal solution was added to the hot [PPN]Cl solution dropwise. A white solid was observed which was filtered off using a closed frit and washed with warm degassed water. While the solid was dried *in vacuo* the color changed from white to light green. The light green product was weighed and kept in the dry box (Yield: 1.02 g, 54.1%).

**$^1$H–NMR (400 MHz, $CD_3OD$) [ppm]:** 7.74 – 7.46 (aromatic, 30H, $PPN^+$).

**$^{13}$C–NMR (100 MHz, $CD_3OD$) [ppm]:** 145.58 (*C*≡$N^-$); 145.22, 135.08, 133.65, 133.62, 133.57, 133.51, 133.48, 130.85, 130.83, 130.76, 130.69, 130.66, 129.27, 129.26, 128.20, 128.18 ($PPN^+$).

**Electrochemistry:** $E_{½}$ ($\Delta E_p$) = –86 mV (irreversible) 1.0 mM in $CH_3CN$ vs. Ag/AgCl, oxidation.

**Infrared ($CH_3CN$):** $\nu_{CN}$ = 2020 $cm^{-1}$.

**Synthesis of $[PPN]_3[Os^{III}(CN)_6]$**

In a 100 mL Schlenk flask, $[PPN]_4[Os^{II}(CN)_6]$ (0.200 g, 0.080 mmol) was dissolved in 50 mL of $CH_2Cl_2$. The solution was stirred for 24 hours at room temperature. The reaction was monitored by IR. Crystals were grown by vapor diffusion of methylene chloride and diethyl ether (Yield: 0.067 g, 42.9%)

**Infrared ($H_2O$):** 2147 $cm^{-1}$.

**Unit Cell:** Orthorhombic, *Pbcn*, a = 23.8163(2) Å, b = 20.3376(2) Å, c = 19.33450(10) Å, α = β = γ = 90°, V = 9364.98(13) $Å^3$.

A light green plate crystal measuring 0.65 × 0.45 × 0.10 $mm^3$ was mounted using a nylon loop and centered on the X–ray beam at 100 K. Crystals were grown by vapor diffusion using methylene chloride and diethyl ether within one week. The accurate unit cell was obtained using reflection with 2θ = 3.30 – 32.31°: a = 23.8163(2) Å, b = 20.3376(2) Å, c = 19.33450(10) Å, α = β = γ = 90°, V = 9364.98(13) $Å^3$. The structure was solved under a primitive orthorhombic

crystal system (space group *Pbcn*) using 15982 reflections. The asymmetric unit consists of one–half molecule of the osmium complex anion and 1.5 molecules of the $PPN^+$ cation. The data reduction was done using CryAlisPro and the structure refinement was done with SHELXL–97 (Sheldrick). All the non–hydrogen atoms were located by Direct Methods and were refined anisotopically by a full–matrix least–squares method. The positions of the remaining hydrogen atoms were calculated. The crystallographic parameters and atomic coordinates for this compound are located in **Table A–16**.

**Attempted Synthesis of $[PPN]_3[Os^{II}(CN)_5(CO)]$**

In a 100 mL Schlenk flask, $[PPN]_4[Os^{II}(CN)_6]$ (0.200 g , 0.080 mmol) was dissolved in 1–propanol (20 mL). The solution was placed under carbon monoxide atmosphere and refluxed for twelve hours. The reaction was monitored by IR. The solution was cooled to room temperature and the solution was placed under dinitrogen atmosphere. The solvent was removed which resulted in a yellow–green solid. The yellow–green solid was purified by adding 20 mL of 1:1 $CH_2Cl_2/H_2O$ mixture. The organic layer was separated by using a separatory funnel. The organic layer was dried using anhydrous magnesium sulfate. The solution was filtered and the solvent was removed *in vacuo*, which resulted in a yellow–green solid (Yield: 0.086 g, 54.7%).

**Infrared (1–propanol):** $\nu_{CO}$ = 2006 $cm^{-1}$; $\nu_{CN}$ = 2106 and 2089 $cm^{-1}$.

## 4.3 Results and Discussion

### 4.3.1 Synthesis and Infrared Studies of the Ruthenium and Osmium Complexes

The low solubility of cyanometallates in organic solvents is due to the nature of the counterion, usually an alkali metal, and can be problematic when performing certain reactions.[18] The solubility of cyanometallates was improved by replacing the alkali metal counterion with bis(triphenylphosphino)iminium ion, $[N(PPh_3)_2]^+$ or $[PPN]^+$.[20] It has been shown that the substitution of the potassium ion with $[PPN]^+$ allowed the reactivity of cyanometallates to be changed. Pelizzi *et al.* reacted $[PPN]_3[Fe^{III}(CN)_6]$ with $Ph_3SnCl$ in DMSO to produce an unusual trinuclear anion, $[(Ph_3SnCl)_2(\mu–CN)_2Fe(CN)_2(DMSO)_2]^{2–}$, which could not be produced using $K_3[Fe^{III}(CN)_6]$.[21–22]

Overall scheme of synthesized complexes are illustrated in **Figure IV–5** and **Figure IV–6**. The $[PPN]_4[Ru^{II}(CN)_6]$ was prepared in moderate yield, 50 – 60%, by precipitation from a

warm aqueous solution of [PPN]Cl added to a aqueous solution of $K_4[Ru^{II}(CN)_6]$. It is very important to maintain the aqueous solution at a moderately hot temperature (50 – 65 $^oC$) to avoid the formation of an oily suspension. The precipitate was filtered using a closed frit, which upon drying, resulted in a brown solid being observed. Infrared analysis was performed to confirm the purity of the desired product (**Figure IV–7**). The product was shown to be soluble in a wide range of solvents: acetonitrile, acetone, DMSO, alcohols, methylene chloride, but insoluble in diethyl ether and aromatic hydrocarbons. This compound was fairly unstable and oxidized slowly to a yellow solid, when exposed to the air. A methylene chloride solution of $[PPN]_4[Ru^{II}(CN)_6]$, open to the air, caused the oxidation of the compound from $Ru^{II}$ to $Ru^{III}$. **Figure IV–8** shows the infrared spectrum of $[PPN]_3[Ru^{III}(CN)_6]$. As a result, this compound was stored in the Dry–box.

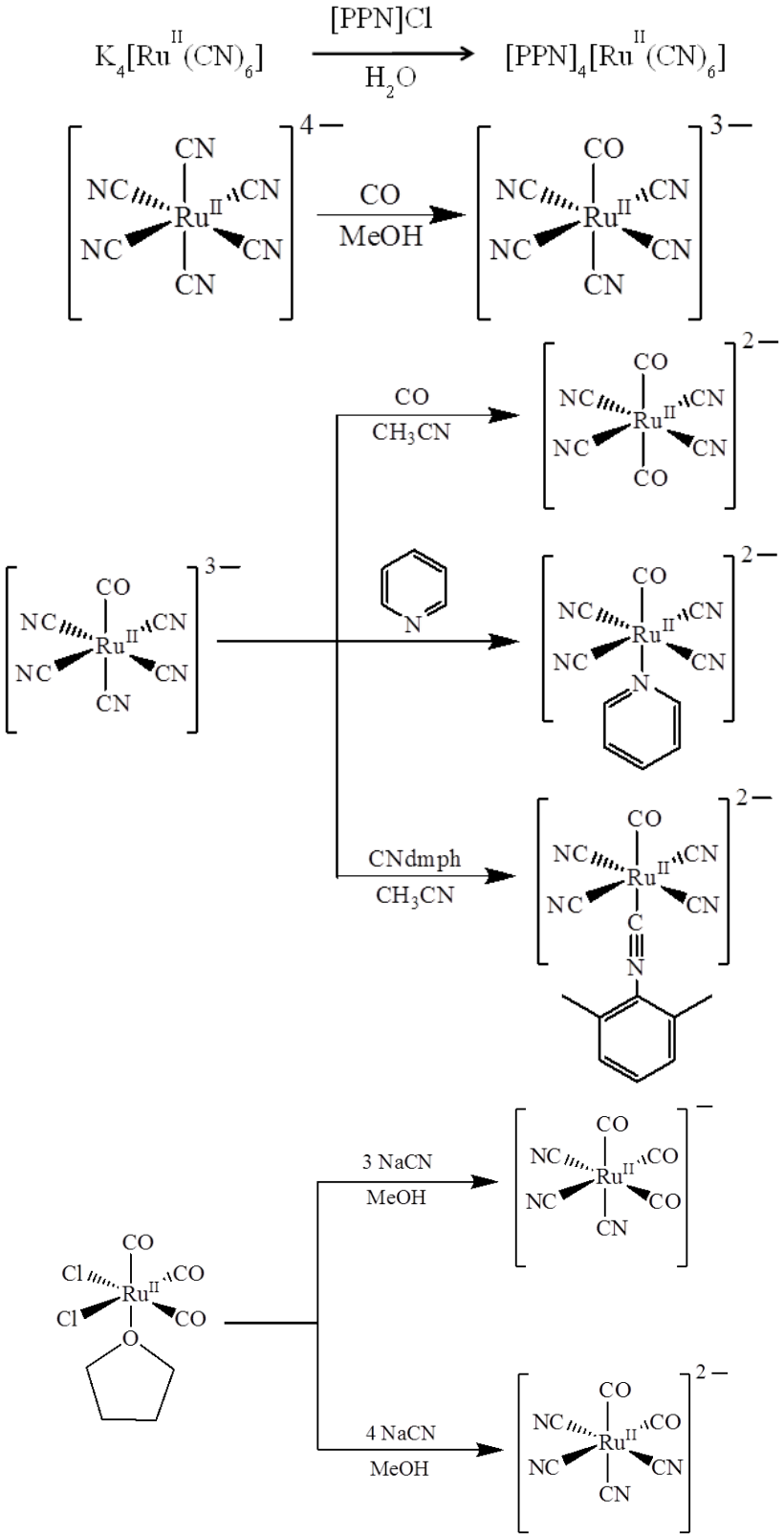


**Figure IV–5. Overall Scheme of Synthesized Ruthenium Compounds.**

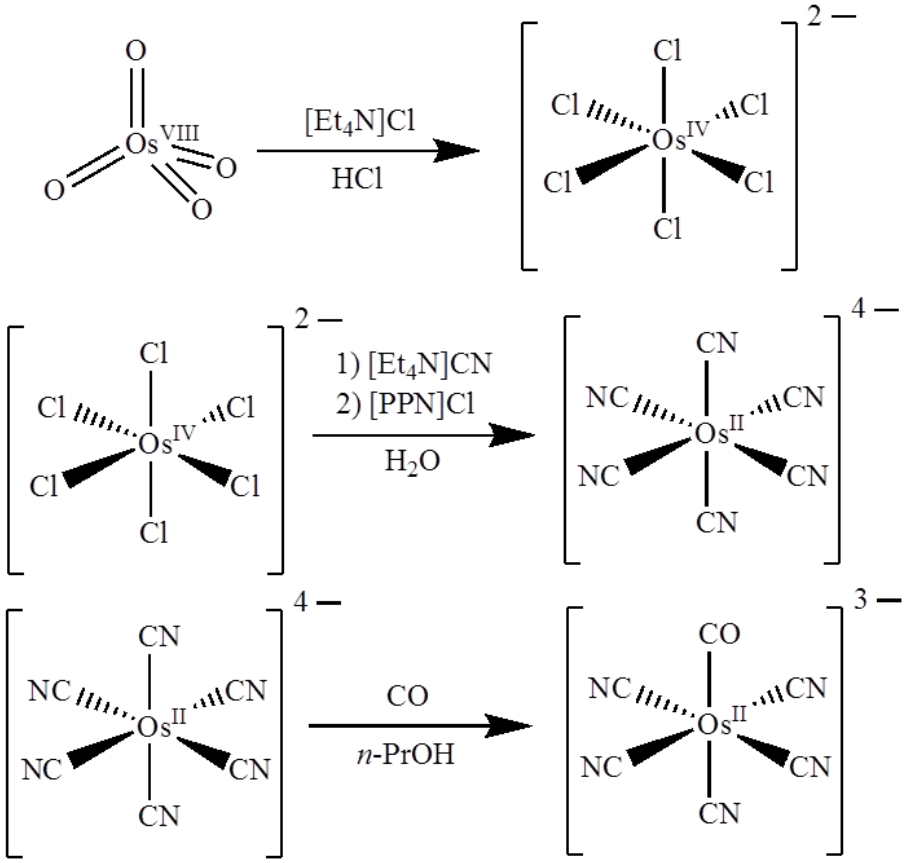


**Figure IV–6. Overall Scheme of Synthesized Osmium Compounds.**

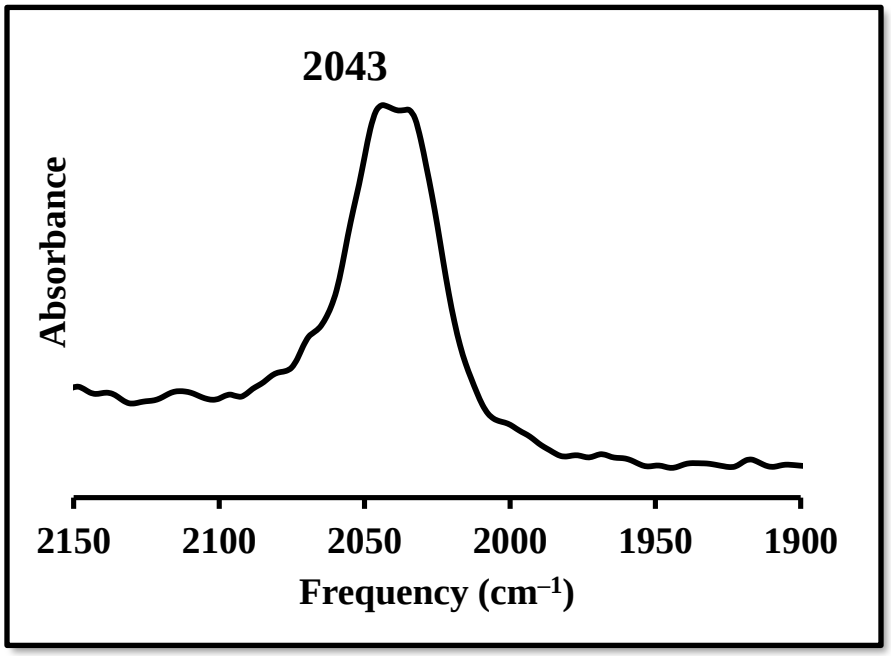


**Figure IV–7. Infrared Spectrum of $[PPN]_4[Ru^{II}(CN)_6]$ in MeOH.**

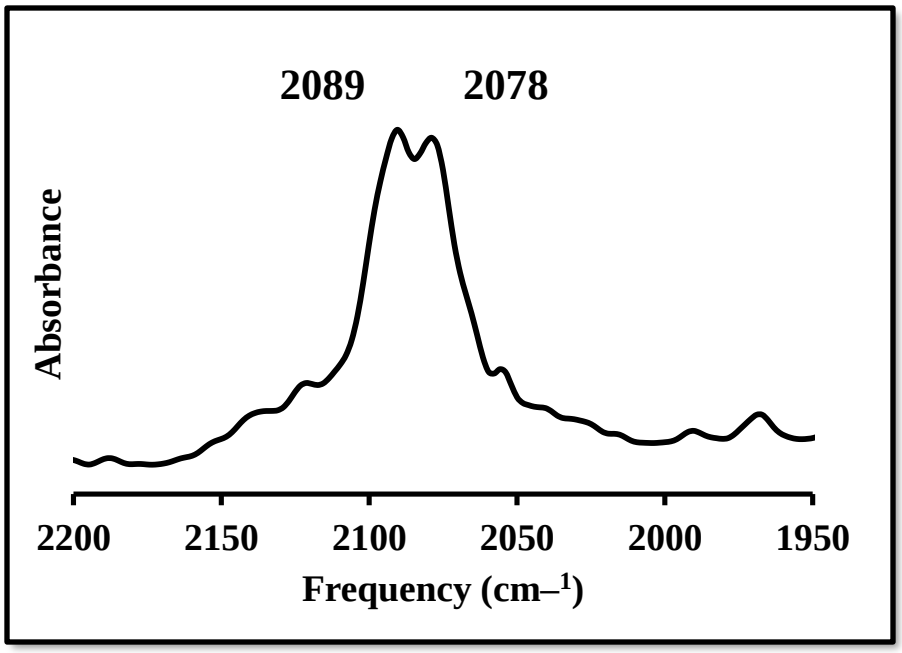


**Figure IV–8. Infrared Spectrum of $[PPN]_3[Ru^{III}(CN)_6]$ in $CH_2Cl_2$.**

As previously mentioned, in 1959 Cotton *et al.* found that $[Fe^{II}(CN)_5(CO)]^{3-}$ can be synthesized using $[Fe^{II}(CN)_6]^{4-}$ under a CO atmosphere. However, this synthetic route was achieved under high temperatures (300°C) and pressures (100 atm). This results in the iron compound that was highly inert to substitution. Since $K_4[Ru^{II}(CN)_6]$ is an expensive compound (~$150/gram), using the same synthetic route as Cotton was not economically favorable. Since replacing the potassium ion with $PPN^+$ has been shown to improve reactivity of the starting material, this method was applied.

A methanolic solution of $[PPN]_4[Ru^{II}(CN)_6]$ was placed under a CO atmosphere and refluxed which resulted in the formation of $[PPN]_3[Ru^{II}(CN)_5(CO)]$. Infrared analysis was performed to confirm the purity of the desired product (**Figure IV–9**). The peak at 1983 $cm^{-1}$ has been assigned to the CO ligand, while the 2086 $cm^{-1}$ peak to the cyanide ligand. The desired product was purified using a 1:1 methylene chloride/distilled water solution to remove [PPN]CN. The mixture was separated using a separatory funnel, which the organic layer ($CH_2Cl_2$ layer) was collected and removed *in vacuo*. The resulting yellow oil was gently heated which resulted in a yellow powder. The desired yellow product was stored under anaerobic conditions. $[PPN]_3[Ru^{II}(CN)_5(CO)]$ is stable under air, under light and in solution. When left open to the air, the yellow powder absorbs moisture to produce a yellow tarry solid.

The $[Ru^{II}(CN)_5(CO)]^{3-}$ anion has a $C_{4v}$ molecular symmetry. There are two different $CN^-$ ligands which are the axial and equatorial $CN^-$. The equatorial $CN^-$ ligands are equivalent due to symmetry. Theoretically, the infrared spectrum should show four peaks for the CO and $CN^-$ stretching frequencies. However, the infrared spectrum shows three peaks, one for CO and two for $CN^-$. This is because the $CN^-$ stretching frequencies are close enough in energy that only two peaks can be distinguished.

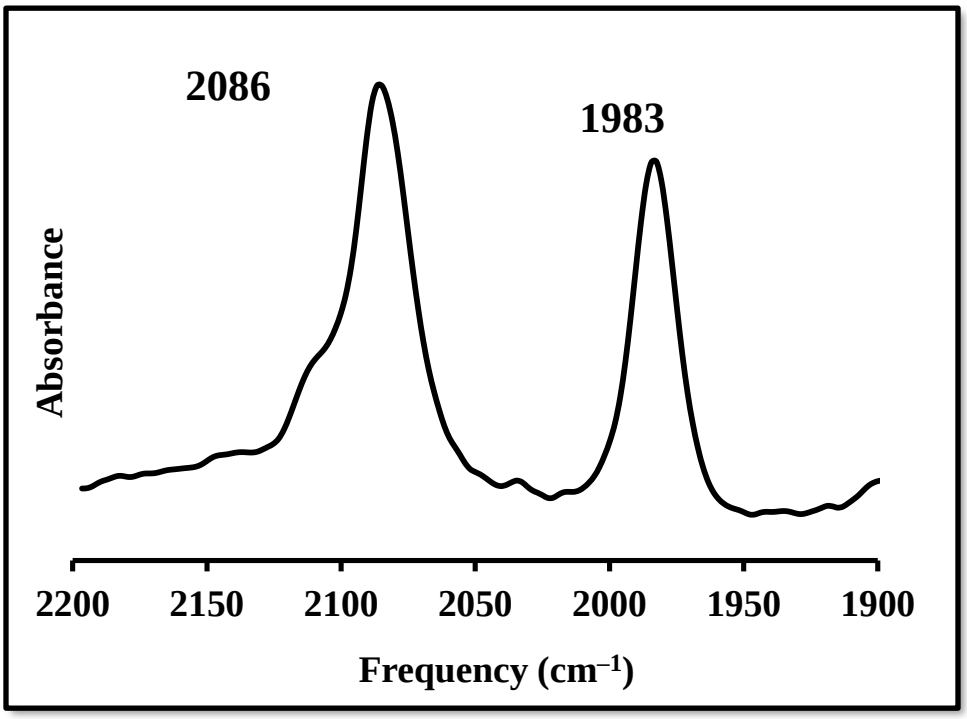


**Figure IV–9. Infrared Spectrum of $[PPN]_3[Ru^{II}(CN)_5(CO)]$ in MeOH.**

In 2002, the iron analog of $[Ru^{II}(CN)_5(CO)]^{3-}$ anion was synthesized and characterized by Jiang *et al.*[23] The infrared spectrum for the iron complex was found to be similar to the ruthenium complex; this is summarized in **Table IV–1**. The slight differences in the infrared spectra are contributed to the interaction between the ligand and the transition metal. The $CN^-$ stretching frequencies differ by 10 $cm^{-1}$ due to the change in σ donation. There is less σ donation from the cyanide to the ruthenium, which weakens the ruthenium cyanide bond but simultaneously strengthens the carbon–nitrogen triple bond of the cyanide. Due to the increased strength of the triple bond, the stretching frequency would increase.

| Table IV–1. Infrared Spectra Comparison of $[M^{II}(CN)_5(CO)]^{3-}$ in MeOH. | | | |
|---|---|---|---|
| **M** | **Cation** | **$\nu_{CO}$ ($cm^{-1}$)** | **$\nu_{CN}$ ($cm^{-1}$)** |
| Fe | $[PPN]^+$ | 1986 | 2076, 2096 |
| Ru | $[PPN]^+$ | 1983 | 2086, 2109(sh) |

The $[Ru^{II}(CN)_5(CO)]^{3-}$ served as an intermediate for the formation of various other complexes. The first complex that was generated was *trans*–$[Ru^{II}(CN)_4(CO)_2]^{2-}$ by further reacting $[Ru^{II}(CN)_5(CO)]^{3-}$ under a CO atmosphere. Infrared analysis was performed to confirm the purity of the desired product (**Figure IV–10**). Using infrared spectroscopy, the symmetry of the compound could be determined. The peak at 2007 $cm^{-1}$ has been assigned to the carbon monoxide ligand, while the 2107 $cm^{-1}$ peak has been assigned to the cyanide ligand. The observation that there is one peak for each ligand is consistent a trans *trans*–$[Ru^{II}(CN)_4(CO)_2]^{2-}$ structure. The desired product was purified using the same procedure described for the $[Ru^{II}(CN)_5(CO)]^{3-}$ complex. The organic layer was placed in a Schlenk flask to which the solvent was removed *in vacuo*. The resulting tan oil was gently heated which resulted in a tan powder. The desired tan product was stored under anaerobic conditions. The complex, *trans*–$[PPN]_2[Ru^{II}(CN)_4(CO)_2]$, was stable under air, under light and in solution.

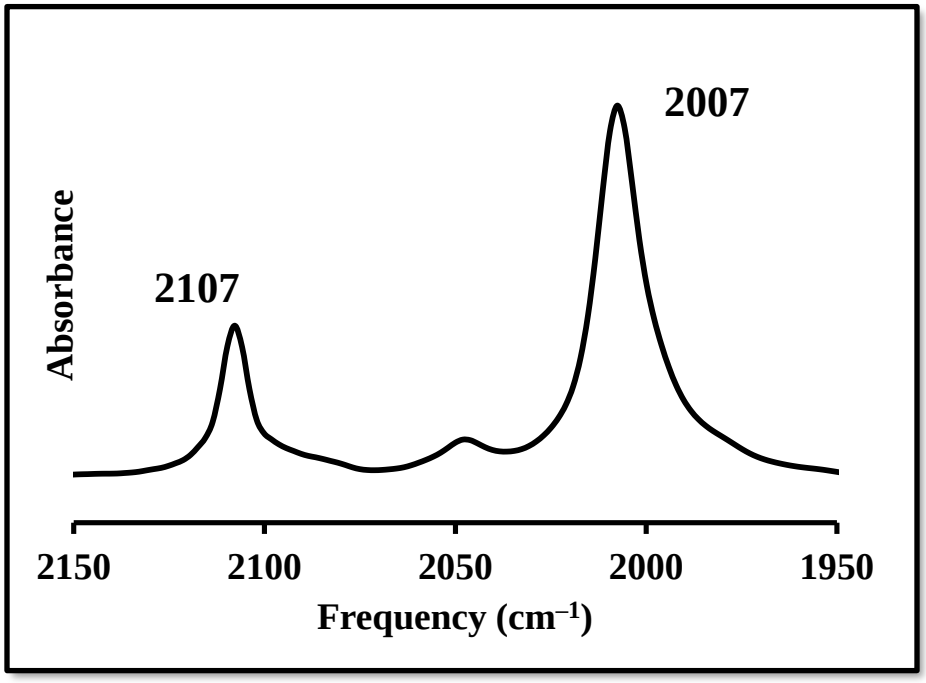


**Figure IV–10. Infrared Spectrum of *trans*–$[PPN]_2[Ru^{II}(CN)_4(CO)_2]$ in $CH_3CN$.**

Jiang *et al*. had synthesized and characterized the iron analog of *trans*–$[Ru^{II}(CN)_4(CO)_2]^{2-}$, which was later revisited by Rauchfuss and coworkers.[16,24,27] Using infrared spectroscopy, it was demonstrated how the stretching frequencies can differ for carbon monoxide and cyanide based on different transition metals, illustrated in **Table IV–2**, and how the quantity of each ligand which is illustrated in **Table IV–4**. As stated above, there is less σ donation when moving down a family in the periodic table. Less σ donation from the ligand to the metal will increase the bond strength of the carbon–oxygen triple bond (C≡O) and the carbon–nitrogen triple bond ($C{\equiv}N^-$), which results in higher stretching frequencies (i.e. blue shift).

**Table IV–2. Infrared Spectra Comparison of *trans*–$[M^{II}(CN)_4(CO)_2]^{2-}$ in $CH_3CN$.**

| M | Cation | $\nu_{CO}$ ($cm^{-1}$) | $\nu_{CN}$ ($cm^{-1}$) |
|---|---|---|---|
| Fe | $[PPh_4]^+$ | 1999 | 2103 |
| Ru | $[PPN]^+$ | 2007 | 2107 |

The number of carbon–monoxide and cyanide has a significant effect in the stretching frequencies found in the infrared spectra. Carbon monoxide binds to the transition metal center through π–backbonding. As the number of carbon monoxide ligands increases there would be higher demand for π–backbonding from the transition metal to the carbon monoxide, which results in a decrease in the metal–ligand bond strength and therefore increases the C≡O bond. This effect would increase the stretching frequency of the carbon–oxygen triple bond. Cyanide binds to the transition metal through σ donation. As the amount of cyanide ligand decreases there would be less σ donation that weakens the metal–ligand bond and therefore strengthen the $C{\equiv}N^-$ bond. This effect would increase the stretching frequency of the carbon–nitrogen triple bond.

The *cis*–$[Ru^{II}(CN)_4(CO)_2]^{2-}$ isomer was synthesized using *fac*–$[Ru^{II}(CO)_3Cl_2THF]$, description of this starting material can be found in Chapter 5. Synthesis of *cis*–$[Ru^{II}(CN)_4(CO)_2]^-$ was performed by reacting *fac*–$[Ru^{II}(CO)_3Cl_2THF]$ with four equivalence of NaCN in a methanolic solution. Infrared analysis was performed to confirm the purity of the desired product. The peaks at 2006 and 2050 $cm^{-1}$ have been assigned to the carbon monoxide ligand, while the 2083 and 2123 $cm^{-1}$ peaks was assigned to the cyanide ligand (**Figure IV–11**). Attempts to synthesize the *cis* isomer using the $[Ru^{II}(CN)_5(CO)]^{3-}$ intermediate have proven unsuccessful. All attempts, using various solvents (i.e. 1–propanol, propionitrile) resulted in the

formation of the *trans* isomer. The infrared spectrum shows the CO in the *cis* orientation, due to the split in the stretching frequencies. The desired product was isolates as the $[PPN]^+$ salt. Jiang *et al*. had, also, synthesized and characterized the iron analog of *cis*–$[Ru^{II}(CN)_4(CO)_2]^{2-}$. The infrared spectra of the two complexes are summarized in **Table IV–3**. The carbonyl and cyanide stretching frequencies are blue shifted for the ruthenium complex according to the explanations previously stated. The complex, *cis*–$[PPN]_2[Ru^{II}(CN)_4(CO)_2]$, was stable under air, under light and in solution.

**Table IV–3. Infrared Spectra Comparison of *cis*–$[M^{II}(CN)_4(CO)_2]^{2-}$ in MeOH.**

| M | Cation | $\nu_{CO}$ ($cm^{-1}$) | $\nu_{CN}$ ($cm^{-1}$) |
|---|---|---|---|
| Fe | $[Na]^+$ | 1967, 2022 | 2080, 2106, 2115(sh) |
| Ru | $[PPN]^+$ | 2006, 2050 | 2083, 2123 |

The comparison of the *cis*– and *trans*–$[Ru^{II}(CN)_4(CO)_2]^{2-}$ infrared spectra show a shift in the carbonyl and cyanide stretching frequencies (**Table IV–4**). The *trans*–$[Ru^{II}(CN)_4(CO)_2]^{2-}$ has a $D_{4h}$ molecular symmetry, while the *cis*–$[Ru^{II}(CN)_4(CO)_2]^{2-}$ has a $C_{2v}$ molecular symmetry. The $CN^-$ and CO in the *trans* complex are related by symmetry, while the *cis* complex only one set of $CN^-$ are related by symmetry. Due to the different orientations of the carbonyl and cyanide ligands, IR peaks will shift due to the *trans* effect. Since the CO ligands are bound to the transition metal through π–backbonding and the $CN^-$ ligands are bound through σ donation, the IR peaks will shift depending on which ligands are *trans* to each other because those ligands will be competing for the same *d* orbital.

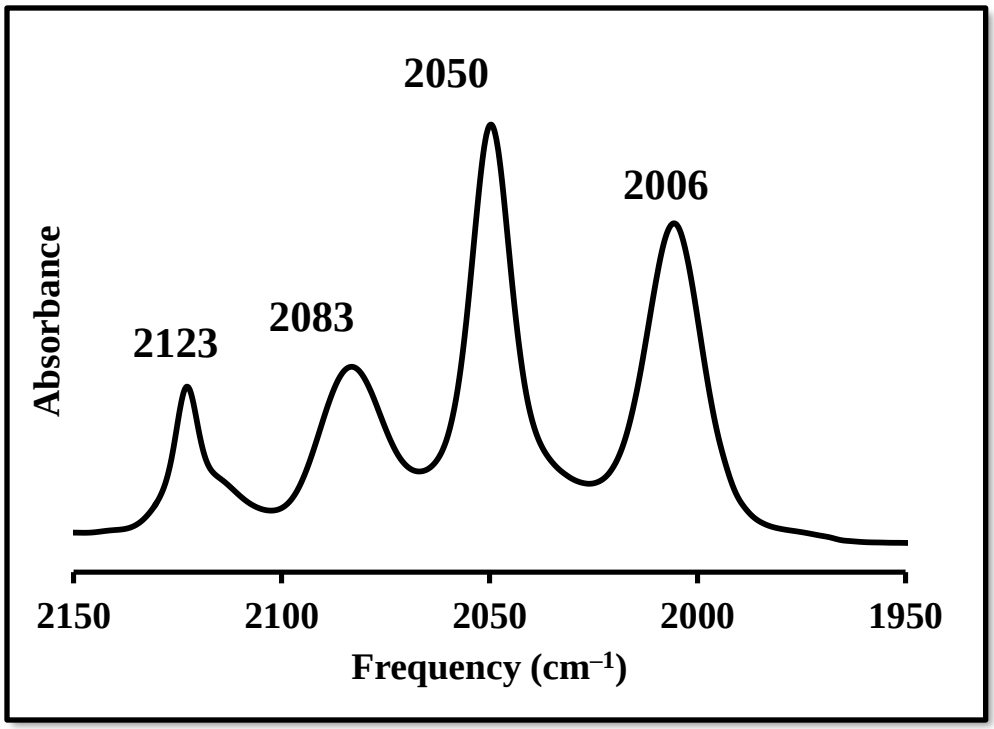


**Figure IV–11. Infrared Spectrum of *cis*–$[PPN]_2[Ru^{II}(CN)_4(CO)_2]$ in MeOH.**

The *fac*–$[Ru^{II}(CN)_3(CO)_3]^-$ isomer was synthesized using *fac*–$[Ru^{II}(CO)_3Cl_2THF]$. Synthesis of this complex was performed by Contakes *et al*. using a similar procedure.[24] Attempts were made to synthesize *fac*–$[Ru^{II}(CN)_3(CO)_3]^-$ using the $[Ru^{II}(CN)_5(CO)]^{3-}$ intermediate and *trans*–$[Ru^{II}(CN)_4(CO)_2]^{2-}$, but were not successful. Synthesis of *fac*–$[Ru^{II}(CN)_3(CO)_3]^-$ was performed by reacting *fac*–$Ru^{II}(CO)_3Cl_2THF$ with three equivalence of NaCN in a methanolic solution. Infrared analysis was performed to confirm the purity of the desired product and agree with the literature. The peaks at 2077 and 2118 $cm^{-1}$ were assigned to the carbon monoxide ligand, while the 2145 and 2164 $cm^{-1}$ peaks were assigned to the cyanide ligand. The peaks are split due the facial geometry that is found in the complex. A variety of countercations were used (e.g $[PPh_4]^+$, $[AsPh_4]^+$, $[PPN]^+$) to isolate the desired product, which all countercations gave similar yields. The carbon monoxide and cyanide stretching frequencies found using infrared spectroscopy shift according to explanations that were previously stated. This is summarized in **Table IV–5**. Jiang *et al*. had synthesized and characterized the iron analog of *fac*–$[Ru^{II}(CN)_3(CO)_3]^-$. **Table IV–5** summarizes the comparison of the two complexes.

| Table IV–4. Infrared Spectra Comparison of $[Ru^{II}(CN)_{6-x}(CO)_x]^{(x-4)}$. | | | | | |
|---|---|---|---|---|---|
| **ν ($cm^{-1}$)** | **x = 0** | **x = 1** | **x = 2 (trans)** | **x = 2 (cis)** | **x = 3** |
| CO | N/A | 1983 | 2007 | 2006, 2050 | 2077, 2118 |
| $CN^-$ | 2043 | 2086, 2109(sh) | 2107 | 2083, 2123 | 2145, 2164 |

| Table IV–5. Infrared Spectra Comparison of $[M^{II}(CN)_3(CO)_3]^-$ in MeOH. | | | |
|---|---|---|---|
| **M** | **Cation** | **$\nu_{CO}$ ($cm^{-1}$)** | **$\nu_{CN}$ ($cm^{-1}$)** |
| Fe | $[Na]^+$ | 2080, 2118 | 2146, 2160 |
| Ru | $[AsPh_4]^+$ | 2077, 2118 | 2145, 2164 |

The second complex that was generated was *trans*–$[Ru^{II}(CN)_4(CO)(py)]^{2-}$ by reacting $[Ru^{II}(CN)_5(CO)]^{3-}$ in a pyridine solution. Infrared analysis was performed to confirm the purity of the desired product (**Figure IV–12**). The desired product was purified using the same procedure described for the $[Ru^{II}(CN)_5(CO)]^{3-}$ complex. The organic layer was placed in a Schlenk flask to which the solvent was removed *in vacuo*. The resulting dark tan oil was gently heated which resulted in a dark tan powder. The desired dark tan product was stored under anaerobic conditions. The complex, *trans*–$[PPN]_2[Ru^{II}(CN)_4(CO)(py)]$, was stable under air, under light and in solution.

Chiarella *et al.* had synthesized and characterized the iron analog of *trans*–$[Ru^{II}(CN)_4(CO)(py)]^{2-}$.[17] **Table IV–6** summarizes the comparison of the two complexes. The CO and $CN^-$ stretching frequencies are shifted to lower wavenumbers ($cm^{-1}$) for the iron complex due to the reasons that have been previously stated.

| Table IV–6. Infrared Spectra Comparison of *trans*–$[M^{II}(CN)_4(CO)(py)]^-$ in pyridine. | | | |
|---|---|---|---|
| **M** | **Cation** | **$\nu_{CO}$ ($cm^{-1}$)** | **$\nu_{CN}$ ($cm^{-1}$)** |
| Fe | $[Bu_4N]^+$ | 1947 | 2081 |
| Ru | $[PPN]^+$ | 1950 | 2089 |

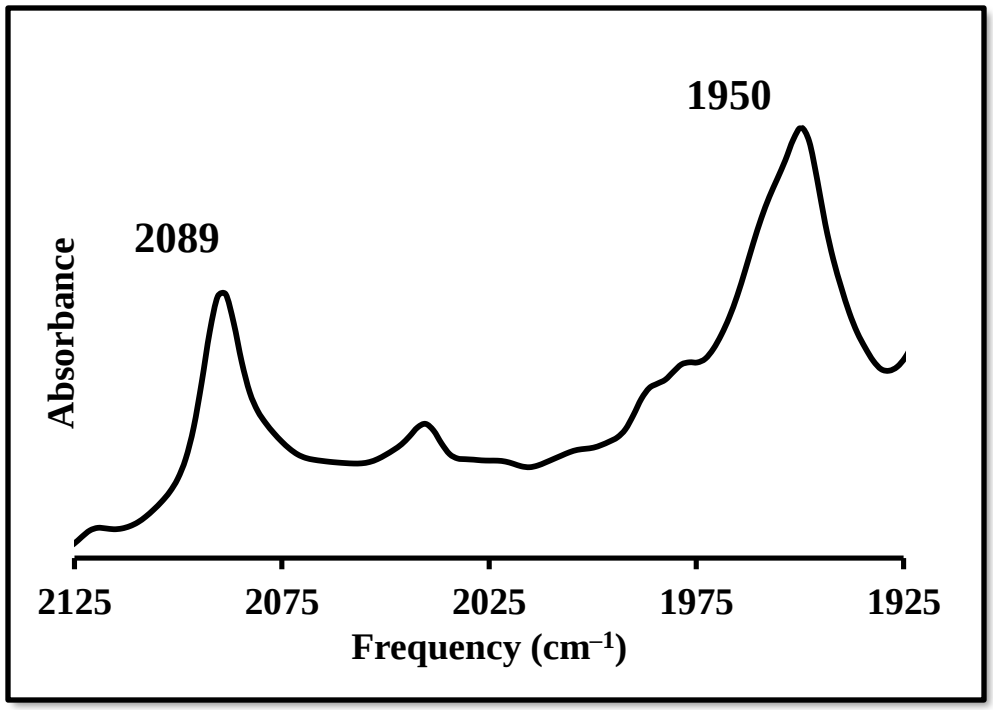


**Figure IV–12. Infrared Spectrum of *trans*–$[PPN]_2[Ru^{II}(CN)_4(CO)(py)]$ in pyridine.**

The third complex that was generated was *trans*–$[Ru^{II}(CN)_4(CO)(CN–dmph)]^{2–}$ by reacting $[Ru^{II}(CN)_5(CO)]^{3–}$ in a methanolic solution with a five molar excess of the isocyanide. Infrared analysis was performed to confirm the purity of the desired product (**Figure IV–13**). The peak at 1986 $cm^{–1}$ has been assigned to the carbon monoxide ligand, while the 2096 and 2121 $cm^{–1}$ peaks was assigned to the cyanide ligand and isocyanide ligand respectively. The desired product was purified using the same procedure described for the $[Ru^{II}(CN)_5(CO)]^{3–}$ complex. The organic layer was placed in a Schlenk flask to which the solvent was removed *in vacuo*. The resulting in dark yellow oil was gently heated which resulted in dark yellow powder. The desired dark yellow product was stored under anaerobic conditions. The complex, *trans*–$[PPN]_2[Ru^{II}(CN)_4(CO)(CN–dmph)]$, was stable under air, under light and in solution.

The comparison between *trans*–$[PPN]_2[Ru^{II}(CN)_4(CO)(CN–dmph)]$ and $[PPN]_3[Ru^{II}(CN)_5(CO)]$ is summarized in **Table IV–7**. Upon comparing the CO and $CN^–$ stretching frequencies, it was observed that there is a slight shift from the $CN^–$ to CN–dmph. This is due to the electron–withdrawing effect of the phenyl ring on the isocyanide. The isocyanide, being electron–withdrawing, removes electron density from the transition metal which decreases

the π–backbonding effect of the CO. This result will strengthen the C≡O bonds, which will blue shift the stretching frequency of the carbonyl.

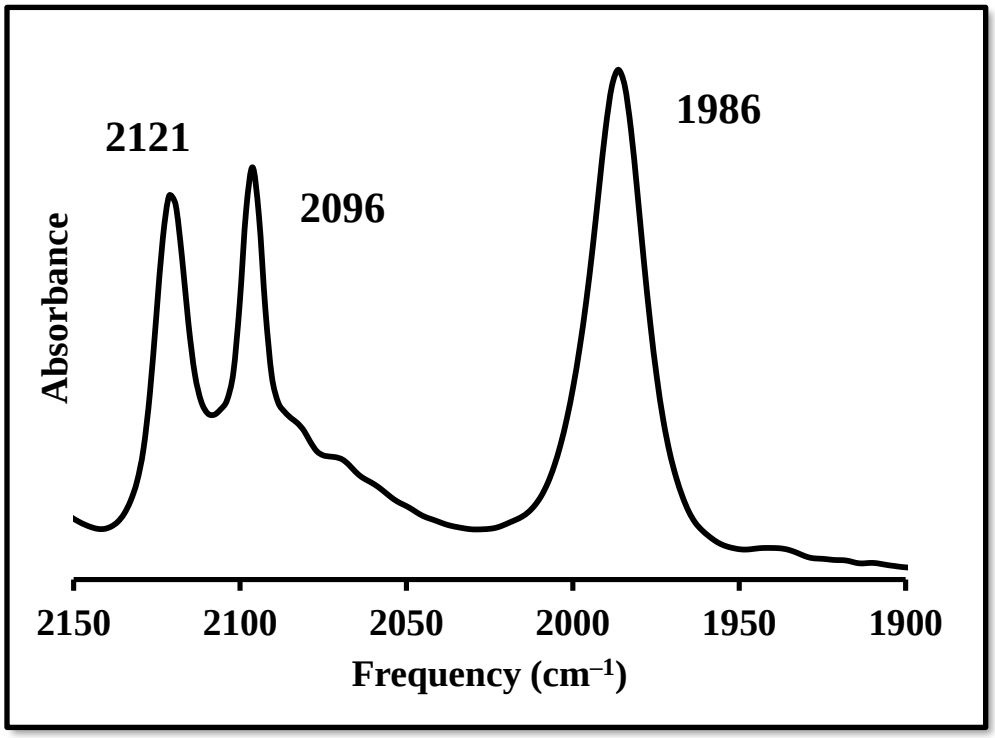


**Figure IV–13. Infrared Spectrum of *trans*–[PPN]$_2$[Ru$^{II}$(CN)$_4$(CO)(CN–dmph)] in $CH_3CN$.**

| **Table IV–7. Infrared Spectra Comparison of [Ru$^{II}$(CN)$_{5-x}$(CO)(L)$_x$]$^{(x-3)}$ in MeOH.** | | | |
|---|---|---|---|
| **x** | **L** | **$\nu_{CO}$ (cm$^{-1}$)** | **$\nu_{CN}$ (cm$^{-1}$)** |
| 0 | CN | 1983 | 2086, 2109(sh) |
| 1 | CN–dmph | 1986 | 2096 |

The [PPN]$_4$[Os$^{II}$(CN)$_6$] was prepared in moderate yield, 50 – 60%, by reacting an aqueous solution of [Et$_4$N]$_2$[Os$^{IV}$Cl$_6$] with ten molar equivalence of [Et$_4$N]CN for seventy–two hours. Infrared analysis was performed to confirm the purity of the desired product (**Figure IV–14**). Allowing the reaction to reflux for forty–eight hours produced [PPN]$_3$[Os$^{III}$(CN)$_6$]. This oxidation was, also, achieved by dissolving [PPN]$_4$[Os$^{II}$(CN)$_6$] in methylene chloride and allowed to stir under air. **Figure IV–15** shows the infrared spectrum of the oxidized product. A warm aqueous solution of [PPN]Cl was added to the reaction mixture. It is very important to maintain the aqueous solution moderately hot to avoid the formation of an oily suspension. The

precipitate was filtered using a closed frit, which, upon drying, resulted in a green solid being observed. The product was shown to be soluble in a wide range of solvents: acetonitrile, acetone, DMSO, alcohols, methylene chloride, but insoluble in diethyl ether and aromatic hydrocarbons. This compound was unstable and oxidizes slowly to a yellow–green solid, when exposed to the air. As a result, this compound was stored in the Dry–box.

Synthesis of $[PPN]_3[Os^{II}(CN)_5(CO)]$ was attempted by reacting $[PPN]_4[Os^{II}(CN)_6]$ under a CO atmosphere in a 1–propanol solution. Infrared analysis was performed to confirm the purity of the desired product (**Figure IV–16**). Purification was performed under the same conditions as the $[PPN]_3[Ru^{II}(CN)_5(CO)]$. The resulting light green oil was gently heated which resulted in a light green powder. $[PPN]_3[Os^{II}(CN)_5(CO)]$ was stable under air, under light and in solution. The characterization of this compound as $[PPN]_3[Os^{II}(CN)_5(CO)]$ was not confirmed due to the lack of additional spectroscopic and crystallographic characterization.

The infrared comparison of the $[M^{II}(CN)_5(CO)]^{3-}$ (where M = Fe, Ru and Os) are summarized in **Table IV–8**. The carbon monoxide and cyanide stretching frequencies are increasing by moving from iron to osmium. This trend is due to the decrease of the σ donation that was explained before.

**Table IV–8. Infrared Spectra Comparison of $[M^{II}(CN)_5(CO)]^{3-}$.**

| M | Cation | Solvent | $\nu_{CO}$ ($cm^{-1}$) | $\nu_{CN}$ ($cm^{-1}$) |
|---|---|---|---|---|
| Fe | $[PPN]^+$ | MeOH | 1986 | 2076, 2096 |
| Ru | $[PPN]^+$ | MeOH | 1983 | 2086, 2109(sh) |
| Os | $[PPN]^+$ | *n*–PrOH | 2006 | 2089, 2106 |

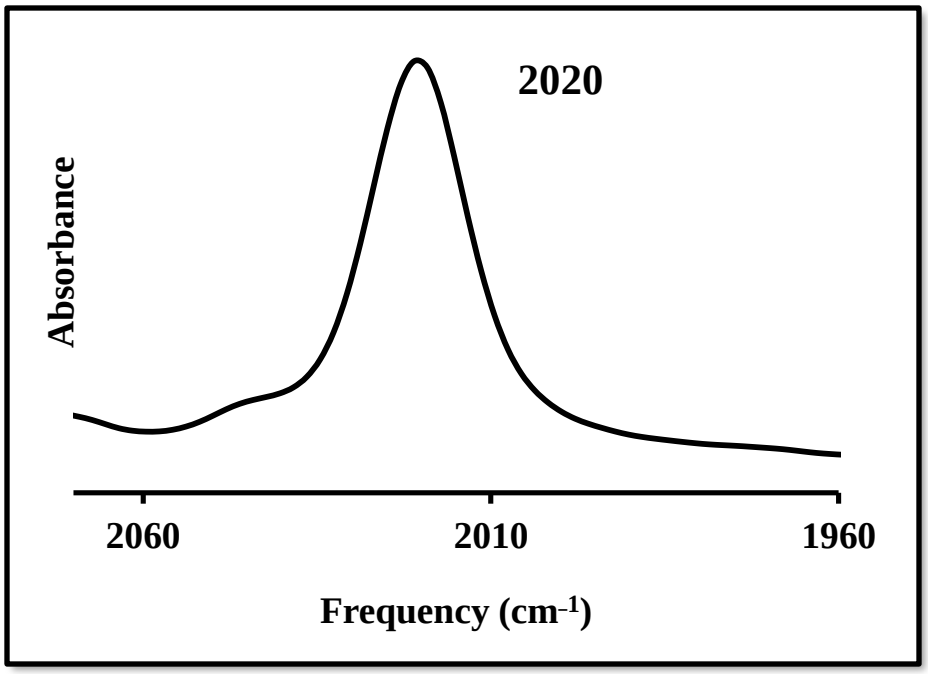


**Figure IV–14. Infrared Spectrum of $[PPN]_4[Os^{II}(CN)_6]$ in $CH_3CN$.**

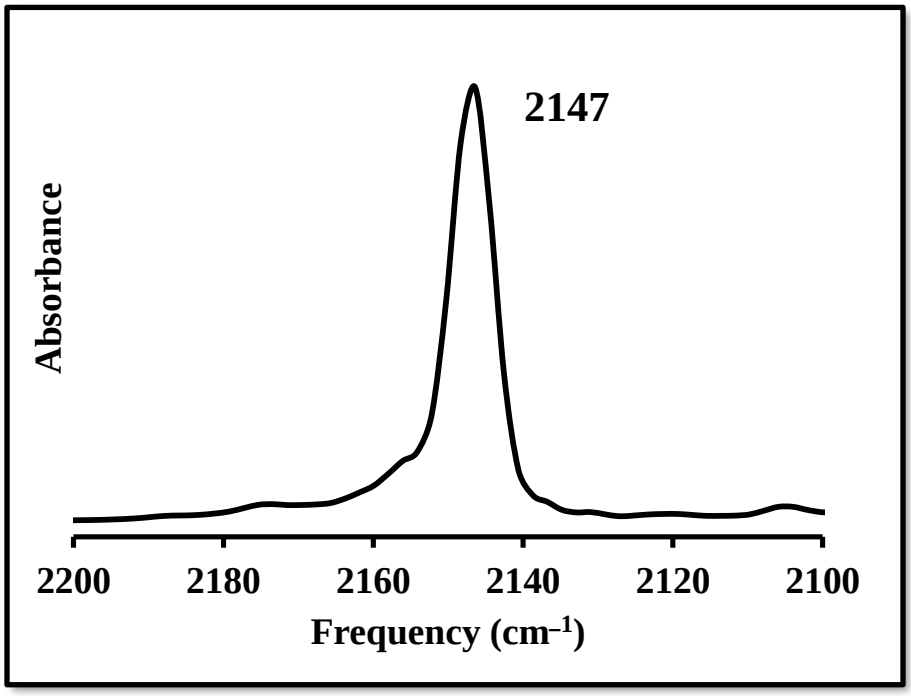


**Figure IV–15. Infrared Spectrum of $[PPN]_3[Os^{III}(CN)_6]$ in $H_2O$.**

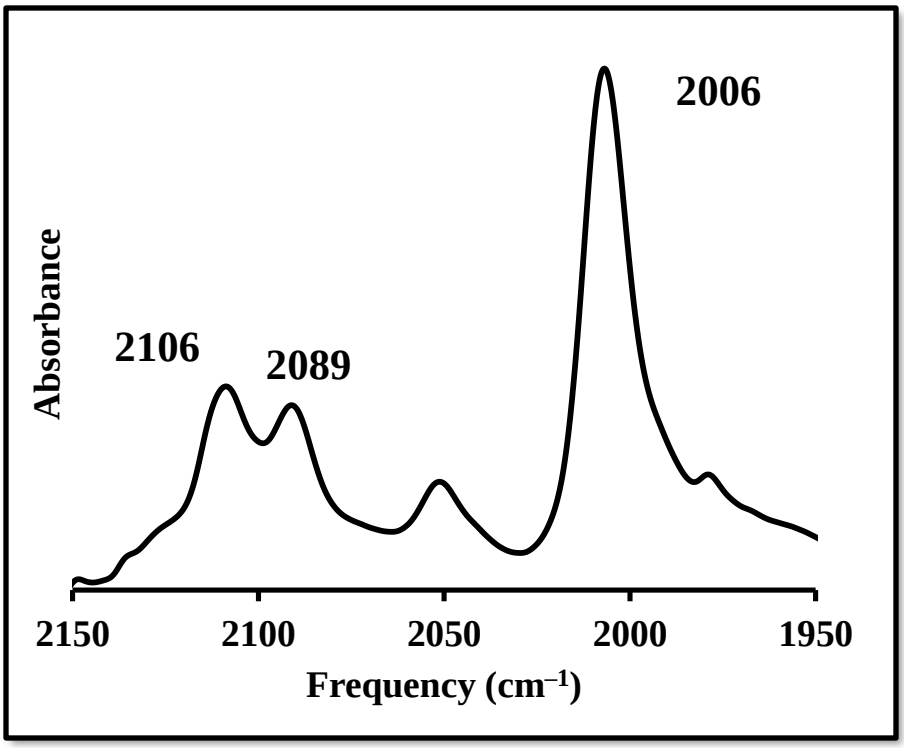


**Figure IV–16. Infrared Spectrum of $[PPN]_3[Os^{II}(CN)_5(CO)]$ in *n*–PrOH.**

Using the infrared spectra collected from the $[PPN]_4[Fe^{II}(CN)_6]$[18], $[PPN]_4[Ru^{II}(CN)_6]$ and $[PPN]_4[Os^{II}(CN)_6]$, there is noticeable trend of the $CN^-$ stretching frequencies. The trend shows that moving down the periodic table, within a family, the $CN^-$ stretching frequencies decrease. This trend is due to the delocalization of the charge from the transition metal to the $CN^-$. This tends to weaken the $CN^-$ bond which results in a red shift.[25] The cyanide stretching frequency for iron and ruthenium are comparable.This trend is illustrated in **Figure IV–17** and summarized in **Table IV–9**.

**Table IV–9. Infrared Spectra Comparison of $[M^{II}(CN)_6]^{4-}$.**

| M | Cation | Solvent | $\nu_{CN}$ ($cm^{-1}$) |
|---|---|---|---|
| Fe | $[PPN]^+$ | $CH_3CN$ | 2041 |
| Ru | $[PPN]^+$ | $CH_3CN$ | 2043 |
| Os | $[PPN]^+$ | $CH_3CN$ | 2020 |

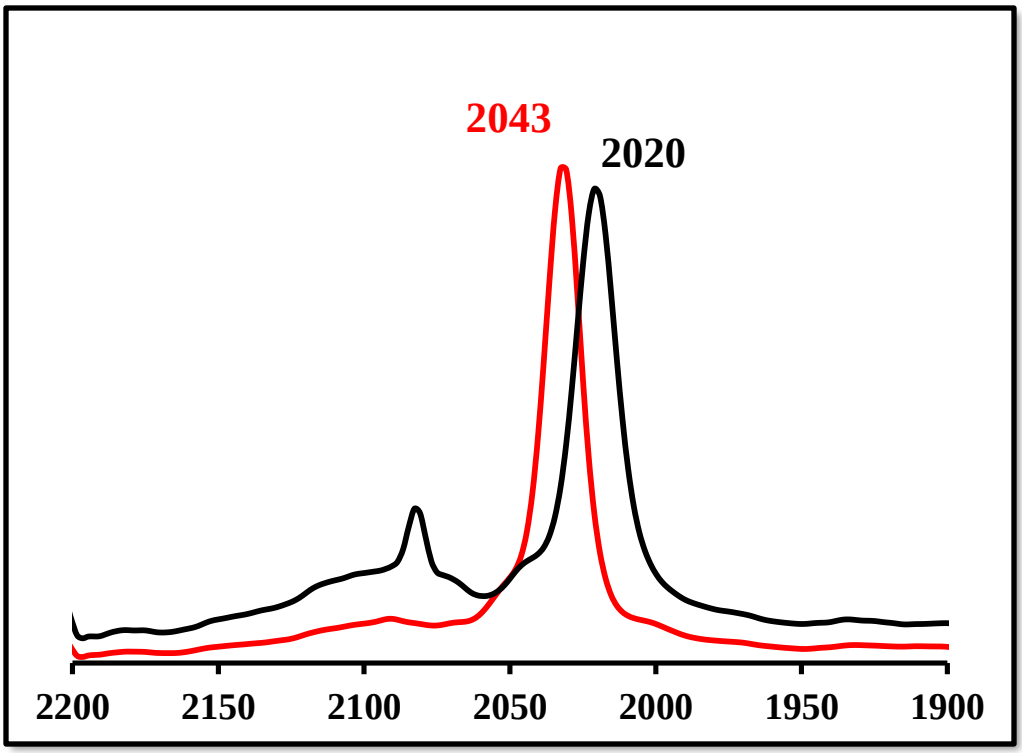


**Figure IV–17. Infrared Spectrum of $[PPN]_4[M^{II}(CN)_6]$ in $CH_3CN$ (where M = Ru (red); and Os (black)).**

### 4.3.2 NMR Studies of the Ruthenium and Osmium Complexes

Proton and carbon ($^1H$ and $^{13}C$) studies were performed on $[PPN]_4[Ru^{II}(CN)_6]$, $[PPN]_3[Ru^{II}(CN)_5(CO)]$, *trans*–$[PPN]_2[Ru^{II}(CN)_4(CO)_2]$, *fac*–$[AsPh_4][Ru^{II}(CN)_3(CO)_3]$, *trans*–$[PPN]_2[Ru^{II}(CN)_4(CO)(py)]$ and $[PPN]_4[Os^{II}(CN)_6]$. All spectra were performed in $CD_3OD$ with the exception of $[AsPh_4][Ru^{II}(CN)_3(CO)_3]$, which was done in $CDCl_3$ due to the resolution of the carbonyl and cyanide peaks. Since the $[PPN]^+$ cation is present in all compounds, except one, and the cation is not coordinated to the transition metal, the peaks in the $^1H$–NMR and $^{13}C$–NMR will not shift by any significant amount. In light of this observation, the $[PPN]^+$ cation peaks have been represented by **Figure IV–18** ($^1H$–NMR) and **Figure IV–19** ($^{13}C$–NMR). The $[AsPh_4]^+$ peaks are represented, in the same fashion as the $[PPN]^+$, by **Figure IV–20** ($^1H$–NMR) and **Figure IV–21** ($^{13}C$–NMR).

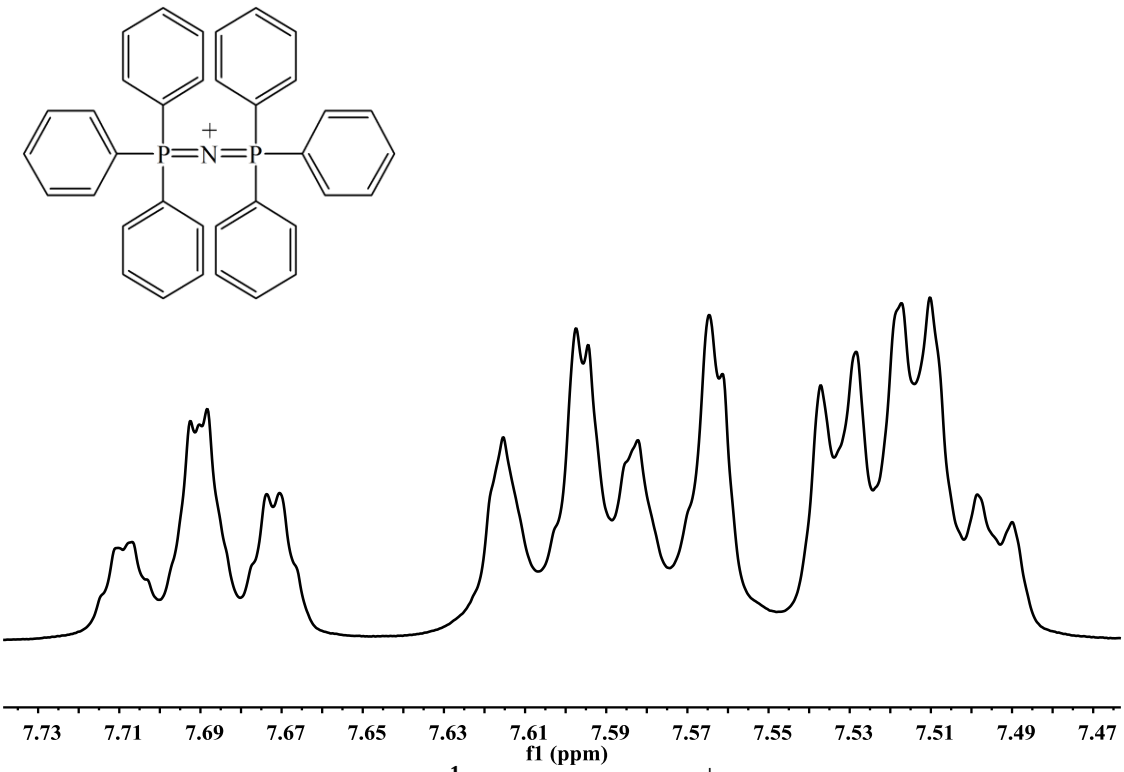


**Figure IV–18. $^{1}$H–NMR of $[PPN]^{+}$ in $CD_3OD$.**

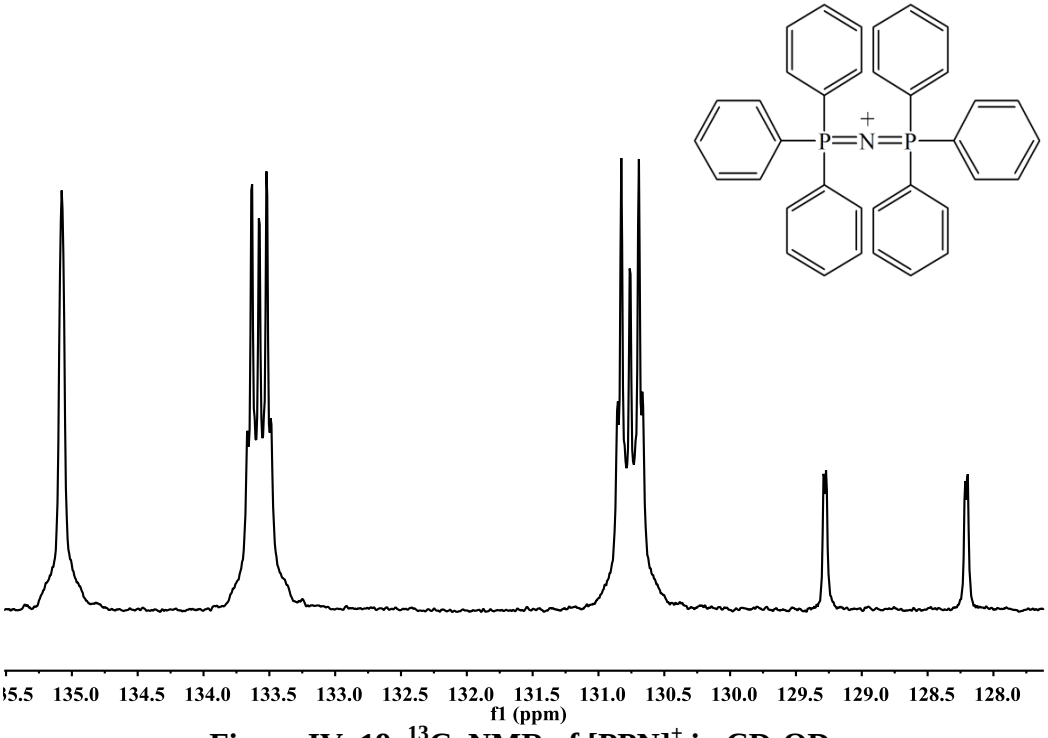


**Figure IV–19. $^{13}$C–NMR of $[PPN]^{+}$ in $CD_3OD$.**

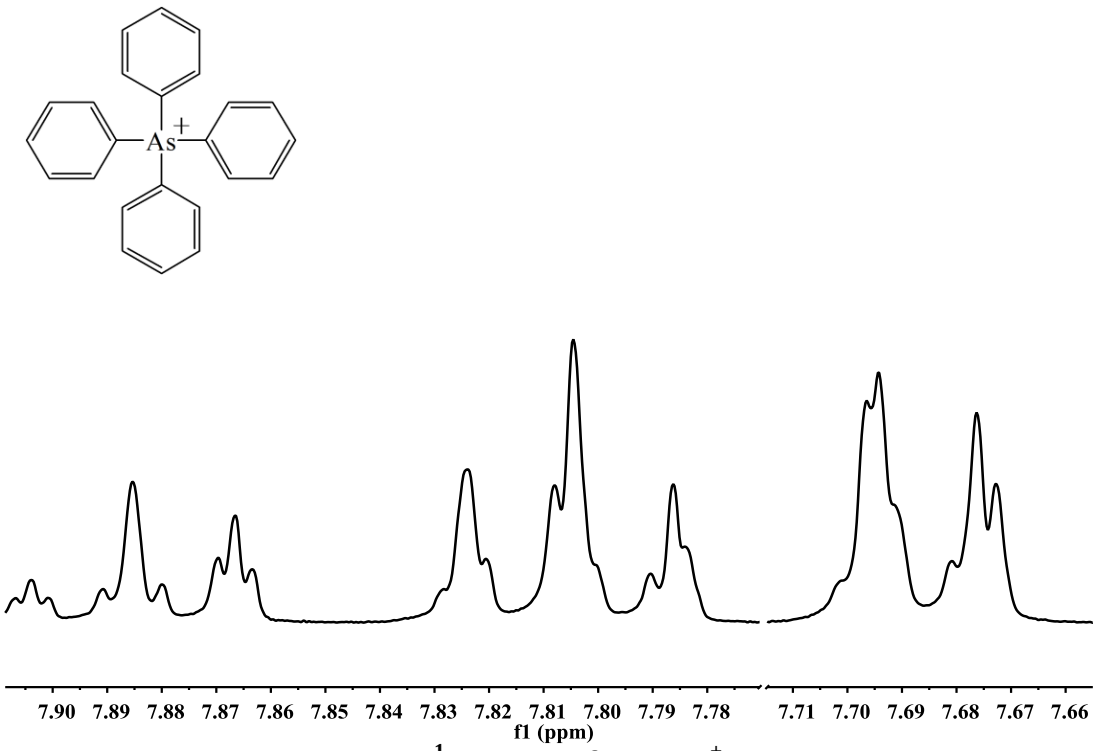


**Figure IV–20. $^{1}H$–NMR of $[AsPh_4]^+$ in $CDCl_3$.**

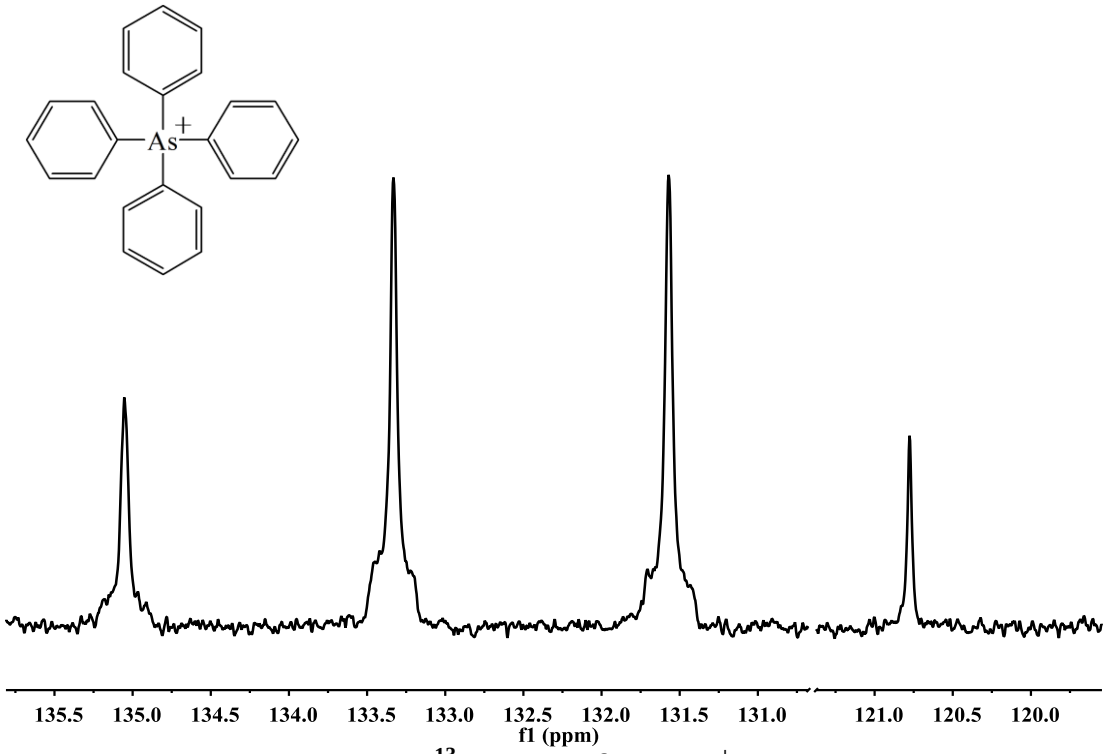


**Figure IV–21. $^{13}C$–NMR of $[AsPh_4]^+$ in $CDCl_3$.**

The $^{13}C$–NMR of the $[M^{II}(CN)_6]^{4-}$ (where M = $Fe^6$, Ru [**Figure IV–22**] and Os [**Figure IV–23**]) show that the $CN^-$ shifts upfield when moving from iron to ruthenium to osmium. This shift, summarized in **Table IV–10**, is due to the increasing electron density from the transition metal. The increasing electron density acts as a shield around the nuclei that is being scanned. The greater the shielding effect on the nuclei, the lower the peak would be observed in the NMR (greater shielding leads to the peaks moving upfield).

| **Table IV–10. $^{13}C$–NMR Comparison of $[M^{II}(CN)_6]^{4-}$.** | | | |
|---|---|---|---|
| **M** | **Cation** | **Solvent** | **$CN^-$ δ (ppm)** |
| $Fe^6$ | $[Et_4N]^+$ | $CD_3CD$ | 177.20 |
| Ru | $[PPN]^+$ | $CD_3CD$ | 165.15 |
| Os | $[PPN]^+$ | $CD_3CD$ | 145.58 |

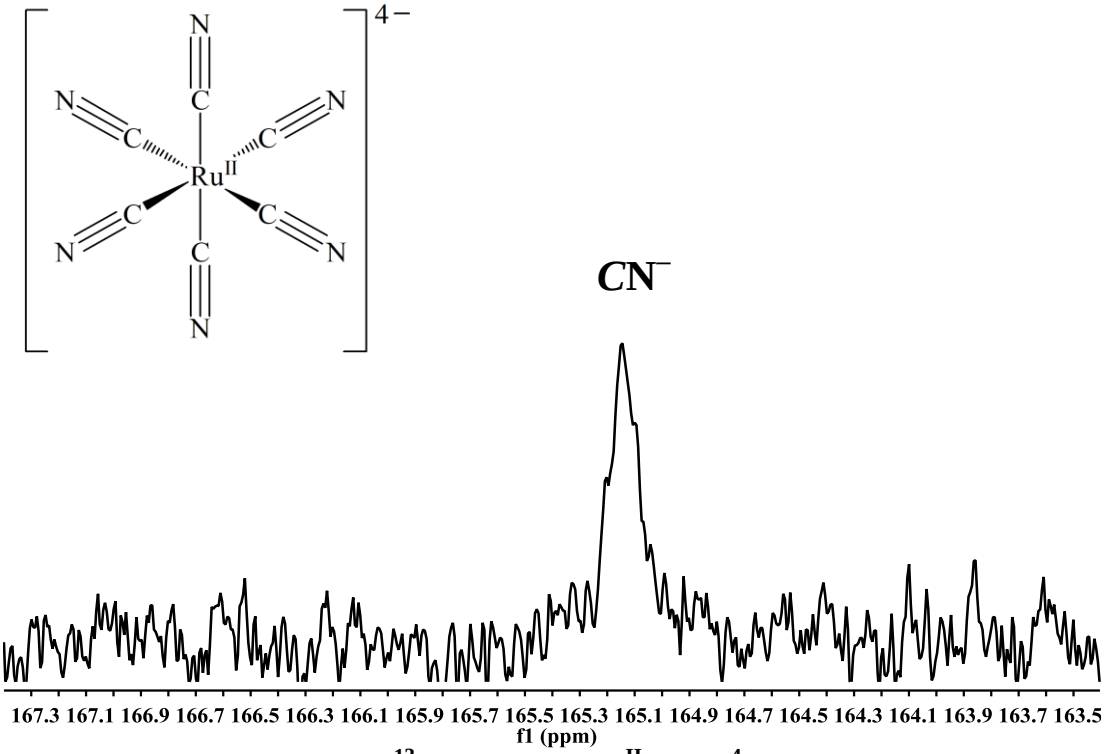


**Figure IV–22. $^{13}C$–NMR of $[Ru^{II}(CN)_6]^{4-}$ in $CD_3OD$.**

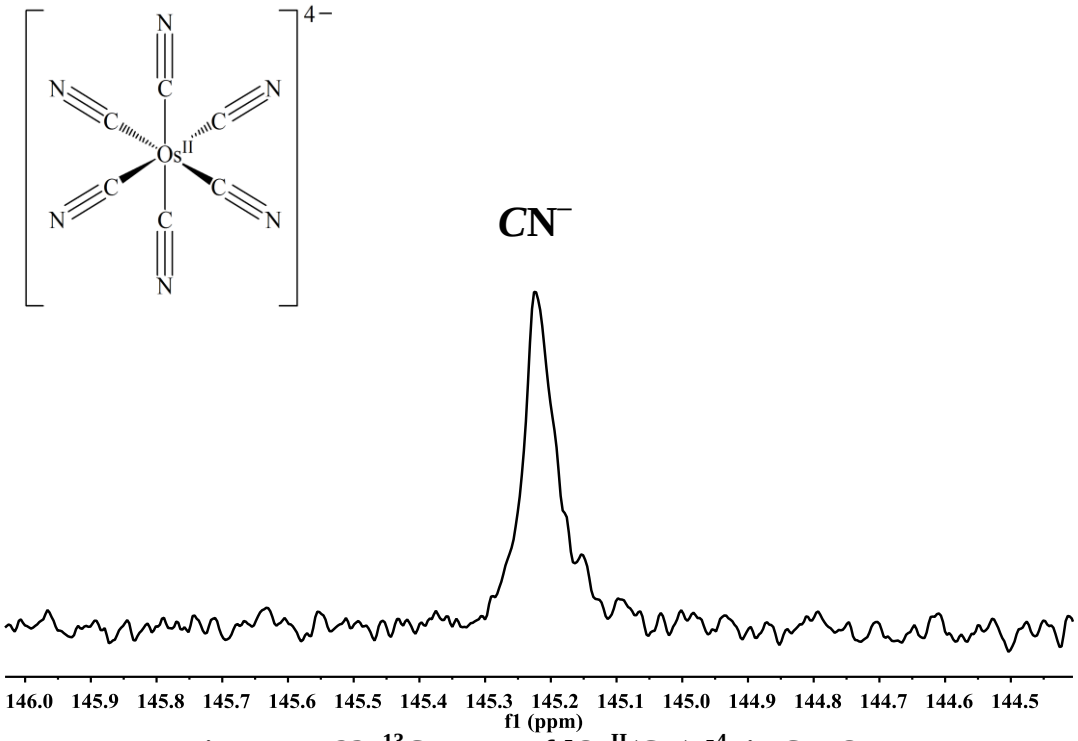


**Figure IV–23. $^{13}C$–NMR of $[Os^{II}(CN)_6]^{4-}$ in $CD_3OD$.**

The $^{13}C$–NMR spectra for $[PPN]_4[Ru^{II}(CN)_6]$ (**Figure IV–22**), $[PPN]_3[Ru^{II}(CN)_5(CO)]$ (**Figure IV–24**), *trans*–$[PPN]_2[Ru^{II}(CN)_4(CO)_2]$ (**Figure IV–25**) and *fac*–$[AsPh_4][Ru^{II}(CN)_3(CO)_3]$ (**Figure IV–26**) show an interesting feature. The observation shows, as the cyanide are substituted by carbon monoxide, the $^{13}C$ signals move upfield. The $^{13}C$ signals for these compounds are summarized in **Table IV–11**. Various explanations have been reported to explain this surprising behavior. It has been suggested that increasing π–donation from the metal to the CO groups would increase the positive charge on the carbon. This increase in positive charge on the carbon leads to a contraction of the carbon 2*p* orbitals and to an expansion of the oxygen 2*p* orbitals.[26] Due to this contraction, the carbon becomes more shielded which results in the $^{13}C$ signals to move upfield. The cyanide $^{13}C$ signals are split for $[PPN]_3[Ru^{II}(CN)_5(CO)]$ due to the fact that one of the cyanide is *trans* to the carbonyl ligand. This results in a different chemical environment than the other cyanide.

| Table IV–11. $^{13}$C–NMR Comparison of $[Ru^{II}(CN)_{6-x}(CO)_x]^{(x-4)}$. | | | |
|---|---|---|---|
| **x** | **Solvent** | **CO δ (ppm)** | **$CN^-$ δ (ppm)** |
| 0 | $CD_3CD$ | N/A | 165.15 |
| 1 | $CD_3CD$ | 200.55 | 151.17 (*cis*), 150.65 (*trans*) |
| 2 | $CD_3CD$ | 193.87 | 134.85 |
| 3 | $CDCl_3$ | 186.14 | 123.16 |

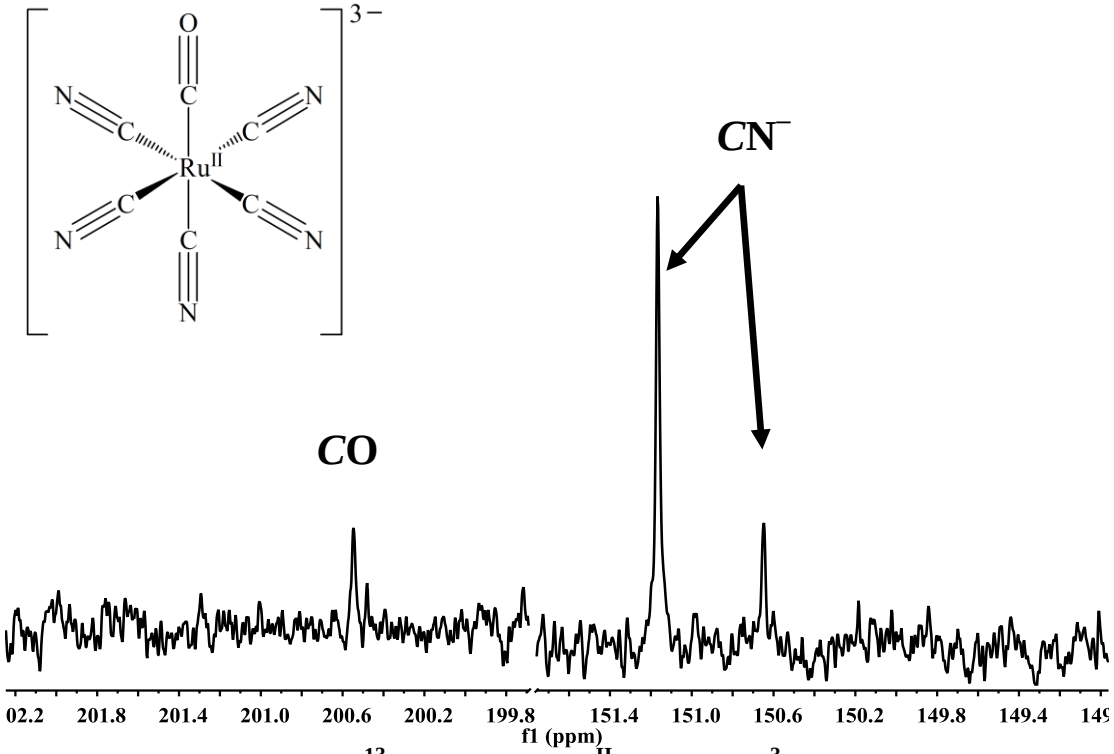


**Figure IV–24. $^{13}$C–NMR of $[Ru^{II}(CN)_5(CO)]^{3-}$ in $CD_3OD$.**

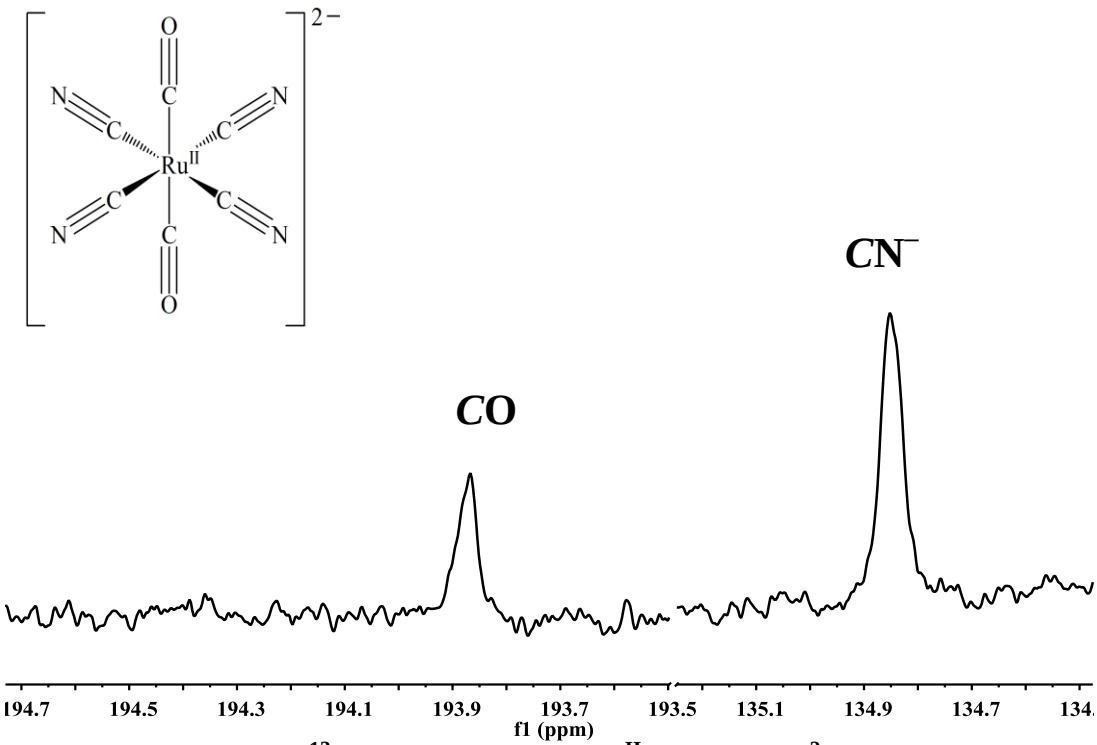


**Figure IV–25. $^{13}$C–NMR of *trans*–$[Ru^{II}(CN)_4(CO)_2]^{2-}$ in $CD_3OD$.**

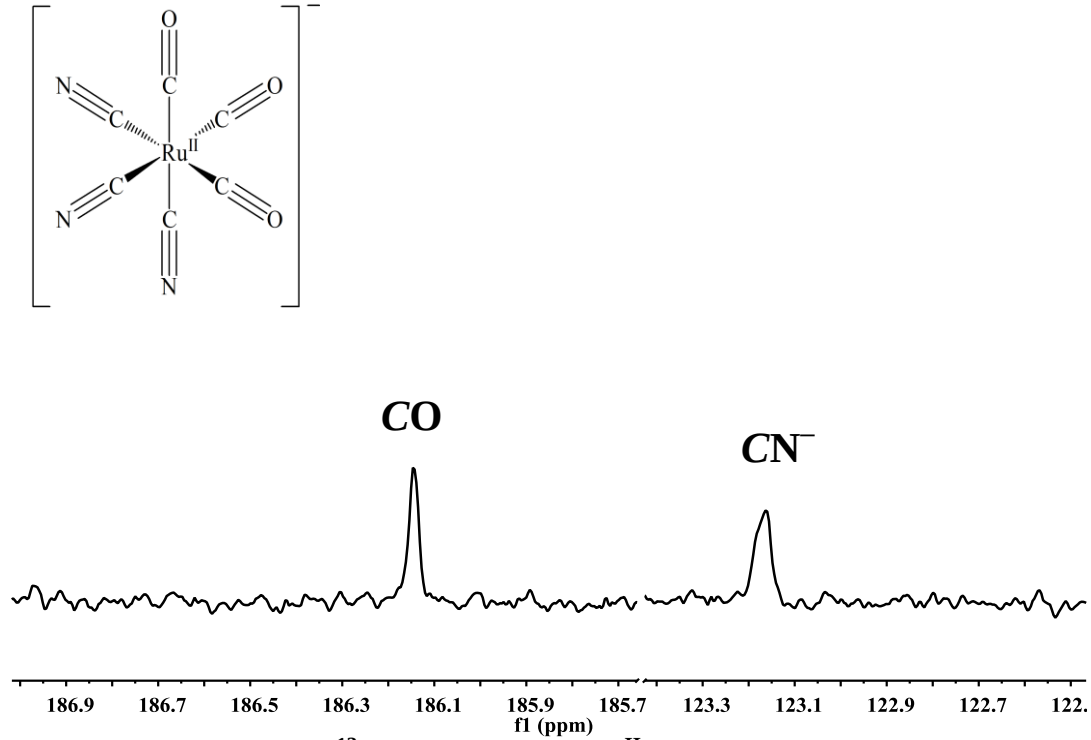


**Figure IV–26. $^{13}$C–NMR of *fac*–$[Ru^{II}(CN)_3(CO)_3]^-$ in $CDCl_3$.**

In 2006, Chiarella *et al.* synthesized the iron analog of *trans*–$[Ru^{II}(CN)_4(CO)(py)]^{2-}$.[17] The $^1$H–NMR (**Figure IV–27**) and $^{13}$C–NMR (**Figure IV–28**) signals does not show any significant shifts on the pyridine hydrogens and carbons when comparing the two complexes. The one exception is that the *ortho* hydrogens and carbons on the pyridine have a slight shift. The peaks move upfield upon comparing ruthenium to iron due to the proximity those nuclei have to the transition metal. The $CN^-$ and CO $^{13}$C signals do show a significant change since they are directly bonded to the metal. This NMR comparison has been summarized in **Table IV–12**. The $CN^-$ and CO $^{13}$C signals for the ruthenium complex are positioned upfield compared to the iron complex. This is due to the extra electron density that belongs to the ruthenium. This extra electron density shields the carbon of the $CN^-$ and CO.

**Table IV–12. NMR Comparison of $[M^{II}(CN)_4(CO)(py)]^{2-}$ in $CD_3OD$.**

| **$^1$H–NMR** | | | |
|---|---|---|---|
| **Fe[17]** | | **Ru** | |
| **δ (ppm)** | **Assignment** | **δ (ppm)** | **Assignment** |
| 9.26 | Bound pyridine $H_{ortho}$ | 9.12–9.09 | Bound pyridine $H_{ortho}$ |
| 7.78 | Bound pyridine $H_{para}$ | 7.81–7.75 | Bound pyridine $H_{para}$ |
| 7.30 | Bound pyridine $H_{meta}$ | 7.34–7.29 | Bound pyridine $H_{meta}$ |
| **$^{13}$C–NMR** | | | |
| **Fe** | | **Ru** | |
| **δ (ppm)** | **Assignment** | **δ (ppm)** | **Assignment** |
| 220.42 | CO | 202.81 | CO |
| 162.12 | $CN^-$ | 156.86 | $CN^-$ |
| 157.67 | Bound pyridine $C_{ortho}$ | 152.43 | Bound pyridine $C_{ortho}$ |
| 137.70 | Bound pyridine $C_{para}$ | 138.33 | Bound pyridine $C_{para}$ |
| 124.67 | Bound pyridine $C_{meta}$ | 125.35 | Bound pyridine $C_{meta}$ |

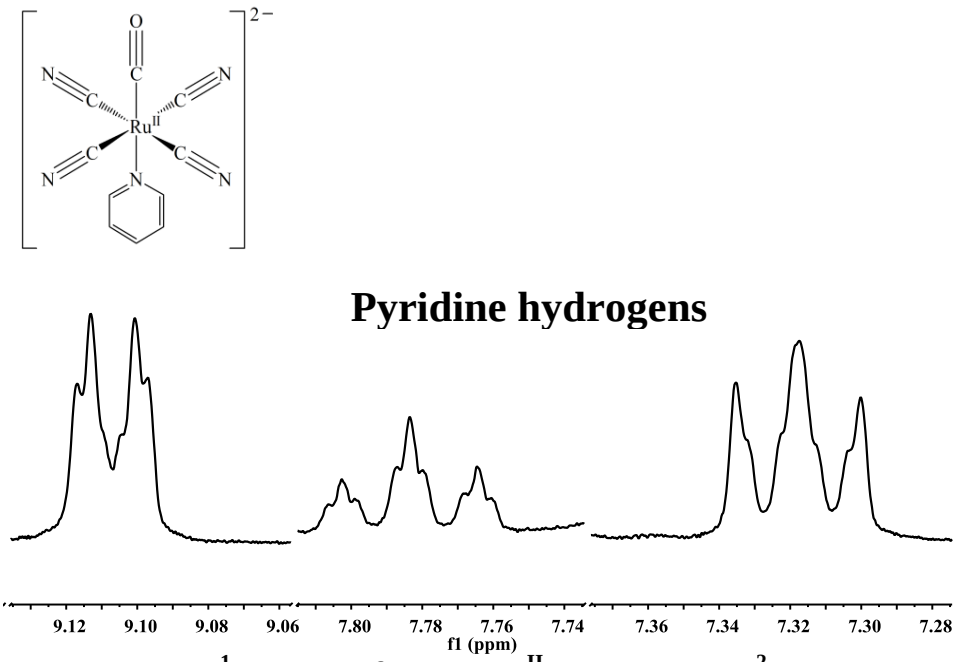


**Figure IV–27. $^{1}$H–NMR of *trans*–$[Ru^{II}(CN)_4(CO)(py)]^{2-}$ in $CD_3OD$.**

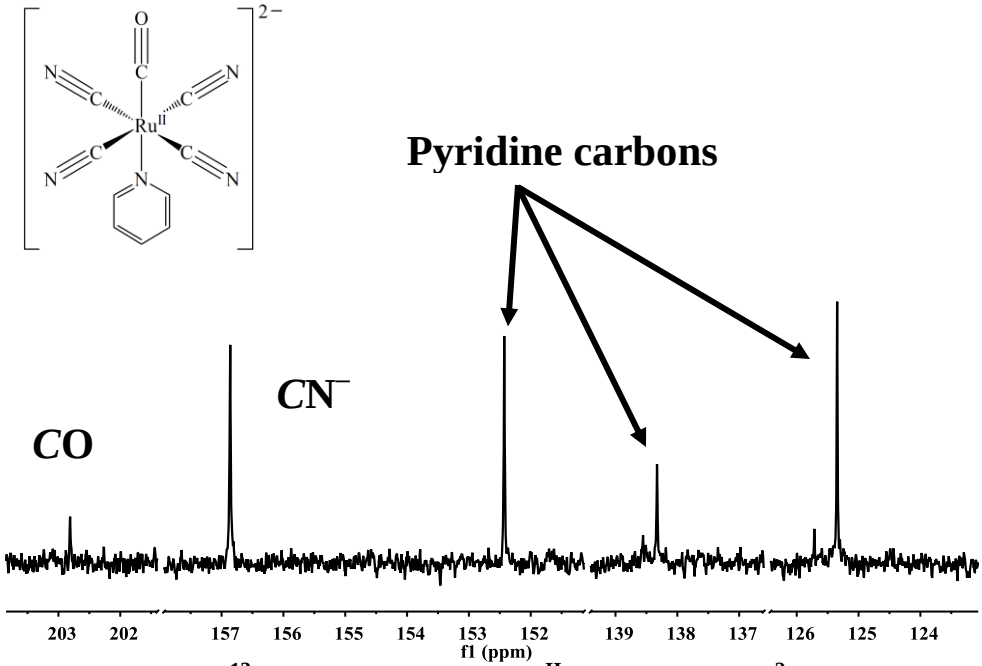


**Figure IV–28. $^{13}$C–NMR of *trans*–$[Ru^{II}(CN)_4(CO)(py)]^{2-}$ in $CD_3OD$.**

### 4.3.3 X–ray Structures of Transition Metal Carbonyl/Cyanide Complexes

The X–ray structure of $[PPN]_3[M^{III}(CN)_6]$ (where M = Fe[18], Ru and Os) confirmed an octahedral structure consisting of six cyanide ligands that are bound to the transition metal and

the $PPN^+$ cation. The average bond distances of the $CN^-$ to metal are 1.941(7) Å, 2.044(6) Å and 2.064(2) Å for Fe, Ru and Os respectively. The average bond distances for the $C{\equiv}N^-$ are 1.162(10) Å, 1.159(6) Å and 1.156(3) Å for Fe, Ru and Os respectively. The transition metal lies on a two–fold axis so that the $[M^{III}(CN)_6]^{3-}$ anion has an imposed $C_2$ symmetry. There are two crystallographically independent $PPN^+$ cations present in the unit cell. One cation occupies a general position whereas the nitrogen atom of the other lies on a two–fold axis. Since there is different multiplicity of the two types of cations, the cations exist in a 2:1 ratio. The general structure of the complex anion is shown in **Figure IV–29**. The crystal structure for all the $[M^{III}(CN)_6]^{3-}$ complexes were solved under an orthorhombic crystal system *Pbcn*. These compounds are classified as isomorphous and isostructural. Crystals of the ruthenium and osmium compounds were grown by vapor diffusion of methylene chloride and diethyl ether, and were grown within a week. Crystallization of the $[M^{II}(CN)_6]^{4-}$ were attempted using various solvents and techniques without success. All attempts have resulted in the oxidation product, $[M^{III}(CN)_6]^{3-}$. Selective bond distances and angles are summarized in **Table IV–13**.

**Table IV–13. Selective Crystallographic Data for $[PPN]_3[M^{III}(CN)_6]$.**

| **Fe**[18] | | **Ru** | | **Os** | |
|---|---|---|---|---|---|
| **Bond Distances (Å)** | | **Bond Distances (Å)** | | **Bond Distances (Å)** | |
| Fe(1)–C(1) | 1.952(8) | Ru(1)–C(1) | 2.030(6) | Os(1)–C(1) | 2.069(2) |
| Fe(1)–C(2) | 1.935(7) | Ru(1)–C(2) | 2.052(6) | Os(1)–C(2) | 2.061(2) |
| Fe(1)–C(3) | 1.935(7) | Ru(1)–C(3) | 2.050(6) | Os(1)–C(3) | 2.063(2) |
| C(1)–N(1) | 1.151(10) | C(1)–N(1) | 1.160(6) | C(1)–N(1) | 1.154(3) |
| C(2)–N(2) | 1.165(10) | C(2)–N(2) | 1.151(6) | C(2)–N(2) | 1.154(3) |
| C(3)–N(3) | 1.169(10) | C(3)–N(3) | 1.166(6) | C(3)–N(3) | 1.161(3) |
| **Bond Angles (°)** | | **Bond Angles (°)** | | **Bond Angles (°)** | |
| C(1)–Fe(1)–C(2) | 90.5(3) | C(1)–Ru(1)–C(2) | 89.48(19) | C(1)–Os(1)–C(2) | 90.16(8) |
| C(1)–Fe(1)–C(3) | 91.4(3) | C(1)–Ru(1)–C(3) | 92.1(2) | C(1)–Os(1)–C(3) | 91.67(8) |
| C(2)–Fe(1)–C(3) | 92.6(3) | C(2)–Ru(1)–C(3) | 89.1(2) | C(2)–Os(1)–C(3) | 89.99(8) |
| Fe(1)–C(1)–N(1) | 179.4(7) | Ru(1)–C(1)–N(1) | 177.6(4) | Os(1)–C(1)–N(1) | 178.8(2) |
| Fe(1)–C(2)–N(2) | 177.4(6) | Ru(1)–C(2)–N(2) | 179.1(5) | Os(1)–C(2)–N(2) | 177.23(19) |
| Fe(1)–C(3)–N(3) | 178.4(7) | Ru(1)–C(3)–N(3) | 178.9(5) | Os(1)–C(3)–N(3) | 178.5(2) |

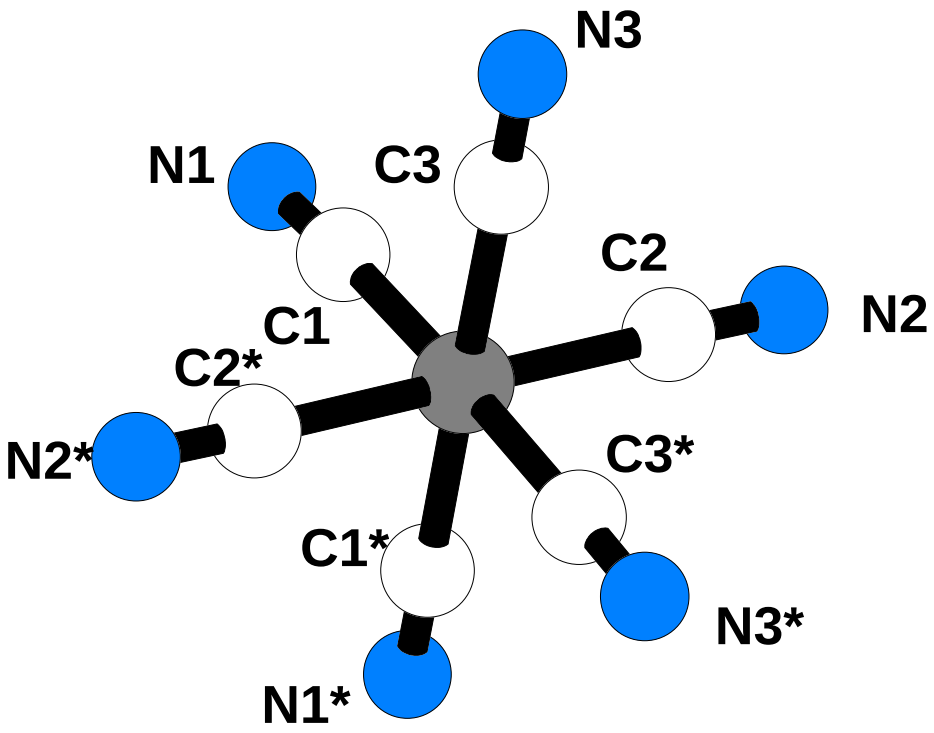


**Figure IV–29. X–ray structure of $[PPN]_3[M^{III}(CN)_6]$ (cations were removed for clarity).**

Using X–ray crystallography and infrared spectroscopy, the correlation between bond distances and cyanide stretching frequencies can be explained. Using **Table IV–13** and infrared data on the $[M^{III}(CN)_6]^{3-}$, the observation can be made that, moving from iron to ruthenium to osmium, the metal–carbon bond increases due to the increasing atomic radius of the transition metal. As a result the carbon–nitrogen triple bond strength will decrease, which results in a blue shift of the cyanide stretching frequencies.

The X–ray structure of *trans*–$[M^{II}(CN)_4(CO)_2]^{2-}$ (where M = Fe[23], Ru) confirmed an octahedral structure with four cyanide ligands and two carbonyl ligands that are bound to the transition metal and the $[PPN]^+$ cation for the ruthenium compound and $[Na]^+$ cation for the iron. The X–ray structure shows the carbonyl ligands to be in a *trans* orientation. The ruthenium atom lies on a two–fold axis so that the *trans*–$[Ru^{II}(CN)_4(CO)_2]^{2-}$ anion has an imposed $C_2$ symmetry, while the $[PPN]^+$ cation is located on a general position. This implies that the ratio of the

ruthenium complex ion and the cation is 1:2. The general structure of the complex anion is shown in **Figure IV–30**. The crystal structure for both compounds was solved under a monoclinic crystal system $P2_1/n$. The *trans*–$[Fe^{II}(CN)_4(CO)_2]^{2-}$ uses the same numbering system as the ruthenium analog. Crystals of the ruthenium compound were grown by vapor diffusion of methylene chloride and diethyl ether after three days. Selective bond distances and angles are summarized in **Table IV–14**. The average metal to cyanide bond distance is 1.926(4) Å for Fe and 2.0590(17) Å for Ru.

**Table IV–14. Selective Crystallographic Data for *trans*–$[M^{II}(CN)_4(CO)_2]^{2-}$.**

| **Fe**[23] | | **Ru** | |
|---|---|---|---|
| **Bond Distances (Å)** | | **Bond Distances (Å)** | |
| Fe(1)–C(1) | 1.800(5) | Ru(1)–C(1) | 1.9360(17) |
| Fe(1)–C(2) | 1.929(4) | Ru(1)–C(2) | 2.0588(17) |
| Fe(1)–C(3) | 1.923(3) | Ru(1)–C(3) | 2.0596(17) |
| C(1)–O(1) | 1.122(5) | C(1)–O(1) | 1.131(2) |
| C(2)–N(1) | 1.144(4) | C(2)–N(1) | 1.146(2) |
| C(3)–N(2) | 1.150(4) | C(3)–N(2) | 1.143(2) |
| **Bond Angles (°)** | | **Bond Angles (°)** | |
| C(1)–Fe(1)–C(2) | 90.09(15) | C(1)–Ru(1)–C(2) | 89.96(7) |
| C(1)–Fe(1)–C(3) | 90.51(15) | C(1)–Ru(1)–C(3) | 89.91(7) |
| C(2)–Fe(1)–C(3) | 90.05(12) | C(2)–Ru(1)–C(3) | 92.63(6) |
| Fe(1)–C(1)–O(1) | 178.8(4) | Ru(1)–C(1)–O(1) | 177.46(14) |
| Fe(1)–C(2)–N(1) | 178.5(3) | Ru(1)–C(2)–N(1) | 178.19(15) |
| Fe(1)–C(3)–N(2) | 179.5(3) | Ru(1)–C(3)–N(2) | 178.65(15) |

Using X–ray crystallography and infrared spectroscopy, the correlation between bond distances and cyanide/carbonyl stretching frequencies can be explained. Using **Table IV–14** and the infrared spectra (**Table IV–2**), the observation can be made that, moving from iron to ruthenium, the metal–carbon bond will increase due to the increasing atomic radius of the transition metal. As a result the carbon–nitrogen and carbon–oxygen triple bond will decrease, which will blue shift the cyanide/carbonyl stretching frequencies. Since the carbonyl ligands are in a *trans* orientation and carbonyl binds to a transition metal using π–backbonding, this will also affect the metal–carbon bond. Since the carbonyl ligands are competing for electrons in the same *d* orbital the bond distances will increase as a result.

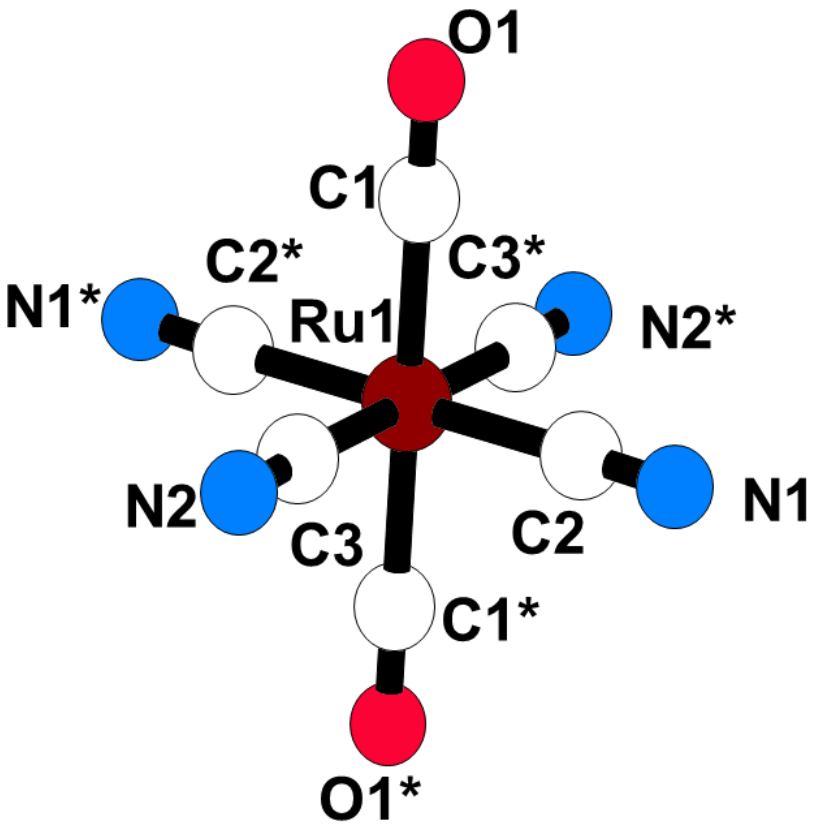


**Figure IV–30. X–ray structure of *trans*–$[PPN]_2[Ru^{II}(CN)_4(CO)_2]$ (cations were removed for clarity).**

The X–ray structure determination of *cis*–$[PPN]_2[Ru^{II}(CN)_4(CO)_2]$ was done. Crystals of *cis*–$[PPN]_2[Ru^{II}(CN)_4(CO)_2]^{2-}$ were grown by vapor diffusion of methylene chloride and diethyl ether after one week. The $[Ru^{II}(CN)_4(CO)_2]^{2-}$ ion and two $[PPN]^+$ cations are located in a general position within the unit cell. It should be noted that the *cis*–$[PPN]_2[Ru^{II}(CN)_4(CO)_2]$ crystallizes in a different unit cell than that found for its isomer, *trans*–$[PPN]_2[Ru^{II}(CN)_4(CO)_2]$. Whereas the CO and CN ligands are ordered in the centrosymmetric *trans*–$[Ru^{II}(CN)_4(CO)_2]^{2-}$ the, $CN^-$ and CO ligands are apparently disordered in the *cis*–$[Ru^{II}(CN)_4(CO)_2]^{2-}$. Refinement does not reveal two short Ru–C(O) bonds and four longer Ru–C(N). The pattern of shorter Ru–C(O) distances for the carbonyl ligand and longer but equal Ru–C(N) bonds were found in the structures of *trans*–$[PPN]_2[Ru^{II}(CN)_4(CO)_2]$ (**Figure IV–30**) and $[PPN][Ru^{II}(CN)_4(CO)(pyridine)]$. The problem of disorder of CO and CN ligands in $[M(CO)_x(CN)_{(6-x)}]^n$ compounds is a frequent one. It was possible to overcome the problem by using cations (e.g $K^+$ or $Na^+$) or hydrogen bonding

solvents of crystallization that preferentially interact with the CN ligands. Unfortunately, these strategies did not work in this case. The overall crystal structure is shown in **Figure IV–31**.

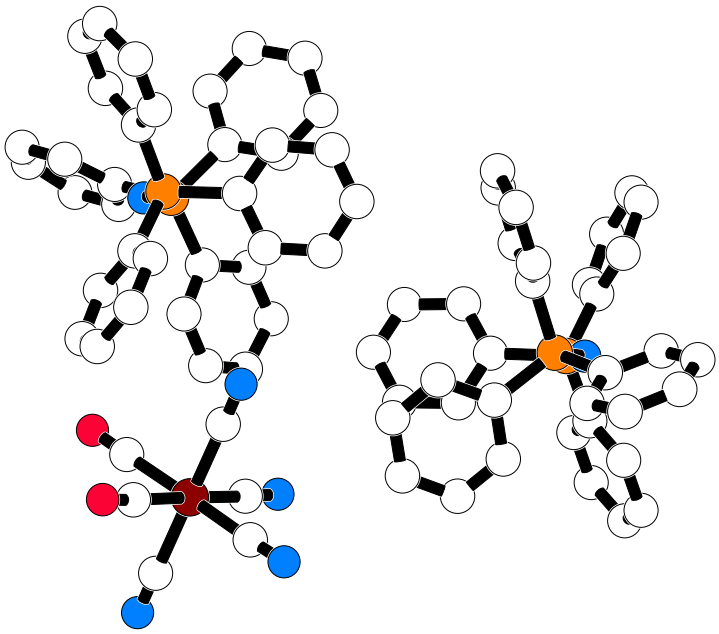

**Figure IV–31. X–ray structure of *cis*–$[PPN]_2[Ru^{II}(CN)_4(CO)_2]$ (hydrogens were removed for clarity).**

Using X–ray crystallography and infrared spectroscopy, the correlation between bond distances and cyanide/carbonyl stretching frequencies can be explained. A true comparison cannot be determined using the data provided when comparing the *cis*–$[M^{II}(CN)_4(CO)_2]^{2-}$ (where M = Fe and Ru). The reason is that the crystal structures for these compounds were grown using different cations ($Na^+$ for Fe and $PPN^+$ for Ru). It has been shown that cations can affect bond distances and angles due to the electrostatic interactions between the cation and the ligands[22] and that the *cis*–$[Ru^{II}(CN)_4(CO)_2]$ crystal structure is too disordered to analysize the data correctly.

The X–ray structure of *trans*–$[M^{II}(CN)_4(CO)(py)]^{2-}$ (where M = Fe[17], Ru) confirmed an octahedral structure with four cyanide ligands, one carbonyl ligand and one pyridine ligand that are bound to the transition metal and the $[PPN]^+$ cation for the ruthenium compound and $[NBu_4]^+$ cation for the iron. The X–ray structure shows the carbonyl ligand *trans* to the pyridine. The

ruthenium compound was solved under the triclinic crystal system *P*1bar. The two compounds, with respect to the complex anion, are isostructural. Crystals of *trans*–$[Ru^{II}(CN)_4(CO)(py)]^{2-}$ were grown by vapor diffusion of acetonitrile and diethyl ether after four days. The ruthenium complex ion and two $PPN^+$ cations are located in a general position within the unit cell (**Figure IV–32**). The general structure of the complex anion is shown in **Figure IV–33**. The X–ray structure for the iron compound follows the same numbering system as the ruthenium (**Figure IV–33**). Selective bond distances and angles are summarized in **Table IV–15**. The *trans*–$[Fe^{II}(CN)_4(CO)(py)]^{2-}$ anion has crystallographic $C_2$ symmetry, which results in only one carbonyl, one–half of the pyridine ligand, one $[NBu_4]^+$ cation and two cyanide ligands in the asymmetric unit. The average metal to cyanide bond distance is 1.932(4) Å for Fe and 2.054(18) Å for Ru. The bond distances for the CO, $CN^-$ and pyridine ligands increase when moving from iron to ruthenium.

Using X–ray crystallography and infrared spectroscopy, the correlation between bond distances and cyanide/carbonyl stretching frequencies can be explained. Using **Table IV–15** and the infrared spectra (**Table IV–6**), the observation can be made that, moving from iron to ruthenium, the metal–carbon bond will increase due to the increasing atomic radius of the transition metal. As a result the carbon–nitrogen and carbon–oxygen triple bond will decrease, which will blue shift the cyanide/carbonyl stretching frequencies.

| Table IV–15. Selective Crystallographic Data for *trans*– $[M^{II}(CN)_4(CO)(py)]^{2-}$. | | | |
|---|---|---|---|
| **Fe**[17] | | **Ru** | |
| **Bond Distances (Å)** | | **Bond Distances (Å)** | |
| Fe(1)–C(1) | 1.722(6) | Ru(1)–C(1) | 1.8238(17) |
| Fe(1)–C(2) | 1.933(3) | Ru(1)–C(2) | 2.0634(19) |
| Fe(1)–C(3) | 1.931(3) | Ru(1)–C(3) | 2.0448(18) |
| Fe(1)–C(4) | 1.931(3) | Ru(1)–C(4) | 2.0543(18) |
| Fe(1)–C(5) | 1.933(3) | Ru(1)–C(5) | 2.0537(19) |
| Fe(1)–N(5) | 2.066(3) | Ru(1)–N(5) | 2.1632(13) |
| C(1)–O(1) | 1.153(5) | C(1)–O(1) | 1.146(2) |
| C(2)–N(1) | 1.141(3) | C(2)–N(1) | 1.152(2) |
| C(3)–N(2) | 1.141(3) | C(3)–N(2) | 1.149(2) |
| C(4)–N(3) | 1.141(3) | C(4)–N(3) | 1.153(2) |
| C(5)–N(4) | 1.141(3) | C(5)–N(4) | 1.156(2) |
| **Bond Angles (°)** | | **Bond Angles (°)** | |
| C(1)–Fe(1)–C(2) | 90.92(15) | C(1)–Ru(1)–C(2) | 90.70(7) |
| C(1)–Fe(1)–C(3) | 90.62(15) | C(1)–Ru(1)–C(3) | 90.46(8) |
| C(1)–Fe(1)–C(4) | 90.62(15) | C(1)–Ru(1)–C(4) | 90.65(7) |
| C(1)–Fe(1)–C(5) | 90.92(15) | C(1)–Ru(1)–C(5) | 94.70(8) |
| C(1)–Fe(1)–N(5) | 179.16(18) | C(1)–Ru(1)–N(5) | 179.35(7) |
| C(2)–Fe(1)–C(3) | 90.37(12) | C(2)–Ru(1)–C(3) | 90.96(7) |
| C(2)–Fe(1)–C(4) | 178.38(13) | C(2)–Ru(1)–C(4) | 178.25(6) |
| C(2)–Fe(1)–C(5) | 89.08(16) | C(2)–Ru(1)–C(5) | 90.27(7) |
| C(2)–Fe(1)–N(5) | 89.68(11) | C(2)–Ru(1)–N(5) | 89.15(6) |
| C(3)–Fe(1)–C(4) | 90.13(17) | C(3)–Ru(1)–C(4) | 90.15(7) |
| C(3)–Fe(1)–C(5) | 178.38(13) | C(3)–Ru(1)–C(5) | 174.68(7) |
| C(3)–Fe(1)–N(5) | 88.79(11) | C(3)–Ru(1)–N(5) | 88.90(6) |
| C(4)–Fe(1)–C(5) | 90.37(12) | C(4)–Ru(1)–C(5) | 88.50(7) |
| C(4)–Fe(1)–N(5) | 88.79(11) | C(4)–Ru(1)–N(5) | 89.52(6) |
| C(5)–Fe(1)–N(5) | 89.68(11) | C(5)–Ru(1)–N(5) | 85.94(6) |
| Fe(1)–C(1)–O(1) | 179.9(5) | Ru(1)–C(1)–O(1) | 178.37(17) |
| Fe(1)–C(2)–N(1) | 179.7(3) | Ru(1)–C(2)–N(1) | 179.24(17) |
| Fe(1)–C(3)–N(2) | 178.8(3) | Ru(1)–C(3)–N(2) | 179.37(17) |
| Fe(1)–C(4)–N(3) | 178.8(3) | Ru(1)–C(4)–N(3) | 178.13(15) |
| Fe(1)–C(5)–N(4) | 179.7(3) | Ru(1)–C(5)–N(4) | 173.68(16) |

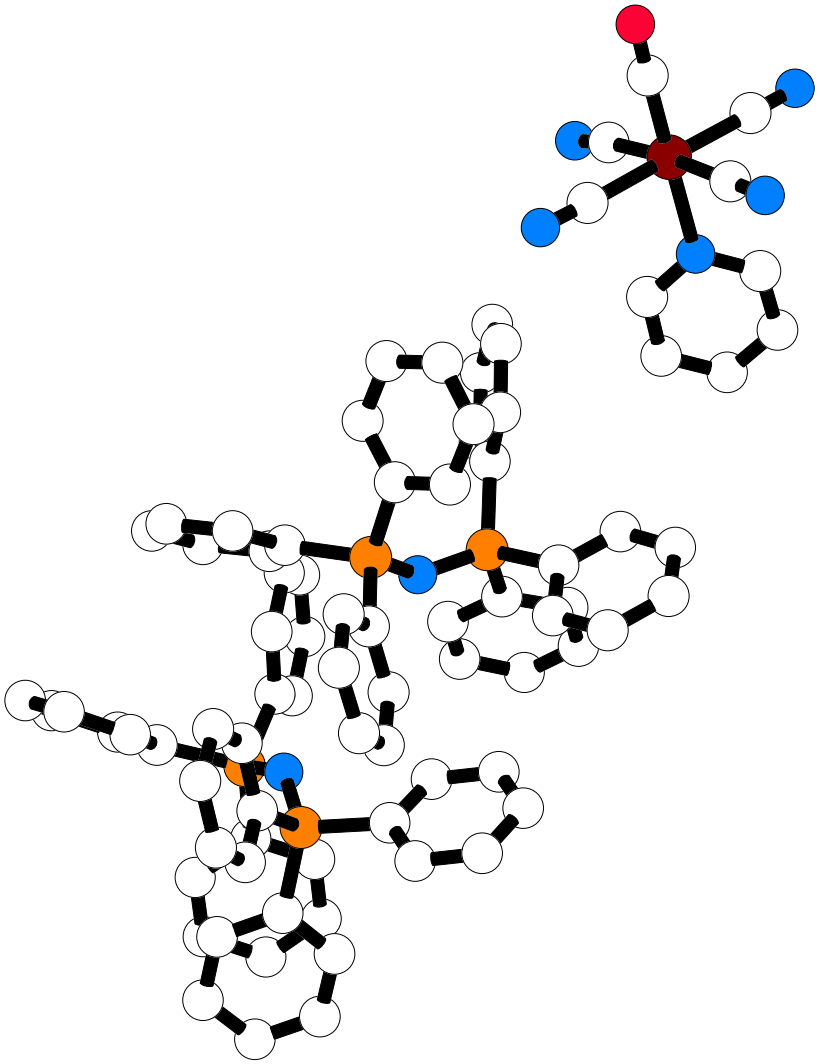

**Figure IV–32. X–ray structure of *trans*–$[PPN]_2[Ru^{II}(CN)_4(CO)(py)]$ unit cell (hydrogens were removed for clarity).**

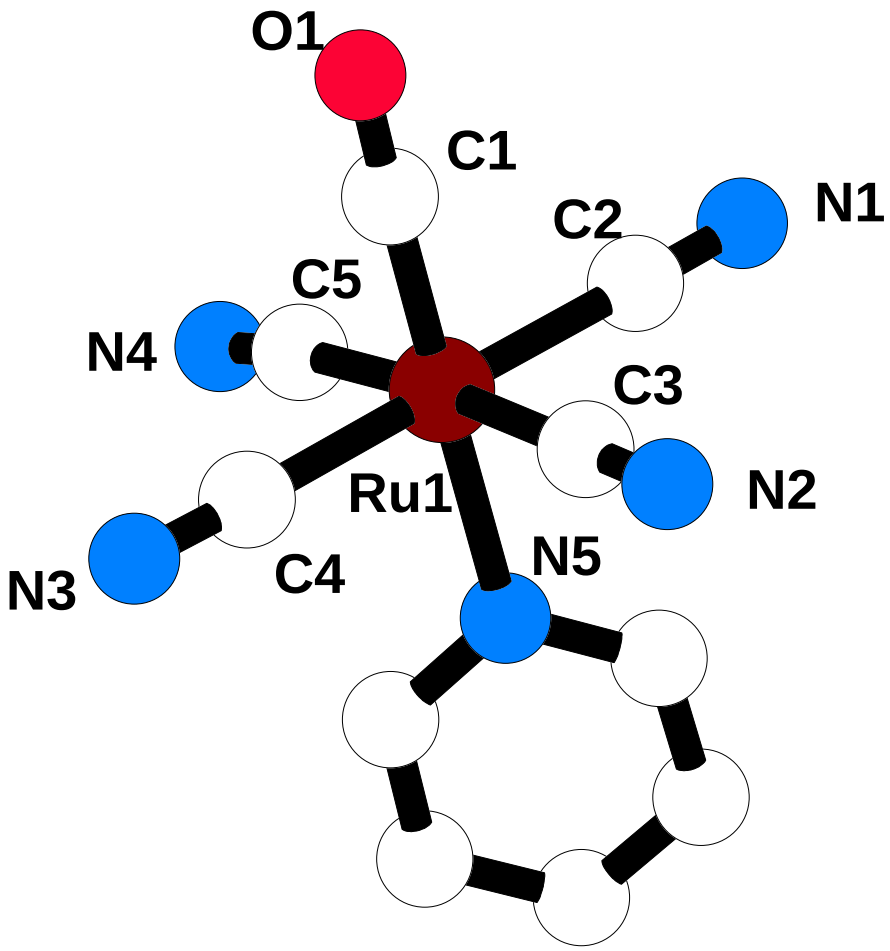


**Figure IV–33. X–ray structure of *trans*–[PPN]$_2$[Ru$^{II}$(CN)$_4$(CO)(py)] (cations and hydrogens were removed for clarity).**

### 4.3.4 Electrochemistry

The cyclic voltammetry of [PPN]$_4$[M$^{II}$(CN)$_6$] (where M = Ru and Os) in acetonitrile shows a reversible oxidation at $E_{½}$ = 0.136 V for Ru and an irreversible oxidation at –0.086 V for Os vs Ag/AgCl (**Figure IV–34**). It is easier to oxidize the osmium compound than the ruthenium. This follows a general trend of the periodic table, as one goes down the periodic table the elements are easier to oxidize.

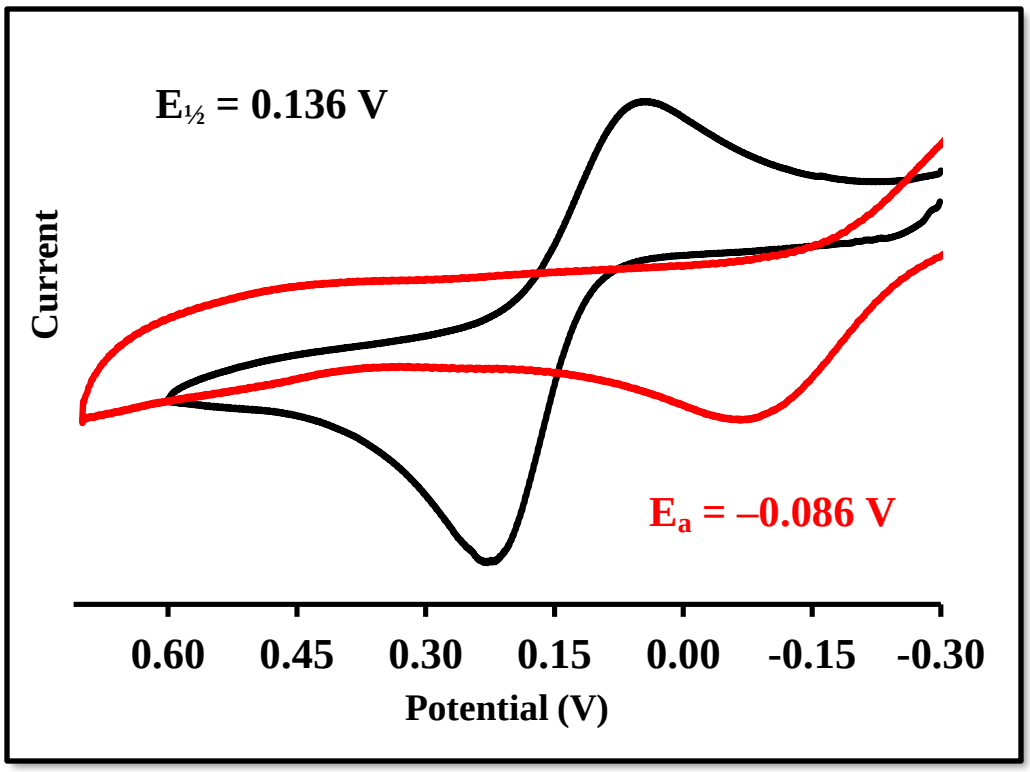


**Figure IV–34. Cyclic Voltammogram of $[PPN]_4[M^{II}(CN)_6]$ in $CH_3CN$, where M = Ru (black) and Os (red).**

The cyclic voltammetry of $[PPN]_3[Ru^{II}(CN)_5(CO)]$ in *N*,*N*–dimethylformamide shows a reversible oxidation at $E_{½}$ = 0.995 V vs Ag/AgCl (**Figure IV–35**). The oxidation of *cis* and *trans*–$[PPN]_2[Ru^{II}(CN)_4(CO)_2]$ and *fac*–$[AsPh_4][Ru^{II}(CN)_3(CO)_3]$ in *N*,*N*–dimethylformamide solution were not observed. Various solvents, i.e. acetonitrile, methylene chloride, methanol and ethanol, were used in order to observe any possible redox potential for these three compounds; however, no redox potentials were observed. Other conditions were attempted, i.e. changing the working electrode from Pt to glassy carbon while changing the solvent; however, all attempts were unsuccessful.

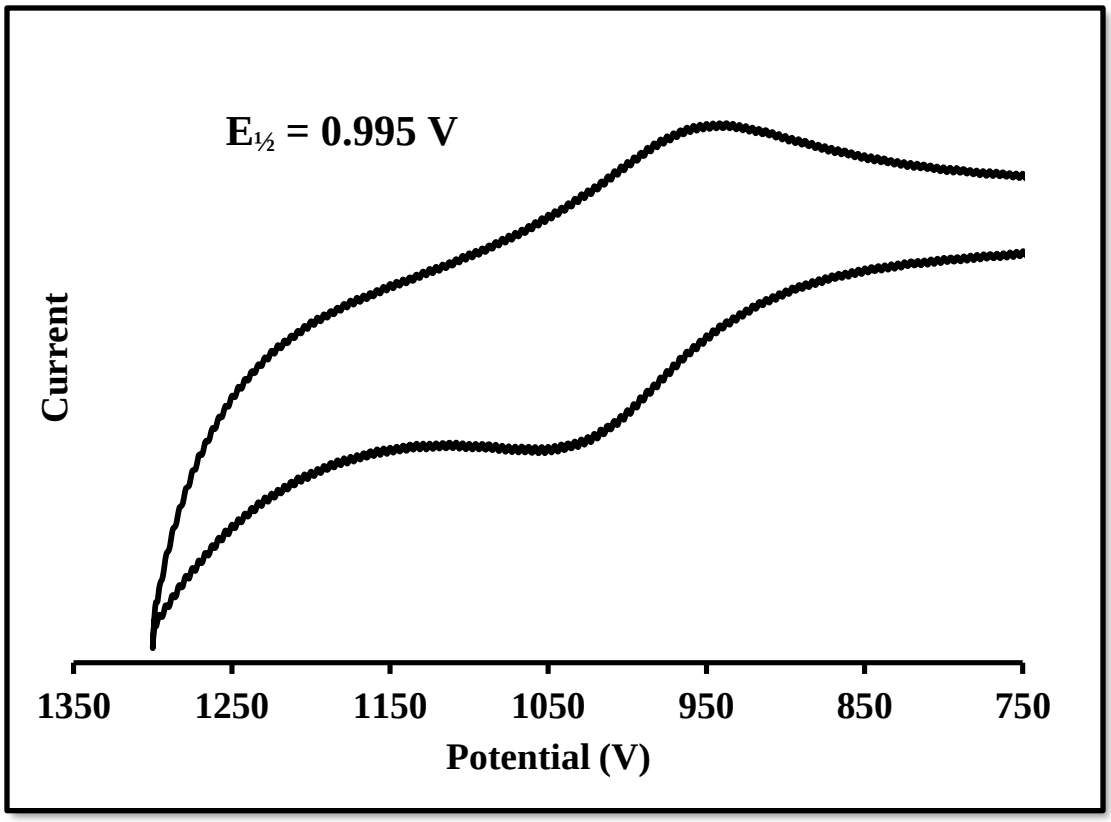


**Figure IV–35. Cyclic Voltammogram of $[PPN]_3[Ru^{II}(CN)_5(CO)]$ in DMF.**

It is known that cyano transition metal compounds favor high oxidation states and transition metal carbonyl compounds favor low oxidation states, e.g. $Fe^0(CO)_5$. This series of compounds show the redox potential trend of stepwise substitution of $CN^-$ to CO from $[Ru^{II}(CN)_6]^{4-}$. Since CO ligands favors low oxidation states while the $CN^-$ ligand favor high oxidation states, there is no redox potential for *cis* and *trans*–$[PPN]_2[Ru^{II}(CN)_4(CO)_2]$ and *fac*–$[AsPh_4][Ru^{II}(CN)_3(CO)_3]$ in DMF which has a potential range from –2.5 to +1.5 V.

The cyclic voltammetry of *trans*–$[PPN]_2[Ru^{II}(CN)_4(CO)(py)]$ in acetonitrile shows a quasi–reversible oxidation at $E_{½}$ = 0.538 V vs Ag/AgCl (**Figure IV–36**).The high positive redox potential is consistent with for the stabilization of the $Ru^{II}$ compound by the presence of the CO. The iron analog shows a reversible oxidation at $E_{½}$ = 0.717 V vs Ag/AgCl. This is another example where it is easier to oxidize the ruthenium compound than the iron, due to the previous explanation.

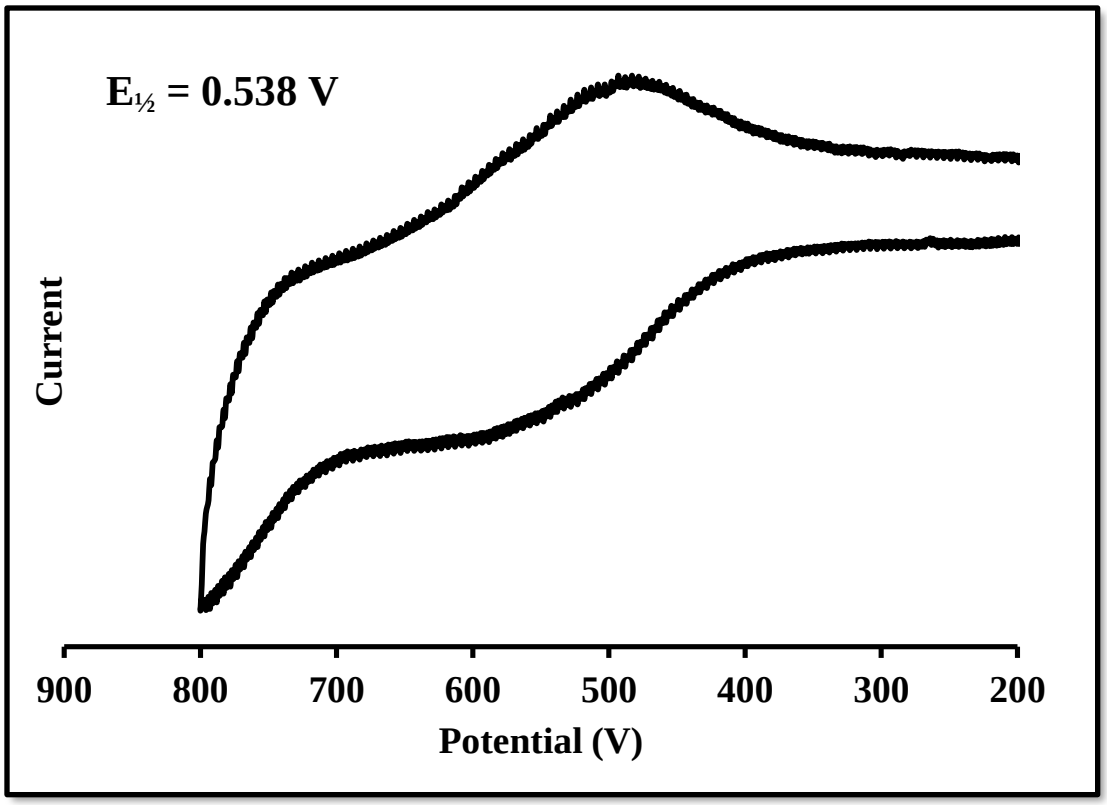


**Figure IV–36. Cyclic Voltammogram of *trans*–$[PPN]_2[Ru^{II}(CN)_4(CO)(py)]$ in $CH_3CN$.**

## 4.4 Conclusions

In conclusion, $[M^{II}(CN)_{(6-x)}(CO)_x]^{(x-4)}$ (where M = Ru and Os) were synthesized, while only the ruthenium complexes were structurally characterized, complexes were also characterized by IR, electrochemistry, NMR ($^1H$ and $^{13}C$) and UV–Vis. Ligand substitution of $CN^-$ with CO in $M_4[Fe^{II}(CN)_6]$ (where M = alkali metal) was only achieved through high CO pressures and temperatures. Counter cation exchange was performed, from $[Na]^+$ to $[R_4N]^+$, to lower the interaction between the counter cation and the complex anion and therefore made the $CN^-$ more liable. Due to the increased reactivity of $[R_4N]_4[Fe^{II}(CN)_6]$, this concept was applied to ruthenium and osmium. A counter cation exchange was performed on $K_4[Ru^{II}(CN)_6]$ using [PPN]Cl. Reacting $[PPN]_4[Ru^{II}(CN)_6]$ with CO under mild conditions proved successful where the isolated product was $[PPN_3][Ru^{II}(CN)_5(CO)]$, which was used an intermediate to synthesize other [Ru(CN)(CO)(L)] complexes. Isolation of *cis*–$[PPN]_2[Ru^{II}(CN)_4(CO)_2]$ and *fac*–

[PPN][$Ru^{II}(CN)_3(CO)_3$] were done using *fac*–[$Ru^{II}(CO)_3Cl_2(THF)$] using four or three equivalence of $CN^-$, respectively.

The X–ray structures of the ruthenium complexes were compared with the iron analogs. The M–L bond distances increased due to the increasing size of the atomic radii moving from iron to ruthenium. Infrared studies and X–ray crystallography confirmed the geometric arrangement of the cyanide and carbonyl ligands. Infrared studies showed an increase in both cyanide and carbonyl stretching frequencies upon substitution of cyanide for carbonyl. The X–ray structure of the *cis*–$[PPN]_2[Ru^{II}(CN)_4(CO)_2]$ determined that the structure is disordered due to the $[PPN]^+$ cation which suggests a counter cation exchange, i.e. alkali metals, to eliminate the disorder.

Electrochemical studies showed the [Ru(CN)(CO)] complexes have high oxidation potentials which shows these complexes are stable in terms of oxidation when compared to the iron analogs.

## 4.5 References


1. Sharpe, A. G. *The Chemistry of Cyano Complexes of the Transition Metals*. Academic Press: New York, 1976.
2. Dunbar, K. R.; Heintz, R. A. Chemistry of Transition Metal Cyanide Compounds: Modern Perspectives. *Prog. Inorg. Chem.* **1997**, *45*, 283.
3. http://www.ibiblio.org/wm/paint/auth/gogh/starry–night/
4. http://www.fda.gov/Drugs/EmergencyPreparedness/BioterrorismandDrugPreparedness/ucm130337.htm
5. http://www.builderssquare.com/xp_34839867–Morton_Kosher_Salt_Coarse_3_lb_1_36_kg_Box_of_12_4499.aspx
6. Gina Chiarella, PhD dissertation, Stony Brook University, Stony Brook, **2006**.
7. Goedken, V. L. *J. Chem. Soc., Chem. Commun.* **1972**, 207–208.
8. Cotton, F. A.; Monchamp, R. R.; Henry, R. J. M.; Young, R. C.; *J. Inorg. Nucl. Chem.*, **1959**, *10*, 28.
9. Gmelin, **1932**, 59B, 704.

10. Gmelin, **1976**, 36B, 24.
11. Toma, H. E.; Creutz, C. *Inorg. Chem.*, **1977**, *16*, 545.
12. Toma, H. E.; Moroi, N. M.; Iha, N. Y. M. *An. Acad. Bras. Cienc.*, **1982**, *54*, 315.
13. Mullar, J. A.; Hebd, C. R. *Seances, Acad. Sci.*; **1887**, *104*, 992.
14. Manchot, W.; Merry, E., Woringer, P. *Chem. Ber.*, **1912**, *45*, 2879.
15. Kenney, D. J.; Flynn, T. P.; Gallini, J. B. *J. Inorg. Nucl. Chem.*, **1961**, *20*, 75
16. Jiang, J.; Koch, S. A. *Angew. Chem., Int. Ed.* **2001**, *40*, 2629–2631.
17. Chiarella, G. M.; Melgarejo, D. Y.; Koch, S. A. *J. Am. Chem. Soc.*, **2006**, *128*, 1416–1417.
18. Cauzzi, D. A.; Mori, G.; Predieri, G.; Tiripicchio, A. *Inorg. Chim. Acta*, **1993**, *204*, 181–187.
19. Gusev, D. G.; Dolgushin, F. M.; Antipin, M. Y.. *Organometallics* **2001**, *20*, 1001.
20. Martinsen, A.; Songstad, J. *Acta Chem. Scand., Ser. A* **1977**, *31*, 645.
21. Carini, C.; Pelizzi, C.; Peilzzi, G.; Predieri, G.; Tarasconi, P.; Vitali, F. *J. Chem. Soc., Chem. Commun.* **1990**, 613.
22. Bonardi, A.; Carini, C.; Pelizzi, C.; Pelizzi, G.; Predieri, G.; Tarasconi, P.; Zoroddu, M. A.; Molloy, K. C. *J. Organomet. Chem.* **1991**, *401*, 283.
23. Jiang, J.; Koch, S. A. *Inorg. Chem.* **2002**, *41*, 158–160.
24. Contakes, S. M.; Hsu, S. C. N.; Rauchfuss, T. B.; Wilson, S. R. *Inorg. Chem.* **2002**, *41*, 1670–1678.
25. Kettle, S. F. A.; Aschero, G. L.; Diana, E.; Rossetti, R.; Stanghellinim P. L.; *Inorg. Chem.* **2006**, *45*, 4928–4937.
26. Buchner, W.;Schenk, W. A. *Inorg. Chem.* **1984**, *23*, 132–137.
27. Jianfeng Jiang, PhD dissertation, Stony Brook University, Stony Brook, **2002**.

# CHAPTER 5. Synthesis and Characterization of Ruthenium(II) Carbonyl Complexes using Phosphine–Thiolate and Amine–Thiolate Ligands

## 5.1 Introduction

Due to their interesting reactivity and structures, researchers have investigated sulfur–coordinated transition metal complexes. These complexes were designed, primarily, to resemble the active site of metal–sulfur enzymes, e.g. hydrogenase and rubredoxin (**Figure V–1**). These active sites are associated with specific redox reactions, e.g. the reversible reduction of dihydrogen for the hydrogenase enzymes and electron transfer processes for rubredoxin. To understand these active sites further, researchers have been synthesizing various model complexes while studying their structure, chemical and physical properties in order to compare them with the original active site. These active sites show unusual ligands, for example, the hydrogenase enzymes contain carbonyl (CO) and cyanide ($CN^-$) ligands. Ligands such as CO and $CN^-$ are toxic to any biological system and can be fatal if inhaled or ingested. Why did nature go through the trouble of using these fatal ligands in designing these enzymes? To date this question, along with others, puzzles scientists.

Iron–thiolate chemistry has been extensively studied, however ruthenium analogs remain comparatively unknown.[1–5] The Koch and Millar groups[1,6–8] primarily synthesized examples of ruthenium–thiolate complexes; however, developments in this area have remained unseen in the literature (**Figure V–2**).

Ruthenium complexes have shown interest in the industrial arena. Ruthenium thiolate compounds may serve as hydrodesulfurization catalysts in the petroleum industry. These hydrodesulfurization catalysts are industrial catalysts used in the removal of sulfur from hydrocarbon petroleum products (**Reaction V–1**).

$$C_xH_yS + 2\,H_2 \xrightarrow{\text{catalyst}} C_xH_{y+2} + H_2S$$

**Reaction V–1. General reaction for hydrodesulfurization.**

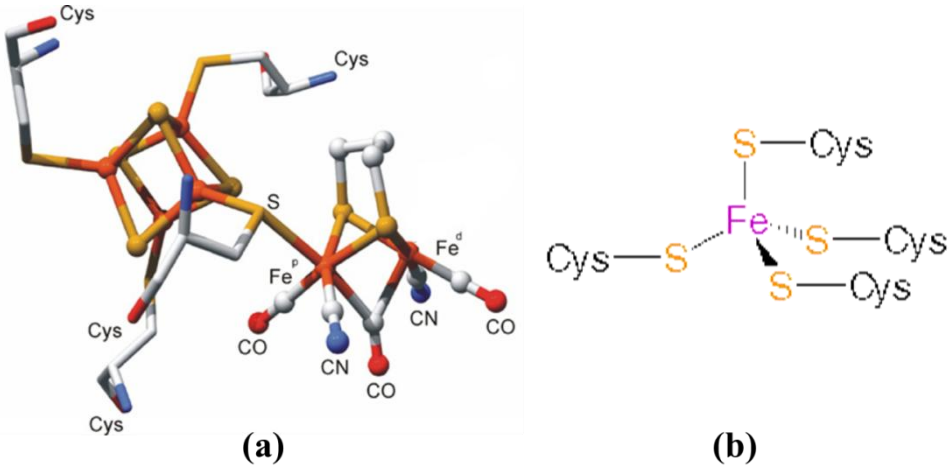


**Figure V–1. (a) [FeFe] hydrogenase, H–cluster[9] (b) Active site of rubredoxin.[10]**

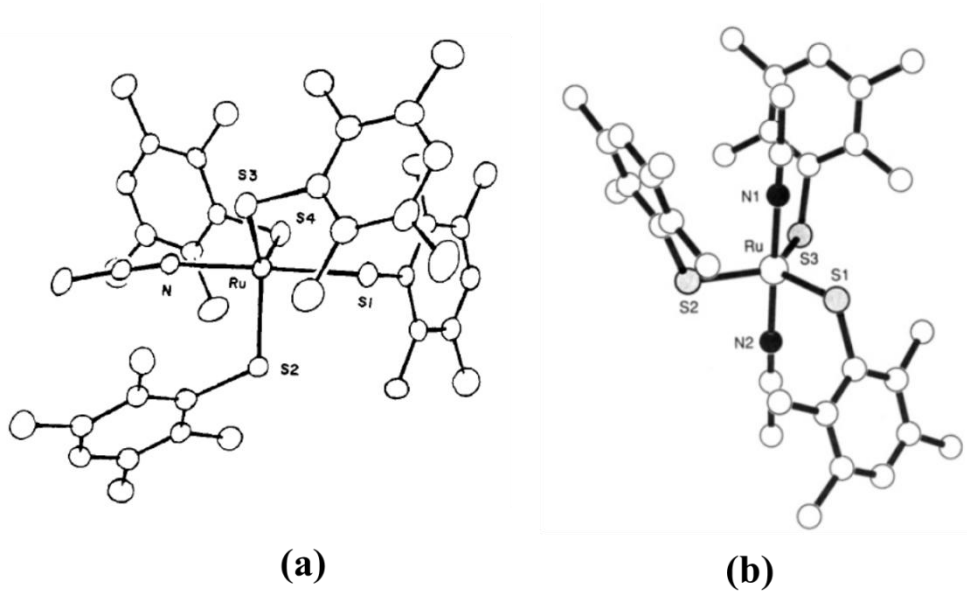


**Figure V–2. X–ray structures of Ruthenium–Thiolate Complexes. (a) [$Ru^{IV}$(S–2,3,5,6–$Me_4C_6H)_4(CH_3CN)$][1] (b) [$Ru^{III}$(S–2,3,5,6–$Me_4C_6H)_3(CH_3CN)_2$][7]**

There are various amounts of sulfur in crude oil in the form of carbon–sulfur hydrocarbons. When these compounds are burned, i.e. combustion, one by–product that is generated is sulfur dioxide, $SO_2$. This compound can be oxidized, from $S^{4+}$ to $S^{6+}$, by ozone or peroxides which results in the environmentally destructive acid rain. Thiophenes ($C_4H_4S$), which are present in petroleum, are extremely difficult to desulfurize; however, certain ruthenium compounds have been shown to be extremely effective catalysts for desulfurizing petroleum.[11]

Another type of ruthenium compounds that are of great interest are ruthenium carbonyl compounds. These compounds have been shown to be excellent catalysts in carbon dioxide reduction to carbon monoxide or methanol[12–13] and sulfur dioxide reduction.[14] These reactions are of particular interest to environmental chemists. One main goal of these compounds is to convert greenhouse gases, such as $CO_2$, to usable fuels. Using these types of materials, there is a high probability of solving the pollution problems that affect our planet.

Various iron complexes have been synthesized to model the active site of hydrogenase. To date researchers have not focused on synthesizing the ruthenium or osmium analogs. Synthesizing these types of compounds can prove to be a useful tool in understanding the structural and chemical properties of the active site. This can be done using transition metals that are isoelectronic to the transition metals found in the active site. Ruthenium and osmium were chosen because both of these transition metals have similar chemical properties as iron. Another advantage of using ruthenium and osmium are the compounds generated tend to be more inert and easier to handle. Recall that hydrogenase enzymes contain transition metal active sites as well as CO and $CN^-$ ligands. The primary goal of this research is to synthesize compounds with this moiety using ruthenium and osmium.

## 5.2 Experimental

**Synthesis of *fac*–[$Ru^{II}(CO)_3Cl_2(THF)$]**

The product was prepared by a modified literature procedure.[15] In a 250 mL Schlenk flask, "$Ru^{III}Cl_3 \bullet 3H_2O$" (5 g, mmol) was dissolved in 50 mL of 1:1 formic acid/hydrochloric acid. The solution was allowed to reflux until the solution changes from dark red to bright yellow. The acid solvent was distilled off leaving a bright yellow solid. The yellow solid was dissolved with 100 mL of acetone and stirred for 30 minutes. The solution was filtered through an opened frit packed with celite. The solvent was removed under vacuum resulting in a yellow solid. The solid was distilled with 25 mL of THF and was felt standing overnight which resulted in white needle crystals. The product was filtered and washed with hexanes. Additional crops of the desired product can be collected by adding excess hexanes to the filtrate. The collected crops were added together to afford 4.05 g, 64.6%, of the desired product.

**$^1$H–NMR (400 MHz, $CD_3CN$) [ppm]:** 5.07 (s, 2H), 4.19–4.13 (m, $J$ = 4.17, 6H).

**$^{13}$C–NMR (100 MHz, $CD_3CN$) [ppm]:** 187.44, 184.12 (*C*≡O).

**Infrared ($CH_3OH$):** $\nu_{CO}$ = 2066 and 2138 $cm^{-1}$.

**Unit Cell:** Monoclinic, $P2_1/n$, a = 5.9680(8) Å, b = 18.200(3) Å, c = 9.7870(1) Å, $\alpha = \gamma = 90^o$, $\beta = 96.891(1)^o$, V = 1055.4(5) $Å^3$.

A colorless needle crystal measuring 1.0 × 0.45 × 0.20 $mm^3$ was mounted using a nylon loop and centered on the X–ray beam at 100 K. Crystals were grown by layering a hexanes to a THF solution of *fac*–[$Ru^{II}(CO)_3Cl_2(THF)$]. Crystals were grown within one day. The accurate unit cell was obtained using reflection with $2\theta = 3.62 – 32.84^o$: a = 5.968(8) Å, b = 18.200(3) Å, c = 9.787(1) Å, $\alpha = \gamma = 90^o$, $\beta = 96.891(1)^o$, V = 1055.4(5) $Å^3$. The structure was solved under a primitive monoclinic crystal system (space group $P2_1/n$) using 3719 reflections. The asymmetric unit consists of one molecule of the ruthenium complex. The data reduction was done using CryAlisPro and the structure refinement was done with SHELXL–97 (Sheldrick). All the non–hydrogen atoms were located by Direct Methods and were refined anisotopically by a full–matrix least–squares method. The positions of the remaining hydrogen atoms were calculated. The crystallographic parameters and atomic coordinates for this compound are located in **Table A–17**.

**Synthesis of *fac*–[$Ru^{II}(CO)_3$(PS2')]**

In a 100 mL Schlenk flask, *fac*–[$Ru^{II}(CO)_3Cl_2(THF)$] (0.500 g, 1.52 mmol) was dissolved in 15 mL of methanol. In a separate 100 mL Schlenk flask, $Li_2$PS2' was generated in a methanol (20 mL) solution using lithium wire (0.023 g , 3.35 mmol) and $H_2$PS2' (0.594 g, 1.68 mmol). The lithium–PS2' solution was allowed to stir until all the reagents had dissolved. The $Li_2$PS2' and metal solutions were cooled to –78 $^o$C using a dry ice/acetone bath. The metal solution was then added to the $Li_2$PS2' solution, dropwise, which resulted in the solution turning from colorless to bright yellow. The mixture was allowed to stir for three hours. The dry ice/acetone bath was removed and immediately the solvent was removed *in vacuo*. The resulting bright yellow solid was observed and extracted using a 2:1 hexanes/diethyl ether solution. The solution was allowed to stir for one hour, then filtered through a closed frit packed with celite. The solvent was removed *in vacuo* to afford the pure yellow product. Crystals suitable for X–ray crystallography were grown by slow evaporation of a concentrated solution of hexanes. Yield: 0.457 g, 55.8%.

**$^{1}$H–NMR (400 MHz, $CD_3CN$) [ppm]:** 7.71–7.61 (s, 3H, aromatic), 7.51–7.43 (m, *J* = 7.48, 2H, aromatic), 7.40–7.35 (dd, *J* = 7.38, 2H, aromatic), 7.33–7.27 (d, *J* = 7.30, 2H, aromatic), 7.07–7.02 (d, *J* = 7.05, 2H, aromatic), 2.20 (s, 6H, C*H*$_3$).

**$^{13}$C–NMR (100 MHz, $CD_3CN$) [ppm]:** 188.92, 188.30, 188.19, 188.04 (*C*≡O); 151.83, 151.55, 132.16, 132.08, 131.86, 131.26, 131.07, 130.96, 130.77, 130.53, 130.21, 129.91, 129.78, 129.68, 129.03, 128.87 (aromatic); 19.95, 19.92 (*C*H$_3$).

**$^{31}$P–NMR (162 MHz, $CD_3CN$) [ppm]:** 91.96 (s)

**UV–Vis:** $\lambda_{max}$, nm ($\varepsilon_m$, $M^{-1}$ $cm^{-1}$) = 237 (100600), 273 (51000).

**Unit Cell:** Monoclinic, *C*2/*c*, a = 27.821(5) Å, b = 9.771(5) Å, c = 17.902(5) Å, $\alpha = \gamma = 90^o$, $\beta$ = 99.952(5)$^o$, V = 4793(3) Å$^3$.

**Infrared ($CH_2Cl_2$):** $\nu_{CO}$ = 2030, 2057 and 2109 $cm^{-1}$.

A yellow prism crystal measuring 0.08 × 0.10 × 0.05 mm$^3$ was mounted using a nylon loop and centered on the X–ray beam at 100 K. Crystals were grown by slow evaporation of hexane solution at –20$^o$C. Crystals were grown within two weeks. The accurate unit cell was obtained using reflection with $2\theta$ = 3.40 – 28.02$^o$: a = 27.821(5) Å, b = 9.771(5) Å, c = 17.902(5) Å, $\alpha = \gamma = 90^o$, $\beta$ = 99.952(5)$^o$, V = 976.4(2) Å$^3$. The structure was solved under a C–centered monoclinic crystal system (space group *C*2/*c*) using 3342 reflections. The asymmetric unit consists of one molecule of the ruthenium complex. The data reduction was done using CryAlisPro and the structure refinement was done with SHELXL–97 (Sheldrick). All the non–hydrogen atoms were located by Direct Methods and were refined anisotopically by a full–matrix least–squares method. The positions of the remaining hydrogen atoms were calculated. The crystallographic parameters and atomic coordinates for this compound are located in **Table A–18**.

**Synthesis of *fac*–[Ru$^{II}$(CO)$_3$(PS2)]**

In a 100 mL Schlenk flask, *fac*–[Ru$^{II}$(CO)$_3$Cl$_2$(THF)] (0.500 g, 1.52 mmol) was dissolved in 15 mL of methanol. In a separate 100 mL Schlenk flask, $Li_2$PS2 was generated in a 20 mL methanol solution using lithium wire (0.233 g, 3.36 mmol) and $H_2$PS2 (0.548 g, 1.68 mmol). The lithium–PS2 solution was allowed to stir until all the reagents had dissolved. The $Li_2$PS2 and metal solutions was cooled to –78 $^o$C using a dry ice/acetone bath. The metal solution was added to the $Li_2$PS2 solution, dropwise, which resulted in the solution turning from colorless to bright yellow. The mixture was allowed to stir for three hours. The dry ice/acetone bath was removed

and immediately the solvent was removed *in vacuo*. The resulting bright yellow solid was observed and extracted using a 2:1 hexanes/diethyl ether solution. The solution was stirred for one hour and filtered through a closed frit packed with celite. The solvent was removed to afford pure yellow product. Crystals suitable for crystallography were grown by slow evaporation of a concentrated solution of hexanes. Yield: 0.494 g, 67.2%.

**$^{1}$H–NMR (400 MHz, DMSO–$d_6$) [ppm]:** 7.51–7.42 (m, *J* = 7.48, 4H, aromatic), 7.39–7.29 (m, *J* = 7.34, 3H, aromatic), 7.24–7.16 (t, *J* = 7.21, 2H, aromatic), 7.00–6.91 (t, *J* = 6.96, 2H, aromatic), 6.82–6.75 (t, *J* = 6.79, 2H, aromatic).

**$^{31}$P–NMR (162 MHz, DMSO–$d_6$) [ppm]:** 83.56 (s)

**UV–Vis:** $\lambda_{max}$, nm ($\varepsilon_m$, $M^{-1}$ $cm^{-1}$) = 279 (68100), 356 (16300).

**Unit Cell:** Triclinic, *P*–1, a = 9.8294(13) Å, b = 10.3375(14) Å, c = 10.7609(15) Å, $\alpha$ = 90.132(11)$^o$, $\beta$ = 116.213(13)$^o$, $\gamma$ = 94.891(11)$^o$, V = 976.43(72) Å$^3$.

**Infrared ($CH_2Cl_2$):** $\nu_{CO}$ = 2032, 2059 and 2110 $cm^{-1}$.

A yellow prism crystal measuring 0.10 × 0.10 × 0.08 $mm^3$ was mounted using a nylon loop and centered on the X–ray beam at 100 K. Crystals were grown by slow evaporation of hexane solution at –20$^o$C. Crystals were grown within two weeks. The accurate unit cell was obtained using reflection with 2$\theta$ = 3.15 – 25.18$^o$: a = 9.8294(13) Å, b = 10.3375(14) Å, c = 10.7609(15) Å, $\alpha$ = 90.132(11)$^o$, $\beta$ = 116.213(13)$^o$, $\gamma$ = 94.891(11)$^o$, V = 976.4(2) Å$^3$. The structure was solved under a primitive triclinic crystal system (space group *P*–1) using 2245 reflections. The asymmetric unit consists of one molecule of the ruthenium complex. The data reduction was done using CryAlisPro and the structure refinement was done with SHELXL–97 (Sheldrick). All the non–hydrogen atoms were located by Direct Methods and were refined anisotopically by a full–matrix least–squares method. The positions of the remaining hydrogen atoms were calculated. The crystallographic parameters and atomic coordinates for this compound are located in **Table A–19**.

**Synthesis of [$Ru^{II}_3(CO)_5(PS2')_3$]**

In a 100 mL Schlenk flask, *fac*–[$Ru^{II}(CO)_3(PS2')$] (0.30 g, 0.558 mmol) was dissolved in methylene chloride (30 mL). The solution was allowed to stir at room temperature until the color of the solution changed from yellow to orange (ca five days). The reaction was monitored by infrared spectroscopy. Diethyl ether was added slowly to the reaction flask and was left

undisturbed for two weeks which produced gold plate crystals that were suitable for X–ray crystallography. Yield: 0.072 g, 33.1%.

**Infrared (hexanes):** $\nu_{CO}$ = 1995, 2036, 2050, 2126 and 2154 $cm^{-1}$.

**UV–Vis:** $\lambda_{max}$, nm ($\varepsilon_m$, $M^{-1}$ $cm^{-1}$) = 302 (6500)

**Electrochemistry:** $E_{ox}$ = 858 mV; 1.0 mM in $CH_2Cl_2$ vs. Ag/AgCl.

**Unit Cell:** Monoclinic, $P2_1/c$, a = 24.7504(14) Å, b = 14.2885(8) Å, c = 19.1832(15) Å, $\alpha = \gamma = 90^o$, $\beta = 106.836(7)^o$, V = 6493.3(7) $Å^3$.

A gold plate crystal measuring 0.45 × 0.40 × 0.15 $mm^3$ was mounted using a nylon loop and centered on the X–ray beam at 100 K. Crystals were grown by vapor diffusion of methylene chloride and diethyl ether. Crystals were grown within three weeks. The accurate unit cell was obtained using reflection with $2\theta = 3.21 – 29.64^o$: a = 24.7504(14) Å, b = 14.2885(8) Å, c = 19.1832(15) Å, $\alpha = \gamma = 90^o$, $\beta = 106.836(7)^o$, V = 6493.3(7) $Å^3$. The structure was solved under a primitive monoclinic crystal system (space group $P2_1/c$) using 15431 reflections. The asymmetric unit consists of one molecule of the ruthenium complex. The data reduction was done using CryAlisPro and the structure refinement was done with SHELXL–97 (Sheldrick). All the non–hydrogen atoms were located by Direct Methods and were refined anisotopically by a full–matrix least–squares method. The positions of the remaining hydrogen atoms were calculated. The crystallographic parameters and atomic coordinates for this compound are located in **Table A–20**.

**Attempted Synthesis of *fac*–[$Ru^{II}(CO)_3$(NS2)]**

In a 100 mL Schlenk flask, *fac*–[$Ru^{II}(CO)_3Cl_2$(THF)] (0.500 g, 1.52 mmol) was dissolved in 15 mL of methanol. In a separate 100 mL Schlenk flask, $Li_2$NS2 (0.609 g, 1.68 mmol) was dissolved in 20 mL of methanol. The $Li_2$NS2 and metal solutions was cooled to $–78^oC$ using a dry ice/acetone bath. The metal solution was added to the $Li_2$NS2 solution, dropwise, which resulted in the solution turning from colorless to a dull yellow. The mixture was stirred for three hours. The dry ice/acetone bath was removed and the solvent was removed *in vacuo*. The resulting yellow–orange solid was observed and extracted using a 2:1 hexanes/diethyl ether solution. The solution was stirred for one hour and filtered through a closed frit packed with celite. The solvent was removed to afford the pure yellow–orange product. Yield: 0.608 g, 74.6%.

**Infrared ($CH_2Cl_2$):** $\nu_{CO}$ = 1956, 2026 and 2102 $cm^{-1}$.

**Attempted Synthesis of *fac*–[$Ru^{II}(CO)_3$(NS2')]**

In a 100 mL Schlenk flask, *fac*–[$Ru^{II}(CO)_3Cl_2$(THF)] (0.500 g, 1.52 mmol) was dissolved in 15 mL of methanol. In a separate 100 mL Schlenk flask, $Li_2$NS2' (0.633 g, 1.68 mmol) was dissolved in 20 mL of methanol. The $Li_2$NS2' and metal solutions was cooled to –78 $^oC$ using a dry ice/acetone bath. The metal solution was added to the $Li_2$NS2' solution, dropwise, which resulted in the solution turning from colorless to a dull yellow. The mixture was stirred for three hours. The dry ice/acetone bath was removed and the solvent was removed *in vacuo*. The resulting yellow–orange solid was observed and extracted using a 2:1 hexanes/diethyl ether solution. The solution was stirred for one hour and filtered through a closed frit packed with celite. The solvent was removed to afford the pure yellow–orange product. Yield: 0.688 g, 82.3%.

**Infrared ($CH_2Cl_2$):** $\nu_{CO}$ = 1954, 2022 and 2100 $cm^{-1}$.

**Synthesis of [$Ru^{II}(CO)_2$(NS2')]$_2$**

In a 100 mL Schlenk flask, *fac*–[$Ru^{II}(CO)_3$(NS2')] (0.25 g, 0.46 mmol) was dissolved in 50 mL of hexanes. The solution was allowed to stir at room temperature until the color of the solution changed from yellow to orange (ca three days). The reaction was monitored by infrared spectroscopy. Diethyl ether was added slowly to the reaction flask and left undisturbed for one week, which produced orange needle crystals. Yield: 0.129 g, 59.6%.

**Infrared (hexanes):** $\nu_{CO}$ = 2035, 2054, 2126 and 2156 $cm^{-1}$.

**UV–Vis:** $\lambda_{max}$, nm ($\varepsilon_m$, $M^{-1}$ $cm^{-1}$) = 300 (4080).

**Electrochemistry:** $E_{ox}$ = 1110 mV; 1.0 mM in $CH_2Cl_2$ vs. Ag/AgCl.

**Unit Cell:** Monoclinic, *C*2/*c*, a = 26.2359(17) Å, b = 8.5698(4) Å, c = 22.4842(14) Å, $\alpha = \gamma = 90^o$, $\beta = 121.808(9)^o$, V = 4296.1(3) $Å^3$.

A orange needle crystal measuring 0.45 × 0.35 × 0.30 $mm^3$ was mounted using a nylon loop and centered on the X–ray beam at 100 K. Crystals were grown by slow evaporation of hexane solution of *fac*–[$Ru^{II}(CO)_3$(NS2′)] at room temperature. Crystals were grown within one weeks. The accurate unit cell was obtained using reflection with $2\theta$ = 3.35 – 27.09$^o$: a = 26.2359(17) Å, b = 8.5698(4) Å, c = 22.4842(14) Å, $\alpha = \gamma = 90^o$, $\beta = 121.808(9)^o$, V = 4296.1(3) $Å^3$. The structure was solved under a C–centered monoclinic crystal system (space group *C*2/*c*) using 3809 reflections. The asymmetric unit consists of one–half molecule of the ruthenium complex which contains a crystallographic $C_2$ axis. The data reduction was done using

CryAlisPro and the structure refinement was done with SHELXL–97 (Sheldrick). All the non–hydrogen atoms were located by Direct Methods and were refined anisotopically by a full–matrix least–squares method. The positions of the remaining hydrogen atoms were calculated. The crystallographic parameters and atomic coordinates for this compound are located in **Table A–21**.

**Synthesis of *fac*–[$Me_3NBz$][$Ru^{II}(CO)_3(S–2,3,5,6–Me_4C_6H)_3$]**

In a 100 mL Schlenk flask, *fac*–[$Ru^{II}(CO)_3Cl_2(THF)$] (0.500 g, 1.52 mmol) was dissolved in 15 mL of methanol. In a separate 100 mL Schlenk flask, lithium–2,3,5,6–tetramethylbenzenethiolate was generated in a methanol (20 mL) solution using lithium wire (0.032 g, 4.57 mmol) and 2,3,5,6–tetramethylbenzenethiol (0.760 g, 4.57 mmol). The lithium–thiol solution was allowed to stir until all the reagents had dissolved. The ruthenium solution was added *via* cannula to the thiolate solution, which resulted in an immediate color change, from colorless to dull yellow. The solution was allowed to stir for three hours at room temperature. A methanolic solution of [$Me_3NBz$]Cl (0.340 g, 1.83 mmol) was added slowly to the reaction mixture, which was left standing and undisturbed overnight. Yellow–orange prism crystals were observed and were suitable for X–ray crystallography. The compound was filtered using a closed frit and washed with diethyl ether. Yield: 0.852 g, 67.3%.

**$^1$H–NMR (400 MHz, $d_6$–DMSO) [ppm]:** 7.53 (s, 5H, [$(CH_3)_3N–CH_2(C_6H_5)]^+$), 6.59 (s, 3H, (–S–(2,3,5,6–$CH_3$–($C_6H$))$_3$), 4.51 (s, 2H, [$(CH_3)_3N–CH_2(C_6H_5)]^+$), 3.02 (s, 9H, [$(CH_3)_3N–CH_2(C_6H_5)]^+$), 2.57 and 2.10 (s, 36H, (–S–(2,3,5,6–$CH_3$–($C_6H$))$_3$).

**$^{13}$C–NMR (100 MHz, $d_6$–DMSO) [ppm]:** 189.97 (*C*≡O); 146.31, 138.49, 131.43, 127.26 ((–S–(2,3,5,6–$CH_3$–($C_6H$))$_3$); 132.75, 130.26, 128.90, 128.27 ([$(CH_3)_3N–CH_2(C_6H_5)]^+$); 67.90 ([$(CH_3)_3N–CH_2(C_6H_5)]^+$); 51.77 ([$(CH_3)_3N–CH_2(C_6H_5)]^+$); 20.89, 20.20 ((–S–(2,3,5,6–$CH_3$–($C_6H$))$_3$).

**Electrochemistry:** $E_{½}$ ($\Delta E_p$) = 581 mV (61 mV); 1.0 mM in $CH_3CN$ vs. Ag/AgCl, oxidation.

**Unit Cell:** Triclinic, *P*–1, a = 11.980(3) Å, b = 12.114(4) Å, c = 15.508(5) Å, $\alpha$ = 107.69(3)$^o$, $\beta$ = 96.05(2)$^o$, $\gamma$ = 103.60(3)$^o$, V = 2045.7(4) Å$^3$.

**Infrared ($CH_3OH$):** $\nu_{CO}$ = 2008, 2025(sh) and 2080 cm$^{-1}$.

A light yellow prism crystal measuring 0.65 × 0.40 × 0.25 mm$^3$ was mounted using a nylon loop and centered on the X–ray beam at 100K. Crystals were grown by layering a concentrated methanol solution of [$Me_3NBz$]Cl to a methanolic solution of Li[$Ru^{II}(CO)_3(tmbt)_3$].

Crystals were grown within one day. The accurate unit cell was obtained using reflection with 2θ = 3.30 – 30.79°: a = 11.980(3) Å, b = 12.114(4) Å, c = 15.508(5) Å, α = 107.69(3)°, β = 96.05(2)°, γ = 103.60(3)°,V = 2045.7(3) Å$^3$. The structure was solved under a primitive triclinic crystal system (space group *P*–1) using 11535 reflections. The asymmetric unit consists of one molecule of the ruthenium complex and one cation. The data reduction was done using CryAlisPro and the structure refinement was done with SHELXL–97 (Sheldrick). All the non–hydrogen atoms were located by Direct Methods and were refined anisotopically by a full–matrix least–squares method. The positions of the remaining hydrogen atoms were calculated. The crystallographic parameters and atomic coordinates for this compound are located in **Table A–22**.

**Synthesis of $[Ru^{I}(CO)_3(S–2,4,6–i–Pr_3C_6H_2)]_2$**

In a 100 mL Schlenk flask, *fac*–$[Ru^{II}(CO)_3Cl_2(THF)]$ (0.300 g , 0.914 mmol) was dissolved in methanol (10 mL). In a separate 100 mL Schlenk flask, 2,4,6–triisopropylbenzenethiol (1.08 g, 4.57 mmol) and lithium wire (0.32 g, 4.57 mmol) were added to and stirred until all the reagents had dissolved in 20 mL of methanol. The thiolate solution was transferred, dropwise, to the ruthenium *via* cannula. The solution was stirred at room temperature for five hours. A partial vacuum was placed on the reaction flak and air was introduced to the system, which this process was performed five times. The solution was allowed to stand overnight. Orange crystals were observed and were identified as triisopropylbenzenedisulfide by x–ray crystallography. The orange crystals were filtered using an open frit. The filtrate was placed in a 100 mL rotovap flask and the solvent was removed which resulted in a yellow–orange solid and finally the solid was redissolved in hexanes (10 mL). The solution was columned using a 30 mL open frit as a column packed with neutral alumina. The column was prewashed with pentane to which the yellow–orange solution was columned, which resulted in a yellow solution to be collected. The solution was concentrated and placed in a –20°C freezer. Yellow needle plate crystals were collected and washed with diethyl ether. The crystals were suitable for x–ray crystallography however insufficient amount of product was formed to get an accurate yield.

**Infrared (pentane):** $\nu_{CO}$ = 1961, 1973 and 2038 cm$^{-1}$.

**Unit Cell:** Monoclinic, $P2_1/c$, a = 13.490(3) Å, b = 27.608(6) Å, c = 10.713(2) Å, α = γ = 90°, β = 110.167(2)°, V = 3745.25(4) Å$^3$.

A light yellow prism crystal measuring 0.30 × 0.30 × 0.20 $mm^3$ was mounted using a nylon loop and centered on the X–ray beam at 100 K. Crystals were grown by slow evaporation of a concentrated pentane solution. Crystals were grown within one week. The accurate unit cell was obtained using reflection with $2\theta = 3.22 – 29.50^o$: a = 13.4896(3) Å, b = 27.6084(6) Å, c = 10.7129(2) Å, $\alpha = \gamma = 90^o$, $\beta = 110.167(2)^o$, V = 3745.18(14) $Å^3$. The structure was solved under a primitive monoclinic crystal system (space group $P2_1/c$) using 9279 reflections. The asymmetric unit consists of one molecule of the ruthenium complex. The data reduction was done using CryAlisPro and the structure refinement was done with SHELXL–97 (Sheldrick). All the non–hydrogen atoms were located by Direct Methods and were refined anisotopically by a full–matrix least–squares method. The positions of the remaining hydrogen atoms were calculated. The crystallographic parameters and atomic coordinates for this compound are located in **Table A–23**.

**Attempted Synthesis of *fac*–[$Ru^{II}(CO)_3$(POS2)]**

In a 100 mL Schlenk flask, *fac*–[$Ru^{II}(CO)_3Cl_2$(THF)] (0.500 g, 1.52 mmol) was dissolved in 15 mL of methanol. In a separate 100 mL Schlenk flask, $Li_2$POS2 was generated in a methanol (20 mL) solution using lithium wire (0.23 g, 3.35 mmol) and $H_2$POS2 (0.574 g, 1.68 mmol). The lithium–POS2 solution was allowed to stir until all the reagents had dissolved. The $Li_2$POS2 and metal solutions were cooled to –78 $^oC$ using a dry ice/acetone bath. The metal solution was added to the $Li_2$POS2 solution, dropwise, which resulted in the solution turning from colorless to orange. The mixture was stirred for three hours. The dry ice/acetone bath was removed and the solvent was immediately removed *in vacuo*. The resulting orange solid was observed and extracted using a 2:1 hexanes/diethyl ether solution. The solution was stirred for one hour and filtered through a closed frit packed with celite. The solvent was removed to afford the pure orange product. Yield: 0.522 g, 65.3%.

**Infrared ($CH_2Cl_2$):** $\nu_{CO}$ = 1984, 2048 and 2111 $cm^{-1}$.

## 5.3 Results and Discussion

The synthesis of the compounds reported in this chapter is shown in **Figure V–3**.

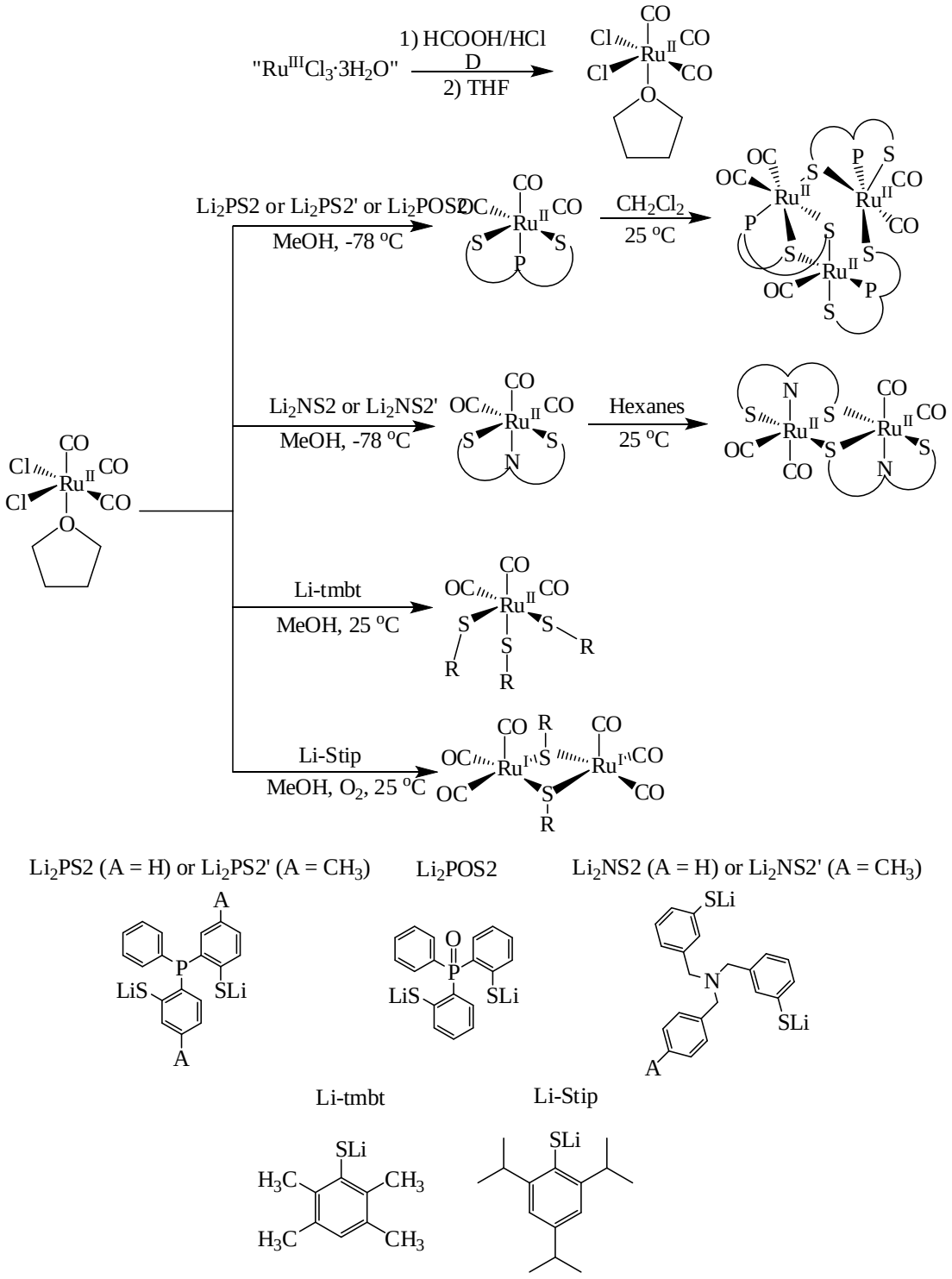


**Figure V–3. Overall scheme of synthesized ruthenium complexes.**

### 5.3.1 Synthesis and Characterization of the Starting Material, *fac*–[$Ru^{II}(CO)_3Cl_2(THF)$]

In the past, several ruthenium carbonyl compounds were known; however, only a few on these compounds contained thiolate ligands.[6,16–17] In an attempt to generate ruthenium–carbonyl thiolate compounds, *fac*–[$Ru^{II}(CO)_3Cl_2(THF)$] was prepared as the starting material. The *fac*–[$Ru^{II}(CO)_3Cl_2(THF)$] synthesis was modified from the literature procedure. According to the literature[15], "$Ru^{III}Cl_3 \bullet 3H_2O$" should be refluxed using a 1:1 formic acid/hydrochloric acid solution under a dinitrogen atmosphere. This acidic solution should be refluxed for twenty–four, which should produce a gold colored solution. However, all attempts made to follow this literature procedure were unsuccessful. The solution did not change color, despite refluxing for several days. The discovery of the modified procedure was accidental when the spectrum popped off during the first night of heating. The next day, the acidic solution had changed color from a deep red to yellow–orange. The reaction continued to reflux until a gold solution was observed. It was concluded that the oxygen from the air aided in the reaction. Several attempts were performed to corroborate this theory and all attempts were proven successfully.

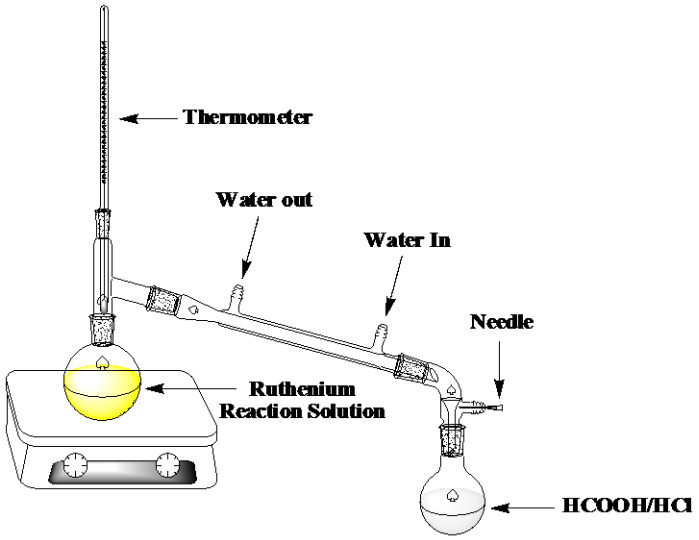


**Figure V–4. Simple distillation apparatus for *fac*–[$Ru^{II}(CO)_3Cl_2(THF)$].**

After refluxing, the solution was transferred from a heating mantle to an oil bath and a simple distillation apparatus was used (**Figure V–4**), i.e. heating mantle cannot be used during distillation due to direct heating of the resulting solid, which caused decomposition of the product. The purpose of adding the needle to the distillation adaptor was to create a partial vacuum while distilling the formic and hydrochloric acids. Upon completion of the distillation,

the resulting yellow solid was cooled to room temperature and impurities were removed by dissolving the solid in reagent grade acetone followed by filtration. The solvent was removed either by use of rotary evaporator or *in vacuo*. The resulting yellow solid was redissolved using distilled THF and a white crystalline solid was observed. Hexanes were added to the solution to precipitate additional amounts of the desired product. The IR spectrum of *fac*–$[Ru^{II}(CO)_3Cl_2(THF)]$ is shown in **Figure V–5**. The IR shows two peaks, at 2066 and 2138 $cm^{-1}$, that were assigned to the facial CO ligands.

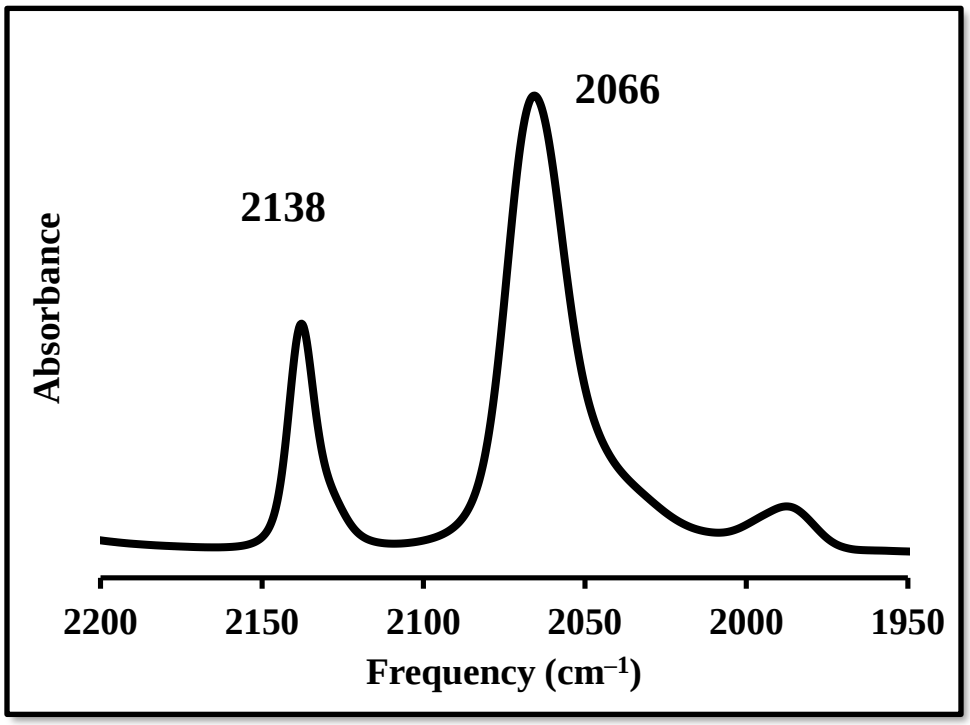


**Figure V–5. Infrared spectrum of *fac*–$[Ru^{II}(CO)_3Cl_2(THF)]$ in MeOH.**

The $^1H$–NMR for *fac*–$[Ru^{II}(CO)_3Cl_2(THF)]$ shows a singlet at 5.07 ppm and a multiplet at 4.15 ppm, which corresponds to the bound tetrahydrofuran ligand (**Figure V–6**).

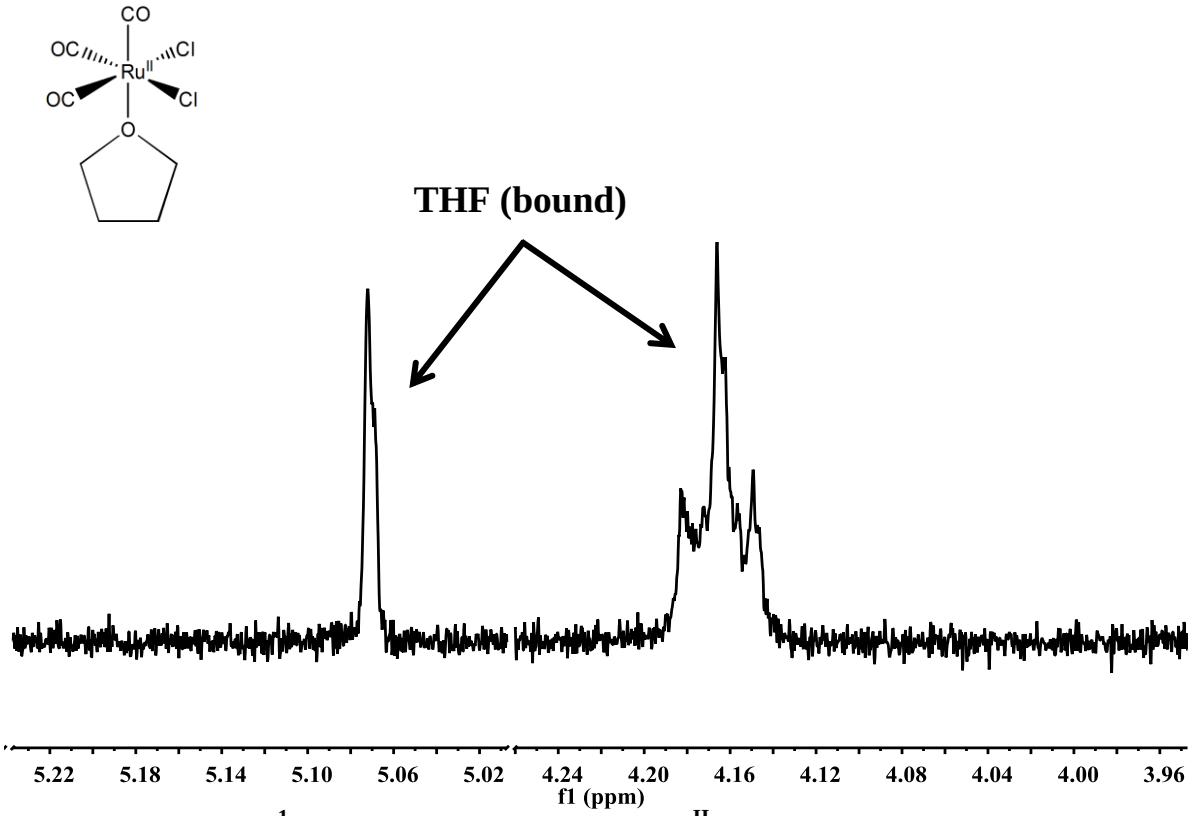


**Figure V–6. $^{1}$H–NMR spectrum of *fac*–[Ru$^{II}$(CO)$_3$Cl$_2$(THF)] in CD$_3$CN.**

The $^{13}$C–NMR for *fac*–[Ru$^{II}$(CO)$_3$Cl$_2$(THF)] shows two carbonyl peaks at 187.44 and 184.12 ppm (**Figure V–7**). The carbonyl signals split into two peaks because two of the three carbonyl ligands are *trans* to the chloride ligands while the third carbonyl is *trans* to the THF. The peak at 184.12 ppm was assigned to the carbonyl ligands *trans* to the chloride while the 187.44 ppm peak was assigned to the carbonyl ligand *trans* to the THF. The carbon peaks for the THF ligand were not assigned due to the long exposure time required to collect the $^{13}$C–NMR data, which resulted in the THF ligand no longer being bound to the ruthenium. This was confirmed by observing free THF in the $^{13}$C–NMR spectrum.

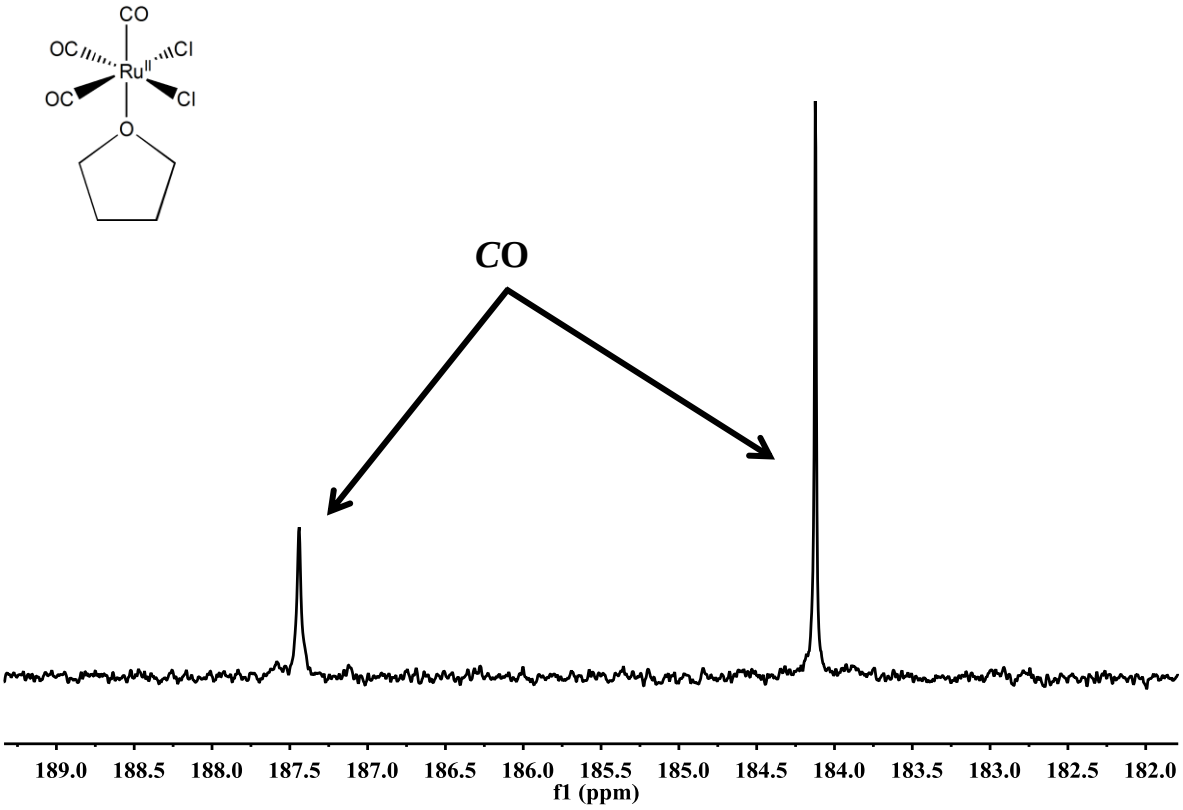


**Figure V–7. $^{13}$C–NMR spectrum of *fac*–[$Ru^{II}(CO)_3Cl_2(THF)$] in $CD_3CN$.**

The X–ray structure of *fac*–[$Ru^{II}(CO)_3Cl_2(THF)$] confirmed a ruthenium(II) compound which displays a slightly distorted octahedral geometry with three carbonyl ligands in the facial arrangement, two chloride ligands and the THF *trans* to one of the carbonyls. The general structure of the ruthenium compound is shown in **Figure V–8**. In 1996, the X–ray structure was first reported by Gray *et al*.[27] This compound was initially reported as [$Ru^{II}(CO)_3Cl_2$]•0.75 THF, based on elemental analysis.[28] Obtaining the X–ray structure was the only conclusive way to determine the amount of THF present in the compound. Crystals, suitable for X–ray crystallography, were grown from the reaction solution of THF layered with hexanes at room temperature. The Ru–$C_{avg}$, Ru–$Cl_{avg}$ and C–$O_{avg}$ bond distances are 1.9073(5) Å, 2.3995(2) Å and 1.1275(8) Å, respectively. The Ru(1)–O(4) bond distance was measured to be 2.146(4) Å. The distorted octahedral geometry was indicated by the dihedral angles between the four least–squares planes through the ruthenium and the coordinating atoms (91.0$^o$, 88.1$^o$, 89.6$^o$ and 88.2$^o$). The crystal structure was solved under a monoclinic crystal system $P2_1/n$. The ruthenium structure is located on a general position. The important geometrical parameters of *fac*–

$[Ru^{II}(CO)_3Cl_2(THF)]$, reported in this dissertation, are compared with Gray's *fac*–$[Ru^{II}(CO)_3Cl_2(THF)]$ (**Table V–1**). Comparison of crystallographic data parameters are shown in **Table V–2**. The crystallographic data of both structures are within experimental error (~2%).

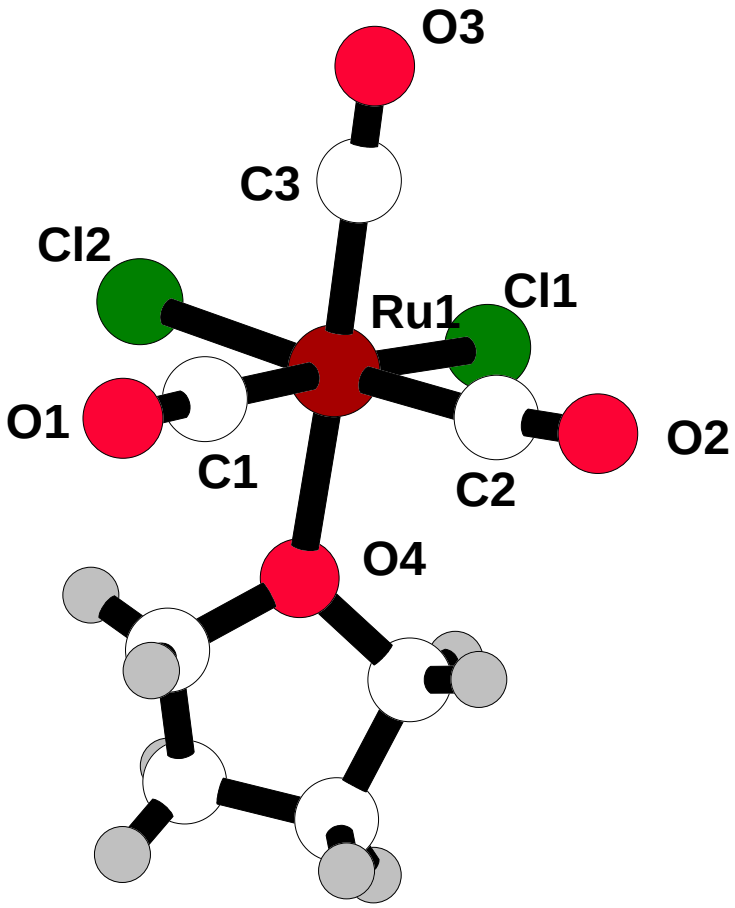


**Figure V–8. X–ray structure of *fac*–$[Ru^{II}(CO)_3Cl_2(THF)]$.**

| **Table V–1. Comparison of Selective Crystallographic Data for *fac*–[$Ru^{II}(CO)_3Cl_2(THF)$].** | | | |
|---|---|---|---|
| **Gray[27]** | | | |
| **Bond Distances (Å)** | | **Bond Angles (°)** | |
| Ru(1) – C(1) | 1.916(6) | C(1) – Ru(1) – C(2) | 94.2(3) |
| Ru(1) – C(2) | 1.918(6) | C(2) – Ru(1) – C(3) | 92.5(3) |
| Ru(1) – C(3) | 1.873(6) | C(1) – Ru(1) – O(4) | 93.5(2) |
| Ru(1) – O(4) | 2.146(4) | C(2) – Ru(1) – O(4) | 89.7(2) |
| Ru(1) – Cl(1) | 2.402(2) | C(3) – Ru(1) – O(4) | 176.1(2) |
| Ru(1) – Cl(2) | 2.390(2) | C(1) – Ru(1) – Cl(1) | 176.9(2) |
| C(1) – O(1) | 1.111(8) | C(2) – Ru(1) – Cl(1) | 87.8(2) |
| C(2) – O(2) | 1.124(8) | C(3) – Ru(1) – Cl(1) | 87.9(2) |
| C(3) – O(3) | 1.127(8) | C(1) – Ru(1) – Cl(2) | 87.4(2) |
| | | C(2) – Ru(1) – Cl(2) | 176.4(2) |
| | | C(3) – Ru(1) – Cl(2) | 90.8(2) |
| | | O(4) – Ru(1) – Cl(1) | 89.0(1) |
| | | O(4) – Ru(1) – Cl(2) | 86.9(1) |
| | | Ru(1) – C(1) – O(1) | 173.2(6) |
| | | Ru(1) – C(2) – O(2) | 175.9(6) |
| | | Ru(1) – C(3) – O(3) | 177.5(5) |
| **This Work** | | | |
| **Bond Distances (Å)** | | **Bond Angles (°)** | |
| Ru(1) – C(1) | 1.9168(14) | C(1) – Ru(1) – C(2) | 94.50(5) |
| Ru(1) – C(2) | 1.9153(13) | C(2) – Ru(1) – C(3) | 89.44(5) |
| Ru(1) – C(3) | 1.8899(13) | C(1) – Ru(1) – O(4) | 90.74(5) |
| Ru(1) – O(4) | 2.1356(9) | C(2) – Ru(1) – O(4) | 94.73(4) |
| Ru(1) – Cl(1) | 2.3946(3) | C(3) – Ru(1) – O(4) | 174.82(5) |
| Ru(1) – Cl(2) | 2.4044(3) | C(1) – Ru(1) – Cl(1) | 176.85(4) |
| C(1) – O(1) | 1.1287(16) | C(2) – Ru(1) – Cl(1) | 86.57(4) |
| C(2) – O(2) | 1.1268(16) | C(3) – Ru(1) – Cl(1) | 90.97(4) |
| C(3) – O(3) | 1.1269(16) | C(1) – Ru(1) – Cl(2) | 87.95(4) |
| | | C(2) – Ru(1) – Cl(2) | 176.63(4) |
| | | C(3) – Ru(1) – Cl(2) | 88.17(4) |
| | | O(4) – Ru(1) – Cl(1) | 86.21(3) |
| | | O(4) – Ru(1) – Cl(2) | 87.54(3) |
| | | Ru(1) – C(1) – O(1) | 176.45(12) |
| | | Ru(1) – C(2) – O(2) | 173.60(11) |
| | | Ru(1) – C(3) – O(3) | 178.36(12) |

| Table V–2. Comparison of Crystallographic Data Parameters for *fac*–[$Ru^{II}(CO)_3Cl_2(THF)$]. | | |
|---|---|---|
| **Data** | **Gray[27]** | **This Work** |
| Empirical Formula | $C_7H_8Cl_2O_4Ru$ | $C_7H_8Cl_2O_4Ru$ |
| Formula Weight | 328.12 | 328.10 |
| Temperature (K) | 298(2) | 100(2) |
| Crystal System | Monoclinic | Monoclinic |
| Space Group | $P2_1/n$ | $P2_1/n$ |
| Unit Dimensions | | |
| a (Å) | 6.0904(9) | 5.968(8) |
| b (Å) | 18.414(4) | 18.200(3) |
| c (Å) | 9.940(2) | 9.787(1) |
| $\alpha$ ($^o$) | 90 | 90 |
| $\beta$ ($^o$) | 96.999(12) | 96.891(1) |
| $\gamma$ ($^o$) | 90 | 90 |
| Volume ($Å^3$) | 1106.5(4) | 1055.4(5) |
| Density (calculated) (g $cm^{-3}$) | 1.97 | 2.065 |
| Z | 4 | 4 |
| Absorption Coefficient ($mm^{-1}$) | 1.863 | 1.975 |
| R | 0.039 | 0.0181 |
| $R_w$ | 0.048 | 0.0413 |

### 5.3.2 Synthesis and Characterization of Ruthenium Carbonyl complexes with the [PS2] and [PS2'] Ligands

The *fac*–[$Fe^{II}(CO)_3$(PS2')] compound was previously synthesized and structurally characterized by Doris Melgarejo.[19] It was prepared by the reaction of $Fe^{II}(CO)_4X_2$ (where X = $Br^-$ or $I^-$) with one equivalent of $Li_2$PS2' at –78$^o$C. When the reactions were done at room temperature, dimeric compounds were obtained. Unsuccessful attempts to synthesize ruthenium–carbonyl compounds using [PS] ligands were first made by Janet Haff.[18] In an attempt to prepare the Ru analog, *fac*–[$Ru^{II}(CO)_3$(PS2')], *fac*–[$Ru^{II}(CO)_3Cl_2$(THF)] was used as the starting material in place of $Ru^{II}(CO)_4X_2$ due to its stability and ease of synthesis. The reaction of [$Ru^{II}(CO)_3Cl_2$(THF)] with one equivalent of $Li_2$PS2 or $Li_2$PS2' in MeOH at –78$^o$C generated *fac*–[$Ru^{II}(CO)_3$(PS2)] and *fac*–[$Ru^{II}(CO)_3$(PS2')]. Reactions were monitored by infrared spectroscopy. The IR spectra, in methanol, for *fac*–[$Ru^{II}(CO)_3$(PS2)] and *fac*–[$Ru^{II}(CO)_3$(PS2')] are illustrated in **Figure V–9**. The desired products, *fac*–[$Ru^{II}(CO)_3$(PS2)] and *fac*–[$Ru^{II}(CO)_3$(PS2')] were purified using the same purification steps as described by Melgarejo for

the Fe analog. The reaction solvent, methanol, was removed *in vacuo* and the resulting yellow solid was partially redissolved using a 2:1 hexanes/diethyl ether solution. The solution was kept stirring at 0 $^{o}$C for several hours, then filtered and solvent was removed *in vacuo*. The IR spectra, in methylene chloride of the purified products, are illustrated in **Figure V–10**. The spectra are very similar to those of the crystallographically characterized *fac*–[$Fe^{II}(CO)_3$(PS2')] and are consistent with a facial $M(CO)_3$ with $C_s$ symmetry.

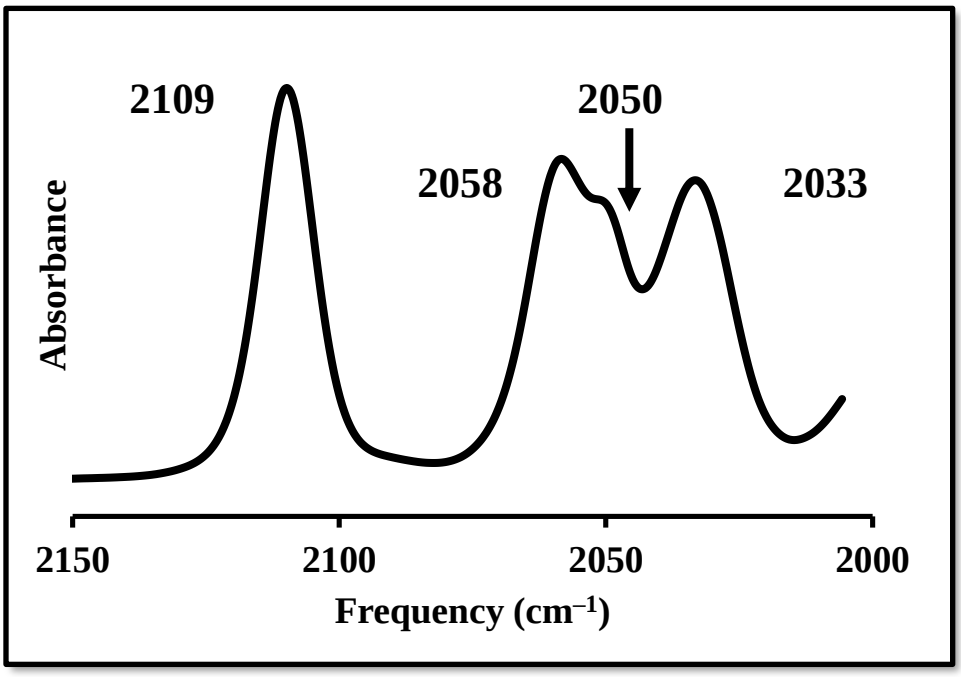


**Figure V–9. Infrared spectrum of *fac*–[$Ru^{II}(CO)_3$(PS2')] in MeOH.**

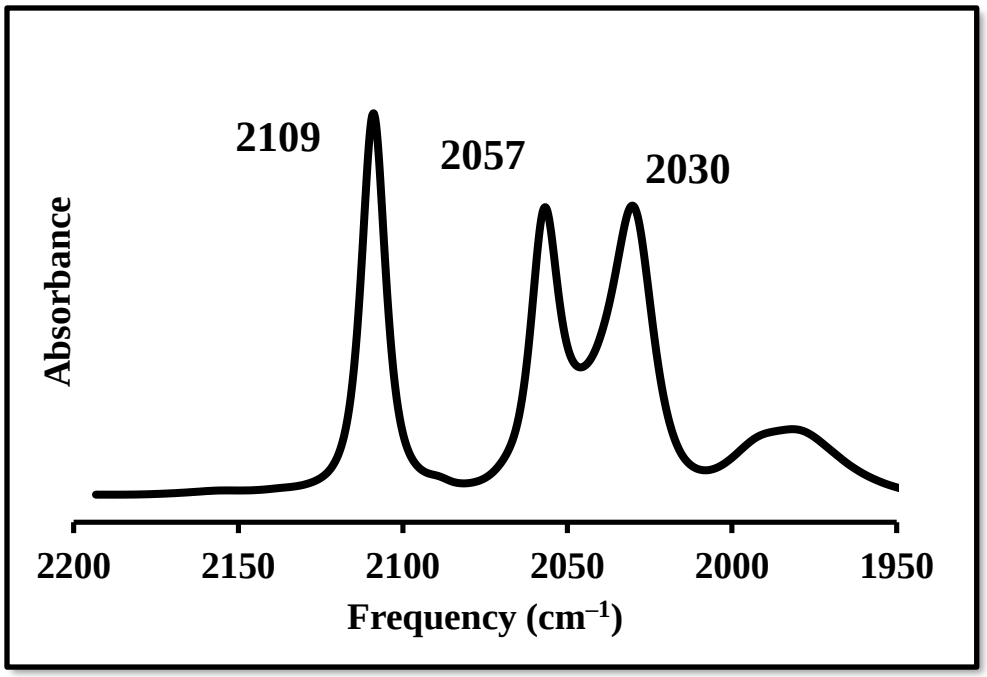


**Figure V–10. Infrared spectrum of *fac*–[$Ru^{II}(CO)_3$(PS2')] in $CH_2Cl_2$.**

The *fac*–[$Ru^{II}(CO)_3$(PS2)] and *fac*–[$Ru^{II}(CO)_3$(PS2')] compounds are thermally unstable at room temperature in the solid–state and especially in solution. The compounds must be kept in a –20$^{o}$C freezer under a dinitrogen atmosphere. The compounds showed changes in color, i.e. yellow to orange, when left at room temperature for three weeks in the solid state. This reaction was accelerated when the *fac*–[$Ru^{II}(CO)_3$(PS2')] was dissolved in methylene chloride and left for one week. The infrared spectrum began to show new multiple peaks (**Figure V–11**). Infrared spectrum was monitored for several days and upon reaction completion, diethyl ether was slowly added to the solution to form large orange prism crystals, see section 5.3.3. The compound was confirmed to be a ruthenium trimer containing five carbonyls and three [PS2'] ligands, [$Ru^{II}_3(CO)_5$(PS2')$_3$]. Two ruthenium metal centers showed to have two carbonyl ligands each while the third ruthenium metal center had one carbonyl. This agrees with the infrared spectrum showing that the four carbonyls, on the two metal centers, are in the *cis* arrangements due to the split of the symmetrical and asymmetrical peaks. The ruthenium trimer was found to be thermally stable for a period of three months, as shown *via* infrared spectra taken at periodic intervals.

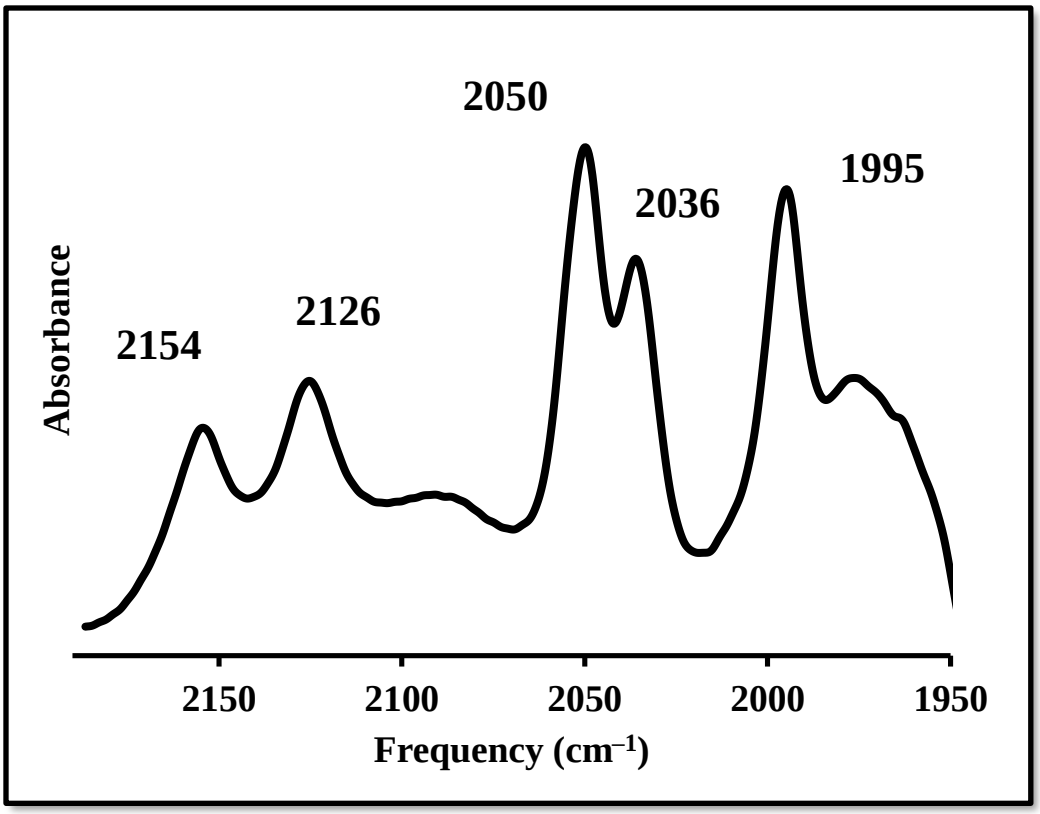


**Figure V–11. Infrared spectrum of $Ru^{II}_3(CO)_5(PS2')_3$ in $CH_2Cl_2$.**

The carbonyl stretching frequencies for the *fac*–[$Ru^{II}(CO)_3Cl_2(THF)$] are shown to be at higher energy than the *fac*–[$Ru^{II}(CO)_3(PS2)$] (**Figure V–12**), *fac*–[$Ru^{II}(CO)_3(PS2')$] and *fac*–[$Ru^{II}(CO)_3(POS2)$] (**Figure V–13**). Since chloride ligands are poorer sigma donors than thiolate ligands there is less electron density being donated to the transition metal center resulting in a decrease in π–backbonding to the carbonyl ligand, which would strengthen the C≡O bond. The IR peaks for all the complexes, including the iron, are summarized in **Table V–3**.

Comparing the infrared spectra of *fac*–[$Fe^{II}(CO)_3(PS2')$] and *fac*–[$Ru^{II}(CO)_3(PS2')$], in $CH_2Cl_2$, the carbonyl stretching frequencies are at higher energy for the ruthenium compound than for the iron. This indicates in this series of compounds that Fe is a better π–donor than Ru.

The very small shifts to lower energy in the infrared peaks for *fac*–[$Ru^{II}(CO)_3(PS2')$] compared *fac*–[$Ru^{II}(CO)_3(PS2)$] are consistent with the electron donation of the methyl groups which are found *para* to the thiolate groups.

| Table V–3. Overall Infrared Data for $[M^{II}(CO)_3(L)]$ (where M = Fe and Ru;L = PS2, PS2' and POS2) | | |
|---|---|---|
| **Compound** | **Solvent** | **$\nu_{CO}$ ($cm^{-1}$)** |
| *fac*–$Fe^{II}(CO)_3$(PS2') | MeOH | 2024, 2043, 2088 |
| *fac*–$Ru^{II}(CO)_3$(PS2') | MeOH | 2033, 2050(sh), 2058, 2109 |
| *fac*–$Ru^{II}(CO)_3$(PS2) | MeOH | 2034, 2050(sh), 2058, 2110 |
| *fac*–$Ru^{II}(CO)_3$(PS2') | $CH_2Cl_2$ | 2030, 2057, 2109 |
| *fac*–$Ru^{II}(CO)_3$(PS2) | $CH_2Cl_2$ | 2032, 2059, 2110 |
| *fac*–$Ru^{II}(CO)_3$(POS2) | $CH_2Cl_2$ | 1984, 2048, 2111 |

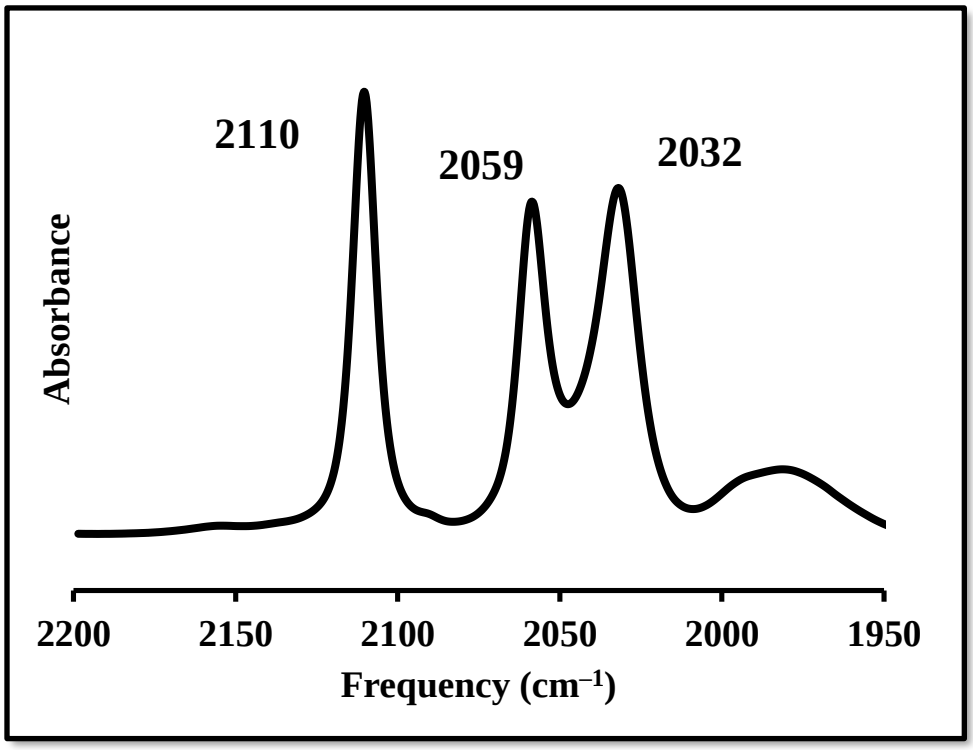


**Figure V–12. Infrared spectrum of *fac*–$[Ru^{II}(CO)_3(PS2)]$ in $CH_2Cl_2$.**

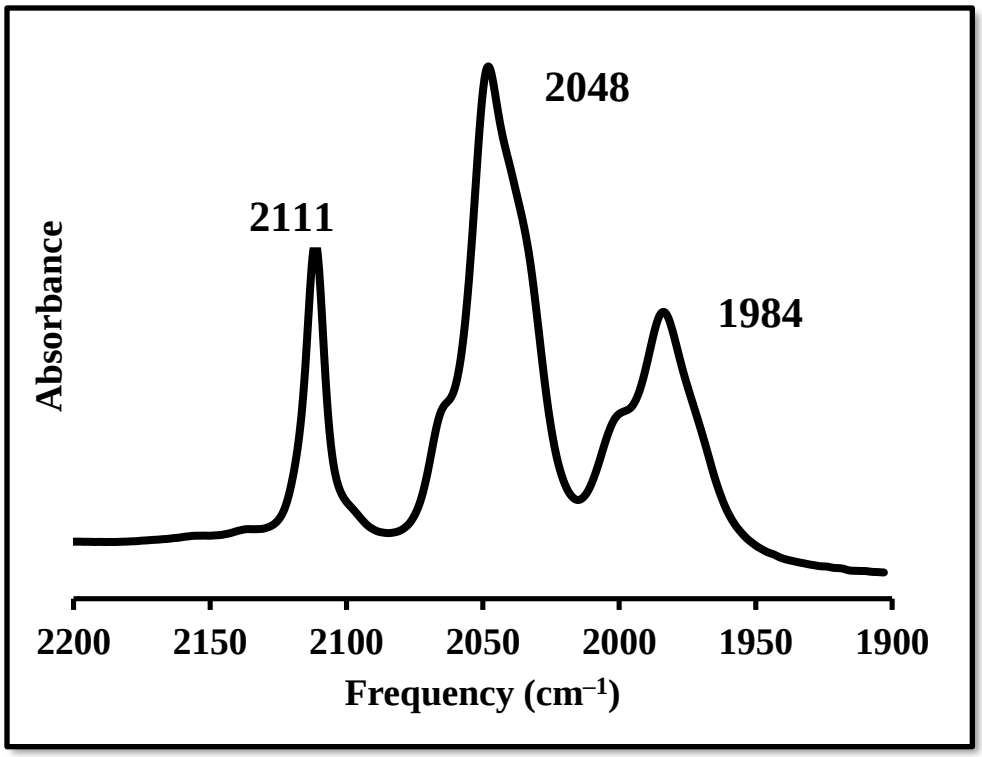


**Figure V–13. Infrared spectrum of *fac*–[$Ru^{II}(CO)_3$(POS2)] in $CH_2Cl_2$.**

### 5.3.3 X–ray Structures of *fac*–[$Ru^{II}(CO)_3$(PS2')], *fac*–[$Ru^{II}(CO)_3$(PS2)] and [$Ru^{II}_3(CO)_5$(PS2')$_3$]

The X–ray structure of *fac*–[$Ru^{II}(CO)_3$(PS2)] confirmed a ruthenium(II) compound which displays a slightly distorted octahedral geometry with three carbonyl ligands in the facial arrangement, which was also confirmed by infrared spectroscopy, and one [PS2] ligand. The structure of the ruthenium compound is shown in **Figure V–14**. Crystals, suitable for X–ray crystallography, were grown from a concentrated hexanes solution at –20$^o$C. The crystal structure was solved under a triclinic crystal system *P*–1(P1bar). The structure has non–crystallographic $C_s$ symmetry. This is the first example of a monomeric ruthenium–carbonyl complex with the [PS2] ligand while other examples, such as the iron compounds, were dimers.[19,29] The Ru–$C_{avg}$, Ru–$S_{avg}$ and C–$O_{avg}$ bond distances are 1.937(18) Å, 2.428(5) Å and 1.135(2) Å respectively. The Ru(1)–P(1) bond distance was measured to be 2.320(4) Å. The distorted octahedral geometry was indicated by the dihedral angles between the four least–squares planes through the ruthenium and the coordinating atoms (88.5$^o$, 89.2$^o$, 95.9$^o$ and 97.4$^o$). Selective bond distances and angles for *fac*–[$Ru^{II}(CO)_3$(PS2)] are summarized in **Table V–4**.

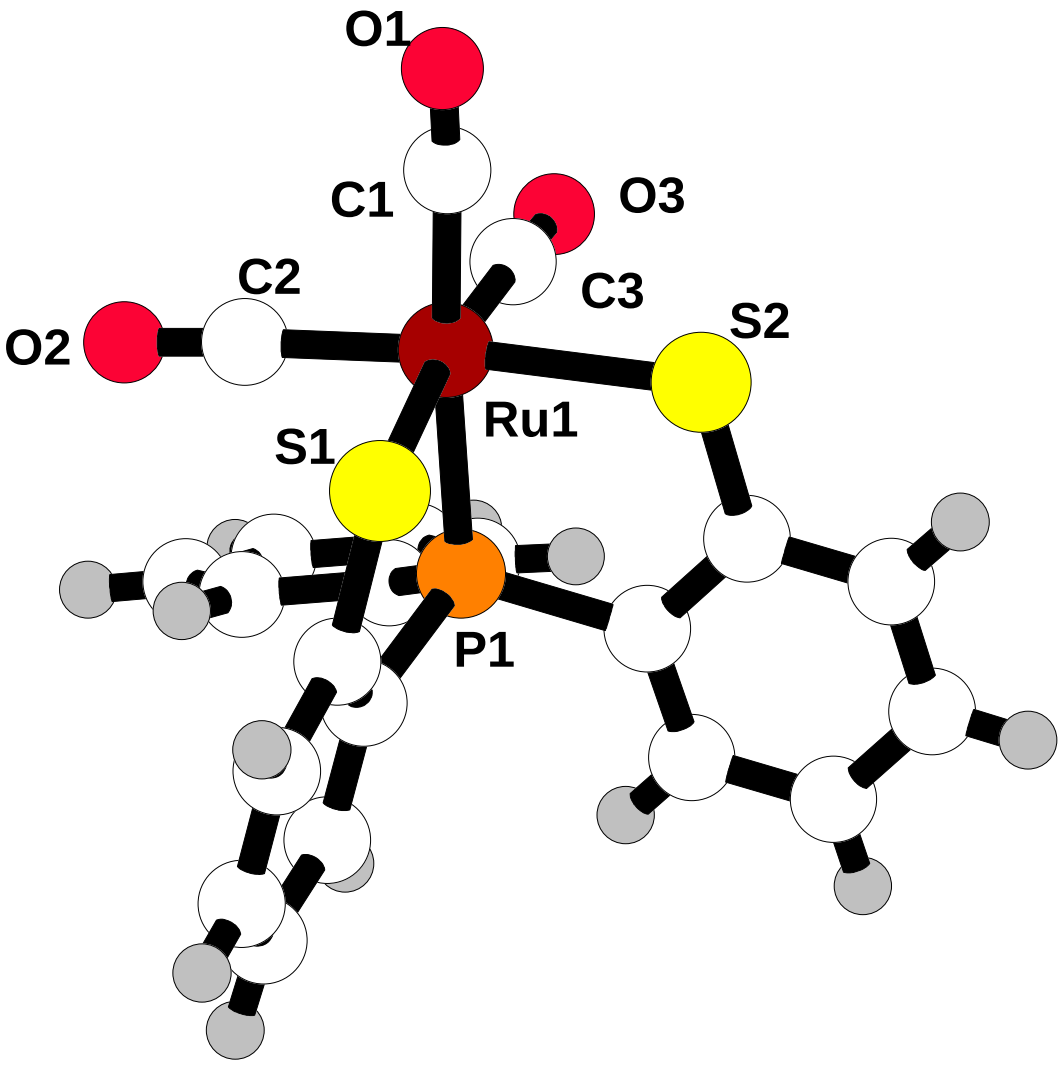


**Figure V–14. X–ray structure of *fac*–[$Ru^{II}(CO)_3$(PS2)].**

| Table V–4. Selective Crystallographic Data for *fac*–[$Ru^{II}(CO)_3$(PS2)]. | | | |
|---|---|---|---|
| **Bond Distances (Å)** | | **Bond Angles (°)** | |
| Ru(1) – C(1) | 2.008(17) | C(1) – Ru(1) – C(2) | 94.9(7) |
| Ru(1) – C(2) | 1.900(19) | C(1) – Ru(1) – C(3) | 96.7(6) |
| Ru(1) – C(3) | 1.904(17) | C(2) – Ru(1) – C(3) | 96.7(6) |
| Ru(1) – S(1) | 2.429(4) | C(1) – Ru(1) – S(1) | 89.2(4) |
| Ru(1) – S(2) | 2.426(5) | C(2) – Ru(1) – S(1) | 86.3(4) |
| Ru(1) – P(1) | 2.320(4) | C(3) – Ru(1) – S(1) | 172.3(5) |
| C(1) – O(1) | 1.100(19) | C(1) – Ru(1) – S(2) | 89.3(6) |
| C(2) – O(2) | 1.15(2) | C(2) – Ru(1) – S(2) | 175.1(4) |
| C(3) – O(3) | 1.155(19) | C(3) – Ru(1) – S(2) | 83.9(6) |
| | | C(1) – Ru(1) – P(1) | 170.8(5) |
| | | C(2) – Ru(1) – P(1) | 90.5(4) |
| | | C(3) – Ru(1) – P(1) | 89.9(4) |
| | | S(1) – Ru(1) – P(1) | 83.72(13) |
| | | S(2) – Ru(1) – P(1) | 85.09(15) |
| | | S(1) – Ru(1) – S(2) | 91.20(15) |
| | | Ru(1) – C(1) – O(1) | 176.4(17) |
| | | Ru(1) – C(2) – O(2) | 177.3(13) |
| | | Ru(1) – C(3) – O(3) | 177.3(12) |

The x–ray structure of *fac*–[$Ru^{II}(CO)_3$(PS2')] (**Figure V–15**) was virtually identical to, but not isomorphous with, *fac*–[$Ru^{II}(CO)_3$(PS2)]. Crystals, suitable for X–ray crystallography, were grown from a concentrated hexanes solution at –20°C. The crystal structure was solved using the monoclinic crystal system *C*2/*c*. The structure has non–crystallographic $C_s$ symmetry. The ruthenium structure is located on a general position. The Ru–$C_{avg}$, Ru–$S_{avg}$ and C–$O_{avg}$ bond distances are 1.938(2) Å, 2.431(5) Å and 1.133(2) Å, respectively. The Ru(1)–P(1) bond distance was measured to be 2.327(5) Å. The distorted octahedral geometry was indicated by the dihedral angles between the four least–squares planes through the ruthenium and the coordinating atoms (85.1°, 89.3°, 96.6° and 95.5°). Selective bond distances and angles for *fac*–[$Ru^{II}(CO)_3$(PS2')] are summarized in **Table V–5**.

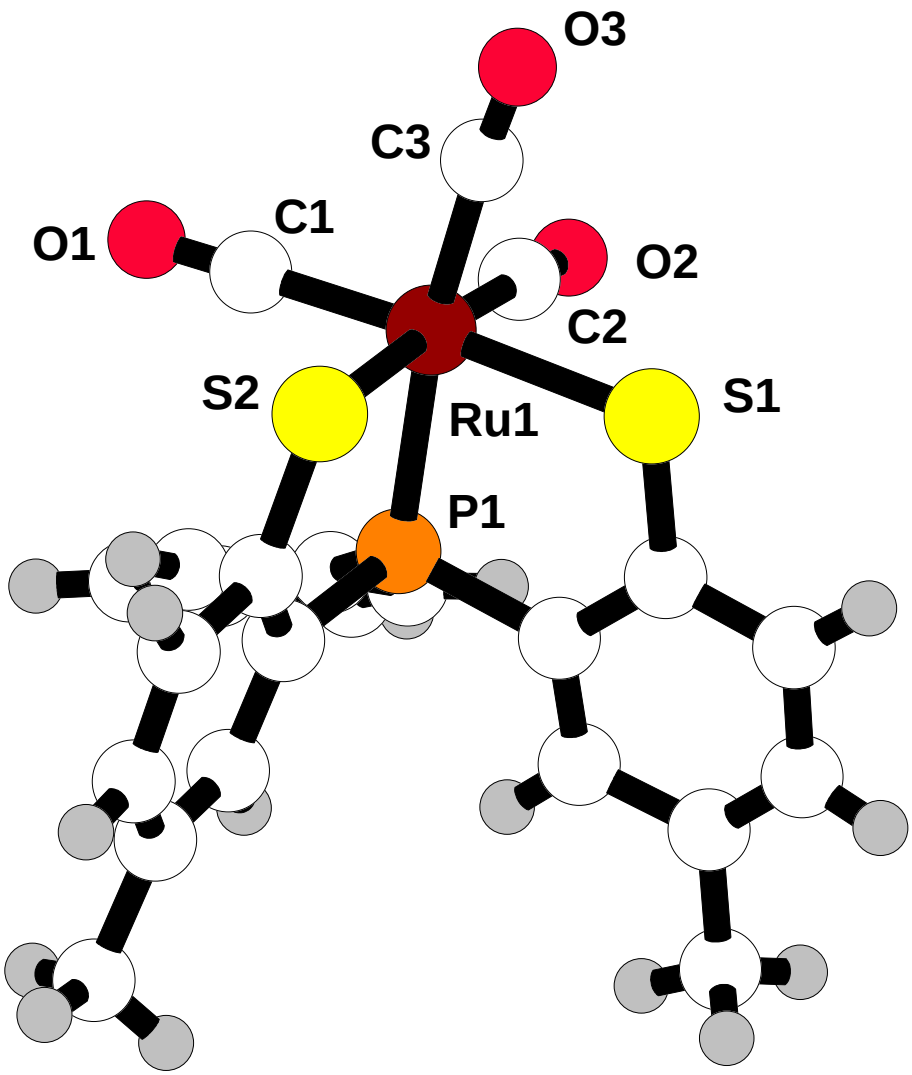


**Figure V–15. X–ray structure of *fac*–[$Ru^{II}(CO)_3$(PS2')].**

| Table V–5. Selective Crystallographic Data for *fac*–[$Ru^{II}(CO)_3$(PS2')]. | | | |
|---|---|---|---|
| **Bond Distances (Å)** | | **Bond Angles (°)** | |
| Ru(1) – C(1) | 1.926(16) | C(1) – Ru(1) – C(2) | 95.9(7) |
| Ru(1) – C(2) | 1.92(2) | C(1) – Ru(1) – C(3) | 96.5(7) |
| Ru(1) – C(3) | 1.97(2) | C(2) – Ru(1) – C(3) | 94.9(7) |
| Ru(1) – S(1) | 2.424(4) | C(1) – Ru(1) – S(1) | 175.8(5) |
| Ru(1) – S(2) | 2.437(5) | C(2) – Ru(1) – S(1) | 87.6(5) |
| Ru(1) – P(1) | 2.327(5) | C(3) – Ru(1) – S(1) | 85.4(5) |
| C(1) – O(1) | 1.110(17) | C(1) – Ru(1) – S(2) | 85.1(5) |
| C(2) – O(2) | 1.16(2) | C(2) – Ru(1) – S(2) | 175.5(5) |
| C(3) – O(3) | 1.13(2) | C(3) – Ru(1) – S(2) | 89.3(5) |
| | | C(1) – Ru(1) – P(1) | 93.2(5) |
| | | C(2) – Ru(1) – P(1) | 90.7(5) |
| | | C(3) – Ru(1) – P(1) | 168.3(4) |
| | | S(1) – Ru(1) – P(1) | 84.57(17) |
| | | S(2) – Ru(1) – P(1) | 84.89(18) |
| | | S(1) – Ru(1) – S(2) | 91.15(17) |
| | | Ru(1) – C(1) – O(1) | 179.6(17) |
| | | Ru(1) – C(2) – O(2) | 175.5(16) |
| | | Ru(1) – C(3) – O(3) | 175.4(13) |

As expected, the comparison of *fac*–[$Ru^{II}(CO)_3$(PS2)] and *fac*–[$Ru^{II}(CO)_3$(PS2')] X–ray structures shows little to no difference in the bond distances and bond angles. The average Ru–C, Ru–S and C–O are comparable.

The iron analog of *fac*–[$Ru^{II}(CO)_3$(PS2')] had been previously synthesized and structurally characterized by X–ray crystallography. The general structure of the iron compound is shown in **Figure V–16**.[19] Just as with the ruthenium complexes the iron compound shows a distorted octahedral geometry. Selective bond distances and angles for *fac*–[$Fe^{II}(CO)_3$(PS2')] are summarized in **Table V–6**. The $Fe–C_{avg}$, $Fe–S_{avg}$ and $C–O_{avg}$ bond distances are 1.771(9) Å, 2.311(3) Å and 1.152(8) Å, respectively. The average bond distances for the ruthenium compound are longer than the iron compound. This occurs because ruthenium has a larger atomic radius than iron.

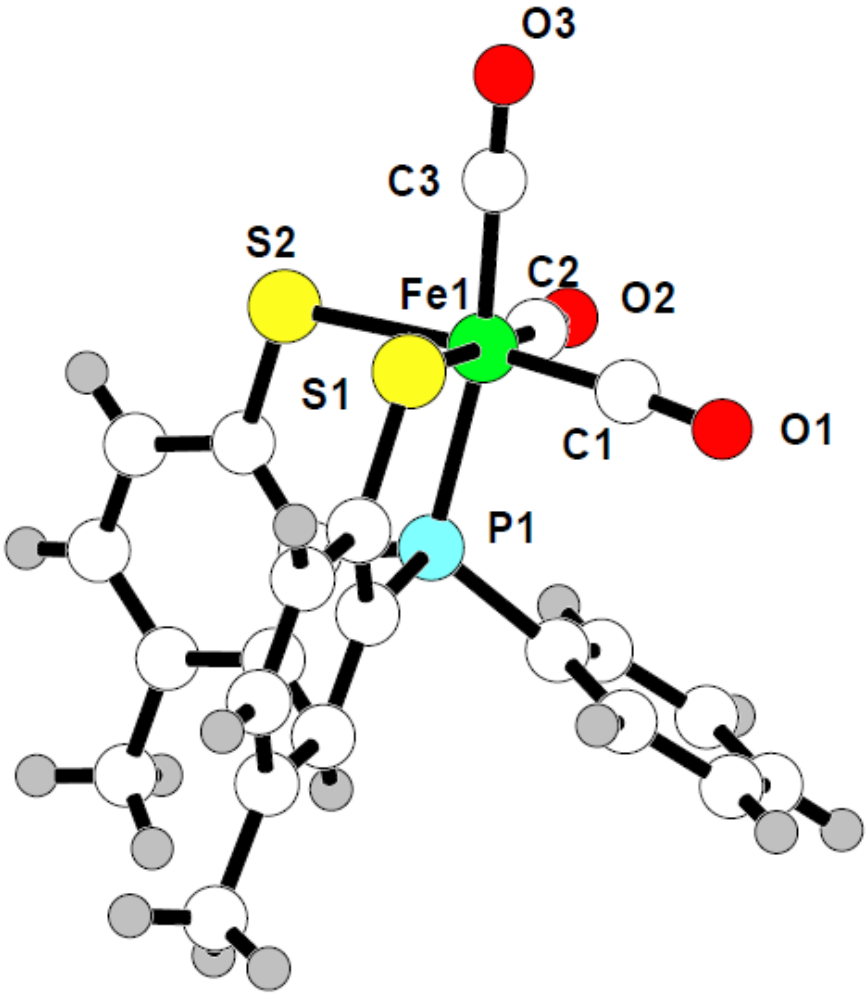


**Figure V–16. X–ray structure of *fac*–[$Fe^{II}(CO)_3$(PS2')].**

| Table V–6. Selective Crystallographic Data for *fac*–[$Fe^{II}(CO)_3$(PS2')]. | | | |
|---|---|---|---|
| **Bond Distances (Å)** | | **Bond Angles (°)** | |
| Fe(1) – C(1) | 1.734(10) | C(1) – Fe(1) – C(2) | 96.2(5) |
| Fe(1) – C(2) | 1.771(9) | C(1) – Fe(1) – C(3) | 97.2(4) |
| Fe(1) – C(3) | 1.809(8) | C(2) – Fe(1) – C(3) | 93.6(4) |
| Fe(1) – S(1) | 2.314(2) | C(1) – Fe(1) – S(1) | 84.6(3) |
| Fe(1) – S(2) | 2.307(3) | C(2) – Fe(1) – S(1) | 179.0(3) |
| Fe(1) – P(1) | 2.217(2) | C(3) – Fe(1) – S(1) | 86.9(3) |
| C(1) – O(1) | 1.169(9) | C(1) – Fe(1) – S(2) | 174.8(3) |
| C(2) – O(2) | 1.150(8) | C(2) – Fe(1) – S(2) | 86.6(3) |
| C(3) – O(3) | 1.136(8) | C(3) – Fe(1) – S(2) | 86.9(3) |
| | | C(1) – Fe(1) – P(1) | 91.4(3) |
| | | C(2) – Fe(1) – P(1) | 91.6(3) |
| | | C(3) – Fe(1) – P(1) | 169.5(3) |
| | | S(1) – Fe(1) – P(1) | 87.76(8) |
| | | S(2) – Fe(1) – P(1) | 84.24(9) |
| | | S(1) – Fe(1) – S(2) | 92.49(9) |
| | | Fe(1) – C(1) – O(1) | 175.6(10) |
| | | Fe(1) – C(2) – O(2) | 178.4(10) |
| | | Fe(1) – C(3) – O(3) | 179.0(10) |

The structure of one of the thermal decomposition products of *fac*–[$Ru^{II}(CO)_3$(PS2')] was determined by X–ray crystallography. The X–ray structure of [$Ru^{II}_3(CO)_5$(PS2')$_3$] confirmed a ruthenium(II) trimer which displays an octahedral geometry around each ruthenium center, five carbonyl ligands and three bridging [PS2′] ligands. Crystals, suitable for X–ray crystallography, were grown by layering diethyl ether over a concentrated methylene chloride solution at room temperature. The crystal structure was solved under a monoclinic crystal system $P2_1/c$. The ruthenium structure is located on a general position. The general structure of the ruthenium trimer is illustrated in **Figure V–17**. Using X–ray crystallography and infrared spectroscopy, confirms that the two sets of the carbonyl ligands are in the *cis* orientation while one carbonyl stands alone. The Ru–$C_{avg}$, Ru–$S_{non–bridged(avg)}$, Ru–$S_{bridged(avg)}$, Ru–$P_{avg}$ and C–$O_{avg}$ bond distances are 1.902(10) Å, 2.434(2) Å, 2.464(2) Å and 1.134(12) Å, respectively. Selective bond distances and angles for [$Ru^{II}_3(CO)_5$(PS2')$_3$] are summarized in **Table V–7**.

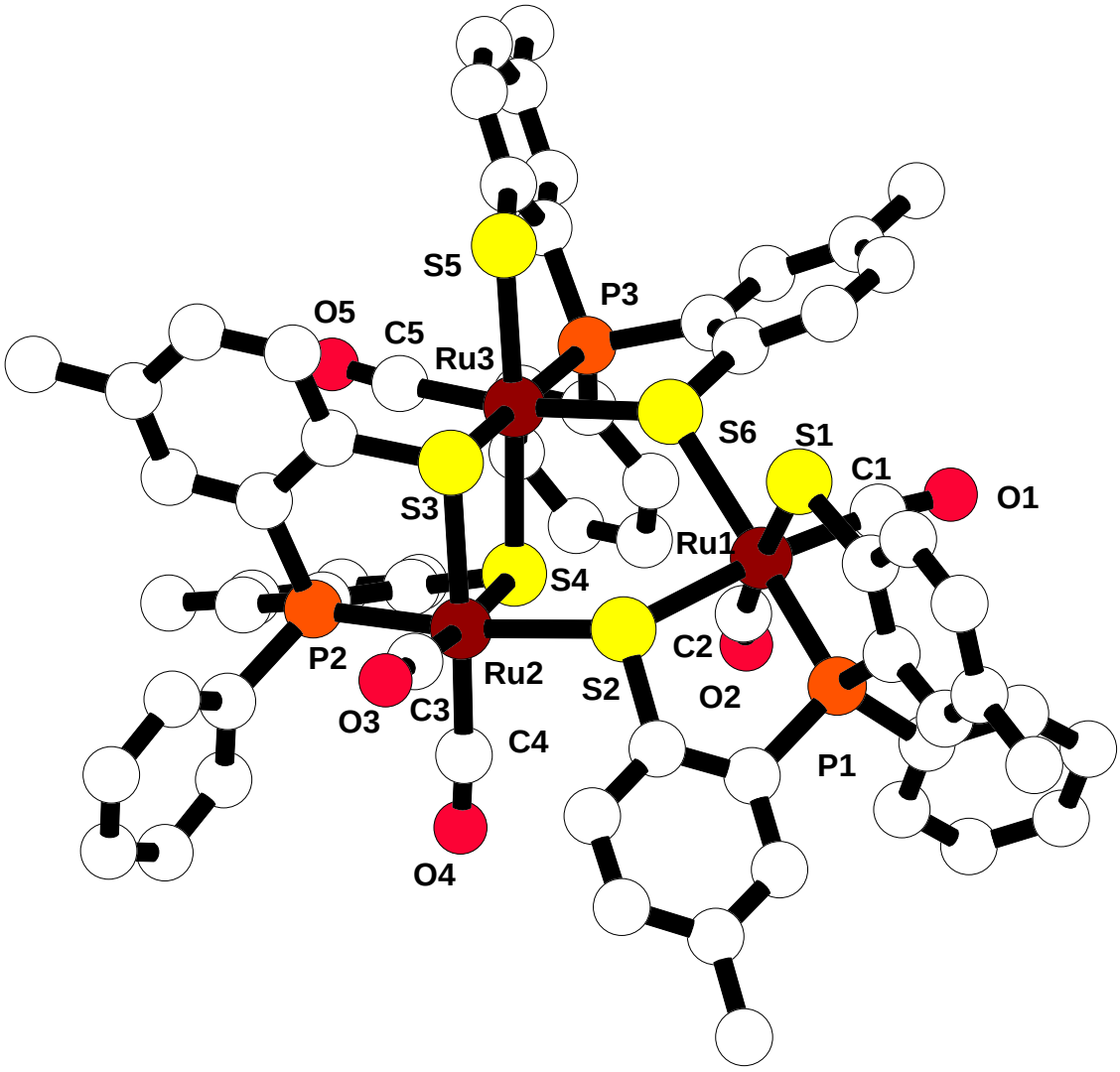


**Figure V–17. X–ray structure of $[Ru^{II}_3(CO)_5(PS2')_3]$.**

| Table V–7. Selective Crystallographic Data for $Ru^{II}_3(CO)_5(PS2')_3$]. | | | | | |
|---|---|---|---|---|---|
| **Bond Distances (Å)** | | **Bond Angles (°)** | | **Bond Angles (°)** | |
| Ru(1) – C(1) | 1.900(10) | C(1) – Ru(1) – C(2) | 87.3(4) | S(3) – Ru(2) – S(2) | 88.55(8) |
| Ru(1) – C(2) | 1.916(8) | C(1) – Ru(1) – P(1) | 89.4(3) | P(2) – Ru(2) – S(2) | 173.32(9) |
| Ru(2) – C(3) | 1.918(12) | C(2) – Ru(1) – P(1) | 94.5(3) | S(4) – Ru(2) – S(2) | 92.16(8) |
| Ru(2) – C(4) | 1.914(11) | C(1) – Ru(1) – S(1) | 86.9(3) | C(5) – Ru(3) – P(3) | 88.9(3) |
| Ru(3) – C(5) | 1.864(10) | C(2) – Ru(1) – S(1) | 174.2(3) | C(5) – Ru(3) – S(5) | 84.2(3) |
| Ru(1) – S(1) | 2.415(2) | P(1) – Ru(1) – S(1) | 85.53(8) | P(3) – Ru(3) – S(5) | 82.42(9) |
| Ru(1) – S(2) | 2.464(2) | C(1) – Ru(1) – S(2) | 171.3(3) | C(5) – Ru(3) – S(4) | 94.1(3) |
| Ru(2) – S(2) | 2.471(2) | C(2) – Ru(1) – S(2) | 97.5(3) | P(3) – Ru(3) – S(4) | 101.89(8) |
| Ru(2) – S(3) | 2.425(2) | P(1) – Ru(1) – S(2) | 82.92(8) | S(5) – Ru(3) – S(4) | 175.36(9) |
| Ru(2) – S(4) | 2.425(2) | S(1) – Ru(1) – S(2) | 88.24(8) | C(5) – Ru(3) – S(6) | 171.3(3) |
| Ru(3) – S(4) | 2.445(2) | C(1) – Ru(1) – S(6) | 96.6(3) | P(3) – Ru(3) – S(6) | 85.72(8) |
| Ru(3) – S(5) | 2.384(2) | C(2) – Ru(1) – S(6) | 97.8(3) | S(5) – Ru(3) – S(6) | 88.39(8) |
| Ru(3) – S(6) | 2.446(2) | P(1) – Ru(1) – S(6) | 166.50(8) | S(4) – Ru(3) – S(6) | 93.62(8) |
| Ru(1) – P(1) | 2.282(2) | S(1) – Ru(1) – S(6) | 82.78(8) | C(5) – Ru(3) – S(3) | 97.8(3) |
| Ru(2) – P(2) | 2.276(3) | S(2) – Ru(1) –S(6) | 89.98(8) | P(3) – Ru(3) – S(3) | 171.32(8) |
| Ru(3) – P(3) | 2.243(3) | C(4) – Ru(2) – C(3) | 94.7(4) | S(5) – Ru(3) – S(3) | 92.73(9) |
| C(1) – O(1) | 1.131(12) | C(4) – Ru(2) – P(2) | 90.7(3) | S(4) – Ru(3) – S(3) | 83.21(8) |
| C(2) – O(2) | 1.124(12) | C(3) – Ru(2) – P(2) | 92.4(3) | S(6) – Ru(3) – S(3) | 86.96(8) |
| C(3) – O(3) | 1.143(14) | C(4) – Ru(2) – S(3) | 173.7(3) | Ru(3) – S(6) –Ru(1) | 124.51(9) |
| C(4) – O(4) | 1.124(12) | C(3) – Ru(2) – S(3) | 90.1(3) | Ru(1) – S(2) –Ru(2) | 125.33(9) |
| C(5) – O(5) | 1.148(12) | P(2) – Ru(2) – S(3) | 84.98(9) | Ru(2) – S(3) –Ru(3) | 94.92(8) |
| | | C(4) – Ru(2) – S(4) | 89.8(3) | Ru(2) – S(4) –Ru(3) | 96.41(8) |
| | | C(3) – Ru(2) – S(4) | 175.1(3) | Ru(1) – C(1) – O(1) | 173.0(9) |
| | | P(2) – Ru(2) – S(4) | 85.62(8) | Ru(1) – C(2) – O(2) | 170.2(8) |
| | | S(3) – Ru(2) – S(4) | 85.30(8) | Ru(2) – C(3) – O(3) | 179.0(9) |
| | | C(4) – Ru(2) – S(2) | 95.6(3) | Ru(2) – C(4) – O(4) | 174.5(9) |
| | | C(3) – Ru(2) – S(2) | 89.3(3) | Ru(3) – C(5) – O(5) | 175.6(9) |

### 5.3.4 NMR Spectroscopy of *fac*–[$Ru^{II}(CO)_3$(PS2)] and *fac*–[$Ru^{II}(CO)_3$(PS2')]

The *fac*–[$Ru^{II}(CO)_3$(PS2)] and *fac*–[$Ru^{II}(CO)_3$(PS2')] compounds were characterized by $^1H$, $^{13}C$ and $^{31}P$ NMR studies. The NMR spectra were measured in either $d_6$–DMSO or $CD_3CN$. The $^1H$–NMR of *fac*–[$Ru^{II}(CO)_3$(PS2)] shows multiple peaks in the aromatic region, 7.5 to 6.7 ppm (**Figure V–18**). The NMR does show some minor impurities; however. the major peaks integrate to the exact amout of hydrogens for the ruthenium compound. The percent of impurities found in the $^1H$–NMR was approximately 28%. The $^{13}C$–NMR spectra taken in various deutrated solvents, but none showed any reportable data. The $^{31}P$–NMR spectrum shows four peaks at 85.99, 84.06, 83.56 and 83.48, where 83.56 was assigned to the *fac*–[$Ru^{II}(CO)_3$(PS2)] compound (**Figure V–19**). Assignment for the other three peaks have been determined; however, these peaks could be associated with a ruthenium dimer or trimer.

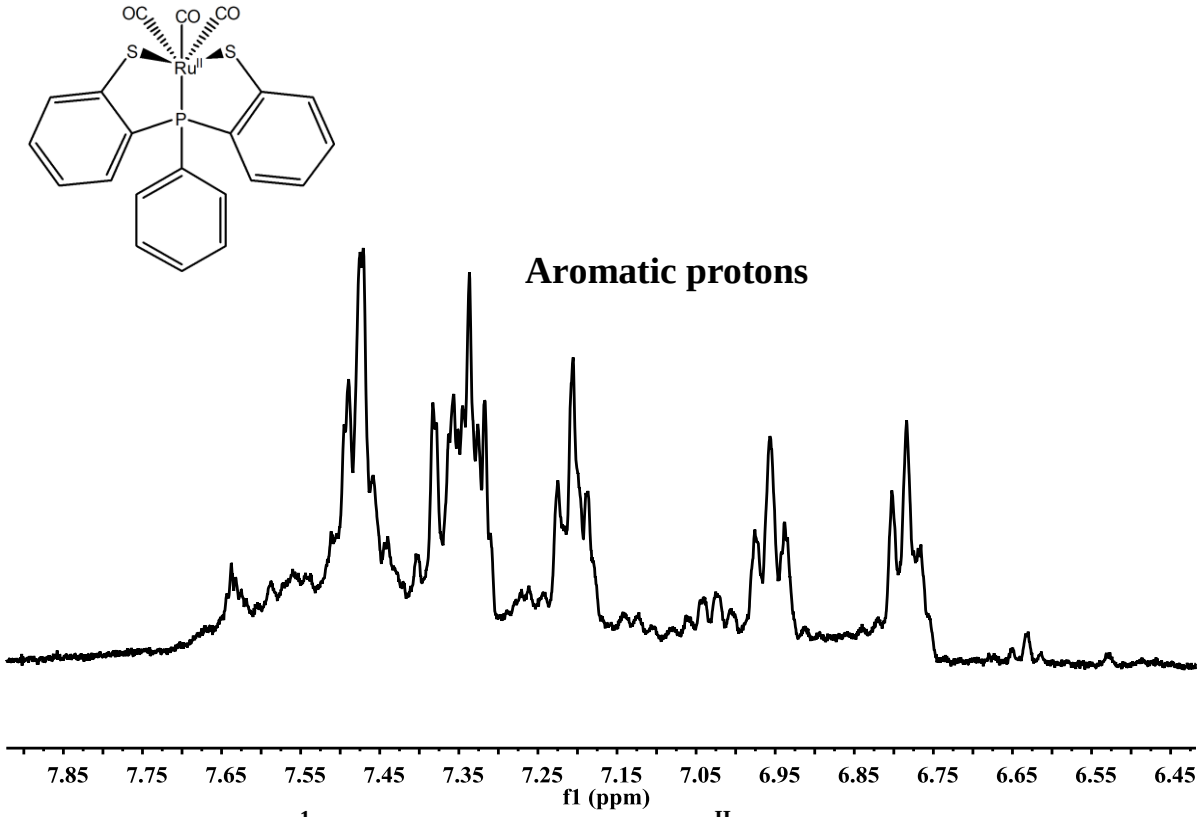


**Figure V–18. $^1H$–NMR spectrum of *fac*–[$Ru^{II}(CO)_3$(PS2)] in $d_6$–DMSO.**

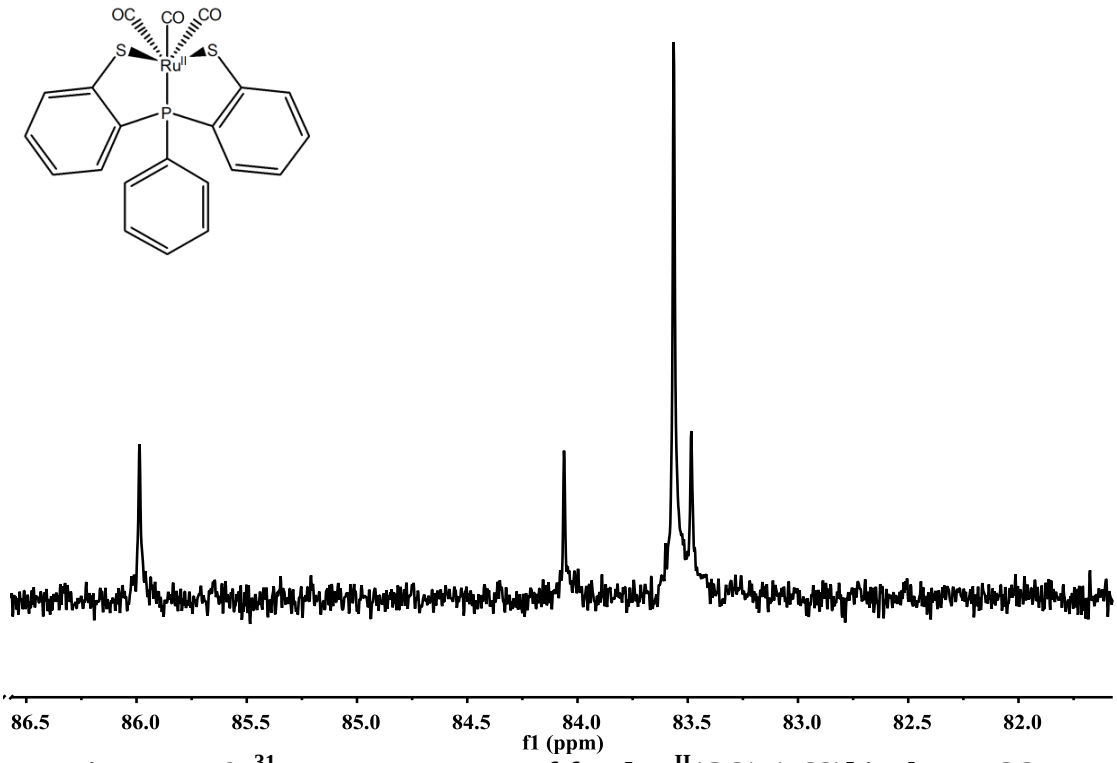


**Figure V–19. $^{31}$P–NMR spectrum of *fac*–[Ru$^{II}$(CO)$_3$(PS2)] in d$_6$–DMSO.**

The $^{1}$H–NMR of *fac*–[Ru$^{II}$(CO)$_3$(PS2')] shows multiple peaks in the aromatic region, 7.7 to 6.9 ppm, and shows a singlet at 2.20 ppm which corresponds to the methyl group ($CH_3$) located on the [PS2'] ligand (**Figure V–20**). The $^{13}$C–NMR of *fac*–[Ru$^{II}$(CO)$_3$(PS2')] shows multiple peaks in the armoatic region, 152 to 129 ppm (**Figure V–21**). The carbonyl peaks are found at 189 and 188 ppm. The carbonyl peaks are split, into four peaks, due to the phosphorous coupling (**Figure V–22**). The methyl carbon, found at 19.9 ppm, also shows a doublet caused by the phosphorous coupling. The $^{31}$P–NMR shows a singlet at 91.96 ppm indicating that the phosphorous is bound to the ruthenium (**Figure V–23**). The phosphorous peak for the free ligand, $H_2$PS2', was found at –17.16 ppm.

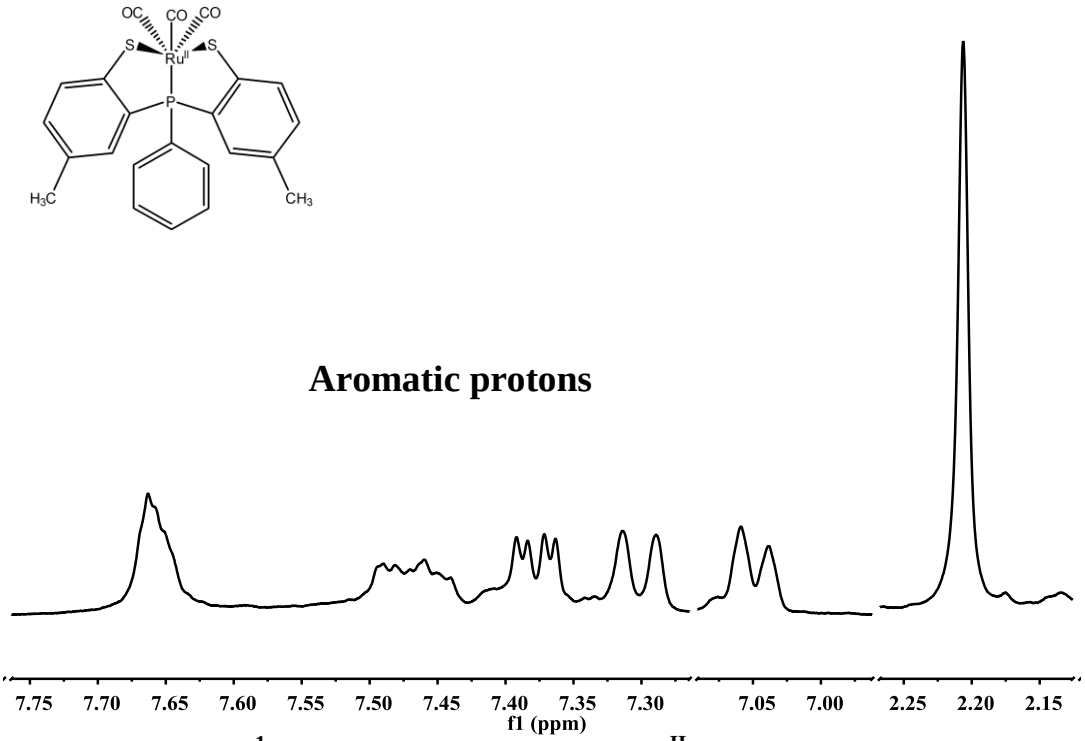


**Figure V–20. $^{1}$H–NMR spectrum of *fac*–[Ru$^{II}$(CO)$_3$(PS2')] in $CD_3CN$.**

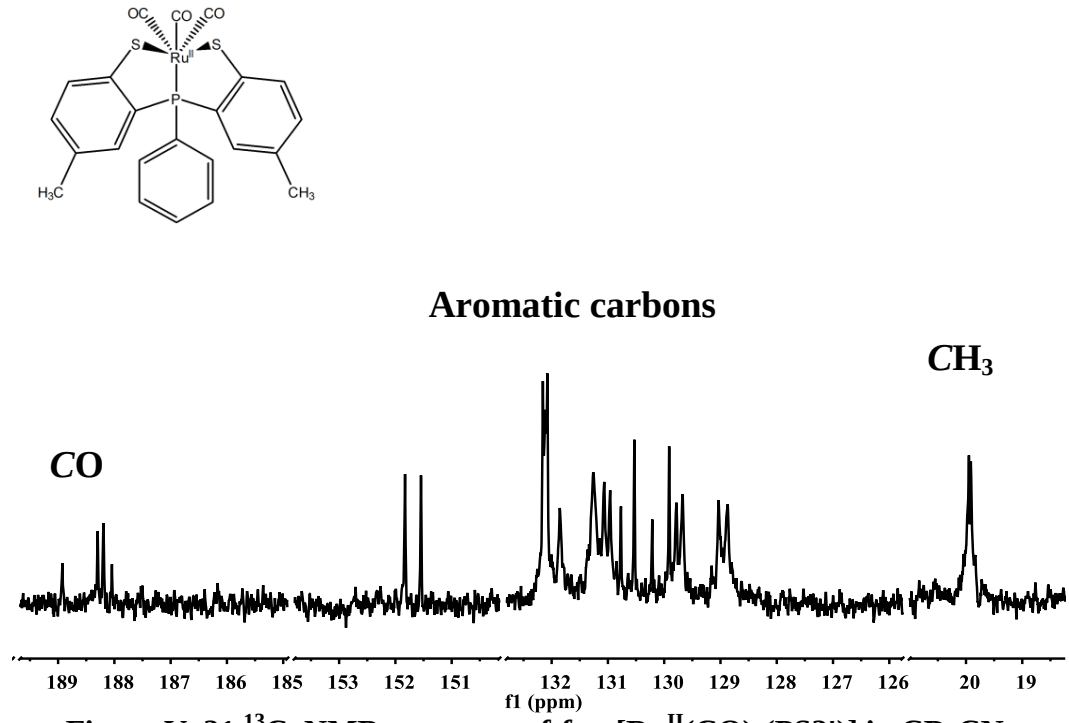


**Figure V–21 $^{13}$C–NMR spectrum of *fac*–[Ru$^{II}$(CO)$_3$(PS2')] in $CD_3CN$.**

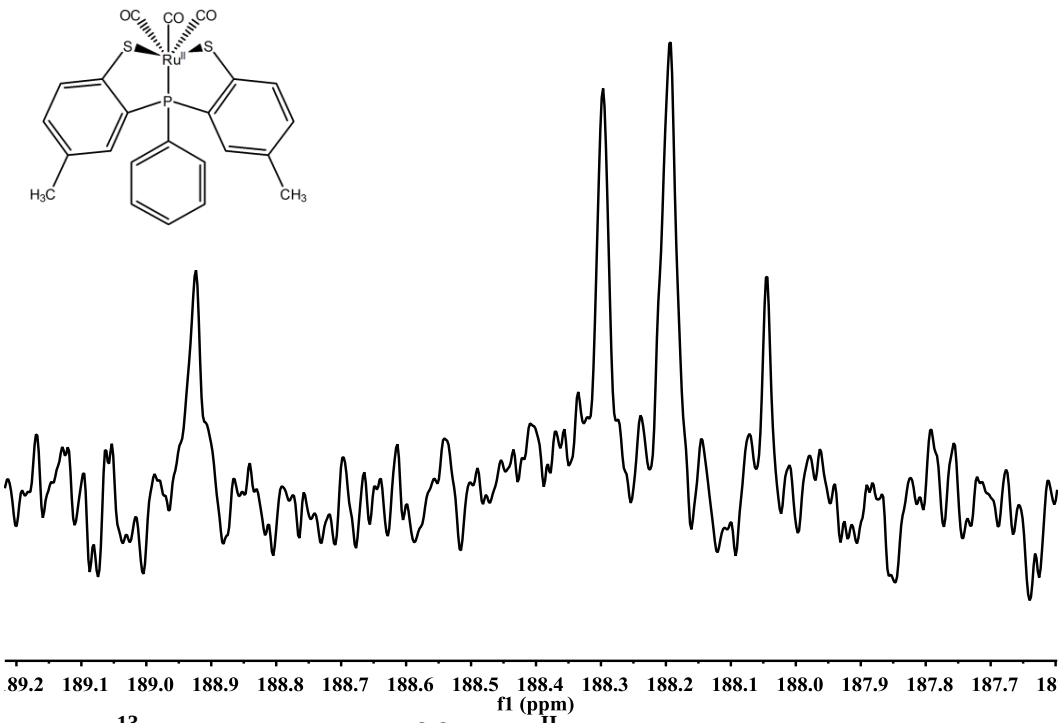


**Figure V–22. $^{13}$C–NMR spectrum of *fac*–[Ru$^{II}$(CO)$_3$(PS2')] in CD$_3$CN, expanded view of carbonyl region.**

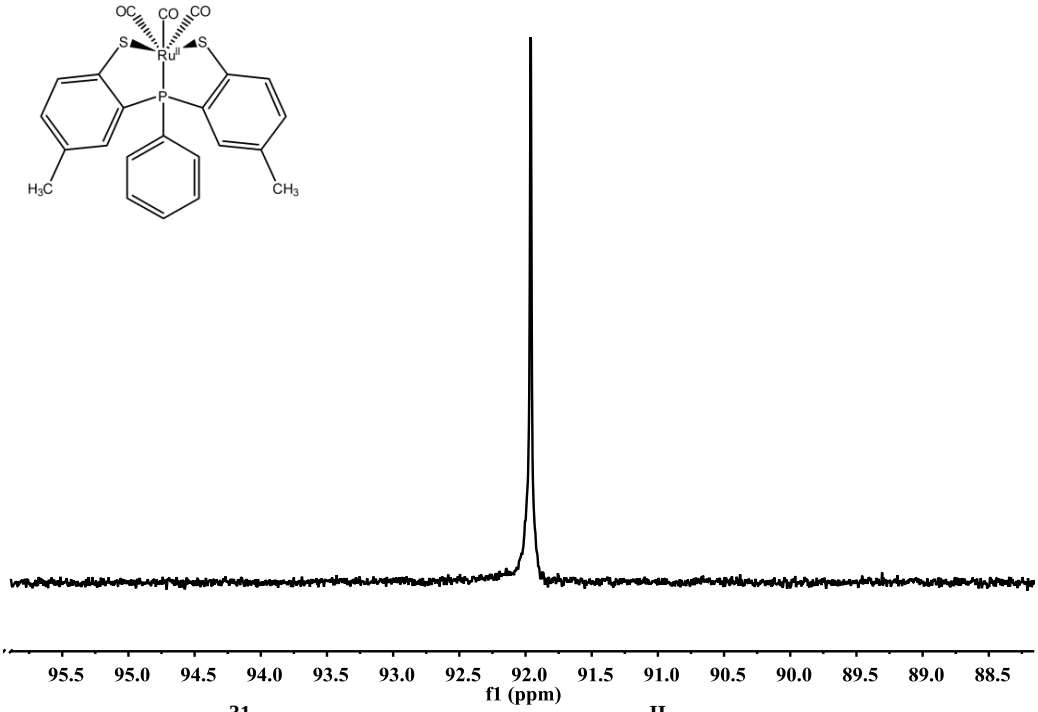


**Figure V–23. $^{31}$P–NMR spectrum of *fac*–[Ru$^{II}$(CO)$_3$(PS2')] in CD$_3$CN.**

As previously stated, the iron analog of *fac*–[$Ru^{II}(CO)_3$(PS2')] was synthesized and characterized by Doris Melgarejo, PhD.[19] Comparing the $^1$H–NMR of both compounds, there were no significant differences between them; however, the $^{13}$C–NMR does show some significant shifts. The carbonyl peaks for the iron compound are located at 205 and 204 ppm, while the ruthenium carbonyl peaks are located at 189 and 188 ppm.

### 5.3.5 Synthesis and Characterization of Ruthenium Carbonyl complexes with the [NS2] and [NS2'] Ligands

The successful synthesis of ruthenium carbonyl complexes using [PS2] and [PS2'] prompted the use other types of tridentate ligands, i.e. [NS2] and [NS2']. These [NS2] ligands are similar to the [PS2] ligands with two major differences. First, the P atom is replaced with a N atom and second, the phenyl groups are replaced with benzyl groups. The same reactions conditions were used for the [NS2] complexes as for the [PS2] complexes. Infrared spectroscopy for the *fac*–[$Ru^{II}(CO)_3$(NS2)] and *fac*–[$Ru^{II}(CO)_3$(NS2')] are illustrated in **Figure V–24** and **Figure V–25** respectively. The IR peaks suggest that the carbonyl ligands are in the facial arrangement. The comparison of the infrared spectra of the [PS2] and [NS2] complexes show an interesting result. Nitrogen is a better sigma donor than phosphorous which increases the electron density on the ruthenium metal center. This increase in electron density would strengthen the π–backbonding the carbonyl ligand and as a result would decrease the C≡O bond strength. This change in bond strength results in a red shift in the carbonyl stretching frequency from the [PS2] complexes to the [NS2]. This is summarized in **Table V–8**.

**Table V–8. Infrared Spectra Comparison of *fac*–[$Ru^{II}(CO)_3$(L)] (where L = PS2, PS2', NS2 and NS2')**

| Compound | $\nu_{CO}$ ($cm^{-1}$) |
|---|---|
| *fac*–[$Ru(CO)_3$(PS2)] | 2032, 2059, 2110 |
| *fac*–[$Ru(CO)_3$(PS2')] | 2030, 2057, 2109 |
| *fac*–[$Ru(CO)_3$(NS2)] | 1956, 2026, 2102 |
| *fac*–[$Ru(CO)_3$(NS2')] | 1954, 2022, 2100 |

The thermal instability of the assumed *fac*–[$Ru^{II}(CO)_3$(NS2)] compounds prevented their crystal structure determination. Several attempts to grow crystals of the *fac*–[$Ru^{II}(CO)_3$(NS2)] and *fac*–[$Ru^{II}(CO)_3$(NS2')] were unsuccessful. Similar to the [PS2] complexes, the [NS2]

complexes must be kept at –20 $^{o}$C freezer to prevent thermal decomposition. Compounds have shown changes in color, i.e. yellow–orange to dark orange, when left at room temperature after one month in the solid state. This reaction was accelerated when the *fac*–[$Ru^{II}(CO)_3$(NS2')] was dissolved in hexanes and left for one week.

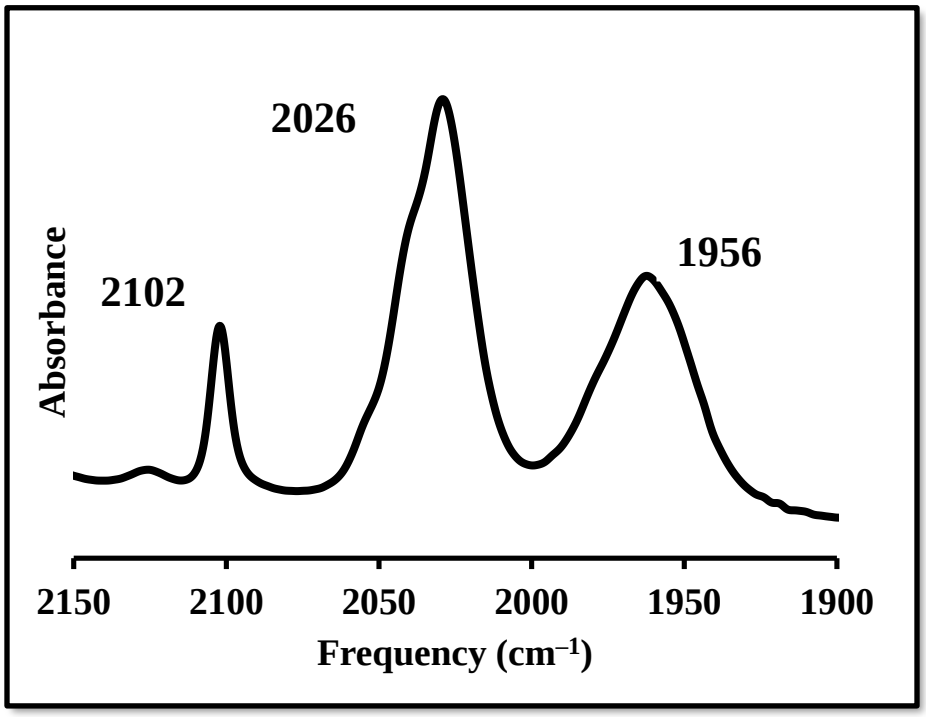


**Figure V–24. Infrared spectrum of *fac*–[$Ru^{II}(CO)_3$(NS2)] in $CH_2Cl_2$.**

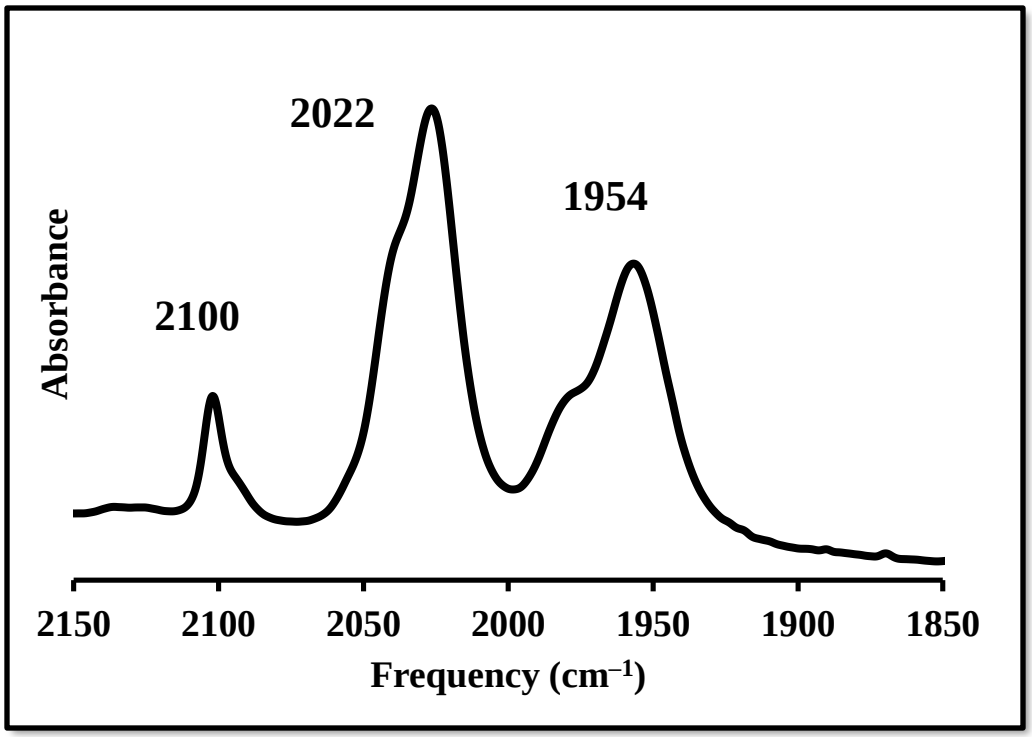


**Figure V–25. Infrared spectrum of *fac*–[$Ru^{II}(CO)_3$(NS2')] in $CH_2Cl_2$.**

The thermal reaction was monitored by IR spectroscopy. After several days, the change in the IR spectrum was complete. (**Figure V–26**). Diethyl ether was slowly added to the solution to form orange needle crystals. The compound was confirmed by X–ray crystallography to be a ruthenium dimer containing four carbonyls and two [NS2'] ligands, $[Ru^{II}(CO)_2(NS2')]_2$. The ruthenium dimer was found be thermally stable for a period of five months, which was proven *via* infrared analysis taken at periodic intervals.

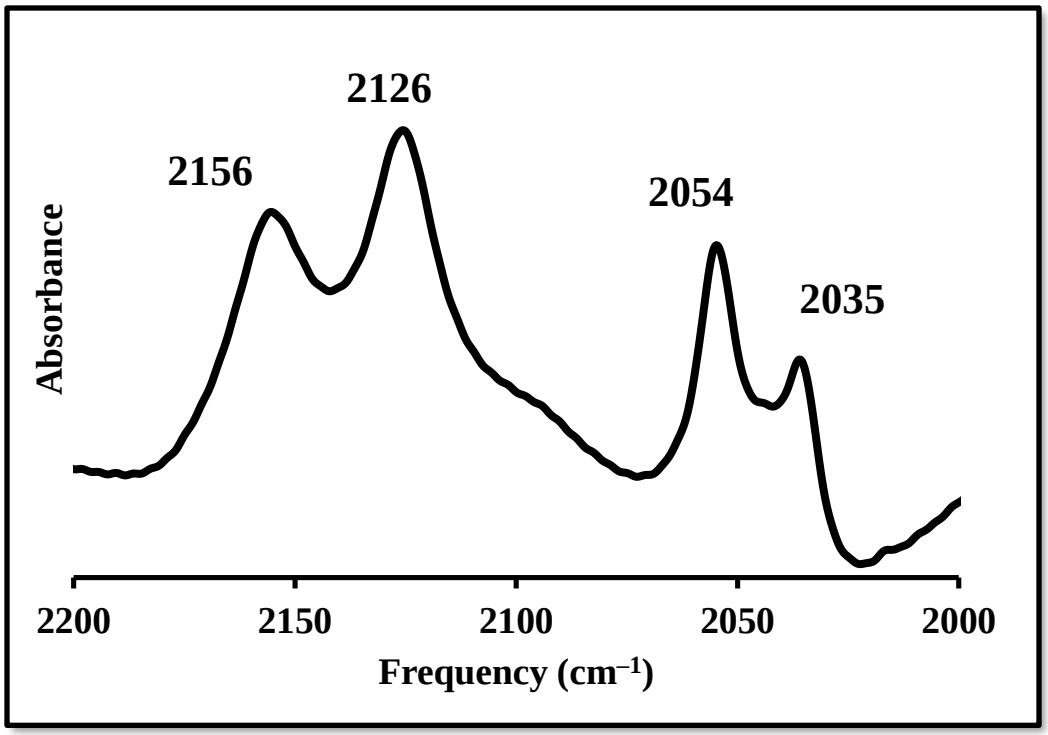


**Figure V–26. Infrared spectrum of $[Ru^{II}(CO)_2(NS2')]_2$ in $CH_2Cl_2$.**

X–ray quality crystals of the dimer, were grown from a concentrated hexanes solution of the *fac*–$[Ru^{II}(CO)_3(NS2')]$ at room temperature. The X–ray structure revealed a centrosymmetric dimer $[Ru^{II}(CO)_2(NS2')]_2$ with two ruthenium octahedron linked by two bridging thiolates. Each ruthenium also has a terminal thiolate, an amine and two carbonyl ligands. The crystal structure was solved under a monoclinic crystal system *C*2/*c*. The transition metal lies on a two–fold axis so that the $[Ru^{II}(CO)_2(NS2)]$ has an imposed $C_2$ symmetry. The general structure of the ruthenium dimer is shown in **Figure V–27**. The Ru–$C_{avg}$, Ru–$S_{avg}$ and C–$O_{avg}$ bond distances are 1.878(8) Å, 2.427(2) Å and 1.134(9) Å, respectively. The bond distance of the bridging thiolate, Ru(1)–$S(2)_{bridging}$, was measured to be 2.487(2) Å. The Ru(1)–N(1) bond distance was measured to be 2.279(5) Å. Both X–ray crystallography and infrared spectroscopy, confirmed that the carbonyl ligands are in the *cis* orientation. Selective bond distances and angles for $[Ru^{II}(CO)_3(NS2')]_2$ are summarized in **Table V–9**.

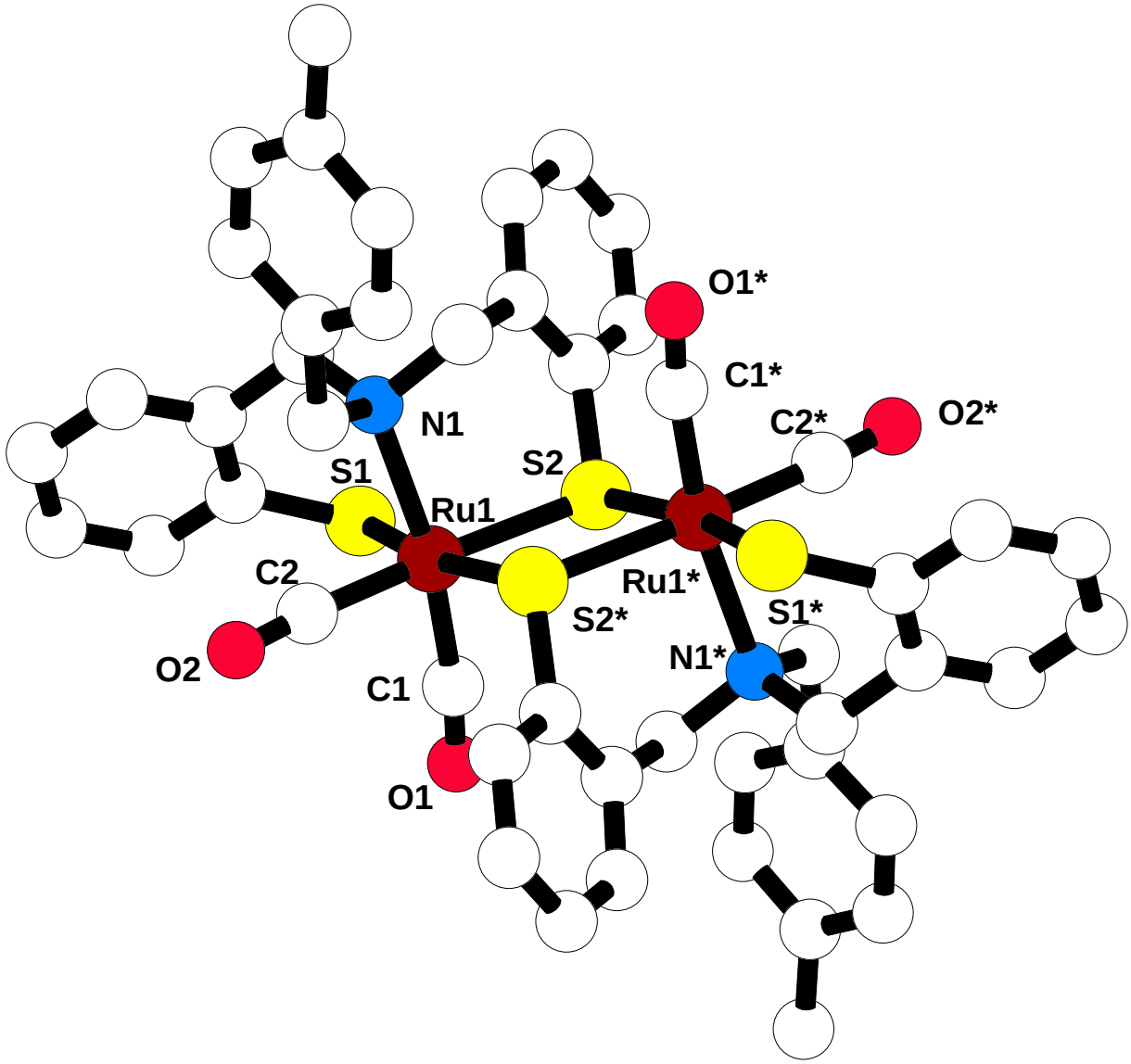


**Figure V–27. X–ray structure of $[Ru^{II}(CO)_2(NS2')]_2$ (hydrogens were removed for clarity).**

| Table V–9. Selective Crystallographic Data for $[Ru^{II}(CO)_2(NS2')]_2$. | | | |
|---|---|---|---|
| **Bond Distances (Å)** | | **Bond Angles (°)** | |
| Ru(1) – C(1) | 1.867(7) | C(1) – Ru(1) – C(2) | 86.4(3) |
| Ru(1) – C(2) | 1.888(8) | C(1) – Ru(1) – N(1) | 168.8(3) |
| Ru(1) – S(1) | 2.403(2) | C(2) – Ru(1) – N(1) | 87.0(2) |
| Ru(1) – S(2) | 2.4500(18) | C(1) – Ru(1) – S(1) | 82.9(2) |
| Ru(1) – N(1) | 2.279(5) | C(2) – Ru(1) – S(1) | 92.8(2) |
| C(1) – O(1) | 1.136(8) | C(1) – Ru(1) – S(2) | 92.8(2) |
| C(2) – O(2) | 1.132(9) | C(2) – Ru(1) – S(2) | 176.4(2) |
| Ru(1) – S(2)* | 2.487(2) | N(1) – Ru(1) – S(1) | 88.39(15) |
| | | N(1) – Ru(1) – S(2) | 94.36(14) |
| | | S(1) – Ru(1) – S(2) | 90.57(2) |
| | | C(1) – Ru(1) – S(2)* | 99.1(2) |
| | | C(2) – Ru(1) – S(2)* | 97.6(2) |
| | | N(1) – Ru(1) – S(2)* | 90.79(15) |
| | | S(1) – Ru(1) – S(2)* | 169.55(7) |
| | | Ru(1) – S(2) – Ru(1)* | 100.90(7) |
| | | Ru(1) – C(1) – O(1) | 173.0(6) |
| | | Ru(1) – C(2) – O(2) | 175.9(6) |

### 5.3.6 The Synthesis and Characterization of *fac*–$[Ru^{II}(CO)_3(SR)_3]^-$ Monomers and a $[Ru^{I}_2(CO)_6(\mu_2–SR)_2]$ Dimer

The *fac*–$[Ru^{II}(CO)_3(S–2,3,5,6–Me_4C_6H)_3]^{1-}$ complex was originally synthesized by Janet Haff.[18] The original synthesis of this compound was performed by reacting *fac*–$[Ru^{II}(CO)_3Cl_2(THF)]$ with 2,3,5,6–tetramethylbenzenethiolate, in which the thiolate was deprotantated by dicyclohexylamine. The reagents were left to stir at room temperature producing a yellow solution within minutes of adding the two reagents. A yellow precpitiate was observed after approximately thirty minutes.

The modified procedure reported in this work shows that the same two reagents are added together; however, the 2,3,5,6–tetramethylbenzenethiolate was deprotonated using lithium wire. This method allows precipitation using various cations to isolate the desired product. Crystallization of the desired product was achieved using $[Et_4N]^+$, [*n*–Pr4N]$^+$, $[Bu_4N]^+$, $[Me_3NBz]^+$, and $[PPN]^+$ cations; however, crystals containing the $[Me_3NBz]^+$ were the most

suitable for X–ray crystallography. The yields using Haff's synthesis and the modified synthesis are comparable at ~85% of pure compound.

The IR spectrum of *fac*–[$Me_3NBz$][$Ru^{II}(CO)_3$(S–2,3,5,6–$Me_4C_6H)_3$] showed two peaks which are characteristic of three facial carbonyl ligands in a facial arrangement (**Figure V–28**). The IR spectrum is comparable to Haff's work. The $^1$H–NMR of *fac*–[$Ru^{II}(CO)_3$(S–2,3,5,6–$Me_4C_6H)_3]^-$ was first reported by Janet Haff.[18] However, the cations were different, $[(Cy)_2NH_2]^+$ cation was used Haff's work and $[Me_3NBz]^+$ was used in this work.

The $^1$H–NMR spectrum shows two peaks in the aromatic region, 7.53 ppm corresponds to the hydrogens on the benzyl group located on the cation while the peak at 6.59 ppm corresponds to the *para* hydrogen located on the thiolate ligand (**Figure V–29**). Two singlets were observed at 2.57 and 2.10 ppm which correspond to the methyl protons located on the thiolate. The methylene protons and the methyl protons of the cation were located on 4.51 and 3.02 ppm, respectively.

The $^{13}$C–NMR of *fac*–[$Ru^{II}(CO)_3$(S–2,3,5,6–$Me_4C_6H)_3]^-$ shows the aromatic carbons on both the thiolate and cation in the range of 146 to 128 ppm. The methyl carbons corresponding to the thiolate are located at 20.89 and 20.20 ppm. The methyl and methylene carbons of the cation are located at 51.77 and 67.90 ppm, respectively. The $^{13}$C–NMR of the *fac*–[$Ru^{II}(CO)_3$(S–2,3,5,6–$Me_4C_6H)_3]^-$ is illustrated in **Figure V–30**.

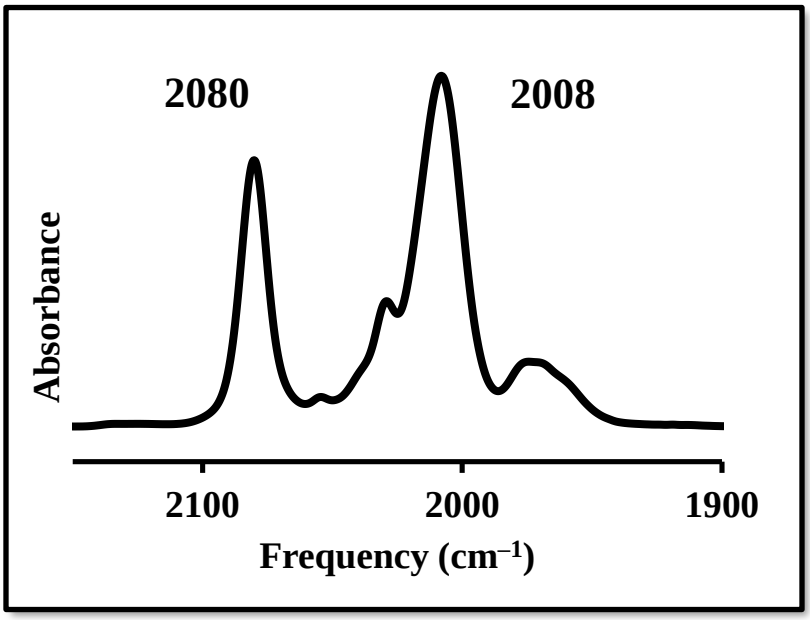


**Figure V–28. Infrared spectrum of *fac*–[$Me_3NBz$][$Ru^{II}(CO)_3$(S–2,3,5,6–$Me_4C_6H)_3$] in MeOH.**

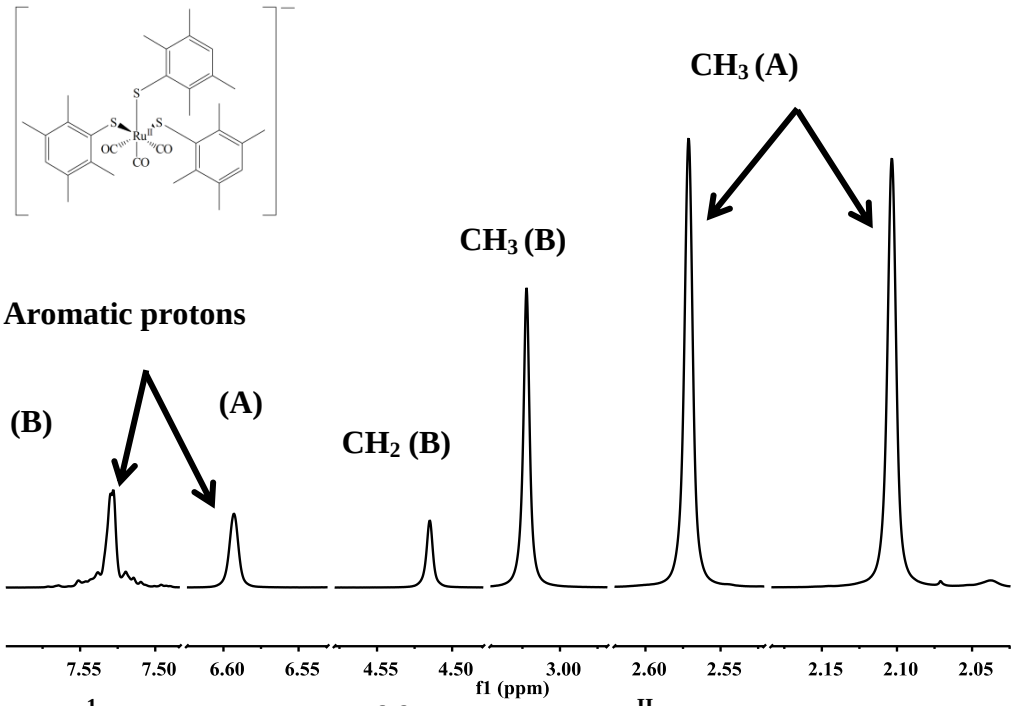


**Figure V–29. $^{1}$H–NMR spectrum of *fac*–[$Me_3NBz$][$Ru^{II}(CO)_3$($S$–2,3,5,6–$Me_4C_6H)_3$] in $d_6$–DMSO (where A = thiolate protons and B = cation protons).**

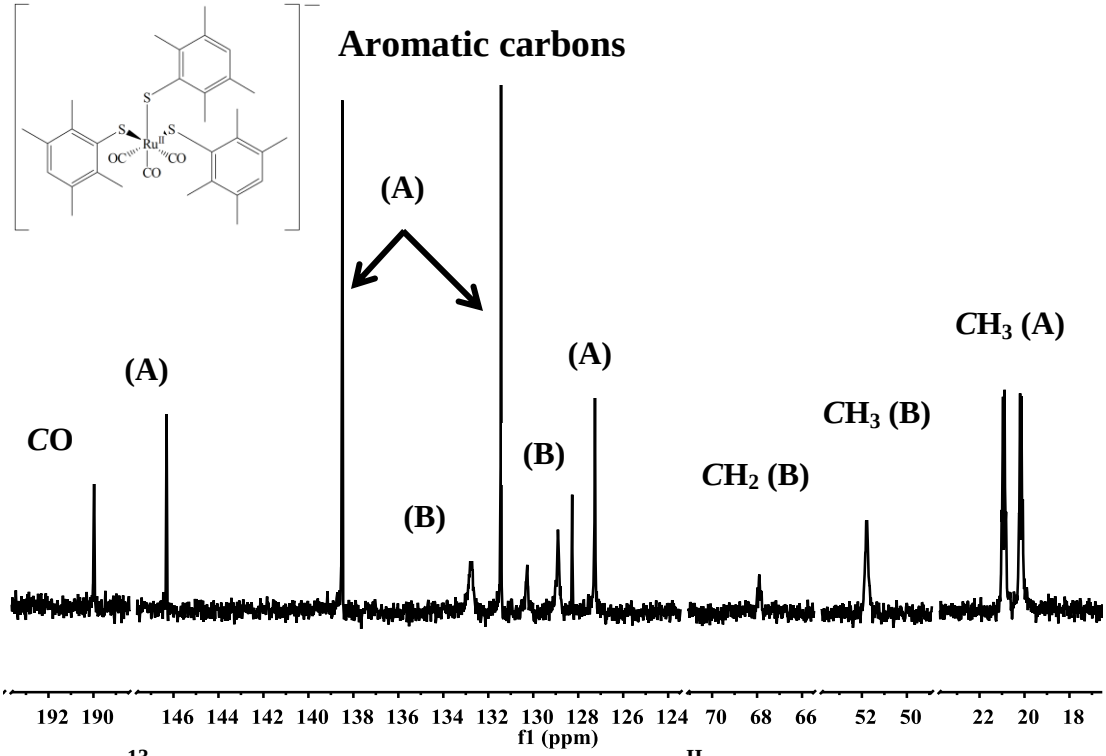


**Figure V–30. $^{13}$C–NMR spectrum of *fac*–[$Me_3NBz$][$Ru^{II}(CO)_3$($S$–2,3,5,6–$Me_4C_6H)_3$] in $d_6$–DMSO (where A = thiolate carbons and B = cation carbons).**

The X–ray structure of *fac*–[$Me_3NBz$][$Ru^{II}(CO)_3$(S–2,3,5,6–$Me_4C_6H)_3$] confirmed a ruthenium(II) anion displaying an octahedral geometry which consists of three carbonyl ligands in the facial arrangement, three 2,3,5,6–tetramethylbenzenethiolate ligands and one $[Me_3NBz]^+$ cation. Crystals, suitable for X–ray crystallography, were grown from layering a concentrated methanolic solution of [$Me_3$NBz]Cl over the reaction solution at room temperature. The crystal structure was solved under a triclinic crystal system *P*1bar. Both structures, ours and Haffs, are isomorphous despite the change in cation. The ruthenium structure is located on a general position. The general structure of the ruthenium monomer is illustrated in **Figure V–31**.

The X–ray structure of *fac*–$[Ru^{II}(CO)_3$(S–2,3,5,6–$Me_4C_6H)_3]^-$ was first reported by Janet Haff, PhD using dicyclohexylammonium, $[(Cy)_2NH_2]^+$, as the counter cation. The Ru–$S_{avg}$, Ru–$C_{avg}$ and C–$O_{avg}$ for *fac*–[$Me_3$NBz][$Ru^{II}(CO)_3$(S–2,3,5,6–$Me_4C_6H)_3$] bond distances are 2.4603(6) Å, 1.918(2) Å and 1.132(3) Å, respectively. The ruthenium–thiolate bond distances are within range of those for published compounds where the thiolate is *trans* to a carbonyl ligand[6,16–17,33–34]. These ruthenium–thiolate bonds, when *trans* to a carbonyl, are typically longer than those *trans* to weaker π acceptor ligands like phosphines[35], acetonitrile[1] or thioethers[35–36].

The important geometrical parameters of *fac*–$[Ru^{II}(CO)_3$(S–2,3,5,6–$Me_4C_6H)_3]^-$, reported in this dissertation, are compared with Haff's *fac*–$[Ru^{II}(CO)_3$(S–2,3,5,6–$Me_4C_6H)_3]^-$ (**Table V–10**). Selective bond distances and angles for *fac*–[$Me_3$NBz][$Ru^{II}(CO)_3$(S–2,3,5,6–$Me_4C_6H)_3$] are summarized in **Table V–11**.

The bond distances of both structures are comparable. This displays that changing of the cation does not have a significant effect on the bond distances of the anion, in this example.

**Table V–10. Comparison of Selective Crystallographic Data for *fac*–$[Ru^{II}(CO)_3$(S–2,3,5,6–$Me_4C_6H)_3]^-$.**

| **This Work** | | **Haff[18]** | |
|---|---|---|---|
| **Bond Distances (Å)** | | **Bond Distances (Å)** | |
| Ru(1) – S(1) | 2.4650(6) | Ru(1) – S(1) | 2.462(2) |
| Ru(1) – S(2) | 2.4395(6) | Ru(1) – S(2) | 2.448(2) |
| Ru(1) – S(3) | 2.4764(5) | Ru(1) – S(3) | 2.481(2) |
| Ru(1) – C(1) | 1.912(2) | Ru(1) – C(1) | 1.90(1) |
| Ru(1) – C(2) | 1.923(2) | Ru(1) – C(2) | 1.92(1) |
| Ru(1) – C(3) | 1.918(2) | Ru(1) – C(3) | 1.90(1) |

| Table V–11. Selective Crystallographic Data for *fac*–[$Me_3NBz$][$Ru^{II}(CO)_3(S–2,3,5,6–Me_4C_6H)_3$]. | | | |
|---|---|---|---|
| **Bond Distances (Å)** | | **Bond Angles (°)** | |
| Ru(1) – S(1) | 2.4650(6) | C(1) – Ru(1) – C(3) | 89.58(9) |
| Ru(1) – S(2) | 2.4395(6) | C(1) –Ru(1) – C(2) | 95.63(10) |
| Ru(1) – S(3) | 2.4764(5) | C(3) – Ru(1) – C(2) | 94.05(10) |
| Ru(1) – C(1) | 1.912(2) | C(1) – Ru(1) – S(2) | 90.06(7) |
| Ru(1) – C(2) | 1.923(2) | C(3) – Ru(1) – S(2) | 92.70(7) |
| Ru(1) – C(3) | 1.918(2) | C(2) – Ru(1) – S(2) | 171.20(7) |
| C(1) – O(1) | 1.132(3) | C(1) – Ru(1) – S(1) | 173.33(7) |
| C(2) – O(2) | 1.135(3) | C(3) – Ru(1) – S(1) | 91.85(7) |
| C(3) – O(3) | 1.130(3) | C(2) – Ru(1) – S(1) | 90.77(7) |
| | | S(2) – Ru(1) – S(1) | 83.367(19) |
| | | C(1) – Ru(1) – S(3) | 92.45(6) |
| | | C(3) – Ru(1) – S(3) | 177.77(7) |
| | | C(2) – Ru(1) – S(3) | 86.67(7) |
| | | S(2) – Ru(1) – S(3) | 86.377(19) |
| | | S(1) – Ru(1) – S(3) | 86.028(19) |
| | | O(1) – C(1) – Ru(1) | 177.95(19) |
| | | O(2) – C(2) – Ru(1) | 178.1(2) |
| | | O(3) – C(3) – Ru(1) | 176.8(2) |

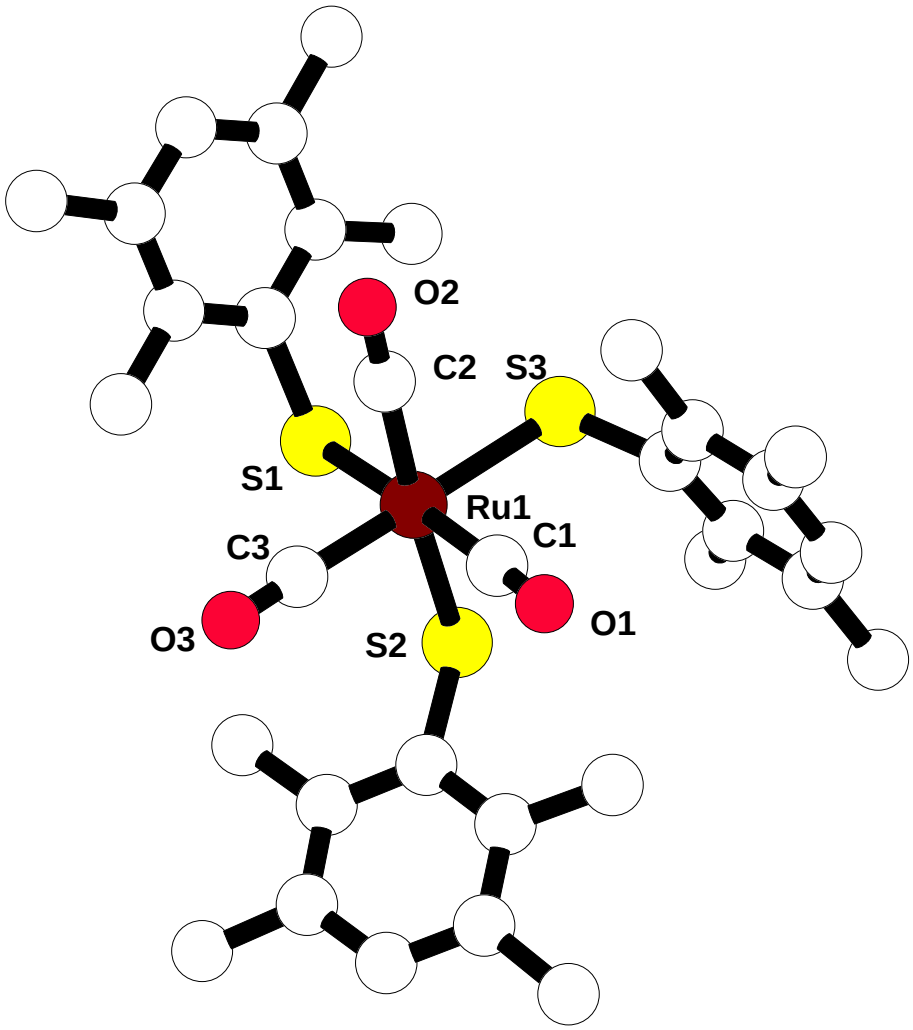


**Figure V–31. X–ray structure of *fac*–[$Me_3NBz$][$Ru^{II}(CO)_3(S–2,3,5,6–Me_4C_6H)_3$] (hydrogens and cation were removed for clarity).**

Attempts to synthesize the analogous compound with a more sterically hindered thiolate, 2,4,6–triisopropylbenzenethiolate resulted in isolation of a Ru(I) dimer through an a unusual reaction. The family of butterfly structures, $M_2(SR)_2(CO)_{6-x}L_2$, resembles the active site of the [FeFe] hydrogenase.[20] In the past, scientists have been synthesizing these butterfly structures using iron. This has been problematic due to the instability in the diiron complexes.[21–22] Recently, scientists have extended this research using ruthenium due to the metal's stability and ease of manipulation.[23–25] In 2006, a series of diruthenium dithiolato carbonyls were synthesized and characterizated.[26] One example of this type of compound was synthesized by Justice *et al.*,

$[Ru^{I}_{2}(S_2C_3H_6)(CO)_6]$ (where $S_2C_3H_6$ = 1,3–propanedithiolate).[26] Synthesis of this compound was performed similarly to the compound synthesized in this work.

The reaction of *fac*–$[Ru^{II}(CO)_3Cl_2(THF)]$ with excess thiolate in MeOH generates a solution whose IR spectrum is consistent with $[Ru^{II}(CO)_3(S–2,4,6–i–Pr_3C_6H_2)_3]^{1–}$ (**Figure V–32**) due to its similarity to the IR spectrum of *fac*–$[Me_3NBz][Ru^{II}(CO)_3(S–2,3,5,6–Me_4C_6H)_3]$ compound. The intensity of two peaks in the spectrum are consistent with a facial $M(CO)_3$ unit and the lower energy of these peaks is consistent with the greater donating ability of [S–2,4,6–*i*–$Pr_3C_6H_2$] vs **[**S–2,3,5,6–$Me_4C_6H$]**.** Addition of oxygen to the reaction mixture resulted in its transformation to the reduced $Ru^{I}Ru^{I}$ dimer, $[Ru^{I}(CO)_3(S–2,4,6–i–Pr_3C_6H_2)]_2$. It is counter intuitive for the addition of $O_2$ to lead to the reduction of the metal. These process was repeated five times and an immeditate color change was observed, from yellow to orange upon the addition of $O_2$. Infrared spectroscopy was used to monitor the reaction, **Figure V–32** illustrates the reaction before oxygen was introduced while **Figure V–33** illustrates the reaction after oxygen was introduced. The purpose of the excess thiolate was to act as a reducing agent. The intermediate product, before the oxygen was applied, was thought to be *fac*–$[Ru^{II}(CO)_3(S–2,4,6–i–Pr_3C_6H_2)_3]^{–}$ due to the similarity to the IR spectrum of *fac*–$[Me_3NBz][Ru^{II}(CO)_3(S–2,3,5,6–Me_4C_6H)_3]$. Upon the addition of $O_2$, the reaction was left to stir overnight and large orange crystals were observed, which were identified to be tri–isopropylbenzenedisulfide by X–ray crystallography. The disulfide was filtered off and the solvent was removed *in vacuo*. The resulting orange precipitate was purified by column chromatography. The solution was collected until the yellow band was removed from the column. The resulting yellow solvent was concentrated to approximately one–fifth of the original volume and placed in a –20 $^{o}$C freezer for several days. The resulting yellow needle crystals, suitable for X–ray crystallography, were collected. Infrared analysis of the yellow crystals was comparable to **Figure V–33**.

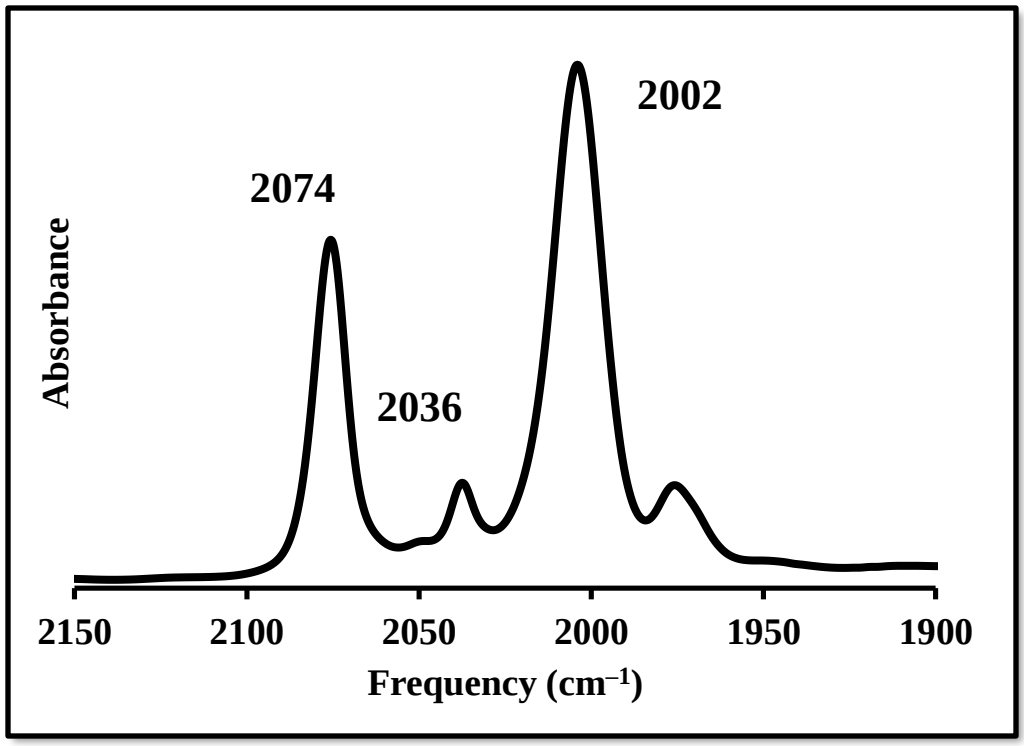


**Figure V–32. Infrared spectrum of $[Ru^{II}(CO)_3(S–2,4,6–i–Pr_3C_6H_2)_3]^{1–}$, before air was applied, in MeOH.**

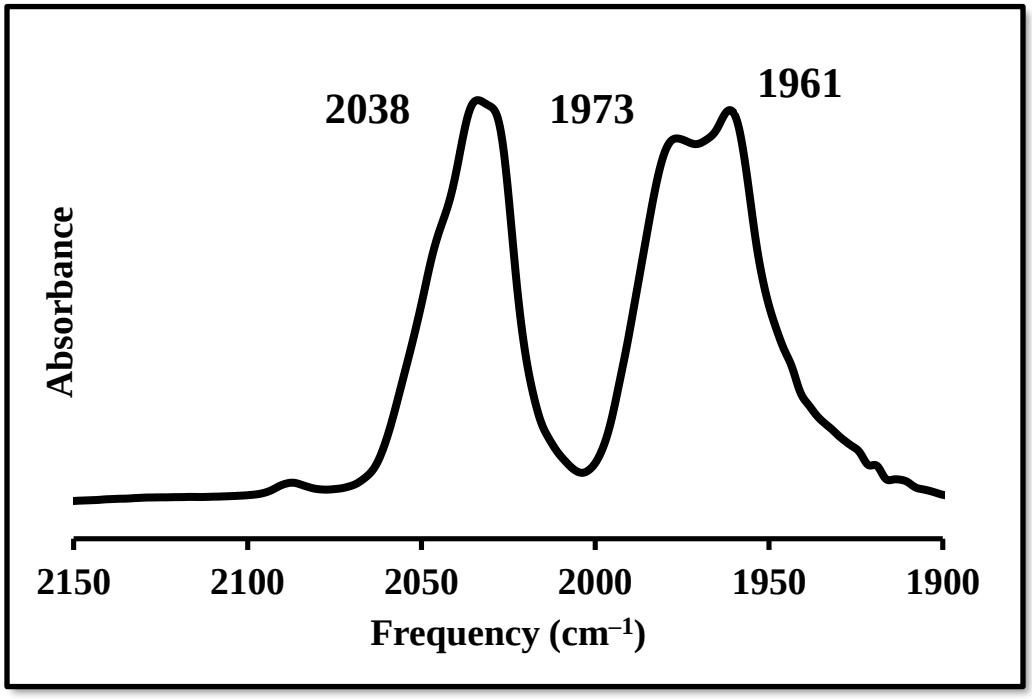


**Figure V–33. Infrared spectrum of $[Ru^{I}(CO)_3(S–2,4,6–i–Pr_3C_6H_2)]_2$ in pentane.**

The role being played by $O_2$ is unknown. The excess thiolate ligand should be sufficient to supply the reducing equivalent and explain the production of the disulfide.

The X–ray structure of $[Ru^{I}(CO)_3(S–2,4,6–i–Pr_3C_6H_2)]_2$ confirmed a ruthenium(I) dimer which displays a butterfly arrangement with six carbonyl ligands and two bridging triisopropylbenzenethiolates. Crystals, suitable for X–ray crystallography, were grown from a concentrated pentane solution at –20 $^{o}$C. The crystal structure was solved under a monoclinic crystal system $P2_1/c$. The general structure of the ruthenium dimer is illustrated in **Figure V–34**. To date, this structure is only the fifth compound, of this type, that has been reported in the literature. The general structures, $[Ru^{I}(CO)_3(S)]_2$ (where S = 2,2,6,6–tetramethylcyclohexylidenemethanethiolate $[C_{11}H_{18}S]$)[30] and $[Ru^{I}(CO)_6(SS)]$ (where SS = 1,3–propanedithiolate [pdt][26], 1,2–ethanedithiolate [edt][31] and 1,2–benzenedithiolate [bdt][32]), have been reported with the earliest report from Seitz *et al*. in 1988 while the next few structures were not reported until after the turn of the new century. The $Ru–C_{axial(avg)}$, $Ru–C_{basal(avg)}$, $Ru–S_{avg}$ and $C–O_{axial(avg)}$ and $C–O_{basal(avg)}$ bond distances for $[Ru^{I}(CO)_3(S–2,4,6–i–Pr_3C_6H_2)]_2$ are 1.955(9) Å, 1.899(8) Å, 2.4520(2) Å, 1.137(2) Å and 1.138(2) Å respectively. The Ru–Ru bond distance of $[Ru^{I}(CO)_3(S–2,4,6–i–Pr_3C_6H_2)]_2$ was measured to be 2.6244(2) Å, which is the shortest Ru–Ru bond out of all the compounds of this class. The $Ru–S_{avg}$ bond distance of $[Ru^{I}(CO)_3(Stip)]_2$ was measured to be the longest out of all the compounds. This is due to the steric effects of the isopropyl groups, located on the *ortho* positions, of the thiolate. The ruthenium–carbonyl bond distances, both axial and basal, are within range from the other previously reported compounds. All the bond distances of the five compounds are summarized in **Table V–12**. Selective bond distances and angles for $[Ru^{I}(CO)_3(S–2,4,6–i–Pr_3C_6H_2)]_2$ are summarized in **Table V–13**.

**Table V–12. Comparison of Bond Distances for $[Ru^{I}(CO)_6(SS)$.**

| Bond | This Work | pdt | edt | bdt | $C_{11}H_{18}S$ |
|---|---|---|---|---|---|
| Ru – Ru | 2.6244(2) | 2.6743(13) | 2.6790(8) | 2.650(2) | 2.678(1) |
| $Ru – S_{avg}$ | 2.4521 | 2.396 | 2.373 | 2.408 | 2.419 |
| $Ru – C_{axial}$ | 1.955 | 1.941 | 1.919 | 1.949 | 1.954 |
| $Ru – C_{basal}$ | 1.899 | 1.912 | 1.906 | 1.893 | 1.904 |
| $C – O_{axial}$ | 1.137 | not listed | 1.136 | 1.124 | 1.117 |
| $C –O_{basal}$ | 1.138 | not listed | 1.134 | 1.130 | 1.131 |

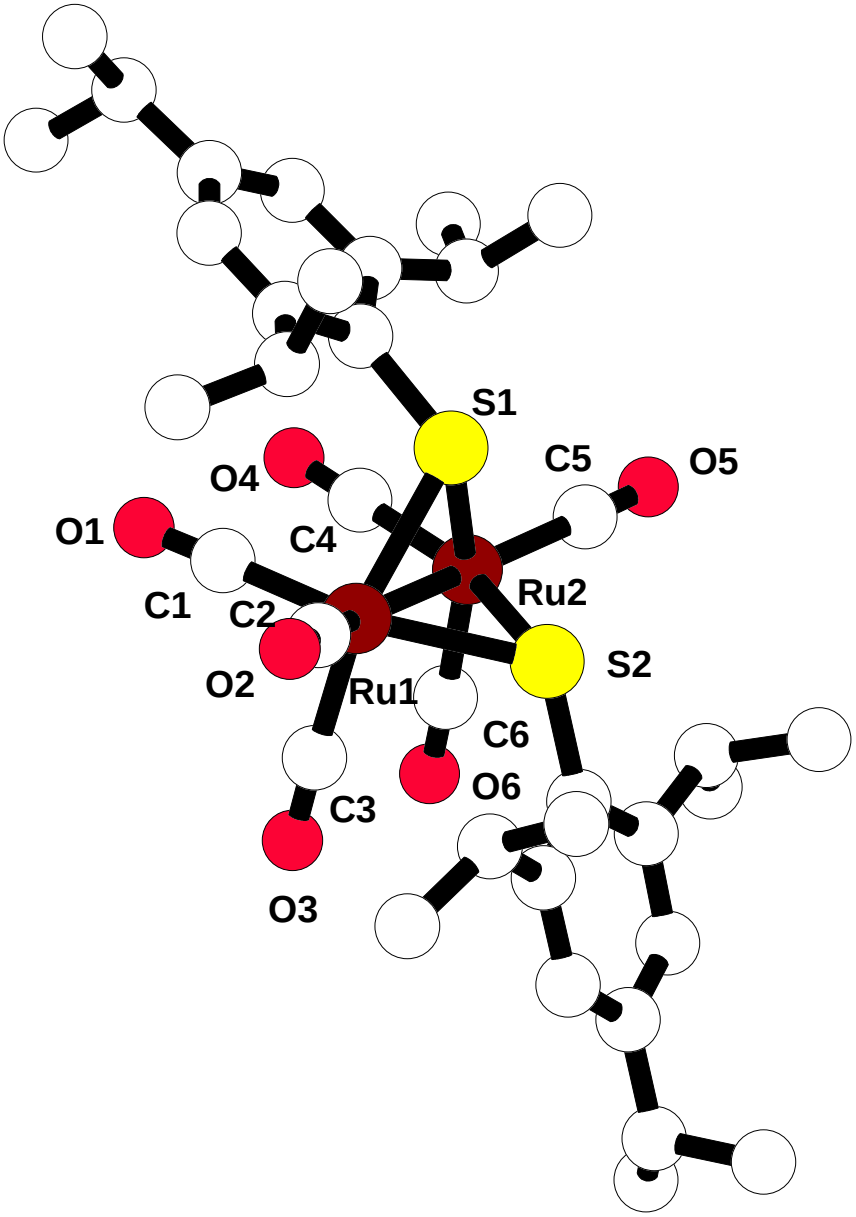


**Figure V–35. X–ray structure of $[Ru^{I}(CO)_3(S–2,4,6–i–Pr_3C_6H_2)]_2$.**

| Table V–13. Selective Crystallographic Data for $[Ru^{I}(CO)_3(S–2,4,6–i–Pr_3C_6H_2)]_2$. | | | | | |
|---|---|---|---|---|---|
| **Bond Distances (Å)** | | **Bond Angles (°)** | | **Bond Angles (°)** | |
| Ru(1) – C(1) | 1.900(10) | Ru(2)–S(2)–Ru(1) | 64.646(14) | C(4)–Ru(2)–S(2) | 156.41(7) |
| Ru(1) – C(2) | 1.916(8) | C(3)–Ru(1)–C(1) | 91.31(9) | C(6)–Ru(2)–S(2) | 93.82(6) |
| Ru(1) – C(3) | 1.918(12) | C(3)–Ru(1)–C(2) | 96.81(9) | C(5)–Ru(2)–S(2) | 106.92(6) |
| Ru(2) – C(4) | 1.914(11) | C(1)–Ru(1)–C(2) | 96.54(9) | S(1)–Ru(2)–S(2) | 73.241(18) |
| Ru(2) – C(5) | 1.864(10) | C(3)–Ru(1)–S(1) | 154.70(7) | C(4)–Ru(2)–Ru(1) | 98.76(6) |
| Ru(2) – C(6) | 2.415(2) | C(1)–Ru(1)–S(1) | 93.74(7) | C(6)–Ru(2)–Ru(1) | 98.18(7) |
| Ru(1) – S(1) | 2.464(2) | C(2)–Ru(1)–S(1) | 107.18(7) | C(5)–Ru(2)–Ru(1) | 159.34(6) |
| Ru(1) – S(2) | 2.471(2) | C(3)–Ru(1)–S(2) | 92.48(7) | S(1)–Ru(2)–Ru(1) | 57.588(13) |
| Ru(2) – S(1) | 2.425(2) | C(1)–Ru(1)–S(2) | 155.61(6) | S(2)–Ru(2)–Ru(1) | 57.696(13) |
| Ru(2) – S(2) | 2.425(2) | C(2)–Ru(1)–S(2) | 106.90(7) | Ru(1)–S(1)–Ru(2) | 64.768(14) |
| C(1) – O(1) | 2.445(2) | S(1)–Ru(1)–S(2) | 73.250(18) | O(1)–C(1)–Ru(1) | 177.21(19) |
| C(2) – O(2) | 2.384(2) | C(3)–Ru(1)–Ru(2) | 97.11(6) | O(2)–C(2)–Ru(1) | 175.1(2) |
| C(3) – O(3) | 2.446(2) | C(1)–Ru(1)–Ru(2) | 97.96(6) | O(3)–C(3)–Ru(1) | 176.9(2) |
| C(4) – O(4) | 2.282(2) | C(2)–Ru(1)–Ru(2) | 159.60(7) | O(4)–C(4)–Ru(2) | 178.4(2) |
| C(5) – O(5) | 2.276(3) | S(1)–Ru(1)–Ru(2) | 57.644(13) | O(5)–C(5)–Ru(2) | 174.69(19) |
| C(6) – O(6) | 2.243(3) | S(2)–Ru(1)–Ru(2) | 57.659(12) | O(6)–C(6)–Ru(2) | 177.9(2) |
| | | C(4)–Ru(2)–C(6) | 90.97(9) | C(4)–Ru(2)–S(1) | 93.46(7) |
| | | C(4)–Ru(2)–C(5) | 95.44(9) | C(6)–Ru(2)–S(1) | 155.76(7) |
| | | C(6)–Ru(2)–C(5) | 96.49(9) | C(5)–Ru(2)–S(1) | 106.77(7) |

## 5.4 Conclusions

In conclusion, various *fac*–$[Ru^{II}(CO)_3(L_3)]$ (where $L_3$ = PS2, PS2', POS2, NS2 and NS2') where synthesized and characterized by IR, NMR ($^1H$ and $^{13}C$), X–ray crystallography, UV–Vis and electrochemistry. All *fac*–$[Ru^{II}(CO)_3(L_3)]$ were synthesized using *fac*–$[Ru^{II}(CO)_3Cl_2(THF)]$ at –78 °C to afford the desired product. Synthesis of *fac*–$[Ru^{II}(CO)_3Cl_2(THF)]$ was performed by a modified procedure where the reaction takes place in air as opposed to under a dinitrogen atmosphere.

The X–ray structures of *fac*–[$Ru^{II}(CO)_3$(PS2)] and *fac*–[$Ru^{II}(CO)_3$(PS2')] confirmed a distorted octahedron where the M–L bond distances decreased from the [PS2] complex to [PS2'] complex due to the electron donating effects of the methyl groups on the [PS2'] ligand. The X–ray structure confirmed a ruthenium trimer, [$Ru^{II}_3(CO)_5(PS2')_3$], from the thermal decomposition of *fac*–[$Ru^{II}(CO)_3$(PS2')] in methylene chloride. The same observation was seen when *fac*–[$Ru^{II}(CO)_3$(NS2')] went under a thermal decomposition to form a ruthenium dimer, [$Ru^{II}(CO)_2$(NS2')]$_2$. Infrared studies and X–ray crystallography confirmed the geometric arrangement of the carbonyl ligands. The X–ray structures of the iron and ruthenium complexes were compared and the M–L bond distances increased from iron to ruthenium due to the increasing atomic radii.

Synthesis of *fac*–[$Ru^{II}(CO)_3Cl_2$(THF)] with three equivalence of a monodentate thiolate ligand formed *fac*–[$Ru^{II}(CO)_3(SR)_3]^-$ complex which was confirmed by X–ray crystallography. Synthesis of *fac*–[$Ru^{II}(CO)_3Cl_2$(THF)] with excess monodentate thiolate ligand, in the presence of air, formed [$Ru^{I}(CO)_3(SR)_3$] which was confirmed by X–ray crystallography. The role of $O_2$ is not currently understood; however, this observation is currently being investigated.

## 5.5 References


1. Koch, S. A.; Millar, M. *J. Am. Chem. Soc.*, **1983**, *105*, 3362–3363.
2. Foster, M. W.; Cowan, J. A. *J. Am. Chem. Soc.* **1999**, *121*, 4093–4100.
3. Kerbs, C.; Henshaw, T. F.; Cheek, J.; Huynh, B. H.; Broderick, J. B. *J. Am. Chem. Soc.* **2000**, *122*, 12497–12506.
4. Wiler, J .J.; Lippard, S. J. *Inorg. Chem.* **1999**, *38*, 3569–3574.
5. Nakamura, A. *Inorg. Chem.* **1996**, *35*, 6473–6484.
6. Millar, M.; O'Sullivan, T.; deVries, N.; Koch, S. A. *J. Am. Chem. Soc.* **1985**, *107*, 3714.
7. Soong, S.; Hain, Jr., J. H.; Millar, M.; Koch, S. A. *Organometallics* **1988**, *7*, 556–557.
8. Satsangee, S. P.; Hain, Jr., J. H.; Cooper, P. T.; Koch, S. A. *Inorg. Chem.* **1992**, *31*, 5160–5161.
9. http://www.mpg.de/350372/forschungsSchwerpunkt
10. http://metallo.scripps.edu/PROMISE/RUBREDOXIN.html

11. Bianchini, C.; Meli, A.; Moneti, S.; Vizza, F. *Organometallic* **1998**, *17*, 2636–2645.
12. Tanaka, K.; Mizukawa, T. *Appl. Organometal. Chem.* **2000**, *14*, 863–866.
13. Tanaka, K.; Ooyama, D. *Coor. Chem. Rev.* **2002**, *226*, 211–218.
14. Ishiguro, A.; Liu, Y.; Nakajima, T.; Wakatsuki, Y. J.*Catalysis*, **2002**, *206*, 159–164.
15. Cleare, M. J.; Griffith, W. P. *J. Chem. Soc. A* **1969**, 372.
16. Panda, B. K.; Chattopadhyay, S.; Ghosh, K.; Chakravorty, A. *Polyhedron*, **2002**, *21*, 899–904.
17. Shiu, K. B.; Yu, S. J.; Wang, Y.; Lee, G. H. *J. Organometal. Chem.*, **2002**, *650*. 37–42.
18. Janet Haff, PhD dissertation, Stony Brook University, Stony Brook, 2002.
19. Doris Melgarejo, PhD dissertation, Stony Brook University, Stony Brook, 2006.
20. Frey, M. *ChemBioChem* **2002**, *3*, 153–160.
21. Schmidt, M.; Contakes, S. M.; Rauchfuss, T. B. *J. Am. Chem. Soc.* **1999**, *121*, 9736–9737.
22. Zhao, X.; Georgakaki, I. P.; Miller, M. L.; Yarbrough, J. C.; Darensbourg, M. Y. *J. Am. Chem. Soc.* **2001**, *123*, 11010–11018.
23. Gloaguen, F.; Lawreence, J .D.; Rauchfuss, T. B. *J. Am. Chem. Soc.* **2001**, *123*, 9476–9477.
24. Borg, S. J.; Behrsing, T.; Best, S. P.; Razavet, M.; Liu, X.; Pickett, C. J. *J. Am. Chem. Soc.* **2004**, *126*, 16988–16999.
25. Mejia–Rodriguez, R.; Chong, D.; Reibenspies, J. H.; Soriaga, M. P.; Darensbourg, M. Y. *J. Am. Chem. Soc.* **2004**, *126*, 12004–12014.
26. Justice, A. K.; Linck, R. C.; Rauchfuss, T. B. *Inorg. Chem.* **2006**, *45*, 2406–2412.
27. Gray, G. M.; Duffey, C. H. *Acta Crystallographica Sec. C* **1996**, C52, 861–863.
28. Reddy, V. V. S.; Whitten, J. E.; Redmill, K. A.; Varshney, A.; Gray, G. M. *J. Organomet. Chem.* **1989**, *372*, 207–216.
29. Gina Chiarella, PhD dissertation, Stony Brook University, Stony Brook, 2006.
30. Seitz, K.; Behrens, U. *J. Organomet. Chem.* **1988**, *345*, 351.
31. Hanif, K. M.; Kabir, S. E.; Mottalib, M. A.; Hursthouse, M. B.; Malik, K. M. A; Rosenberg, E. *Polyhedron* **2000**, *19*, 1073.
32. Cabeza, J. A.; Martinez–Gomez, M. A.; Riera, V.; Arhura, D.; Garcia–Granda, S. *Organometallics*, **1998**, *17*, 1471.

33. Shiu, K. B.; Wang, Y.; Liao, F. L.; Chiang, M. Y.; Peng, S. M.; Lee, G. H.; Wang, J. C.; Liou, L, S. *Organometallics* **1998**, *17*, 1790–1797.
34. Jessop, P. G.; Rettig, S. J.; Lee, C. L.; James, B, R. *Inorg. Chem.* **1991**, *30*, 4617–4627.
35. Grapperhaus, C. A.; Poturovic, S.; Masguta, M. S. *Inorg. Chem.* **2002**, *41*, 4309–4311.
36. Sekkmann, D.; Heinemann, F. W.; Gottschlak,–Gaudig, T. *Inorg. Chem.* **1998**, *37*, 3982–3988.

# CHAPTER 6. Synthesis and Characterization of New Models of [NiFe] Hydrogenase

## 6.1 Introduction

There are several microorganisms, classified as hydrogenase enzymes, which catalyze the reversible formation and consumption of dihydrogen (**Reaction VI–1**).[1–3]

$$2\,H^{+} + 2\,e^{-} \leftrightarrows H_2$$

**Reaction VI–1. Redox reaction of dihydrogen.**

Several crystal structures of [NiFe] hydrogenases have shown that these enzymes have a common but unique active site. The construction of the active site is a dithiolate–bridged Ni–Fe center with two cyanides ($CN^{-}$) and a carbonyl ligand (CO) coordinated to the Fe atom (**Figure VI–1**). Crystallographic studies of the oxidized form of the enzyme indicate the presence of a third bridging ligand, which is represented in **Figure VI–1** as X. It has been thought that the third bridging ligand could be an $O^{2-}$, $OH^{-}$ or $OOH^{-}$.[4] This bridging ligand has shown to be replaced by a spectroscopically detected hydride in some reduced forms of these enzymes.[5]

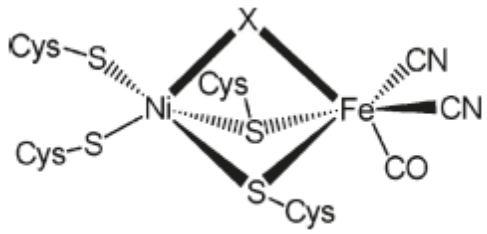


**Figure VI–1. Active site of [NiFe] hydrogenase.**

The synthesis of these analogues, for this dinuclear center, has been extremely challenging. First, there are two different metals in the active site. Second, there are five different ligands to account for. In 2005, the closest synthetic analogue for the [NiFe] center was $[Fe^{II}(CN)_2(CO)_2(\mu\text{–pdt})Ni^{II}(S_2CNR_2)]^{-}$ (where pdt = 1,3–propanedithiolate; $S_2CNR_2$ = dithiocarbamate, where R = Et, piperdine), which was reported by Tatsumi *et al*. (**Figure VI–2**).[6] The reported compounds differ from the geometry of the Fe centers found in the enzymes. The

noted difference of the geometry is in the enzyme where the cyanide ($CN^-$) is found in the *cis* arrangement, while the synthetic complexes the $CN^-$ ligands are found in the *trans* arrangement. The second noted difference is that the enzyme contains one carbon monoxide (CO) ligand while the synthetic complex contains two CO ligands.

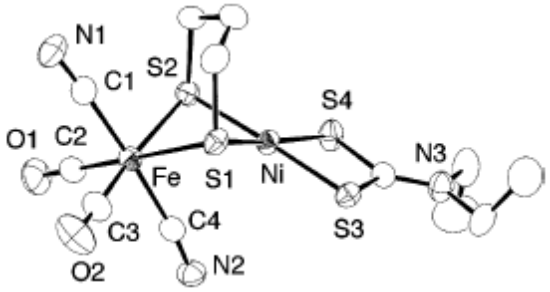


**Figure VI–2. X–ray structure of $[Fe^{II}(CN)_2(CO)_2(\mu\text{–pdt})Ni^{II}(S_2CNEt_2)]^-$.**

In 2009, another set of Ni–Fe dimers were synthesized by Jiang *et al.*[7] Here the starting material used to synthesize the dimer was different from Tatsumi's *et al*. synthetic route. Tatsumi used *trans,mer*–$[Fe^{II}(CN)_2(CO)_3Br]^-$ while Jiang *et al*. used *fac*–$[Fe^{II}(CN)_2(CO)_3I]^-$. There are two notable differences from the two starting material, the first being one complex contains bromide and the other iodide. The second, most important, difference is the cyanide ($CN^-$) ligands are *trans* in Tatsumie's complex while *cis* in Jiang's complex. This difference in geometry for the cyanide is important due to the fact that the enzyme has the cyanide in the *cis* configuration. Using *fac*–$[Fe^{II}(CN)_2(CO)_3I]^-$, Jiang *et al.* were able to synthesize two new analogues of the [NiFe] hydrogenase a hexamer, $[(dppe)Ni^{II}(\mu\text{–}SEt)_2Fe^{II}(CN)_2(CO)_2]_6$ (where dppe = 1,2–bis(diphenylphosphino)ethane and SEt = ethanethiolate) where the cyanide ligands are in a *cis* configuration, and a dimer, $[(dppe)Ni^{II}(\mu\text{–pdt})Fe^{II}(CN)_2(CO)_2]$ (**Figures VI–3** and **Figure VI–4** respectively) where the cyanide ligands are in the *trans* configuration.

There has been models of the [NiFe]–hydrogenase, see Chapter 1; however, only a few have the same ligation as found in the enzyme active site. The primary goal of this research is to synthesize nickel–iron dimers containing cyanide, carbonyls and thiolates to model the active site as well as study the catalytic activity.

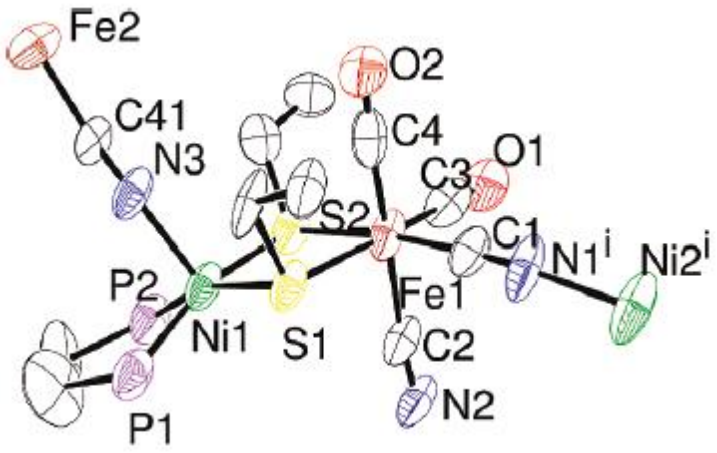


**Figure VI–3. ORTEP drawing of one Ni–Fe unit of $[(dppe)Ni^{II}(\mu\text{–}SEt)_2Fe^{II}(CN)_2(CO)_2]_6$ (phenyl groups and hydrogens were omitted for clarity).**

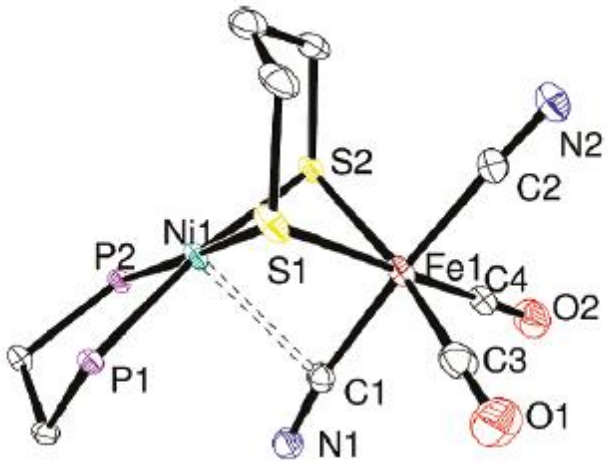


**Figure VI–4. ORTEP drawing of $[(dppe)Ni^{II}(\mu\text{–}pdt)Fe^{II}(CN)_2(CO)_2]$ (phenyl groups and hydrogens were omitted for clarity).**

## 6.2 Experimental

**Synthesis of *cis*–$[Fe^{II}(CO)_4I_2]$**

The product was synthesized according to a literature procedure.[8] A solution of $I_2$ (25.99 g, 102 mmol) in 60 mL of dry diethyl ether was added dropwise onto a solution of $Fe^0(CO)_5$ (14 mL, 20.86 g, 106 mmol) in 30 mL of dry diethyl ether at 0 $^oC$ under nitrogen during 30 minutes. After addition of iodine, reaction mixture was keep stirring for another 150 minutes at 0 $^oC$. The

final reaction mixture had a red wine color. The solvent was removed by rotary–evaporation. Solid product was dried under vacuum for 20 minutes and stored at –20°C. Final product weight = 40.3 g (97.8 mmol). Yield = 94%. Infrared spectrum was taken to verify purity.

**Infrared (hexane):** $\nu_{CO}$ = 2062, 2085 and 2130 $cm^{-1}$

**Synthesis of *fac*–K[$Fe^{II}(CN)_2(CO)_3I$]**

The product was synthesized according to a literature procedure.[9] All manipulations were performed in air and in absence of light. To a solution of $Fe^{II}(CO)_4I_2$ (5 g, 11.9 mmol) in 100 mL of methanol was added KCN (1.54 g, 23.7mmol). The mixture was allowed to stir overnight at room temperature. A black precipitate was filtered off and the solvent was removed using a rotary evaporator resulting in a dark red solid to be observed. The red solid was dissolved in minimum amount of absolute ethanol (~20 mL). The suspension was centrifuged for ten minutes to remove any potassium iodide. The dark red solution was decanted and placed in a 100 mL Schlenk flask. The solvent was removed *in vacuo*. Infrared spectra were taken to verify purity (Yield: 3.47 g, 81.7%)

**Infrared ($CH_3OH$):** $\nu_{CO}$ = 2064 and 2103 $cm^{-1}$; $\nu_{CN}$ = 2145 and 2133 $cm^{-1}$.

**Synthesis of $Ni^{II}$(S4)**

The product was synthesized according to a literature procedure.[10] To a stirred solution of 4.5 g (18.9 mmol) of $NiCl_2 \cdot 6H_2O$ in 100 mL of water and 60 mL of ethanol was added a solution of 4.5 g (19.7 mmol) of $H_2S4$ and 18 mL of 17.5% NaOH (78.8 mmol) in 50 mL of water at 50°C. The resulting brown solution was refluxed for 30 minutes and filtered while hot. The filtrate was stored in the refrigerator for 24 hours to afford red–black needles. The product was filtered, washed with ethanol and dried *in vacuo*. Crystals were grown from reaction mixture at − 20 °C Yield: 4.5 g, 80%

**Unit Cell:** Monoclinic, $P2_1/n$, a = 9.3839(3) Å, b = 8.5363(2) Å, c = 13.5316(4) Å, $\alpha = \gamma = 90^o$ $\beta = 92.032(3)^o$, V = 1083.25(5) $Å^3$.

A red–black needle crystal measuring 0.50 × 0.35 × 0.15 $mm^3$ was mounted using a nylon loop and centered on the X–ray beam at 100 K. Crystals were grown from reaction mixture at –20°C. Crystals were grown within one day. The accurate unit cell was obtained using reflection with $2\theta = 3.23 – 29.57^o$: a = 9.3839(3) Å, b = 8.5363(2) Å, c = 13.5316(4) Å, $\alpha = \gamma = 90^o$ $\beta = 92.032(3)^o$, V = 1083.25(5) $Å^3$. The structure was solved under a primitive monoclinic crystal system (space group $P2_1/n$) using 2680 reflections. The asymmetric unit consists of one

molecule of the nickel complex. The data reduction was done using CryAlisPro and the structure refinement was done with SHELXL–97 (Sheldrick). All the non–hydrogen atoms were located by Direct Methods and were refined anisotopically by a full–matrix least–squares method. The positions of the remaining hydrogen atoms were calculated. The crystallographic parameters and atomic coordinates for this compound are located in **Table A–24**.

**Synthesis of *cis*–[$Ni^{II}$(dppe)$Cl_2$]**

The product was synthesized according to a literature procedure.[11] In a 100 mL Schlenk flask, a solution of 1,2–bis(diphenylphosphino)ethane (dppe) (2.00 g, 5.04 mmol) in $CH_2Cl_2$ (25 mL) was added dropwise, *via* cannula, to a solution of $Ni^{II}Cl_2$•$6H_2O$ (1.19 g, 5.01 mmol) in ethanol (20 mL), which became dark red. The mixture was stirred for thirty minutes at room temperature. Dark orange microcrystalline precipitate was filtered using an open frit. Product was washed with diethyl ether (4 x 20 mL) and dried under vacuum. Crystals were grown by vapor diffusion using methylene chloride and diethyl ether at −20 $^oC$. Yield: 2.44 g, 92%

**Unit Cell:** Monoclinic, $P2_1/c$, a = 12.1826(2) Å, b = 15.2299(3) Å, c = 15.1924(3) Å, $\alpha = \gamma = 90^o$ $\beta = 105.666(2)^o$, V = 2714.08(9) $Å^3$.

A green–yellow prism crystal measuring 0.80 × 0.50 × 0.50 $mm^3$ was mounted using a nylon loop and centered on the X–ray beam at 100 K. Crystals were grown by laying of methylene chloride and diethyl ether at room temperature. Crystals were grown within one week. The accurate unit cell was obtained using reflection with $2\theta = 3.19 – 29.48^o$: a = 12.1826(2) Å, b = 15.2299(3) Å, c = 15.1924(3) Å, $\alpha = \gamma = 90^o$ $\beta = 105.666(2)^o$, V = 2714.08(9) $Å^3$. The structure was solved under a primitive monoclinic crystal system (space group $P2_1/c$) using 6474 reflections. The asymmetric unit consists of one molecule of the nickel complex and one molecule of methylene chloride. The data reduction was done using CryAlisPro and the structure refinement was done with SHELXL–97 (Sheldrick). All the non–hydrogen atoms were located by Direct Methods and were refined anisotopically by a full–matrix least–squares method. The positions of the remaining hydrogen atoms were calculated. The crystallographic parameters and atomic coordinates for this compound are located in **Table A–25**.

**Synthesis of *trans*,*cis*–[$Fe^{II}(CN)_2(CO)_2Ni^{II}$(S4)]**

Synthesis of this complex was done in absence of light. To a stirred solution of K[$Fe^{II}(CN)_2(CO)_3$I] (0.25 g, 0.69 mmol) in 50 mL of methanol was added $Ni^{II}$(S4) (0.10 g, 0.35 mmol). The mixture was allowed to stir for three hours. A light yellow precipitate was observed

and was filtered off using a closed frit packed with celite. The solvent was removed *in vacuo*. The resulting dark red product was purified with minimum amount of $CH_2Cl_2$ and stirred for two hours. The suspension was filtered using a closed frit packed with celite. The solvent was removed to afford a dark red–brown solid. Yield: 0.085 g, 53.9%. Crystals were grown using vapor diffusion using methylene chloride and diethyl ether at –20°C.

**Infrared ($CH_2Cl_2$):** $\nu_{CO}$ = 2011 and 2057 $cm^{-1}$; $\nu_{CN}$ = 2099 and 2119 $cm^{-1}$.

**Unit Cell:** Triclinic, *P*–1, a = 7.8344(5) Å, b = 10.2131(6) Å, c = 13.0208(8) Å, α = 76.188(5)°, β = 78.263(5)°, γ = 73.029(5)°, V = 957.57(10) $Å^3$.

A red–brown plate crystal measuring 0.20 × 0.15 × 0.15 $mm^3$ was mounted using a nylon loop and centered on the X–ray beam at 100 K. Crystals were grown by vapor diffusion of methylene chloride and diethyl ether at –20 °C. Crystals were grown within one week. The accurate unit cell was obtained using reflection with 2θ = 2.91 – 29.58°: a = 7.8344(5) Å, b = 10.2131(6) Å, c = 13.0208(8) Å, α = 76.188(5)°, β = 78.263(5)°, γ = 73.029(5)°, V = 957.57(10) $Å^3$. The structure was solved under a primitive triclinic crystal system (space group *P*–1) using 4976 reflections. The asymmetric unit consists of one molecule of the nickel–iron dimer. The data reduction was done using CryAlisPro and the structure refinement was done with SHELXL–97 (Sheldrick). All the non–hydrogen atoms were located by Direct Methods and were refined anisotopically by a full–matrix least–squares method. The positions of the remaining hydrogen atoms were calculated. The crystallographic parameters and atomic coordinates for this compound are located in **Table A–26**.

**Attempted Synthesis of [$Fe^{II}(CN)_2(CO)_2$(*μ*–ndt)$Ni^{II}$(dppe)]**

Synthesis of this complex was done in the dark. To a stirred solution of $K[Fe^{II}(CN)_2(CO)_3I]$ (0.25 g, 0.69 mmol) in 15 mL of methanol was added, *via* cannula, $Li_2$ndt (where ndt = norbornanedithiolate). $Li_2$ndt was generated in a 10 mL of methanol solution using $H_2$ndt (0.067 g, 0.42 mmol) and lithium wire (0.006 g, 0.84 mmol) placed in a 50 mL Schlenk flask. Solution was transferred when all reagents were dissolved. The reaction mixture was stirred for three hours at room temperature. The solvent was removed *in vacuo* which resulted in a dark red solid. Approximately 20 mL of $CH_2Cl_2$ was added to the reaction flask and was stirred for twenty minutes. To the $CH_2Cl_2$ solution, $Ni^{II}$(dppe)$Cl_2$ (0.11 g, 0.21 mmol) was added and the solution changed color from dark red to purple. The solution was stirred for an additional two

hours. The solution was filtered *via* closed frit packed with celite. The filtrate was removed *in vacuo* which resulted in a red–brown solid. Yield: 0.153 g, 46.7%.

**Infrared ($CH_2Cl_2$):** $\nu_{CO}$ = 2056 and 2014 $cm^{-1}$; $\nu_{CN}$ = 2125 $cm^{-1}$.

**Attempted Synthesis of [$Fe^{II}(CN)_2(CO)_2$(*μ*–*o*–xyl)$Ni^{II}$(dppe)]**

Synthesis of this complex was done in the dark. To a stirred solution of $K[Fe^{II}(CN)_2(CO)_3I]$ (0.25 g, 0.69 mmol) in 15 mL of methanol was added, *via* cannula, $Li_2$*o*–xyl (where *o*–xyl = *o*–xylene–*α*,*α*'–dithiolate). $Li_2$*o*–xyl was generated in a 10 mL of methanol solution using $H_2$*o*–xyl (0.071 g, 0.42 mmol) and lithium wire (0.006 g, 0.84 mmol) placed in a 50 mL Schlenk flask. Solution was transferred when all reagents were dissolved. The reaction mixture was stirred for four hours at room temperature. The solvent was removed *in vacuo* which resulted in a dark red solid. Approximately 20 mL of $CH_2Cl_2$ was added to the reaction flask and was stirred for twenty minutes. To the $CH_2Cl_2$ solution, $Ni^{II}(dppe)Cl_2$ (0.11 g, 0.21 mmol) was added and the solution changed color from dark red to purple. The solution was stirred for an additional two hours. The solution was filtered *via* closed frit packed with celite. The filtrate was removed *in vacuo* which resulted in a dark red–brown solid. Yield: 0.173 g, 52.6%.

**Infrared ($CH_2Cl_2$):** $\nu_{CO}$ = 2056 and 2016 $cm^{-1}$; $\nu_{CN}$ = 2134 $cm^{-1}$.

## 6.3 Results and Discussion

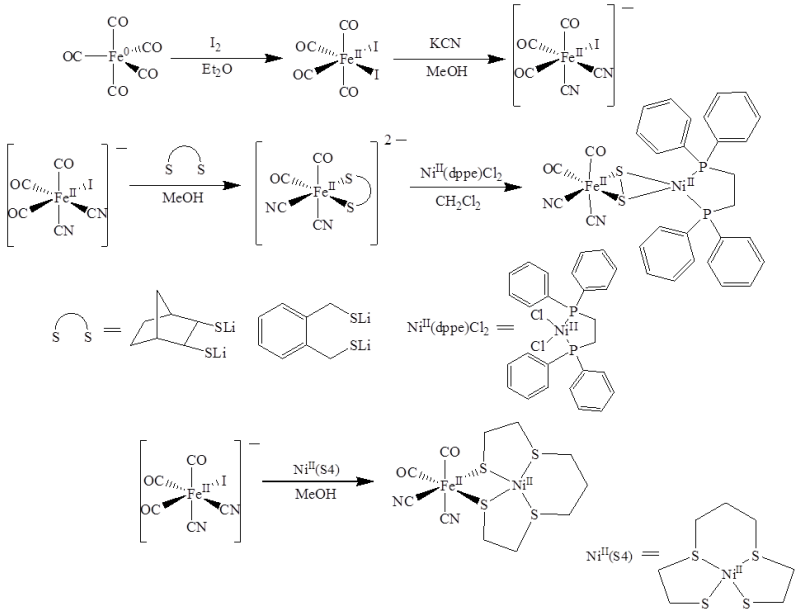


**Figure VI–5. Overall reaction scheme of iron and nickel complexes.**

### 6.3.1 Synthesis and Infrared Studies of the Iron Starting Material

Synthesis of *cis*–[$Fe^{II}(CO)_4I_2$] was prepared in a very direct and simple procedure. This redox reaction was performed under anaerobic conditions in a solution of diethyl ether. Storage of the desired product was stored in a freezer at –20 $^oC$; however, thr compound is stable at room temperature for long periods of time. The overall reaction scheme is illustrated in **Figure VI–5**.

The infrared spectrum shows three peaks, which correspond to the carbonyl ligands. The infrared spectrum for this compound can be found in Gina Chiarella's PhD dissertation, IR was comparable to those found in her dissertation.[8]

Synthesis of *fac*–[$Fe^{II}(CN)_2(CO)_3I]^-$ was performed in air and in the dark. To a methanolic solution of $Fe^{II}(CO)_4I_2$ was added two molar equivalence of potassium cyanide (KCN), which was stirred overnight at room temperature.

A black precipitate, which may be a polymer, was observed and filtered to give a dark red solution. The starting material, *cis*–[$Fe^{II}(CO)_4I_2$], has been shown to polymerize at room temperature under long exposure to air where the iodide act as bridging ligands.[12] The black precipitate is insoluble in a wide range of solvents including strong acid or strong base.

The dark red solution was transferred to a round bottom flask and placed on a rotary evaporator to remove the solvent. The resulting dark red solid was redissolved in a minimum amount of absolute ethanol and was centrifuged for ten minutes, at maximum speed, to remove any undissolved potassium iodide. The supernatant was transferred to a flask and the solvent was removed *in vacuo*, which resulted in a red–orange solid. The solvent cannot be removed using a rotary evaporator due to decomposition and isomerization of the desired product. Storage of the desired product was kept in a freezer at –20 $^oC$ as the product is not thermodynamically or photochemically stable.

The infrared spectrum shows two peaks at 2066 and 2103 $cm^{-1}$, which correspond to the carbonyl ligands. One peak appears broad with a slight shoulder, while the other peak is straight and narrow. This common spectrum corresponds to the carbonyl ligands being in *fac* orientation (**Figure VI–6**).

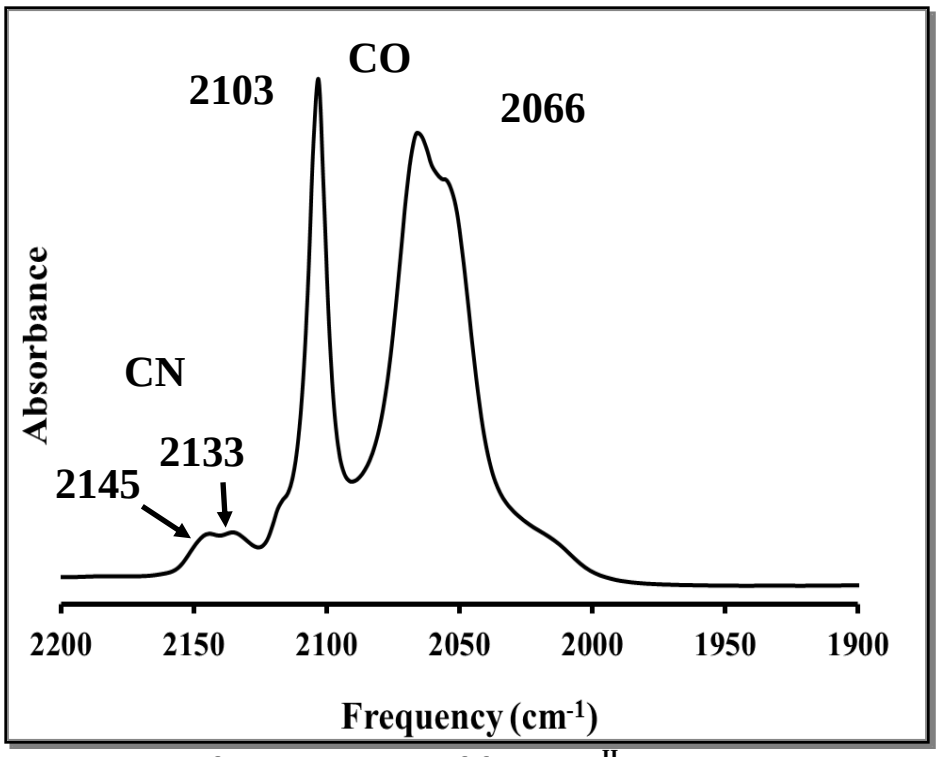


**Figure VI–6. Infrared spectrum of *fac*–K[$Fe^{II}(CN)_2(CO)_3I$] in MeOH.**

### 6.3.2 Synthesis and Infrared Studies of the Ni – Fe dimers

Syntheses of the Ni – Fe dimers were performed under anaerobic conditions while in the absence of light. The syntheses were performed using a two–step procedure, with the exception of the *trans,cis*–[$Fe^{II}(CN)_2(CO)_2Ni^{II}$(S4)] which used a one–step procedure.

The first step in the formation of the iron–thiolate complexes was lithiation of the dithiol compound. Norbornanedithiol or *o*–xylene–*α,α*'–dithiol was dissolved in methanol, in which two molar equivalence of lithium wire was placed and stirred until all reagents were dissolved. The lithiated thiol was transferred *via* cannula, dropwise, to a methanolic solution of *fac*–$[Fe^{II}(CN)_2(CO)_3I]^-$ and the solution was stirred for three hours. Upon addition of the lithiated thiol the solution changed from a bright red to a deep red (maroon) color.

Due to the lack of purity of the *fac*–$[Fe^{II}(CN)_2(CO)_3I]^-$ complex, a titration of 1,3–propanedithiolate was performed. This titration was performed to understand the amount of thiolate that must be added to maintain the thiolate as the limiting reagent. Having excess thiolate would make crystallization of the final product extremely difficult. The starting material, *fac*–$[Fe^{II}(CN)_2(CO)_3I]^-$, is insoluble in the final extractions of the desired complexes from methylene chloride. It was found that adding 70% thiolate ligand versus *fac*–$[Fe^{II}(CN)_2(CO)_3I]^-$ was an

adequate amount of reagent. The titration was monitored by infrared spectroscopy (**Figure VI–7**).

These reactions were monitored by infrared spectroscopy, norbornanedithiolate is shown in **Figure VI–8** while *o*–xylene–*α,α*'–dithiolate is shown in **Figure VI–9**. Reactions were complete after three hours of stirring at room temperature based on infrared studies. Longer reaction time does not change the infrared spectrum for either experiment. In both infrared spectra there are two peaks which have been assigned as the carbonyl ligands, for norbornanedithiolate (2023 $cm^{-1}$ and 1974 $cm^{-1}$) and for *o*–xylene–*α,α*'–dithiolate (2030 $cm^{-1}$ and 1981 $cm^{-1}$). Based on the infrared spectra the conclusion is the carbonyl ligands are in a *cis* arrangement. This would imply that were was a loss of CO due to the absence of the *fac*–CO arrangement seen in the infrared spectrum of *fac*–$[Fe^{II}(CN)_2(CO)_3I]^-$.

The carbonyl peaks in the *fac*–$[Fe^{II}(CN)_2(CO)_3I]^-$ spectrum are red shifted due to the presence of the sulfur on the dithiolate ligands. Thiolates are better σ–donors than iodide and CO, which results in extra electron density on the metal. This excess electron density strengthens the π–backbonding of the carbonyl, which weakens the C≡O bond.

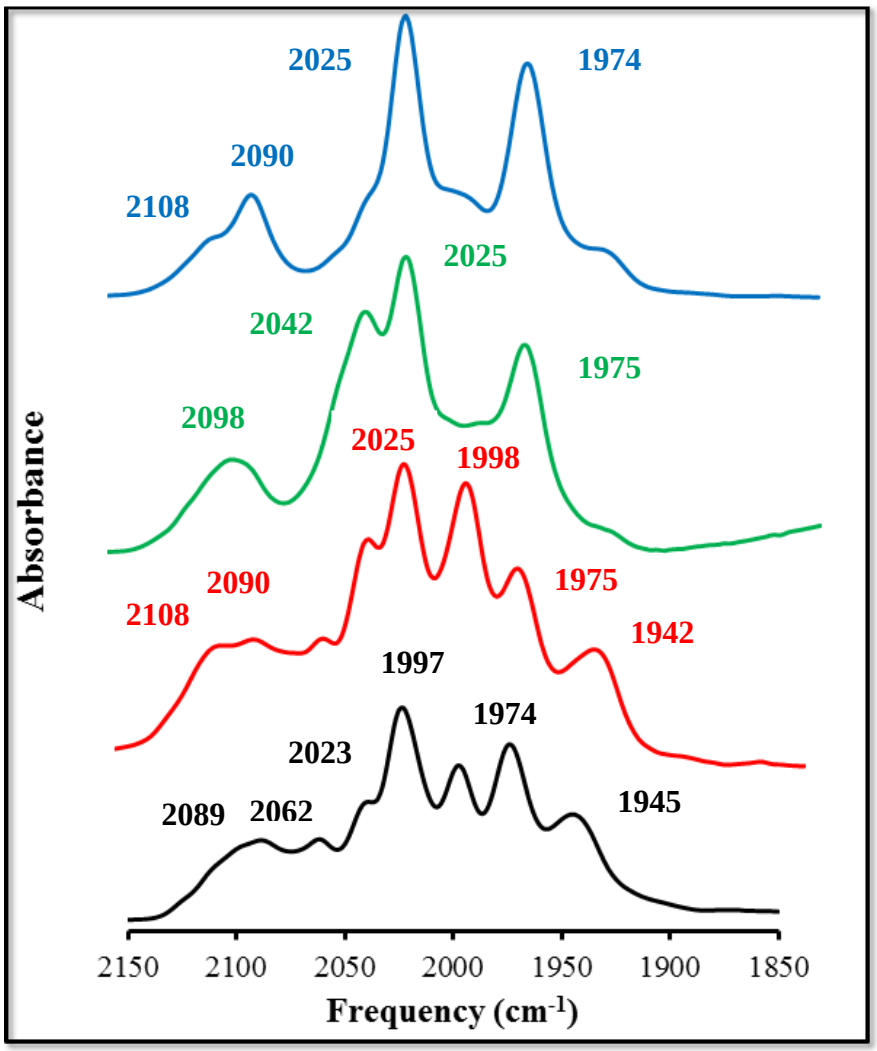


**Figure VI–7. Titration of 1,3–propanedithiolate to *fac*–$[Fe^{II}(CN)_2(CO)_3I]^-$ in MeOH. (black) 10% 1,3–propanedithiolate; (red) 30% 1,3–propanedithiolate; (green) 50% 1,3–propanedithiolate; (blue) 70% 1,3–propanedithiolate.**

In both infrared spectra there is one board peak; under close observation it can be seen that the peak is split. This board peak, in both infrared spectra, has been assigned to the cyanide ($CN^-$) ligands, for norbornanedithiolate (2094 $cm^{-1}$) and for *o*–xylene–*α*,*α*'–dithiolate (2097 $cm^{-1}$). Based on the infrared spectra the conclusion is the cyanide ligands remain in the *cis* orientation as in the *fac*–$[Fe^{II}(CN)_2(CO)_3I]^-$ complex. Using the infrared spectrum and based on the conclusions that were made for the loss of CO, it can be concluded that the second ligand to be removed is the iodide ($I^-$).

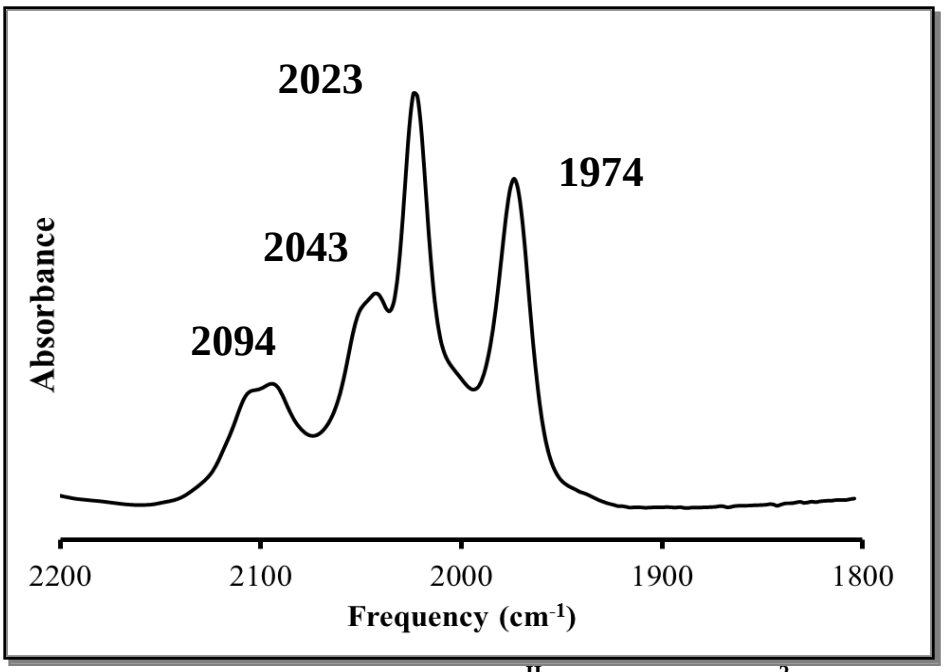


**Figure VI–8. Infrared spectrum of $[Fe^{II}(CN)_2(CO)_2(ndt)]^{2-}$ in MeOH.**

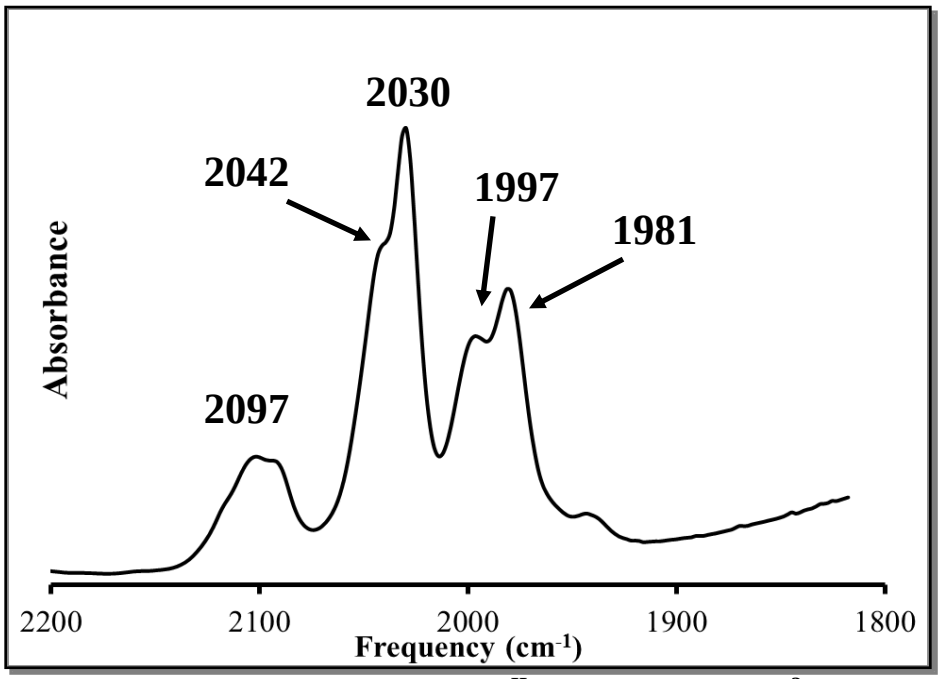


**Figure VI–9. Infrared spectrum of $[Fe^{II}(CN)_2(CO)_2(o\text{–xyl})]^{2-}$ in MeOH.**

In the second step of the procedure, following formation of the $[Fe^{II}(CN)_2(CO)_2(SS)]^{2-}$ (where SS = norbornanedithiolate or *o*–xylene–*α*,*α*'–dithiolate), the solvent was removed *in vacuo*. The resulting red–brown solid was redissolved in $CH_2Cl_2$, solid $Ni^{II}(dppe)Cl_2$ was added,

approximately 0.5 molar equivalence, and the resulting $CH_2Cl_2$ solution was quickly degassed under dinitrogen atmosphere. Upon the addition of $Ni^{II}(dppe)Cl_2$, the solution changed from deep red to purple. The mixture was stirred for two hours and was monitored by IR; norbornanedithiolate (**Figure VI–10**) and *o*–xylene–*α,α*'–dithiolate (**Figure VI–11**). The mixture was filtered and the solvent was removed *in vacuo* to produce a red–orange solid.

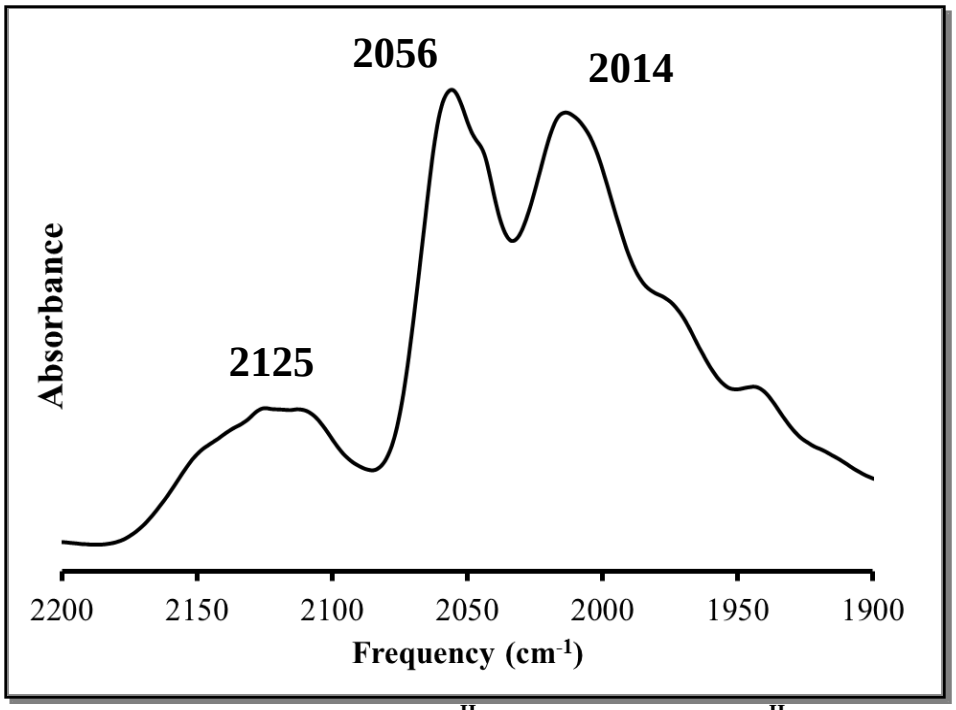


**Figure VI–10. Infrared spectrum of $[Fe^{II}(CN)_2(CO)_2(\mu$–ndt)$Ni^{II}(dppe)]$ in $CH_2Cl_2$.**

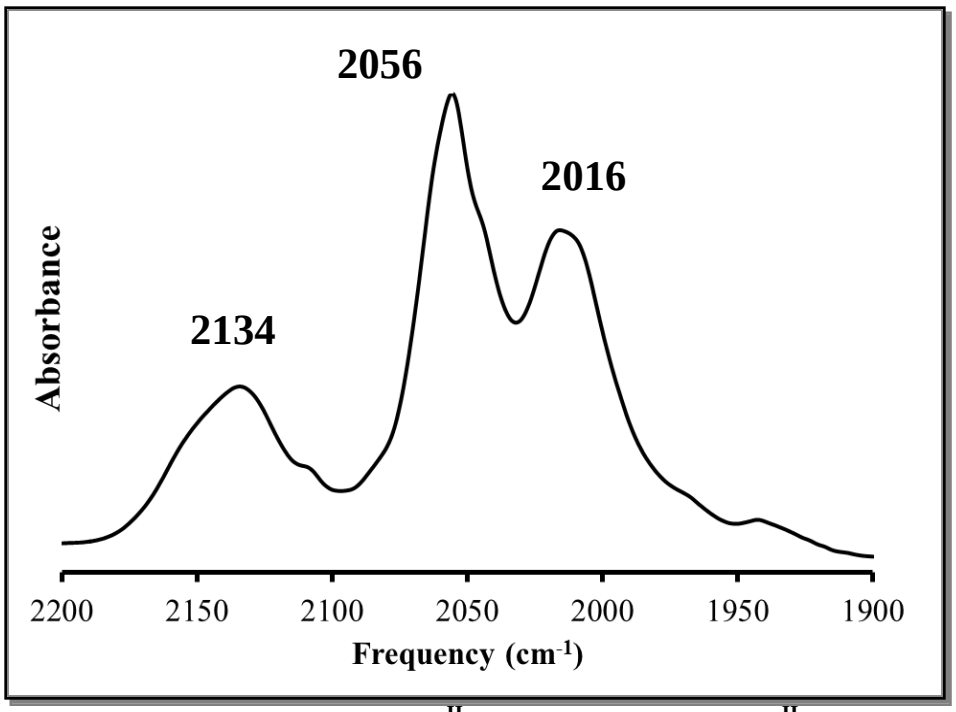


**Figure VI–11. Infrared spectrum of $[Fe^{II}(CN)_2(CO)_2(\mu\text{–}o\text{–xyl})Ni^{II}(dppe)]$ in $CH_2Cl_2$.**

Reactions were complete after two hours of stirring at room temperature based on infrared studies. Longer reaction time does not change the infrared spectrum for either experiment. In both infrared spectra there are two peaks, at lower frequencies, which have been assigned as the carbonyl ligands, for norbornanedithiolate (2056 $cm^{-1}$ and 2014 $cm^{-1}$) and for *o*–xylene–*α*,*α*'–dithiolate (2056 $cm^{-1}$ and 2016 $cm^{-1}$). The infrared spectra support the conclusion that the carbonyl ligands are still in a *cis* orientation.

The carbonyl peaks of the Ni–Fe dimer are blue shifted from the $[Fe^{II}(CN)_2(CO)_2(SS)]^{2-}$ spectrum due to the presence of the nickel complex being bound by the bridging dithiolate compound. As a result the electron density around the thiolate is being distributed among both metals. By this shift in electron density the σ–donation of the thiolate has weakened which in turn weakens the π–backbonding effect of the carbonyl ligands and strengthens the C≡O bond.

In both infrared spectra there is one board peak, which has been assigned to the cyanide ($CN^-$) ligands, for norbornanedithiolate (2125 $cm^{-1}$) and for *o*–xylene–*α*,*α*'–dithiolate (2134 $cm^{-1}$). The infrared spectra are inconclusive as to whether the cyanide ligands remained in the *cis* orientation or if a rearrangement occurred and the cyanide ligands are in the *trans* orientation.

Synthesis of *trans,cis*–[$Fe^{II}(CN)_2(CO)_2Ni^{II}$(S4)] was performed *in sito*. Solid $Ni^{II}$(S4), 0.5 molar equivalence, was added to a methanolic solution of *fac*–[$Fe^{II}(CN)_2(CO)_3I]^-$ under dinitrogen atmosphere. The reaction is monitored using infrared spectroscopy (**Figure VI–12**). The mixture changed from a bright red to a dark purple. An orange–yellow precipitate was observed and the mixture was stirred until all of the $Ni^{II}$(S4) had dissolved, which the solution was filtered. The orange–yellow precipitate was isolated and an IR (KBr pellet) was performed to help identify the material (**Figure VI–13**). The filtrate was collected and the solvent was removed *in vacuo*. The resulting red–orange solid was redissolved in $CH_2Cl_2$, filtered and the solvent removed *in vacuo*, which resulted in a dark red–brown solid.

The carbonyl peaks in the $Fe^{II}$–$Ni^{II}$(S4) complex are red shifted from the *fac*–[$Fe^{II}(CN)_2(CO)_3I]^-$ spectrum due to the presence of the nickel complex. The loss of the *fac* carbonyl peaks in the IR spectrum shows a loss of one CO ligand. The CO ligands, 2057 $cm^{-1}$ and 2011 $cm^{-1}$, indicate that the ligands are in a *cis* orientation. The peaks at 2119 $cm^{-1}$ and 2099 $cm^{-1}$ were assigned as the cyanide peaks, indicating that the cyanides could be in the *cis* orientation. According to the crystal structure, see section 6.3.2, the orientation of the cyanide ligands do not coincide with the IR spectrum.

The orange–yellow precipitate that was isolated from the first step of extraction could not be fully identified due to its lack of solubility. The presence of carbonyl and cyanides peaks in the IR spectrum gave a clue to what may be the mystery compound. Based on the solubility of the compound, the precipitate could be a polymer of the desired product. Precipitate was insoluble in a wide range of solvents ($CH_2Cl_2$, alcohols, pyridine, toluene, acetonitrile, DMF, and DMSO), which made crystallization of compound nearly impossible.

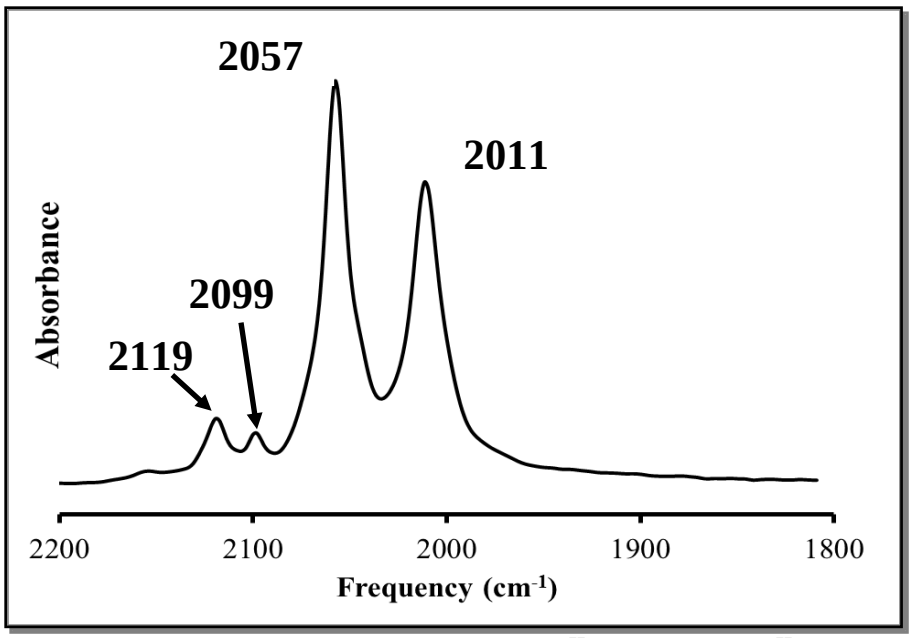


**Figure VI–12. Infrared spectrum of *trans,cis*–[$Fe^{II}(CN)_2(CO)_2Ni^{II}(S4)$] in $CH_2Cl_2$.**

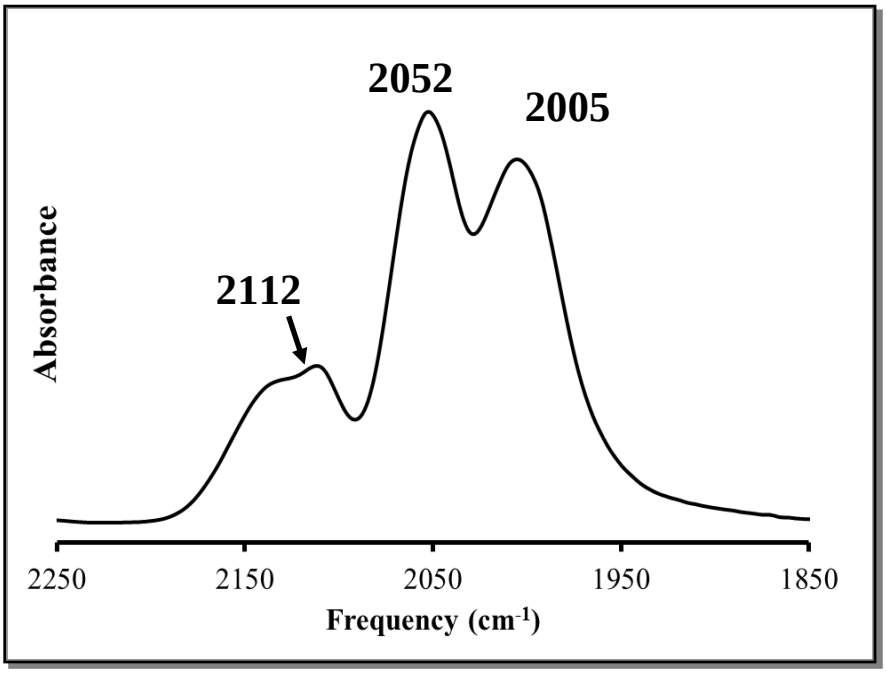


**Figure VI–13. Infrared spectrum of orange–yellow preciptate from the reaction of *trans,cis*–[$Fe^{II}(CN)_2(CO)_2Ni^{II}(S4)$], KBr pellet.**

### 6.3.3 X–ray Structures

The result for the X–ray structure of *cis*–$Ni^{II}(dppe)Cl_2 \bullet CH_2Cl_2$ (**Figure VI–14**) shows the nickel in a slightly distorted square planar environment. This confirms that the structure contains one dppe ligand, two chloride ions and one molecule of $CH_2Cl_2$ in the asymmetric unit. In 1987, the crystal structure of $Ni^{II}(dppe)Cl_2 \bullet CH_2Cl_2$ was first reported by Spek *et al.*[13] The most recent comparison study, using X–ray crystallography, on $Ni^{II}(dppe)Cl_2 \bullet CH_2Cl_2$ was done in 2003 by Bomfim *et al.*[11] The important geometrical parameters of $Ni^{II}(dppe)Cl_2 \bullet CH_2Cl_2$, reported in this dissertation, are compared with Bomfim's $Ni^{II}(dppe)Cl_2 \bullet CH_2Cl_2$ (**Table VI–1**). Comparison of crystallographic data parameters are shown in **Table VI–2**.

**Table VI–1. Comparison of Selective Crystallographic Data for *cis*–$Ni^{II}(dppe)Cl_2 \bullet CH_2Cl_2$.**

| **Bomfim[13]** | | | |
|---|---|---|---|
| **Bond Distances (Å)** | | **Bond Angles (°)** | |
| Ni(1) – P(1) | 2.145(1) | P(1) – Ni(1) – P(2) | 86.99(5) |
| Ni(1) – P(2) | 2.160(1) | P(1) – Ni(1) – Cl(1) | 88.78(5) |
| Ni(1) – Cl(1) | 2.208(1) | P(1) – Ni(1) – Cl(2) | 175.11(5) |
| Ni(1) – Cl(2) | 2.200(1) | P(2) – Ni(1) – Cl(1) | 175.29(5) |
| P(1) – C(1) | 1.841(4) | P(2) – Ni(1) – Cl(2) | 88.92(5) |
| P(2) – C(2) | 1.826(4) | Cl(1) – Ni(1) – Cl(2) | 95.41(5) |
| C(1) – C(2) | 1.505(6) | | |
| **This Work** | | | |
| **Bond Distances (Å)** | | **Bond Angles (°)** | |
| Ni(1) – P(1) | 2.1422(5) | P(1) – Ni(1) – P(2) | 86.846(19) |
| Ni(1) – P(2) | 2.1515(5) | P(1) – Ni(1) – Cl(1) | 88.680(19) |
| Ni(1) – Cl(1) | 2.2004(5) | P(1) – Ni(1) – Cl(2) | 174.43(2) |
| Ni(1) – Cl(2) | 2.2065(5) | P(2) – Ni(1) – Cl(1) | 174.89(2) |
| P(1) – C(1) | 1.8367(19) | P(2) – Ni(1) – Cl(2) | 88.649(18) |
| P(2) – C(2) | 1.8337(18) | Cl(1) – Ni(1) – Cl(2) | 95.955(19) |
| C(1) – C(2) | 1.523(3) | | |

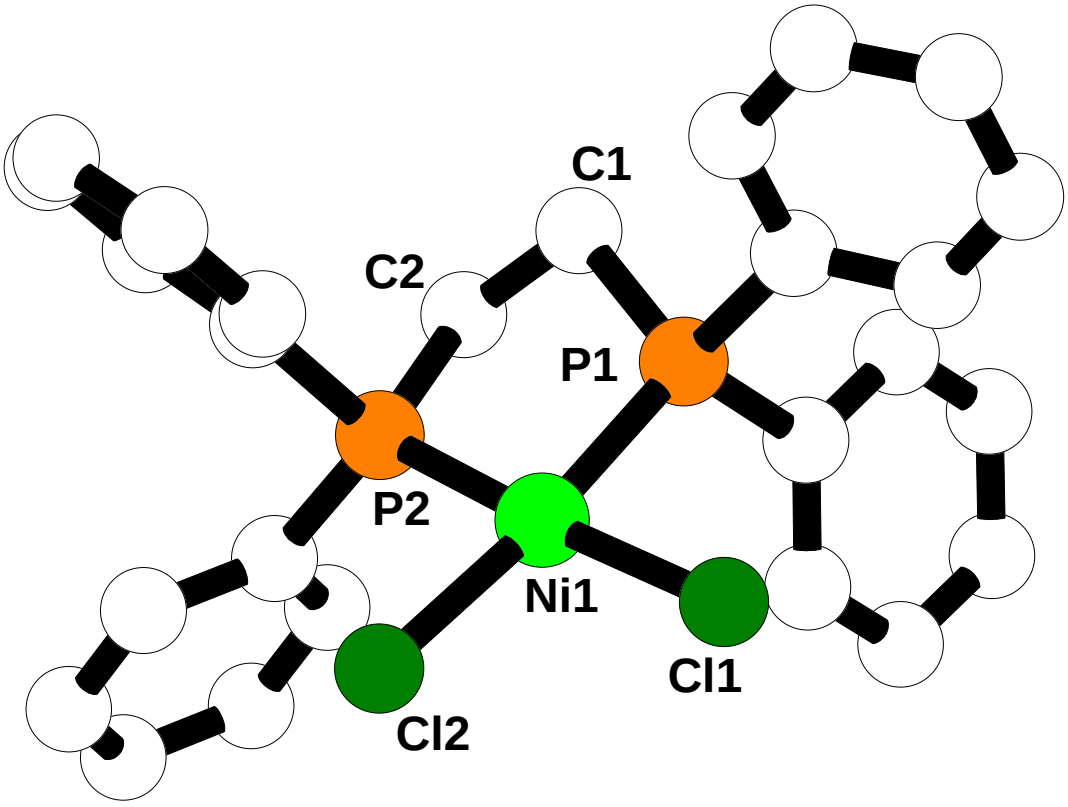


**Figure VI–14. X–ray structure of *cis*–$Ni^{II}(dppe)Cl_2 \bullet CH_2Cl_2$ (hydrogens and solvent molecule were removed for clarity).**

| **Table VI–2. Comparison of Crystallographic Data Parameters for *cis*–$Ni^{II}(dppe)Cl_2 \bullet CH_2Cl_2$.** | | |
|---|---|---|
| **Data** | **Bomfim[13]** | **This Work** |
| Empirical Formula | $C_{27}H_{26}Cl_4NiP_2$ | $C_{27}H_{26}Cl_4NiP_2$ |
| Formula Weight | 612.93 | 612.93 |
| Temperature (K) | 298(2) | 100(2) |
| Crystal System | Monoclinic | Monoclinic |
| Space Group | $P2_1/c$ | $P2_1/c$ |
| Unit Dimensions | | |
| a (Å) | 12.258(1) | 12.1826(2) |
| b (Å) | 15.403(3) | 15.2299(3) |
| c (Å) | 15.299(2) | 15.1924(3) |
| $\alpha$ ($^o$) | 90 | 90 |
| $\beta$ ($^o$) | 104.804(8) | 105.666(2) |
| $\gamma$ ($^o$) | 90 | 90 |
| Volume ($Å^3$) | 2792.7(6) | 2714.08(9) |
| Density (calculated) (g $cm^{-3}$) | 1.458 | 1.500 |
| Z | 4 | 4 |
| Absorption Coefficient ($mm^{-1}$) | 1.207 | 1.242 |
| R | 0.053 | 0.0306 |
| $R_w$ | 0.123 | 0.0769 |

The result for the X–ray structure of $Ni^{II}$(S4) (**Figure VI–15**) shows the nickel in a slightly distorted square planar environment. In 1990, the crystal structure of $Ni^{II}$(S4) was first reported by Yamamura *et al.*[14] The important geometrical parameters of $Ni^{II}$(S4), reported in this dissertation, are compared with Yamamura's $Ni^{II}$(S4) (**Table VI–3**). Comparison of crystallographic data parameters are shown in **Table VI–4**. The average nickel–sulfur (neutral) bond distance for $Ni^{II}$(S4), Ni–S, is 2.1669(4) Å and the average nickel–sulfur (anionic) bond distance, Ni–$S^-$, is 2.1772(4) Å. When comparing these bond distances from $[Ni^{II}(ttp)](BF_4)_2$ (where ttp = 1,4,8,11–tetrathiacyclotetradecane), which is a pure Ni–S case has an average bond distance of 2.176 Å, and $(PPh_4)_2[Ni^{II}(edt)_2]$ (where edt = 1,2–ethanedithiolate), which is a pure Ni–$S^-$ case has an average bond distance of 2.195 Å, it was found that the $Ni^{II}$(S4) bonds are stronger than those of the pure cases.

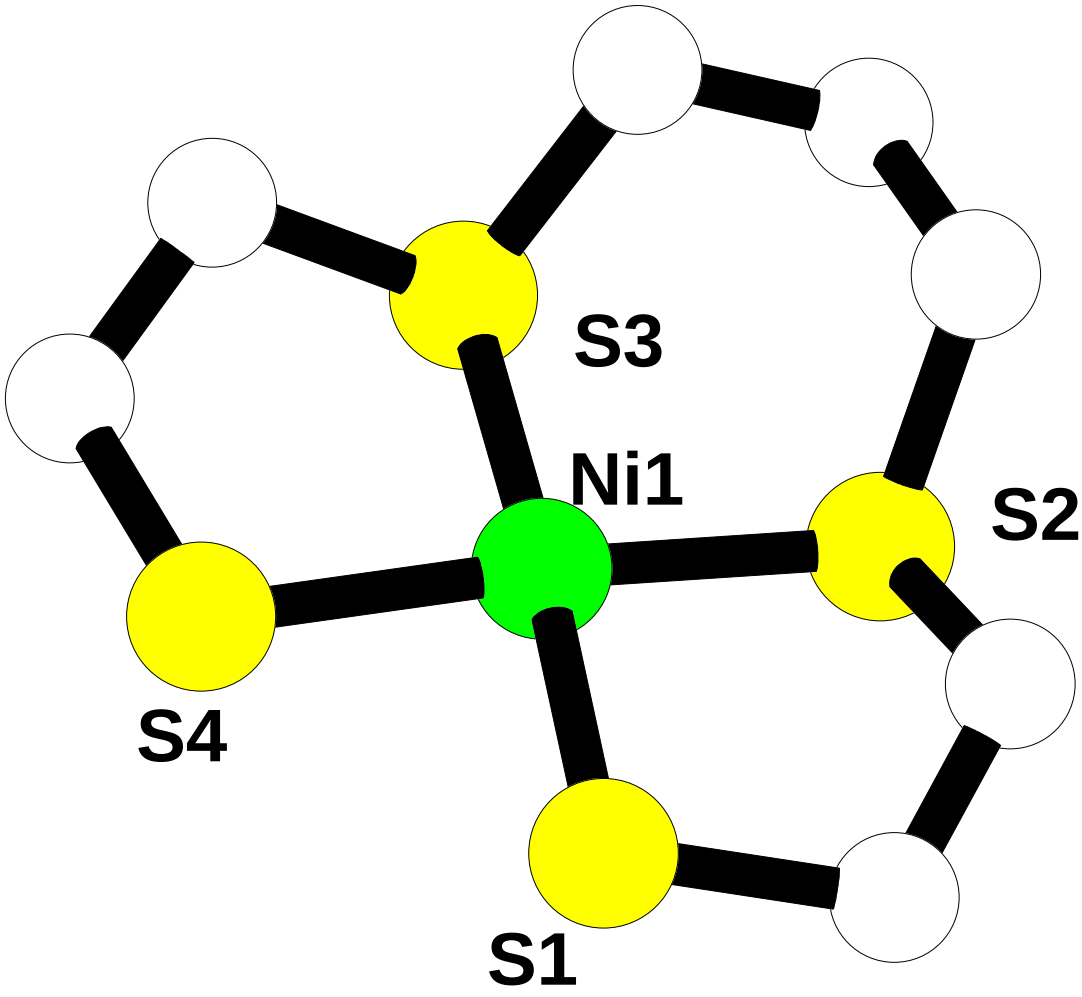


**Figure VI–15. X–ray structure of $Ni^{II}$(S4) (hydrogens were removed for clarity).**

| Table VI–3. Comparison of Selective Crystallographic Data for $Ni^{II}$(S4). | | | |
|---|---|---|---|
| **Yamamura[14]** | | | |
| **Bond Distances (Å)** | | **Bond Angles (°)** | |
| Ni(1) – S(1) | 2.177(2) | S(1) – Ni(1) – S(2) | 90.17(6) |
| Ni(1) – S(2) | 2.179(2) | S(1) – Ni(1) – S(3) | 175.85(6) |
| Ni(1) – S(3) | 2.166(2) | S(1) – Ni(1) – S(4) | 87.05(6) |
| Ni(1) – S(4) | 2.173(1) | S(2) – Ni(1) – S(3) | 92.85(5) |
| | | S(2) – Ni(1) – S(4) | 177.02(6) |
| | | S(3) – Ni(1) – S(4) | 89.87(5) |
| **This Work** | | | |
| **Bond Distances (Å)** | | **Bond Angles (°)** | |
| Ni(1) – S(1) | 2.1751(4) | S(1) – Ni(1) – S(2) | 89.858(16) |
| Ni(1) – S(2) | 2.1635(4) | S(1) – Ni(1) – S(3) | 176.857(17) |
| Ni(1) – S(3) | 2.1704(4) | S(1) – Ni(1) – S(4) | 87.058(16) |
| Ni(1) – S(4) | 2.1794(4) | S(2) – Ni(1) – S(3) | 92.914(15) |
| | | S(2) – Ni(1) – S(4) | 175.794(18) |
| | | S(3) – Ni(1) – S(4) | 90.097(16) |

| Table VI–4. Comparison of Crystallographic Data Parameters for $Ni^{II}$(S4). | | |
|---|---|---|
| **Data** | **Yamamura[14]** | **This Work** |
| Empirical Formula | $C_7H_{14}NiS_4$ | $C_7H_{14}NiS_4$ |
| Formula Weight | 286.142 | 285.13 |
| Temperature (K) | 298(2) | 100(2) |
| Crystal System | Monoclinic | Monoclinic |
| Space Group | $P2_1/n$ | $P2_1/n$ |
| Unit Dimensions | | |
| a (Å) | 9.461(3) | 9.3839(3) |
| b (Å) | 8.650(2) | 8.5363(2) |
| c (Å) | 13.721(2) | 13.5316(4) |
| α (°) | 90 | 90 |
| β (°) | 92.60(2) | 92.032(3) |
| γ (°) | 90 | 90 |
| Volume ($Å^3$) | 1121.7(4) | 1083.25(5) |
| Density (calculated) (g $cm^{-3}$) | 1.688 | 1.748 |
| Z | 2 | 4 |
| Absorption Coefficient ($mm^{-1}$) | 2.40 | 2.506 |
| R | 0.0643 | 0.0211 |
| $R_w$ | 0.0531 | 0.0443 |

Comparing the Ni–S bond distances of the free $Ni^{II}(S4)$ with the bound $Ni^{II}(S4)$, in *trans,cis*–$[Fe^{II}(CN)_2(CO)_2Ni^{II}(S4)]$, it was found the pure Ni–S and Ni–$S^-$ bond distances became longer in the bound complex (*trans,cis*–$[Fe^{II}(CN)_2(CO)_2Ni^{II}(S4)]$) than in the free $Ni^{II}(S4)$ , 2.1910(15) Å from 2.1669(4) Å and 2.1710(15) Å from 2.1772(4) Å, respectively. This difference in bond distance is due to the anionic sulfurs on the $Ni^{II}(S4)$ which are bridging the nickel and iron centers. Due to the electron density being distributed between two transition metals the bond strength becomes weaker, which this is demonstrated in the two crystal structures.

X–ray analysis of *trans,cis*–$[Fe^{II}(CN)_2(CO)_2Ni^{II}(S4)]$ (**Figure VI–15**) confirmed that the two sulfur atoms of $Ni^{II}(S4)$ bridge the iron to the nickel and that the two $CN^-$ ligands on the iron are *trans* to each other, while the CO ligands are *cis*. The *trans,cis*–$[Fe^{II}(CN)_2(CO)_2Ni^{II}(S4)]$ has a similar structural framework as the active site of [NiFe] hydrogenase.

The distinction between CO and $CN^-$ ligands was made clear based on the difference in Fe—CN and Fe—CO distances (avg. 1.927 Å vs avg. 1.794 Å respectively). The important geometrical parameters of *trans,cis*–$[Fe^{II}(CN)_2(CO)_2Ni^{II}(S4)]$ are compared to the oxidized forms of *D. gigas* and *D. fructosovorans* as well as complexes reported by Tatsumi *et. al.*[6] and Jiang *et. al.*[7] (**Table VI–5**).

**Table VI–5. Comparison of Selected Bond Distances (Å) and Fe—S—Ni Angle of Synthetic Analogues of [NiFe] Hydrogenase and Oxidized form of *D. gigas* and *D. fructosovorans***

| | **This Work** | **Tatsumi [6]** | **Jiang[7]** | ***D. gigas*[15–16]** | ***D. fructosovorans*[14]** |
|---|---|---|---|---|---|
| Fe—Ni | 3.133(7) | 3.0587(6) | 2.809(1) | 2.9 | 2.9 |
| Fe—S—Ni[a] | 88.06 | 84.43 | 78.12 | 73.7 | *b* |
| Fe—S (bridge)[a] | 2.333 | 2.337 | 2.341 | 2.2 | 2.4 |
| Ni—S (bridge)[a] | 2.172 | 2.213 | 2.219 | 2.6 | 2.4 |
| Ni—S (terminal)[a] | 2.191 | 2.206 | N/A | 2.2 | 2.3 |

[a] Averaged. [b] Data not deposited in the protein data bank (PDB).

The Fe—S, Ni—S, and Fe—Ni bond distances are all comparable, except for the long Ni—S (bridge) bond distance in *D. gigas*. The oxidized form of *D. gigas* has a triply bridged structure, which results in a smaller Fe—S—Ni angle, and yet the Fe—Ni bond distance remains long. However, the doubly bridged Fe—Ni bond of the reduced form of *D. vulgaris* is

substantially shorter.[15–16] Through this observation, it is not likely that the Fe—Ni bond distance is determined by the number of bridging atoms, but rather it is controlled by the oxidation state and/or the spin state of the metal centers.[6,17–19] The coordination geometry of the Ni in *trans*,*cis*–[$Fe^{II}(CN)_2(CO)_2Ni^{II}$(S4)] is close to square planar with an average bond angle of 89.91°. This is a contrast to the highly distorted $NiS_4$ geometry found in the oxidized and reduced forms of [NiFe] hydrogenases. The second $CN^-$, C(2) – N(2), bond distance is slightly longer (1.243 Å vs 1.116 Å for C(1) – N(2)) due to a distortion on C(2). A summary of selective bond distances and bond angles for *trans*,*cis*–[$Fe^{II}(CN)_2(CO)_2Ni^{II}$(S4)] are listed in **TableVI–6**.

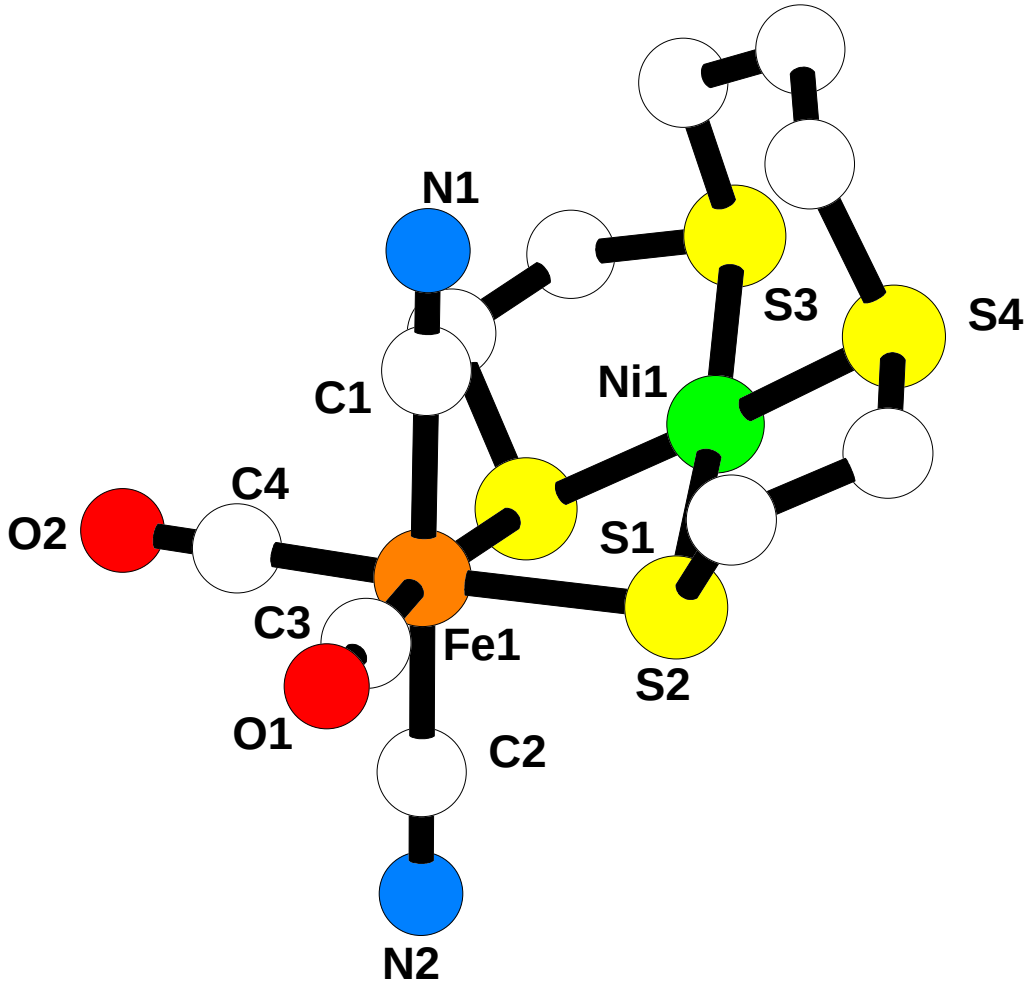


**Figure VI–16. X–ray structure of *trans*,*cis*–[$Fe^{II}(CN)_2(CO)_2Ni^{II}$(S4)] (hydrogens were removed for clarity).**

| Table VI–6. Selective Crystallographic Data for *trans,cis*–$[Fe^{II}(CN)_2(CO)_2Ni^{II}(S4)]$. | | | |
|---|---|---|---|
| **Bond Distances (Å)** | | **Bond Angles (°)** | |
| Fe(1) – C(1) | 1.963(5) | C(1) – Fe(1) – C(2) | 177.8(3) |
| Fe(1) – C(2) | 1.869(8) | C(1) – Fe(1) – C(3) | 91.7(2) |
| Fe(1) – C(3) | 1.787(6) | C(1) – Fe(1) – S(1) | 90.87(15) |
| Fe(1) – C(4) | 1.786(5) | C(1) – Fe(1) – S(2) | 91.88(16) |
| Fe(1) – S(1) | 2.3295(15) | C(3) – Fe(1) – S(1) | 172.0(2) |
| Fe(1) – S(2) | 2.3365(15) | C(3) – Fe(1) – S(2) | 94.26(19) |
| C(1) – N(1) | 1.116(6) | C(4) – Fe(1) – S(1) | 92.67(17) |
| C(1) – N(2) | 1.243(10) | C(4) – Fe(1) – S(2) | 172.77(17) |
| C(3) – O(1) | 1.134(7) | S(1) – Fe(1) – S(2) | 78.13(5) |
| C(4) – O(2) | 1.129(6) | S(1) – Ni(1) – S(2) | 85.22(5) |
| Ni(1) – S(1) | 2.1723(15) | S(1) – Ni(1) – S(3) | 91.80(6) |
| Ni(1) – S(2) | 2.1710(15) | S(1) – Ni(1) – S(4) | 174.30(6) |
| Ni(1) – S(3) | 2.1907(15) | S(2) – Ni(1) – S(3) | 175.07(6) |
| Ni(1) – S(4) | 2.1914(15) | S(2) – Ni(1) – S(4) | 91.58(6) |
| | | S(3) – Ni(1) – S(4) | 91.06(6) |

## 6.4 Conclusions

In conclusion, NiFe–dimers can be synthesized using *fac*–$[Fe^{II}(CN)_2(CO)_3I]^-$ with a deprotonate thiolate followed by the addition of a $Ni^{II}$–complex, i.e. $Ni^{II}Cl_2$(dppe) and $Ni^{II}$(S4). Characterization of NiFe–dimers was performed by IR and X–ray crystallography. The infrared studies showed a red shift in the carbonyl and cyanide stretching frequencies when *fac*–$[Fe^{II}(CN)_2(CO)_3I]^-$ reacts with a dithiolate which is caused by increased σ–donation affecting the π–backbonding of the carbonyl ligands and σ–bonding of the cyanide ligands. The infrared studies showed when the $[Fe^{II}(CN)_2(CO)_2(SS)]^{2-}$ reacts with a $Ni^{II}$–complex to result in a blue shift for the cyanide and carbonyl stretching frequencies. The σ–donation caused by the dithiolate is weakened due the distribution to both transition metals, which affects the π–backbonding of the carbonyl ligands and σ–bonding of the cyanide ligands.

The X-ray structure of *trans,cis*-$[Fe^{II}(CN)_2(CO)_2Ni^{II}(S4)]$ confirmed a dimeric complex with iron having an octahedral geometry while the nickel was square planar. This neutral complex is the first to be structurally characterized that models the [NiFe]-hydrogenase having

all the key components. Catalytic studies need to be investigated to show if this complex truly models the enzyme active site.

## 6.5 References


1. Vignais, P. M.; Billoud, B. *Chem. Rev.* **2007**, *107*, 4206–4272.
2. Fomtecilla–Camps, J. C.; Volbeda, A.; Cavazza, C.; Nicolet, Y. *Chem. Rev.* **2007**, *107*, 4273–4303.
3. Armstrong, F. A.; Belsey, N. A.; Cracknell, J. A.; Goldet, G.; Parkin, A.; Reisner, E.; Vincent, K. A.; Wait, A. F. *Chem. Soc. Rev*. **2009**, *38*, 36–51.
4. Volbeda, A.; Martin, L.; Cavazza, C.; Matho, M.; Faber, B. W.; Roseboom, W.; Albracht, S. P. J.; Garcin, E.; Rousset, M.; Fomtecilla–Camps, J. C. *J. Biol. Inorg. Chem.* **2005**, *10*, 239–249.
5. Lubitz, W.; Reijerse, E.; van Gastel, M. *Chem. Rev.* **2007**, *107*, 4331–4365.
6. Zilong, L.; Ohki, Y.; Tatsumi, K. *J. Am. Chem. Soc.* **2005**, *127*, 8950–8951.
7. Jiang, J.; Maruani, M.; Solaimanzadeh, J.; Lo, W.; Koch, S. A., Millar, M. *Inorg. Chem.* **2009**, 6359–6361.
8. Gina Chiarella, PhD dissertation, Stony Brook University, Stony Brook, **2006**.
9. Jianfeng Jiang, PhD dissertation, Stony Brook University, Stony Brook, **2002**.
10. F. Osterloh; W. Saak; S. Pohl. *J. Am. Chem. Soc.* **1997**, *119*, 5648.
11. Bomfim J. A. S.; de Souza, F. P.; Filgueiras, C. A. L.; de Sousa, A. G.; Gambardell, M. T. P. *Polyhedron*, **2003**, 1567–1573.
12. Hieber, W.; Lagally, H.; Wirsching A. *Z. Anorg. Allgem. Chem.* **1940**, *245*, 35.
13. Spek, A. L.; van Eijck, B. P. *Acta Cryst. C* **1987**, *C43*, 1879–1880.
14. Yamamura, T.; Arai, H.; Nakamura, N.; Miyamae, H. *Chemistry Letters* **1990**, 2121–2124.
15. Higuchi, Y.; Yagi, T.; Yasuoka, N. *Structure* **1997**, 5, 1671–1680.
16. Higuchi, Y.; Ogata, H.; Miki, K.; Yasuoka, N.; Yagi, T. *Structure* **1999**, 7, 549–556.
17. Volbeda, A.; Charon, M. H.; Piras, C.; Hatchikian, E. C.; Frey, M.; Fontecilla–Camps, J. C. *Nature* **1995**, *373*, 580–587.

18. Volbeda, A.; Garcin, E.; Piras, C.; de Lacey, A. L.; Fernandez, V. M.; Hatchikian, E. C.; Frey, M.; Fontecilla–Camps, J. C. *J. Am. Chem. Soc.* **1996**, *118*, 12989–12996.
19. Rousset, M.; Montet, Y.; Guigliarelli, B.; Forget, N.; Asso, M.; Bertrand, P.; Fontecilla–Camps, J. C.; Hatchikian, E. C. *Proc. Natl. Acad. Sci. U.S.A.* **1998**, *95*, 11625–11630.

# Dissertation References

**Chapter 1:**


1. Lippard, S. J.; Berg, J. M. *Principles of Bioinorganic Chemistry*; University Science Books; 1994.
2. Lubitz, W.; Tumas, W. *Chem. Rev.* **2007**, *107*, 3900.
3. Gordon, R.B.; Bertram, M.; Graedel, T.E. *Proc. Natl. Acad. Sci. USA* **2006**, *103*, 1209.
4. http://greenecon.net/solar–and–hydrogen–energy–economics/energy_economics.html
5. Akhmanova, A.; Voncken, F.; van Alen, T.; van Hoek, A.; Boxma, B.; Vogels, G.; Veehuis, M.; Hackstein, J. H. P. *Nature* **1998**, *396*, 527.
6. Shima, S.; Pilak, O.; Vogt, S; Schick, M.; Stagni, M. S.; Meyer–Klaucke, W.; Warkentin, E.; Thauer, R. K.; Ermler, U. *Science* **2008**, *321*, 572.
7. Crabtree, R. H.. *Inorg. Chim. Acta* **1986**, *125*, L7.
8. Volbeda, A.; Charon, M. H.; Piras, C.; Hatchikian, E. C.; Frey, M.; Fontecilla–Camps J. C. *Nature* **1995**, *373*, 580.
9. Volbeda, A.; Garcin, E.; Pirasl, C.; De Lacey, A .L.; Fernandez, V. M.; Hatchikian, E. C.; Frey, M.; Fontecilla–Camps, J. C.. *J. Am. Chem. Soc.* **1996**, *118*, 12989.
10. Ogata, H.; Hirota, S.; Nakahara, A.; Komori, H.; Shibata, N.; Kato, T.; Kano, K.; Higuchi, Y. *Structure* **2005**, *13*, 1635.
11. Volbeda, A.; Martin, L; Cavazza, C.; Matho, M.; Faber, B. W.; Roseboom, W.; Albracht, S. P. J.; Garcin, E.; Rousset, M.; Fontecilla–Camps J. C. *J. Biol. Inorg. Chem.* **2005**, *10*, 239.
12. Lamle, S. E.; Albracht, S. P. J.; Armstrong, F. A. *J. Am. Chem. Soc.* **2004**, *126*, 14899.
13. Ogata, H.; Mizoguchi, Y.; Mizuno, N.; Miki, K.; Adachi, S.; Yasuoka, N.; Yagi, T.; Yamacuchi, O; Hirota, S.; Higuchi, Y. *J. Am. Chem. Soc.* **2002**, *124*, 11628.
14. Higuchi, Y.; Ogata, H.; Miki, K.; Yasuoka, N.; Yagi, T. *Structure* **1999**, *7*, 549.
15. Leroux, F.; Dementin, S.; Burlatt, B.; Cournac, L.; Volbeda, A,; Champ, S.; Martin, L.; Guigliarelli, B.; Bertrand, P.; Fontecilla–Camps J. C.; Rousset, M.; Leger, C. *Proc. Natl. Acad. Sci. U. S. A.* **2008**, *105*, 11188.
16. Tard, C.; Pickett, C. J. *Chem. Rev.* **2009**, *109*, 2245.
17. De Lacey, A. L.; Fernandez, V. M.; Rousset, M.; Cammack, R. *Chem. Rev.* **2007**, *107*, 4304.

18. Van der Waan, J. W.; Coremans, J.; Bouwens, E. C. M.; Albracht, S. P. J.; *Biochim. Biophys. Acta* **1990**, *1041*, 101.
19. Trofanchuk, O.; Stein, M.; Gessner, C.; Lendzin, F.; Higuchi, Y.; Lubitz, W. *J. Biol. Inorg. Chem.* **2000**, *5*, 36.
20. Gessner, C.; Trofanchuck, O.; Kawagoe, K.; Higuchi, Y.; Yasuoka, N.; Lubitz, W. *Chem. Phys. Lett.* **1996**, *256*, 518.
21. Carepo, M.; Tierney, D. L.; Brondino, C. D.; Yang, T. C.; Pamplona, A; Telser, J.; Moura, I.; Moura, J. J. G.; Hoffman, B. M. *J. Am. Chem. Soc.* **2002**, *124*, 281.
22. Osz, J.; Bagyinka, C. *Biophys. J.* **2005**, *89*, 1984.
23. De Lacey, A. L.; Moiroux, J.; Bourdillon, C. *Eur. J. Biochem.* **2000**, *267*, 6560.
24. Leger, C.; Jones, A. K.; Roseboom, W.; Albracht, S. P. J.; Armstrong, F. A.*Biochemistry* **2002**, *41*, 15736.
25. Niu, S. Q.; Thomson, L. M.; Hall, M. B. *J. Am. Chem. Soc.* **1999**, *121*, 4000.
26. Foerster, S.; Stein, M.; Brecht, M.; Ogata, H.; Higuchi, Y.; Lubitz, W. *J. Am. Chem. Soc.* **2003**, *125*, 83.
27. Pardo, A.; De Lacey, A. L.; Fernandez, V. M.; Fan, H. J.; Fan, Y. B.; Hall, M. B. *J. Biol. Inorg. Chem.* **2006**, *11*, 286.
28. Brecht, M.; van Gastel, M.; Buhrke, T.; Friedrich, B.; Lubtiz, W. *J. Am. Chem. Soc.* **2003**, *125*, 13075.
29. Siegbahn, P. E. M. *Advances in Inorganic Chemistry – Including Bioinorganic Studies, Vol 56*; Elsevier Academic Press Inc: San Diego, 2004; p 101.
30. Foerster, S.; van Gastel, M.; Brecht, M; Lubtiz, W. *J. Biol. Inorg. Chem.* **2005**, *10*, 51.
31. De Gioia, L.; Fantucci, P.; Guigliarelli; B.; Bertrand, P. *Int. J. Quantum Chem.* **1999**, *73*, 187.
32. Volbeda, A.; Fontecilla–Camps J. C. *Coord. Chem. Rev.* **2005**, *249*, 1609.
33. Leger, C.; Jones, A. K.; Albracht, S. P. J.; Armstrong, F. A. *J. Phys. Chem. B* **2002**, *106*, 13058.
34. Foerster, S.; Stein, M.; Brecht, M.; Ogata, H.; Higuchi, Y.; Lubitz, W. *J. Am. Chem. Soc.* **2003**, *125*, 83.
35. Fichtner, C.; van Gastel, M.; Lubitz, W. *Phys. Chem. Chem. Phys.* **2003**, *5*, 5507.
36. Halcrow, M. A.; Christou, G. *Chem. Rev.* **1994**, *94*, 2421.

37. Mullar, J. A.; Hebd, C. R. *Seances, Acad. Sci.*; **1887**, *104*, 992.

38. Manchot, W.; Merry, E., Woringer, P. *Chem. Ber.*, **1912**, *45*, 2879.

39. Kenney, D. J.; Flynn, T. P.; Gallini, J. B. *J. Inorg. Nucl. Chem.*, **1961**, *20*, 75.

40. Cotton, F. A.; Monchamp, R. R.; Henry, R. J. M.; Young, R. C.; *J. Inorg. Nucl. Chem.*, **1959**, *10*, 28.

41. (a) Jiang, J.; Koch, S. A. *Angew. Chem., Int. Ed.* **2001**, *40*, 2629–2631. (b) Jiang, J.; Maruani, M.; Sclaimanzadeh, J.; Lo, W.; Koch, S. A.; Millar, M. *Inorg. Chem.* **2009**, *48*, 6359.

42. Chiarella, G. M.; Melgarejo, D. Y.; Koch, S. A. *J. Am. Chem. Soc.*, **2006**, *128*, 1416–1417.

43. Lai, C. H.; Reibenspies, J. H.; Darenbourg, M. Y.; *Angew. Chem. Int. Ed.* **1996**, *35*, 2390.

44. Osterloh, F.; Saak, W.; Haase, D.; Pohl, S. *Chem. Commun.* **1997**, 979.

45. Davies, S. C.; Evans, D. J.; Hughes, D. L.; Longhurst, S.; Sanders, J. R.*Chem. Commun.* **1999**, 1935.

46. Smith, M. C.; Barcely, J. E.; Cramer, S. P.; Davies, S. C.; Gu, W. W.; Hughes, D. L.; Longhurst, S.; Evans, D. J. *J. Chem. Soc. Dalton Trans.* **2002**, 3410.

47. Zhu, W. F.; Marr, A. C.; Wang, Q.; Neese, F.; Spencer, D. J. E.; Blake, A .J.; Cooke, P. A.; Wilson, C.; Schroder, M. *Proc. Natl. Acad. Sci. U. S. A.* **2005**, *102*, 18280.

48. Sellmann, D.; Geipel, F.; Lauderbach, F.; Heinemann, F. W.; *Angew Chem. Int. Ed.* **2002**, *41*, 632.

49. Li, Z. L.; Ohki, Y.; Tatsumi, K. *J. Am. Chem. Soc.* **2005**, *127*, 8950.

50. Chen, C. H.; Chang, Y. S.; Yang, C. Y.; Chen, T. N.; Lee, C.; Liaw, W .F. *Dalton Trans.* **2004**, 137.

51. Contakes, S. M.; Hsu, S.C. N.; Rauchfuss, T. B.; Wilson, S. R.; *Inorg. Chem.* **2002**, *41*, 4610.

52. Jiang, J. F.; Koch, S. A. *Inorg. Chem.* **2002**, *41*, 158.

53. Jiang, J. F.; Acunzo, A.; Koch, S. A. *J. Am. Chem. Soc.* **2001**, *123*, 12109.

54. Liaw, W. F.; Lee, J. H.; Gau, H. B.; Chen, C. H.; Jung, S. J.; Hung, C. H.; Chen, W. Y.; Hu, C. H.; Lee, G. H. *J. Am. Chem. Soc.* **2002**, *124*, 1680.

55. Liaw, W. F.; Lee, J. H.; Chen, C. H.; Lee, C. H.; Lee, G. H.; Peng, S. M. *J. Am. Chem. Soc.* **2000**, *122*, 488.

56. Kayal, A.; Rauchfuss, T. B. *Inorg. Chem.* **2003**, *42*, 5046.
57. Sellmann, D.; Geipel, F.; Heinemann, F. W. *Chem. Eur. J.* **2002**, *8*, 958.
58. Perra, A.; Davies, E .S.; Hyde, J. R.; Wang, Q.; McMaster, J.; Schroder, M. *Chem. Commun.* **2006**, 1103.
59. Adams, M. W. W. *Biochim. Biophys. Acta* **1990**, *1020*, 115.
60. Vignais, P. M.; Billoud, B.; Meyer, J. *Fems Microbiol. Rev.* **2001**, *25*, 455.
61. Heinekey, D. M. *J. Organomet. Chem.* **2009**, *694*, 2671.
62. Peters, J. W.; Lanzilotta, W. N.; Lemon, B. J.; Seefeldt, L. C. *Science*, **1998**, *282*, 1853.
63. Nicolet, Y.; Piras, C.; Legrand, P.; Hatchikian, C. E.; Fontecilla–Camps J. C. *Struct. Fold. Des.* **1999**, *7*, 13.
64. Nicolet, Y.; Cavazza, C.; Fontecilla–Camps, J.C. *Journal of Inorganic Biochemistry* **2002**, *91*, 1.
65. Siegbahn, P. E. M.; Tye, J. W.; Hall, M. B. *Chem. Rev.* **2007**, *107*, 4414.
66. De Lacey, A. L.; Standler, C.; Cavazza, C.; Hatchikian, E. C.; Fernandez, V. M. *J. Am. Chem. Soc.* **2000**, *122*, 11232.
67. Popescu, C. V.; Munck, E. *J. Am. Chem. Soc.* **1999**, *121*, 7877.
68. Cao, Z. X.; Hall, M. B. J. *J. Am. Chem. Soc.* **2001**, *123*, 3734.
69. Bruschi, M.; Fantucci, P.; De Dioia, L. *Inorg. Chem.* **2003**, *42*, 4773.
70. Zhou, T. J.; Mo, Y. R.; Liu, A. M.; Zhou, Z. H.; Tsai, K. R. *Inorg. Chem.* **2004**, *43*, 923.
71. Zhou, T.; Mo, Y.; Zhou, Z.; Tsai, K. *Inorg. Chem.* **2005**, *44*, 4941.
72. Bruschi, M.; Fantucci, P.; De Gioia, L. *Inorg. Chem.* **2002**, *41*, 1421.
73. Albracht, S. P. J.; Roseboom, W.; Hatchikian, E. C. *J. Biol. Inorg.Chem.* **2006**, *11*, 88.
74. Lyon, E. J.; Georgakai, I. P.; Reibenspies, J. H.; Darensbourg, M. Y. *Angew. Chem. Int. Ed.* **1999**, *38*, 3178.
75. Schmidt, M.; Contakes, S. M.; Rauchfuss T. B. *J. Am. Chem. Soc.* **1999**, *121*, 9736.
76. Le Cloirec A.; Best, S. P.; Borg, S.; Davies, S. C.; Evans, D. J.; Hughes, D. L.; Pickett, C. J. *Chem. Commun*. **1999**, 2285.
77. Gloaguen, F.; Lawrence, J. D.; Rauchfuss, T. B. *J. Am. Chem. Soc.* **2001**, *123*, 9476.
78. Nehring, J. L.; Heinekey, D. M. *Inorg. Chem.* **2003**, *42*, 4288.
79. Zhao, X.; Georgakaki, I. P.; Miller, M. L.; Mejia–Rodriguez, R.; Chiang, C. Y.; Darensbourg, M. Y. *Inorg. Chem.* **2002**, *41*, 3917.

80. Chong, D.; Georgakaki, I. P.; Mejia–Rodriguez, R.; Sanabria–Chinchilla, J.; Soriaga, M. P.; Darensbourg, M. Y. *J. Chem. Soc., Dalton Trans.* **2003**,*89*, 4158.
81. Aguirre De Carcer, I.; DiPasquale, A.; Rheingold, A. L.; Heinekey, D. M. *Inorg.Chem.* **2006**, *45*, 8000.
82. Tard, C.; Liu, X.; Ibrahim, S. K.; Bruschi, M.; De Gioia, L.; Davies, S.; Yang, X.; Wang, L. S.; Sawers, G.; Pickett, C. J. *Nature* **2005** *434*, 610.
83. Nicolet, Y.; De Lacey, A. L.; Vernde, X.; Fernandez, V. M.; Hatchikian, E.C.; Fontecilla–Camps, J. C. *J. Am. Chem. Soc.* **2001**, *123*, 1596.
84. Pandey, A. S.; Harris, T. V.; Giles, L. J.; Peters, J. W.; Szilagyi, R. K. *J. Am. Chem. Soc.* **2008**, *130*, 4533.
85. Li, H.; Rauchfuss, T. B. *J. Am. Chem. Soc.* **2002**, *124*, 726.
86. Popescu, C. V.; Münck, E. J. *J. Am. Chem. Soc.* **1999**, *121*, 7877.
87. Zirngibl, C.; Hedderich, R.; Thauer, R. K. *FEBS Lett.* **1990**, *216*, 112.
88. Thauer, R. K.; Klein, A. R.; Hartmann, G. C. *Chem. Rev.* **1996**, *96*, 3031.
89. Lyon, E. J.; Shima, S.; Buurman, G.; Chowdhuri, S.; Batschauer, A.; Steinbach, K.; Thauer, R. K. *Eur. J. Biochem.* **2004**, *271*, 195.
90. Lyon, E. J.; Sordel–Kippert, M. S.; Kauss, M.; Kahnt, J.; Thauer, R. K.; Steinbach, K.; Xie, X. L.; Verdier, L.; Griesenger, C. *Angew. Chem., Int. Ed. Engl.* **2004**, *43*, 2547.
91. Shima, S.; Lyon, E. J.; Thauer, R. K.; Mienert, B.; Bill, E. *J. Am. Chem. Soc.* **2005**, *127*, 10430.
92. Shima, S.; Pilak, O.; Vogt, S.; Schick, M.; Stagni, M. S.; Meyer–Klaucke, W.; Warkentin, E.; Thauer, R. K.; Ermler, U. *Science* **2008**, *321*, 572.
93. Hiromoto, T.; Ataka, K.; Pilak, O.; Vogt, S.; Stagni, M. S.; Meyer–Klaucke, W.; Warkentin, E.; Thauer, R. K.; Shima, S.; Ermler, U. *FEBS Lett.* **2009**, *583*, 585.
94. Wang, X.; Li, Z.; Zeng, X.; Luo, Q.; Evans, D. J.; Pickett, C. J.; Liu, X. *Chem. Commun.* **2008**, 3555.

**Chapter 2:**

1. Figuly, G. D.; Loop, C. K.; Martin, J. C. *J. Am. Chem. Soc.* **1989**, *111*, 654.
2. Block, E.; Eswarakrishnan, V.; Gernon, M.; Ofori–Okai, G.; Saha, C.; Tang, K.; Zubieta, J. *J. Am. Chem. Soc.* **1989**, *111*, 658.
3. Smith, K.; Lindsay, C. M.; Pritchard, G. J. *J. Am. Chem. Soc.* **1989**, *111*, 665.

4. Block, E.; Ofori–Okai, G.; Zubieta, J. *J. Am. Chem. Soc.* **1989**, *111*, 2327.
5. Fernandez, P.; Sousa–Pedrares, A.; Romero, J.; Garcia–Vazquez, J. A.; Sousa, A.; Perez–Lourido, P. *Inorg. Chem.* **2008**, *47*, 2121.
6. Dilworth, J. R.; Wheatley, N. *Coord. Chem. Rev.* **2000**, *199*, 89.
7. Cotton, F. A.; Eglin, J. L.; Hong, B.; James, C. A. *J. Am. Chem. Soc.* **1992**, *114*, 4915.
8. *Organic Synthesis* **1987**, *65*, 150.
9. Perez–Lourido, P.; Garcia–Vasquez, J. A.; Romero, J.; Sousa, A.; Block, E.; Maresca, K. P.; Zubieta, J. *Inorg. Chem.* **1999**, *38*, 538.
10. Hildebrand, A.; Lönnecke, P.; Silaghi–Dumitrescu, L.; Hey–Hawkins, E. *Dalton Trans.* **2008**, 4639.
11. Iwasaki, F.; Iwasaki, H. *Acta Crystallogr. B* **1972**, *28*, 3370.
12. Chen, Q.; Buss, C. B.; Young, V. G.; Fox, S. *J. Chem. Crystallogr.* **2005**, *35*, 177.

**Chapter 3:**

1. Berg, J. M.; Holm, R. H. *Metals Ions in Biology*; Spiro, T. G., Ed; Wiley: New York, 1982; vol. 4; pp. 1–66.
2. Blower, P. J.; Dilworth, J. R. *Coord. Chem. Rev.* **1987**, *76*, 121.
3. Dilworth, J. R.; Zheng, Y.; Miller, J. R. *J. Chem. Soc, Dalton Trans.* **1992**, 1757–1758.
4. Zhu, W.; Marr, A. C.; Wang, Q.; Neese, F.; Spencer, D. J. E.; Blake, A. J.; Cooke, P. A.; Wilson, C.; Schröder, M. *PNAS*, **2005**, *102*, 18280–18285.
5. Corbett, M. C.; Hu, Y.; Fay, A. W.; Ribbe, M. W.; Hedman, B.; Hodgson, K. O. *PNAS*, **2006**, *103*, 1238–1243.
6. Lippard, S. J.; Berg, J. M. *Principles of Bioinorganic Chemistry*; University Science Books; 1994.
7. Sellmann, D.; Geck, M.; Knoch, F.; Ritter, G.; Dengler, J. *J. Am. Chem. Soc.*, **1991,** *113*, 1819.
8. Sellmann, D.; Lechner, P.; Knoch, F.; Moll, M. *Angew. Chem., Int. Ed. Engl.*, **1991**, *30*, 552.
9. Sellmann, D.; Barth, I.; *Z. Anorg. Allg. Chem.*, **1989,** *577*, 234.
10. Sellmann, D.; Binker, G.; Moll, M.; Herdtweck, E. *J. Organomet. Chem.* **1987**, *327*, 403.
11. Sellmann, D.; Kaeppler, O. *Z. Naturforsch., Teil B*, **1987**, *42*, 1291.
12. Sellmann, D.; Binker, G.; Moll, M.; Campana, C. E. *Inorg. Chim. Acta* **1987**, *130*, 221.

13. Sellmann, D.; Reineke, U.; Huttner, G.; Zsolnai, L. *J. Organomet. Chem.* **1987**, *310*, 83.
14. Issleib, V. K.; Gans, W. *Z. Anorg. Allg. Chem.* **1982**, *491*, 163.
15. Stephan, D. W.; *Inorg. Chem.* **1984**, *23*, 2207.
16. Block, E.; Eswarakrishman, V.; Gernon, M.; Ofori–Okai, G.; Saha, C.; Tang, K.; Zubieta, J. *J. Am. Chem. Soc.* **1989**, *111*, 658.
17. Block, E.; Ofori–Okai, G.; Zubieta, J. *J. Am. Chem. Soc.* **1989**, *111*, 2647.
18. Vries, N.; Davison, A.; Jones, A. G. *Inorg. Chim. Acta* **1989**, *165*, 346.
19. Dilworth, J. R.; Hutson, A. J.; Lewis, J. S.; Miller, J. R.; Zheng, Y.; Chen, Q.; Zubieta, J. *J. Chem. Soc., Dalton Trans.* **1996**, 1093–1104.
20. I.P. Evans; A. Spencer; G. Wilkinson. *J. Chem. Soc. Dalton* **1973**, 204.
21. Dehand, J.; Rose, J. *Inorg. Chim. Acta* **1979**, *37*, 249.
22. Elliott, G. P.' McAuley, N. M.; Roper, W. R. *Inorg. Synth.* **1989**, *26*, 185.
23. John Franolic, PhD dissertation, Stony Brook University, Stony Brook, **1993**.
24. Susan T. Beatty, PhD dissertation, Stony Brook University, Stony Brook, **1995**.
25. Kou–Suein Ai, PhD dissertation, Stony Brook University, Stony Brook, **1996**.
26. Doris Melgarejo, PhD dissertation, Stony Brook University, Stony Brook, **2006**.

**Chapter 4:**

1. Sharpe, A. G. *The Chemistry of Cyano Complexes of the Transition Metals*. Academic Press: New York, 1976.
2. Dunbar, K. R.; Heintz, R. A. Chemistry of Transition Metal Cyanide Compounds: Modern Perspectives. *Prog. Inorg. Chem.* **1997**, *45*, 283.
3. http://www.ibiblio.org/wm/paint/auth/gogh/starry–night/
4. http://www.fda.gov/Drugs/EmergencyPreparedness/BioterrorismandDrugPreparedness/ucm130337.htm
5. http://www.builderssquare.com/xp_34839867–Morton_Kosher_Salt_Coarse_3_lb_1_36_kg_Box_of_12_4499.aspx
6. Gina Chiarella, PhD dissertation, Stony Brook University, Stony Brook, **2006**.
7. Goedken, V. L. *J. Chem. Soc., Chem. Commun.* **1972**, 207–208.
8. Cotton, F. A.; Monchamp, R. R.; Henry, R. J. M.; Young, R. C.; *J. Inorg. Nucl. Chem.*, **1959**, *10*, 28.
9. Gmelin, **1932**, 59B, 704.

10. Gmelin, **1976**, 36B, 24.
11. Toma, H. E.; Creutz, C. *Inorg. Chem.*, **1977**, *16*, 545.
12. Toma, H. E.; Moroi, N. M.; Iha, N. Y. M. *An. Acad. Bras. Cienc.*, **1982**, *54*, 315.
13. Mullar, J. A.; Hebd, C. R. *Seances, Acad. Sci.*; **1887**, *104*, 992.
14. Manchot, W.; Merry, E., Woringer, P. *Chem. Ber.*, **1912**, *45*, 2879.
15. Kenney, D. J.; Flynn, T. P.; Gallini, J. B. *J. Inorg. Nucl. Chem.*, **1961**, *20*, 75
16. Jiang, J.; Koch, S. A. *Angew. Chem., Int. Ed.* **2001**, *40*, 2629–2631.
17. Chiarella, G. M.; Melgarejo, D. Y.; Koch, S. A. *J. Am. Chem. Soc.*, **2006**, *128*, 1416–1417.
18. Cauzzi, D. A.; Mori, G.; Predieri, G.; Tiripicchio, A. *Inorg. Chim. Acta*, **1993**, *204*, 181–187.
19. Gusev, D. G.; Dolgushin, F. M.; Antipin, M. Y.. *Organometallics* **2001**, *20*, 1001.
20. Martinsen, A.; Songstad, J. *Acta Chem. Scand., Ser. A* **1977**, *31*, 645.
21. Carini, C.; Pelizzi, C.; Peilzzi, G.; Predieri, G.; Tarasconi, P.; Vitali, F. *J. Chem. Soc., Chem. Commun.* **1990**, 613.
22. Bonardi, A.; Carini, C.; Pelizzi, C.; Pelizzi, G.; Predieri, G.; Tarasconi, P.; Zoroddu, M. A.; Molloy, K. C. *J. Organomet. Chem.* **1991**, *401*, 283.
23. Jiang, J.; Koch, S. A. *Inorg. Chem.* **2002**, *41*, 158–160.
24. Contakes, S. M.; Hsu, S. C. N.; Rauchfuss, T. B.; Wilson, S. R. *Inorg. Chem.* **2002**, *41*, 1670–1678.
25. Kettle, S. F. A.; Aschero, G. L.; Diana, E.; Rossetti, R.; Stanghellinim P. L.; *Inorg. Chem.* **2006**, *45*, 4928–4937.
26. Buchner, W.;Schenk, W. A. *Inorg. Chem.* **1984**, *23*, 132–137.
27. Jianfeng Jiang, PhD dissertation, Stony Brook University, Stony Brook, **2002**.

**Chapter 5:**

1. Koch, S. A.; Millar, M. *J. Am. Chem. Soc.*, **1983**, *105*, 3362–3363.
2. Foster, M. W.; Cowan, J. A. *J. Am. Chem. Soc.* **1999**, *121*, 4093–4100.
3. Kerbs, C.; Henshaw, T. F.; Cheek, J.; Huynh, B. H.; Broderick, J. B. *J. Am. Chem. Soc.* **2000**, *122*, 12497–12506.
4. Wiler, J J.; Lippard, S. J. *Inorg. Chem.* **1999**, *38*, 3569–3574.
5. Nakamura, A. *Inorg. Chem.* **1996**, *35*, 6473–6484.

6. Millar, M.; O'Sullivan, T.; deVries, N.; Koch, S. A. *J. Am. Chem. Soc.* **1985**, *107*, 3714.
7. Soong, S.; Hain, Jr., J. H.; Millar, M.; Koch, S. A. *Organometallics* **1988**, *7*, 556–557.
8. Satsangee, S. P.; Hain, Jr., J. H.; Cooper, P. T.; Koch, S. A. *Inorg. Chem.* **1992**, *31*, 5160–5161.
9. http://www.mpg.de/350372/forschungsSchwerpunkt
10. http://metallo.scripps.edu/PROMISE/RUBREDOXIN.html
11. Bianchini, C.; Meli, A.; Moneti, S.; Vizza, F. *Organometallic* **1998**, *17*, 2636–2645.
12. Tanaka, K.; Mizukawa, T. *Appl. Organometal. Chem.* **2000**, *14*, 863–866.
13. Tanaka, K.; Ooyama, D. *Coor. Chem. Rev.* **2002**, *226*, 211–218.
14. Ishiguro, A.; Liu, Y.; Nakajima, T.; Wakatsuki, Y. J.*Catalysis*, **2002**, *206*, 159–164.
15. Cleare, M. J.; Griffith, W. P. *J. Chem. Soc. A* **1969**, 372.
16. Panda, B. K.; Chattopadhyay, S.; Ghosh, K.; Chakravorty, A. *Polyhedron*, **2002**, *21*, 899–904.
17. Shiu, K. B.; Yu, S. J.; Wang, Y.; Lee, G. H. *J. Organometal. Chem.*, **2002**, *650*. 37–42.
18. Janet Haff, PhD dissertation, Stony Brook University, Stony Brook, 2002.
19. Doris Melgarejo, PhD dissertation, Stony Brook University, Stony Brook, 2006.
20. Frey, M. *ChemBioChem* **2002**, *3*, 153–160.
21. Schmidt, M.; Contakes, S. M.; Rauchfuss, T. B. *J. Am. Chem. Soc.* **1999**, *121*, 9736–9737.
22. Zhao, X.; Georgakaki, I. P.; Miller, M. L.; Yarbrough, J. C.; Darensbourg, M. Y. *J. Am. Chem. Soc.* **2001**, *123*, 11010–11018.
23. Gloaguen, F.; Lawreence, J .D.; Rauchfuss, T. B. *J. Am. Chem. Soc.* **2001**, *123*, 9476–9477.
24. Borg, S. J.; Behrsing, T.; Best, S. P.; Razavet, M.; Liu, X.; Pickett, C. J. *J. Am. Chem. Soc.* **2004**, *126*, 16988–16999.
25. Mejia–Rodriguez, R.; Chong, D.; Reibenspies, J. H.; Soriaga, M. P.; Darensbourg, M. Y. *J. Am. Chem. Soc.* **2004**, *126*, 12004–12014.
26. Justice, A. K.; Linck, R. C.; Rauchfuss, T. B. *Inorg. Chem.* **2006**, *45*, 2406–2412.
27. Gray, G. M.; Duffey, C. H. *Acta Crystallographica Sec. C* **1996**, C52, 861–863.
28. Reddy, V. V. S.; Whitten, J. E.; Redmill, K. A.; Varshney, A.; Gray, G. M. *J. Organomet. Chem.* **1989**, *372*, 207–216.

29. Gina Chiarella, PhD dissertation, Stony Brook University, Stony Brook, 2006.
30. Seitz, K.; Behrens, U. *J. Organomet. Chem.* **1988**, *345*, 351.
31. Hanif, K. M.; Kabir, S. E.; Mottalib, M. A.; Hursthouse, M. B.; Malik, K. M. A; Rosenberg, E. *Polyhedron* **2000**, *19*, 1073.
32. Cabeza, J. A.; Martinez–Gomez, M. A.; Riera, V.; Arhura, D.; Garcia–Granda, S. *Organometallics*, **1998**, *17*, 1471.
33. Shiu, K. B.; Wang, Y.; Liao, F. L.; Chiang, M. Y.; Peng, S. M.; Lee, G. H.; Wang, J. C.; Liou, L, S. *Organometallics* **1998**, *17*, 1790–1797.
34. Jessop, P. G.; Rettig, S. J.; Lee, C. L.; James, B, R. *Inorg. Chem.* **1991**, *30*, 4617–4627.
35. Grapperhaus, C. A.; Poturovic, S.; Masguta, M. S. *Inorg. Chem.* **2002**, *41*, 4309–4311.
36. Sekkmann, D.; Heinemann, F. W.; Gottschlak,–Gaudig, T. *Inorg. Chem.* **1998**, *37*, 3982–3988.

**Chapter 6:**

1. Vignais, P. M.; Billoud, B. *Chem. Rev.* **2007**, *107*, 4206–4272.
2. Fomtecilla–Camps, J. C.; Volbeda, A.; Cavazza, C.; Nicolet, Y. *Chem. Rev.* **2007**, *107*, 4273–4303.
3. Armstrong, F. A.; Belsey, N. A.; Cracknell, J. A.; Goldet, G.; Parkin, A.; Reisner, E.; Vincent, K. A.; Wait, A. F. *Chem. Soc. Rev*. **2009**, *38*, 36–51.
4. Volbeda, A.; Martin, L.; Cavazza, C.; Matho, M.; Faber, B. W.; Roseboom, W.; Albracht, S. P. J.; Garcin, E.; Rousset, M.; Fomtecilla–Camps, J. C. *J. Biol. Inorg. Chem.* **2005**, *10*, 239–249.
5. Lubitz, W.; Reijerse, E.; van Gastel, M. *Chem. Rev.* **2007**, *107*, 4331–4365.
6. Zilong, L.; Ohki, Y.; Tatsumi, K. *J. Am. Chem. Soc.* **2005**, *127*, 8950–8951.
7. Jiang, J.; Maruani, M.; Solaimanzadeh, J.; Lo, W.; Koch, S. A., Millar, M. *Inorg. Chem.* **2009**, 6359–6361.
8. Gina Chiarella, PhD dissertation, Stony Brook University, Stony Brook, **2006**.
9. Jianfeng Jiang, PhD dissertation, Stony Brook University, Stony Brook, **2002**.
10. F. Osterloh; W. Saak; S. Pohl. *J. Am. Chem. Soc.* **1997**, *119*, 5648.
11. Bomfim J. A. S.; de Souza, F. P.; Filgueiras, C. A. L.; de Sousa, A. G.; Gambardell, M. T. P. *Polyhedron*, **2003**, 1567–1573.
12. Hieber, W.; Lagally, H.; Wirsching A. *Z. Anorg. Allgem. Chem.* **1940**, *245*, 35.

13. Spek, A. L.; van Eijck, B. P. *Acta Cryst. C* **1987**, *C43*, 1879–1880.

14. Yamamura, T.; Arai, H.; Nakamura, N.; Miyamae, H. *Chemistry Letters* **1990**, 2121–2124.

15. Higuchi, Y.; Yagi, T.; Yasuoka, N. *Structure* **1997**, 5, 1671–1680.

16. Higuchi, Y.; Ogata, H.; Miki, K.; Yasuoka, N.; Yagi, T. *Structure* **1999**, 7, 549–556.

17. Volbeda, A.; Charon, M. H.; Piras, C.; Hatchikian, E. C.; Frey, M.; Fontecilla–Camps, J. C. *Nature* **1995**, *373*, 580–587.

18. Volbeda, A.; Garcin, E.; Piras, C.; de Lacey, A. L.; Fernandez, V. M.; Hatchikian, E. C.; Frey, M.; Fontecilla–Camps, J. C. *J. Am. Chem. Soc.* **1996**, *118*, 12989–12996.

19. Rousset, M.; Montet, Y.; Guigliarelli, B.; Forget, N.; Asso, M.; Bertrand, P.; Fontecilla–Camps, J. C.; Hatchikian, E. C. *Proc. Natl. Acad. Sci. U.S.A.* **1998**, *95*, 11625–11630.

**Table A–1. Crystal data and structure refinement for $H_2PS2$.**

| | | |
|---|---|---|
| Identification code | $H_2PS2$ | |
| Empirical formula | $C_{18}H_{15}PS_2$ | |
| Formula weight | 326.39 | |
| Temperature | 100(2) K | |
| Wavelength | 0.71073 Å | |
| Crystal system | Monoclinic | |
| Space group | $P2_1/n$ | |
| Unit cell dimensions | a = 7.6555(2) Å | α = 90° |
| | b = 8.0505(2) Å | β = 97.476(2)° |
| | c = 26.6533(6) Å | γ = 90° |
| Volume | 1628.70(7) $Å^3$ | |
| Z | 4 | |
| Density (calculated) | 1.331 $Mg/m^3$ | |
| Absorption coefficient | 0.415 $mm^{-1}$ | |
| F(000) | 680 | |
| Crystal size | 0.45 x 0.35 x 0.25 $mm^3$ | |
| Theta range for data collection | 3.31 to 29.70° | |
| Index ranges | –10<=h<=10, –11<=k<=11, –36<=l<=37 | |
| Reflections collected | 21679 | |
| Independent reflections | 4238 [R(int) = 0.0275] | |
| Completeness to theta = 29.70° | 91.8 % | |
| Absorption correction | Sphere | |
| Refinement method | Full–matrix least–squares on $F^2$ | |
| Data / restraints / parameters | 4238 / 0 / 198 | |
| Goodness–of–fit on $F^2$ | 1.044 | |
| Final R indices [I>2sigma(I)] | R1 = 0.0394, wR2 = 0.1012 | |
| R indices (all data) | R1 = 0.0470, wR2 = 0.1043 | |
| Largest diff. peak and hole | 1.158 and –0.458 e.$Å^{-3}$ | |

**Table A–2. Crystal data and structure refinement for $H_2PS2'$.**

| | | |
|---|---|---|
| Identification code | $H_2PS2'$ | |
| Empirical formula | $C_{20}H_{19}PS_2$ | |
| Formula weight | 354.44 | |
| Temperature | 100(2) K | |
| Wavelength | 0.71073 Å | |
| Crystal system | Monoclinic | |
| Space group | $P2_1/n$ | |
| Unit cell dimensions | a = 9.4007(2) Å | α = 90° |
| | b = 9.5810(2) Å | β = 98.492(2)° |
| | c = 20.0653(5) Å | γ = 90° |
| Volume | 1787.43(7) $Å^3$ | |
| Z | 4 | |
| Density (calculated) | 1.317 $Mg/m^3$ | |
| Absorption coefficient | 0.384 $mm^{-1}$ | |
| F(000) | 744 | |
| Crystal size | 0.85 x 0.40 x 0.35 $mm^3$ | |
| Theta range for data collection | 3.49 to 31.40° | |
| Index ranges | –12<=h<=13, –13<=k<=13, –28<=l<=23 | |
| Reflections collected | 17723 | |
| Independent reflections | 5301 [R(int) = 0.0241] | |
| Completeness to theta = 31.40° | 89.8 % | |
| Absorption correction | Sphere | |
| Refinement method | Full–matrix least–squares on $F^2$ | |
| Data / restraints / parameters | 5301 / 0 / 216 | |
| Goodness–of–fit on $F^2$ | 1.117 | |
| Final R indices [I>2sigma(I)] | R1 = 0.0392, wR2 = 0.1220 | |
| R indices (all data) | R1 = 0.0550, wR2 = 0.1271 | |
| Largest diff. peak and hole | 0.547 and –0.518 e.$Å^{-3}$ | |

**Table A–3. Crystal data and structure refinement for NBr2'.**

| | | |
|---|---|---|
| Identification code | NBr2' | |
| Empirical formula | $C_{22}H_{21}Br_2N$ | |
| Formula weight | 459.22 | |
| Temperature | 100(2) K | |
| Wavelength | 0.71073 Å | |
| Crystal system | Monoclinic | |
| Space group | $P2_1/c$ | |
| Unit cell dimensions | a = 7.5884(4) Å | α = 90° |
| | b = 29.730(2) Å | β = 94.891(5)° |
| | c = 8.8523(4) Å | γ = 90° |
| Volume | 1989.8(2) $Å^3$ | |
| Z | 4 | |
| Density (calculated) | 1.533 $Mg/m^3$ | |
| Absorption coefficient | 4.078 $mm^{-1}$ | |
| F(000) | 920 | |
| Crystal size | 0.90 x 0.70 x 0.40 $mm^3$ | |
| Theta range for data collection | 3.39 to 32.78° | |
| Index ranges | –11<=h<=11, –44<=k<=41, –7<=l<=13 | |
| Reflections collected | 10803 | |
| Independent reflections | 6147 [R(int) = 0.0853] | |
| Completeness to theta = 32.78° | 83.3 % | |
| Absorption correction | Sphere | |
| Refinement method | Full–matrix least–squares on $F^2$ | |
| Data / restraints / parameters | 6147 / 0 / 226 | |
| Goodness–of–fit on $F^2$ | 1.041 | |
| Final R indices [I>2sigma(I)] | R1 = 0.1384, wR2 = 0.3461 | |
| R indices (all data) | R1 = 0.1748, wR2 = 0.3688 | |
| Largest diff. peak and hole | 3.401 and –4.468 e.$Å^{-3}$ | |

**Table A–4. Crystal data and structure refinement for NBr3.**

| | | |
|---|---|---|
| Identification code | NBr3 | |
| Empirical formula | $C_{21}H_{18}Br_3N$ | |
| Formula weight | 524.09 | |
| Temperature | 100(2) K | |
| Wavelength | 0.71073 Å | |
| Crystal system | Triclinic | |
| Space group | *P*–1 | |
| Unit cell dimensions | a = 7.6219(2) Å | α = 79.071(3)° |
| | b = 9.0494(3) Å | β = 81.768(2)° |
| | c = 14.5748(4) Å | γ = 85.510(3)° |
| Volume | 975.52(5) $Å^3$ | |
| Z | 2 | |
| Density (calculated) | 1.784 $Mg/m^3$ | |
| Absorption coefficient | 6.206 $mm^{-1}$ | |
| F(000) | 512 | |
| Crystal size | 0.65 x 0.50 x 0.30 $mm^3$ | |
| Theta range for data collection | 3.34 to 32.81° | |
| Index ranges | –9<=h<=11, –12<=k<=13, –20<=l<=17 | |
| Reflections collected | 10962 | |
| Independent reflections | 6394 [R(int) = 0.0310] | |
| Completeness to theta = 32.81° | 88.2 % | |
| Absorption correction | Sphere | |
| Refinement method | Full–matrix least–squares on $F^2$ | |
| Data / restraints / parameters | 6394 / 0 / 226 | |
| Goodness–of–fit on $F^2$ | 0.915 | |
| Final R indices [I>2sigma(I)] | R1 = 0.0365, wR2 = 0.0671 | |
| R indices (all data) | R1 = 0.0636, wR2 = 0.0711 | |
| Largest diff. peak and hole | 0.680 and –0.887 e.$Å^{-3}$ | |

**Table A–5. Crystal data and structure refinement for *trans*–[*n*–$Pr_4N$][$Ru^{III}(PS2)_2$].**

| | | |
|---|---|---|
| Identification code | *trans*–[*n*–$Pr_4N$][$Ru^{III}(PS2)_2$] | |
| Empirical formula | $C_{48}H_{54}NP_2RuS_4$ | |
| Formula weight | 936.17 | |
| Temperature | 100(2) K | |
| Wavelength | 0.71073 Å | |
| Crystal system | Monoclinic | |
| Space group | $P2_1/n$ | |
| Unit cell dimensions | a = 9.39420(10) Å | α = 90° |
| | b = 23.2295(4) Å | β = 101.551(2)° |
| | c = 20.5371(3) Å | γ = 90° |
| Volume | 4390.89(11) $Å^3$ | |
| Z | 4 | |
| Density (calculated) | 1.416 $Mg/m^3$ | |
| Absorption coefficient | 0.655 $mm^{-1}$ | |
| F(000) | 1948 | |
| Crystal size | 0.25 x 0.15 x 0.15 $mm^3$ | |
| Theta range for data collection | 3.16 to 28.47° | |
| Index ranges | –11<=h<=12, –28<=k<=30, –27<=l<=24 | |
| Reflections collected | 69277 | |
| Independent reflections | 10184 [R(int) = 0.0449] | |
| Completeness to theta = 28.47° | 91.7 % | |
| Absorption correction | Sphere | |
| Refinement method | Full–matrix least–squares on $F^2$ | |
| Data / restraints / parameters | 10184 / 0 / 505 | |
| Goodness–of–fit on $F^2$ | 0.998 | |
| Final R indices [I>2sigma(I)] | R1 = 0.0339, wR2 = 0.0718 | |
| R indices (all data) | R1 = 0.0557, wR2 = 0.0750 | |
| Largest diff. peak and hole | 0.954 and –0.933 e.$Å^{-3}$ | |

**Table A–6. Crystal data and structure refinement for *trans*–[$Et_4N$][$Ru^{III}(PS2')_2$].**

| | | |
|---|---|---|
| Identification code | *trans*–[$Et_4N$][$Ru^{III}(PS2')_2$] | |
| Empirical formula | $C_{48}H_{54}NP_2RuS_4$ | |
| Formula weight | 936.17 | |
| Temperature | 100(2) K | |
| Wavelength | 0.71073 Å | |
| Crystal system | Triclinic | |
| Space group | *P*–1 | |
| Unit cell dimensions | a = 9.2808(2) Å | α = 72.968(3)° |
| | b = 13.8541(4) Å | β = 88.488(2)° |
| | c = 19.3704(6) Å | γ = 80.802(2)° |
| Volume | 2350.19(11) $Å^3$ | |
| Z | 2 | |
| Density (calculated) | 1.323 $Mg/m^3$ | |
| Absorption coefficient | 0.612 $mm^{-1}$ | |
| F(000) | 974 | |
| Crystal size | 0.35 x 0.15 x 0.15 $mm^3$ | |
| Theta range for data collection | 3.12 to 29.53° | |
| Index ranges | –12<=h<=12, –18<=k<=19, –26<=l<=26 | |
| Reflections collected | 40425 | |
| Independent reflections | 11647 [R(int) = 0.0423] | |
| Completeness to theta = 29.53° | 88.6 % | |
| Absorption correction | Sphere | |
| Refinement method | Full–matrix least–squares on $F^2$ | |
| Data / restraints / parameters | 11647 / 0 / 508 | |
| Goodness–of–fit on $F^2$ | 0.926 | |
| Final R indices [I>2sigma(I)] | R1 = 0.0328, wR2 = 0.0793 | |
| R indices (all data) | R1 = 0.0530, wR2 = 0.0824 | |
| Largest diff. peak and hole | 0.758 and –0.478 e.$Å^{-3}$ | |

**Table A–7. Crystal data and structure refinement for *cis*–[$Et_4N$][$Ru^{II}$(PS3')(HPS3')](“S–S” disulfide).**

| | | |
|---|---|---|
| Identification code | *cis*–[$Et_4N$][$Ru^{II}$(PS3')(HPS3')](“S–S” disulfide) | |
| Empirical formula | $C_{50}H_{56}NP_2RuS_6$ | |
| Formula weight | 1026.33 | |
| Temperature | 100(2) K | |
| Wavelength | 0.71069 Å | |
| Crystal system | Monoclinic | |
| Space group | $P2_1/c$ | |
| Unit cell dimensions | a = 15.094(5) Å | α = 90.000(5)° |
| | b = 17.482(5) Å | β = 93.140(5)° |
| | c = 18.799(5) Å | γ = 90.000(5)° |
| Volume | 4953(3) $Å^3$ | |
| Z | 4 | |
| Density (calculated) | 1.376 $Mg/m^3$ | |
| Absorption coefficient | 0.669 $mm^{-1}$ | |
| F(000) | 2132 | |
| Crystal size | 0.30 x 0.20 x 0.10 $mm^3$ | |
| Theta range for data collection | 3.18 to 27.12° | |
| Index ranges | –18<=h<=19, –20<=k<=21, –22<=l<=23 | |
| Reflections collected | 42008 | |
| Independent reflections | 9493 [R(int) = 0.0342] | |
| Completeness to theta = 27.12° | 86.7 % | |
| Refinement method | Full–matrix least–squares on $F^2$ | |
| Data / restraints / parameters | 9493 / 0 / 541 | |
| Goodness–of–fit on $F^2$ | 1.049 | |
| Final R indices [I>2sigma(I)] | R1 = 0.0592, wR2 = 0.1409 | |
| R indices (all data) | R1 = 0.0775, wR2 = 0.1471 | |
| Largest diff. peak and hole | 1.576 and –0.624 e.$Å^{-3}$ | |

**Table A–8. Crystal data and structure refinement for *trans*–[*n*–$Pr_4N$][$Ru^{III}(NS2)_2$].**

| | | |
|---|---|---|
| Identification code | *trans*–[*n*–$Pr_4N$][$Ru^{III}(NS2)_2$] | |
| Empirical formula | $C_{54}H_{66}N_3RuS_4$ | |
| Formula weight | 986.41 | |
| Temperature | 100(2) K | |
| Wavelength | 0.71073 Å | |
| Crystal system | Monoclinic | |
| Space group | $P2_1/n$ | |
| Unit cell dimensions | a = 11.4340(3) Å | α = 90° |
| | b = 23.6791(6) Å | β = 96.415(2)° |
| | c = 18.3050(4) Å | γ = 90° |
| Volume | 4925.0(2) $Å^3$ | |
| Z | 4 | |
| Density (calculated) | 1.330 $Mg/m^3$ | |
| Absorption coefficient | 0.527 $mm^{-1}$ | |
| F(000) | 2076 | |
| Crystal size | 0.30 x 0.20 x 0.10 $mm^3$ | |
| Theta range for data collection | 3.14 to 29.57° | |
| Index ranges | –15<=h<=15, –23<=k<=32, –18<=l<=25 | |
| Reflections collected | 27554 | |
| Independent reflections | 11700 [R(int) = 0.0520] | |
| Completeness to theta = 29.57° | 84.7 % | |
| Absorption correction | Sphere | |
| Refinement method | Full–matrix least–squares on $F^2$ | |
| Data / restraints / parameters | 11700 / 0 / 559 | |
| Goodness–of–fit on $F^2$ | 0.687 | |
| Final R indices [I>2sigma(I)] | R1 = 0.0372, wR2 = 0.0526 | |
| R indices (all data) | R1 = 0.0929, wR2 = 0.0576 | |
| Largest diff. peak and hole | 0.539 and –0.603 e.$Å^{-3}$ | |

**Table A–9. Crystal data and structure refinement for *trans*–[*n*–$Pr_4N$][$Ru^{III}(NS2')_2$].**

| | | |
|---|---|---|
| Identification code | *trans*–[*n*–$Pr_4N$][$Ru^{III}(NS2')_2$] | |
| Empirical formula | $C_{56}H_{70}N_3RuS_4$ | |
| Formula weight | 1014.46 | |
| Temperature | 100(2) K | |
| Wavelength | 0.71069 Å | |
| Crystal system | Monoclinic | |
| Space group | $P2_1/c$ | |
| Unit cell dimensions | a = 11.417(5) Å | a= 90° |
| | b = 24.770(5) Å | b= 95.739(5)° |
| | c = 18.287(5) Å | g = 90° |
| Volume | 5146(3) $Å^3$ | |
| Z | 4 | |
| Density (calculated) | 1.310 $Mg/m^3$ | |
| Absorption coefficient | 0.506 $mm^{-1}$ | |
| F(000) | 2140 | |
| Crystal size | 0.25 x 0.20 x 0.10 $mm^3$ | |
| Theta range for data collection | 3.19 to 29.44° | |
| Index ranges | –15<=h<=15, –31<=k<=25, –18<=l<=24 | |
| Reflections collected | 18130 | |
| Independent reflections | 10576 [R(int) = 0.0311] | |
| Completeness to theta = 29.44° | 74.1 % | |
| Refinement method | Full–matrix least–squares on $F^2$ | |
| Data / restraints / parameters | 10576 / 0 / 578 | |
| Goodness–of–fit on $F^2$ | 0.845 | |
| Final R indices [I>2sigma(I)] | R1 = 0.0424, wR2 = 0.0923 | |
| R indices (all data) | R1 = 0.0802, wR2 = 0.0983 | |
| Extinction coefficient | 0.00000(13) | |
| Largest diff. peak and hole | 1.248 and –1.186 e.$Å^{-3}$ | |

**Table A–10. Crystal data and structure refinement for *trans*–[$Me_3NBz$][$Os^{III}(PS2)_2$].**

| | | |
|---|---|---|
| Identification code | *trans*–[$Me_3NBz$][$Os^{III}(PS2)_2$] | |
| Empirical formula | $C_{46}H_{42}NOsP_2S_4$ | |
| Formula weight | 989.19 | |
| Temperature | 100(2) K | |
| Wavelength | 0.71073 Å | |
| Crystal system | Triclinic | |
| Space group | *P*–1 | |
| Unit cell dimensions | a = 9.3142(3) Å | α = 83.493(2)° |
| | b = 12.8318(4) Å | β = 77.059(3)° |
| | c = 18.4460(5) Å | γ = 71.708(3)° |
| Volume | 2037.87(11) $Å^3$ | |
| Z | 2 | |
| Density (calculated) | 1.612 $Mg/m^3$ | |
| Absorption coefficient | 3.447 $mm^{-1}$ | |
| F(000) | 990 | |
| Crystal size | 0.35 x 0.15 x 0.10 $mm^3$ | |
| Theta range for data collection | 3.27 to 29.68° | |
| Index ranges | –12<=h<=12, –17<=k<=17, –24<=l<=25 | |
| Reflections collected | 68284 | |
| Independent reflections | 10607 [R(int) = 0.1065] | |
| Completeness to theta = 29.68° | 92.0 % | |
| Refinement method | Full–matrix least–squares on $F^2$ | |
| Data / restraints / parameters | 10607 / 0 / 490 | |
| Goodness–of–fit on $F^2$ | 1.009 | |
| Final R indices [I>2sigma(I)] | R1 = 0.0533, wR2 = 0.1119 | |
| R indices (all data) | R1 = 0.1215, wR2 = 0.1252 | |
| Largest diff. peak and hole | 2.073 and –0.950 e.$Å^{-3}$ | |

**Table A–11. Crystal data and structure refinement for *cis*–[$Me_3NBz$][$Os^{III}(PS2')_2$].**

| | | |
|---|---|---|
| Identification code | *cis*–[$Me_3NBz$][$Os^{III}(PS2')_2$] | |
| Empirical formula | $C_{50}H_{48}NOsP_2S_4$ | |
| Formula weight | 1043.27 | |
| Temperature | 100(2) K | |
| Wavelength | 0.71073 Å | |
| Crystal system | Triclinic | |
| Space group | *P*–1 | |
| Unit cell dimensions | a = 9.0659(3) Å | α = 78.314(3)° |
| | b = 15.3938(5) Å | β = 88.340(2)° |
| | c = 16.6074(5) Å | γ = 86.192(2)° |
| Volume | 2264.37(13) $Å^3$ | |
| Z | 2 | |
| Density (calculated) | 1.530 $Mg/m^3$ | |
| Absorption coefficient | 3.107 $mm^{-1}$ | |
| F(000) | 1050 | |
| Crystal size | 0.35 x 0.15 x 0.05 $mm^3$ | |
| Theta range for data collection | 3.20 to 28.40° | |
| Index ranges | –10<=h<=11, –20<=k<=20, –21<=l<=21 | |
| Reflections collected | 25449 | |
| Independent reflections | 9484 [R(int) = 0.0512] | |
| Completeness to theta = 28.40° | 83.5 % | |
| Refinement method | Full–matrix least–squares on $F^2$ | |
| Data / restraints / parameters | 9484 / 0 / 523 | |
| Goodness–of–fit on $F^2$ | 1.012 | |
| Final R indices [I>2sigma(I)] | R1 = 0.0405, wR2 = 0.0897 | |
| R indices (all data) | R1 = 0.0612, wR2 = 0.0925 | |
| Largest diff. peak and hole | 1.354 and –1.520 e.$Å^{-3}$ | |

**Table A–12. Crystal data and structure refinement for $[PPN]_3[Ru^{III}(CN)_6]$.**

| | | |
|---|---|---|
| Identification code | $[PPN]_3[Ru^{III}(CN)_6]$ | |
| Empirical formula | $C_{57}H_{45}N_{4.50}P_3Ru_{0.50}$ | |
| Formula weight | 936.42 | |
| Temperature | 100(2) K | |
| Wavelength | 0.71073 Å | |
| Crystal system | Orthorhombic | |
| Space group | *Pbcn* | |
| Unit cell dimensions | a = 24.009(3) Å | α = 90° |
| | b = 20.583(2) Å | β = 90° |
| | c = 19.4679(19) Å | γ = 90° |
| Volume | 9620.6(17) $Å^3$ | |
| Z | 8 | |
| Density (calculated) | 1.293 $Mg/m^3$ | |
| Absorption coefficient | 0.318 $mm^{-1}$ | |
| F(000) | 3884 | |
| Crystal size | 0.60 x 0.30 x 0.10 $mm^3$ | |
| Theta range for data collection | 1.67 to 20.83°. | |
| Index ranges | –24<=h<=22, –19<=k<=20, –19<=l<=19 | |
| Reflections collected | 32472 | |
| Independent reflections | 5047 [R(int) = 0.0894] | |
| Completeness to theta = 20.83° | 99.9 % | |
| Absorption correction | Sphere | |
| Refinement method | Full–matrix least–squares on $F^2$ | |
| Data / restraints / parameters | 5047 / 0 / 587 | |
| Goodness–of–fit on $F^2$ | 1.121 | |
| Final R indices [I>2sigma(I)] | R1 = 0.0462, wR2 = 0.1135 | |
| R indices (all data) | R1 = 0.0735, wR2 = 0.1246 | |
| Largest diff. peak and hole | 0.304 and –0.392 e.$Å^{-3}$ | |

**Table A–13. Crystal data and structure refinement for *trans*–$[PPN]_2[Ru^{II}(CN)_4(CO)_2]$.**

| | | |
|---|---|---|
| Identification code | *trans*–$[PPN]_2[Ru^{II}(CN)_4(CO)_2]$ | |
| Empirical formula | $C_{39}H_{30}N_3OP_2Ru_{0.50}$ | |
| Formula weight | 669.14 | |
| Temperature | 100(2) K | |
| Wavelength | 0.71073 Å | |
| Crystal system | Monoclinic | |
| Space group | $P2_1/c$ | |
| Unit cell dimensions | a = 12.9848(2) Å | α = 90° |
| | b = 13.21920(10) Å | β = 106.5600(10)° |
| | c = 19.8902(3) Å | γ = 90° |
| Volume | 3272.51(7) $Å^3$ | |
| Z | 4 | |
| Density (calculated) | 1.358 $Mg/m^3$ | |
| Absorption coefficient | 0.391 $mm^{-1}$ | |
| F(000) | 1380 | |
| Crystal size | 0.45 x 0.25 x 0.10 $mm^3$ | |
| Theta range for data collection | 3.26 to 32.97° | |
| Index ranges | –17<=h<=19, –20<=k<=12, –24<=l<=27 | |
| Reflections collected | 21196 | |
| Independent reflections | 10534 [R(int) = 0.0237] | |
| Completeness to theta = 32.97° | 85.6 % | |
| Absorption correction | Sphere | |
| Refinement method | Full–matrix least–squares on $F^2$ | |
| Data / restraints / parameters | 10534 / 0 / 412 | |
| Goodness–of–fit on $F^2$ | 0.939 | |
| Final R indices [I>2sigma(I)] | R1 = 0.0332, wR2 = 0.0836 | |
| R indices (all data) | R1 = 0.0578, wR2 = 0.0874 | |
| Largest diff. peak and hole | 0.482 and –0.537 $e.Å^{-3}$ | |

**Table A–14. Crystal data and structure refinement for *cis*–$[PPN]_2[Ru^{II}(CN)_4(CO)_2]$.**

| | | |
|---|---|---|
| Identification code | *cis*–$[PPN]_2[Ru^{II}(CN)_4(CO)_2]$ | |
| Empirical formula | $C_{78}H_{60}N_6O_2P_4Ru$ | |
| Formula weight | 1338.27 | |
| Temperature | 100(2) K | |
| Wavelength | 0.71073 Å | |
| Crystal system | Monoclinic | |
| Space group | $P2_1/c$ | |
| Unit cell dimensions | a = 25.0458(8) Å | α = 90° |
| | b = 13.0964(6) Å | β = 107.143(3)° |
| | c = 20.6277(5) Å | γ = 90° |
| Volume | 6465.5(4) $Å^3$ | |
| Z | 4 | |
| Density (calculated) | 1.375 $Mg/m^3$ | |
| Absorption coefficient | 0.396 $mm^{-1}$ | |
| F(000) | 2760 | |
| Crystal size | 0.35 x 0.25 x 0.20 $mm^3$ | |
| Theta range for data collection | 3.35 to 28.12° | |
| Index ranges | –32<=h<=16, –11<=k<=13, –27<=l<=21 | |
| Reflections collected | 10718 | |
| Independent reflections | 7515 [R(int) = 0.0180] | |
| Completeness to theta = 28.12° | 47.5 % | |
| Absorption correction | Sphere | |
| Refinement method | Full–matrix least–squares on $F^2$ | |
| Data / restraints / parameters | 7515 / 0 / 821 | |
| Goodness–of–fit on $F^2$ | 1.107 | |
| Final R indices [I>2sigma(I)] | R1 = 0.0557, wR2 = 0.1579 | |
| R indices (all data) | R1 = 0.0702, wR2 = 0.1620 | |
| Extinction coefficient | 0.00000(13) | |
| Largest diff. peak and hole | 0.652 and –0.400 $e.Å^{-3}$ | |

**Table A–15. Crystal data and structure refinement for *trans*–[PPN]$_2$[Ru$^{II}$(CN)$_4$(CO)(py)].**

| | | |
|---|---|---|
| Identification code | *trans*–[PPN]$_2$[Ru$^{II}$(CN)$_4$(CO)(py)] | |
| Empirical formula | $C_{82}H_{65}N_7OP_4Ru$ | |
| Formula weight | 1389.36 | |
| Temperature | 100(2) K | |
| Wavelength | 0.71073 Å | |
| Crystal system | Triclinic | |
| Space group | *P*–1 | |
| Unit cell dimensions | a = 13.7375(4) Å | α = 73.931(2)° |
| | b = 16.1926(5) Å | β = 71.636(2)° |
| | c = 17.1100(5) Å | γ = 71.625(3)° |
| Volume | 3360.84(17) Å$^3$ | |
| Z | 2 | |
| Density (calculated) | 1.373 Mg/m$^3$ | |
| Absorption coefficient | 0.383 mm$^{-1}$ | |
| F(000) | 1436 | |
| Crystal size | 0.45 x 0.30 x 0.15 mm$^3$ | |
| Theta range for data collection | 3.23 to 30.11° | |
| Index ranges | –16<=h<=19, –21<=k<=22, –23<=l<=23 | |
| Reflections collected | 33219 | |
| Independent reflections | 16991 [R(int) = 0.0177] | |
| Completeness to theta = 30.11° | 85.8 % | |
| Absorption correction | Sphere | |
| Refinement method | Full–matrix least–squares on F$^2$ | |
| Data / restraints / parameters | 16991 / 0 / 856 | |
| Goodness–of–fit on F$^2$ | 1.069 | |
| Final R indices [I>2sigma(I)] | R1 = 0.0311, wR2 = 0.0829 | |
| R indices (all data) | R1 = 0.0419, wR2 = 0.0856 | |
| Largest diff. peak and hole | 0.491 and –0.843 e.Å$^{-3}$ | |

**Table A–16. Crystal data and structure refinement for $[PPN]_3[Os^{III}(CN)_6]$.**

| | | |
|---|---|---|
| Identification code | $[PPN]_3[Os^{III}(CN)_6]$ | |
| Empirical formula | $C_{57}H_{45}N_{4.50}Os_{0.50}P_3$ | |
| Formula weight | 980.98 | |
| Temperature | 100(2) K | |
| Wavelength | 0.71073 Å | |
| Crystal system | Orthorhombic | |
| Space group | *Pbcn* | |
| Unit cell dimensions | a = 23.8163(2) Å | α = 90° |
| | b = 20.3376(2) Å | β = 90° |
| | c = 19.33450(10) Å | γ = 90° |
| Volume | 9364.98(13) $Å^3$ | |
| Z | 8 | |
| Density (calculated) | 1.392 $Mg/m^3$ | |
| Absorption coefficient | 1.521 $mm^{-1}$ | |
| F(000) | 4012 | |
| Crystal size | 0.65 x 0.45 x 0.10 $mm^3$ | |
| Theta range for data collection | 3.30 to 32.31° | |
| Index ranges | –35<=h<=35, –29<=k<=30, –28<=l<=28 | |
| Reflections collected | 188800 | |
| Independent reflections | 15982 [R(int) = 0.0494] | |
| Completeness to theta = 32.31° | 95.7 % | |
| Absorption correction | Sphere | |
| Refinement method | Full–matrix least–squares on $F^2$ | |
| Data / restraints / parameters | 15982 / 0 / 587 | |
| Goodness–of–fit on $F^2$ | 1.181 | |
| Final R indices [I>2sigma(I)] | R1 = 0.0424, wR2 = 0.0742 | |
| R indices (all data) | R1 = 0.0527, wR2 = 0.0767 | |
| Largest diff. peak and hole | 1.336 and –0.651 e.$Å^{-3}$ | |

**Table A–17. Crystal data and structure refinement for *fac*–[$Ru^{II}(CO)_3Cl_2(THF)$].**

| | | |
|---|---|---|
| Identification code | *fac*–[$Ru^{II}(CO)_3Cl_2(THF)$] | |
| Empirical formula | $C_7H_8Cl_2O_4Ru$ | |
| Formula weight | 328.10 | |
| Temperature | 100(2) K | |
| Wavelength | 0.71073 Å | |
| Crystal system | Monoclinic | |
| Space group | $P2_1/n$ | |
| Unit cell dimensions | a = 5.968(8) Å | α = 90° |
| | b = 18.200(3) Å | β = 96.891(1)° |
| | c = 9.787(1) Å | γ = 90°. |
| Volume | 1055.4(5) Å | |
| Z | 4 | |
| Density (calculated) | 2.065 $Mg/m^3$ | |
| Absorption coefficient | 1.975 $mm^{-1}$ | |
| F(000) | 640 | |
| Crystal size | 1.0 x 0.45 x 0.20 $mm^3$ | |
| Theta range for data collection | 3.62 to 32.84° | |
| Index ranges | –9<=h<=8, –27<=k<=26, –14<=l<=14 | |
| Reflections collected | 22141 | |
| Independent reflections | 3719 [R(int) = 0.0284] | |
| Completeness to theta = 32.84° | 94.9 % | |
| Refinement method | Full–matrix least–squares on $F^2$ | |
| Data / restraints / parameters | 3719 / 0 / 127 | |
| Goodness–of–fit on $F^2$ | 1.081 | |
| Final R indices [I>2sigma(I)] | R1 = 0.0181, wR2 = 0.0413 | |
| R indices (all data) | R1 = 0.0248, wR2 = 0.0424 | |
| Largest diff. peak and hole | 0.419 and –0.884 e.$Å^{-3}$ | |

**Table A–18. Crystal data and structure refinement for *fac*–[$Me_3NBz$][$Ru^{II}(CO)_3(tmbt)_3$].**

| | | |
|---|---|---|
| Identification code | *fac*–[$Me_3NBz$][$Ru^{II}(CO)_3(tmbt)_3$] | |
| Empirical formula | $C_{43}H_{55}NO_3RuS_3$ | |
| Formula weight | 831.13 | |
| Temperature | 100(2) K | |
| Wavelength | 0.71073 Å | |
| Crystal system | Triclinic | |
| Space group | *P*–1 | |
| Unit cell dimensions | a = 11.980(3) Å | α = 107.69(3)° |
| | b = 12.114(4) Å | β = 96.05(2)° |
| | c = 15.508(5) Å | γ = 103.60(3)° |
| Volume | 2045.7(3) $Å^3$ | |
| Z | 2 | |
| Density (calculated) | 1.349 $Mg/m^3$ | |
| Absorption coefficient | 0.575 $mm^{-1}$ | |
| F(000) | 872 | |
| Crystal size | 0.65 x 0.40 x 0.25 $mm^3$ | |
| Theta range for data collection | 3.30 to 30.79° | |
| Index ranges | –16<=h<=16, –16<=k<=17, –22<=l<=20 | |
| Reflections collected | 37555 | |
| Independent reflections | 11535 [R(int) = 0.0355] | |
| Completeness to theta = 30.79° | 90.0 % | |
| Refinement method | Full–matrix least–squares on $F^2$ | |
| Data / restraints / parameters | 11535 / 0 / 460 | |
| Goodness–of–fit on $F^2$ | 1.057 | |
| Final R indices [I>2sigma(I)] | R1 = 0.0393, wR2 = 0.1143 | |
| R indices (all data) | R1 = 0.0506, wR2 = 0.1196 | |
| Largest diff. peak and hole | 0.775 and –1.452 e.$Å^{-3}$ | |

**Table A–19. Crystal data and structure refinement for *fac*–[$Ru^{II}(CO)_3$(PS2')].**

| | | |
|---|---|---|
| Identification code | *fac*–[$Ru^{II}(CO)_3$(PS2')] | |
| Empirical formula | $C_{23}H_{17}O_3PRuS_2$ | |
| Formula weight | 537.53 | |
| Temperature | 100(2) K | |
| Wavelength | 0.71069 Å | |
| Crystal system | Monoclinic | |
| Space group | C2/*c* | |
| Unit cell dimensions | a = 27.821(5) Å | α = 90° |
| | b = 9.771(5) Å | β = 99.952(5)° |
| | c = 17.902(5) Å | γ = 90° |
| Volume | 4793(3) $Å^3$ | |
| Z | 8 | |
| Density (calculated) | 1.490 $Mg/m^3$ | |
| Absorption coefficient | 0.916 $mm^{-1}$ | |
| F(000) | 2160 | |
| Crystal size | 0.10 x 0.08 x 0.05 $mm^3$ | |
| Theta range for data collection | 3.40 to 28.02° | |
| Index ranges | –21<=h<=32, –11<=k<=9, –23<=l<=11 | |
| Reflections collected | 5887 | |
| Independent reflections | 3342 [R(int) = 0.0648] | |
| Completeness to theta = 28.02° | 57.7 % | |
| Refinement method | Full–matrix least–squares on $F^2$ | |
| Data / restraints / parameters | 3342 / 0 / 246 | |
| Goodness–of–fit on $F^2$ | 1.213 | |
| Final R indices [I>2sigma(I)] | R1 = 0.1073, wR2 = 0.2376 | |
| R indices (all data) | R1 = 0.1545, wR2 = 0.2479 | |
| Largest diff. peak and hole | 0.750 and –0.677 e.$Å^{-3}$ | |

**Table A–20. Crystal data and structure refinement for *fac*–[$Ru^{II}(CO)_3$(PS2)].**

| | | |
|---|---|---|
| Identification code | *fac*–[$Ru^{II}(CO)_3$(PS2)] | |
| Empirical formula | $C_{21}H_{13}O_3PRuS_2$ | |
| Formula weight | 509.47 | |
| Temperature | 100(2) K | |
| Wavelength | 0.71073 Å | |
| Crystal system | Triclinic | |
| Space group | *P*–1 | |
| Unit cell dimensions | a = 9.8294(13) Å | α = 90.132(11)° |
| | b = 10.3375(14) Å | β = 116.213(13)° |
| | c = 10.7609(15) Å | γ = 94.891(11)° |
| Volume | 976.4(2) $Å^3$ | |
| Z | 2 | |
| Density (calculated) | 1.733 $Mg/m^3$ | |
| Absorption coefficient | 1.119 $mm^{-1}$ | |
| F(000) | 508 | |
| Crystal size | 0.10 x 0.10 x 0.08 $mm^3$ | |
| Theta range for data collection | 3.15 to 25.18° | |
| Index ranges | –11<=h<=9, –11<=k<=11, –11<=l<=10 | |
| Reflections collected | 3229 | |
| Independent reflections | 2245 [R(int) = 0.0415] | |
| Completeness to theta = 25.18° | 63.9 % | |
| Refinement method | Full–matrix least–squares on $F^2$ | |
| Data / restraints / parameters | 2245 / 0 / 233 | |
| Goodness–of–fit on $F^2$ | 1.225 | |
| Final R indices [I>2sigma(I)] | R1 = 0.0753, wR2 = 0.2045 | |
| R indices (all data) | R1 = 0.0934, wR2 = 0.2099 | |
| Largest diff. peak and hole | 1.991 and –0.903 e.$Å^{-3}$ | |

**Table A–21. Crystal data and structure refinement for $[Ru^{II}(CO)_2(NS2')]_2$.**

| | | |
|---|---|---|
| Identification code | $[Ru^{II}(CO)_2(NS2')]_2$ | |
| Empirical formula | $C_{24}H_{19}NO_2RuS_2$ | |
| Formula weight | 518.59 | |
| Temperature | 100(2) K | |
| Wavelength | 0.71073 Å | |
| Crystal system | Monoclinic | |
| Space group | *C*2/*c* | |
| Unit cell dimensions | a = 26.2359(17) Å | α = 90° |
| | b = 8.5698(4) Å | β = 121.808(9)° |
| | c = 22.4842(14) Å | γ = 90° |
| Volume | 4296.1(4) $Å^3$ | |
| Z | 8 | |
| Density (calculated) | 1.604 $Mg/m^3$ | |
| Absorption coefficient | 0.945 $mm^{-1}$ | |
| F(000) | 2096 | |
| Crystal size | 0.45 x 0.35 x 0.30 $mm^3$ | |
| Theta range for data collection | 3.35 to 27.10° | |
| Index ranges | –33<=h<=27, –10<=k<=9, –24<=l<=28 | |
| Reflections collected | 8872 | |
| Independent reflections | 3809 [R(int) = 0.0546] | |
| Completeness to theta = 27.10° | 80.4 % | |
| Refinement method | Full–matrix least–squares on $F^2$ | |
| Data / restraints / parameters | 3809 / 0 / 271 | |
| Goodness–of–fit on $F^2$ | 0.748 | |
| Final R indices [I>2sigma(I)] | R1 = 0.0649, wR2 = 0.1789 | |
| R indices (all data) | R1 = 0.0982, wR2 = 0.2019 | |
| Largest diff. peak and hole | 3.023 and –1.093 e.$Å^{-3}$ | |

**Table A–22. Crystal data and structure refinement for $[Ru^{II}_3(CO)_5(PS2')_3]$.**

| | | |
|---|---|---|
| Identification code | $[Ru^{II}_3(CO)_5(PS2')_3]$ | |
| Empirical formula | $C_{65}H_{51}O_5P_3Ru_3S_6$ | |
| Formula weight | 1500.54 | |
| Temperature | 100(2) K | |
| Wavelength | 0.71073 Å | |
| Crystal system | Monoclinic | |
| Space group | $P2_1/c$ | |
| Unit cell dimensions | a = 24.7504(14) Å | α = 90° |
| | b = 14.2885(8) Å | β = 106.836(7)° |
| | c = 19.1832(15) Å | γ = 90° |
| Volume | 6493.3(7) $Å^3$ | |
| Z | 4 | |
| Density (calculated) | 1.535 $Mg/m^3$ | |
| Absorption coefficient | 1.003 $mm^{-1}$ | |
| F(000) | 3016 | |
| Crystal size | 0.45 x 0.40 x 0.15 $mm^3$ | |
| Theta range for data collection | 3.21 to 29.64° | |
| Index ranges | –31<=h<=32, –19<=k<=19, –23<=l<=26 | |
| Reflections collected | 38027 | |
| Independent reflections | 15431 [R(int) = 0.0452] | |
| Completeness to theta = 29.64° | 84.2 % | |
| Refinement method | Full–matrix least–squares on $F^2$ | |
| Data / restraints / parameters | 15431 / 0 / 739 | |
| Goodness–of–fit on $F^2$ | 1.182 | |
| Final R indices [I>2sigma(I)] | R1 = 0.0901, wR2 = 0.2170 | |
| R indices (all data) | R1 = 0.1144, wR2 = 0.2248 | |
| Largest diff. peak and hole | 2.413 and –2.368 e.$Å^{-3}$ | |

**Table A–23. Crystal data and structure refinement for $[Ru^{I}(CO)_3(Stip)]_2$.**

| | | |
|---|---|---|
| Identification code | $[Ru^{I}(CO)_3(Stip)]_2$ | |
| Empirical formula | $C_{36}H_{46}O_6Ru_2S_2$ | |
| Formula weight | 840.99 | |
| Temperature | 100(2) K | |
| Wavelength | 0.71073 Å | |
| Crystal system | Monoclinic | |
| Space group | $P2_1/c$ | |
| Unit cell dimensions | a = 13.4896(3) Å | α = 90° |
| | b = 27.6084(6) Å | β = 110.167(2)° |
| | c = 10.7129(2) Å | γ = 90° |
| Volume | 3745.18(14) $Å^3$ | |
| Z | 4 | |
| Density (calculated) | 1.492 $Mg/m^3$ | |
| Absorption coefficient | 0.959 $mm^{-1}$ | |
| F(000) | 1720 | |
| Crystal size | 0.30 x 0.30 x 0.20 $mm^3$ | |
| Theta range for data collection | 3.22 to 29.50° | |
| Index ranges | –16<=h<=17, –36<=k<=34, –13<=l<=13 | |
| Reflections collected | 34846 | |
| Independent reflections | 9279 [R(int) = 0.0399] | |
| Completeness to theta = 29.50° | 88.9 % | |
| Absorption correction | Sphere | |
| Refinement method | Full–matrix least–squares on $F^2$ | |
| Data / restraints / parameters | 9279 / 0 / 415 | |
| Goodness–of–fit on $F^2$ | 0.863 | |
| Final R indices [I>2sigma(I)] | R1 = 0.0275, wR2 = 0.0481 | |
| R indices (all data) | R1 = 0.0528, wR2 = 0.0504 | |
| Largest diff. peak and hole | 0.957 and –0.456 e.$Å^{-3}$ | |

**Table A–24. Crystal data and structure refinement for $Ni^{II}$(S4).**

| | | |
|---|---|---|
| Identification code | $Ni^{II}$(S4) | |
| Empirical formula | $C_7H_{14}NiS_4$ | |
| Formula weight | 285.13 | |
| Temperature | 100(2) K | |
| Wavelength | 0.71073 Å | |
| Crystal system | Monoclinic | |
| Space group | $P2_1/c$ | |
| Unit cell dimensions | a = 9.3839(3) Å | α = 90° |
| | b = 8.5363(2) Å | β = 92.032(3)° |
| | c = 13.5316(4) Å | γ = 90° |
| Volume | 1083.25(5) $Å^3$ | |
| Z | 4 | |
| Density (calculated) | 1.748 $Mg/m^3$ | |
| Absorption coefficient | 2.506 $mm^{-1}$ | |
| F(000) | 592 | |
| Crystal size | 0.50 x 0.35 x 0.15 $mm^3$ | |
| Theta range for data collection | 3.23 to 29.57° | |
| Index ranges | –12<=h<=10, –10<=k<=11, –18<=l<=17 | |
| Reflections collected | 8455 | |
| Independent reflections | 2680 [R(int) = 0.0253] | |
| Completeness to theta = 29.58° | 88.2 % | |
| Absorption correction | Sphere | |
| Refinement method | Full–matrix least–squares on $F^2$ | |
| Data / restraints / parameters | 2680 / 0 / 109 | |
| Goodness–of–fit on $F^2$ | 0.938 | |
| Final R indices [I>2sigma(I)] | R1 = 0.0211, wR2 = 0.0443 | |
| R indices (all data) | R1 = 0.0307, wR2 = 0.0457 | |
| Largest diff. peak and hole | 0.385 and –0.322 e.$Å^{-3}$ | |

**Table A–25. Crystal data and structure refinement for $Ni^{II}(dppe)Cl_2 \cdot CH_2Cl_2$.**

| | | |
|---|---|---|
| Identification code | $Ni^{II}(dppe)Cl_2 \cdot CH_2Cl_2$ | |
| Empirical formula | $C_{27}H_{26}Cl_4NiP_2$ | |
| Formula weight | 612.93 | |
| Temperature | 100(2) K | |
| Wavelength | 0.71073 Å | |
| Crystal system | Monoclinic | |
| Space group | $P2_1/c$ | |
| Unit cell dimensions | a = 12.1826(2) Å | α = 90° |
| | b = 15.2299(3) Å | β = 105.666(2)° |
| | c = 15.1924(3) Å | γ = 90° |
| Volume | 2714.08(9) $Å^3$ | |
| Z | 4 | |
| Density (calculated) | 1.500 $Mg/m^3$ | |
| Absorption coefficient | 1.242 $mm^{-1}$ | |
| F(000) | 1256 | |
| Crystal size | 0.80 x 0.50 x 0.50 $mm^3$ | |
| Theta range for data collection | 3.19 to 29.48° | |
| Index ranges | –16<=h<=12, –20<=k<=20, –20<=l<=20 | |
| Reflections collected | 15000 | |
| Independent reflections | 6474 [R(int) = 0.0187] | |
| Completeness to theta = 29.48° | 85.9 % | |
| Absorption correction | Sphere | |
| Refinement method | Full–matrix least–squares on $F^2$ | |
| Data / restraints / parameters | 6474 / 0 / 307 | |
| Goodness–of–fit on $F^2$ | 1.076 | |
| Final R indices [I>2sigma(I)] | R1 = 0.0306, wR2 = 0.0769 | |
| R indices (all data) | R1 = 0.0408, wR2 = 0.0793 | |
| Largest diff. peak and hole | 0.724 and –0.873 e.$Å^{-3}$ | |

**Table A–26. Crystal data and structure refinement for *trans,cis*–[$Fe^{II}(CN)_2(CO)_2Ni^{II}(S4)$].**

| | | |
|---|---|---|
| Identification code | *trans,cis*–[$Fe^{II}(CN)_2(CO)_2Ni^{II}(S4)$] | |
| Empirical formula | $C_{12}H_{14}FeN_2NiO_2S_4$ | |
| Formula weight | 461.05 | |
| Temperature | 100(2) K | |
| Wavelength | 0.71073 Å | |
| Crystal system | Triclinic | |
| Space group | *P*–1 | |
| Unit cell dimensions | a = 7.8344(5) Å | α = 76.188(5)° |
| | b = 10.2131(6) Å | β = 78.263(5)° |
| | c = 13.0208(8) Å | γ = 73.029(5)° |
| Volume | 957.57(10) $Å^3$ | |
| Z | 2 | |
| Density (calculated) | 1.599 $Mg/m^3$ | |
| Absorption coefficient | 2.180 $mm^{-1}$ | |
| F(000) | 468 | |
| Crystal size | 0.20 x 0.15 x 0.15 $mm^3$ | |
| Theta range for data collection | 2.91 to 29.58° | |
| Index ranges | –10<=h<=10, –14<=k<=13, –17<=l<=18 | |
| Reflections collected | 30818 | |
| Independent reflections | 4976 [R(int) = 0.1194] | |
| Completeness to theta = 29.58° | 92.7 % | |
| Absorption correction | Sphere | |
| Refinement method | Full–matrix least–squares on $F^2$ | |
| Data / restraints / parameters | 4976 / 0 / 194 | |
| Goodness–of–fit on $F^2$ | 0.544 | |
| Final R indices [I>2sigma(I)] | R1 = 0.0499, wR2 = 0.1480 | |
| R indices (all data) | R1 = 0.1161, wR2 = 0.1833 | |
| Largest diff. peak and hole | 0.582 and –0.723 e.$Å^{-3}$ | |

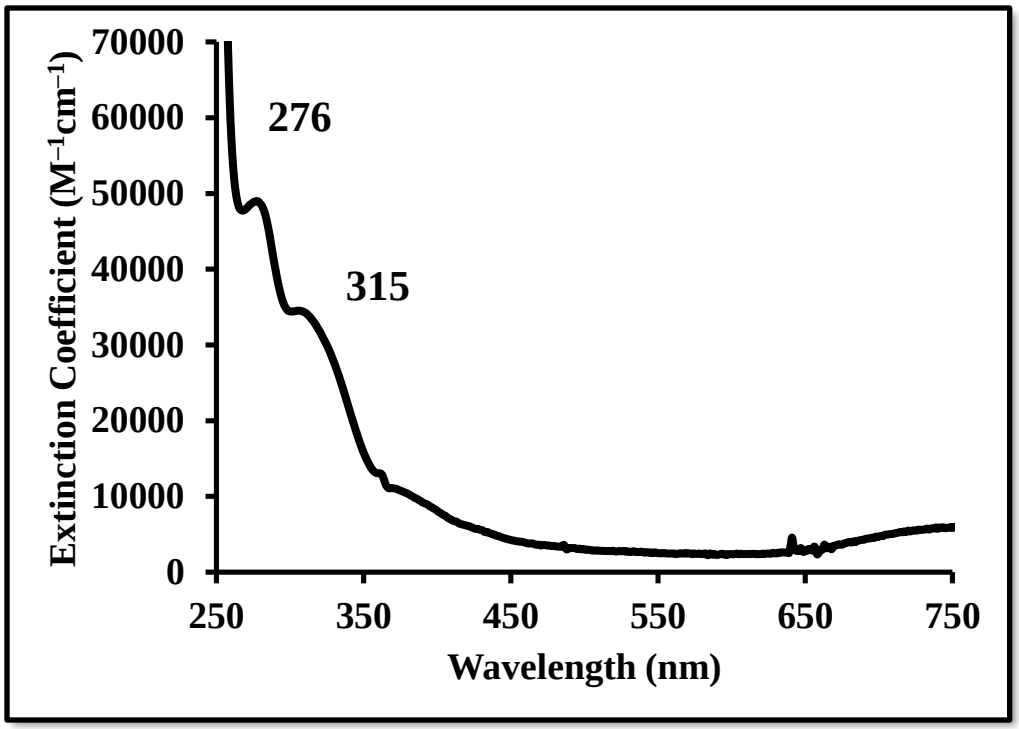


**Figure B–1. UV–Vis Spectrum of *trans*–[*n*–$Pr_4N$][$Ru^{III}(PS2)_2$] in DMF.**

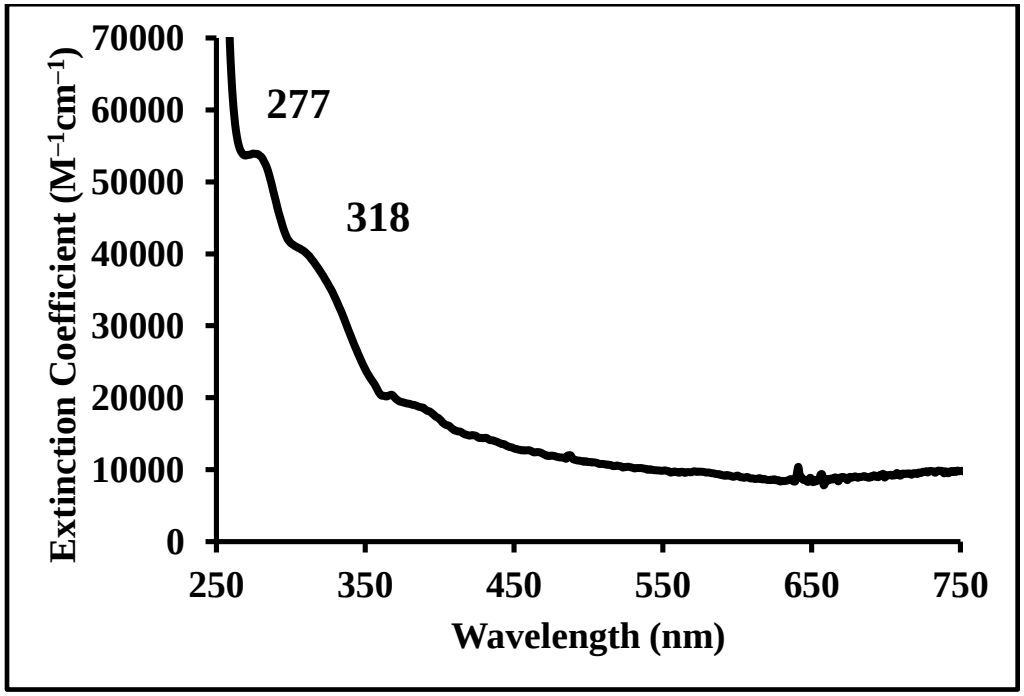


**Figure B–2. UV–Vis Spectrum of *trans*–[$Et_4N$][$Ru^{III}(PS2')_2$] in DMF.**

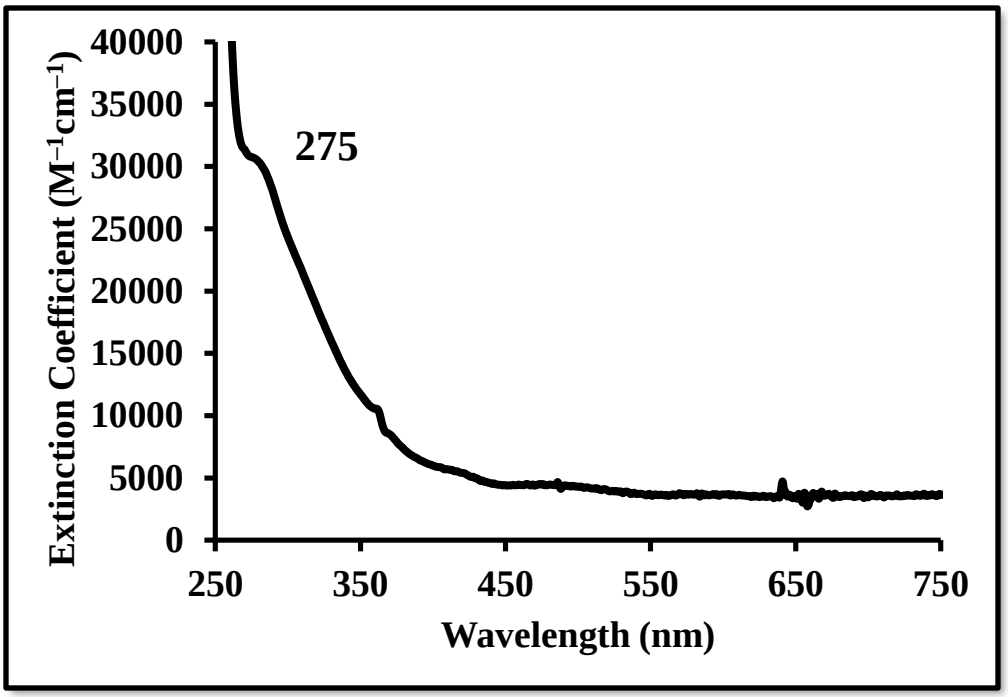


**Figure B–3. UV–Vis Spectrum of *trans*–[$Me_3NBz$][$Os^{III}(PS2)_2$] in DMF.**

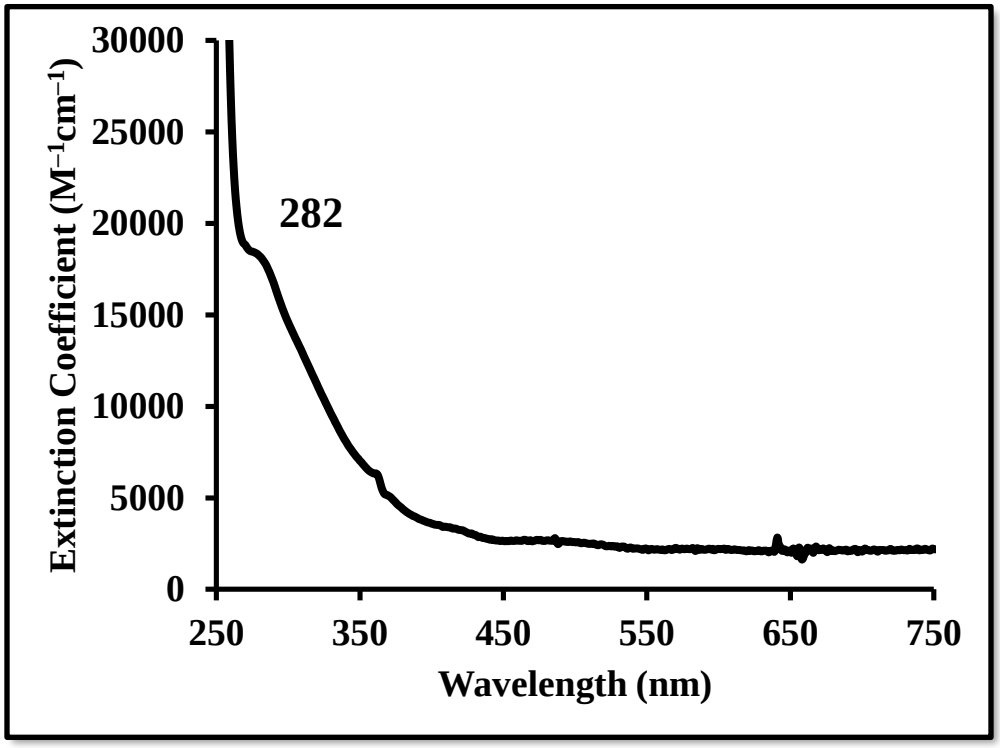


**Figure B–4. UV–Vis Spectrum of *cis*–[$Me_3NBz$][$Os^{III}(PS2')_2$] in DMF.**

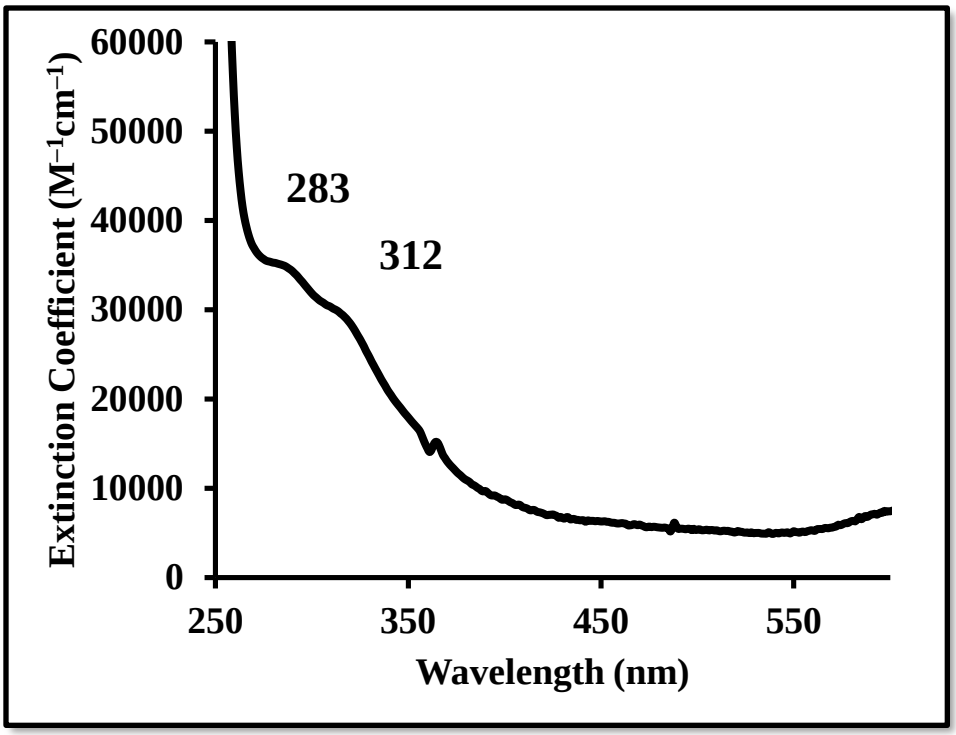


**Figure B–5. UV–Vis Spectrum of *trans*–[*n*–$Pr_4N$][$Ru^{III}(NS2)_2$] in DMF.**

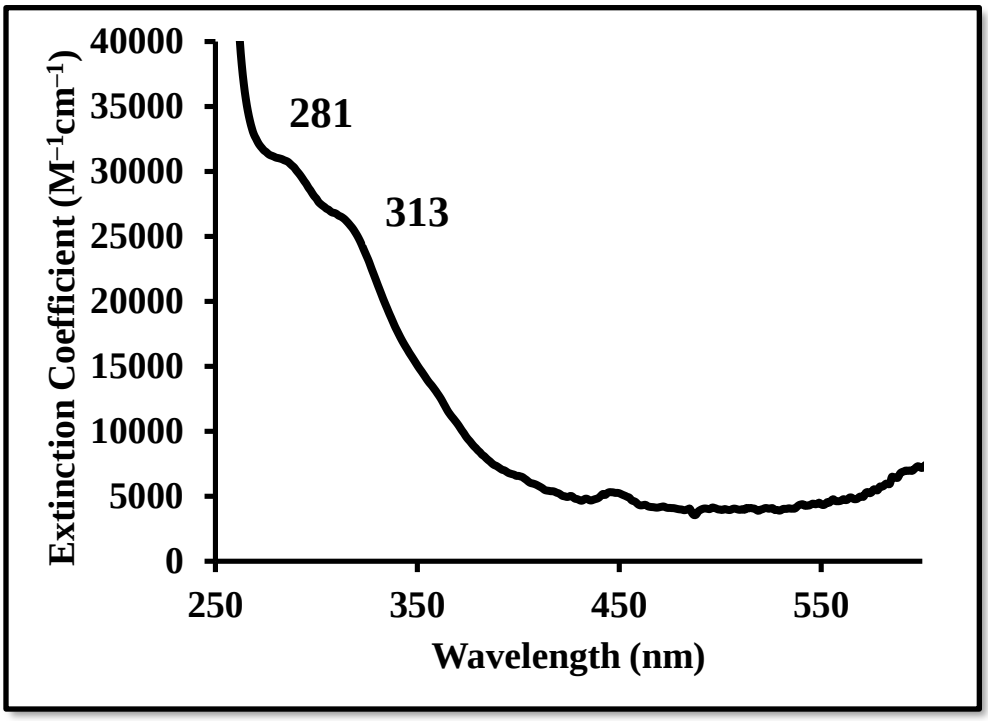


**Figure B–6. UV–Vis Spectrum of *trans*–[*n*–$Pr_4N$][$Ru^{III}(NS2')_2$] in DMF.**

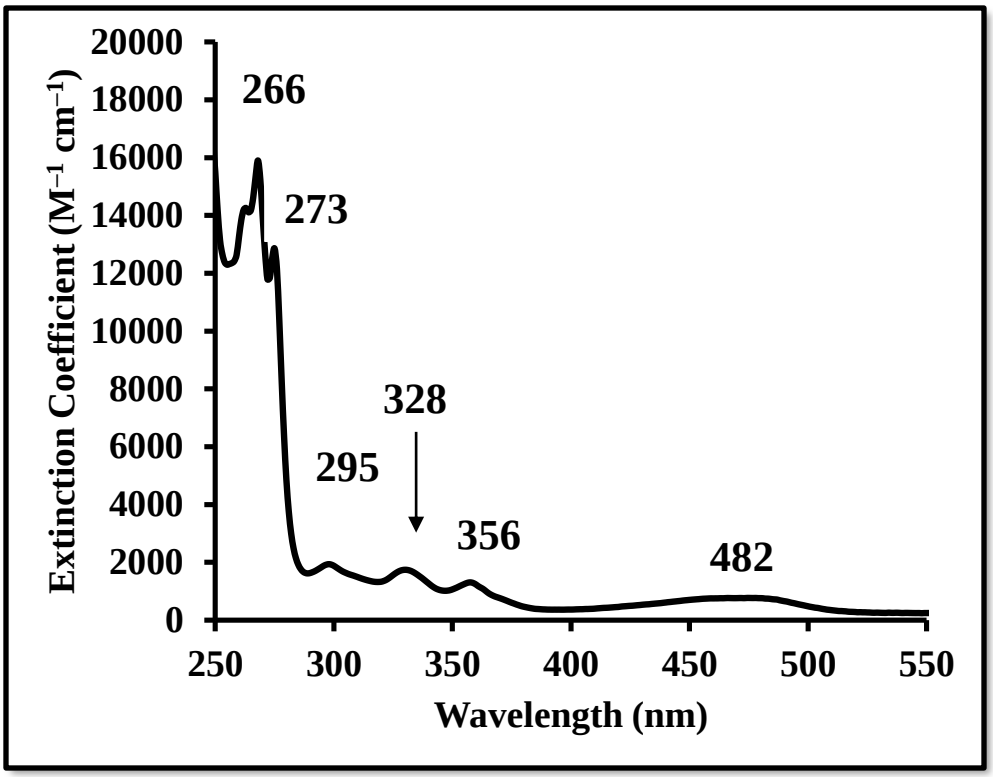


**Figure B–7. UV–Vis Spectrum of $[PPN]_4[Ru^{II}(CN)_6]$ in $CH_3CN$.**

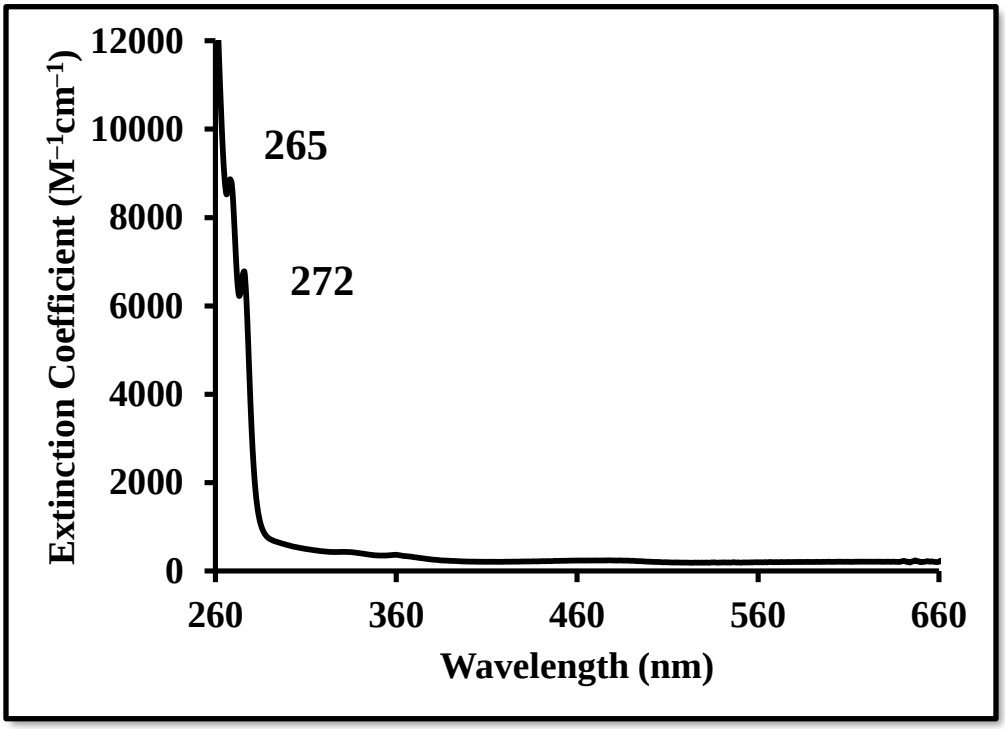


**Figure B–8. UV–Vis Spectrum of $[PPN]_3[Ru^{II}(CN)_5(CO)]$ in $CH_3CN$.**

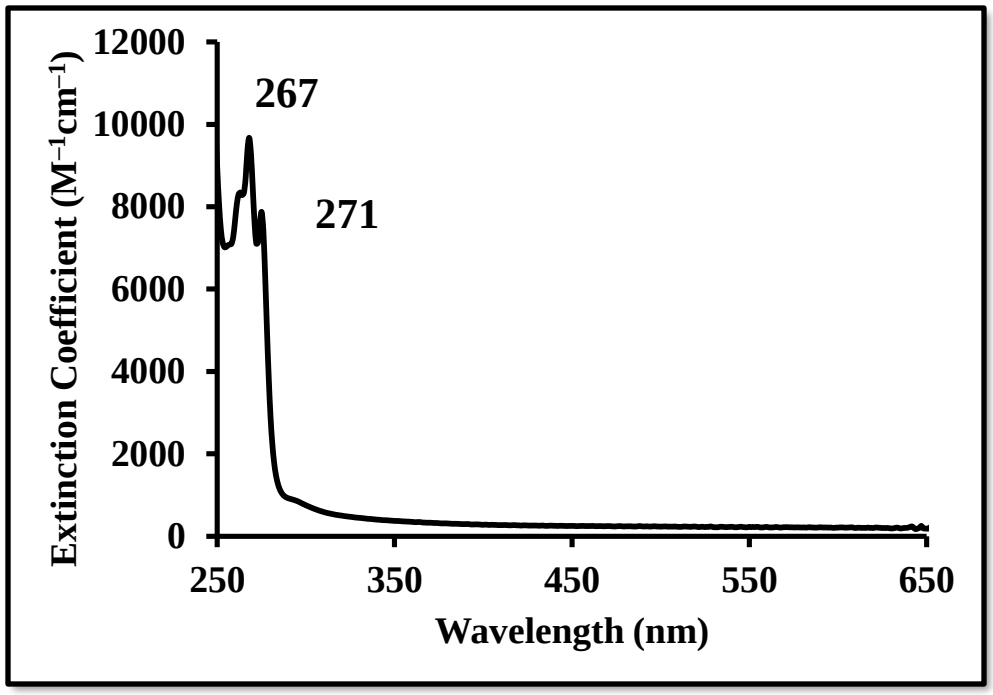


**Figure B–9. UV–Vis Spectrum of *trans*–$[PPN]_2[Ru^{II}(CN)_4(CO)_2]$ in $CH_3CN$.**

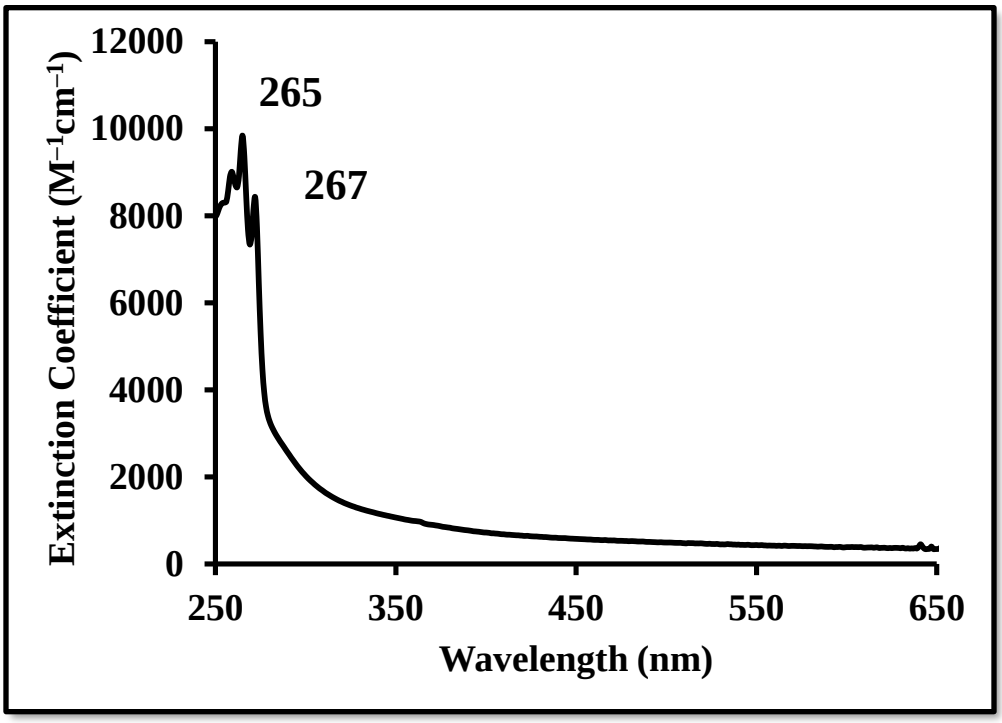


**Figure B–10. UV–Vis Spectrum of *cis*–$[PPN]_2[Ru^{II}(CN)_4(CO)_2]$ in $CH_3CN$.**

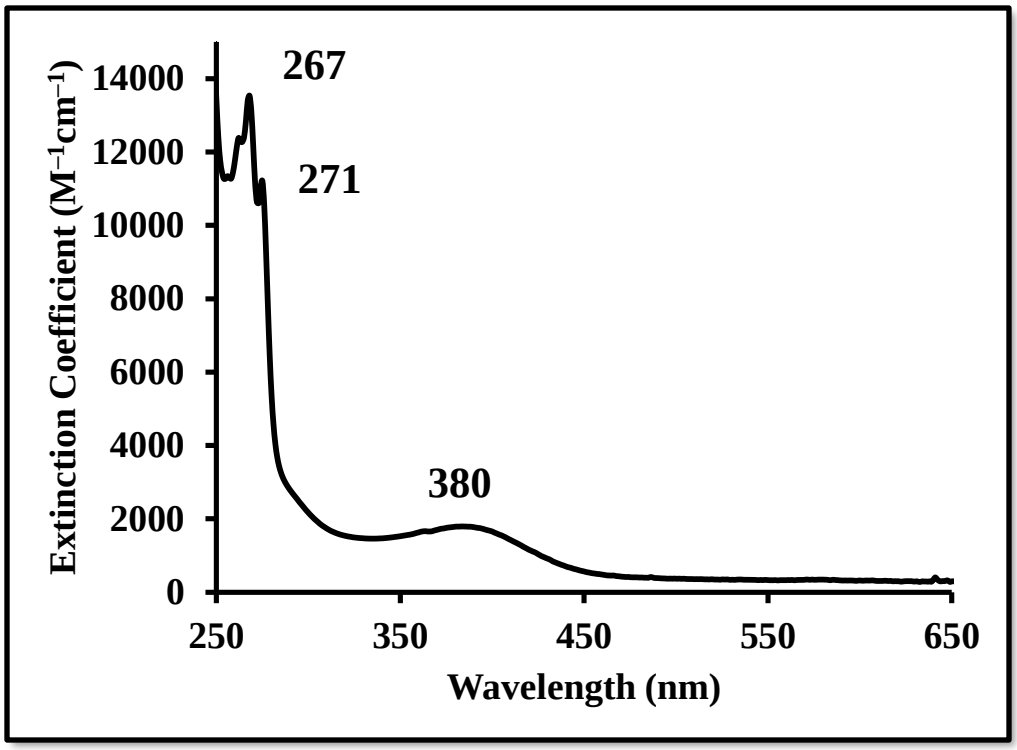


**Figure B–11. UV–Vis spectrum of *trans*–$[PPN]_2[Ru^{II}(CN)_4(CO)(py)]$ in $CH_3CN$.**

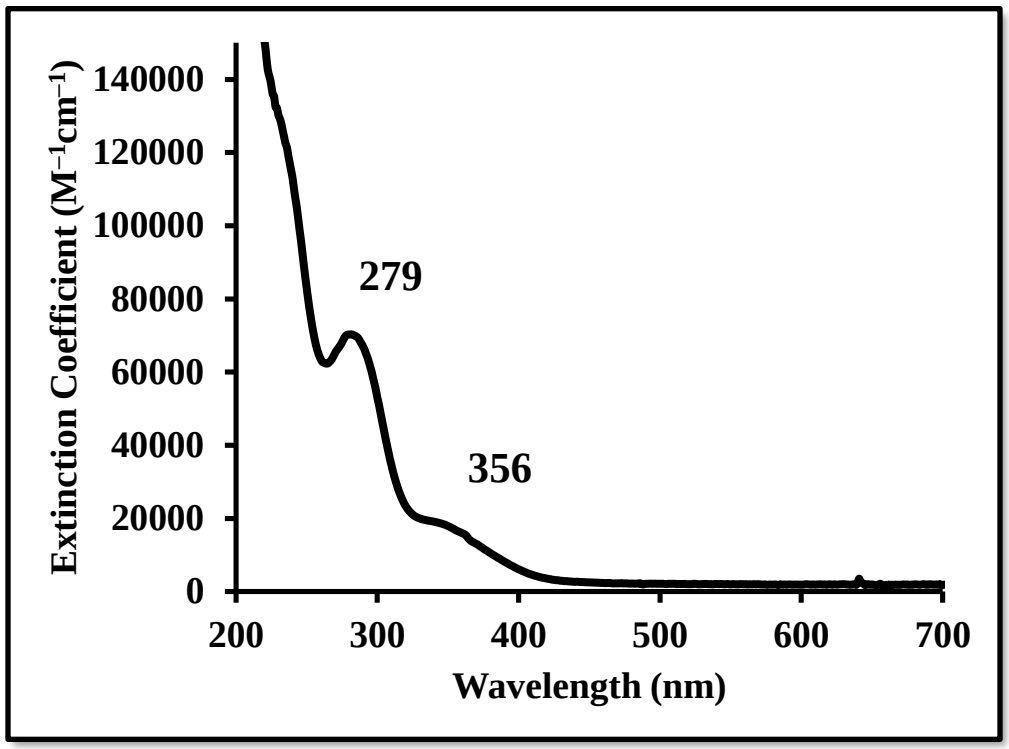


**Figure B–12. UV–Vis Spectrum of *fac*–$[Ru^{II}(CO)_3(PS2)]$ in DMF.**

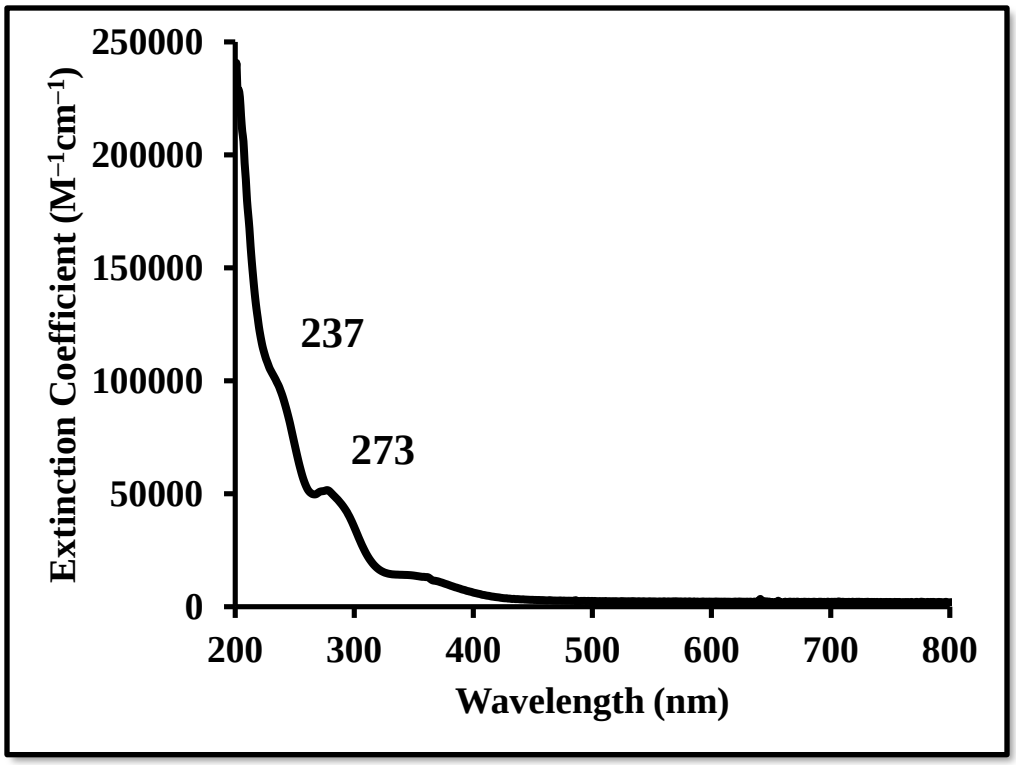


**Figure B–13. UV–Vis Spectrum of *fac*–[$Ru^{II}(CO)_3$(PS2′)] in DMF.**

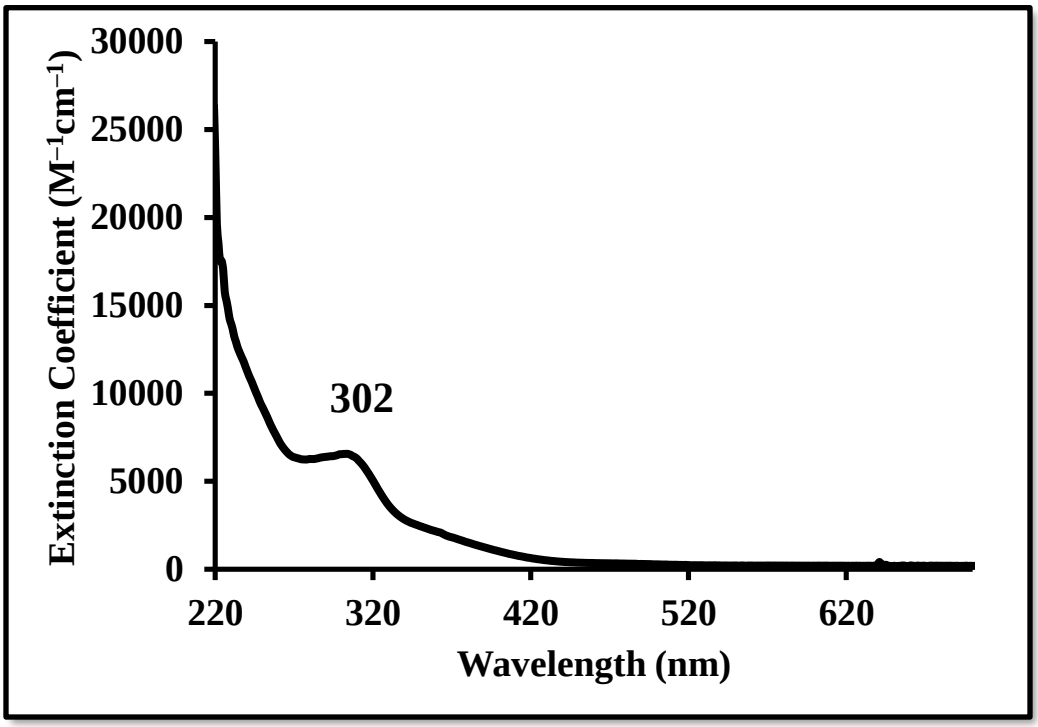


**Figure B–14. UV–Vis Spectrum of [$Ru^{II}_3(CO)_5$(PS2′)$_3$] in DMF.**

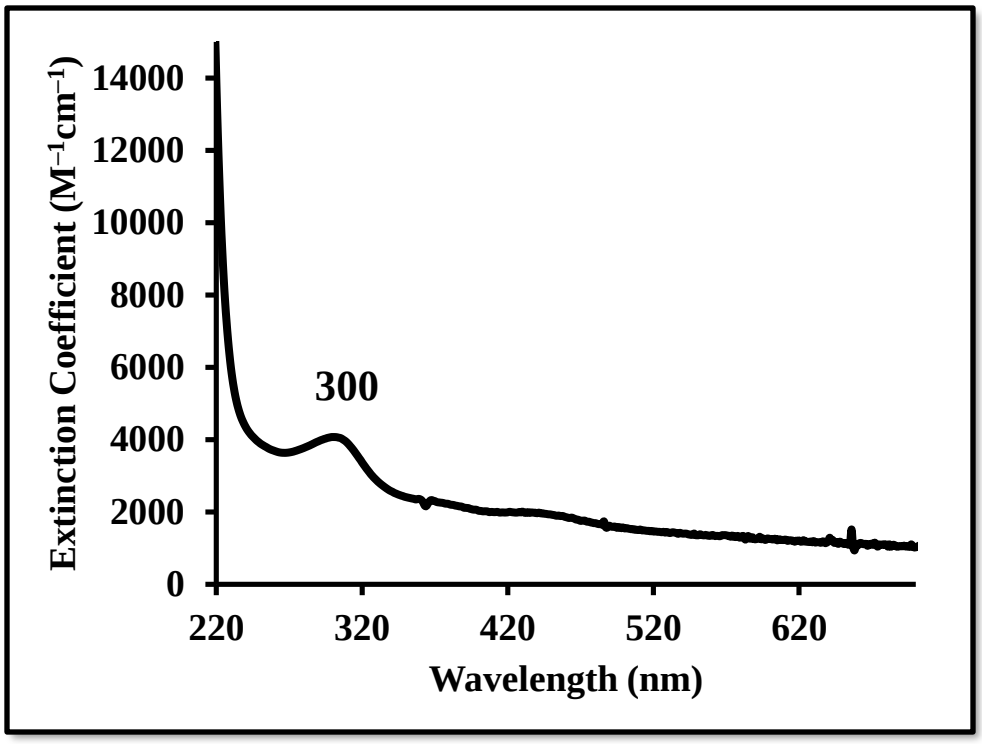


**Figure B–15. UV–Vis Spectrum of $[Ru^{II}(CO)_2(NS2')]_2$ in DMF.**